UNCLASSIFIED

AD NUMBER
AD382136

CLASSIFICATION CHANGES

TO: **unclassified**

FROM: **confidential**

LIMITATION CHANGES

TO:

Approved for public release, distribution unlimited

FROM:

Distribution authorized to U.S. Gov't. agencies and their contractors; Critical Technology; JUN 1967. Other requests shall be referred to Air Force Rocket Propulsion Laboratory, Attn: RPPR-STINFO, Edwards AFB, CA 93523.

AUTHORITY

30 Jun 1979, per document marking, DoDD 5200.10; AFRPL ltr, 3 Jan 1986

THIS PAGE IS UNCLASSIFIED

AD 382 136

AUTHORITY:

AFAPL
ltr 3 JAN 86

SECURITY

MARKING

The classified or limited status of this report applies
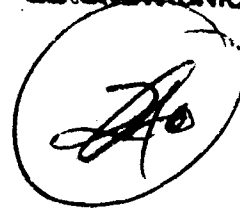
to each page, unless otherwise marked.

Separate page printouts MUST be marked accordingly.

CONFIDENTIAL

AFRPL-TR-67-82

(UNCLASSIFIED TITLE)

BERYLLIUM EROSION CORROSION INVESTIGATION FOR SOLID ROCKET NOZZLES

Final Report

W. L. Smallwood, et al.

Space and Re-entry Systems
Division of Philco-Ford Corporation
Newport Beach Operations

TECHNICAL REPORT AFRPL-TR-67-82

June 1967

AD382136

Air Force Rocket Propulsion Laboratory
Research and Technology Division
Air Force Systems Command
Edwards Air Force Base, California

CONFIDENTIAL

Qualified requestors may obtain copies of this report from DDC.

CONFIDENTIAL

Secondary Publication No. CG-3969

(UNCLASSIFIED TITLE)
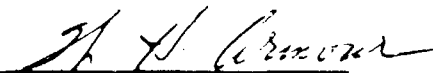
BERYLLIUM EROSION CORROSION INVESTIGATION FOR SOLID ROCKET NOZZLES

Final Report

W. L. Smallwood, et al.
Space and Re-entry Systems
Division of Philco-Ford Corporation
Newport Beach Operations

In addition to security requirements which must be met, this document is subject to special export controls and each transmittal to foreign governments or foreign nationals may be made only with prior approval of AFRPL (RPPR-STINFO), Edwards, California 93523

Classification Reviewed by _W. H. Armour_

W. H. Armour, Supervisor
Advanced Propulsion
Technology Section,
Mechanical Engineering Department

for homogeneous and inhomogeneous conditions resp. For system analysis instead of $\Delta\lambda$, describing a rectangular wavelength band only, the spectral responsivity $\mathcal{R}_\lambda$ of the receiver has to be included as another factor in the integral. The integrals are equivalent to broad band radiant fluxes, given in W.

If an average extinction coefficient $\overline{\sigma_{\lambda, \Delta\lambda}}$ for the wavelength band under consideration is used to calculate the transmission by Eq. (5), i.e. the exponential law, instead of Eq. (9), i.e. the correct integration, the calculated transmission values for short ranges would be higher than the actual ones. That for long ranges would be lower. Physically this results simply because at the beginning of the transmission range the radiation at wavelengths with high σ_λ is attenuated much more than that with low σ_λ. Therefore the spectral content of the radiation is changing along the transmission range, so that wavelengths with low σ_λ are dominating more and more. These results for long range transmission in an overall extinction law flater than an exponential one.

For wavelength bands comparable with atmospheric windows, see section 2.4.1 and 2.5 (Fig.2 and 3), the extinction coefficient for the dominating wavelengths after transmission ranges between some 100 m and 1 km is more or less wavelength independent. Therefore the exponential extinction law can be used for long range window transmission, including a correction term, as a good approximation. This is very helpful for system analysis because of the simple handling of exponential relations and these ranges R > 1 km, quite comparable with operational ranges sensitive to atmospheric limitations.

2.3 Atmospheric Absorption and Scattering

With respect to absorption, it may be mentioned only, that it is defined as the transfer of radiant energy to other kinds of energy, caused by interaction between radiation and matter. The absorption coefficient α, as introduced by Eq. (6) is related to the complex index of refraction $m = n - ix$, suitable to describe absorbing matter, by

$$\alpha = \frac{R_a}{R} \frac{4\pi x}{\lambda} , \qquad (11)$$

with R_a = interaction pathlength, R = macroscopical transmission range. Absorption was indicated in Fig.2 of lecture 1 by $\longrightarrow$o. Absorption effects of atmospheric constituents will be discussed in section 2.4.

More general comments are necessary on scattering, i.e. within this context the deflection of radiation from its original direction, if striking a surface or propagating through a medium. It is described by the volume scattering function

$$\beta(\varphi) = \frac{dI(\varphi)}{E \, dV} , \qquad (12)$$

given in $sr^{-1} m^{-1}$ with $I(\varphi)$ = radiant intensity in $W sr^{-1}$ for a certain angle φ with respect to the original direction, E = irradiance in Wm^{-2} of the volume element dV in m^3, see Fig.1. The scattering coefficient β, covering all losses by scattering, follows by integration:

$$\beta = 2\pi \int_0^{180} \beta(\varphi) \sin\varphi \, d\varphi , \qquad (13)$$

FOREWORD

UNCLASSIFIED ABSTRACT

Contract AF 04(611)-10753 was conducted over the period June 1965 to
March 1967. The program was directed toward understanding erosion-corrosion
mechanisms of nozzle heat sink and insulation materials in state-of-the-art
beryllium solid propellant exhausts. The major task was the design, fabri-
cation, and evaluation of the results of the 29 motor tests. Primary design
variables included propellant, grain design, motor configuration, nozzle
contour, materials and nozzle scale. Four beryllium propellants were tested
in 5 designs (100 and 500 pound grains) in 25 tests. Aluminum analogs were
used in 4 tests. Submerged, conventional and steep inlet nozzles were
designed to exceed 5000°F with pyrolytic graphite, ATJ graphite, dense
tungsten, carbon cloth and asbestos phenolic materials. The hardware, wall
deposits and exhaust plume particles are described. Measured nozzle temp-
eratures and ballistic performance were used to determine throat tempera-
ture, corrosion and oxide deposition histories. Design parameter effects
on nozzle and ballistic performance and material failure mechanisms are
discussed. Supporting chemical reaction, arc plasma, cold flow modeling,
data correlation and analytical studies are described. A generalized
model for nozzle design and performance evaluation is presented. The
model includes improved heat transfer, corrosion and deposition analyses.
Standard materials can be used with either beryllium or aluminum propellants
in properly designed motors. Poor nozzle and ballistic performance relates
to incomplete metal combustion and inadequate thermostructural design.
Oxide deposits are thermally and chemically protective. Most of the con-
clusions and recommendations pertain as well to liquid, hybrid and other
solid systems.

(THIS PAGE INTENTIONALLY LEFT BLANK)

iv

CONTENTS

CONTENTS (Continued)

ILLUSTRATIONS

ILLUSTRATIONS (Continued)

ILLUDSTRATIONS (Continued)

ILLUSTRATIONS (Continued)

ILLUSTRATIONS (Continued)

xi

ILLUSTRATIONS (Continued)

ILLUSTRATIONS (Continued)

ILLUSTRATIONS (Continued)

ILLUSTRATIONS (Continued)

ILLUSTRATIONS (Continued)

ILLUSTRATIONS (Continued)

ILLUSTRATIONS (Continued)

ILLUSTRATIONS (Continued)

TABLES

TABLES (Continued)

(THIS PAGE INTENTIONALLY LEFT BLANK)

SECTION I (C)

INTRODUCTION

1.1 (U) REPORT OBJECTIVES AND SCOPE

This is the Final Report for Contract AF 04(611)-10753, "Berylium Erosion Corrosion Investigation for Solid Rocket Nozzles." The technical program was conducted over the period 1 June 1965 to 17 March 1967. During this period, a series of four technical progress reports were issued. These reports, References 1 through 4, provide thorough coverage of all of the program technical results. In total, there are 500 figures, 108 tables and over 500 pages of text. The volume and complexity of these reports inhibits information transfer to the reader with general interests. Consequently, the primary objectives of the Final Report are to:

(1) Provide a concise summary of the program results, conclusions and recommendations.

(2) Provide a guide and index to more detailed derivations and discussions of the program results contained in the Technical Progress Reports.

(3) Group some of the more interesting motor test data in appendices for easy reference and comparison.

(4) Discuss the projection of program results and philosophy to future solid and non-solid chemical propulsion systems.

-1-

The remainder of Section I briefly describes the program objectives, scope and technical approach. A summary of the program results and conclusions is given in Section II. Section III describes the design and results of the 29 program motor tests and summarizes the results of the supporting laboratory and data correlation studies. Section IV presents a generalized nozzle design and performance analysis technique. Conclusions and recommendations are presented in Sections V and VI, respectively.

1.2 (C) BACKGROUND

During the past decade, the development of solid propellants containing beryllium metal has been stimulated by a potential gain of about 10% in specific impulse relative to comparable aluminum systems. High performance beryllium propellants were under consideration for application in future upper stage solid motors. During early development, three major technical problems were associated with the beryllium systems. Thus, the toxic beryllium compounds automatically posed fabrication, testing hazard and atmospheric pollution problems. Secondly, delivered performance did not meet the theroetical expectations. Finally, materials erosion problems were considerably more severe than initially estimated. It was evident that materials performance could not be entirely controlled by application of the design technology developed for aluminum propellant systems.

At the present time, delivered performance efficiencies, comparable to or better than aluminum systems, have been demonstrated by intermediate and advanced beryllium propellants. This report describes the results of a program directed toward understanding nozzle design problems with beryllium propellants. It follows that, with the control of the motor/nozzle performance problems, beryllium propellants can be selected for use in upper stage motors as originally planned. However, economic penalties are associated with the use of beryllium and the control of the toxic hazards. The greatest payoff, then, would be associated with high performance, weight or volume limited systems. In such systems, there appears to be no technical reason why advanced aluminum propellant candidates could not be replaced by higher performance beryllium analogs.

1.3 (U) PROGRAM OBJECTIVES

The overall objectives of this research and development program were:

> (1) To provide an understanding of the mechanisms
>   of erosion and corrosion with beryllium
>   propellants.

> (2) To determine what nozzle materials and designs
>   can be used with beryllium propellants.

-2-

(3) To successfully demonstrate the performance
     of a test weight nozzle system with a beryllium
     propellant.

1.4 (C) PROGRAM SCOPE

The following limitations and restrictions were placed on the scope of the
investigation:

(1) (C) This program was to involve:

(a) (U) Analyses, laboratory test and rocket
          motor test firings to determine the
          mechanisms of surface regression with
          beryllium propellants.

(b) (U) Correlation of available motor test
          firing data.

(c) (U) Design, fabrication and testing of
          nozzles to demonstrate a test weight
          design for use with beryllium pro-
          pellants. The design was to be readily
          capable of redesign without conceptual
          changes to a lightweight design.

(d) (U) The application of tungsten, graphite,
          carbon or reinforced plastics as
          materials in nozzle design.

(e) (U) The generation of technology appli-
          cable to both conventional and sub-
          merged convergent-divergent nozzle
          configuration, with demonstration
          of only one design.

(f) (C) Testing of hardware with four dif-
          ferent propellant compositions in
          the 280-285 theoretical specific
          impulse range.

(g) (U) Consideration of both composite and
          nitroplasticized double-based pro-
          pellant compositions.

(2) (U) The program was not to include cooled
          nozzle designs. Ablative-plastics and
          impregnated tungsten were not defined as
          cooled materials.

-3-

(3) (U) It was required that the laboratory study
and motor testing phases of the contract
be supported by an effective industrial
hygiene program.

1.5 (C) PROGRAM TECHNICAL APPROACH

a. (U) Phases of Work

The program was segmented into a series of six technical phases defined
as follows:

(1) Phase I - Theoretical Analysis and Studies:

(a) Analyses were performed to determine the
exhaust composition, ballistic performance,
particle flow mechanics, propellant grain
configuration effects, heat transfer and
corrosion.

(b) Thermal and structural analyses were pro-
vided in support of motor/nozzle design
and testing.

(c) Heat transfer analysis techniques were
developed to include the effects of depo-
sition. Nozzles tested under Phases III
and V were instrumented in support of this
effort.

(2) Phase II - Laboratory Studies

(a) The chemical reactivity of nozzle materials
with concensed species unique to beryllium
propellants were studied.

(b) Particle impaction and deposition effects
were studied using cold flow modeling and
arc plasma techniques.

(c) Post-test analyses of the hardware, con-
densed phase deposits and exhaust plume
particle samples were conducted to character-
ize motor performance and material failure
modes.

(3) Phase III - Small Scale Rocket Motor Testing

    (a) A series of eight tests were conducted to provide a direct comparison between aluminum and beryllium propellants of similar compositions.

    (b) A series of seventeen tests were conducted to determine beryllia deposition, impaction, grain configuration effects and specific corrosion data with beryllium propellants.

    (c) All tests in this phase were conducted with the following conditions:

        Throat Diameter: 1 to 1-1/4 inch
        Chamber Pressure: 800 psia (nominal)
        Test Duration: 20 seconds (nominal)

(4) Phase IV - Comparative Analysis

    (a) A comparative analysis of all nozzle test firing data accumulated in this program and from the available information from other beryllium motor programs was performed. The data were compared with similar aluminized propellant test data.

(5) Phase V - Development Testing

    (a) Additional nozzle performance and nozzle scale data were obtained in a series of four development nozzle tests. All nozzles in this series were submerged.

    (b) The nominal development testing conditions were:

        Throat Diameter: 2 to 2-1/2 inches
        Chamber Pressure: 800 psia
        Test Duration: 25 seconds

(6) Phase VI - Analysis Technique Demonstration

    (a) The analytical prediction techniques developed in this program were demonstrated for a motor to be tested on another program.

b. (U) General Requirements

The following general requirements were incorporated into the program technical approach:

(1) All motor tests firings were conducted by the Air Force Rocket Propulsion Laboratory, Edwards Air Force Base, California, using Aerojet ADOBE, 600 pound motor cases.

(2) All solid propellant grains were of the cartridge loading type.

(3) Motor assembly, disassembly and data reduction were accomplished by AFRPL. Tested hardware, without decontamination, and reduced test data were delivered to Philco-Ford for further analysis.

(4) All program operations involving the handling or potential exposure to toxic beryllium compounds were conducted in strict accordance with an Industrial Hygiene Plan approved by the Air Force.

(5) A series of four technical progress reports were prepared and distributed in accordance with the CPIA distribution list, Groups 2 and 4. A program Demonstration Phase Report, Analytical Nozzle Performance Study for the Hercules X259-C2 Motor," February 1967, was distributed only to the Government and Hercules Incorporated.

c. (U) Program Technical Premises

The program technical approach was formulated to evaluate three related premises which offered a logical explanation of the observed behavior of motor materials in beryllium propellant exhausts. These were:

(1) A significant fraction of the incidences of poor nozzle materials performance with both beryllium and aluminum propellants derive from underestimation of the convective heat transfer.

(2) The formation and behavior of condensed phase surface deposits along the nozzle contour has a strong influence on materials performance.

(3) The mechanics of beryllium metal combustion are more restrictive relative to aluminum. Major differences in heat transfer, corrosion and deposition result.

-6-

SECTION II (C)

SUMMARY

The results of early development testing of beryllium solid propellants
indicated that a severe nozzle materials problem existed. Consequently,
this program was directed to improving the understanding of the mechanisms
of erosion and corrosion in beryllium exhausts and to determining which
nozzle materials can be successfully applied with beryllium propellants.
These issues and the associated one of poor ballistic performance recorded
by beryllium propellants have been successfully resolved, at least quali-
tatively. The extensive similarity between beryllium and aluminum propellant
systems has been demonstrated. An improved general approach to nozzle
design and performance evaluation has been developed. Specific improvements
have been made in heat transfer, corrosion, ballistic performance and oxide
deposition analyses. The utility of and requirements for supplemental lab-
oratory and scale motor testing have been clarified. The conclusions and
recommendations are jointly based on the detailed interpretation of the
program solid motor tests and analytical study of the interaction of the
rocket exhaust with motor materials.

The program results are summarized and reviewed in Section III. Section 3.1
and Appendix I describe the seven propellants used in this program. Formu-
lation, ideal performance and nonideal performance data are described. The
propellants include two beryllium and two aluminum analog CMDB formulations
and two beryllium and one aluminum composite formulations. A qualitative
metal combustion model is described and it is shown that poor combustion
may increase the exhaust corrosivity by an order of magnitude or more.
Beryllium metal combustion is inherently slower than aluminum. Metal
agglomeration at the grain surface and low flame temperatures prior to metal
combustion are identified as major causes of incomplete combustion. In some
cases, required metal particle residence times have been greater than those

-7-

available in solid motors. All of the beryllium and one of the aluminum analogs tested are shown to be potentially poor with respect to achieving complete combustion in short times.

Section 3.2 reviews the results of studies conducted in support of the main rocket motor test phases of the program. Laboratory chemical reaction studies showed that low melting tungsten carbide and tungsten-beryllium (or aluminum) alloys may be formed. Beryllia, beryllium nitride and beryllium carbide were shown to be inert at reasonable rocket pressures and temperatures. Arc plasma studies of beryllia impingement on graphite and plastic insulation were relatively unsuccessful. Deposits were formed but sticking thresholds could not be identified in the low pressure tests. Cold flow modeling studies were conducted to examine the particle impingement process as a function of grain and nozzle contour designs. The results were qualitatively useful in interpreting the detailed grain port flow effects on the magnitude and location of particle impingement in the solid motor tests. The use of grease on the nozzle model contour was shown to be useful in visualizing the gas shear flow patterns with complex grain designs. Correlation studies showed that the general lack of heat transfer and deposition data tended to nullify the value of tests conducted in other programs. A unique pressure dependence of corrosion rate was shown for one composite beryllium propellant. This suggested that incomplete propellant combustion occurred below a critical pressure near 700 psia. The analytical techniques developed (or improved) for treating corrosion, heat transfer, deposition and ballistic performance are briefly reviewed. The application of these analytical techniques in the program demonstration phase is briefly discussed. A more extensive discussion of the program analytical methods is included in Section IV.

Section 3.3 and Appendices I and II describe the objectives and design of the 29 motors and nozzles tested in the program. The major design parameters were: (1) propellant, (2) grain design, (3) motor configuration, (4) nozzle contour. (5) nozzle throat diameter, and (6) nozzle materials. Each test featured at least one design change. Four grain designs were used with 100 pound grains. The four 500 pound grains were of a single design. Submerged, steep inlet and conventional nozzle contours were tested. End burning grains were tested in two positions relative to the nozzle throat. Pyrolytic graphite heat sink designs were used in the majority of the tests to facilitate thermal data acquisition. Five tungsten insert nozzles were tested. ATJ graphite, carbon cloth and asbestos phenolic materials were used away from the throat sections. All nozzles were designed to exceed surface temperatures of 5000 F in the 20 and 25 second burn times. Four tests used aluminum analog propellants. Extensive thermal and ballistic instrumentation were provided on each test.

Section 3.4 and Appendix III describe the motor test results and the post test condition of the nozzles. The test results include: (1) visual examination of the hardware, (2) ballistic data, (3) thermocouple data,

(4) motion pictures of the tests, and (5) exhaust plume particl   mples. The majority of the actual data is not included in this report which concentrates on the interpretation of the results. Basically, the physical condition of the nozzles and aft closure insulators was excellent. The small nozzles tested with the axially slotted grain designs were slightly grooved at 0 and 180 degrees relative to the grain slot. The large nozzles were submerged (slotted grain design) and the nose cap was slotted through in line with the grain slot. Complex grooves developed downstream of the nose cap slot. Only two nozzle failures occurred. The large scale tungsten insert (500-pound grain test) was ejected at 20 seconds. This was a result of extensive carbide formation followed by buckling and obtrusion. The failure of one of the small nozzles (100 pound grain) occurred in the pr -gram and that was a direct result of a gas leak at the aft closure - nozzle inlet interface. Some of the pressure and thermocouple data were lost due to the two nozzle failures and poor installation. The great majority of the specific test objectives were achieved.

Section 3.3 and Appendices IV through IX describe the results of the post test analyses applied to characterize nozzle performance. Cross sectional views of the nozzles after removal of loose deposits are shown in Appendix IV. The condition of each nozzle is discussed. The nozzle deposits and chamber slag were sampled and analyzed by X-ray diffraction. The samples were predominantly composed of the oxides, asbestos decomposition products and carbon. Beryllium carbide, tungsten species and aluminum metal were also found on the appropriate tests. Typical hollow, spherical alumina particles were collected from the plume on the aluminum grain tests. The berylli appeared as hexagonal rods, the majority of which were much smaller than the alumina particles. No impurities were detected in any of the plume samples collected. Nozzle throat deposition/erosion histories were calculated for each test and are given in Appendix V. Throat deposit thicknesses depend on the propellant, grain design, motor configuration, nozzle contour and throat heat sink capacity. The deposit thickness histories appear to be reproducible. On one 500 pound grain test with the nozzle submerged to 15 percent, there was no net decrease in throat radius. The throat erosion on that test was over 100 percent greater than for an identical test with 10 percent submergence. Aluminum propellant tests gave results qualitatively similar to the beryllium results. The depos histories show that throat corrosion occurred before the arrival of deposits to protect the throat on several tests but normally occurred after the deposits had melted and flowed away from the throat. A calculation method using thrust and pressure data is preferred to one using grain burning rate and pressure data. Schematic representations of exhaust flow fields and relative particle impingement rates are given in Appendix VII. The qualitative flow field analysis is used to explain the nozzle grooving which occurred on the slotted grain tests. The ballistic performance efficiencies were calculated for each test and adjusted to approximately account for heat transfer, deposition, deposit expulsion and divergence losses (Appendix VI). Analysis of the results indicated that poor combustion had occurred on some tests

while the majority were highly efficient. Errors in the data and averaging effects are discussed. Nozzle throat temperature histories and heat transfer coefficients are given in Appendix VIII. These data agreed well with theoretical predictions. Deposits and poor propellant combustion reduce the effective nozzle heat transfer considerably. Circumferentially non-uniform heating was associated with the slotted grain tests. The slotted grains and submerged nozzles gave results above predicted values. Nozzle throat corrosion data are given in Appendix IX. On a large number of tests, no corrosion occurred at all. The others yielded results which compare reasonably well with previous experience and simple corrosion rate prediction theory. The corrosion rate data is somewhat confused by non-uniform oxide deposition. Deposition protection prevailed over most of the firing period and must be accounted for in determining corrosion rates.

Section 3.6 briefly discusses the program results in terms of the program objectives and future motor/nozzle design requirements. Tungsten, graphite and plastic insulation materials can be used with either beryllium or aluminum propellants. There are no essential differences in the chemical or thermophysical degradation mechanisms in these systems. Incomplete combustion of beryllium propellants is the primary cause of excessive graphite nozzle corrosion. Poor combustion may be accompanied by an increase in deposition which will temporarily protect the nozzle. The high melting point of beryllia permits deposition protection to persist longer relative to alumina. Order of magnitude increases in corrosion can result when poor combustion is not accompanied by deposition protection. This is most likely to occur when unusually high turbulence or exhaust flow stagnation occurs locally along the motor/nozzle contour. It can also occur for deeply submerged nozzles which prevent deposit formation. Thermal stress induced surface spallation of graphites will extensively increase the surface regression. Chemical reaction heat absorption, blowing and surface roughness effects should be accounted for in heat transfer predictions for graphite nozzles. Low Prandtl numbers and unequal diffusional mass transfer coefficients should be accounted for in boundary layer transport analysis. Water, carbon dioxide, hydrogen and nitrogen are the dominant exhaust species which attack graphites. Tungsten fails by thermal shock fragmentation, plastic deformation and/or formation of low melting carbides. Low melting aluminum and beryllium alloys of tungsten may also be formed but have not been observed. Many nozzle failures in the past are attributed to underestimation of nozzle heat transfer and nonuniform exhaust flow field effects. Future designs should insure a high degree of metal combustion, uniform exhaust flow fields and control of oxide deposition. Improved awareness of the influence of propellant selection, grain design and motor/nozzle contour effects on nozzle materials performance will lead to optimum nozzle materials and ballistic performance. Beryllium propellants studied in this program are marginal in terms of metal combustion efficiency. Their use could require design restrictions which are potentially undesirable.

Section IV qualitatively describes an improved approach to nozzle design
and performance analysis. Basically, it requires that specific considera-
tion be given to the motor design parameters which have a recognized
influence on nozzle materials performance. In the absence of specific data
or prior experience, laboratory and scale motor tests are required to
validate important assumptions or to provide empirical adjustments. Once
decisions or assumptions are made concerning the metal combustion efficiency,
internal flow field details and particle impingement, parametric characteri-
zation of the deposition radiation, convection, corrosion and surface erosion
processes are required. Well developed analytical techniques are recommended
when they are available. Otherwise, approximate or preliminary techniques
are suggested. Then, the nozzle thermal response, deposition, nozzle corro-
sion and motor pressure are calculated simultaneously, with coupling effects
included. The structural stability of the nozzle and its contour is evaluated
using the calculated thermal response. Iteration can be used to determine
the importance of any assumptions made in the process and/or to optimize
the nozzle or motor/nozzle design. The extension of the analytical method
to other solid and liquid propulsion systems is briefly discussed.

The major program conclusions are presented in Section V. These are organized
under the following headings: (1) Nozzle materials performance, (2) Pro-
pellant combustion efficiency, (3) Effects of poor metal combustion,
(4) Nozzle heat transfer, (5) Nozzle corrosion, (6) Nozzle mechanical erosion,
(7) Oxide deposition, (8) Grain design, (9) Nozzle design, (10) Motor testing,
and (11) Analytical developments. Emphasis is placed on the means of
achieving adequate nozzle and motor ballistic performance. Ultimately, this
requires an improved understanding of the character of the propellant
exhaust, its actions upon the hardware and the reactions of the hardware to
such actions. The conclusions qualitatively describe the important char-
acteristics of beryllium propellants and, more generally, solid propellants.
In some areas, more detailed conclusions may be found in the technical prog-
ress reports.

The major program recommendations are presented in Section VI. These are
organized under the following headings: (1) Propellant selection,
(2) Advanced nozzle design, (3) Motor testing, (4) Analyses development,
and (5) Program results. Again, the emphasis is placed on the further
development and application of the program results to optimize nozzle per-
formance and minimize the occurrence of nozzle performance problems. Pro-
pellant selection criteria should include consideration of combustion
mechanics and efficiency. Propellant selection should also be compatible
with the motor configuration and grain design requirements. The selection
of advanced and cooled nozzle designs should consider the detailed effects,
disadvantages and advantages of oxide deposition. Future motor testing is
desirable to further clarify the effects of the major motor design parameters
on nozzle corrosion, deposition and heat transfer in aluminum and beryllium
systems. Further development of the analytical characterization of these
processes is also required. The relatively general and basic character of
the program results suggest that they should be extended to hybrid, fuel
rich, gel and liquid propellant systems.

-11-

SECTION III (C)

ROCKET MOTOR TEST PROGRAM RESULTS

3.1 (C) PROPELLANT SELECTION AND CHARACTERIZATION

a. (C) Program Propellant Selection

An initial step in the program was to classify the available beryllium
propellants. Candidate state-of-the-art formulations were required to have
standard impulse values above 280 seconds and ideal flame temperatures
above 3400°K. Composite modified double base propellants were classified
according to their ingredients as shown in Table I. Similarly, composite
propellants were grouped as shown in Table II. Within each group, propel-
lants were rated according to a particular oxidation ratio referred to as
XSO (excess oxygen). This parameter is related to the oxidation potential
of the ideal exhaust and is defined as the number of gram atoms of oxygen
less the sum of the gram atoms of carbon and beryllium in the formula.

Four beryllium propellants were selected to provide reasonable ranges in
flame temperature, XSO and ingredients. Each of these propellant charac-
teristics was assumed to be closely related to the propellant combustion,
oxide deposition and/or nozzle heat transfer phenomena. A CMDB propellant
was chosen from Group I to have a high flame temperature and XSO = 0.15.
A companion CMDB propellant was chosen from Group III to more closely approx-
imate a double base propellant and to have XSO = 0.05. Two composite pro-
pellants were chosen from Group I to obtain XSO = 0.15 and 0.30. The nom-
inal beryllium metal content was set at 12 percent for all propellants.
The selected propellants were named according to the closest, standard,
Atlantic Research Corporation propellant with the letter "F" appended to
designated this particular series. Relatively minor tailoring of the
standard propellants was necessary to achieve the desired XSO values and

-12-

TABLE I. COMPOSITE MODIFIED DOUBLE BASE PROPELLANTS

Group I	Group II	Group III	Group IV
TMETN	TMETN	TMETN	Resorcinol
Resorcinol	Resorcinol	Resorcinol	Triacetin
Triacetin	2-NDPA	Triacetin	2-NDPA
2-NDPA	HMX	2-NDPA	RDX or HMX (large quantities)
Plasticized Nitrocellulose	Nitroglycerine (small quantities)	RDX	Nitroglycerine (large quantities)
Beryllium	Plasticized Nitrocellulose	Nitroglycerine (small quantities)	Plasticized Nitrocellulose
Ammonium Perchlorate (large quantities)	Beryllium	Plasticized Nitrocellulose	Beryllium
	Ammonium Perchlorate	Beryllium	Ammonium Perchlorate (small quantities)
		Ammonium Perchlorate	

Typical Propellants

Arcocel 317	Arcocel 319B	Arcocel 319BR	Hercules VCP
Arcocel 191C	Lockheed 1009		Hercules VCN

TABLE II. COMPOSITE PROPELLANTS (C)

Group I	Group II	Group III
Polyurethane	Nitroplasticized Polyurethane	Polybutadiene
Beryllium	Beryllium	Beryllium
Ammonium Perchlorate	Ammonium Perchlorate	Ammonium Perchlorate

Typical Propellants

Arcane 54	Aerojet ANP 2991	NOTS CB-11
Arcane 24		Thiokol TP-H-1092
		Aerojet ANB-3084-2

a common nominal burn rate. The specific formulas for the Arcocel 191F, 319BRF, Arcane 54F and 24F propellants are given in Appendix I. Additional discussion of the propellant characterization and selection process may be found in Section 2.2 of Reference 1.

To obtain a direct comparison between beryllium and aluminum propellants, three aluminum analog formulations were selected. These were developed by using the same ingredients as for the beryllium propellants, excluding the Arcane 24F. It was further required that XSO and ideal flame temperature be matched within analog pairs. The aluminum propellants were designated Arcocel 389, 390 and Arcane 60. Specific formulas of these propellants are given in Appendix I.

b. (C) Ideal and Nonideal Propellant Performance

Standard isentropic expansion calculations were performed for all seven of the selected propellants. Ideal ballistic performance data (C^*, Isp and C_F) were obtained for both the equilibrium and frozen expansion assumptions. The results are summarized in Table VI of Reference 1. These data were subsequently used in computing delivered performance efficiencies for the actual motor tests. All calculations were based on the nominal 800 psia chamber pressure and an ambient pressure of 13.2 psia. The beryllium propellants had impulse values close to 280 seconds compared to about 260 for the aluminum analogs. Beryllium C^* values ranged from about 5400 to 5510 ft/sec. The aluminum analog values ranged from 5120 to 5280 ft/sec.

The first order, nonideal combustion effect was believed to derive directly from the slow or incomplete combustion of the metal additive. This effect was examined by varying the percentage of metal entering the thermodynamically simulated combustion reaction. The unburned metal was carried as an inert specie with the specific heat of the condensed metal. No vapor specie for the unburned metal was admitted. Standard performance calculations were then performed over the range of 0 to 90 percent metal combustion. Typical variations in C^* and Isp for the program propellants are plotted in Figures 4 through 7 in Reference 1 and the ranges in performance are tabulated on Page 16 of Reference 2 for all seven propellants. Both C^* and Isp were found to be approximately linear functions of the percent metal combustion. With 0 percent metal burned, the minimum C^* and Isp efficiencies were in the range of 76 to 80 percent. It follows directly that measured motor performance values, once corrected for other losses, can be used to estimate metal combustion efficiency.

c. (C) Ideal and Nonideal Exhaust Composition

Equilibrium exhaust compositions were obtained along with the ballistic performance data. Major specie concentration data for the case of ideal combustion are given in Table VII of Reference 1 for the seven propellants. The most prevalent species were CO, H_2, N_2, H_2O, CO_2, H, OH and the condensed

oxides. These data are compared with similar data for the case of 0 percent Be metal combustion in Table I of Reference 3. Large increases in the concentration of CO_2, H_2O and HCl are accompanied by commensurate reductions in the amounts of CO, H_2, H and minor chlorine species. Thus, the formula quantity of oxygen which does not combine with the metal additive appears as gaseous species which are known to contribute to nozzle corrosion. With no metal combustion, the value of the XSO parameter may increase from $[0 - (Be + C)]$ to $X[0 - C]$; where X is 0.68 for both the beryllium composites, 0.57 for Arcocel 191F and 0.78 for Arcocel 319BRF.

A more dramatic illustration of the effect of incomplete metal combustion on the exhaust oxidation potential (relative to both the unburned metal particles and the motor/nozzle materials) can be seen in Figures 8 and 9 of Reference 1. There, the sum of the moles of oxidizing species (CHO, CO_2, OH, H_2O, NO, O and O_2) are plotted against percent metal burned. This sum should be closely related to the XSO parameter since each specie (except for O_2) has only one available oxygen atom. However, at 100 percent combustion, the number of moles of oxidizing species is greater than XSO (approximately twice). This is primarily because some of the beryllium metal appears as chlorides and not all of the carbon appears as CO. The variation of the moles of oxidizing species is approximately a linear function of the amount of metal burned. The magnification of the apparent exhaust oxidation potential is approximately a factor of 9 to 12 for the XSO = 0.15 propellant, 25 for the XSO = 0.05 propellant and 5 for the XSO = 0.30 propellant. These results generally indicate that the Be and Al metal particles must burn primarily via reactions with H_2O and CO_2, the concentrations of which decrease in proportion to the amount of metal actually burned. Obviously, it will be difficult to burn all the metal, while it remains in condensed form, unless the propellant is adequately over oxidized. It follows that, the lower the ideal flame temperature and/or chamber velocity, the higher the oxidation ratio or XSO should be to achieve complete combustion of the metal.

A brief investigation of the effects of diluting the exhaust gases with phenolic insulation pyrolysis products was conducted. The results are presented and discussed on Pages 18-21 of Reference 2. Basically, it was shown that the carbon and hydrogen rich pyrolysis gases would tend to extinguish any burning metal particles immersed in exhaust/pyrolysis gas mixtures. The mixture temperatures were not greatly altered by gas-gas reactions, although such reactions were found to be slightly endothermic. It was concluded from this limited study that the mixing of incompletely burned exhausts with pyrolysis gases would not lead to excessive nozzle corrosion, or heating. However, such mixtures would be significantly enriched in hydrogen, hydrocarbons and carbon monoxide. This would occur regardless of the degree of beryllium or aluminum combustion. The exhaust/pyrolysis gas mixtures would be more corrosive than the pure propellant exhaust gases via the graphite-hydrogen and tungsten-hydrocarbon reactions. In fact, the exposure of tungsten to hydrocarbon pyrolysis gases and

acetylene (graphite or carbon char-hydrogen reaction product) has been suggested as a primary causal factor in tungsten insert failures.

d. (C) Metal Combustion Mechanics

In support of the premise that poor beryllium metal combustion is a major contributor to the nozzle performance problem, a simplified qualitative combustion model was formulated. This model provided a basis for selecting specific thermochemical and ballistic performance calculations, some of which have been described in the preceding paragraphs. In addition, the selection of many of the motor/nozzle designs and the interpretation of test results were strongly influenced by the qualitative model. Actually, the model was progressively developed as is described in Sections 2.2.a of References 1 through 4. The essence of the model and the practical implications are briefly discussed below.

The qualitative combustion model concentrates on the behavior or life history of the metal particles. Typically, the beryllium or aluminum particles are approximately spherical with a mass mean diameter of 15 to 20 microns and a size range of 1 to 40 or 50 microns. Usually, most of the oxidizer is also in a dispersed particulate form. HMX or RDX ball powder is about the same size as the metal and ammonium perchlorate particles may reach 300 microns in diameter. The particulate or solid phases are presumed to be uniformly distributed in the relatively continuous binder phase. A key assumption of the model is that the propellant ingredients, exclusive of the metal particles, burn to near thermodynamic equilibrium at or very close to the grain surface. In other words, the first stage of solid propellant combustion proceeds essentially as though the metal were not present. When some or all of the oxidizer is in particulate form, the flame will have a complex structure. Significant thermal and chemical gradients are likely to persist to distances from the grain surface of the order of 5 to 10 times the diameter of the largest oxidizer particles. The roughness of the grain surface will also depend on the size and behavior of the particulate ingredients. However, the grain surface is assumed to retreat in a nominally linear fashion.

The metal particles initially exist within the propellant at the preignition grain soak temperature. As a metal particle "approaches" the grain surface, it is heated somewhat because heat conduction into the propellant establishes a significant gradient normal to the burning surface. Due to its superior heat sink qualities, the metal particle temperature will lag that of the binder phase in which it resides. The particle eventually emerges at the grain surface which may be essentially solid (composite propellants) or a "fizz" layer (double base propellants). While the particle resides at the grain surface, it will be heated by convection, radiation and surface oxidation reactions. During this time the particles may melt, melt and agglomerate, and/or develop a significant oxide skin. Ultimately, the particles and agglomerates will be lifted or ejected from the grain surface

and carried away by the gaseous combustion products. The second key assumption of the model is that the majority, if not all, of the metal particles and agglomerates ignite and burn only after they have been detached from the grain surface. The particles are presumed to undergo only surface oxidation reactions until their ignition temperatures are reached, after which combustion proceeds primarily via vapor phase reactions. Finite times, which depend on the metal particle or agglomerate size, are required before ignition occurs or metal combustion is completed. Should these times be excessive, metal may pass the nozzle throat or exit plane without reacting. The implications in terms of ballistic performance have already been discussed while the attendant corrosion, heat transfer and deposition effects will be described in subsequent paragraphs. For the present, attention will be focused on comparing the combustion of aluminum and beryllium. Because of the importance of metal particle size in the combustion process, the metal agglomeration question is emphasized.

The aluminum and beryllium analog tests utilized grains which contained approximately the same number of metal particles with similar size distributions. Note that the density of aluminum is about 150 percent of that of beryllium and aluminum weights are about 165 percent of the beryllium weights. The specific heat of beryllium is about 2 to 3 times that of aluminum over the temperature range from ambient to their melting points. The heats of fusion for the two metals is approximately the same. The melting point of aluminum is $930°K$ compared to $1550°K$ for beryllium. Noting that flame standoff distances are typically greater than the metal particle diameter, it follows that it may be considerably more difficult to melt beryllium at the grain surface than aluminum. Significant surface oxidation of the particles can accelerate melting but it is not likely that such oxides would also melt. Melting is presumed to be necessary to permit metal particle agglomeration. However, the development of a solid oxide shell on the metal particle could retard agglomeration. Evidently then, the agglomeration phenomenon may depend on the oxygen-carbon ratio of the binder and the size of the oxidizer particles. Of course, the metal particles may move about on the burning surface, colliding with oxidizer and other metal particles.

In composite propellants, the metal particles may become trapped between the large ammonium perchlorate particles. While they may melt under these circumstances, their gaseous environment will probably not favor surface oxidation. Such agglomerates may be blown off the surface due to the gasification of the underlying binder via heat conduction through the metal. Double base propellants may not restrict the motion of the metal particles (relative to composites) and agglomeration should occur via a direct collision mechanism. CMDB propellants would logically behave in an intermediate manner.

In composite-aluminum systems, it is predicted that surface agglomeration will be essentially independent of flame temperature. Agglomeration will be proportional to the ammonium perchlorate particle size and, therefore, inversely proportional to burn rate. In the composite-beryllium system, there may be a sharp change in agglomeration behavior as the flame temperature is increased. At low ideal flame temperatures, there may not be any agglomeration; at very high temperatures the metal will melt and agglomerate as in the aluminum system; at intermediate temperatures the metal particles may stick together, forming aggregates. Ammonium perchlorate particle size effects should be similar for both metals when melting actually occurs. However, consideration of the density differences between the metals suggests that the beryllium particles will be more easily lifted from the grain surface, possibly tending to reduce the number and size of agglomerates relative to aluminum. Note that the smallest particles will be relatively easy to remove from the grain surface. Rotational and axial acceleration effects may also be important in combustion.

In double base aluminum systems, it is predicted that agglomeration will be less extensive and more strongly dependent on burn rate than for composites. Agglomeration may be inversely proportional to the ratio of nitroglycerine and nitrocellulose to the particulate oxidizer (such as HMX). In the double base-beryllium system, a demarkation could again occur when the flame temperature becomes high enough to cause melting of the particle surface. Again, the CMDB-aluminum and beryllium system should exhibit a combination of the agglomeration characteristics of both the composite and double base systems. Metal density and particle size effects should be the same as for composites.

Eventually, all metal particles and agglomerates will be lifted from the grain surface, pass through the flame and enter the higher temperature exhaust. From this point on, it is argued that the determining factors in combustion are the local flame temperature, the particle size distribution, the local exhaust gas composition, the nature of the particular metal and the exhaust flow field. Obviously, the flame temperature can only increase if the metal actually burns. An ignition delay occurs primarily because the metal leaves the grain surface before being heated to the ignition temperature. Both surface oxidation and particle lag induced convective heating (and possibly radiation) will occur. The surface reactions are likely to promote the development of an oxide shell which will act as a diffusion barrier against further reactions. The velocity lag heating will depend on the difference between the particle surface and the local exhaust temperatures as well as the difference between the gas and particle velocities. If the exhaust gas temperature should be less than the ignition temperature, ignition may not occur at all. (It should be noted that as long as some surface oxidation reactions occur, the particle temperature may rise to levels above the local exhaust gas temperature.)

-18-

Ignition is said to occur when the reactions begin to accelerate. For beryllium and aluminum, this occurs when the partial pressures of metal vapor above the liquid becomes significant. This vapor diffuses through the oxide shell to the particle surface and beyond. When the vapor reacts with the exhaust gases (primarily H_2O and CO_2), heat is generated. Some of the heat is transferred back to the metal, causing its temperature and vapor generation rate to increase. The post-ignition combustion process may be extremely rapid unless (1) the oxide reaction product condenses on the particle surface, restricting the vapor diffusion, or (2) there is not sufficient oxygen available in the exhaust to sustain the reaction. Presumably secondary reactions between water vapor and the surface oxides can produce gaseous hydroxides which may limit the oxide shell growth. If the oxygen supply is locally depleated, the unburned metal will continue to evaporate. Unburned metal vapor would burn completely as air mixes with the plume while unevaporated metal might survive the expansion and plume mixing processes.

Flame temperatures were calculated as a function of the fraction of the metal burned for all of the program propellants. Sample results may be seen in Figures 10 and 11 of Reference 1. The temperature varies in a nearly linear fashion between the 0 and 100 percent metal combustion extremes. According to the combustion model, the flame temperature prior to any significant metal combustion must be above the metal ignition temperature to achieve rapid combustion. The upper limit for the ignition temperatures of aluminum and beryllium may be taken to be the metal oxide melting points, 2300°K and 2835°K, respectively (Reference 5). The minimum ignition temperatures depend on the oxidizing species, the concentration of the oxidizing species and the system pressure. In the presence of significant amounts of water vapor, beryllium may ignite at temperatures as low as 1900°K. Aluminum ignition temperatures apparently are not so easily lowered. It is likely that the diffusivity of the oxidizing and metal vapor species through the oxide shell and the gaseous hydroxide stability are not the same in the two metal systems. At least as a first approximation, the aluminum ignition temperature is presumed to be close to 2300°K while that for beryllium may vary from 1900°K to 2835°K as the water vapor concentration decreases.

The aluminum propellants, Arcocel 389, 390 and Arcane 60, have minimum flame temperatures (0 percent metal combustion) of 2500, 2390 and 2060°K, respectively. Note that metal ignition may be most difficult for the Arcane 60 propellant. The beryllium propellants, Arcocel 191F, 319BRF, Arcane 54F and 24F, have minimum flame temperatures of 2393, 2287, 1978 and 2034°K, respectively. Evidently, ignition should be relatively more difficult in the composite systems while all four propellants could exhibit marginal combustion characteristics. Note that 25 percent of the beryllium in the Arcocel 191F must burn before the exhaust flame temperature reaches the beryllia melting point: the corresponding figure is nearly 50 percent for the Arcane 54F propellant.

The smallest particles should have the shortest ignition delays and total combustion times. Conversely, metal agglomerates or the largest original metal particles will require the longest times to complete combustion. The lower density, higher melting point and higher heat capacity of the beryllium suggest that ignition delays may be about 5 times the values for equal sized aluminum particles. As long as the flame temperature remains below the beryllia melting point, beryllium combustion is likely to be slower than for aluminum. Clearly then, in comparing the metal combustion delays for different propellants, the agglomeration and flame temperature characteristics must be considered. It is predicted that when the minimum propellant flame temperatures (no metal combustion) are above 2300°K for aluminum and above 2835°K for beryllium, both the agglomeration and metal combustion processes will be quantitatively similar for analog propellant formulations. However, the longer ignition delay will persist for beryllium.

Based on the qualitative combustion model alone, it is expected that beryllium will be more difficult to burn than aluminum. An exception to the rule may occur when aluminum agglomerates at the grain surface and beryllium does not, in otherwise comparable situations. The time actually available, to complete metal combustion before the exhaust reaches the motor walls, may vary from less than a millisecond (especially for shallow nozzle submergence) to as much as a second. Motor residence times with respect to the nozzle throat may vary over about the same range. Residence times vary considerably over the firing period, with motor configuration and with motor scale. The times required to complete the combustion of a metal particle will depend on its size, the amount of available oxygen, flame temperatures and velocity lag. The results of laboratory combustion studies and available motor test data suggest that particles above about 10 microns may require from 1 to more than 100 milliseconds to burn. It should be noted that particle agglomerate sizes have been observed to exceed 1000 microns in fuel rich propellants.

In summary then, complete metal combustion cannot be assumed for most beryllium and some aluminum propellants. The specific degree of metal combustion at points of interest along the wall contour will depend on propellant formulation, propellant grain microstructure and motor design. Specific combustion mechanics depend on the original metal particle size distribution, metal melting point, metal oxide melting point, metal heat capacity, metal density, particle ignition temperature, exhaust flow velocities and acceleration loads. It remains to be shown how poor combustion may influence motor materials performance. This will be done in succeeding paragraphs.

    e. (C) Combustion Efficiency Effects on Nozzle Performance

There are three major ways in which nozzle materials performance will be affected by metal combustion efficiency. These are: (1) corrosion, (2) heat transfer, and (3) condensed phase impaction and deposition. These areas were examined in an ideal analytical or qualitative manner for the program propellants. Each area is discussed individually below.

(1) (C) Chemical Corrosion

The corrosivity of the solid propellant exhaust, with respect to any particular motor material, is represented by the thermodynamic B value. B is simply the mass of wall material required to chemically saturate a unit mass of propellant exhaust. It is defined for the state of thermo-dynamic equilibrium so that any computer program which can find the equilibrium state as a function of given values of pressure, temperature and atomic composition can be used to find B values. When the wall material is solid and both reactants and products are gaseous, the B value is proportional to the nozzle surface regression rate (see Section 2.2 of Reference 1). In addition to computing the B value, the composition of the exhaust, saturated with wall material, is available. Comparison of the original and final compositions indicate which net chemical reactions have taken place. The ideal exhausts of the program propellants contain gases species composed of carbon, hydrogen, nitrogen, oxygen, chlorine and aluminum or beryllium. The only condensed species which appear are the beryllia and alumina. (Note that a true double base propellant con-tains no chlorine and that advanced propellants may contain flourine.) The only new species which appeared over the range of metal combustion efficiency were the condensed metal and, sometimes, the condensed metal nitrides and carbides. The chemical stability of the latter condensed species, relative to graphite and tungsten, was examined experimentally. The results are discussed in a subsequent paragraph.

Regardless of the degree of metal combustion assumed, it was confirmed that the major reactions with graphite were:

$$H_2O + C = CO + H_2$$

$$CO_2 + C = 2CO$$

$$H_2 + 2C = C_2H_2 \text{ (above 4000°F)}$$
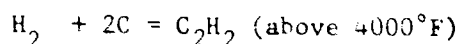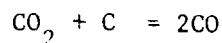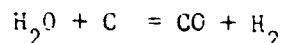
Of course, minor oxygen species, OH, O, O_2, CHO, NO and NO_2 also react. In some propellants, significant amounts of CN and HCN may appear as reaction products. Considerably more of the BeOH and $Be(OH)_2$ species appear compared to the analogous aluminum species. However, in the aluminum system, significantly greater amounts of the gaseous suboxides appear compared to the beryllium system. These gaseous hydroxides and suboxides will react with carbon to form condensed carbides and CO as long as the carbide product is thermally stable. At temperatures near 5000°F, the reaction will produce the metal vapor and CO. Even if these species should exist in greater quantities than are thermochemically indicated, they could not increase the exhaust corrosivity by more than a few percent. The metal vapors will not be dangerous when they form a condensed carbide

film which will inhibit further reaction. At temperatures approaching 6000°F, carbon sublimation begins and C_2H will form via the hydrogen reaction. However, these temperatures are seldom, if ever, reached in solid propellant systems.

The gaseous reactions of primary interest are the usual ones given above. The B values for the gas phase reactions with graphite are shown for the Arcocel 191F and 389 aluminum analog propellants in Figures 14 and 15 of Reference 1. The curves for the other propellants are very similar in shape. For ideal combustion, the B value curves are shifted up or down in accordance with the XSO or oxidation ratio. The percent metal combustion curves also shift due to changes in the total oxygen and carbon to oxygen ratio. Negative B values occur below temperatures near 1000°K. This indicates that the exhaust is supersaturated with carbon. However, the thermochemically indicated conversion of $2CO$ to CO_2 and carbon will not necessarily occur. A plateau is established in the 1500 to 2500°K range. The B value corresponding to such plateaus reflects the total effect of all carbon-oxygen reactions to form carbon monoxide. Above about 2500°K, the carbon-hydrogen reactions begin to cause the B values to rise rapidly. In contrast to the oxygen reactions, the hydrogen reaction is strongly temperature dependent. It should be noted that when no metal combustion is allowed, the hydrogen reactions are not important, since the graphite surface temperature could not exceed 2500°K for any of the program propellants. Considering that the graphite would be significantly below the flame temperature, the primary effect of poor metal combustion on exhaust corrosivity is an increase in the available oxygen for reaction with carbon. This increase will be inversely proportional to the XSO and proportional to the metal combustion efficiency. The major difference between the beryllium and aluminum systems will be confined to the metal combustion effect.

Similar results were obtained for the exhausts without eliminating the condensed oxides. These may be seen in Figures 12 and 13 of Reference 1. In this case the calculation of equilibria is not realistic. That is, most of the alumina and beryllia is in particulate form and cannot equilibrate with either the gaseous exhaust component or the nozzle wall. In general, the reactions of the condensed oxides with either graphite or tungsten may be neglected entirely except as indicated in the discussion of the laboratory studies results.

The preceding results can be directly extended to tungsten. The usual oxygen and chlorine reactions will occur in either the beryllium or aluminum system. For all practical purposes, such reactions will not promote significant surface regression. However, there are two reactions which can occur that may precipitate catastrophic failure of tungsten inserts. Thus, the exposure of tungsten to either beryllium (metal or vapor) or carbon will lead to the formation of beryllides and carbides which have melting points well below that of tungsten. There are three

-22-

potential sources of carbon in either the beryllium or aluminum system. These are: (1) carbon or graphite supporting material, (2) condensed carbon eroded from upstream surfaces, and (3) hydrocarbons from insulation pyrolysis or graphite-hydrogen reactions upstream. The third source is currently regarded as the most important. The important source of beryllium is unburned metal. B values were not calculated for tungsten since they would not relate directly to the corrosion rate when condensed species are the dominant reaction products.

In summary then, there is no indication that nozzle materials corrosion will be significantly different in the beryllium system relative to the aluminum system, provided that the materials see only the products of complete combustion. In either system, poor combustion will lead to increased oxygen attack. The increase may be by more than an order of magnitude. The oxygen and hydrogen reactions will dominate for graphite materials. Oxygen and chlorine attack of tungsten can normally be neglected. Low melting tungsten carbides and beryllides may be formed when exposure to gaseous hydrocarbons or beryllium metal occurs. This action may precipitate catastrophic structural failure of tungsten inserts.

(2) (C) Heat Transfer

The convective heat transfer to the wall can be treated as the product of a transfer coefficient and a driving potential. Simplified temperature or enthalpy driving potentials may be used as follows:

$$q = h\ (T_{aw} - T_w)$$

$$q = h/\bar{C}p\ (H_{aw} - H_w)$$

where:

q = local convective heat flux, Btu/in^2 sec

T_{aw} = local adiabatic wall temperature, $^\circ F$

T_w = local wall temperature, $^\circ F$

H_{aw} = adiabatic stagnation enthalpy of the exhaust at the wall temperature, Btu/lbm

$\bar{C}_p$ = local average boundary layer specific heat, $Btu/lbm\ ^\circ F$

h = convective heat transfer coefficient, Btu/in^2 sec $^\circ F$.

Assuming the nozzle expansion process to be isentropic, the chamber stagnation enthalpy will be conserved except in the boundary layer. If we disregard boundary layer recovery effects, H_{aw} may be set equal to H_o, the chamber enthalpy. However T_{aw} is always less than T_o (chamber stagnation flame temperature) where the local static pressure is below the chamber pressure.

-23-

For example, T_{aw} drops about $600^{\circ}K$ over the pressure range 800 to 13 psia for the Arcocel 191F propellant (see Figure 1, Reference 1). The average boundary layer specific heat is dependent on wall temperature, pressure and the particular exhaust composition. These dependencies may be seen, for the ideal case of no wall reactions, in Appendix VIII. According to the simplified Bartz equation, (Reference 6), the value of h is most strongly dependent on $\bar{C}p$ and $C*$ at constant chamber pressure.

When the metal additive has not completely burned, all of the heat transfer parameters will change. Major decreases in H_{aw} and T_{aw} will occur. Compensating decreases in the chamber pressure and $C*$ should leave $h/\bar{C}p$ relatively unaffected. However, $\bar{C}p$ will decrease due to the smaller drop in exhaust temperature relative to a given decrease in stagnation enthalpy. The net effect will be a decrease in the heat flux. The reduction in flame temperature level will have a direct effect on nozzle performance. Thus, the maximum materials temperature which can be reached could fall well below maximum allowable design values. This effect will be most pronounced when the ideal flame temperature is close to the metal oxide melting point while there are oxide deposits along the nozzle contour. It is by this mechanism that extremely high nozzle performance can be achieved with beryllium composites (such as the Arcane 54F). Nozzle performance in analog aluminum systems could be considerably less impressive simply because the oxide coating can not be retained to as high temperatures as in the beryllium system. When no deposits are present, the nozzle performance will reflect the increase in oxygen reactions associated with poor metal combustion. As previously discussed, the beryllium propellants would precipitate the poorer nozzle materials performance in such a situation.

The effects of the corrosion reactions on the wall heat flux must not be neglected. The net effect of the exhaust gas reactions with the graphite materials is that heat is absorbed. The hydrogen reaction is the most endothermic. Since hydrogen becomes more reactive as the surface temperature rises above $2500^{\circ}K$, the surface temperature rise will lag well behind values calculated for the case of no reactions. Actually the surface temperature will essentially reach a plateau below T_{aw} instead of asymtotically approaching it. The sum of all the oxygen reactions with graphite is also endothermic. Above about $1500^{\circ}K$, the heat blocking effect will be essentially independent of surface temperature. A similar situation exists for tungsten. Empirical convective heat transfer correlations have primarily been developed for "cold" walls without significant chemical reactions or blowing. The extension of such correlations to advanced propellants and wall temperatures above about 2500 to $2700^{\circ}K$ would lead to overestimation of both the predicted surface temperature and corrosion rate. However, there is reason to believe that these same correlations underestimate the heat transfer coefficient for other reasons. These include the use of high Prandtl numbers, neglect of surface roughness and underestimation of the boundary layer specific heat.

On the other hand, film cooling effects associated with insulation pyrolysis are neglected and may cause overestimation of the heat transfer. The net result is that the original empirical correlations may well be accurate enough for many propellant/motor systems. Their application in new propellant systems or when poor combustion occurs should be undertaken with considerable caution.

(3) (C) Oxide Impaction and Deposition

Under conditions of complete propellant combustion, the condensed oxide products exist in particulate form. These particles cannot precisely follow the gas streamlines. Consequently, they may be centrifuged to or away from the wall whenever the gas streamlines are turned near the motor/nozzle contour. In general, particles which impact on the contour may rebound or stick. Rebounding is most likely to occur at high impact energies, when gaseous reaction products form during impaction or the surface material breaks down. Sticking is known to occur but threshold conditions have not been found. Both mechanical sticking and chemical bonding occur for alumina and beryllia on graphite. Both oxides wet tungsten. When sticking occurs, wall deposits will form in the impingement area, shielding the surface from the corrosive gases and heat transfer. As the deposits build up, the surface will melt and flow downstream. Thus, the deposit will propagate over the entire contour until the liquid flows away faster than it is replenished by impaction. The liquid may also become unstable as it thins, breaking up into streams or beads. As long as deposits cover the nozzle surface, there will be no corrosion. The insulating nature of the oxides will reduce the heat conduction to the substrate and reduce the convection heating by forcing the gas side surface temperature to rise rapidly to values above the oxide melting point.

Poor metal combustion may effect oxide impingement most directly through the increase in particle diameters. The largest metal particles, agglomerates or condensed oxide particles will experience the greatest slip relative to the gas streamlines. Impacting particles which contain metal should be well below the local gas temperature and may not contribute significantly to wall heating. Deposits containing metal will have a lower melting point than pure oxide deposits. Deposited metal should continue to vaporize as it flows along the contour. The vapor should burn in the boundary layer, increasing the heat transfer to the deposit surface and sustaining the metal vaporization process. It is likely that some of the metal in wall deposits could be expelled from the motor. In some cases this could constitute a significant performance loss, probably confined to the early portion of the motor test.

It is emphasized that the predicted increase in exhaust corrosivity, associated with poor metal combustion or flow stratification, will not influence nozzle materials performance as long as deposits shield them from the exhaust. The corrosivity calculations suggest that excessive corrosion could occur prior to the arrival of any deposit, provided that the surface temperatures are

above about 1000 to 1500°K. The lower melting point of alumina should permit it to flow over the contour to the throat more rapidly than the beryllia. As long as poor metal combustion persists, the deposits will be relatively difficult to remove, since the flame temperatures will be significantly closer to the oxide melting point. Especially for beryllium propellants then, corrosion after deposit removal will not be very much worse than under ideal combustion conditions. Of course, when no deposition occurs or it is nonuniform, the higher corrosion rates would occur. Such conditions should be associated with shallowly submerged nozzles and with some internal burning grains with noncircular ports.

3.2 (C) SUPPORTING LABORATORY AND ANALYTICAL STUDIES

A number of specific laboratory and analytical study efforts were conducted to clarify certain aspects of the nozzle erosion problem. The laboratory studies were predominantly completed prior to the initiation of motor testing. The analytical studies described in this section were conducted over the entire span of the program. The scope and results of each of these tasks are described separately below.

a. (U) Condensed Phase Reaction Studies

The objective of this laboratory study was to determine the extent to which the condensed phases present in beryllium propellant exhausts would react with tungsten and graphite nozzle material. Exhaust sampling results from prior programs and B-value analyses for the Arcocel 333E propellant indicated that beryllium nitride and beryllium carbide could accompany the unburned beryllium and beryllia. The reactions of these condensed phases with wall materials in a rocket cannot be conveniently treated by analytical techniques which depend on the equilibrium assumption. Quick look experiments were defined to determine which of these materials could potentially contribute to extreme behavior of nozzle materials. The results of these studies are discussed in Sections 3.2 of References 1 and 2.

In reviewing the discussions of the reactivity of alumina and beryllia with graphite in References 1 through 4, several errors were noted. Consequently, the present discussion supercedes the earlier ones where disagreements occur. Basically, the exposure of beryllia to graphite at subatmospheric pressures led to significant reactions beginning at about 2560°K (4150°F), well below the melting point of beryllia. The rate of the reaction suggested that an intermediate, liquid phase was present. Presumably, such a phase would be an oxycarbide or beryllium metal. Post-test analysis indicated that residual beryllia samples contained beryllium carbide. Such samples were from tests in which visual smoke products had ceased to appear and in which the beryllia had melted. It was also noted that there was no oxide or carbide residue associated with the graphite reaction surface. Evidently, the reaction ceased when the gaseous products separated the beryllia from the graphite. These results are qualitatively similar to those previously obtained for

alumina and graphite. In order to evaluate the behavior of the oxides with respect to graphite at rocket pressures, a reasonable physical model was established. This model, in conjunction with equilibrium B-value calculations, provides a means of predicting the chemical stability of the oxides with respect to the nozzle materials of interest.

At low temperatures, condensed beryllia reacts with solid carbon to form solid Be_2C and CO gas. Similarly, alumina reacts with carbon to form Al_4C_3 and CO gas. In either case, intermediate condensed oxycarbide phases may form. At high temperatures, the carbide and oxycarbide become unstable with respect to alternate gaseous decomposition products. Thus, the primary beryllia reaction products become: CO, Be (vapor), Be (liquid) and BeC_2 (gas). Similarly, the primary alumina reaction products become: CO, Al (vapor), Al (liquid) and Al_2O (gas). In each case the dominant gaseous product is CO. Temperatures must exceed about 3200°K before the beryllium carbide gas becomes important relative to the metal vapor. Above the melting point of alumina (2300°K) the aluminum suboxide gas is a slightly more important product than aluminum vapor.

In the rocket environment, a continuous coating of either oxide may form on the graphite surfaces. The reactions proceeded to form condensed products at the interface. At low surface temperatures, the carbides and oxycarbides will form. At high temperatures the metal will be produced. These condensed phases will act as a diffusion barrier and the reactions will essentially stop unless the products are physically removed from the reaction zone. The CO will tend to diffuse through the oxide deposit, provided that the external partial pressure of CO (prominant exhaust product) is less than the equilibrium pressure of CO at the reaction interface. It is interesting to note that composite propellant exhausts typically yield less CO than double base propellants. Thus, diffusional transport of CO away from the reaction zone (and consequently acceleration of the reaction rate) will occur at lower surface temperatures then in double base systems. For beryllia the CO diffusion should begin in the range of 2700 to 2900°K; for alumina it should begin in the range 2500 to 2700°K. The loss of CO from the reaction site will, of course, tend to promote the formation of additional condensed products so the reaction will still be diffusion controlled and very slow.

As surface temperatures continue to rise, the carbides and oxycarbides will begin to decompose. Both the reduction of the diffusion barrier and the diffusion of the other gaseous products will tend to increase reaction rates. Eventually, the total pressure of the gaseous reaction products could excede the local static pressure in the nozzle. Then, bubbling or boiling would occur to relieve the pressures. The entire deposit could be blown off the surface if it happened to be solid. The "boiling points" of beryllia on graphite are 2400, 2700 and 3200°K at nozzle pressures of 10, 100 and 1000 psia, respectively. At the same pressures, these temperatures are 2200, 2500 and 2900°K for alumina on graphite. For alumina, boiling will almost always occur as the pressure relief mechanism since it melts at 2300°K. Beryllia will boil when the nozzle pressures are above about

400 psia while it may be blown off at lower pressures, since it melts at 2835°K. Impurities in the beryllia could lower the melting point and permit boiling to occur at lower pressures.

The boiloff of the gaseous reaction products could lead to local pitting and higher average reaction rates. Because condensed reaction products will still form, the maximum reaction rates will not be achieved until the partial pressures of the metal species at the reaction site approach the local nozzle pressure. For beryllia, surface temperatures must exceed about 3400°K at pressures above 100 psia to achieve the maximum rate condition. Actually then, very high beryllia graphite reaction rates will not be achieved in practical cases while a continuous coating persists. For alumina, temperatures must be above 3000°K at pressures above 100 psia to achieve the maximum rate condition. Again, very rapid reaction rates are not likely to occur in actual nozzles.

The continuous deposit model is not always applicable in the nozzle environment. Thus, when a continuous deposit of the liquid oxides becomes too thin, it will become unstable. The thin deposit film will break up into sheets or beads. Then, the gaseous reaction products will escape from the reaction zone by flowing or diffusing to the edge of the stream or bead rather than diffusing through the oxide. The escaping gas may propel the oxide along the surface or tend to expel it from the surface at the high range of graphite surface temperatures. The net effect will be that the bead or stream will tend to form a narrow axial groove as it flows along the contour.

Thus far, there are few notable differences in the beryllia and alumina reactions with graphite. Special note should be taken of the fact that alumina melts at 2300°K (3700°F). The gas shear forces will tend to remove the deposits at wall temperatures well below the chemical stability limit (above about 3000°K). Thus, the deposits which were originally trapped along the contour, early in the test, will not contribute to significant corrosion. Assuming that oxide particle impaction continues, the discontinuous modes of oxide deposit flow will be established. The uncoated graphite surfaces will be exposed to the exhaust gases and the usual gas-solid reactions will occur. It is not obvious whether such reactions would proceed at the expected rates or not. It is possible that the discontinuous deposits may contribute to local increases in boundary layer turbulence which would tend to increase the reaction rates. The discontinuous flow of beryllia deposits should only differ in that it will occur at significantly higher surface temperatures (above about 4650°F). When large amounts of beryllia may be stored along the nozzle contour, the surface temperatures will probably exceed 5000°F before the continuous deposits degenerate to stream or bead form.

The thermal conductivity of beryllia is believed to be about 3 times that of alumina. Less significant variations in viscosity, density, specific

-28-

heats, heat of fusion and surface tension are recognized. It is probable
that the solubility of exhaust gases and condensed ablative insulation
decomposition products will be different for the two oxides. All of these
factors will influence the specific behavior of the wall deposits and their
flow characteristics. Final interpretations of their relative importance
must await the generation of improved property values at high temperatures,
especially for the liquid phases. However, it is apparent that potential
differences in the amounts of deposit formed and the melting point of the
oxides are dominant factors. The nozzle thermal design and oxide con-
ductivity should determine the endurance of continuous deposits. When poor
metal combustion occurs, it should be expected that the quantity, endurance,
composition and flow characteristics of deposits will be extensively altered.
Once again, there is apparently no reason to expect that graphite nozzle
corrosion can be attributed directly to the oxides in either the beryllium
or aluminum system.

Comparable studies of the reactions of the metal oxides with tungsten were
conducted. Experimental studies, in this and other programs, generally
indicate that essentially no reactions occur. This may be a result of the
formation of an intermediate molecular layer of tungsten suboxides. It is
also noted that the diffusional transport of tungsten would be considerably
slower than that of carbon. Some surface polishing and grain boundary
attack of tungsten have been observed. This action is presumed to be the
source of the tungsten found in or on the surface of the oxides in post-test
examination of reaction samples. Both beryllia and alumina wet tungsten.
It should be expected, then, that contour deposits would form in essentially
the same manner as for graphite nozzles. Equilibrium B value calculations
indicate that the interface pressure of gaseous reaction products will be
less than 1.0 psia at tungsten temperatures below $3400°K$ with both beryllia
and alumina. This suggests that deposit boiling will not occur and that the
discontinuous deposit flow modes will not increase the oxide reactivities
significantly. For either oxide, the primary reaction products are the
condensed metal and its vapor. The metal could be involved in the grain
boundary attack.

No reactions were observed between beryllium nitride and graphite or tungsten
to temperatures of 4800 and $4600°F$, respectively. It is probable that the
nitride would be well dispersed in the rocket exhaust. Consequently, the
absence of reactions with the pure material suggests that no reactions will
occur in the rocket environment. Similarly, aluminum nitride is not regarded
as a threat to the nozzle materials.

In an experimental survey for low melting compounds of tungsten, two eutectic
Be-W alloys were found. The WBe_{12} phase has a melting point near $1600°K$.
The WBe_2 phase is thought to have a melting point near $2000°K$. At tempera-
ture levels where the beryllium carbide begins to decompose, tungsten
carbides (WC_2 and WC) were formed. In the tungsten aluminum system, WAl_{12}
also has a melting point of $1600°K$ and the WAl_4 phase melts at $1900°K$. It is

-29-

quite apparent that the exposure of tungsten to aluminum, beryllium and/or carbon would produce surface melting. Note that the metal or carbon rich phases will form first (at the leading edge of a tungsten insert) and that these phases will continue to dissolve more tungsten as they flow along the contour. In this respect, the beryllium will be the most dangerous. The more refractory carbides are always found in melted regions of tested inserts. Apparently the aluminum and beryllium alloys have not been found. Such alloys could have been removed before or during carburization. Even without experimental confirmation of the production of the metal alloys, they constitute a real hazard to tungsten inserts.

There are several possible sources of beryllium or aluminum for alloying. The most obvious is unburned metal which flows, from the impingement area, along the contour to the tungsten. The decomposition of the metal oxycarbides and carbides (on graphite surfaces upstream) also produce both the liquid metal and its vapor. The exhaust contains relatively small amounts of the metal vapor but metal chlorides, suboxides and/or hydroxides could form the alloys when they react with the tungsten. The direct reduction of the condensed oxides by tungsten also produces metal for alloying. The sources of carbon include hydrocarbon gases, mechanically eroded material from upstream surfaces, metal carbide decomposition products and supporting graphite structures. The hydrocarbon source is currently regarded as the most serious. Large quantities of hydrocarbons are evolved during the pyrolysis of plastic insulation materials. Acetylene is also the primary product of hydrogen attack of graphite contour materials, such gases will tend to flow along the contour and over the hot tungsten surface. The hydrogen-graphite reactions can be controlled by holding surface temperatures below about 5000°F. Submerging the nozzle could minimize pyrolysis gas flow over the tungsten throat. Oxide deposit protection of tungsten should be effective in preventing carburization. The maximum deposit protection of tungsten would be found in the relatively low flame temperature beryllium composite propellant system.

b. (U) Arc Plasma Studies

A plasmadyne SG-1 arc jet was used to study the impingement and deposition characteristics of alumina and beryllia on graphite and asbestos phenolic. The results of this study may be found in Section 3.3 of References 1 and 2. Very few of the experimental objectives were actually achieved for two basic reasons. First, the tests were run at pressures just below atmospheric to minimize the possibility of beryllia leakage. According to the beryllia-carbon reaction model, this condition would not be similar to the actual rocket case in that wetting would not occur. The test conditions were somewhat more reasonable for the alumina impingement experiments. The second problem involved the lack of temperature control of the test materials. The samples tended to cool off rapidly (by radiation) as soon as insulating deposits formed on the impingement surface.

-30-

The experimental results appear to be reasonable when interpreted in terms of the oxide-graphite reaction model. With graphite surface temperatures initially below the alumina melting point, there was some evidence of carbide formation and the deposits had normal crystal habits. When the sample temperature was raised above the alumina melting point, extensive carbide formation was observed. Apparently, only random mechanical sticking of beryllia on graphite occurred. Sample temperatures did not reach the minimum reaction temperature (about 4100°F) or the beryllia melting point. With initial sample temperatures above about 3600°F, some reflection of alumina particles was observed. Most of the beryllia particles were reflected during impact.

Sticking was observed for both oxides on asbestos phenolic. Sticking appeared to follow the initial development of a char layer. Molten asbestos decomposition products appeared to be directly involved in the capture of the oxide particles. Thicker alumina deposits were formed compared to beryllia. The alumina also reacted with the asbestos phases while the beryllia probably fused too rapidly to permit significant reaction.

Future attempts to examine the effects of impaction parameters on sticking and reaction should not be conducted at low pressures. It is also believed that deposit flow mechanics should only be studied using surface configurations and gas shear levels which resemble those of an actual nozzle. It is also possible that equivalent results could be obtained from actual solid motor firings. The low pressure plasma would be suitable for studying tungsten alloying effects.

c. (U) Cold Flow Modeling

A detailed description and discussion of the results of the cold flow modeling study conducted in this program are presented Section 3.3 of References 1 and 2. Selected cold flow modeling results obtained under another program (NASA Contract NAS 7-408) are also presented in Section 3.3 of Reference 2. The results of these studies were primarily used as an aid in qualitatively interpreting the rocket motor test results. They were of particular value in the estimation of the exhaust flow fields, locating impingement areas and in understanding the effects of circumferentially nonuniform flow.

The experimental techniques were extensions of those developed under Contract AF 04(611)-9072 (Reference 7). Basically, the rocket exhaust conditions are analytically translated to the modeling situation which features the flow of nitrogen containing dispersed polyethylene particles (spherical). A wide range of particle sizes were used in each test to model actual rocket exhaust particle sizes up to 30 microns. Particles which impinge on the model contour are retained on a sticky tape and then counted. In the NASA study, the model contour was coated with grease to obtain a visual representation of the gas flow pattern as well as impingement data. End burner, circular port and star grains were modeled in this program. The axial location of the

grains relative to the model nozzle throat was varied. Several circular port diameters were tested. Conventional nozzle contours, two aft closure angles and a submerged nozzle were modeled. The effects of surface roughness and contour discontinuities (due to wall deposits) were also examined. In general, the results are presented graphically, showing the relationship of particle impingement flux as a function of distance along the closure/nozzle wall. In principle, these results could be extrapolated to the actual rocket case via the modeling equations. This would facilitate the prediction of particle impingement heat fluxes, quantitative characterization of the source of oxide wall deposits and location of boundary layer starting points in either uniform of nonuniform flow situations. Rather than attempting to summarize the results of the cold flow studies, it is more pertinent here to consider the limitations of the techniques and results.

A major limitation of the cold flow modeling technique is that the particle size in the actual rocket cannot be determined. It is not obvious that the rocket particles can be satisfactorily represented by a single modeling particle size or size distribution. Thus, the original metal particle size distribution may shift as a result of grain surface agglomeration. Then, during rapid combustion, the metal oxide may temporarily exist as a vapor cloud rather than as discrete particles. Through condensation and particle interactions, an entirely new size distribution may be created. The entire process is highly transient and there may be little similarity between the particles in the chamber and those collected in the exhaust plume.

The modeling studies conducted in this program utilized solid particles while the particles in the rocket are normally liquid or partially liquid. The impact mechanics are not obviously the same over the potential range of impact velocities. Furthermore, particle sticking will lead to surface shielding which will also alter the impact mechanics. Sticking is believed to depend on a number of special factors which include chemical interaction, wall temperature and surface character effects.

More sophisticated modeling techniques are required to simulate the particle injection and stratification effects associated with internal burning grains. The flow field visualization techniques developed in the NASA study offers real promise, provided that combustion transient, flow turbulence and variable burn rate effects can be neglected. However, there may not be a more practical or accurate way to understand the specific flow field character associated with complex grain and nozzle geometries. In this case, two-phase flow effects may be of secondary importance.

Ultimately, the object of cold flow modeling is to produce quantitative data for direct use in motor insulation and nozzle design or failure diagnosis. The results of the present program suggest that (1) high impingement rates, (2) incomplete combustion induced increases in exhaust corrosivity, and (3) locally extreme convective heat transfer and wall shear will all occur in approximately the same areas of the aft closure or nozzle

entrance section. It should be expected that correlations of cold flow impingement data with actual insulation erosion profiles can be established and used in design. It should be recalled that the particle impingement is not necessarily the primary cause of high local erosion. Fortunately, it appears that corrective redesign would be effective even if impingement is not the primary surface regression mechanism. Cold flow modeling may profitably be used as an aid to visualizing the interaction of the exhaust flow with the motor/nozzle walls. The results could be directly used in an empirical manner to adjust the grain/motor design, to indicate potential areas of high erosion or to diagnose failures.

d. (C) Correlation Studies

It was expected at the outset of the program that a significant amount of data could be obtained from the results of other beryllium motor programs. Motor designs and test data were acquired from contract reports prepared by Aerojet Gene .1, Atlantic Research, Hercules and Thiokol. From the veiy large number of tests considered, only a few groups could actually be used for correlation purposes.

There was a serious lack of nozzle thermal response, deposition, erosion and/or ballistic performance data. The majority of the test data acquired in this effort has not been published under this contract and is regarded as being of little general value. Some of the erosion data was used in establishing the aft closure insulation designs used in this program. A few specific observations concerning data quality and trends were discussed in Section 4.2 of References 1 and 2. The more successful correlation efforts are reviewed below.

Atlantic Research 10-pound tailoring motor tests, with propellants similar to those used in this program, were examined in detail (see Pages 184 to 189, Reference 2). Analysis of the test data indicated that throat deposition effects were almost negligible. Then, the throat heating and corrosion were assumed to depend only on motor pressure and propellant type. The total measured throat erosion was then plotted against average motor pressure. The Arcocel 191 and 319B propellant data (Figure 93, Reference 2) correlated with the average chamber pressure raised to a power slightly less than 0.8 over a pressure range of 400 to 1600 psia. Such a power dependency is predicted from corrosion theory. This tends to rule out mechanical or physical erosion. The throat corrosion rate was close to zero at 400 psia (2.5-seconds duration) which suggests that both deposition and surface temperature effects would have to be given some consideration in a more rigorous analysis. Throat deposits were retained on one test of less than 0.5-second duration.

Similar treatment of the Arcane 24, 53, and 54 composite propellant data gave an interesting result. Above 700 psia, the throat corrosion rate also exhibited an 0.8 power dependence on pressure (data to 1020 psia). However,

entrance section. It should be expected that correlations of cold flow impingement data with actual insulation erosion profiles can be established and used in design. It should be recalled that the particle impingement is not necessarily the primary cause of high local erosion. Fortunately, it appears that corrective redesign would be effective even if impingement is not the primary surface regression mechanism. Cold flow modeling may profitably be used as an aid to visualizing the interaction of the exhaust flow with the motor/nozzle walls. The results could be directly used in an empirical manner to adjust the grain/motor design, to indicate potential areas of high erosion or to diagnose failures.

d. (C) Correlation Studies

It was expected at the outset of the program that a significant amount of data could be obtained from the results of other beryllium motor programs. Motor designs and test data were acquired from contract reports prepared by Aerojet General, Atlantic Research, Hercules and Thiokol. From the very large number of tests considered, only a few groups could actually be used for correlation purposes.

There was a serious lack of nozzle thermal response, deposition, erosion and/or ballistic performance data. The majority of the test data acquired in this effort has not been published under this contract and is regarded as being of little general value. Some of the erosion data was used in establishing the aft closure insulation designs used in this program. A few specific observations concerning data quality and trends were discussed in Section 4.2 of References 1 and 2. The more successful correlation efforts are reviewed below.

Atlantic Research 10-pound tailoring motor tests, with propellants similar to those used in this program, were examined in detail (see Pages 184 to 189, Reference 2). Analysis of the test data indicated that throat deposition effects were almost negligible. Then, the throat heating and corrosion were assumed to depend only on motor pressure and propellant type. The total measured throat erosion was then plotted against average motor pressure. The Arcocel 191 and 319B propellant data (Figure 93, Reference 2) correlated with the average chamber pressure raised to a power slightly less than 0.8 over a pressure range of 400 to 1600 psia. Such a power dependency is predicted from corrosion theory. This tends to rule out mechanical or physical erosion. The throat corrosion rate was close to zero at 400 psia (2.5-seconds duration) which suggests that both deposition and surface temperature effects would have to be given some consideration in a more rigorous analysis. Throat deposits were retained on one test of less than 0.5-second duration.

Similar treatment of the Arcane 24, 53, and 54 composite propellant data gave an interesting result. Above 700 psia, the throat corrosion rate also exhibited an 0.8 power dependence on pressure (data to 1020 psia). However,

as the pressure fell below 700 psia, the throat erosion rate increased at a rapid rate (to the minimum test pressure of 550 psia). The Arcane 24 propellant has a higher oxidation ratio and deposits protected the throat from erosion. These data suggest a progressive decrease in metal combustion efficiency as the pressure falls below 700 psia (1.0 mil/sec minimum erosion rate over 4.6 seconds). The data generally supports the qualitative metal combustion model. The chamber residence times (to the nozzle throat) were slightly greater than 3 milliseconds at the low pressures and approached 5 milliseconds at the higher pressures. It is suspected that the double base propellants would exhibit similar behavior at pressures below about 400 psia (residence times below about 1.5 milliseconds). Similar relations might be observed for any propellant which experienced surface agglomeration. When metal agglomeration occurs, the minimum erosion rate will occur at a chamber pressure which is inversely proportional to both the flame temperature and the oxidation ratio. If agglomeration does not occur, complete combustion may occur in less than a millisecond for all practical pressures. Shorter residence times would be a difficult condition to produce experimentally over significant test durations.

Sections of a silver infiltrated tungsten ring tested in the Atlantic Research PALLAS program were examined (see Pages 225 to 226, Reference 3). The ring had been located upstream of the nozzle throat section. Extensive flame-side surface melting and flow had occurred. X-ray diffraction analysis of the damaged areas showed large amounts of tungsten carbide. No beryllium alloys were detected. Some silver was found at the back side surface of the ring segments. Evidently, the depletion of the silver infiltrant permitted direct exposure of the tungsten to the upstream source of carbon. This particular insert indicates that the carbide degradation mechanism pertains to the powder metallurgy tungsten products as well as to the dense forms. Of course, infiltrants should be at least partially effective in preventing exposure of the flame-side surface to the carbon source. There has been no correlation of the predicted aluminum or beryllium alloying degradation mechanism with the post-test analysis of tungsten inserts examined to date. Since several metal sources have been identified, this problem should be examined further.

Nozzles tested on the Aerojet ADOBE program were visually examined and photographed. Several of the photographs and a discussion of the general appearance of these nozzles may be found on Pages 125 to 133 of Reference 4. The primary nozzle throat materials were silver infiltrated tungsten, pyrolytic graphite and Graph-i-tite GX. The performance of the thick tungsten inserts and entrance caps was generally good. There was no indication of extensive carbide formation or excessive silver depletion. Both silver and metal oxide deposition protection are believed to be partly responsible for this result. The Graph-i-tite nozzle was also in good condition. This is believed to derive from the sacrificial ablation of the plastic entrance section material and oxide deposition. The pyrolytic graphite nozzles were severely eroded. This probably derives from the

development of extreme thermal expansion stresses at the surface, leading to plastic deformation of the washer edges and nodule spallation. Nozzle heat transfer and deposition data were not available. The general performance of these nozzles appears to correlate well with the qualitative models developed in this program.

Ballistic data for nozzles tested on the Thiokol ADOBE program were analyzed to develop throat deposition/erosion curves. Five tests, each with a different throat heat sink design, were selected. The results are presented and discussed in Section 4.2 of Reference 4. Deposit histories (see Appendix V) were generally similar to those developed for the nozzles tested in this program. This is taken as an indication that nozzle/motor scale effects will not reverse or nullify the results of the present program. The deposit histories correlated well with the throat heat sink capacity. The thick tungsten and pyrolytic graphite washer inserts exhibited the highest deposit thicknesses, the thin tungsten insert and Graph-i-tite inserts gave intermediate results, and the pyrolytic graphite shell permitted only thin (probably liquid) beryllia deposits to develop.

The Thoikol nozzle throat erosion rates were generally consistant with expectations. The tungsten did not corrode or erode. The thick insert experienced significant plastic deformation during the test while the thin insert deformed after the test. The Graph-i-tite erosion was near 5 mils/sec late in the test and somewhat less during the middle third of the test after deposits were removed. Nonuniform and diminishing flow of beryllia following the main deposit pulse would explain this. The pyrolytic graphite throat washer erosion rate was highest after deposit removal and decreased with time. Surface spallation and washer deformation probably occurred after deposit removal, accounting for the higher initial erosion rate (the hardware was not examined). The average rate was near 2 mils/second. The pyrolytic graphite shell evidently eroded mechanically (about 10 mils/sec) after the loss of the protective deposit film. The erosion rate decreased steadily until the HLM85 substrate was exposed. The decreasing rate suggests that the erosion tended to relieve material stresses which caused the surface layers to break down.

Efforts to obtain erosion, heat transfer and deposition data for aluminum propellant tests were equally unsuccessful. However, from experience and available test data, it is apparent that motor/nozzle materials grossly behave in the same manner with either type of propellant. It is clear that motor, grain and nozzle design have a strong influence on materials behavior in either propellant system. It is obvious from the available data that beryllium propellants do not always lead to more corrosion than aluminum propellants, even in identical motors. Metal combustion efficiency, heat transfer and oxide deposition effects offer reasonably complete explanations for observed performance variations in the two propellant systems.

-35-

e. (U) Analytical Technique Development

A significant fraction of the program effort was devoted to the development of improved analytical techniques for predicting and characterizing nozzle performance. The major emphasis was placed on the convective heat transfer, corrosion rate prediction and oxide deposit flow characterization. The influences of two-phase flow, incomplete metal combustion, wall roughness and boundary layer injection on these fundamental processes were considered in a more qualitative manner. A great deal of progress was made but further development of the theories and correlation with test data are still desired.

Sections II and V of References 1 through 4 contain extensive descriptions and discussions of the analytical technique developments. Section IV of this report is devoted exclusively to summarizing the philosophy and method of nozzle design and performance analysis as developed in this program. However, a few brief comments are pertinent at this point.

(1) Convective Heat Transfer

Program efforts to improve nozzle convective heat transfer theory were based on the belief that commonly used analyses, typified by the simplified Bartz Equation (Reference 6), significantly underestimate convective heating by high energy propellant exhausts. It was argued that this would be a direct result of misapplication of the theories developed for and evaluated in low performance nozzle systems. Although a detailed boundary layer analysis should be performed in general, the advantages of closed form equations cannot be easily ignored. The real danger in using such equations is that the inherent assumptions and approximations are not obvious. The nature of high energy propellant exhausts demands the use of enthalpy driving potential and the inclusion of chemical wall reaction, blowing and surface roughness effects, as opposed to using a temperature potential and ignoring the other effects.

The objective of this discussion is to show why the closed form convective heat transfer equations appear to work as well as they do and to indicate when they will not work. To begin with, high energy propellants necessarily must exhibit high ratios of flame temperature to exhaust molecular weight. In practical systems, a relatively large fraction of the total energy is accommodated by dissociation of molecular species and vaporization of condensed products. In fact, this is what limits the propellant flame temperature and makes temperature gradient an inadequate measure of heat transfer potential. To include the exhaust energy that does not appear as temperature, an enthalpy potential may be used directly or the temperature potential may be used in combination with an appropriate exhaust specific heat. Chamber values, either frozen or equilibrium, of the exhaust specific

heat should not be used. The appropriate value, for first approximations, is the average boundary layer specific heat at the particular axial station of interest. Thus:

$$\left(\bar{C}_p\right)_x = \left(\frac{H_o - H_w}{T_o - T_w}\right)_x$$

where:

$\bar{C}_p$ = average boundary layer specific heat

H_o = boundary layer edge stagnation enthalpy

H_w = exhaust stagnation enthalpy at the nozzle wall

T_o = boundary layer edge stagnation temperature

T_w = exhaust stagnation temperature at the nozzle wall

x = reference axial location

The above equation permits the user to establish convective heat transfer coefficients as a function of local nozzle wall temperature as required in the nozzle conduction analysis. Note that T_o is dependent if the local pressure while H_o is not. Both H_o and T_o may be replaced by the appropriate recovery values if desired. Of course, the conventional convective heat transfer coefficient is linearly related to $\bar{C}_p$ as long as the film reference condition is acceptable. At low wall temperatures, $\bar{C}_p$ is weakly dependent on surface temperature. At high wall temperatures, it depends strongly on wall temperature.

Now, the local convective heat flux can be written as:

$$(q)_x = \left[(h/\bar{C}_p) \, \bar{C}_p \, (T_o - T_w)\right]_x$$

As expressed in the simplified Bartz equation, the convective coefficient $(h/\bar{C}_p)$ depends on wall temperature due to the variation of boundary layer density and viscosity. Since, the chamber values are used for reference, the value of $h/\bar{C}_p$ steadily increases as the surface temperature drops below the stagnation value. With the added temperature dependence of $\bar{C}_p$, a plot of h against wall temperature will have a "U" shape. A plot of q against wall temperature will have a more complex shape. Initially, q will decrease; then it will level out; finally it will decrease again as $(T_o - T_w)$ approaches zero. In the "flat" zone, q may actually rise slightly as the wall temperature increases.

Because they contain large amounts of hydrogen, high performance propellants will exhibit a wide range of species molecular weights. As shown in Section 2.2 of Reference 4, this will depress the Prandtl number to values near 0.5. Since such values are well below unity, the conventional power dependence of h on Pr must be replaced. The low Prandtl numbers lead to increased values of h compared to results using values near unity. This increase is roughly independent of wall temperature. At this point, it should be realized that the value of h/C_p pertains to either (1) a hydraulically smooth wall, or (2) a particular wall roughness if an empirical constant has been introduced. The convective coefficient increases as the wall roughness and gradually becomes independent of the local Reynold's number.

Incomplete combustion of metal additives will decrease $\bar{C}_p$, H_o and T_o while h/C_p will be relatively unaffected. The net effect will be a reduction in q. If wall deposits are present (especially beryllia), the value of T_o may approach T_w because of the oxide insulation effect. Thus, very large reductions in heat transfer may be associated with poor combustion. Deposition alone will also reduce the heat transfer, since it always forces T_w to higher values than would otherwise prevail.

Chemical reactions at the nozzle surface will have several effects. The common reactions are endothermic. This will tie the surface temperature rise directly to the corrosion rate. The corrosion reaction product mass injection (blowing) effect will favorably distort the boundary layer mechanical structure. Finally, the change in boundary layer species concentrations will alter $\bar{C}_p$, viscosity and Prandtl number. The reaction heat absorption and blowing effects probably dominate in reducing the heat flux. The reaction heat effect should be included in defining the enthalpy driving potential.

The injection of insulation pyrolysis gases into the boundary layer may also reduce the heat transfer. Low insulation surface temperatures and high ablation rates will introduce potentially significant film cooling. Reactions between the exhaust and pyrolysis gases are likely to be endothermic for most plastics in common use. Again the boundary layer composition and corrosion reactions may be altered significantly.

Under some circumstances, the combination of the above effects could be cancelling in nature. This may be especially true if measured heat transfer coefficients or heat fluxes are averaged over the entire test firing. However, the combination of poor combustion and deposition (many composite propellants) may cause the actual heat transfer to be far below expectations. Conversely, high flame temperatures, good combustion, no deposition and a rough wall can lead to higher actual heat transfer rates than predicted. In the latter case, high corrosion rates will oppose the other effects. Note that graphite corrosion will normally be more effective than tungsten in this respect. However, tungsten may remain smooth compared to the graphite because of its superior microstructure (physical erosion resistance).

There are some applications when the closed form nozzle convection equations cannot be used directly. A good example is the plug nozzle system. However, they are also not useful in the motor aft closure region or in the vicinity of flow stagnation or separation regions anywhere along the nozzle contour. In these cases, boundary layer development analyses should be used. Note that no restriction has been placed on the type of chemical propulsion system. The use of a boundary layer analysis is subject, in general, to the same conditions discussed above as are the closed form equations. It is apparent that nozzles have and could continue to be doomed to failure simply because the heat transfer was underestimated. In some cases, the degree of error may be greater than a factor of 2. The less extreme cases are believed to involve error factors in the range of 0.5 to 1.5, with the average being relatively close to unity. Because of the dominance of the surface roughness and surface temperature effects (which are resisted primarily by the corrosion and blowing effects), average convective heat transfer coefficients will appear to increase as the firing time increases. There is a great danger in using correlations and data from short time firings, whether or not deposition protection is involved. The accurate prediction of heat transfer with unrealistic analyses is simply the result of the cancellation of neglected effects.

(2) Corrosion Rate Theory

Corrosion of nozzle contour materials is the limiting surface degradation mechanism in the absence of the more spectacular mechanical failure mechanisms. The prediction and measurement of corrosion rates of graphite materials is a matter of major interest. The present discussion is also restricted to gas-solid reactions with all gas products. However, the principles can be extended to other materials and types of reactions if desired.

The gas solid reactions of interest proceed via a series of five steps, namely:

(a) Transport of the reactive gas species to the graphite surface,

(b) Absorption of the reactive species at a potential surface reaction site,

(c) Reaction,

(d) Desorption of the product gas(s),

(e) Transport of the products away from the reaction site.

Because the system is essentially in steady flow, mass storage effects can usually be neglected. Regardless of the rates of reactant and product

transport rates, the chemical potentials will act to establish a local
equilibrium concentration at the gas-solid boundary. If this condition is
closely approximated, the rate of consumption of the wall material will be
entirely determined by the rate at which the reactants are transported to
the wall or the rate of product removal. In the event that the adsorption,
desportion or reaction steps are slow, the capacity of the surface to react
may be less than the capacity of the system to transport the reactants or
products. In this case, corrosion is said to be limited by chemical kinetics
as opposed to being mass transport limited. When kinetics pertain, the con-
centration of the reaction products (at the gas-solid interface) will be
less than (and the reactant concentrations more than) if local thermochemical
equilibrium pertained. Note, that the mass transport processes must continue
in a steady flow system regardless of kinetic limitations. The mass transport
limited case implies local thermochemical equilibrium and maximum corrosion
rat .

When kinetic limitations pertain, empirical information must be available
concerning the capacity of the surface to react as a function of reactant
and product concentrations. Consequently, the mass transport rates must
also be determined, in general, to find the appropriate reaction site con-
centrations. Similarly, the problem of determining the composition of the
gas phase adjacent to the wall is a simple matter, provided that the elemental
composition, temperature and pressure are known. Again, the boundary layer
mass transport processes must be characterized to find the elemental
compositions.

Reactive and reaction product species flow with the other exhaust components
a ng the gas streamlines which approximately parallel the nozzle contour.
As a result of the reactions at the gas-solid interface, the concentrations
of the species involved change with respect to their concentrations at some
distance from the wall. The differences in these concentrations are driving
potentials for ordinary molecular diffusion (pressure and thermal diffusion
may also occur). The transport of molecular species occurs in the direction
of the gradient and, usually, in the wall normal direction (across flow
streamlines). Because of the fundamental similarity of molecular diffusion
to energy and momentum diffusion, the process is of the boundary layer type.
In fact, under certain specific conditions, the thermal, velocity and con-
centration boundary layers are mathematically identical. It is possible then
to calculate the mass transfer in the same manner used to find the convective
heat transfer and wall shear. Strictly speaking, the idea of concentration
gradient induced molecular diffusion applies only to the laminar flow case.
When the flow is turbulent, bulk or eddy diffusion dominates. However,
the transport of energy and momentum occurs in the same manner and the
processes remain similar. Large, uncooled nozzles will have turbulent boundary
layers. Thus it is reasonable to proceed to calculate reactive specie and
product mass transport using turbulent boundary layer theory.

A relatively advanced mathematical model of the boundary layer diffusion mass transport has been described in Reference 4 (Pages 11 to 23). This model includes the improvements in the convective boundary layer theory. It also is shown how the general results reduce to the simpler forms described in Section 2.2 of References 1, 2, and 3. Since the advanced analysis was not programmed, it is not presented here. However, several comments are pertinent. First, it should be observed that the wide variation of molecular weights of diffusing species negates the simplifying assumption that all specie mass transfer coefficients are equal. Further, since each chemical reaction absorbs or releases different amounts of heat energy, an average mass transfer coefficient can usually not be defined. The diffusion of species at different rates, necessarily alters the elemental concentrations at the reaction site relative to that obtained by saturating the undisturbed exhaust with wall material (normal B value calculation). Consequently, corrosion rate predictions which depend on unity or average boundary layer Lewis numbers should be treated as coarse estimates only. The program test results make it emphatically clear that oxide deposition, poor metal combustion and chemical reaction heat effects should be appropriately treated in estimating the convective heat transfer coefficients used to predict corrosion rates.

There are a number of practical situations for which the advanced corrosion theory will not apply. In general, this occurs when the initial and/or boundary conditions for the momentum, energy and mass transport processes are not similar. Changes in wall material (including deposits) along the flow path, foreign gas injection and variation in contour temperature violate the initial condition similarity requirement. (Note that the coupling of all the transport processes causes errors in the heat transfer and skin friction predictions when such changes occur.) A good example of this situation involves a tungsten throat insert preceded by a graphite inlet section. Instead of being exposed to only the propellant exhaust, the upstream edge of the tungsten also sees the acetylene product of the carbon-hydrogen reaction. The acetylene will react with the tungsten, forming condensed carbides and hydrogen. The acetylene will diffuse both toward and away from the tungsten surface until it is completely consumed or passes beyond the tungsten. The tungsten carbide will tend to melt and flow downstream, dissolving more tungsten. This process will continue as long as a fresh supply of carbon-hydrogen reaction products is available.

A similar situation can arise when pyrolytic graphite is preceded by polycrystalline graphite. The inlet section is likely to have higher surface temperatures than the throat. Especially if the pyrolytic graphite kinetically resists reaction with hydrogen (relative to the polycrystalline graphite), an excess of acetylene will flow over the throat section. In this case, the acetylene will prevent or retard the hydrogen reaction relative to corrosion model predictions. On the other hand, the inlet section may be coated with an oxide deposit. Then the boundary layer will be deficient in acetylene and rich in oxidizing species. Even though the

boundary layer development has been otherwise normal, the corrosion rates just beyond the deposit edge will be very much higher than predicted. The injection of hydrocarbon pyrolysis gases can also lead to two direction diffusion with carburization of tungsten and protection of graphite.

The breakdown of the transport similarity assumptions should not be confused with boundary layer starting effects. Thus stagnation point, boundary layer separation, surface roughness and free stream turbulence have a common effect on the transport processes. The problem here is to anticipate the increase in the transport coefficients associated with those effects. Another potential problem involves the question of reaction kinetics. The requirements for obtaining accurate data for the hydrogen and nitrogen reactions with graphite and the correct use of that data should be obvious (see References 8 and 9). There may also be a problem with the boundary layer gas phase reactions. Thus, the recombination reactions and the reaction of acetylene with oxidizing species are potentially subject to kinetic rate controls. Note that the C_2H_2 reactions with H_2O and CO_2 may eliminate wall oxidation while only slightly accelerating the C_2H_2 formation rate. This, along with inaccu. e diffusion analysis, could be mistaken for hydrogen-carbon surface reaction kinetics.

A significant gain in the understanding of the solid rocket nozzle corrosion mechanics has been made. Coupled with the improved mathematical models for convection and diffusion, it should now be possible to improve the accuracy of nozzle performance predictions. Ultimately, it is also necessary to accurately characterize the nozzle deposition. Eventually, it should be possible to improve the performance of nozzle throat materials by taking appropriate advantage of deposition, pyrolysis gas injection and sacrificial corrosion.

(3) Oxide Deposition

A qualitative model of the wall deposit flow process was formulated and is described in Section 2.5 of Reference 1. A preliminary analytical model is described in Section 2.5 of Reference 4. This model considers the transient heat transfer to and through the deposit, as well as the viscous transport of the molten material along the nozzle wall. The only attempts to carry out a numerical example were frustrated by mathematical instability.

The deposition process is necessarily a transient one. The particle impaction rate will probably change considerably with time due to transients in the propellant combustion process and chamber flow field variation. Then, sticking of the particles may depend both on the impaction parameters and the specific temperature or physical condition of the surface. Apparently, the transient thermal response of the nozzle wall materials has the most pronounced effect. As long as the nozzle surface temperature remains below the deposit melting point, some of it will be solid. The deposit thickness will normally be made up of the solid layer and a liquid layer. The

thickness of the solid layer will gradually decrease for heat sink designs.
The liquid layer thickness will depend on the melting rate, and flow from
the upstream source, the local impingement rate, the oxide viscosity,
oxide conductivity and local gas shear. Basically, the nozzle will accumu-
late oxide as long as it can be frozen along the contour. Once the deposits
are completely melted, they will flow away faster than new material can be
impinged. Apparently, the endurance of the deposits can be extended in
time by nozzle cooling and, to a lesser extent, by increasing the deposition
rate. The retention of alumina for long periods would be impractical com-
pared to beryllia. However, alumina deposition is not necessarily negligible
in terms of its effects on heat transfer, corrosion and ballistic perform-
ance, particularly in small nozzles and short tests.

The analytical technique using measured thrust and pressure (see Section 5,
Reference 4) is recommended for determining the nozzle throat deposition
erosion history. Several other techniques were also used in the program
and are described in Section 5 of Reference 2. The resulting variation in
nozzle throat area can be used directly in the evaluation of ballistic
performance efficiency. In design, the predicted variation in throat area
should be used to find the chamber pressure history. For small nozzles,
deposition can cause major excursions in chamber pressure and significant
variations in burn time.

    f. (U) Program Demonstration Phase

A demonstration of some of the analytical techniques developed in this
program was conducted at the completion of the rocket motor test phases
The motor selected for this purpose was the X259-C2, designed and built by
Hercules Incorporated under Contract AF04(694)-762 sponsored by Ballistic
Systems Division, Norton Air Force Base, San Bernardino, California. The
motor uses the Hercules VID propellant and a Graph-i-tite G-90 submerged
nozzle. The study was limited to the prediction of the graphite nozzle
thermal and chemical response and the motor pressure history. A variety
of cases were calculated to illustrate the importance of deposition and
chemical reaction kinetics.

The results of the study were summarized in a report which was distributed
only to the Air Force and Hercules Incorporated. The X259-C2 motor test
had not been conducted at the completion of the program technical perform-
ance period. Since the predictions cannot be compared with actual results,
the demonstration study will not be described here. The objectives,
approach and a brief description of the analytical results may be found in
Reference 4, pages 207 to 210.

    g. (U) Industrial Hygiene and Safety

An extensive industrial hygiene and safety program was formulated and
carried out in support of the laboratory studies involving toxic materials.
The plan and results are described in Sections 6 of References 1 through 4.
Section 5 of Reference 4 is a final summary report for the Industrial
Hygiene Program.

3.3 (U) ROCKET MOTOR TEST OBJECTIVES AND DESIGN

a. Test Objectives

A series of 29 motor test firings were conducted during the program. Each test involved the change of at least one basic design parameter. The objective of this approach was simply to produce a maximum amount of detailed data concerning the effect of major design parameters on nozzle performance. The design parameters selected were:

(1) Propellant formulation,

(2) Grain design,

(3) Motor configuration,

(4) Nozzle configuration,

(5) Nozzle materials,

(6) Nozzle scale.

The small motor test series (designated T-1 through T-25) were conducted with 1 to 1-1/4 inch nozzle throat diameters, nominal pressure of 800 psia and nominal burn time of 20 seconds. The second major series (designated T-51 through T-54) were conducted with 2.4 inch throat diameters and 25 second nominal burn times. In each test, the nozzles were designed to reach throat surface temperatures in the 5000 to 5500°F range to simulate longer firing times.

The motor tests were grouped according to the major design parameters under investigation. The objective of the first seven tests, designated T-1 through T-7, was to produce baseline heat transfer and corrosion data representative of complete metal combustion for each of the program propellants. Tests T-5 through T-8 used aluminum analogs of the four beryllium propellants tested in T-1 through T-4. The objective of the analog tests was to provide a direct comparison of the heat transfer and corrosion mechanics between the two metal additive systems.

Tests T-8 through T-11, T-14 and T-15 featured major grain design changes, with internal variation of propellant formulation, relative to the design used in Tests T-1 through T-7. Tests T-12 and T-13 featured the first significant variations in nozzle configuration. Tests T-16 through T-20 featured the variation of nozzle materials with an otherwise standard motor/nozzle configuration. Tests T-21 through T-24 were deliberately designed to achieve poor metal combustion for three beryllium propellants and two nozzle configurations. The objective of Test T-25 was to demonstrate the influence of nozzle heat sink capacity on nozzle deposition, heat transfer and corrosion.

The development motor tests, T-51 through T-54, featured a change in nozzle scale. The nozzle materials and propellant formulation were varied within this series. Tests T-51 and T-53 featured a variation in degree of nozzle submergence. Test T-52 featured a change in propellant and the nozzle material was changed on Test T-54. The nozzles in this series were also designed to reach temperature levels characteristic of long firing times relative to the nominal test duration.

The measure of success, in terms of the achievement of the test objectives, was necessarily more complicated than in propellant development programs. Basically, it was required that reasonably accurate nozzle thermal response, deposition and corrosion data be obtained on each test. Further, it was required that ballistic and photographic data be obtained for each test. It was also required that the hardware be recovered from each test, without unnecessary decontamination, for detailed physical and chemical examination. Specific nozzle erosion or motor ballistic performance goals were not established as a measure of test success. The maintenance of overall nozzle/motor integrity was regarded as a basic requirement.

The remainder of Section 3.3 describes the detailed design of the motors tested in this program. Specific design data has been accumulated in Appendix I and II. Table III of Appendix I presents a summary of the design parameters and nozzle materials by motor test for easy reference. Section 3.4 and 3.5 will subsequently describe the test results and the post test analysis results, respectively. These results are discussed in Section 3.6 in terms of the achievement of the test objectives. The interpretations of the test results are also reflected in the other sections of this report.

b. Propellant Formulations

The philosophy of propellant selection was discussed in Section 3.1.a. The actual formulas are given in Appendix I for the 4 beryllium and 3 aluminum propellants. The tests in which each propellant was used are indicated with the formula. It is emphasized that the propellants were tailored for use in this program. Consequently, they are not standards in any sense.

c. Grain Design

Cross-sectional views and dimensional data for the five grain designs used in this program are given in Appendix I. The designs were developed specifically for use in this program. The grain configuration merely provided the means of achieving the desired exhaus flow field characteristics. The tests in which each design was used are indicated on the cross-sectional views.

The 600-pound Aerojet ADOBE motor cases were used in all tests. This imposed limits on the grain diameters and lengths. In the process of developing the

-45-

grain designs, it was found that limitations were also imposed on the specific choice of configuration. Consequently, it was not possible to achieve all of the potentially desirable grain design/flow field effects. Although the grain designs were frozen as late in the program as possible, there was no opportunity to effect changes after evaluation of the motor test results.

The end burning grain design was selected for the basic propellant/nozzle performance Tests T-1 through T-7. The objectives were to achieve neutral burning and a highly uniform flow field. The grain was located approximately 24 inches from the nozzle throat to achieve very large chamber residence times and a reasonably small percentage variation of the residence time over the firing period. This same design was also used in Tests T-21 through T-24. For these tests, the grain was translated 12 inches aft to shorten the initial chamber residence times to essentially zero at the aft closure outer diameter. The residence time relative to the nozzle throat was also reduced to about half the original value. Significant changes in the residence times over the test period were unavoidable.

The Type I grain design was developed to achieve neutral burning and circumferentially uniform flow with the simplest internal burning configuration. The circular port diameter was a maximum value for the ADOBE motor without altering the common grain burn rate established for all tests. The relatively low flow velocity associated with the 7-inch port presumably minimized the possibility of dramatic insulation or nozzle materials failure. This design was tested first to determine its suitability for use in the succeeding nozzle material tests, T-16 through T-20 and T-25. The design was used in Tests T-9, T-11 and T-14 with three beryllium propellants for direct comparison with the end burning grain tests (T-1, T-3, T-4, T-21, T-22 and T-24) using those same propellants. All of the internal burning grains were to be bonded to the aft closure to preclude possible failures of aft end inhibitors. Aft end burning grain designs could not be evaluated with the limited number of tests available.

The Type II grain design was developed to achieve neutral burning and a simple type of circumferentially nonuniform exhaust flow. The circular port diameter was chosen to be the same as for the Type I grain to permit direct comparison of results. The termination of the single axial slot short of the grain O.D. and the slot width of 1 inch were established for convenience and to achieve nominally neutral burning. This design was used in Tests T-10 and T-8 with a beryllium propellant and its aluminum analog to extend the metal base comparison from the end burner to complex internal burning grain designs. The design was also used in Tests T-12 and T-13. Thus, with T-10, a comparison of three nozzle configurations was possible with all other parameters fixed. The variation of slot width, number of slots and slot shape could not be investigated with the number of tests available. It was generally assumed that such effects could be predicted from the results of the single slot test.

The Type III grain design was developed primarily to achieve a near maximum grain port velocity. It was expected that the Arcocel 319BRF propellant, because of its low oxidation ratio (XSO), would achieve low metal combustion efficiency in this design. Thus, T-14 and T-15 comprised an internal burning grain design pair likely to effect wide variation in nozzle materials performance. It was expected that the slotted Type II and Type III grain test results could be compared to find port velocity effects in non-uniform flow.

The 500-pound grain design was seriously restricted by the motor length which could not accommodate an extension of the Type I design. A scaled up version of the Type II design was selected. This selection was in part based on the observation from the small scale tests that submerged nozzles would tend to damp out the exhaust flow nonuniformities. The aft end of the 500-pound grain was designed to be compatible with the submerged nozzle and the aft closure insulator. The grain circular port diameter was 3.8 inches and the slot width was held at one inch. Except for the epoxy filler at the forward end of the grain, this design closely approached a reasonable volume fraction for this motor. It was believed that further increases represented a serious threat to achieving reasonable motor/materials performance.

All of the grain designs were nominally neutral. This requirement was imposed primarily to minimize the complexity of dealing with motor pressure variations in the post-test analysis of nozzle performance It was also expected that deposition effects would be more visible in the motor pressure trace with neutral grains. The grains were all designed for cartridge loading. This was done to accommodate the plan to conduct the tests at A.F.R.P.L. facilities while the grains were to be fabricated by Atlantic Research Corporation, Alexandria, Virginia. The grains were shipped in temperature controlled vans and subsequently placed in controlled temperature storage at R.P.L. Actual storage times were kept to a minimum since the grains were shipped in small lots just ahead of the motor test schedule.

　　　d. Motor Configurations

Schematic representations of the basic motor configurations for each test are shown in Appendix I. The excess volume in the forward end of the ADOBE motor case was filled with wood blocks. The end burning grains were installed in insulation sleeves which were bonded to the aft closure insulation during assembly. The internal burning grains were bonded to micarta or asbestos phenolic casting sleeves which were also bonded to the aft closure insulator during motor assembly. Asbestos phenolic plates provided base support and insulation in all tests. Aluminum and steel bearing plates were also used in the small motor tests. Thin aluminum spacers (forward of the asbestos plate) were used to accommodate grain length variations and to insure positive axial compression of all components after assembly of the motor.

-47-

The aft closure insulators were potted in place with RTV-60 to effect a good seal. Failure of the asbestos base plate o-ring seal on Tests T-1 and T-2 (near burnout) caused some damage to the ADOBE barrels. Redundant seals were added in this area to prevent further leakage. Otherwise, the o-ring seal proved to be sufficient to prevent pressurization of the forward section of the motors. The leakage experienced on Tests T-1, T-2 and T-13 and the corrective action taken are discussed in Section 5.2 of References 2 and 3. Other details of the development motor configuration (T-51 through T-54) may be found in Section 5.3 of References 3 and 4.

e. Nozzle Designs

Cross-sectional views of the nozzles tested in this program were presented and described in Section 5.2 of References 1, 2, and 3 and in Section 5.3 of Reference 3. These figures are included in this report in Appendix I. The critical dimensions have been added and the tests using each design are indicated. In all cases, the designs represent a simple approach to the use of the heat sink concept. The design of nozzle subcomponents was standardized as much as possible. To some extent the designs were limited because of the existing ADOBE aft closure bolt circle, the thermal instrumentation requirement and the aft closure insulation requirement. Initially, the aft closure insulation thicknesses were set to accommodate the maximum erosion experienced on other programs. Eventually the aft closures were made in two concentric parts, with only the section exposed to the flame being replaced for each test. The small nozzle expansion ratio was optimum for the RPL ambient pressure of 13.2 psia. This could not be done on the larger nozzles which were limited to an area ratio of 5.

The pyrolytic graphite heat sink nozzles were used in the majority of tests. This was done to take advantage of the low thermal conductivity in the axial direction. Thus, each washer acts somewhat like a calorimeter. This permitted the convenience of measuring temperature responses at the outer diameter of the washers. The outer diameter of the washers was held constant for the small motor nozzles except for T-25. The slight variations in nozzle throat diameters did not significantly alter the heat sink capacity. A significant change in radial washer thickness was introduced in the T-25 nozzle to clarify the effect of heat sink capacity on oxide deposit behavior.

The tungsten inserts used in Tests T-16 through T-19 were nominally identical. The design analysis indicated that these inserts would not be significantly deformed during the test. Based on the assumptions employed in the analysis, the tungsten insert used on T-54 was also safe. A secondary support ring was used in this test. This ring was broken into four segments during assembly. (Apparently this was not a cause of the failure which ultimately occurred.) The tungsten inserts used in the small nozzles were also cracked (not segmented) during manufacture. The axial cracks

apparently did not affect the insert performance. The tungsten inserts were installed in ATJ graphite support rings. The outer diameter of the ATJ rings was equal to that of the ATJ sleeve used with the pyrolytic graphite washer design. Roughly, then, the heat sinks were approximately the same, thermally, for both heat sink types.

Nozzles T-17 and T-20 utilized carbon cloth phenolic in place of the ATJ graphite in the entrance section of the conventionally contoured nozzles. This was done to examine the tungsten carbide formation effect (T-17) and pyrolysis gas film effect on pyrolytic graphite (T-20). Carbon cloth nose caps were used on T-12, T-18, T-19 and T-23, all of which were submerged. With the expectation that the details of the flow field induced erosion would be clearer, asbestos phenolic nose caps (instead of carbon cloth) were used on Tests T-51 through T-54. Asbestos phenolic was used to insulate the aft closure and nozzle holders in all tests, primarily because of its low cost.

The three nozzle contours (conventional, steep inlet and submerged) used in the small motor tests were chosen to establish a significant range in this design variable. Deep submergence of the small nozzle conflicted with the thermal instrumentation requirement and would have introduced unnecessary failure risks. This aspect of nozzle contour design was reserved for the larger nozzle Tests T-51 and T-53. These nozzles were submerged to approximately 10 and 15 percent, respectively (percent of grain burning surface behind the nozzle). Note that the T-23 nozzle is more deeply submerged than the T-12, T-18 and T-19 nozzles.

The thermal expansion allowance for the pyrolytic graphite washers was located between the first washer and the entrance section. The thermal expansion gap allowed for the washers to be heated to the design temperature (about $5000°F$) and for the residual char of the RTV-102 filler. The pyrolytic graphite washers were lightly glued with epoxy to facilitate machining. The washer stack was glued to the ATJ graphite sleeve which was also glued to the asbestos phenolic insulator. It was not expected that the glue would retard free expansion of the washers or contribute to the axial expansion allowance. Other nozzle components were glued together to provide rigidity. The joint between the nozzle and the asbestos phenolic aft closure insulator was filled with RTV-60 during motor assembly.

More detailed discussions of the nozzle designs and assembly procedures may be found in Section V of References 1 through 4. It should be noted that the designs are relatively rugged and somewhat conservative. However, it should be apparent that the designs could easily be converted to light or flight weight if desired. The nozzle inlet, exit cone and insulation design is approximately representative of a 40 to 60 second test duration.

f. Test Instrumentation

A detailed motor test instrumentation plan was formulated and carried out in support of the objective of providing maximum characterization of nozzle performance. Redundant thrust and motor pressure measurements were required. Condensed phase plume samples were obtained and motion picture coverage (3 or 4 views) were scheduled for each test. The major effort was devoted to measuring the nozzle thermal response and post-test soak down. The instrumentation plan and the specific problems which developed are dis-cussed in detail in Section 4.3 of References 1 through 4.

A relatively standard approach was taken in obtaining axial thrust and aft end pressure data. Extremely simple grab sampling techniques were used to capture condensed particles. The approach and technique used to obtain the thermal response data should be of general interest and concern. Con-sequently, the thermocouple designs, locations in the nozzles tested and a performance summary are presented in Appendix II.

g. Fabrication and Assembly

The general procedures employed in the fabrication and assembly of the motor insulation, nozzles, grains and motors has been described in Section V of References 1 through 4. A number of specific incidents involving near failure or failure of components are also described and discussed. Swelling of some plastic nozzle and grain insulation sleeves required minor rework of the part or motor. Marginal igniter design or poor igniter placement apparently precipitated the hang fires experienced on Tests T-6, T-24 and T-52.

The sealing failures experienced on Tests T-1, T-2 and T-13 were due to inadequate design or lack of seal refurbishment. Except for Test T-54, there were no major or minor failures which did not directly stem from design or assembly errors. The failure of Test T-13 was the only one which led to extensive loss of useful test results. The great majority of the tests were actually carried out with ut incidents and the tests met or exceeded design expectations.

The instrumentation plan was not carried out as successfully. Improper thermocouple installation at the test site, loss of camera coverage, plugging of pressure ports during assembly and premature shut down of data recording equipment seriously compromised the results of four tests. These problems and the consequences were discussed in detail in Section 4.3 of References 2, 3, and 4.

Considering that there were two component manufacturers involved and that a third party conducted the motor assembly and test, the overall test plan was reasonably effective. It is emphasized that the basic designs proved to be highly effective. In no case was a major or minor failure attributed

to unusual characteristics of beryllium propellants. Apparently then, relatively ordinary fabrication, bonding, assembly and sealin, techniques developed for aluminum propellant testing are equally applicab'₂ to beryllium propellants.

3.4 (C) MOTOR TEST RESULTS

   a.   (C) Post-Test Condition of Hardware

The tested motor components were disassembled and examined before and after decontamination operations. The nozzles, aft closure insulation, chamber liners, asbestos base plates and chamber residue were appropriately packaged and transported to Philco-Ford for post-test examination. The ADOBE motor components were decontaminated and reloaded at the test site.

Inadequate sealing at the base of the end burning grains on Tests T-1 and T-2 led to a partial burn through of the chamber wall. The extent of the damage did not prevent the continued use of the chambers after appropriate modification. On Test T-13, the potting compound, used to seal the aft closure nozzle bolts, failed or was missing. A leak through one of the bolt holes caused a dramatic failure of the aft closure/nozzle assembly approximately midway through the test. The steel aft closure could not be repaired. Pictures of the damage may be seen in Section 3.4 of Reference 3. On Test T-54, the ADOBE barrel and aft closure were partially burned. The damage occurred at the bonded joint between the asbestos phenolic grain sleeve and aft closure insulator at the end of the grain slot. Minor burning of the aft closure also occurred at the two pressure ports.

The internal motor insulation, grain filler blocks and grain casting sleeves were normally in excellent condition. There appeared to be more chamber residue associated with the four aluminum propellant tes₊₊ compared to the beryllium. Many of the asbestos base plates and aft closure insulators were decontaminated and reused. Photographs of the aft closure insulators, in the as received condition, may be found in Section 3.4 of References 2, 3 and 4. In general there was almost negligible erosion and charing of the asbestos. The only significant damage was caused in the tests using slotted grains. The slot flow caused relatively slight grooving of the insulator with the Type II and Type III grains. The depth of the grooves was much greater on Tests T-51, T-53, and T-54 with about 3/4 inch of material being removed. In contrast, only about 1/4 inch of material was removed on Test T-52 (hangfire). In the majority of these tests, a shallow groove was also formed in the aft closure insulator 180 degrees from the grain slot. The aft closure insulators from the end burning grain tests were extensively coated with oxide deposits. The portions of the insulator exposed to the exhaust flow in the internal burning grain tests were relatively free of deposits. The aft closure insulator from Test T-13 was badly eroded along the exhaust gas leak path, but was otherwise normal in appearance.

-51-

The post-test condition of the nozzles can best be visualized by examining the photographs in Section 3.4 of References 2, 3 and 4. As a rule, the entrance, throat and exit cone sections were coated with oxide deposits and/or carbon soot. It was normally possible to see the axial grooves in the nozzle inlet and throat sections (slotted grain tests). Damage to submerged nozzle nose cap and ATJ graphite entrance sections could also be seen. After sampling the nozzle surface deposits for chemical analysis, the nozzles were cleaned of loose deposits for closer examination. Throat diameter measurements were made before and after this process. Care was taken to ensure that all throat deposits were removed but it is possible that some pyrolytic graphite may also have been removed in the process. In most cases, it was difficult to remove the oxide deposits to examine the actual character of the nozzle surface.

Basically, very little information could be obtained through visual examination of the tested hardware. Removal of the carbon soot (pyrolysis gas cracking during cool down) exposed the oxide deposits. It is difficult to say whether the deposit appearance is actually representative of conditions during the test or not. The long cocking period and dissolution of gases during motor cool down probably caused some change in the character of the deposits. Aft closure deposits were thicker at the bottom of the motor and tended to be irregular with some beading. Entrance section deposits appeared to be denser and more uniform. The majority of the nozzle throats were relatively clean. A thick deposit was removed from the throat of the T-52 nozzle. It was sectioned and examined (see Figure 21, Reference 4). It had a layered structure and was highly porous The exit cone deposits varied considerably from one test to another, both in character and quantity. The beryllia deposits tended to be thicker at the bottom of the exit cone and as the area ratio increased axially. Often, narrow streams extended downstream of the main deposit and waves or ripples could be seen on the surface. Circumferential waves could also be seen in the tungsten insert throat deposits which were retained throughout the test.

     b. (C) Motion Pictures

High speed motion picture coverage of the firings proved to be quite useful in interpreting major failures, thermocouple performance and deposit expulsion characteristics. The plan called for an overhead axial view, an oblique and two normal views of the motor and exhaust plume. Approximately 60 percent of the desired footage was actually produced. For some of the early tests, no film was obtained.

The normal (90 and 270 degrees relative to the plume axis) views were useful in evaluating thermocouple performance. Leakage produced smoke which was visually traced to the appropriate thermocouple. Expelled thermocouples were also identified. Such poor thermocouple performance

was traced to poor installation practices. The leakage often stopped during the test and in no case caused damage to the nozzle or motor. The cause of failure on Test T-13 was clarified considerably as the films showed the initiation and growth of the leak. The normal views also showed that the plume fluctuated considerably during many of the tests. On Test T-22, the use of filters showed that exit cone detachment and condensed phase flow stratification were occurring. Other attempts to see through the plume at the nozzle exit were unsuccessful.

The overhead axial view was particularly dramatic for the firings conducted at night. Deposits were expelled in bursts at irregular intervals over the beryllium motor tests after an initial delay period. Again, the observed behavior of deposit expulsion correlated well with the calculated throat deposit histories (see Section 3.5). The circumferential uniformity of the bursts and the quantity of material expelled varied considerably. Evidently, the deposits came from two sources, the exit cone and the throat. The breakup of small portions of exit cone deposits produced relatively fine sprays confined to a small arc of the plume periphery. Larger amounts of liquid deposit apparently sheared away from the throat and flowed or rolled along the exit cone surface. The resulting bursts tended to contain spherical particles estimated to be up to 1/4 inch in diameter and involved relatively large plume arcs. Deposits sheared away from the wall in the process are believed to be the cause of observed plume flashes. Such droplets would be retained within the plume and not be directly observed. Their large size would probably precipitate shocks in the flow which would accentuate the magnitude of the flash.

These general characteristics of deposit expulsion are in complete agreement with the details of the pressure-thrust histories, the throat deposit histories and the post-test character of contour deposits. The aluminum propellants (limited movie coverage) did not produce significant deposit expulsion external to the plume. Similarly, only minor expulsion was observed for those beryllium firings in which there was very little throat deposition (calculated). It is reasonably clear that plume sampling and thrust measurement planning should consider the wall deposit expulsion, especially with beryllium propellants.

c. (U) Exhaust Plume Particle Sampling

A variety of extremely simple grab sampling techniques were used to collect plume particles. The performance of flat surface, dish and cup type samplers were evaluated on the early tests. These were combined in a single device (see Appendix II). Some glass slide samplers were also used. The majority of the tests were sampled with small glass bottles (one end open) mounted on a vertical post (see Appendix II). The samples were collected at a distance of approximately 50 feet from the nozzle. The glass bottles were used to collect particles at several elevations above the test pad. All sampling techniques provided quantities sufficient for analysis but none produced large samples. All of the program tests were sampled.

d. (C) Pressure-Thrust Measurements

Two pressure and two thrust measurements were planned for each motor test. The two sets of data were examined and evaluated separately. In many cases plugging of one pressure port occurred during the test. On Test T-20, both pressure ports were sealed during motor assembly and no data was obtained The two sets of thrust data did not normally precisely agree. In some instances calibration errors and thrust stand resonance were evident. The normal procedure was to use the highest thrust curve unless there was reason to believe that it was not valid.

The pressure and thrust data used in the post-test analysis are presented in Appendix III for all of the program motor tests. All of the ballistic data is also available in digital form. The pressure-thrust histories were previously presented in Section V of References 2, 3 and 4. It should be noted that the majority of the pressure traces do not approximate the nominal neutral design specification. This is basically a consequence of the nozzle throat deposition. The burn rate of the Arcocel 319BRF grains was somewhat higher than that of the others, giving rise to slightly higher than nominal pressure. Tests T-6, T-24 and T-52 were hangfires. Apparently ignition was marginal on the end burning grain Tests T-1, T-2, T-4 and T-5 due to the large free volume in the chamber. The greatest deviations from neutral burning occurred with the slotted grains. This is believed to have been a result of the radial flow stagnation along the grain surface opposite the slot. This flow essentially promoted the formation of a second (or mirror) slot with the result that the grains burned progressively during the first 10 seconds. There was no evidence that the grains or grain inhibitors had failed on these tests. Evidently, this type of erosive burning will occur whenever the exhaust generated in a slot must flow in a semiradial direction.

The irregularities in the thrust and pressure curves are believed to be real. They correspond to the deposit expulsions observed in the films of the firings. The magnitude of the spikes correspond well with the apparent amount of material expelled in a burst. When both the pressure and thrust curves reflect and expulsion, the material probably originated at or up- stream of the throat. When only the thrust trace reacts, only exit cone deposits are assumed to be involved. Further clarification of the deposit flow and expulsion would be possible with side thrust and motor weight measurements.

e. (U) Thermocouple Data

The measured thermocouple output data were converted to temperature and plotted for each nozzle test. Since this data cannot be interpreted directly, it has not been included in this report. Data for the first seven test: may be found in Section 2.5 of Reference 2. Data for the remaining small motor tests are given in the Appendix of Reference 3.

Data obtained for the development nozzles (T-51 through T-54) are presented in Appendix A of Reference 4. The location of the thermocouples in each nozzle may be determined by referring to Appendix II of this report or to Section 4.3 of References 1 through 4.

The quality of the data was assessed both by direct examination of the results and by post-test examination of the thermocouples. Thermocouples were destroyed during the failures on Tests T-13 and T-54. In other cases, the wrong type thermocouples were installed or were damaged during nozzle assembly (see Appendix II). Aside from the obviously bad data, much of the data could not be used for technical reasons. Thus, when a means of determining the oxide deposit thickness away from the throat is developed, the nozzle inlet and exit cone temperature data may be useful. In the near future, the measurement of temperatures at or near the throat station will be most useful. It should be noted that circumferential variations in temperature were measured in the slotted grain tests. Consequently, multiple throat temperature measurements would be recommended with slotted or star type grains.

3.5 (C) POST-TEST ANALYSES RESULTS

    a. (C) Visual Examination

Each nozzle was cleaned to the extent necessary to distinguish the character-
istics of the surface and to measure the throat diameter. The nozzles were
then sectioned axially and examined. The nozzles and insulation components
were photographed before and after sectioning. These photographs were pre-
sented in Section 3.4 of References 2, 3 and 4. The nozzle cross-section
views are also included in Appendix IV of this report. Both nozzle halves
are shown when there are significant differences in their appearance
(slotted grain tests). A few aft closure cross sections are included to
indicate the extent of insulation erosion and charing.

The most outstanding general observations were that most of the nozzles
appeared to be essentially undamaged and nearly half the nozzles had no
measurable throat regression. With only the few exceptions subsequently
noted, the nozzles which were undamaged and which suffered uniform surface
regression were tested with the end burning and Type I (circular port)
grains. The exceptions to the "perfect condition" and grain design general-
izations are listed below.

      (1) Pyrolytic graphite washer delaminations - observed
          in most tests, usually the upstream washers but
          sometimes only one washer at or near the throat.

      (2) Pyrolytic graphite washer cracks - the upstream
          washer split axially on Tests T-6 and T-7.

      (3) Pyrolytic graphite washer pitting - some very small
          nodule delamination pits were observed in the
          throat washers of the T-1, T-7 and T-9 nozzles, only
          at the top section of the nozzle.

      (4) Tungsten insert cracks - the axial cracks formed
          during machining developed axially and radially,
          several circumferential cracks appeared and surface
          erosion occurred along the major axial crack on T-17.

      (5) ATJ Graphite exit cone pitting - minor and randomly
          located pits were observed in the flame side
          surface of most of the exit cones.

      (6) ATJ Graphite entrance cone cracks - some of the
          entrance cones were radially cracked during the
          test or disassembly, usually forming three sections.

(7) <u>Carbon cloth delamination</u> - some delamination and post test deformation of the carbon cloth entrance cone and nose cap sections was observed (Tests T-17, T-18, T-19 and T-20).

(8) <u>Slotted grain tests</u> - the T-52 (pyrolytic graphite) nozzle throat section was unique among the slotted grain tests in that no throat regression or washer delamination occurred.

It can also be stated that the general appearances of the nozzles tested with the aluminum and beryllium analogs (T-1 through T-7) were exceedingly similar.

The condition of the nozzles tested with the Type II and III grains was strikingly different from the other nozzles in only one major respect. That is that axial grooves were formed in the aft closure insulator, nozzle inlet and pyrolytic graphite throat sections. Except for Test T-13, there were two grooves, one in line with the grain slot and the other 180 degrees from the first. These grooves were quite narrow (not more than the grain slot width). The depth of the two grooves was not the same and both tended to disappear with increasing distance in the flow direction. The groove surfaces were almost as smooth as the adjacent material. This is a strong indication that they were not caused by stress induced mechanical erosion. Actually, it is argued that the grooves were formed by corrosive action alone. On Test T-13, a third groove extended downstream of the point where the exhaust leak occurred. Although deeper, the character of this groove was similar to the others and is believed to have been formed in essentially the same manner. This third groove is obviously not related to the grain design in any way.

The grooves formed on Test T-8 (aluminum analog of T-10) were barely visible compared to the others. The Type III grain test (T-15) produced the deepest and narrowest grooves. Evidently, the three nozzle contours used in Tests T-10, T-12 and T-13 with the Type II grains only slightly influenced the character of the grooves. The submerged T-12 nozzle did not have a major effect. The groove formed opposite the Type II grain slot was the deeper of the two formed. The groove in line with the grain slot was deeper with the Type III grain.

The condition of the development test nozzles, T-51 through T-54, was relatively unique. Although the 500-pound grains were slotted similarly to the 100-pound grains, the nozzles were submerged significantly farther. The slot flow stagnation (radial) cut a slot through both the asbestos phenolic and ATJ graphite sections of the nose cap. Well over an inch of each of these materials was removed in the process. The slot in the ATJ section was not as wide as the grain slot. Extensive loss of the asbestos phenolic

portion of the nose cap permitted leakage under the ATJ ring near the
nose cap slot. Immediately adjacent to the slot in the ATJ ring, there
were relatively high spots (or ridges) followed by secondary grooves which
diminished with distance away from the ridges. The asbestos phenolic was
eroded almost completely away in the vicinity of the saddle shaped depres-
sions in the graphite ring. A very deep and fairly narrow groove was also
cut in the aft closure insulator in line with the grain slot.

Grooves, such as occurred in the small nozzles opposite the grain slot,
were formed, at least on T-54. They were extremely hard to see on the
other nozzles and did not extend into the nozzle inlet or throat sections.
A new kind of groove appeared on the T-51 and T-53 nozzles in line with
the grain and nose cap slots. It is believed that these grooves were a
direct consequence of the nose cap slot and, thus, only indirectly due
to the grain slot. It is believed that a groove was also formed in the
tungsten insert on Test T-54. Such a groove would have permitted buckling
and expulsion of the insert. Only slight grooving of the upstream pyro-
lytic graphite washer occurred in line with the nose cap slot on Test T-52.
This nozzle was still heavily coated with oxide deposits after the test.

The grooves in the T-51 and T-53 nozzles had three general characteristics.
First, the width of the affected area was much greater than in the small
nozzle tests. The affected area was also wider on T-53 than T-51.
Secondly, there was an axial ridge, in line with the original grain slot,
separating the damaged area effectively into two grooves. The third char-
acteristic was the extreme roughness of the damaged area. This is attrib-
uted to the spallation of surface nodules as the primary groove formation
mechanism. Evidently, considerable local surface smoothing and channeling
also occurred via corrosion. More massive spalling occurred in the first
two washers on T-53; the roughness tended to diminish in the flow and
circumferential directions on both T-51 and T-53. Extensive delamination
of the three upstream washers occurred on T-51. The throat and inlet
washer were slightly delaminated on T-53.

The ATJ exit cones were eroded in line with the nozzle throat grooves up
to one inch from the last pyrolytic graphite washer. Steps between the
two materials were not formed and maximum erosion occurred about 1/8 inch
from the pyrolytic graphite washer face. The surface damage was most
extensive for the T-53 and T-54 nozzles. There were only slight indications
of erosion on the T-52 exit cone and the T-51 nozzle was in an intermediate
condition. Exit cone surfaces opposite the nozzle groove areas were
relatively undamaged.

The tungsten insert was expelled during Test T-54. The motion pictures
indicated that the main insert left the nozzle and hit the test pad. The
insert was found near the end of the test pad about 60 feet from the
nozzle. The movies also showed the segments of the tungsten support ring

leaving the nozzle. This probably occurred after the main insert passed
the support ring. Only one support ring fragment was recovered as the
sections were projected well beyond the test pad. The one section recovered
was in very good condition. As may be seen from the photographs, the main
insert was extensively deformed while in a plastic state. By finding the
points where the thermocouples contacted the insert, it was determined
that the missing portion of the main insert was actually in line with the
grain/nose cap slot. Extensive melting and flow of the surface material
had occurred in this general area. This was a direct result of the for-
mation of the low melting carbides. The carbide formation was undoubtedly
accelerated by the extensive corrosion and erosion of the asbestos phenolic
and graphite nose cap sections. The flame side surface of the main insert
had a very shiny appearance which is characteristic of the tungsten carbide.

It is emphasized that locally poor materials performance was clearly
related to the introduction of flow field nonuniformities. Even when this
occurred, the performance of the nozzle materials not influenced by the
flow nonuniformities was as good or better than in the uniform exhaust
flow tests. It would appear, then, that the materials employed in this
program have not and did not "fail" solely as a result of exposure to
beryllium propellant exhausts. However, visual observations and physical
measurements do not provide an adequate basis for interpreting the specific
material failure mechanisms. The remainder of this section describes the
results of the post-test evaluation of nozzle performance. Seven relatively
distinct segments of the total analysis procedure are discussed separately,
even though they are closely interrelated. Section 3.6 presents a more
general discussion of the test program results.

   b. (C) Chemical Analysis of Deposits

Approximately 10 samples of chamber residues and nozzle/aft closure wall
deposits were taken from each set of motor test hardware. These were
analyzed by X-ray diffraction to identify the phases present and their
relative concentrations. While the phase concentrations are valid for
the individual samples, they do not provide an accurate measure of wall
deposit composition during the motor firing. The results of the sample
analyses are tabulated and discussed in Sections 3.4 of References 2, 3
and 4. As would be expected, the major phases were beryllia or alumina.
Other interesting phases were found as described below.

Analysis of deposits from the beryllium propellant tests usually showed
only beryllium carbide, carbon, graphite and asbestos decomposition
products to be mixed with the normal beryllia. The shiny or metallic
appearance of the chamber slag was attributed to the deposition of carbon
and formation of pyrolytic graphite during motor cooldown. For Test T-13
only, a small amount of beryllium metal was found in the chamber residue.

The asbestos decomposition products and beryllium carbide were usually, but not always, found on the nozzle throat and exit cone surfaces. Some tungsten and tungsten carbide was found in the exit cone surface on Tests T-16, T-17 and T-18. The asbestos decomposition and tungsten/tungsten carbide alloys evidently flow along the contour, subsequently freeze on the exit cone and could be expelled in the exhaust plume. Mixtures of beryllia and the asbestos (or silica) decomposition products would probably have a lower melting point than beryllia. It should be noted that beryllium carbide and beryllium present at motor shutdown are likely to decompose and evaporate during the low pressure heat soak period.

Analysis of deposits from the aluminum propellant tests gave similar results with two main exceptions. No aluminum carbide was found but there was some aluminum oxycarbide. The carbide was probably present but hydrolyzed in air after the test. Aluminum metal was found in large quantities, both in the chamber residue and aft closure insulation deposits. Evidently this could be unburned metal or a decomposition product of aluminum carbide. Asbestos-aluminum interactions apparently produced the aluminum silicates found on the aft closure insulator. The asbestos decomposition products were also transported along the nozzle contour as in the beryllium tests. These impurities could depress the melting point of the deposits from that of pure alumina.

    c. (C) Exhaust Plume Particle Analysis

Exhaust plume particles from the program motor tests were found to be beryllia or alumina by X-ray diffraction analysis. The expected beryllium, beta-beryllia, beryllium nitride and beryllium carbide either were not present or existed in undetectable quantities. It is speculated that these phases (except beryllium) would be more likely to appear near the periphery of the plume which was not sampled. However, it is conceivable that such phases could be produced in the combustion process and survive the flight through the nozzle. They would probably not appear as discrete particulate phases. If they should be mixed in low concentrations with beryllia, they would not show up in the X-ray diffraction analyses.

Selected photographs of the particles were presented in Sections 3.4 of References 2 and 4. The number of these pictures was kept to a minimum simply because there were few, if any, significant differences among the samples from different tests or the several elevations sampled in each test. The alumina particles were hollow spheres. Their diameters appeared to continuously vary from about 0.1 to 8 microns. The beryllia particles appeared to be in the form of dense hexagonal rods (crystals). There were a very large number of these particles in the 0.01 to 0.2 micron size range. There was a second distribution of particles in the range of about 0.5 to 5 microns. Samples from the development motor tests appeared to

contain a greater number of these larger particles. However, some of the particles were apparently fused together, giving the impression that the particles were irregular and as large as 10 microns. Attempts to measure the beryllia particle size distribution with a Coulter counter were not successful.

The very small beryllia particles are presumed to have condensed from the vapor phase during rapid combustion of the metal particles. Apparently, nucleation is not difficult and there is little evidence of subsequent particle growth. It is also presumed that the larger particles are the result of metal particle surface oxidation reactions and vapor condensation during metal particle combustion. If this is true, their size distribution should be related to that of the metal in the propellant (including agglomeration effects). It is suggested that the condition of beryllia exhaust particles is more indicative of the beryllium combustion process than is the case in the aluminum system. The beryllia particle sizes suggest that two phase lag losses may be lower than in the aluminum system. The sampling techniques employed in this program (and perhaps others) were not adequate to clarify the combustion or two phase flow processes further.

   d. (C) Throat Deposition/Erosion History

Two basic techniques were developed to determine the variation of nozzle throat radius with time during the test period. One method utilizes adjusted grain burning rate data and the measured chamber pressure history. This technique is most applicable to cases where the grain burns neutrally or, at least, in accordance with the design plan. The second method utilizes the measured thrust and pressure data. These techniques (and variations) are described in detail in Section 5.2 of References 2 and 4. A comparison of the results of the two techniques is also given in Reference 4 for several tests. The F/P method described on Pages 164-175 of Reference 4 is generally preferred when thrust data is available. Both methods are subject to errors associated with the input ballistic or grain burning rate data. Imprecision of the actual calculations will also be significant and will become greater as the nozzle scale (throat diameter) is increased. It is emphasized that the throat deposition/erosion history must be determined and used in the detailed evaluation of heat transfer, corrosion and ballistic performance.

The throat radius histories developed for the program motor tests are included in Appendix V. (In the future, it would be most useful to present this data on the pressure-thrust curves.) A review of these curves indicates that there are several general characteristics. Thus, there is normally a delay of a few seconds before deposits appear at the throat. On Tests T-3 and T-6, corrosion occurred prior to the arrival of the deposit pulse. In spite of the hangfire on T-6, this is strong evidence of analogous behavior of comparable aluminum-beryllium propellants. (The

extensive similarity of the analog pairs can also be seen by comparing the T-1/T-7, T-4/T-5 and T-8/T-10 deposit histories.) Corrosion apparently also occurred before deposition on Test T-20. However, no pressure data were obtained on this test and the deposit curve was approximated from the thrust data using other test results as a guide. The length of the delay period was reduced considerably in the Type II slotted grain tests. This is believed to be a result of direct impingement in the near-throat region induced by the strong radial flow from the grain slot.

A second general characteristic of the deposit curves is that they tend to build up to and retreat from a peak value. This is consistent with the expected transient heat sink response, oxide insulation effect and molten oxide flow model. The lower peaks seen on either side of the maximum corresponds to similar fluctuations in the pressure histories. The early subpeaks may be caused by metal or asbestos decomposition products depression of the oxide melting point. The later subpeaks probably reflect deposit flow instability. That is, large amounts of liquid flowing in the high flow acceleration region (throat) may develop waves, crest or break up. There are some tests in which a plateau, rather than a distinct peak, is established. This corresponds to low flame temperature, low oxide melting point or poor combustion efficiency. This type of deposit behavior could probably be produced by supplementally cooling of the nozzle. The data for T-11, T-14 and T-53 are relatively unique because there was very little deposition. This suggests that no deposit freezing occurred at the throat or that there was actually little or no particle impingement. The former would be expected for T-11 and T-14. Deep nozzle submergence on T-53 apparently minimized deposit formation.

Once again the Type II slotted grains exhibited a unique characteristic. Thus, after a relatively normal deposition pulse, followed by throat corrosion, the deposits built up for a second time. Since only the average deposit thickness can be determined at any instant, these curves are strongly affected by nonuniform deposition. Note that the Type III and 500-pound grain tests did not exhibit the Type II grain deposition characteristics. This is presumably due to the lower strength of the radial slot flow and nozzle submergence. The return of deposits with the Type II grains may be due to the development of the mirror slot in the grain and/or the unusually low pressures during the regressive burning portion of the test.

Comparisons of the deposition curves, according to the major motor design parameters, were presented in Section 4.2 of References 3 and 4 (see Appendix V). The most obvious general results of this comparison are as follows:

(1) The deposit curves are strongly related to the grain design.

(2) Nozzle submergence reduces deposition.

-62-

(3) Poor metal combustion stimulates higher deposition.

(4) Deposition decreases with increasing flame temperature.

(5) Deposition increases with increasing heat sink capacity.

(6) Beryllia and alumina deposition characteristics are similar, probably due to the approximate cancellation of the melting point and thermal conductivity effects.

(7) Qualitative deposit curve characteristics were reproducible.

(8) Tungsten throat deposit curves were similar to those for pyrolytic graphite throats.

(9) Deposit curves were essentially reproduced in tests using the same propellant, grain design and nozzle contour.

(10) Carbon cloth nozzle inlet sections did not alter the deposition characteristics significantly.

The throat radius history curves also provide a relatively detailed picture of the nozzle throat regression. The endurance of the deposits in the small nozzle tests accounted for the small amount or total lack of throat corrosion. It should be noted that the slopes of the erosion portion of the throat radius histories are not normally smooth. This would be a logical result of nonuniform deposit flow. In fact, the corrosion was also nonuniform when it occurred only after deposit removal. It is reasonably certain that the deposits were normally removed first from the top section of the throat surface. The throats were elliptical in this case while they were almost perfectly circular when corrosion occurred prior to the arrival of deposits. Except for the nonuniform deposition effect, the "true" throat corrosion rates can be determined directly from the throat radius history (slope of the erosion portion of the curve). The time when this corrosion occurred can also be identified. This permits the estimation of the throat surface temperature when corrosion occurred.

e. (C) Ballistic Performance

Ballistic performance data were calculated for all of the motor tests except T-8 and T-54. Telecomputing Services, Inc., under contract to AFRPL, computed the average C^* an Isp as part of the normal ballistic and

thermocouple data reduction process. Such results were based on an average
of the initial and final throat areas. This procedure is not realistic
when both deposition and erosion occur or no erosion occurs during the
test. Note that the final throat measurement may not be representative of
the deposition at burnout. Consequently, the performance data were also
hand calculated as described in Section 5.2 of Reference 2. The procedure
employed essentially integrates the complicated throat area history in
lieu of assuming a linear variation. Attempts to determine the instanta-
neous variation in C* were relatively unsuccessful since the exhaust mass
flow rates were not sufficiently well known.

The ballistic performance data are presented in Appendix VI in tabular
form. Action time, propellant weight, chamber pressure, thrust, C* and
impulse data are included. Integral average and maximum values are given
for pressure and thrust. The ideal C* at the nominal design pressure are
given for reference, along with the values computed by Telecomputing
Services Inc. (subscript TSI) and Philco-Ford (subscript ADP). The TSI
and ADP computed values for the integral average impulse are also tabulated.
Note that the C* and Isp data are not representative of instantaneous or
maximum delivered performance. Note also that the ADP performance values
were computed using the throat radius history data given in Appendix V.

The ideal equilibrium performance, corresponding to the actual average
chamber pressure for each test, was computed in order to establish effi-
ciency ratings. This was done for two or three chamber pressures covering
the range of the average motor pressures recorded for each propellant.
The results were plotted and the individual test performance values were
read from the resulting curves (see Appendix VI). The ideal impulse values
are still in error since they correspond to the initial nozzle expansion
area ratio. The ADP values of C* and Isp were then used to compute the
performance efficiencies. The results are included in Appendix VI.
Basically, it was felt that neither the performance data or the efficiency
ratings could be evaluated directly. On the other hand, it was highly
desirable to obtain an estimate of the average metal combustion efficiency
for each test.

The ballistic efficiency data were approximately corrected for three major
losses. The results are included in Appendix VI. The slag effect repre-
sents the reduction of the propellant weight to account for the retention
of slag within the motor and the low performance expulsion of liquid
deposits throughout the test. These estimates range from 1/2 to 4-1/2 per-
cent and affect C* and Isp equally (except for T-13 which developed a
leak). The corrections are based on the post-test examination of the hard-
ware and the deposit expulsion observed in the test movies. The heat
transfer/skin friction losses range from 1 to 2-1/2 percent and are 1/2 per-
cent greater for Isp than C*. The variation of the correction from test
to test reflects the change in exposed nozzle/aft closure surface area and
temperature. A 3 percent divergence angle correction was uniformly applied

to the Isp. A secondary side thrust correction was added to account for the nonuniform slag expulsion and plume detachment observed in the test movies. Note that no correction was made for two-phase lag losses. It is emphasized that the corrections are essentially rough estimates as opposed to rigorous analytical results.

According to the metal combustion model developed in the program, the remaining C* loss should be indicative of the average metal combustion efficiency for the entire test. If none of the metal burned at all, the C* efficiencies would be in the range of 75 to 80%, less the unusual drag loss effect. There is no convenient way to estimate the range of combustion efficiency from the adjusted averages. In reviewing the adjusted C* efficiencies given in Table III of Reference 4, some numerical errors were discovered. The corrected data are included in Appendix VI. Although numerical inaccuracy and poor estimates of the accounted losses can not be ruled out, the most probable errors remaining are associated with the throat deposition/erosion history. Since an integral average throat area is used, such errors are not likely to be greater than about 2 percent. In any case, C* efficiencies above 98 percent are regarded as indicative of high metal combustion efficiency. Evidently then, the majority of the tests satisfied this condition. It appears that the efficiency of the double base propellents decreased in going from the remote end burning grain to the internal burning grains.

The Arcane 54F (Tests T-4 and T-11) showed the opposite trend. The close end burners (T-21 and T-23) gave very low performance for the Arcocel 191F compared to the high residence time design of T-1. This occurred to a lesser degree for the Arcocel 319BRF (T-3 and T-24) and Arcone 54F (T-4 and T-22). Submerged nozzles apparently induced lower performance with the Arcocel 191F but not with the Arcocel 319BRF propellants. The most significant result is believed to be the distinct loss of C* performance corresponding to the reduction of chamber residence time (at low flow velocities) on Tests T-21, T-22 and T-23. It follows that materials upstream of the throat may be exposed to incompletely burned exhausts in general. It is also logical to expect that this problem would be most severe during the earliest portion of the test. Evidently more testing would be required to clarify the dependence of combustion efficiency on propellant, flow velocity, residence time and nozzle contour parameters. The data from these tests do provide preliminary indications that such dependencies actually exist.

The impulse efficiency data indicates that the performance of the 500-pound grains was significantly better than that of the small grains. Evidently this is a combination of the scale effect and the lower expansion area ratio. It is interesting to note, however, that the first 15 small motor tests had significantly higher impulse efficiencies than the last 10 tests. This trend is strong enough to suspect that a thrust stand or calibration

error may be involved. Normally, impulse efficiencies above 94 to 95 percent would be reasonable for the small motor tests. Apparently, the beryllium propellants tested are capable of delivering such performance.

In the future, the accurate measurement of motor performance should be given the greatest possible emphasis. Deposition effects on throat area and thrust should not be neglected. Average C* efficiency data can provide a coarse indication of poor combustion and more particularly, the degree of metal burning. Ultimately, it would be highly desirable to obtain a motor weight history (small motors) to permit the instantaneous evaluation of C* and/or oxide deposition.

f. (C) Fluid Mechanics

Fluid mechanics studies leading to improved boundary layer and fluid properties characterization have been discussed in other sections of this report. Additional efforts were devoted to estimating the flow fields characteristic of the program grain design-nozzle contour combinations. The objectives were to provide approximate locations of the areas along the motor contour where flow stagnation and particle impaction would occur. This was done after the test firings and emphasis was placed on explaining the aft closure-nozzle grooving phenomenon associated with the slotted grains. Schematic representations of the motor flow field and condensed phase impaction profiles are included in Appendix VII.

The estimates of the chamber-nozzle exhaust flow fields were generally influenced by the results of the cold flow modeling studies and experience with potential flow theory. The results for the end burner and center perforated grain designs are quite simple. Basically, when the flow streamlines are turned by the wall, the condensed phases will be centrifuged accordingly. Thus, in a flow stagnation region, the particles will not negotiate the turn and will strike the wall. This occurs in very limited areas. Note that the flow stagnation will induce high heat transfer, corrosion and gas shear in about the same areas where impingement occurs. The opposite effect can also be produced when the centrifugal forces are in a direction away from the contour. This occurs when a submerged nozzle is used. The flow around the submerged nose cap tends to shield it against the axially directed main flow. The more mass flowing around the nozzle, the more effective is the shielding. This shielding reduces particle impingement, heat transfer corrosion and gas shear. At some submergence, impingement along the convergent portion of the contour should be eliminated entirely. This condition was approached on Test T-53 at approximately 15 percent submergence. Note that essentially the same shielding effect occurs once the flow becomes parallel to the steep inlet and conventionally contoured nozzle designs. Thus, as the flow approaches the inlet and/or throat sections, condensed phases near the wall will tend to be centrifuged toward the nozzle centerline. This leads to the ideas of limiting particle

streamlines and condensed phase stratification. It is interesting to speculate that the boundary layer in the throat and exit cone sections is devoid of oxide particles. In the special case when burning metal particles are subjected to centrifuging, the throat and exit cone wall flow may be abnormally rich in oxidizing gas species.

The slotted grains are unique in that the slot exhaust must flow radially while the core flow is primarily axially directed. This results, first, in a partial flow stagnation along the grain surface opposite the slot. Circumferential flow will develop to accommodate the stagnation which may extend axially to the nozzle throat in some cases. The abnormal turbulence (eddys), high heat transfer, high gas shear and high corrosion cause the groove to form in nozzle opposite the grain slot. If the grain port diameter is large relative to some measure of the radial slot jet flow strength, jet viscous dissipation effects may be significant. Otherwise, dissipation effects will only be important in reducing the local turbulence along the stagnation li e with increasing distance from the source of the disturbance. Presumably, oxide impingement will be higher along the stagnation line opposite the grain slot. Unless retarded by turbulence, higher deposition rates would eventually protect the nozzle from the groove forming mechanisms.

There is also a major axial component of the flow within the grain slot, especially near the grain outer diameter. Thus, the slot flow stagnates where it is turned by the aft closure insulator. This led to the formation of a deep groove where the insulator was exposed (no cab-o-sil/grain bond in the slot area). The resulting flow along the aft closure will then have a greater radial velocity component than in other sections of the motor. This radial jet stagnated along the outside of the submerged nose cap sections of the development nozzles (T-51 through T-54). This cutting torch action slotted the nose cap rather dramatically. This will force some of the exhaust to flow circumferentially away from the nose cap stagnation line. There will also be free shear layers developed along the boundaries between the radial slot jet and axial core flows. These shear layers are highly turbulent and can cause extensive erosion where they reach the wall. This apparently caused the "saddles" observed in the nose caps of the development nozzles. A similar interaction between the nozzle inlet flow and the flow through the nose cap slot was evidently a primary cause of the grooving of the T-51 and T-53 nozzles. Either of two mechanisms could have been the primary causal factor in forming the nozzle grooves in line with the Type II and III grain slots. Those would be the free shear layer turbulence or the burning particle centrifuging effect.

The slotted grain flow-field effects are discussed in greater detail in Section 2.4 of References 3 and 4. The extension of the single slot results to the cases of two and three axial slots is also discussed in Reference 3. Basically, the interpretations of the grain slot flow effects can be extended to grains with star cores and forward slots. Ultimately,

the designer should recognize that extreme stagnation, recirculation and free shear layer effects will lead to local breakdown of any material in common use. The best rule would be to eliminate the severe interaction rather than to predict or measure its extent. It should be obvious that high, nonuniform erosion of insulation and nozzle materials will ultimately penalize the system in terms of weight and performance.

g. (C) Nozzle Throat Heat Transfer

Conduction computer analyses were performed to determine the oxide deposit insulation effect and gas side heat transfer coefficients for most of the nozzles tested. The technique employed and the results are described and discussed in Section 2.5 of References 2, 3, and 4. Since the wall deposit thickness history could only be determined at the nozzle throat, attention was primarily devoted to the throat washers of the pyrolytic graphite heat sinks. Efforts to evaluate the heat transfer to the tungsten nozzle inserts were more complex and less successful. The analysis was not carried out for some nozzles due to the lack of suitable temperature data.

Basically, a measurement of the total heat transferred to the wall at a given axial station was obtained by measuring the short time equilibration temperature. That is, the temperature gradients become nearly zero shortly after burnout. Thus, the wall thermocouple indicated the average washer temperature in about 60 seconds after burnout. The total heat of the washers was corrected (by about 2 percent) to account for the nozzle insulation pyrolysis during the first minute after burnout. A trial and error procedure was then used to find the heat transfer coefficient which produced the measured total heat of the washer. The heat transfer coefficient was assumed to depend on pressure to the eight-tenths power. The measured chamber pressure and throat deposit histories were used directly but no attempt was made to account for the nearly insignificant throat corrosion. The final pressure dependent heat transfer coefficient necessarily averages out all surface temperature, surface roughness, combustion and flow field transients. Circumferential variations are also averaged when they occur. The circumferential variation in heat transfer can only be seen by comparing the several temperatures measured for a single washer. Such effects appeared to be significant only on the slotted grain tests.

The data obtained are included in Appendix VIII. The figures show the nozzle throat temperature history and, in most cases, the oxide deposit surface temperature history. The reasonableness of the results can be checked in two ways. First, the measured backwall temperature history can be compared with the calculated value. Differences are associated primarily with poor definition of the oxide thermal properties, errors in the deposition (or pressure) history and averaging effects. In the majority of cases, the agreement is excellent. A second check may be made by noting the relationships of the calculated throat or deposit surface

temperature and the oxide melting point. Thus, the throat deposit thickness should level off or begin to decrease when the deposit surface melts. Then, the deposit should disappear when the throat surface temperature reaches the oxide melting point. Again, agreement is exhibited by most of the results. Heat transfer coefficients are indicated in each temperature history plot. The stagnation reference temperature used was the ideal, equilibrium value at the nominal throat pressure. This value is slightly less than the ideal chamber temperature and is not the turbulent boundary layer recovery temperature. Actually, there is an inconsistency, amounting to ±5 percent, due to variation of the average motor pressure by ±200 psi from the nominal. This is due only to the variation in the free stream stagnation reference temperature dependence on pressure which was ignored.

Within the accuracy of the analyses and data employed, a low heat transfer coefficient indicates that poor metal combustion has occurred. Actually, the stagnation reference temperature is low, not the heat transfer coefficient. The apparent reduction in the coefficient depends on the difference in the values of the stagnation and gas side surface temperatures. Note that the gas side surface temperatures have average values near or above the oxide melting point. For low temperature beryllium propellants, a relatively small degree of incomplete metal combustion can therefore cause a major reduction in the apparent heat transfer coefficient.

All of the heat transfer coefficients were corrected to the nominal chamber pressure (800 psia). This was done to facilitate comparison of the results. The coefficients were also divided by the average boundary layer specific heat (equilibrium) evaluated at the average gas side surface temperature. This tends to eliminate some of the surface temperature dependence of the convective coefficient. As shown in Table V of Reference 4, the improved closed form convection theory indicates that the value of $(h/C_p)_{800}$ should be very close to 0.0090 lbm/in.^{2} sec for all seven of the program propellents (see Appendix VIII). This value should be compared with the experimental results which are tabulated in Appendix VIII in accordance with the major motor design variables. The experimental results are discussed in Reference 4, Pages 71 to 79.

Considering the known problems with the thermal instrumentation, hang fires, nozzle failures and the uncertainties in the deposit insulation effect, there is remarkably good agreement between the theory and the test results. It should also be recalled that the improved closed form theory does not account for pyrolysis gas mass injection, corrosion, poor combustion, boundary layer development length, nonuniform flow or surface roughness effects. Thus, the end burning grains, due to the exposure of the entire aft closure surface to the flow, are likely to promote slightly low throat heat transfer compared to the internal burning grains. If poor metal combustion occurs, it would primarily affect the core flow (near the

motor axis). There may also be significant stratification of condensed phases in the core flow. In contrast, the internal burning grains will achieve the highest degree of metal combustion near the motor axis. Similarly, the slotted grains and submerged nozzles are likely to produce higher than theoretical heat transfer.

There are only two outstanding deviations between theory and experiment. Thus, the tungsten insert nozzles, T-16 through T-18, have uniformly low measured throat heat transfer coefficients. This is attributed to the inability of the post-test analysis procedure to handle the axial conduction effects (due to lack of deposit thickness data). The close end burner tests, T-21 through T-24, also have uniformly low measured coefficients. This is at least partially attributed to poor metal combustion. It should also be noted that the deposit histories used in the analysis may have been somewhat in error (see Section 5.2 of Reference 4). In fact, the use of the revised F/P method for determining throat deposit histories (in lieu of the older C_F and K_n methods) would improve the agreement between the backwall temperatures and alter the heat transfer coefficient on a number of other tests as well.

The theoretical heat transfer coefficient for the development nozzles (at 800 psia) would be 0.0080 lbm/in^2 sec. The results for T-51 and T-52 were significantly higher than this value. This is attributed to the unusual slot flow, corrosion heat absorption (T-51) and nonuniform deposition. The measured value for T-53 was quite low. The post-test analysis did not include any deposit at the throat. The throat erosion history is not compatible with this assumption. The measured result would be significantly higher if a deposit were included (a reasonable value could not be determined from the throat radius history).

The measured throat heat transfer coefficients for both beryllium and aluminum propellants are basically in good agreement with the improved theory. This theory predicts results which are significantly higher than commonly reported nozzle design values. Such design data does not account for deposition or corrosion effects and would, therefore, prove to be reasonably accurate in many cases. However, they would be far from adequate for long motor firing and for propellants whose flame temperatures are well above the oxide melting points. It is reasonable to assume, then, that poor nozzle performance can often be attributed to poor design. The high temperature double base propellants would be particularly susceptible. On the other hand, minor metal combustion inefficiency (leading to increased deposition) would render the low temperature composite propellants nearly harmless. Evidently, tungsten nozzles would give particularly good performance in the low temperature composite systems. Clearly, final conclusions cannot be drawn solely from the results of this program. More data are required to characterize the dependence of the convective heat transfer on motor design, propellant, nozzle material, corrosion and

surface roughness effects. It is believed that such efforts would lead
to vastly improved understanding of the causes of poor nozzle performance.
Such understanding would lead to improved designs and performance. However,
it will become increasingly evident that there are definite limits to the
capabilities of the commonly used nozzle materials. Further improvement
in nozzle performance will then require thermal and/or corrosion protection
for both beryllium and aluminum propellants.

h. (C) Nozzle Throat Corrosion

The interference of wall deposits with the corrosion of the nozzle throats
by the exhaust gases severely limited the amount of data produced. This
had the positive result of confirming the effective inertness of the metal
oxides and permitted extensive clarification of the convective heat trans-
fer question. The corrosion studies were further frustrated by the nearly
insignificant total corrosion, of the order of the expected thermal defor-
mation of the throat, on several tests. Nonuniform corrosion and surface
spallation also complicated the situation. However, the results were
actually adequate to clarify the nature of the corrosion process and to
establish the direction of future efforts.

Theoretically, the combustion products of the propellants studied are
saturated with carbon (CO/CO_2 balance) up to a particular temperature
threshold. The threshold temperature ranges from about 1000 to 1900°F
for no metal combustion and ideal combustion, respectively. Calculated
surface temperatures, at the time when corrosion started or when deposits
arrived at the nozzle throat, were compared with the theoretical threshold
values. Although there were only four tests in which corrosion preceded
deposition, graphite corrosion started above 2000°F. On 14 tests, deposits
arrived when surface temperatures ranged from 1700 to 5000°F. It was
noted that the highest deposit arrival temperatures corresponded to the
highest initial surface temperature rise rates. It is clear that these
results are subject to major errors. However, a corrosion threshold
evidently does exist and probably lies in the 2000 to 3000°F temperature
range. The threshold data are tabulated in Appendix IX. The tungsten
insert tests are omitted since no corrosion was measured and the temperature
threshold for observable corrosion is very high.

The measured corrosion data are presented in Appendix IX. It is important
to note that the surface temperature during the actual period of corrosion
is given. Maximum, minimum and average radial regression are given. The
most representative regression values were selected and corrected to
account for thermally induced throat contraction (about 2 mils at 5000°F).
The corrected corrosion rate was then obtained by dividing the throat
regression by the time period over which the corrosion actually occurred.
Although an attempt was made to eliminate the influence of the grooves
formed in the slotted grain tests, the problem of nonuniform corrosion

could not be resolved. That is, the corrosion rates may actually range
to a maximum of twice the indicated values. This is entirely due to
corrosion occurring at the top of the nozzle while the bottom remained
coated with oxide deposits. In many cases the throats were measurably
elliptical and attack of the top surface of the throat was obvious from
its appearance. This effect would be most pronounced for the shortest
corrosion times (or lowest rates) and for the slotted grains.

Predicted and measured corrosion rates are also compared in Appendix IX.
The predictions were obtained by means of extremely simple hand calculation
techniques (see Pages 15 to 20 of Reference 3). They do not include blow-
ing, combustion efficiency, surface roughness or pyrolysis gas injection
effects. Direct use of the B value (exhaust corrosivity parameter) and the
heat and mass transfer similarity assumption overpredicts the corrosion by
as much as an order of magnitude or more at high surface temperatures. The
second technique independently calculates the corrosion by water vapor and
hydrogen. These are theoretically the most important reactions for the
program propellants. The comparison of these results with the measure-
ments is not entirely conclusive. The water reaction alone provides
reasonable agreement with the measurements up to graphite temperatures of
about 4500°F. Then, at temperatures up to 5500°F, some or all of the
hydrogen contribution is also required. Unfortunately, the quality of
the measured corrosion rates is not adequate to identify a specific trend
or transition. At temperatures above about 4700°F, it is relatively cer-
tain that liquid deposits (bead and stream flow) are influencing the
results. This can best be seen by examining the throat deposition/erosion
curves (particularly for T-1, T-7, T-51 and T-53).

The pyrolytic graphite corrosion data suggests several important things.
These are listed below.

(1) The major effect of deposition protection of the
throat surface can be eliminated from the corro-
sion data. Secondary effects, involving unsym-
metrical deposition, continue to influence the
quality of the corrosion rate data. As a result,
the uncertainty in the average throat corrosion
rate may be above 100 percent.

(2) Appropriate closed form equations can be developed
to approximately predict throat corrosion in the
absence of physical erosion. Specific corre-
lation equations could be developed for a partic-
ular propellant and nozzle design.

(3) There is no indication from the data that
beryllium and aluminum corrosion mechanics
are different.

-72-

(4) The corrosion data neitner supports nor contradicts the thesis that hydrogen attack of pyrolytic graphite is kinetically restricted. More advanced theoretical predictions and more specialized solid motor testing would be required to resolve this issue.

(5) The apparent lack of hydrogen reaction kinetics in a few of the tests suggests that the polycrystalline graphite reaction rates would be slightly higher than for the pyrolytic graphite. This would be due to differences in surface activity, roughness and porosity. Even if kinetics do apply to the pyrolytic graphite, they could be less effective or absent for the polycrystalline graphites.

(6) In the potentially rare cases when corrosion occurs primarily below 4500°F, only the oxidation of graphite need be considered. At higher temperatures, hydrogen attack and the interference between the acetylene product and the oxidizing gases should be considered. (Nitrogen-carbon reactions should also be considered in appropriate cases.)

(7) The most useful data from other programs will be those obtained with the corresponding deposition and heat transfer (surface temperature). End burning and simple, circularly ported grain test data will be the most accurate. Some submerged nozzle data will not involve deposition effects and could be the best of all data.

(8) Nozzle corrosion prediction should be treated as a boundary layer transport problem and should be coupled with the convective heat transfer analysis. hechanical breakdown of the nozzle surface (erosion) should be treated as a separate issue and should be avoided rather than analyzed.

(9) There is no positive indication in the corrosion results to indicate that incomplete propellant combustion occurred. This is a direct consequence of the occurrence of extensive deposition on those tests designed to accentuate the combustion efficiency effect.

Uniform corrosion of tungsten by the exhaust gases was not observed. Formation of the low melting tungsten carbides did occur. The mechanics and rate of this reaction cannot be properly treated until the carbon source has been more clearly identified (see also Section 3.2).

3.6 (C) DISCUSSION OF MOTOR TEST RESULTS

The program motor tests were designed and conducted with two overall objectives. These were to examine the mechanics of corrosion and erosion of nozzle materials exposed to beryllium exhausts and to determine which nozzle materials can be successfully used with beryllium propellants. The basic approach called for the variation in the major motor design parameters and the maximum production of detailed performance data for each test. Finally, the test results were to be interpreted to determine the degree to which the individual test and overall program objectives have been met. Such matters are discussed briefly in this section. Similar discussions may also be found . Sections 7.1 of References 1 through 4.

This program was originated because beryllium motor tests often resulted in dramatic failure or high nozzle erosion. In some instances, nozzle erosion did not occur at all or was less severe than for comparable aluminum propellant tests. The test results clearly indicate that unusually good nozzle performance is a direct result of oxide deposit protection of the contour materials. This applies to graphite, tungsten, carbon cloth and asbestos phenolic materials. The demonstrated inertness of the oxide deposits in the solid motor firings was in complete agreement with predictions based on thermochemical analyses and extrapolation of laboratory experimental studies. The potential exception to the predicted inertness would be the attack of tungsten by aluminum or beryllium metal, forming very low melting alloys. This action was not observed in this program but should not be ruled out. The source of metal for alloying could be either unburned metal mixed with the oxide deposits or the product of aluminum or beryllium carbide (formed at the interface between graphite contour and oxide deposits upstream) decomposition at high temperatures. The formation of low melting tungsten carbides in this program (beryllium propellants only) and in other programs (both aluminum and beryllium propellants) is not obviously related to oxide deposits.

Of the 25 small motor tests conducted, physical failures occurred on only three. Inadequate sealing at the base of the end burning grains on the first two tests (T-1 and T-2) caused partial burnthrough of the steel case. A poor seal permitted leakage through the nozzle to ambient on Test T-13. The damage was quite extensive to the metal and insulation components; the nozzle contour forming materials were relatively unaffected. The extent of the damage on these three tests could have been related to the degree of metal combustion. Thus, slow combustion of beryllium metal could have increased the gas phase oxygen content of the leaking gases.

The nozzle performance on the four development motor tests was considerably more dramatic. The grooving of the aft closure insulator and slotting of the nose cap are believed to have been primarily a consequence of the stagnation flow and free shear layer turbulence associated with the chamber flow field. Again, the extent of the damage could in part be due to poor metal combustion. Less damage occurred on T-52 than on T-51, T-53 and T-54. The Arcocel 319BRF propellant, which is known to have excellent metal combustion characteristics, was used on T-52. Unfortunately, that test was also a hangfire (poor igniter placement) so less efficient combustion of the Arcocel 191F propellant used on the other tests is not confirmed. The damage to the nozzle throat section on these tests is obviously related to the nose cap and/or grain slot. Similar behavior would be expected with aluminum propellants since surface spallation of the pyrolytic graphite and carburization of the tungsten appear to have been the primary causal factors. Based on the results of the pyrolytic graphite nozzle performance (T-51 and T-53), the failure of the thin tungsten insert on Test T-54 might have been predicted.

There is ample evidence that the nozzle materials employed in this program can be successfully used with beryllium propellants. There is no particular indication that other materials used in aluminum systems could not be used with equal success with beryllium propellants. The few aluminum analog propellant tests conducted in this program generally re-enforce the original program hypothesis that the behavior of the two propellant types was a matter of differences in degree rather than kind. That is, no unique characteristics have been discovered in this program which can be attributed only to beryllium propellants. This in no way appears to be a result of an unfortunate selection of propellants in this program. Motor test results and/or hardware from beryllium programs conducted by Atlantic Research, Aerojet, Hercules and Thiokol have also been examined and no contradictions have been found.

Ultimately, the performance of nozzle and motor insulation materials in beryllium exhausts must be compared with their performance in aluminum systems. In this program comparable propellants were judged to be those with (1) identical flame temperatures, (2) equivalent ideal exhaust corrosivity or excess oxygen content, (3) identical propellant ingredients,

excepting the metal additive, and (4) identical grain, motor and nozzle designs. These criteria establish a reasonable basis for comparison of ideal and delivered ballistic performance as well as nozzle materials performance. The beryllium propellant will necessarily have the higher ideal ballistic performance. Basically, the delivered nozzle materials performance and ballistic performance efficiency will only be different if the combustion efficiency and/or condensed phase deposition and lag losses are different. Several of the possible combinations of these factors were demonstrated in this program. The thermal insulation and corrosion protection afforded by alumina and beryllia deposits were demonstrated under complete or comparable combustion conditions (Tests T-1 through T-7). The measured performance (heat transfer, deposition, corrosion and ballistics) were obviously similar for analog pairs of propellants. Later, in Tests T-21 through T-24, it was shown that reduced combustion efficiencies led to higher deposition with lower heat transfer and no corrosion. There is no reason to doubt that aluminum analogs would behave in the same manner. The remaining possibility is that there may be no deposition protection when the combustion efficiencies of analogs pairs are different. Deposition protection was nearly eliminated on Test T-53 but the combustion efficiency was apparently high and the corrosion was normal.

The consequences of poor propellant combustion during periods when the wall materials are not protected by oxide deposits can be predicted with high confidence. Thus, slow or incomplete combustion of the metal additive will greatly increase the relative availability of gaseous oxidizing species in the exhaust. Corrosion rates may be increased by an order of magnitude or more, at exposed materials temperatures above about 1500°F. Such a corrosion rate increase would be very dramatic for plastic insulation and graphite materials but would be only marginally serious for tungsten. Gaseous beryllia, beryllium hydroxides and beryllium vapor could vigorously attack tungsten (if they actually exist or can diffuse to the tungsten) by forming low melting metal alloys. Analogous aluminum species would have the same effect. The program motor tests showed that throat corrosion can occur before the arrival of protective deposits. The higher melting point of the beryllia would be disadvantageous in this special case, especially with low flame temperature propellants.

Laboratory studies of metal particle combustion, conducted by Hercules, NOTS, Atlantic Research and others, indicate that beryllium is normally the more difficult metal to burn. Apparently, excessively slow combustion of either metal can occur and will depend on (at least) grain surface agglomeration and the flame temperature of the nonmetallic propellant ingredients. At the present time it should not be difficult to determine which propellants will be slow to achieve complete combustion using a combination of laboratory and analytical techniques. The present lack of sufficiently detailed knowledge concerning the metal combustion mechanics prevents extensive generalization.

Abnormally high deposition or nozzle corrosion should be anticipated when
(1) propellant flame temperatures are low, (2) metal agglomeration at the
grain surface is known to occur, (3) particle residence times are short
along streamlines which pass near the wall contour, (4) the oxidation
ratio is low, (5) metal loading is high, (6) motor pressures are low, and
(7) origional metal particle sizes are high. Basically, the size of the
particles which must burn, the availability of oxygen to sustain combus-
tion and the flame temperature along the particle streamlines must be
adequate to promote rapid vapor phase combustion within the available time.
Ideally, the minimum propellant flame temperature (without metal combus-
tion) should be close to or above the oxide melting point. The beryllium
and one of the aluminum propellants tested in this program do not meet
this ideal requirement. Fortunately, beryllium particles are known to
ignite in water vapor at temperatures well below the beryllia melting
point. However, this will only make it feasible to achieve complete com-
bustion within finite (as opposed to very short) times.

It is reasonably clear that the majority of the beryllium propellants in
the impulse range being studied, will exhibit individual, rather than
general, characteristics to the extent that their metal combustion charac-
teristics differ. That is, much longer combustion times will be required
relative to typical aluminum analogs or advanced beryllium propellants.
This will be reflected in the deposition, corrosion and heat transfer due
to their direct dependence on the degree of metal combustion. In the
final analysis, the low impulse beryllium propellants just cannot be com-
pared with their aluminum counterparts unless equivalent metal combustion
efficiencies are coincidentially achieved.

Much of the confusion regarding the performance of beryllium relative to
aluminum propellants is undoubtedly due to the detailed lack of similarity
of the combustion and deposition processes. In addition, the studies of
heat transfer and corrosion conducted in this program indicate that nozzle
failures in either propellant system may be traced to poor design. The
motor test results support the contention that the convective heat transfer
is higher than commonly claimed. Test results and analyses show that sur-
face roughness and nonuniform flow field effects can force the convective
heating rates still higher. These increases are normally resisted by
oxide deposit protection, corrosion reaction heat absorption, surface blow-
ing and poor combustion. If the latter effects should dominate, the heat
transfer may be well below conventional predictions. In either case, there
may be considerable variation in the heat transfer, in both time and space,
which would not be predicted by conventional analyses. Probably the
greatest danger in over or underestimating the heat transfer will be that
the capacity and failure mechanisms of nozzle materials can be misjudged.
One result appears to have been that design technology which has proven
successful in one propellant system is only marginally effective in new
systems.

-77-

Grain design and motor/nozzle contour effects on nozzle performance have been clearly illustrated in this program. This emphasizes the need to account for the detailed interaction of the exhaust flow field with the motor contour in the design process. It is also apparent that the degradation of upstream materials can have a pronounced effect on nozzle throat performance by distorting the exhaust chemistry or flow structure near the contour. When these effects are coupled with the propellant combustion and deposition effects, each motor test becomes more individualistic in terms of nozzle performance.

Ultimately, materials degradation occurs by chemical and/or thermo-mechanical routes. Tungsten insert failures involve excessive plastic deformation. Premature failure may be precipitated by carburization, beryllium or aluminum alloy formation, and selective grain boundary attack. Tungsten performance should be best with low flame temperature propellants. High pyrolysis and graphite corrosion rates of upstream materials are not desirable with tungsten throats. Unusually good performance of tungsten will result when deposition protection and/or poor propellant combustion occur.

Ordinary corrosion and thermostructural breakdown of the surface of graphite materials are dominant degradation mechanisms. The attack rates by oxygen and hydrogen bearing gas species depend on the local exhaust composition and boundary layer diffusion. Reaction kinetics and endothermic reaction effects will favorably influence the rates. A well developed, stable boundary layer and complete combustion of the propellant are essential to achieving low attack rates. Oxide deposition protection will have an overriding influence while it lasts. Excessive bulk and differential thermal expansion stresses cause surface spallation. The scale of the surface breakdown appears to be closely related to the nodule or grain size and the radial temperature gradient. A well developed, stable boundary layer (heat transfer rate) and adequate thermal expansion allowances are essential to good graphite performance. Surface spallation is often lumped in with corrosion, confusing the issue considerably. Surface gas shear induced grain erosion and selective grain boundary attack may contribute to surface regression. Surface roughness associated with spallation/erosion will increase the local heat transfer and corrosion rates.

Failure of plastic insulation materials probably involves simultaneous exposure to excessive corrosion, heat transfer, gas shear and particle impingement. The most dramatic failures will be associated with local exhaust flow stagnation, turbulence and/or boundary layer reattachment. A well developed, stable boundary layer, high local combustion efficiency and reasonable exhaust flow velocities are essential to good performance. Pyrolysis gas injection into the nozzle boundary layer may precipitate tungsten insert carburization but will probably improve graphite performance. The program motor test and analytical study results strongly indicate the need for an improvement in the approach to motor insulation and

nozzle design. Greater awareness of the importance of propellant combus-
tion and deposition effects are essential. Improved techniques for charac-
terizing the exhaust flow field and boundary layer processes should be
applied. Nozzle heat transfer and corrosion theory should be upgraded
accordingly. There is also a basic requirement for improving and under-
standing of the chemical, thermal and structural capacities of nozzle
materials. Somewhat more fundamentally, the propellant selection, grain
design and motor configuration criteria should be reviewed. Thus, rapid
combustion, and the development of a uniform exhaust flow field could be
insured at the outset of the motor design process and would minimize the
nozzle design problem. A definite stand should also be taken as to the
desirability of nozzle deposition effects. Note that delivered ballistic
performance can be maximized or optimized in the process. If a propellant
with poor combustion characteristics must be used, it will be necessary
to compromise either stage volumn or mass fraction to achieve high nozzle
or ballistic performance.

In the absence of combustion efficiency, deposition and exhaust flow field
variances, acceptable nozzle performance can be achieved with the commonly
recommended materials in the beryllium and aluminum systems. This will
hold in other chemical propulsion systems as well. The beryllium system
apparently has some unique advantages stemming from the high melting points
of the metal and oxide. However, rapid metal combustion is deterred by
the high metal heat capacity and high oxide melting point. There is some
evidence that beryllium can be best utilized in propellants which do not
promote grain surface agglomeration and/or have high flame temperatures.
Double base propellants may be preferable but the key requirement appears
to be more directly related to the oxidizer particle size and/or binder
decomposition kinetics. However, it should be recognized that the metal
combustion process will not be instantaneous in any propellant. Basically,
this means that small scale propellant evaluation and scale motor testing
should be conducted with due consideration given to the requirements of
scaling the metal combustion process.

Considerable progress has been made in this program in the area of post
test analysis of nozzle performance. It has been demonstrated that detailed
throat deposition, corrosion, ballistic and heat transfer data can be
obtained. The value of such data should not be underestimated nor should
its accuracy be overestimated. The major deterrent to achieving higher
data quantity and quality has been human error. In future propellant
development and materials evaluation programs, greater care should be
taken in obtaining ballistic performance data and in computing performance
efficiencies. The throat deposition/erosion analysis should be developed
further and routinely performed in future programs. Thermal instrumen-
tation techniques used in this program were highly effective. The use of
such techniques in future programs should be encouraged. The post test
measurement of throat corrosion was difficult at best. The circumferential

variation in throat regression can and should be related to the motor design. Maximum and minimum values are useful only when the location is also given. Evidently, much of the nozzle corrosion and heat transfer data obtained in the past may have been strongly influenced by poor metal combustion, nonuniform exhaust flow and/or oxide deposition. Such data should not be used without considerable interpretation in the development of new motor systems or in evaluating theoretical predictions. This generally applies to both aluminum and beryllium propellants.

SECTION 4 (U)

NOZZLE DESIGN AND PERFORMANCE ANALYSIS METHOD

4.1 INTRODUCTION

A major fraction of the program technical effort was devoted to the development of improved analytical methods for post-test characterization of nozzle performance. Parallel efforts were devoted to the improvement of analytical models for predicting nozzle performance. The results of these efforts reflect the achievements in improving the understanding of nozzle/exhaust interaction phenomena which determine nozzle materials performance. This section attempts to organize, condense and generalize these results. The nozzle performance analysis method and philosophy apply to any solid propellant motor and can be extended to other chemical propulsion devices without major revision. Emphasis is placed on philosophy and qualitative analysis. Specific analytical formulations and techniques are outlined or incorporated by reference. The presentation is intended to facilitate the application of the method in the preliminary design and scale testing phases of the motor systems development. If this is actually done, it is believed that many of the problems, such as have been uncovered in the beryllium system, may be circumvented. Of course, the method may still be used in the diagnostic sense in the event that unexpected nozzle or motor insulation performance problems should arise.

A schematic representation of the method is shown in Figure 1. It consists of a series of steps in logical order. Each step provides for the treatment of a well defined segment of the overall analytical problem. It is essential that appropriate decisions be made regarding the technical issues identified in each step. Such decisions are of two basic types. First, the user must decide to include, neglect or ignore the indicated physical features of the problem. Secondly, when an effect is to be included in

INITIAL CONDITIONS:

- PROPELLANT FORMULATION
- NOMINAL MOTOR THRUST PROGRAM
- MOTOR INTERNAL CONFIGURATION
- DESIGN OF NOZZLE COMPONENTS
- MOTOR/NOZZLE MATERIALS

CALCULATION OF IDEAL (THERMODYNAMIC EQUILIBRIUM) PROPELLANT EXHAUST COMPOSITION AND THERMODYNAMIC PROPERTIES.

ESTIMATION OF CHAMBER/NOZZLE FLOW FIELD.

CHARACTERIZATION OF NONIDEAL PROPELLANT COMBUSTION MECHANICS.

ESTIMATION OF ACTUAL PROPELLANT PERFORMANCE, THERMODYNAMIC PROPERTIES, AND EXHAUST COMPOSITION.

SPECIFICATION OF BOUNDARY LAYER EDGE CONDITIONS:

- EXHAUST GAS TRANSPORT PROPERTIES
- MASS FLUX
- RECOVERY ENTHALPY
- CORROSIVE SPECIE CONCENTRATIONS

ESTIMATION OF PARTICLE IMPINGEMENT PROFILE ALONG MOTOR/NOZZLE CONTOUR.

CALCULATION OF EXHAUST/CONTOUR INTERCHANGE FACTORS FOR RADIATION HEAT TRANSFER.

ESTIMATION OF EXPOSED NOZZLE SURFACE CONDITIONS:

- CHEMICAL REACTIONS WITH CORROSIVE EXHAUST GASES
- CHEMICAL REACTIONS WITH CONDENSED PHASE DEPOSITS
- WALL ENTHALPY VARIATION WITH TEMPERATURE, PRESSURE, INSULATION PYROLYSIS, AND CHEMICAL REACTIONS
- SUSCEPTIBILITY TO MECHANICAL EROSION
- MAGNITUDE OF WALL ROUGHNESS

CHARACTERIZATION OF THE BOUNDARY LAYER:

- SKIN-FRICTION COEFFICIENT
- CONVECTIVE HEAT TRANSFER COEFFICIENT
- SPECIE MASS TRANSFER COEFFICIENTS

CALCULATION OF OVERALL NOZZLE THERMOCHEMICAL RESPONSE, SIMULTANEOUSLY COUPLING:

- OVERALL NOZZLE HEAT TRANSFER BY CONDUCTION
- CONVECTIVE AND RADIATIVE HEAT TRANSFER
- FLOW OF SURFACE DEPOSIT
- ABLATION RATES OF SACRIFICIAL INSULATION MATERIALS
- EXPOSED SURFACE REGRESSION DUE TO CHEMICAL CORROSION
- EFFECT OF MASS ADDITION INTO THE BOUNDARY LAYER
- EFFECT OF NOZZLE THROAT AREA VARIATION ON MOTOR BALLISTICS

NOZZLE STRUCTURAL ANALYSIS TO DETERMINE THERMOMECHANICAL EFFECTS

CONCLUSIONS AND RECOMMENDATIONS CONCERNING:

- NOZZLE STRUCTURAL INTEGRITY
- NOZZLE CONTOUR INTEGRITY
- MOTOR BALLISTIC PERFORMANCE
- MODIFICATIONS TO MOTOR NOZZLE DESIGN
- MODIFICATIONS TO MAIN DESIGN
- MODIFICATIONS OF MATERIALS SELECTIONS
- MODIFICATION OF PROPELLANT SELECTION
- FUTURE DEVELOPMENT TEST OBJECTIVES
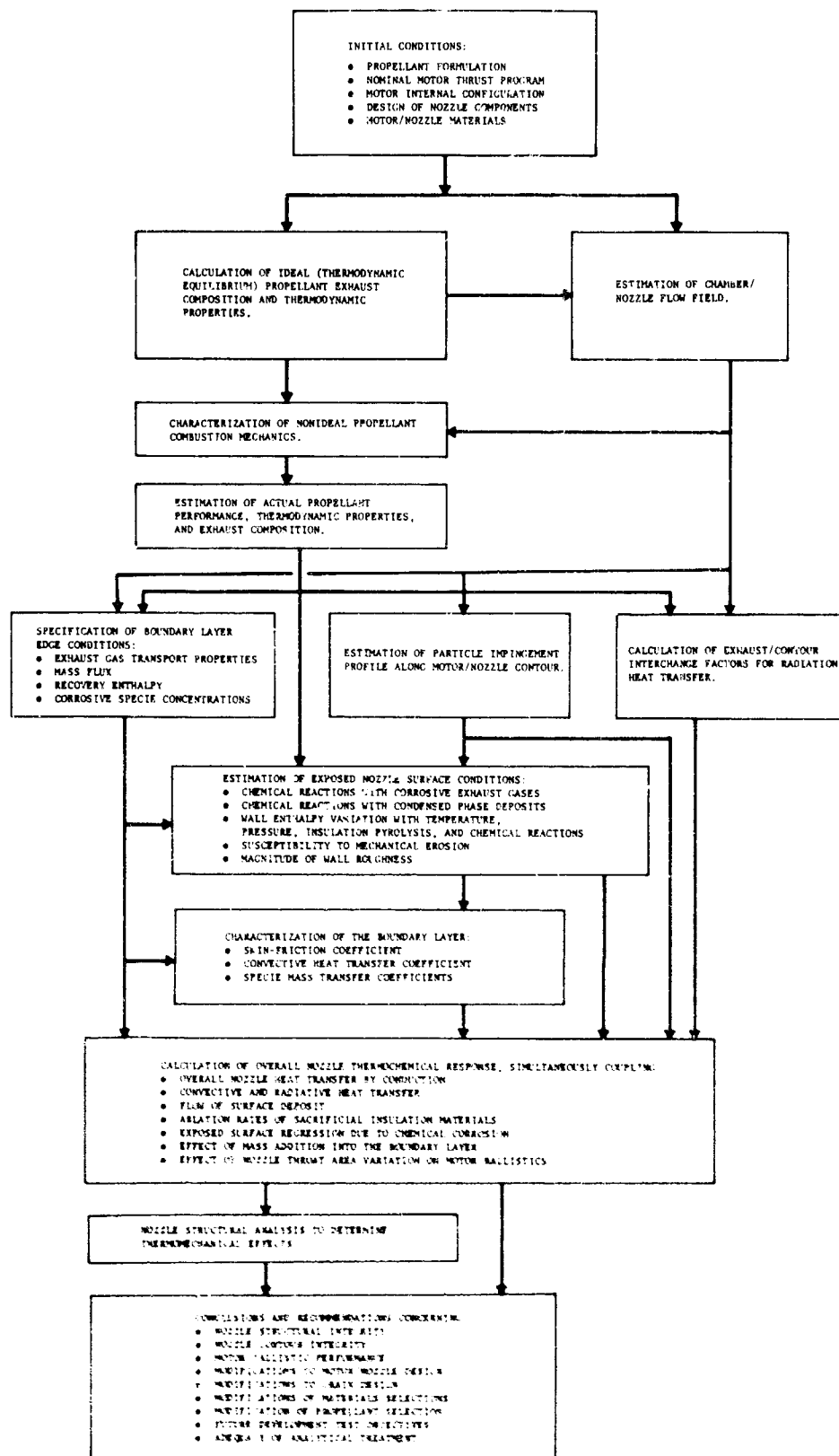- ADEQUACY OF ANALYTICAL TREATMENT

FIGURE 1.   NOZZLE DESIGN AND PERFORMANCE ANALYSIS FLOW CHART

the analytical model, the user must choose a degree of approximation and/or specific analytical or empirical means of treatment. If actual nozzle performance does not agree with design expectations, the validity of these decisions should be re-evaluated. The results of the beryllium motor test program provide numerous examples of how nozzle performance can be misinterpreted if combustion and deposition effects are neglected or ignored. Similarly, the assumption of uniform exhaust flow, hydraulically smooth nozzle contours and thermodynamic equilibrium have been shown to be potentially unrealistic. A matter of particular concern, with respect to the performance of tungsten nozzles, is the consideration of the low melting berylide and carbide formation. In general, the interpretation of scale motor test results, motor performance efficiency data and design concept integrity depend extensively on such decisions. In many instances laboratory and/or motor test experiments are required to provide the basis for, or confirmation of, the technical decisions and results.

The starting point for the analysis would normally be a specific solid propellant rocket motor design. The initial conditions (see Figure 1) to be specified include: the propellant formulation, the nominal motor thrust program (equivalent to the propellant grain design), the motor/nozzle internal contour, the nozzle design, and the heat sink/insulation materials employed. After proceeding through the analytical steps, the user should formulate conclusions and recommendations regarding: (1) the performance of the initial motor/nozzle design (2) modifications to the design and/or materials selection, (3) definition of future development test objectives, and (4) the adequacy and accuracy of the analytical treatment. The motor/nozzle performance primarily includes the overall integrity of the motor/nozzle structure and the stability of the internal contour, and, secondarily, the motor delivered impulse.

In implementing the analytical method, it may be sufficient for the first iteration to use the simplest and most direct techniques in each of the analytical steps. This should permit the rapid detection of the most serious problem areas and indicate where the more sophisticated analytical or experimental techniques are required. It should be noted that some of the simplified techniques described in this section constitute significant improvements over previous idealized first approximations.

As the design iterations proceed, shortcuts may be taken in the implementation of the method. Thus, when the propellant selection becomes fixed, only minor revisions to the propellant combustion analysis need be made. When the motor internal configuration becomes fixed, the flow field, particle impingement, radiation interchange factors, and boundary layer edge conditions need not be re-evaluated. Final selection of the materials leaves only component thermal and structural design details to be worked out.

-83-

It is not unlikely that some of the design modifications suggested by the analysis would involve controversial assumptions employed in the individual analytical steps. This is to be expected in systems employing propellants, materials, and/or design philosophies for which direct engineering experience is minimal. When critical uncertainties arise in characterizing the motor/ nozzle response, encompassing assumptions are made which lead to a range of predicted performance for the particular design. Development tests are then specified to determine the correct analytical formulation. The specification of a test program includes the design of test hardware, the selection of test instrumentation, and the post-test analysis of the data obtained.

Sections 4.2 through 4.10 are organized in accordance with Figure 1. In each subject area, the technical approach, analytical methods and future improvements are discussed. Typical and/or new analyses are outlined or referenced. Section 4.11 briefly discusses the extension of the method of analysis to cooled nozzles and from solids to other chemical propulsion systems.

4.2 PROPELLANT COMBUSTION AND PERFORMANCE ANALYSIS

The characterization of propellant combustion and ballistic performance includes:

    (1) Theoretical calculation of the ideal specific
        impulse, characteristic exhaust velocity,
        adiabatic flame temperature, and the exhaust
        composition,

    (2) Estimation of nonideal combustion effects
        such as excessive internal gas velocities,
        insufficient chamber residence times for
        metal combustion, metal particle agglomera-
        tion, and flow stratification,

    (3) Estimation of actual propellant thermo-
        dynamic characteristics such as specific
        impulse, flame temperature, exhaust compo-
        sition, enthalpy, specific heats, and
        isentropic exponent.

The input requirements for such calculations include:

    (1) The propellant formulation (binder, oxidizer,
        metal, additives, etc.) propellant heat of
        formation, grain microstructure, nominal
        chamber pressure history and nozzle expansion
        ratio,

-84-

(2) Estimation of the internal flow field param-
eters, including internal gas velocities,
condensed particle trajectories, and particle
residence times (see Section 4.3).

The ideal propellant exhaust properties are employed in the estimation of
the internal flow field parameters. The combustion and thermodynamic
data from the estimate of the actual propellant delivered performance is
subsequently used to:

(1) Check the internal flow parameters which were
based upon ideal exhaust properties,

(2) Determine the boundary layer edge conditions,

(3) Estimate the nozzle exposed surface conditions,

(4) Estimate oxide particle impingement profiles,

(5) Calculate interchange factors for radiative
heat transfer.

a. Technical Approach

The ideal characterization of the required propellant exhaust performance
parameters is conducted on a routine basis within the solid propellant
industry. Typical results have been described in Section 3.1. The first
step in the calculation procedure is to find the chamber stagnation condi-
tions, given the propellant formula, ingredient heats of formation, the
thermodynamic properties of all reasonable combustion products and the nominal
chamber pressure history. Adiabatic and equilibrium assumptions are used.
The minimum free energy definition of the equilibrium state is used in the
computerized analysis technique. A key output of this step is the value of
the chamber entropy. The exhaust is then expanded isentropically (in one
dimension) to each of a series of nozzle exit pressures. The nozzle throat
condition is located at the point where the mass flux achieves the maximum
value. Exhaust impulse and C* are calculated from their definitions. At
each specified pressure, all desired thermodynamic state parameters (enthalpy,
temperature, etc.) are calculated. As a matter of option, the exhaust may
be thermochemically frozen at the chamber composition or at any expansion
pressure ratio. Usually, the completely frozen and equilibrium conditions
are calculated. The treatment of rate limited processes (condensation,
fusion and recombination) is usually regarded as being impractical. Since
freezing normally occurs downstream of the nozzle throat, the equilibrium
assumption is preferred in nozzle design. However, freezing in the exit
cone will influence ballistic performance.

In comparing these ideal results with the actual rocket case, the following effects may pertain and introduce significant deviations from ideal:

      (1)   Combustion efficiency losses,

      (2)   Nonadiabatic flow conditions,

      (3)   Incomplete specification of exhaust species and inaccurate thermochemical properties,

      (4)   Nonisentropic flow,

      (5)   Mass flow augmentation and mass storage,

      (6)   Propellant composition variances,

      (7)   Combustion chamber pressure gradients,

      (8)   Multidimensional flow.

The combined result of these effects is an apparent reduction in delivered C^* and ISP efficiency. The delivered efficiency may also be significantly affected by measurement errors and averaging effects. Nevertheless, the ideal propellant/motor performance will continue to be used as a reference in both performance evaluation and design. At this point, the most important question to be resolved is whether or not complete propellant combustion can be achieved in the given motor design. Conversely, the effective degree of combustion in a particular motor test should be ascertained. As discussed in Section 3.1, the failure of the metal additive to burn completely is regarded as the primary factor in poor combustion. This will appear as a ballistic performance loss as well as having a major effect on nozzle performance.

The potential ballistic loss due to poor metal combustion is proportional to the metal loading and, for the propellants used in this program, may be as great as 20 to 25 percent. Combustion losses also include the effects of flow stratification, erosive burning, wall deposition and nonequilibration of condensed phases with gaseous exhaust products. However, the combination of poor metal combustion and flow stratification effects are assumed to dominate in practical cases. Motor/nozzle designs should be developed to minimize these losses and post-test performance analyses should be directed to finding the magnitude of the losses.

It is not obvious that it would ever be required to design a motor to operate under conditions of low average metal combustion efficiency. However, high mass fraction designs are likely to be inefficient during the early portion of the firing. If the hardware is damaged during this period, it may well not survive the full test duration. It is essential then that the designer

estimate the magnitude of the combustion efficiency problem or take positive steps to avoid exposure of hardware to incompletely burned exhausts. With recognition of the problem of properly scaling the metal combustion process, the results of such efforts should be confirmed in actual motor tests. Because of this and the ultimate desirability of maximizing the combustion efficiency, the development of extensive analytical techniques to evaluate the metal combustion phenomenon is not indicated. A more qualitative approach is described below:

(1) Estimate the exhaust gas potential flow field and residence times along streamlines from the grain surface to the points where flow turning occurs at the wall and to the nozzle throat.

(3) Estimate the initial burning particle size distribution. The effect of grain surface agglomeration in distorting the original metal particle size distribution can be evaluated in laboratory propellant combustion studies.

(3) Compute the variation in flame temperature and exhaust composition as a function of degree of metal combustion.

(4) Estimate the required residence times (ignition delay) for particles of various sizes, taking into account variations in particle lag heating, gas velocity, gas temperature and oxidizer concentration along streamlines.

(5) Estimate the tendency of the design to promote stratification and/or deposition of burning metal particles caused by particle slip across streamlines.

(6) Iterate the procedure over the firing period with emphasis on the portions of the test when residence times, the pressure and the chamber velocities are lowest.

(7) For use in post-test analysis, compute C^*, ISP, stagnation enthalpy and exhaust composition as a function of degree of metal combustion. If possible, the motor performance efficiency should be calculated on an instantaneous rather than average basis.

(8) Revise metal combustion efficiency estimates
based on motor ballistic and materials
performance.

(9) If poor metal combustion efficiency is indi-
cated, recommend propellant and/or design
changes.

For either the beryllium or aluminum propellants, the metal combustion
problem will be minimized if metal particle agglomeration does not occur
on the grain surface and the minimum flame temperature (no metal combustion)
is above the oxide melting point. The minimum flame temperature must be
above the minimum particle ignition temperature. The minimum flame tem-
perature could drop below the oxide melting point to account for some frac-
tion of the smaller particles which are certain to ignite very quickly.
Thus, particles up to 5 microns in diameter are likely to ignite in less
than 0.1 millisecond. Evidently, the metal vapor pressure must reach a
critical level (while particles are coated with solid oxides) before rapid
combustion can begin. (Such a combustion criteria would be only meaningful
as long as there was sufficient oxygen available to sustain the vapor phase
reaction.) It should be remembered that the particle residence times rela-
tive to the aft closure insulation and nozzle inlet surfaces may be con-
siderably shorter than those pertaining to the nozzle throat. Consequently,
delivered motor efficiency may not always relate directly to aft closure
or nozzle inlet materials exposure conditions.

The extreme corrosivity of the exhaust during the metal combustion tran-
sient poses a major threat to the hardware. However, wall materials may
survive a poor combustion transient if they are protected by metal and/or
oxide deposits. The use of deep nozzle submergence may lead to some shield-
ing of the nozzle by creating a long flow path for combustion products near
the wall. However, nozzle submergence will tend to eliminate protective
deposit formation. Sacrificial ablation of aft closure and nozzle inlet
surfaces would have a similar shielding effect. In extreme cases, the
propellant or grain design should be changed to avoid the adverse effects
of poor combustion.

The dependence of the combustion transient on the motor design suggests
that prior experience with a given propellant may not be completely relia-
ble in new situations. Propellant tailoring is also likely to influence
the combustion mechanics of the metal additive. The condition or treatment
of the metal itself should not be overlooked.

b. Future Improvements

To the extent that greater emphasis must be placed on the combustion problem
as it relates to motor hardware and ballistic performance, greater emphasis
should also be placed on the study of the combustion of metal additives.

Improved characterization of propellant combustion mechanics, empirical data for motor design, and techniques for acceler ting combustion of metal particles are required. Advanced propellants should be developed to achieve high metal combustion rates. The combustion characteristics of such propellants should be examined as soon in their development as possible. Slurry, gel, fuel rich, liquid and hybrid systems necessarily involve transient combustion processes which may precipitate materials and ballistic performance problems.

4.3 INTERNAL FLOW FIELD ANALYSIS

A complete characterization of the internal flow field (combustion products) would include:

(1) Gas velocity vector throughout the field,

(2) Trajectories of various sized particles,

(3) Chamber residence times for exhaust products from different regions of the grain,

(4) Entropy losses associated with high velocity flow turning and/or heating,

(5) Regions of flow mixing, separation and reattachment,

(6) Variation of the above with grain burn time.

Such a complete analysis is not always necessary or worthwhile. Engineering experience is essential in this step to focus the analytical effort on the more critical aspects of the flow field. The interpretation of scale motor test results or development of scaling criteria are closely related to the evaluation of the motor flow field characteristics.

The input information for the flow field analysis consists of:

(1) The grain and motor/nozzle internal contour,

(2) The thermodynamic properties of the propellant combustion products.

The results and/or assumptions generated in this step are required to:

(1) Select important mechanisms of nonideal combustion,

(2) Calculate boundary layer edge conditions,

(3) Estimate exhaust particle impingement profile,

(4) Calculate radiative interchange factors,

(5) Interpret nonuniform performance of motor materials.

-90-

a. Technical Approach

Internal flow field analyses should be conducted in the preliminary motor configuration design stage, as a part of motor scaling studies and in diagnosing motor materials performance. In most cases, great analytical precision cannot be justified or is not possible. It should be noted that the most convenient assumption, uniform one-dimensional flow, has frequently been treated as a standard in evaluating motor performance and in developing nozzle designs. Pertinent deviations from this ideal are considered below.

The character of the flow field is determined by the grain design, the motor/nozzle contour, the condensed phases and the transient combustion process. Potential flow theory can be used, at least in principle, to establish a first order estimation of the gas flow field. Flow separations, mixing zones, free shear layers and reattachment zones should be approximately located. Again in principle, the condensed phase flow field can be superimposed on the gas flow by neglecting the interaction between the two. Since the condensed phase size distribution will be transient in nature and not well known at any point, the calculation of particle lag and streamlines will be highly approximate. However, it is important to identify flow regions in which the condensed phase will exist in higher or lower than average concentrations. If such regions are formed prior to the completion of metal combustion, the burning particles could be extinguished or the apparent exhaust corrosivity will be distorted. Stratification of the condensed phase may have a significant influence on motor ballistic performance and exhaust plume characteristics.

Internal burning grains with circumferentially nonuniform cores (slots, steps, star points, etc.) will induce the greatest distortion of the flow field from the ideal. Radial jet type flow will interact with the axial core flow to increase turbulence and form free shear layers. As illustrated by the slotted grain tests in this program, the radial jets can induce circumferential nonuniformities in grain burning, nozzle erosion, particle impingement and nozzle convective heating. Such nonuniformities will increase the severity of the local exhaust/wall interactions well above the average or nominal conditions. This could precipitate component and system failure in marginal designs. It is doubtful that more conservative hardware designs could eliminate the problem. Thus, stagnation flow and extreme local turbulence are the causes of locally extreme heat transfer, corrosion and impingement which the wall materials cannot survive. Material changes and wall cooling can only be expected to be partially effective in improving performance. It appears that the most critical materials problems will occur when a submerged nozzle is used with a slotted or star grain. The flow behind the nozzle and along the aft closure insulation will be most difficult to characterize. Extreme turbulence, multiple stagnations and recirculation should be anticipated. Nose cap and insulation materials can simultaneously be subjected to very intense heating, corrosion, shear and impingement.

The evaluation of the internal flow field, for the purposes of estimating the magnitude of the metal combustion problem, was discussed in Section 4.2. It is also important to evaluate the probability of incurring erosive burning. High grain burn rates could alter the character of the metal agglomeration and particle combustion mechanics. Apparently, the effects of high grain surface gas shear, motor axial acceleration and rotation on metal combustion mechanics have not been extensively studied. Strong coupling effects are predicted but the net effect on nozzle performance will not be obvious until the effect of transverse shear and acceleration on metal agglomeration are understood. It should be noted that there will be a major reduction in the chamber flow velocities over the firing period for high mass fraction designs. The highest velocities should relate to the erosive burning limit which may be of the order of 1000 to 2000 ft/sec. A low limit in velocity should probably also be established to account for the reduction in combustion efficiency which could occur due to the reduction of particle lag heating at low gas velocities. (Even a transition from turbulent to laminar lag heating may be critical.) This effect will be offset to some extent by increases in residence time.

b. Future Improvements

Requirements for star and slotted grains will undoubtedly continue. The degree to which insulation and nozzle materials performance will be affected by the flow nonuniformities, with or without transient combustion effects, can only be roughly estimated. More sophisticated experimental or analytical studies should be related as closely as possible to a particular propellant and motor system. Scale and development motor test results should be interpreted in terms of grain design and poor combustion induced erosion. When problems arise, supplemental scale and cold flow testing could be conducted to provide a relative basis for evaluating alternate designs.

4.4 BOUNDARY LAYER EDGE CONDITIONS

The accurate determination of the boundary layer edge conditions and exhaust gas transport properties is essential to the prediction of both heat transfer and corrosion. The following data are required:

(1) Local mass flux of exhaust gases,

(2) Local recovery enthalpy,

(3) Local exhaust gas composition,

(4) Variation of exhaust gas viscosity, thermal conductivity, and Prandtl number with local pressure, temperature, and composition,

(5) Magnitudes of flow nunoniformities as a function of circumferential location near the nozzle surface.

Input information for this step in the analysis is obtained from:

(1) The estimate of the actual propellant performance, thermodynamic properties, and exhaust composition,

(2) The internal flow field analysis.

The data resulting from this step are then employed in the:

(1) Estimation of nozzle surface conditions.

(2) Calculation of boundary layer transport coefficients.

(3) Calculation of nozzle overall thermochemical response.

a. Technical Approach

The basic assumption of the flow field calculations was that the flow is inviscid. The internal contour of the motor and nozzle defines the boundary of the flow field. For most cases, the magnitude of the error introduced by neglecting the boundary layer displacement thickness along the contour is very small. In such cases, the boundary layer edge conditions are equivalent to the flow field conditions along the nominal internal contour. In general these conditions are dependent upon the axial and circumferential location along the motor/nozzle contour and the time from motor ignition.

The first approximation in determining the edge mass flux and recovery enthalpy is to assume a one-dimensional flow field. For this assumption:

$$(\rho u)_e = \frac{P_c \, g}{C^*} \left(\frac{A_t}{A} \right)$$

where:

$(\rho u)_e$ = mass flux at the boundary layer edge, $lbm/(in^2 sec)$

P_c = chamber pressure, psia

g = acceleration due to gravity, $32.174 \, ft/sec^2$

C^* = characteristic exhaust velocity, ft/sec

A_t = nozzle throat area, in^2

A = local nozzle cross-sectional area, in^2

The second approximation accounts for axially symmetric deviations from the one-dimensional flow. The expression for mass flux is the same as in the first approximation except for the substitution of A' for A. The quantity A' is defined as the local flow cross-sectional area and is obtained as a function of axial location from the flow field analysis. Note that A' will be greater than or equal to A. Since the gas shear, heat transfer and mass transfer increase with mass flux, the use of A' rather than A is not conservative. The most refined estimate takes circumferential nonuniformities into account. In this case, the mass flux distribution should be obtained directly from the flow field analysis.

In some boundary layer analyses the mass flux is expressed in terms of the Mach number at the boundary layer edge. For example, Reference 11 uses the following expression for $(\rho u)_e$:

$$(\rho u)_e = \frac{0.203 \, \gamma \, P_c \, M_e}{\left[C_p \, T_c \, (\gamma - 1)\right]^{1/2} \left(1 + \frac{\gamma - 1}{2} M_e^2\right)^{\frac{\gamma + 1}{2(\gamma - 1)}}} \tag{1}$$

where:

M_e = edge Mach number

γ = isentropic expansion exponent

C_p = specific heat at constant pressure (exhaust products), Btu/lbm°R

T_c = adiabatic flame temperature, °R

In employing this expression, γ is chosen to give the proper pressure at the throat. The actual values of P_c and T_c (from the combustion analysis) are used and the value of C_p is chosen such that the maximum value of $(\rho u)_e$ is given by the expression for $M_e = 1$. Then, if the one-dimensional assumption is made, the variation of M_e with axial location is determined from the equation:

$$\frac{A}{A_t} = \frac{1}{M_e} \left(\frac{1 + \frac{\gamma - 1}{2} M_e^2}{\frac{\gamma + 1}{2}}\right)^{\frac{\gamma + 1}{2(\gamma - 1)}}$$

Otherwise, if the mass flux variation does not correspond to one-dimensional flow, the variation in Mach number with axial location is calculated from Equation 1 to match the variation in mass flux determined from the flow field analysis.

Local variations in the mass flux with time should generally be accounted for. In cases where the flow field is uniform and simple, the mass flux will be proportional to pressure. As the grain burns away from the nozzle (particularly submerged nozzles), other mass flux variations will occur and should be accounted for.

The calculation of the convective heat transfer requires a knowledge of the recovery enthalpy along the nozzle contour. For turbulent flow, this enthalpy is calculated from:

$$H_r = h_e + (Pr)^{1/3} (H_e - h_e) \tag{2}$$

where:

H_r = recovery enthalpy, Btu/lbm

h_e = static enthalpy at the boundary layer edge, Btu/lbm

Pr = Prandtl number of the exhaust

H_e = total enthalpy at the boundary layer edge, Btu/lbm

In addition to the enthalpy data, the propellant combustion and performance analysis provides an estimate of the variation in exhaust composition throughout the nozzle. Calculations of the corrosivity of the exhaust depend upon the composition at the boundary layer edge. Both mole fractions and mass fractions of all important species in the exhaust gas should be specified at this point in the analysis. This boundary layer edge composition data is used to characterize the wall conditions and calculate transport properties for the exhaust gas.

Currently, the transport properties for the exhaust gas are calculated by a variety of methods. The simplest of these is that of Reference 6. The most refined method is that described in Section II of Reference 4 which employs the data of Reference 12 and the equations of Reference 13 to obtain values of μ_o, k, and Pr for the exhaust gas mixture. This method is a very good approximation to the rigorous kinetic theory for multi-component gas mixtures (Reference 13), but is not complex to an impractical extreme. The potential improvement in accuracy is brought out by the following example:

T_c = 6794°R $\overline{M}$ = 18.21 γ = 1.16

C_p = 0.492 Btu/lbm°R (frozen)

$\overline{M}$ = mean molecular weight of exhaust gas mixture

The results for the two methods are summarized in the following table. All of the indicated changes tend to significantly increase the predicted values of the convective heat transfer.

Transport Property	Simple Method	Refined Method	% Change
μ_o lbm/in sec	0.392×10^{-5}	0.512×10^{-5}	+31%
k Btu/in sec°R	0.226×10^{-5}	0.575×10^{-5}	+254%
Pr	0.855	0.438	-49%

The discussion of the diffusion coefficients for the species diffusing through the exhaust gas mixture has been included in Section 4.8. The mixture diffusion coefficients are calculated from the binary coefficients for each specie with every other specie in the exhaust mixture. The calculation of the binary diffusion coefficients is discussed in Section II of Reference 4. The standard method of calculating these coefficients is by the expression:

$$D_{ij} = \frac{0.004233 \times T^{1.5} \left(\frac{M_i + M_j}{M_i M_j} \right)^{1/2}}{P \sigma_{ij}^2 \Omega_{P_{ij}}} \tag{3}$$

where

D_{ij} = diffusion coefficient for specie i through specie j, in^2/sec

P = local pressure, psia

T = local temperature, °K

M = molecular weight

σ_{ij} = mean collision diameter for species i and j, angstroms

$\Omega_{P_{ij}}$ = collision cross-section integral for diffusion

The data in References 12 and 14 have been used in conjunction with Equation 3 to obtain the diffusion coefficients.

b. Future Improvements

A shortcoming of the current techniques for specifying the boundary layer conditions is that the effects of adding material (pyrolysis gases and/or

products of surface corrosion reactions) to the boundary layer upstream of the point of interest are not included. The effects of this boundary layer mass addition pertain to the potentials for surface corrosion and convective heat transfer (see Section 4.8). All mass addition effects may be included in the analysis through modifications in the boundary layer structure. However, it is physically realistic and convenient to separate the effects into those influencing the convective heat transfer and surface corrosion coefficients, and those influencing the recovery enthalpy and the effective composition of corrosive boundary layer gases. This separation of effects corresponds to the simplified terminology of "blocking" effects and "dilution" effects.

Relative to the blocking effects, the dilution effects of mass addition at the nozzle surface are difficult to estimate. A physical model of the dilution process includes:

> (1) The addition of pyrolysis gas and products of surface corrosion reactions to the boundary layer,

> (2) The mixing of these gases with the propellant exhaust gases in the boundary layer,

> (3) The establishment of a new thermochemical equilibrium in the mixture and new effective edge enthalpy and composition at some point downstream of the original injection point.

The translation of this physical model into a useful mathematical model is limited by the lack of quantitative knowledge of two key parameters in the model. These are the mixture ratio of injected gases to propellant exhaust products and the distance downstream of the point of injection where the mixture thermochemical equilibrium properties become the effective edge conditions.

To date, the majority of the effort to clarify this problem has been in the area of highly idealized laboratory experiments. Rocket motor test firings, representing the opposite extreme in experimental work, are not well suited to the investigation of the dilution effects because of the relative lack of control. The best experimental approach would probably involve a compromise between the two extremes. The testing would be of the laboratory type and employ:

> (1) "Warm" gases (1500 to 2500°K) of carefully controlled composition,

> (2) Well characterized flow geometries such as a flat plate,

-97-

(3) Materials representative of those employed in
               solid rocket motors.

4.5 PARTICLE IMPINGEMENT ANALYSIS

Discussed in this subsection are the techniques of estimating the particle
impingement profiles for the given motor/nozzle internal contour. The
particle impingement profile data includes:

          (1) Frequency per unit area of condensed particle
               impingement as a function of location on the
               contour, particle size, and propellant consumed,

          (2) Mass, momentum, and energy fluxes to the surface
               due to particle impingement.

The input data for this analysis is obtained from the propellant combustion
and flow field analyses and includes:

          (1) Composition of condensed particles,

          (2) Size distribution of particles in the chamber,

          (3) Particle trajectories.

The results of the impingement profile analysis are employed in:

          (1) Estimating the nozzle exposed surface conditions,

          (2) Calculating the nozzle thermochemical response
               (flow of surface deposit).

As in the flow field analysis, the complete specification of particle impinge-
ment by theoretical methods is impossible for most cases of interest. This
implies a need for reliable empirical techniques to interpret and scale
particle impingement and motor materials performance data.

     a. Technical Approach

Condensed phase impingement has been studied by a variety of analytical,
cold flow modeling and motor test techniques. Each of these is limited in
its ability to represent the actual case. The cold flow and scale motor
testing approach may provide some information concerning impingement area
location, boundary layer starting point and nonuniform flow effects. Cold
flow modeling results from this program may be found in Sections 3.3 of
References 1 and 2. When transient combustion and nonuniform flow effects
are acknowledged, it is apparent that the effort and expense of such work
may not always be justified. The alternate approach is more qualitative in
nature and depends on understanding the results of analytical and experi-
mental studies of particle impingement.

Evidently, both the normal metal oxides and the metals themselves can be impinged on motor surfaces. It is assumed that each particle may stick to the wall or rebound in accordance with the nature of the wall material, its surface character, its temperature, the momentum and energy impact parameters, the physical state of the particle and its physical properties. Except in rare instances (contoured exit cones), it is expected that the impinging particles will be in the liquid state. Lacking specific evidence to the contrary, some or all of the liquid can be assumed to remain on the surface. The most obvious exception to this rule occurs when the impact causes the physical removal of the material in the impact zone. (Ablative and polycrystalline materials in the vicinity of a near normal flow stagnation would probably experience this type of physical erosion.) When the particles do stick, they will contribute to the heating of the surface, both because they will be hotter than the surface and the mechanical impact energy will partially dissipate as heat. When the impact surface is liquid (silica melt, molten alumina, etc.), particle sticking may be more efficient but splashing could occur.

The consequences of impingement are chemical, mechanical and thermal. At least for graphite and tungsten materials, the metal oxides of aluminum and beryllium do not pose a significant chemical interaction problem. However, the deposition of aluminum or beryllium metal on tungsten (and possibly metal motor components) could have disasterous results. Mechanical erosion is most likely to occur in high velocity flow stagnation regions, at high materials surface temperatures and with structurally weak surfaces. This effect could be avoided by eliminating the flow stagnation condition (a design-flow field tradeoff) or by changing materials. It is speculated that, in the past, excessive gas phase corrosion associated with poor metal combustion may have been misinterpreted as impaction induced mechanical erosion. The net thermal effect of impaction depends on whether or not sticking occurs. If sticking does not occur, the local heating rates will be significantly augmented relative to convective heating. When sticking occurs, the deposit insulation effects can more than compensate for the particle heating. Furthermore, the flow of the deposit extends the insulation effects to surfaces downstream where impaction is not occurring. As a matter of choice, the designer could elect to eliminate such deposit formation and flow effects by preventing either particle impaction or sticking. Conversely, by increasing impaction rates, it should be possible to encourage deposit formation to take greater advantage of the insulation effect. Apparently, the accumulation of high temperature slag on motor surfaces, not normally exposed to convective heating, has caused motor case burn throughs in the past. In such cases, minimal insulation has been available to resist the slag heating.

Accurate means of predicting impingement rates in complex motors have not been developed. In the present program, the character of the deposit history at the nozzle throat was evaluated by ballistic and thermal performance analyses. Such data could be used to estimate the fraction of the total

condensed material that was actually deposited. Cold flow modeling data and analytical estimates could also be used to provide a reference for comparative analysis. Post test inspection of fired hardware would al o be useful as would measurement of thermal response along the motor contour. Ultimately, actual motor materials performance will probably provide the best indication of the effectiveness of empirical design techniques employed to control the condensed phase impaction and deposition.

b. Future Improvements

In the future, motor testing should be used to further evaluate the possibility of exploiting the advantages of oxide deposition protection. The effects of nozzle submergence on slag accumulation and deposition control are matters of particular interest. It is emphasized that impingement and deposition are closely related to the degree and rate of metal combustion, the grain design and the motor/nozzle wall contour. The designer should anticipate both the benefits and adverse effects of condensed phase impingement, slag accumulation, deposit protection and slag expulsion. All motor tests and results should be studied to confirm qualitative expectations and to improve the understanding of the behavior of the condensed phases. Gravity field and acceleration effects on slag deposits should be considered in motor test programs.

4.6 RADIATION PARAMETRIC ANALYSIS

This section describes the techniques used to calculate the radiative heat transfer in rocket nozzles. The three sources of radiant energy for heat transfer to a given location on the nozzle surface are:

      (1) Exhaust gases,

      (2) Condensed particles in the exhaust,

      (3) Regions of the nozzle surface with a line-of-sight to the given location.

Effective emissivities for radiation from these sources are dependent upon:

      (1) Absorption and scattering coefficients of the gaseous species and particles,

      (2) Effective path lengths for radiation emitted from the three sources,

      (3) The intersurface view factors,

      (4) The nature of the nozzle surface materials.

The estimation of gas and particle emissivities from scattering and absorption coefficient data is ordinarily not possible for the complex solid propellant exhaust mixtures. In most cases, a method of scaling gas and particle emissivities (in combination) from direct measurements of the radiant energy flux in solid rocket motors is employed.

The input information of primary importance to this analytical step is:

      (1) The motor/nozzle internal contour,

      (2) The composition of the propellant exhaust gases,

      (3) The composition and size distribution of particles
           in the exhaust.

The actual calculation of the contribution to the overall nozzle heat transfer by radiation is performed in the computerized, coupled analysis using the instantaneous surface temperatures and the appropriate emissivity data in parametric form. In many cases, the treatment of radiation may be omitted when it can be shown to be negligible compared to convection.

    a. Technical Approach

The radiation heat flux to the nozzle surface may be written as (see Sections 2.5 of References 1, 2 and 3):

$$q_{rad} = \epsilon_{gw} \, \sigma \left(T_g^4 - T_w^4 \right) \qquad (4)$$

where:

$$\frac{1}{\epsilon_{gw}} = \frac{1}{\epsilon_g} + \frac{1}{\epsilon_w \, \epsilon_{g\infty}} - \frac{1}{\epsilon_{g\infty}}$$

q_{rad} = radiation heat flux, Btu/in^2 sec

ϵ_{gw} = overall emissivity

ϵ_g = local emissivity of combustion products

$\epsilon_{g\infty}$ = maximum emissivity of combustion products

ϵ_w = local surface emissivity

σ = Stefan-Boltzmann constant

$$T_g \quad = \quad \text{local static temperature of combustion products, } °R$$

$$T_w \quad = \quad \text{local surface temperature, } °R$$

Equation 4 is valid primarily for propellant exhausts with significant amounts of condensed species. In such cases, the combustion products radiant emission is primarily from the condensed species. Radiation from surfaces with a line-of-sight to the surface of interest will usually be negligible due to the scattering nature of the condensed phase. For propellant exhausts with no condensed species, the radiation flux is primarily from the gaseous species H_2O, CO, HCl and from nearby surfaces. Techniques for the estimation of radiation view factors are described in Reference 15. The most refined of these techniques is a computer program which integrates the intersurface radiation to any point on the contour of an axisymmetric nozzle.

Referring again to the situation where condensed particle cloud radiation is dominant, the local and maximum cloud emissivities are related by the expression:

$$\epsilon_g \quad = \quad \epsilon_{g_\infty} \left[1 - \exp(-\phi \ell) \right] \tag{5}$$

where:

ϕ = constant dependent upon the optical properties (scattering and adsorption coefficients) of the exhaust,

ℓ = mean path length for radiation from the cloud to the given point on the nozzle surface.

A summary of the underlying theory for this expression is provided in References 1 and 2. Currently, the implementation of this expression for the calculation of ϵ_g is limited by the complexity of the theoretical expressions for ϕ and ϵ_{g_∞}. Experimental data are required for these factors in the analysis. Reference 7 shows the selection of $\ell = 0.9$ times the local nozzle diameter to be valid for alumina particle clouds. Measurements of the terms in Equation 5, reported in References 7 and 16 for alumina clouds, show the influence of static pressure and temperature, mean molecular weight of the exhaust, mean radiation path length, and the weight percent of alumina in the exhaust. The value of the maximum emissivity may vary from 0.2 to 1.0 depending upon the amount of condensed carbon and/or iron oxide particles in the alumina cloud. A value of 0.28 for a beryllia particle cloud was reported in Reference 2. As noted in Reference 2, $\epsilon_g \approx \epsilon_{g_\infty}$ for PD ≥ 450 psia-ft, where P is the local static pressure and D the local nozzle diameter. For regions of the nozzle where PD < 450 psia-ft and the radiation heat flux is likely to be important compared to the convective heat flux, the data of Reference 7 could be used. Similar data for beryllia clouds has not been found. The use of alumina data offers the best available approximation.

The emissivity of the nozzle surface depends on the presence or absence of deposits of condensed exhaust products (primarily BeO or Al_2O_3). Data found in the literature and summarized in Reference 2 indicates an approximate emissivity range of 0.2 to 0.3 for metal oxides deposits and 0.8 to 1.0 for carbon chars and graphite materials.

b. Future Improvements

The weakest point in the parametric radiation analysis is the determination of particle cloud emissivity for clouds composed of particles other than pure alumina. The effects of varying amounts of impurities such as carbon particles and iron oxide upon the cloud maximum emissivity and emissivity correction factor are uncertain. These uncertainties become increasingly important as the motor size is increased. For beryllia clouds, the emissivity data are especially sparse. The amounts of unburned metal particles may be an important variable in the estimation of the maximum and local emissivities of beryllia clouds. The best approach to gathering the basic emissivity data is probably the use of the technique which has proven successful in obtaining the existing data. This involves the use of radiometers in measuring cloud emissivities in actual solid rocket motor firings. The method of analysis of data obtained from these tests is described in Reference 2.

4.7 EXPOSED SURFACE CHARACTERIZATION

The characterization of the exposed motor/nozzle contour surfaces includes the determination of:

(1) Chemical reactions between exposed wall materials, exhaust products, condensed deposits, and insulation pyrolysis gases,

(2) Chemical composition of gases immediatly adjacent to the surface,

(3) Enthalpy of gases adjacent to the surface,

(4) Chemical corrosion potential in terms of differences in corrosive species concentrations between the boundary layer edge and the surface,

(5) Susceptibility of the surface material to mechanical erosion,

(6) Magnitudes of surface roughness.

This data should be obtained in a parametric form to account for transients in surface temperature, pressure, and pyrolysis gas flow.

The inputs required for this parametric characterization are obtained from:

     (1) The specification of nozzle materials,

     (2) The propellant combustion analysis,

     (3) The specification of boundary layer edge conditions,

     (4) The estimation of the particle impingement profile.

The parametric results are required in the final coupled calculation of the nozzle thermochemical response. The chemical composition of the gases adjacent to the surface and the anticipated magnitudes of surface roughness are used in the calculation of the boundary layer heat and mass transport coefficients.

    a. Technical Approach

The identification of the chemical interactions between the exposed surface, exhaust products and pyrolysis gases can be accomplished using existing thermochemistry computer programs. Typically, the thermochemical equilibrium composition and related thermodynamic data for reacting systems are found using the minimization of free energy method. The use of the same technique to analyze the propellant combustion and performance is discussed in Section 4.2. The employment of thermochemistry programs to characterize the chemical corrosion of the exposed nozzle surface is discussed below.

The first approximation in determining the nature and quantitative extent of the surface corrosion is to calculate the chemical equilibrium composition of a unit mass of exhaust products saturated with the surface material. Pyrolysis gases may be added in any desired ratios to the exhaust products. The local pressure and temperature are input to uniquely determine the thermodynamic state of the mixture. The composition of the gases saturated with wall material is compared with the exhaust composition at the boundary layer edge. This comparison is used to identify the important corrosion reactions which are likely to occur.

Limitations to the corrosion reactions predicted from thermodynamic equilibrium considerations arise from three sources. These are:

     (1) Finite gas-solid reaction rates (kinetic limitations),

(2) Unavailability of condensed exhaust products
for corrosive reactions,

(3) Protection of the surface material by a
deposit of condensed exhaust products or
condensed products of corrosion reactions.

The influence of finite corrosion reaction rates on corrosion may be
estimated using the thermodynamic equilibrium program. Knowing the
pressure and temperature, kinetic data for the particular reaction of
interest, and a first estimate of the mass fluxes of the species taking
part in the reaction, the heats of formation of appropriate species may be
adjusted to anticipate the shift in mixture composition at the surface. In
general, some iteration would be required until the calculated specie mass
fluxes agree with the specie rates of production (or consumption) at the
surface. Unfortunately, the results of including reaction kinetic effects
are not easily obtained in the desired parametric form. Reference 8
describes the development of a special computer program to calculate the
kinetically controlled corrosion of graphite exposed to gas mixtures con-
taining CO_2, H_2O, and H_2. This program has a similar shortcoming in that
the corrosion potential is a function of the specific mass transfer coef-
ficient, in addition to the pressure, temperature, and pyrolysis gas flow
rate. A practical approach to including kinetic effects is to estimate
the regimes (temperature, pressure, etc.) where these effects become sig-
nificant and apply empirical factors to the equilibrium estimates of the
potential for surface corrosion.

A second technique is useful for estimating the lower limit for corrosion
in kinetically controlled reactions. After identifying the particular
reactions which will be kinetically controlled, the products of these
reactions may be deleted from the list of acceptable output species for the
equilibrium calculation. The result is a composition at the surface which
reflects a zero reaction rate for the selected corrosion reactions. In
some cases the bracketing of the corrosion potential by this latter tech-
nique is sufficient to provide insight into the importance of reaction
kinetic effects.

When exhaust products such as metal oxides are condensed, they will be in a
particulate form, unable to equilibrate with either the gas phase or the
wall. The particle impingement profile may also indicate that the particles
will not approach the surface. The effect of these conditions upon the
estimate of surface corrosion is obtained by eliminating the condensed
products in the exhaust composition which is input to the chemical equili-
brium corrosion calculation.

When the exhaust products or the products of the corrosion reactions occur
as condensed species, the possibility of their inhibiting gas phase corro-
sion must be examined closely. If such products are in the liquid state,

they might be removed by the gas shear and thus not completely block the gas-solid reactions. If the products form in the solid state, the reactions can only procede via the diffusion of corrosive gases through the solid coating.

The quantitative results of the surface corrosion analysis include the corrosion potential and the enthalpy of the mixture at the surface as functions of pressure, temperature, and pyrolysis gas addition at the surface. As presented in Reference 17 and discussed in Reference 1, the corrosion potential is the "B value" which represents the mass of wall material required to saturate a unit mass of exhaust products. For gas mixtures where all the species in the mixture have identical mass transfer coefficients, it can be shown that:

$$\dot{r} = (\rho u)_e \, C_m \, \frac{B}{\rho_x}$$

where:

$\dot{r}$ = linear surface corrosion rate, in^2 sec

$(\rho u)_e$ = boundary layer edge mass flux, lbm/in^2 sec

C_m = mass transfer coefficient for the gases in the mixture

ρ_x = density of the surface material, lbm/in^2

The parametric data for B as a function of pressure, temperature, and pyrolysis gas flow rate is then part of the input for the calculation of $\dot{r}$ in the final calculation of the nozzle thermochemical response.

The thermochemical equilibrium program, which determines the mixture composition at the surface and the B value, also calculates the mixture enthalpy from,

$$H_w = \sum_i X_i \left(\Delta H_{f_{298_i}} + \Delta H_{T_i} \right)$$

where:

H_w = enthalpy of the composition at the surface, Btu/lbm

X_i = mole fraction of specie i at the surface

$\Delta H_{f_{298_i}}$ = heat of formation of specie i at 298°K, Btu/lbm

ΔH_{T_i} = enthalpy required to raise specie i from 298°K to the local temperature, Btu/lbm

-106-

Then, the convective heat transfer to the surface is expressed as:

$$q = (\rho u)_e \, C_h \, (H_r - H_w)$$

Here the symbols are defined as:

q = convective heat flux, Btu/in^2 sec

C_h = Stanton number

H_r = recovery (adiabatic wall) enthalpy, Btu/lbm

As with the B value, the variation of H_w with pressure, temperature, and pyrolysis gas flow is obtained for the coupled calculation of nozzle response. Note that the standard reference enthalpy for H_{aw} and H_w should be the same for the expression for q to be correct.

The estimation of the susceptibility of the surface material to mechanical erosion and roughening is considerably less refined than the estimation of surface chemical corrosion. It is necessary to identify regions of the surface where erosion is likely to be either completely negligible or completely dominant with respect to corrosion effects. In the former case, the results of the coupled calculation of nozzle thermochemical response are unaffected by erosion. In the latter case, both corrosion and heat transfer rates will be dominated by roughness effects as only turbulent transport processes will occur in the boundary layer.

The qualitative estimate of the susceptibility of the surface to mechanical erosion should be based upon the following specific information:

(1) Microstructure of the surface material,

(2) Likelihood of corrosive reactions occurring beheath the surface of the (porous) material,

(3) Strength properties of the material near the surface,

(4) Local impingement rates and momentum of condensed particles in the exhaust,

(5) Estimates of gas shear at the surface,

(6) Estimates of the pressure drop due to pyrolysis gas flow through the porous char of sacrificial insulation materials.

The magnitude of the surface roughness should be estimated to determine the possibility of increased gas shear, convective heat flux, and corrosive species transport. The surface roughness may have a critical influence upon the boundary layer transport coefficients as a result of altering the boundary layer structure. Order of magnitude estimates for surface roughness heights may be obtained from a knowledge of the microstructure of the material and the mode of surface corrosion/erosion. For example, the magnitubes of surface roughness for polycrystalline graphites is probably of the order of the grain size. The distribution of the roughness elements over the surface is also important in estimating the effect of the surface roughness upon the boundary layer structure.

   b. Future Improvements

while the analytical techniques for characterizing the nozzle surface materials are considered adequate, the quality of materials property data is poor. The data which could be greatly improved through careful laboratory investigation include:

   (1) Properties of liquid and solid metal oxide
        deposits (liquid viscosity, thermal con-
        ductivities, and surface emissivities),

   (2) Additional chemical kinetic rate data for
        charred surfaces of insulation materials.

   (3) Magnitudes of surface roughness developed by
        various materials under flow conditions which
        simulate the rocket nozzle environment.

4.8 BOUNDARY LAYER ANALYSIS

The evaluation of the boundary layer transport coefficients is discussed in this section. The transport coefficients include:

   (1) Skin friction coefficient for gas shear
        calculation,

   (2) Stanton number for convective heat transfer
        rate calculation,

   (3) Species mass transfer coefficients for chemical
        corrosion rate calculation.

The coefficients are determined from a calculation of the local boundary layer which is dependent upon:

(1) Local mass flux at the boundary layer edge,

(2) Transport properties of the gases in the boundary layer,

(3) Surface temperature and pressure,

(4) Pyrolysis gas injection into the boundary layer,

(5) Magnitude of the local surface roughness.

Parametric calculation of the transport coefficients is usually required. The parametric data is then employed in the calculation of the nozzle thermochemical response. Input to the boundary layer analysis is obtained from the specification of boundary layer edge conditions and exposed surface conditions.

a. Technical Approach

The characterization of boundary layers starts with the determination of whether they are laminar or turbulent. This requires the calculation of the local Reynolds number for the boundary layer and a comparison of this parameter with a critical Reynolds number for transition from a laminar to a turbulent structure. The critical Reynold's number is a function of the pressure gradient along the surface, the magnitude of the surface roughness, mass addition, heat transfer at the surface, and external flow field turbulence. In most correlations of boundary layer transition data, the characteristic length employed in the critical Reynold's number is either the boundary layer displacement thickness or momentum thickness. Some data obtained directly from rocket motor firings (Reported in Reference 19) seems to indicate that the boundary layer at the nozzle throat (hydraulically smooth) will be laminar or in transition for sufficiently low values of the Reynold's number based on throat diameter. The general applicability of this data to solid propellant rockets is controversial. In any case, it is desirable to determine the nature of the boundary layer along the entire contour. This task requires the use of more fundamental data than can be obtained from rocket motor firings. Since most solid rockets operate at chamber pressures in excess of 200 psia, the Reynold's numbers for these motors are sufficiently large to insure that the boundary layer will be turbulent throughout the nozzle. Exceptions are noted further on in the discussion.

-109-

The characterization of turbulent boundary layers in rocket nozzles may be accomplished with a variety of techniques. Currently, the best approach to the boundary layer characterization (including the calculation of the required transport coefficients) consists of the following steps:

Step 1. The nozzle boundary layer computer program of either Reference 11 or Reference 19 is used to calculate the boundary layer parameters including the skin-friction coefficient and the Stanton number. Both of these analyses assume the turbulent boundary layer is developing over a hydraulically smooth surface in a flow field with a nonzero pressure gradient. The analysis of Reference 11 assumes the exhaust gases are perfect, but allows an arbitrary boundary layer Mach number distribution to be input independent of the actual nozzle geometry. The program of Reference 19 may employ variable exhaust thermodynamic properties, but assumes the mass flux at the boundary layer edge is related directly to the nozzle geometry. The forms of the Reynold's analogy (between momentum and heat transfer) employed by the two programs differ slightly.

Step 2. The skin-friction coefficient and Stanton number distributions along the nozzle contour are fitted to correlation equations of the following form (see Section 3.?):

$$C_f/2 = C_1 \left(\frac{\mu_o \, C^*}{D_t \, P_c \, g}\right)^{0.2} \left(\frac{D_t}{r_c}\right)^{0.1} \left(\frac{A}{A_t}\right)^n \sigma$$

$$C_h = \frac{C_t/2}{1 - 5 \, (C_f/2)^{1/2} \left[1 - 2r + \ln\left(\frac{6}{5 \, Pr + 1}\right)\right]}$$

where:

C_1 = correlation coefficient

μ_o = viscosity of exhaust gases in the chamber, lbm/in sec

C^* = characteristic exhaust velocity of the propellant, ft/sec

D_t = nozzle throat diameter, in.

P_c = chamber pressure, psia

g = acceleration due to gravity, ft/sec^2

r_c = radius of curvature of the nozzle contour at the nozzle throat, in.

A = local nozzle cross-section area, in^2

A_t = nozzle throat area, in^2

σ = temperature correction factor for gas density and viscosity across the boundary layer

Pr = Prandtl number of the exhaust gas mixture

n = correlating exponent

The values of C_1 and n are adjusted to provide the best fit for both $C_f/2$ and C_h along the contour. Recent studies (Reference 4) indicate that the value of C_1 will be in the range 0.0225 to 0.026 and the value of n will be approximately 0.1.

Step 3. By extending the similarity analysis which related C_h to $C_f/2$ and the Prandtl number of the gas mixture, the relationship between the mass transfer coefficients (Cm_i) and $C_f/2$ may be shown to be:

$$Cm_i = \frac{C_f/2}{1 - 5\,(C_f/2)^{1/2}\left[1 - Sc_i + \ln\left(\frac{6}{5\,Sc_i + 1}\right)\right]}$$

where:

$$Sc_i = \frac{\mu}{\rho D_{i,mix}} = \text{Schmidt number for specie } i$$

μ = gas mixture viscosity, lbm/in sec

ρ = gas mixture density, lbm/in^2

$D_{i,mix}$ = diffusion coefficient of specie i in the gas mixture, in^2/sec

This expression may be derived employing boundary layer assumptions similar to those employed by von Karman in deriving his relation between C_h and $C_f/2$. A summary of von Karman's derivation is presented in Reference 20. Currently, the most practical technique for evaluating the Cm_i's is to assume all the specie Schmidt numbers are identical and equal to the Prandtl number. This assumption leads to the conclusion:

$$Cm_i = C_m = C_h$$

It further implies that the B values obtained in the exposed surface characterization may be used directly in calculating the corrosion rate.

<u>Step 4</u>. The injection of surface material (corrosion products) and/or pyrolysis gases into the boundary layer may have a major effect on the boundary layer structure and, therefore, the transfer coefficients. The magnitude of this effect is estimated through the use of the following parameter:

$$B_t = \frac{(\rho v)_{pyrolysis}}{(\rho u)_e \, C_h} + B$$

where:

B_t = a total B value including net flow of corrosive gases, reaction products, and pyrolysis gases.

$(\rho v)_{pyrolysis}$ = mass flux of pyrolysis gas at the nozzle surface, lbm/in^2 sec

$(\rho u)_e$ = mass flux at the boundary layer edge, lbm/in^2 sec

C_h = Stanton number

B = surface corrosion parameter

This parameter is then employed in a semi-emperical correlation of the form:

$$\frac{(C_f/2)}{(C_f/2)_o} = f(B_t) \leq 1.0$$

Thus, for $B_t > 0$ the skin friction coefficient is reduced by the injection of gases at the surface. Several specific correlations for this transpiration factor are currently in use. References 1, 21, 33, 23, and 8 contain discussions of the more useful correlating functions. The correction factor of Reference 23 is one of the most recent and reasonable for use in rocket nozzles. This is essentially:

$$\frac{(C_f/2)}{(C_f/2)_o} = \frac{0.8 \, B_t}{\exp(0.8 \, B_t) - 1}$$

Here, $(C_f/2)_o$ is the calculated value of the skin-friction coefficient for the case of no mass addition at the surface. The effect of transpiration on the similarity relation between C_h (and the Cm_i's) and the $C_f/2$ is assumed to be negligible as long as the reduced $C_f/2$ is used in the similarity expressions.

Step 5. The effect of surface roughness upon the boundary layer transfer coefficients is the final consideration in the parametric characterization of the boundary layer. The analysis of surface roughness effects contained in Reference 4 provides a guide to the application of specific roughness data. The result of the analysis is an estimate for the rough wall skin-friction coefficient which is obtained from an effective roughness parameter Ks/X. The value of the rough wall skin-friction coefficient may be 50 to 100 percent greater than the smooth wall value. In applying the rough-surface calculation, care should be taken to include the effects of simultaneous mass addition at the surface. The modification of the boundary layer structure by the transpiration of gases into the boundary layer may negate the effect of surface roughness on the skin-friction coefficient or increase the value of the critical roughness height. Experimental data from research on re-entry problems, where this combination of effects occurs, may be applicable for the rocket nozzle boundary layer analysis. Where it has been determined that surface roughness is a dominating factor, the best assumption for determining C_m and C_h from the rough wall skin-friction coefficient is:

$$Sc_i = \overline{Sc} = Pr = 1$$

Here, these similarity parameters are the ones for the case of a completely turbulent boundary layer. This assumption implies:

$$C_m = C_h = (C_f/2)_{rough}$$

The techniques described in the above five steps are valid primarily for turbulent boundary layers in flows with a favorable pressure gradient. Other techniques should be applied in such special flow situations as a stagnation point and any region of separated flow (e.g., in the aft closure around a submerged nozzle). Techniques for these two particular special cases have been developed and are summarized below.

The development of the laminar boundary layer near a stagnation point is a relatively well characterized phenomenon. Reference 20 presents the variation in heat transfer coefficient with distance away from the stagnation point for various body shapes.

Reference 24 is a standard reference for calculations of heat transfer
in separated regions. Both laminar and turbulent reattached boundary
layers are considered with results presented in the form of Stanton number
factors for nonseparated boundary layers of equivalent Reynold's number.
These Stanton number factors are a function of the fluid Prandtl number
and the type of boundary layer (laminar or turbulent). It should be noted
that the Stanton number corrections apply only to the average values over
the separated flow regions. Other more recent data indicate that such
averaging is not sufficiently detailed. Reference 25, for example, presents
data which show a significant peak in the heat transfer coefficient near
the reattachment point of the boundary layer. The effect may be quite sig-
nificant depending upon the flow field of the particular motor under
consideration.

    b. Future Improvements

Two techniques which are nearly developed to the point of implementation
are:

    (1) A computerized calculation of turbulent boundary
layer development in a rocket nozzle environ-
ment including the effect of mass addition at
the surface. This calculation method is an
extension of the analyses of Reference 11 and 19.
The data of Reference 26 relating the skin fric-
tion coefficient to the local transpiration rate
and boundary layer Reynold's number would probably
be employed. Such a computer program would be
used in a manner similar to the two programs dis-
cussed above. The results of the calculation
would provide the parametric variation of $C_f/2$,
C_h, and C_m with wall temperature, mass injec-
tion rate, and location on the nozzle contour.
The use of this program would increase con-
siderably the confidence in predicting the
convective heat transfer and surface corrosion
rates in nozzles with high rates of boundary
layer mass addition.

    (2) A calculation of the corrosion potential employ-
ing unequal Schmidt numbers for the gaseous
species in the mixture. This calculation would
probably best be implemented by modifying the
present B-value computer program to include the
analysis of Section 2.2 of Reference 4. The
results of this modified program would be applied
in exactly the same manner as are the current
B-values. However, the accuracy of the B-values

-114-

would be considerably improved for propellant
exhausts composed of species of widely different
molecular weights (see Section 4.4). Prandtl/
Schmidt number ratios (Lewic numbers) of such
species as CO_2, H_2, and H will be significantly
different from unity. The magnitude of the
effect of the variation of Lewis numbers from
unity, on the B values is estimated to be in
the range of 20 to 50 percent.

It is not unlikely that some of the existing chemical kinetic rate data
will have to be reviewed when more accurate calculation of the gaseous
diffusion effects upon surface corrosion is achieved. Also, the identifica-
tion of dilution effects from laboratory experiments (see Section 4.4) would
depend upon the ability to accurately analyze the test data.

4.9 COUPLED NOZZLE THERMOCHEMICAL ANALYSES

The techniques presented in this section integrate the parametric results of the prior analytical steps into a final calculation of the nozzle overall thermochemical response. The parametric input data is obtained from:

(1) Specification of the boundary layer edge conditions,

(2) Estimation of nozzle exposed surface conditions,

(3) Calculation of the boundary layer transport coefficients,

(4) Estimation of the particle impingement profile,

(5) Calculation of radiative interchange factors,

(6) The detailed nozzle design.

The phenomena modeled in the coupled analyses include:

(1) Conductive heat transfer in the nozzle components,

(2) Convective and radiative heat transfer to the nozzle surface,

(3) Flow of liquid deposit along the nozzle surface,

(4) Internal ablation of sacrificial insulations,

(5) Chemical corrosion of the nozzle surface,

(6) Effects of local mass addition into the boundary layer,

(7) Effects of throat area variation on the motor internal ballistics.

The coupling of these phenomena assures a realistic analytical simulation of the actual nozzle performance. The major interactions between the phenomena which necessitate the coupling of the analyses include the following:

(1) Heat conducted into the nozzle is dependent upon convective and radiative heating rates,

-116-

(2)   Convective and radiative heating rates are
       dependent upon the surface temperature,

(3)   Heat conducted into the nozzle is dependent
       upon the thermal insulation provided by con-
       densed deposits on the nozzle surface,

(4)   The flow of deposit material depends upon the
       surface temperature, the convective and radiative
       heating rates, and the gas shear,

(5)   The radiative heating rate is dependent upon the
       presence of the deposit through the surface
       emissivity,

(6)   The internal ablation rate and effective heat
       of ablation of heat sink insulation depends
       upon the conductive heating rate at the ablation
       front,

(7)   The conduction of heat beyond the ablation front
       is dependent upon the effective heat of ablation,

(8)   The pyrolysis gas flow rate is dependent upon
       the internal ablation rate,

(9)   The pyrolysis gas composition is dependent
       upon the temperature of the charred material,

(10) The chemical corrosion of the nozzle surface is
       dependent upon the surface temperature and pres-
       sure, and the rate of transport of corrosive
       species to the surface,

(11) The convective heating rate is dependent upon
       the heat absorbed or released at the nozzle
       surface by the corrosive chemical reactions,

(12) The chemical reactions occurring at the surface
       depend upon the pyrolysis gas composition and
       flow rate,

(13) The transport of corrosive gaseous species to
       the wall is inhibited by the presence of wall
       deposits,

(14) The gas shear, convective heating rate, and
transport rates of corrosive species are
dependent upon the rate of mass addition into
the boundary layer from the nozzle surface,

(15) The rate of mass addition into the boundary
layer depends on the pyrolysis gas flow rate
and the rate of chemical corrosion of the nozzle
surface,

(16) The motor instantaneous chamber pressure is
dependent upon the nozzle instantaneous throat
area,

(17) The nozzle throat area history is dependent upon
the deposition/corrosion history at the throat,

(18) The gas shear, convective heating rate, and
corrosive species transport depend upon the
instantaneous chamber pressure.

In addition to these interactions, the nozzle surface regression due to
mechanical erosion may be significant. Analytical coupling of the mechanical
erosion rate to particle impingement, gas shear, corrosive weakening of
surface material, and internal ablation phenomena would be desirable in
such cases. Unfortunately, this is extremely difficult in general due to
a lack of understanding of specific erosion mechanics. Where appropriate
test data are available, a mechanical erosion correlation may be included
in the coupled analyses.

The quantitative results of the calculation include:

(1) The overall thermal history of the nozzle,

(2) The internal ablation history of sacrificial
insulation,

(3) The corrosion history of the nozzle contour,

(4) The motor pressure and thrust histories.

The results of this step satisfy two of the original objectives in applying
the method of analysis:

(1) The prediction of nozzle contour integrity,

(2) The prediction of motor ballistic performance.

The nozzle thermochemical response data are essential input to the final structural analysis to determine thermochemical effects upon the nozzle structural integrity.

a. Technical Approach

The calculation of the overall nozzle thermochemical response requires the use of a computer program. Such a program, as documented in Reference 27, basically provides an explicit finite-difference solution to the three dimensional Fourier heat conduction equation. The size and flexibility of other conduction programs must permit the inclusion of equations other than the basic conduction equation. This is very important in solving simultaneously the governing equations for the physically coupled thermochemical phenomena. Just as important is the ability to reprogram the coupled analyses to permit simplified calculation procedures to be used. The formulation of the Fourier conduction equation and the equations of the coupled analyses as they are currently used are discussed in the following paragraphs.

(1) Conduction Heat Transfer

The method employed to solve the Fourier heat conduction equation involves the digital solution of an analogous R-C electrical network. The conduction geometry is programmed as a series of nodes, each with heat-storing capacity and connected by thermal resistors to adjacent nodes. The finite difference equation is an explicit expression for the temperature at each node after a specified time interval has passed. This expression is:

$$T_i (\theta + \Delta\theta) = \frac{\Delta\theta}{C_i} \left[\sum_j \frac{T_j(\theta) - T_i(\theta)}{R_{ij}} + Q_i \right] + T_i(\theta)$$

where:

$T_i (\theta + \Delta\theta)$ = temperature of the ith node at time $\theta + \Delta\theta$, °F

θ = independent time variable, sec

$\Delta\theta$ = time increment, sec

C_i = heat capacity of ith node, Btu/°F

$T_j(\theta)$ = temperature of the jth node, adjacent to the ith node, at time θ, °F

$T_i(\theta)$ = temperature of the ith node at time θ, °F

-119-

$$R_{ij} \qquad = \quad \text{thermal resistance to heat flow between the jth node and the ith node, } °F \text{ sec/Btu}$$

$$Q_i \qquad = \quad \text{strength of internal heat source (or sink) for the ith note, Btu/sec}$$

The sensible heat capacity is usually found from:

$$C_i \quad = \quad \rho_i \, V_i \, C_{pi}$$

where:

$$\rho_i \quad = \quad \text{density of ith node, lbm/in}^3$$

$$V_i \quad = \quad \text{volume of ith node, in}^3$$

$$C_{pi} \quad = \quad \text{specific heat of ith node, Btu/lbm}°F$$

The thermal resistances are usually determined by whether the heat flow is by conduction,

$$R_{ij} \quad = \quad \frac{l_{ij}}{k \, A_{ij}} \tag{6}$$

or by convection,

$$R_{ij} \quad = \quad \frac{1}{h_{ij} \, A_{ij}} \tag{7}$$

or by radiation,

$$R_{ij} \quad = \quad \frac{1}{\sigma \, \epsilon_{ij} \, A_{ij} \, F_{ij} \left[(T_i + 460)^2 + (T_j + 460)^2\right] \left[(T_i + 460) + (T_j + 460)\right]} \tag{8}$$

Here the nomenclature is:

$$l_{ij} \qquad = \quad \text{length of heat path from jth node to the ith node, in}$$

$$A_{ij} \qquad = \quad \text{interface area common to the ith and jth nodes, in}^2$$

$$k \qquad = \quad \text{material thermal conductivity, Btu/in sec}°F$$

$$h_{ij} \qquad = \quad \text{convective film coefficient between the ith and jth nodes, Btu/in}^2 \text{ sec }°$$

σ = Stefan-Boltzmann constant, Btu/in^2 sec°R^4

ϵ_{ij} = emissivity for radiation between the ith and jth nodes

F_{ij} = configuration factor for radiation between the ith and jth nodes

T_i, T_j = temperatures of the ith and jth nodes, °F

Since this formulation of the heat conduction problem involves an explicit expression for temperature T_i $(\theta + \Delta\theta)$, some attention must be given to the question of the stability of the solution. Assuming a small error exists in the solution for the T_i's at a time θ, it must not be allowed to propagate as θ progresses. This criterion determines the maximum size of the time increment which may be used in the explicit expression. The time increment is normally set equal to one fourth of the minimum value of the $(RC)_i$'s of all nodes in the network, where:

$$(RC)_i = C_i \sum_j \frac{1}{R_{ij}}$$

In solving the conduction problem, all values of C_i, R_{ij}, Q_i may be recalculated after the calculation of the new node temperature. This allows variations in all pertinent parameters as the calculation proceeds. The important variations which are usually considered include:

(a) Variations in material properties with temperature,

(b) Variations in the convective boundary condition,

(c) Variations in surface emissivity and oxide deposit thickness.

It is through this capability for instantaneous (time increments of 0.1 sec are normally small enough) variations in the conduction problem that the models of the important physical phenomena occurring in the nozzle are coupled to the solution of the conduction problem.

(2) Convection and Radiation Heat Transfer

Once the nodal network has been established to model the heat conduction in the nozzle components, the convective and radiative heat transfer into all nozzle surface nodes must be specified. For convection, the surface node thermal resistance is given by Equation (7).

When the convective heat transfer into the ith node is expressed in terms of a temperature difference, then:

$$Q_{conv} = h_{ij} A_{ij} (T_j - T_i)$$

However, when an enthalpy driving potential is used, a more convenient method is to employ the heat source term, Q_i. In this case:

$$Q_{conv} = Q_i = \left(\frac{h}{\bar{C}_p}\right)_{ij} A_{ij} (H_j - H_i)$$

This expression is compatible with the result of Section 4.7 since

$$Q_{conv} = q_{conv} A_{ij} = \text{heating rate, Btu/sec}$$

$$\left(\frac{h}{\bar{C}_p}\right)_{ij} = (\rho u)_e C_h = \text{overall convective coefficient, lbm/in}^2 \text{ sec}$$

$$H_j = H_r = \text{local recovery enthalpy, Btu/lbm}$$

$$H_i = H_w = \text{local wall enthalpy, Btu/lbm}$$

$$A_{ij} = \text{area of ith surface convection node, in}^2$$

The term Q_i is dependent upon T_i, the chamber pressure, and the location of the surface node on the nozzle contour. These dependencies arise from the following considerations:

(a) $H_w = H_i$ is a function of T_i and the local pressure.

(b) $H_r = H_j$ is a function of the location of the surface node.

(c) $(\rho u)_e = P_c \, g/C^* \, k_1$, where the k_1 factor depends primarily upon the local area ratio. The local value of k_1 is determined from the analysis of Subsection 4.4.

(d) $C_h = \dfrac{k_2 \left(P_c\right)^{-0.2}}{1 - k_3 \left(P_c\right)^{-0.1}}$ where the values of k_2 and k_3 are obtained from the analysis of Section 4.8.

-122-

The information required to compute the Q_i's is input to the program in tabular form for interpolation as the calculation of the T_i's proceeds. Note that the result for C_h does not include the effects of mass injection into the boundary layer.

For radiation the thermal resistance is given by Equation (8). There may be more than one radiation resistance to the ith surface node. For the particle cloud radiation:

ϵ_{ij} = ϵ_{gw} = overall cloud emissivity obtained from the analysis of Section 4.6

A_{ij} = area of the ith surface node exposed to radiation (usually the same as that for convection), in^2

F_{ij} = 1.0

T_j = local static temperature of the particle cloud, °F

For intersurface radiation, the factors ϵ_{ij} and F_{ij} are determined using the techniques referenced in Section 4.6. The value of T_j is the temperature of the jth surface node radiating to the ith surface node. The major variation, which must be included in the radiation resistance calculation, is that of the emissivity with the presence or absence of a surface deposit on the ith node.

(3) Surface Deposit Flow

When the analysis of Section 4.5 indicates the need, the effects of surface deposits should be included in the nozzle thermochemical response calculation. For solid propellant rockets, the deposit is usually composed of metallic oxides in the liquid and solid phases. The deposit will provide corrosion protection and significant thermal insulation for the surface. A discussion of the physical and analytical modeling of the deposit behavior is contained in Section 2.5 of References 2 and 4. To date, efforts to solve the mathematical formulation by explicit finite difference methods (in conjunction with the conduction solution) have not been successful.

The current technique of including a deposit on the nozzle surface in the solution of the conduction equation consists of:

(a) Specifying as input the time-dependent deposit thickness on each of the surface nodes of the conduction network,

(b) Keying the removal of the deposit to the attainment of the deposit melting point,

-123-

(c) Assuming no surface corrosion and using corre-
     sponding wall enthalpy data while the deposit
     is present,

(d) Neglecting the heat capacity of the deposit
     nodes with respect to the capacity of the
     surface nodes.

The specific assumptions employed in Items (a), (b) and (c) should be
based on experience with deposition behavior (see Section 3.5). Item (d)
is justified by the fact that the deposit is relatively thin and that the
thermal diffusivity is an order of magnitude less for the deposit than for
nozzle heat sink materials. Thus, the insulating capability of the deposit
is relatively more important that its heat absorbing capability.

The thermal resistance between the deposit node and the nozzle surface node
is:

$$R = \frac{\delta_{dep}}{k_{dep} A_i} \tag{9}$$

Where:

δ_{dep} = deposit thickness for the surface node in
                   question, inch

k_{dep} = thermal conductivity of the deposit,
              Btu/(in sec°F)

A_i = area of the ith surface node covered by the
          deposit, in^2

Currently, the required thermal property data for metallic oxide deposits
is scarce. As reported in Reference 2 the best available estimates for
the thermal conductivities are:

$$k_{Al_2O_3} = 0.60 \times 10^{-4} \text{ Btu/(in sec°F)}$$

$$k_{BeO} = 1.85 \times 10^{-4} \text{ Btu/(in sec°F)}$$

(4) Internal Ablation of Insulators

In analyzing nozzle designs which employ reinforced plastic insulation
materials, the effects of the internal ablation of such materials should
be included in the conduction solution. Additionally, large motors may
employ only ablative materials. The physical model of the ablation pro-
cess and the corresponding mathematical model are reviewed in Reference 15.
A summary of the discussion is presented in Reference 3.

In analyzing the ablation process in conjunction with the solution of the
conduction problem, nodes are established for the sacrificial materials as
well as the heat sink materials. As the ablative nodes are heated, the
density and thermal properties of the nodes are modified to account for
the pyrolysis of the plastic. The rate law is of the form:

$$\Delta\rho_i = -\Delta\theta (\rho_v - \rho_c) A \left(\frac{\rho_i - \rho_c}{\rho_v - \rho_c}\right)^n \exp\left[-\frac{E}{R(T_i + 460)}\right]$$

where:

$\Delta\rho_i$ = change in density of the ith ablative node, lbm/in^3

$\Delta\theta$ = time increment, sec

ρ_v = density of the virgin insulation, lbm/in^3

ρ_c = density of the fully charred insulation

A = pyrolysis rate constant, 1/sec

ρ_i = density of the ith ablative node at time θ, lbm/in^3

E = activation energy, Btu/lbm-mole

n = degree of reaction

R = universal gas constant, Btu/lbm-mole°R

T_i = temperature of the ith ablative node at time θ, °F

The pyrolysis gas from the resin decomposition is presumed to flow parallel
to the temperature gradient. The flow rate of pyrolysis gas is calculated
by summing the mass loss of resin from all the nodes in a line parallel to

-125-

the gas flow direction. The heat absorbed by the resin decomposition and percolation of the pyrolysis gas through the char is accounted for in an internal heat sink term for each ablative node. Chemical interactions between the percolating gases and the char can be accounted for by assuming that thermochemical equilibrium pertains. The temperature dependence of the pyrolysis gas, char and virgin material properties are input when they are known.

(5) Corrosion

From the results of Section 4.7, the corrosion parameter for the nozzle surface materials will be known as a function of location, pressure and temperature. This information is in the form of a B value which is employed in the solution of the conduction problem. For the surface nodes:

$$\dot{r}_i = \left(\frac{h}{\overline{C_p}}\right)_{ij} \frac{B_i}{\rho_i}$$

Where:

$\dot{r}_i$ = surface regression rate of the ith surface node, in/sec

B_i = corrosion parameter for the ith surface node (temperature and time dependent)

ρ_i = density of the ith surface node, lbm/in^3

More than one table of B versus temperature may be required for a particular material if it is exposed to widely different pressures. For each B value table, a corresponding table of wall enthalpy versus temperature values is used to ..clude the enthalpy absorbed (or released) by the corrosion reactions.

Currently, the effect of surface regression upon the volume of the surface nodes is not included in the conduction solution. This practice is employed to avoid the difficulties of reformulating the conduction network during the course of the solution of the conduction problem. When the magnitude of the total surface regression becomes large relative to the depth of the surface nodes, this practice should be modified.

(6) Boundary Layer Mass Addition

As discussed in Section 4.8, there are several correction factors which may be applied to the boundary layer transfer coefficients to account for the blocking effects of local mass injection. Currently, the selected

-126-

correction factor (see Section 4.8) is applied in the conduction solution as follows:

$$C_h' = \frac{k_2' \, (P_c)^{-0.2}}{1 - k_3' \, (P_c)^{-0.1}}$$

$$\frac{k_2'}{k_2} = \left(\frac{k_3'}{k_3}\right)^2 = \frac{0.8 \, B_{ti}}{\exp \, (0.8 \, B_{ti}) - 1}$$

$$B_{ti} = B_i + \frac{m_i^+}{\dfrac{P_c \, g}{C^*} \, k_1 \, C_h \, A_i}$$

The primed quantities are those corrected for the mass addition effect. The subscript i refers to the ith surface node. In addition to the symbols previously defined:

B_{ti} = total B value for the ith surface node

m_i^+ = total flow rate of pyrolysis gas leaving the ith surface node, lbm/sec

The corrected convective heat transfer coefficient is used in calculating both the convective heat source strength (or convective resistance) and the corrosion of the surface nodes.

(7) Motor Internal Ballistics

The primary reason for including the claculation of the internal ballistics in the conduction solution is to account for chamber pressure effects upon the nozzle convective heat transfer and surface corrosion. Where desirable, the calculation of the rocket thrust and specific impulse may be included.

The chamber pressure (P_c) is involved in the convective heat transfer and surface corrosion rate in two ways. These are the local mass flux,

$$(\rho u)_e = \frac{P_c \, g}{C^*} \, k_1$$

and the Stanton number,

$$C_h = \frac{k_2 (P_c)^{-0.2}}{1 - k_3 (P_c)^{-0.1}}$$

Due to the nature of solid propellants, the chamber pressure history is closely related to the nozzle throat area history. The throat area may vary as a result of oxide deposition and/or surface corrosion. Neglecting erosive burning effects, the standard expression for the chamber pressure is,

$$P_c = \left(\frac{\rho_p \, a \, C^* \, A_b}{g \, A_t} \right)^{\frac{1}{1 - n}}$$

where:

ρ_p = density of solid propellant

a = propellant burn rate coefficient

C^* = propellant characteristic exhaust velocity

g = acceleration due gravity

A_b = burning area of the propellant grain

A_t = nozzle throat area

n = propellant burn rate exponent

The values of ρ_p, a, n, C^* are assumed constant while the data for A_b, as a function of the propellant grain web consumed, is input to the problem in tabular form. This tabular data is derived from the geometry of the grain design. The web consumed is found from the expression,

$$W_c(\theta + \Delta\theta) = W_c(\theta) + \Delta\theta \, a \, (P_c)^n$$

where:

W_c = propellant grain web consumed

-128-

The value of P_c used in this expression is that calculated at time θ. The throat area is calculated from the diameter.

For the case of deposit present at the throat,

$$D_t(\theta + \Delta\theta) \;=\; D_t(\theta = \theta_d) - 2\delta_{dep_t}$$

or, in the case of surface corrosion at the throat,

$$D_t(\theta + \Delta\theta) \;=\; D_t(\theta) + 2\Delta\theta\, \dot{r}_t$$

Here the symbols are defined as:

$D_t(\theta)$ = nozzle throat diameter

δ_{dep_t} = deposit thickness at the throat

θ_d = time when the deposit appears

$\dot{r}_t$ = surface corrosion rate at the throat

In cases where circumferential nonuniformities have been included at the throat, these effects must be averaged.

In some cases the throat area changes will be of sufficient magnitude to introduce large variations in the nozzle expansion ratio. The effect of the change in expansion ratio on the nozzle thrust coefficient may be calculated independently after the entire chamber pressure, throat area, and exit area histories are obtained from the conduction solution. This calculation may also be included in the conduction solution itself. In general, it is more practical to employ the former alternative since the calculation of the thrust coefficient from the expansion ratio, ambient pressure, and exhaust isentropic exponent (γ) usually requires iteration.

   b.   Future Improvements

The techniques and models currently included in the thermal analyzer computer program described above could be improved in two important areas. These are:

   (1)   Inclusion of a mathematic formulation of the surface deposit flow to be solved by a finite difference technique,

   (2)   Development and inclusion of a mathematic model of the mechanical surface erosion phenomena of importance in rocket nozzles.

The fundamental difficulty which has precluded solving the mathematical model of the flow of deposit along the nozzle surface is the derivation of a stable finite difference technique for the governing equations. As described in Section 2.5 of Reference 4, an explicit finite difference technique, programmed in conjunction with a conduction network, failed to yield a stable solution. The stability criteria derived for this and other explicit techniques are quite complex and are unlikely to be compatible with the stability criterion for the conduction solution. Any reductions in the time increment size may drastically increase the machine computational time and cost for a given problem. A reasonable alternative, to bypass the stability difficulty, is to employ an implicit finite difference technique in solving the deposit flow equations. While this approach involves more computation, it is usually absolutely stable with respect to error propagation.

In addition to the programming of deposit flow equations, the mathematical formulation could be improved by adding terms which have been neglected for the present but which are potentially important. A major shortcoming in the overall deposit analysis is the lack of property data for typical deposit materials (Al_2O_3 and BeO). This data would best be obtained from laboratory testing and would include:

    (1)   Thermal conductivity of the liquid and solid phases and variation with temperature,

    (2)   Specific heat of the liquid phase,

    (3)   Dynamic viscosity of the liquid phase.

The best approach to including mechanical surface erosion is not clear. The erosion process will be transient at best and may be discontinuous. While an overly sophisticated erosion model is not desirable, some relatively simple formulation of the phenomena would be useful in correlating future test data. The following expression is the most primitive which can be formulated:

$$\dot{m}_{erosion} = m_s \dot{N}_s$$

Here the symbols are defined as:

$\dot{m}_{erosion}$ =   mass loss rate of wall materials due to erosion, lbm/in^2 sec

m_s =   average mass of wall material involved at a site of mechanical failure, $lbm/site$

$\dot{N}_s$ =   rate of appearance at the surface of sites of mechanical failure, $sites/in^2$ sec

Physical models of mechanical erosion phenomena would then provide the dependencies of m_s and $\dot{N}_s$ upon:

(1) The nature of the material at the surface,

(2) The surface stress and mode of stress relief at the surface,

(3) Particle impact energies,

(4) Gas shear stress level,

(5) Chemical corrosion of the surface.

Such a formulation could be expanded as appropriate subscale test data became available. Without even as simple as expression as the above, the proper definition of a subscale test program to investigate the mechanical erosion effects would be unlikely to succeed.

4.10 STURCTURAL ANALYSIS

The final analytical step is the performance of structural analyses to determine thermo-mechanical stability of the given nozzle design. The structural analysis includes the estimation of stresses induced in the nozzle components due to:

(1) Pressure loads,

(2) Pyrolysis gas venting,

(3) Thermal expansion,

(4) Rotational and axial acceleration.

Predictions of component failure or satisfactory performance are then made in terms of:

(1) Comparison of calculated stress levels with materials capacity at elevated temperatures,

(2) Excessive component deformation,

(3) Potential for chamber gas leakage due to excessive component mechanical or thermal damage.

The information required from the nozzle thermochemical response calculation
is:

   (1)   The thermal history of the nozzle components,

   (2)   The expected pyrolysis off-gassing rate for
         sacrificial materials,

   (3)   Char depths in sacrificial components,

   (4)   Motor chamber pressure trace,

   (5)   Contour corrosion/erosion history.

   a.   Technical Approach

The two basic requirements of structural analysis are to insure that the
motor functions as a pressure vessel and that the integrity of the internal
contour forming materials is maintained. Without a reasonably accurate
characterization of the nature of the actions of the exhaust on the motor/
nozzle materials and their thermal response, the value of structural anal-
ysis is severely limited. In this program, emphasis has not been placed
on the development of any new techniques for structural analysis. However,
there are a number of specific aspects of the nozzle performance problem
which interrelate with the structural problem and which should be emphasized.

Nozzle component thermal shock failures are frequently a matter of some
concern. It should be noted that the heat transfer coefficient during
the first few seconds of the firing must be known to evaluate thermal
shock stresses. The motor pressure, combustion efficiency, impingement,
pyrolysis gas injection. deposit flow and surface temperature transient
effects make this determination nearly impossible. It is not obvious that
there is any reasonable substitute for direct testing experience in cases
where thermal shock is anticipated. The encouragement of high initial
insulation pyrolysis rates or oxide deposit insulation could probably be
exploited to lessen the possibility of thermal shock damage.

During the initial nozzle temperature transient, it is possible that the
compressive stresses along the nozzle contour may excede ultimate values
while the material is still elastic. Both the radial temperature gradient
and axial thermal expansion and pressure loading can contribute to the
build up of the surface compressive loads. The relief mechanism could be
surface spallation rather than a tensile failure at the cold surface of the
component. Polycrystalline graphites in nozzle entrance sections may suffer
surface spallation before surface or subsurface temperatures reach the
elastic-plastic transformation temperature (in the range of 4000-4500 F).
The resulting surface roughness will promote higher local heat transfer
and corrosion. These effects will be propagated downstream due to the

destruction of the boundary layer or increased boundary layer turbulence. Some smoothing of the surface should occur over the remainder of the firing, obscuring the initial character of the surface failure. Oxide deposition protection could be very effective in preventing such failures.

The performance of nozzle materials at high surface temperatures may be primarily determined by corrosion in a sound structural design. To achieve this, the surface stresses and material temperatures must be controlled such that plastic deformation, physical erosion and surface spallation do not become dominant. Plastic deformation of edge oriented pyrolytic graphite can be controlled to some extent by providing free axial thermal expansion and limiting surface temperatures to the range of 5200-5500°F. Plastic deformation of pyrolytic graphite may actually be of little consequence unless it is directly related to surface spallation. The surface roughness associated with nodule spallation is regarded as being very serious. The precise cause of nodule spallation is not well understood but it probably involves nodule boundary corrosion and stress concentrations as well as surface compressive loading. While the removal of surface nodules may be effective in relieving the stresses, the ensuing roughness augments both the heat transfer and corrosion. Thus, this process could be regenerative.

The porous polycrystalline graphites are more likely to suffer granular surface erosion at high temperatures. This process may be accelerated by chemical attack of intergranular bonds which may have a partially amorphous habit. While surface roughness may be limited to the dimension of the grains or pores, it is currently thought that such roughness is sufficient to markedly increase convective heating, surface shear and corrosion in nozzle inlets and throats. This would especially apply to relatively small nozzles. Evidently then, structural design should consider the specification of materials which develop sufficiently low characteristic roughness values and/or high resistance to physical erosion.

Plastic deformation of tungsten is a more straight forward problem of temperature and stress. Because of the corrosion and spallation resistance normally attributed to dense tungsten, it is frequently expected to survive at much higher temperatures than the graphites. Under such exposure, tungsten can plastically deform, both during and after the test. Thin tungsten inserts can be extruded during the test and, otherwise, are likely to undergo contraction during motor cool down. Relatively thick inserts will undergo deformation primarily during the firing period. Physical erosion of dense tungsten is not likely to occur unless extensive grain boundary attack occurs or the low melting carbon, beryilium or aluminum alloys should form. Power metallurgy tungsten materials probably erode in a manner analagous to that of the polycrystalline graphites.

Flight weight motor cases and insulation are normally limited to a maximum pressure and maximum heating period. It is important to consider the effects of throat area reduction due to oxide deposition. It may be necessary to manipulate the grain design to insure that deposition does not augment nominal peak pressure values. The motor burnout time is also dependent on deposition as well as other factors.

Reference 15 may be consulted for a review of nozzle structural analysis techniques. More recent developments can be found in the literature. Many of these stem from the application of graphite and ablative materials in re-entry applications.

4.11 APPLICATION OF THE METHOD TO OTHER SYSTEMS

The essense of the nozzle design analysis method, as represented in Figure 1, is the systematic consideration of the major thermo-physical parameters which determine nozzle performance. New emphasis has been placed on the solid propellant combustion process, the exhaust flow field mechanics, condensed phase behavior, boundary layer processes and materials surface mechanics. The overall nozzle design and performance analysis method can be extended to other chemical propulsion systems if appropriate revisions are made in the analytical mechanics. This should be preceded by a semi-qualitative evaluation of the nature of the combustion, fluid mechanics and surface mechanics phenomena in each new system.

The propellant combustion process directly influences nozzle and insulation materials performance through the corrosivity, energy level and condensed phase content of the exhaust. Metalized solid propellants are hardly unique in the sense that the combustion process is transient. The combustion mechanics of fuel rich, hydride, and uncured propellants should be more complex than the ordinary beryllium and aluminum systems. The introduction of new binder and oxidizer systems will also alter the combustion mechanics. The hybrid, liquid, slurry, dual chamber and air augmentation systems introduce additional complexity in the mixing of the fuel and oxidizer before complete combustion is achieved. Although extensive combustion research has been conducted, it is not apparent whether the results can be used directly in nozzle design. Such research would be of major immediate interest in the evaluation of actual motor/nozzle materials performance.

Multi-phase combustion chamber flow field mechanics are probably most complex in the air augmentation, dual chamber and pulse motor systems. The use of submerged nozzles, plug nozzles, and complex grain designs in any propulsion system will magnify the problem, even for a single phase exhaust. Maximum materials performance will correspond to the development and maintenance of a stable fluid boundary layer along the motor/nozzle contour. The introduction of free stream turbulence, flow stagnation and flow separation at or near the wall can destroy or reduce the boundary layer

shielding effect. Locally, the wall will see major increases in gas shear, heat transfer, corrosion and particle impingement. Regardless of the propulsion system, such action must be anticipated. Underestimation of the exhaust flow interaction with the motor/nozzle contour is potentionally the most probable indirect cause of system failure.

The consideration of cooled nozzles introduces the requirement to supplement the heat transfer analysis portion of the model. Relatively unique analyses are required to handle regenerative, transpiration, film, liquid metal and radiation cooling. The cooling should be handled in a parametric manner to be compatible with the passive heat sink analysis. The coupling of all the thermochemical responses will probably be more critical in analyzing cooled nozzle designs (see for example Reference 28).

The consideration of plug nozzle designs introduces a relatively unusual slag problem. If deposits reach the annular threat section, they may preferentially adhere to either the plug or the outer body. Part of the annulus could also be sealed off. It will probably require extensive thermal instrumentation and ballistic analysis to interpret the deposit behavior. Plug support struts will be subject to unusual particle impingement and deposition. Free stream turbulence associated with the struts may also influence the nozzle boundary layer stability.

The introduction or consideration of new propellant systems necessitates additional consideration of surface mechanics. The corrosivity of new gaseous and condensed species should be established. Preferential grain boundary attack, surface embrittlement and alloying should be considered in general. Specific chemical reactions and the associated energy release (or absorption) should be determined. In all propulsion systems, greater emphasis should be placed on understanding surface roughness and physical property effects.

Emphasis has been placed on the need to associate a degree of approximation with each analytical technique employed within the overall model. Aside from the sheer complexity of the nozzle performance analysis problem, there are two other major limitations inherrant in the method. One is the designers ability to recognize all of the important thermal, chemical and physical features of the nozzle problem. Normally, the designer will also be required to correctly determine which of these can limit materials and system performance. The second major limitation is the usual lack of sufficient materials property data. Evidently there is a real need to improve the balance among (1) actual design practices, (2) the development of advanced analytical techniques, and (3) improved characterization of material properties.

SECTION V (C)

CONCLUSIONS

The present investigation of erosion and corrosion of nozzles exposed to
beryllium solid propella..t exhausts has led to general conclusions which
apply to metalized solid propellants and to conclusions which apply
specifically to beryllium propellants. Those are summarized in outline
form below. More detailed conclusions have prevously been presented at
the end of Sections II through V in References 1 through 4. Many of those
earlier conclusions have been incorporated in the discussions given in the
preceding sections of this report.

I. DESIGN TECHNOLOGY REQUIREMENTS

Ultimately, motor insulation and nozzle materials must effectively shield
the motor superstructure from the actions of the exhaust to the extent that
overall structural integrity is maintained. Then, the functional inner
contour must be stable to the extent that the efficiency of the energy
conversion device is maintained within acceptable limits. Motor insulation
and nozzle materials are inherently limited in their ability to successfully
resist the thermal, chemical and physical actions of the rocket exhaust at
their exposed surfaces. The specific response of the material is determined
by the nature of the propellant system and the motor configuration as well
as the inherent capacity of the materials. That is, the degree of the
actions of the exhaust on the materials and the degree of their response
depends both on the design and the material.

An adequate design technology must be capable of predicting the contour
surface recession, nozzle component thermal response and nozzle component
structural response. To be successful, the design technology should be
based on a detailed understanding of the mechanics and dynamics of the

-136-

exhaust/ materials interactions. The present program has contributed to the improvement of this understanding. Considerably more progress is required before the design procedures can be divorced from the trial and error method or effectively automated. Consequently, the state-of-the-art design technology must also be capable of inverse application to interpret the results of actual motor firings.

II. MOTOR MATERIALS PERFORMANCE

1. The design technology developed for use with low and medium energy aluminum propellants will not be equally successful with high energy aluminum or any of the beryllium propellants. The older design technology fails in that it tends to underestimate boundary layer convective heat and mass transfer (reactive species) while normally neglecting combustion efficiency, exhaust flow field and oxide deposition effects.

2. The failure of motor insulation and nozzle materials to meet the performance expectations set for similar aluminum systems is due primarily to the appearance of poor metal combustion as a dominant issue and secondarily to inadequate design and fundamental differences in the nature of the aluminum and beryllium exhausts.

3. Good materials performance depends on complete propellant combustion or extensive oxide deposition protection against poor combustion. Poor materials and ballistic performance are closely related to inadequate motor design and/or poor choice of propellant.

III. METAL COMBUSTION EFFICIENCY

1. The ignition and combustion of metal additives occurs as the metal particles are carried along by the exhaust products of the other propellant ingredients and at some distance from the grain surface. The times required to essentially complete metal combustion are much greater than the times required to combust the other propellant ingredients and may exceed available residence times in the motor.

2. A potentially major cause of poor metal combustion is the agglomeration of the original metal particles while they reside at the grain surface. Based on the differences in melting points, aluminum will agglomerate more readily than beryllium, other factors being equal. Collisions between molten particles should result in larger spherical particles unless a solid oxide skin is developed. Partially molten particles may stick together to form aggregates. Such aggregates should eventually complete melting and draw into a spherical shape. Evidently, whether or not the particles melt depends at least on chamber pressure (flame standoff distance), the flame temperature (without metal combustion), the mobility of the particles at the grain surface, the

the size of the oxidizer particles and the forces acting to remove the particle from the grain surface. Many of these factors will also tend to determine the propellant burn rate.

3. It is speculated that the metal particles will not be removed from the grain surface until they conduct enough heat to the underlying or surrounding binder to cause rapid decomposition. Such action should produce enough gases to lift the particle from the surface. However, a motion parallel to the grain surface could also result. In turn, such motion will lead to particle collisions. Alternately, the metal particles may be trapped in pockets formed between large oxidizer particles.

4. Composite and double base propellants will promote surface agglomeration by different mechanisms. The large ammonium perchlorate particles usually used in composite apparently trap the smaller metal particles in natural pockets. The resulting agglomerate sizes should correlate with the oxidizer particle size, metal loading and possibly type of binder. Double base propellants tend to use oxidizer particles of the same order of size as the metal. They also tend to develop a "fizz" layer or zone which may inhibit particle mobility. Double base propellants tend to have higher flame temperatures than composite which favors metal particle melting. Presumably, the CMDB propellants would exhibit intermediate behavior. In any case, the occurrence and degree of metal agglomeration at the grain surface will be a measurable characteristic of the particular propellant and metal system.

5. Internal burning grains impose a shear load at the grain surface. This might increase agglomeration relative to the end burner case. However, higher interparticle collision forces could alter the agglomeration and ejection mechanics considerably.

6. Once the metal particles are removed from the grain surface, they will continue to be heated until the ignition temperature is reached. The length of the ignition delay depends on the local flame temperature, particle size, particle heat capacity, local exhaust composition, local exhaust mass flux, and the amount of surface oxide developed. Even though beryllium may ignite at $1900°K$ relative to $2300°K$ for aluminum, ignition delays will be longer for beryllium particles compared to aluminum particles of equal size. In some cases, beryllium particle ignition temperatures may be as high as $2850°K$, the melting point of the metal oxide. Grain surface agglomeration promotes longer ignition delay times by reducing the number and increasing the size of the unburned metal particles. These effects may be partly offset by melting the metal while at the grain surface. In the most extreme case, metal agglomerates or particles may not reach their ignition temperature within the motor.

7. The primary combustion process (nonmetallic ingredients) must yield temperatures above the ignition limit. Apparently, the depression of the beryllium ignition point below the oxide melting point is dependent on the local water vapor concentration.

8. Vaporization of the metal is the key to achieving complete combustion. After ignition, rapid vapor phase combustion will occur, provided that there is sufficient "oxygen" available and that solid oxides do not excessively restrict beryllium vaporization.

9. Combustion of aluminum above 2300°K should be very similar to beryllium combustion above 2850°K. Slower combustion of beryllium will occur while particle temperatures are in the range of 1900 to 2850°K. The last particles to burn will do so more slowly than the first simply because of the decrease in available oxygen.

10. It would be reasonable to lower the propellant oxidation ratio as flame temperatures increase as long as metal agglomeration does not also increase. High oxidation ratios should not be necessary when agglomeration does not occur.

11. Beryllium and aluminum propellants will only exhibit similar performance characteristics (motor materials and ballistic) when they achieve similar combustion characteristics. The more prevalent case appears to be that the aluminum propellant combustion is normally more efficient than the analog beryllium propellants such as those tested in this program. It is speculated that beryllium propellants with minimum flame temperatures (no metal combustion) above about 2800°K will not exhibit the combustion efficiency problems attributed to the earlier generation of propellants. It is also likely that combustion of the poorer propellants can be improved by appropriate propellant tailoring or accommodated by proper motor design.

IV. EFFECTS OF POOR METAL COMBUSTION

1. At any point in the exhaust where combustion of the metal particles is not complete, the flame temperature will be lower, the exhaust gas corrosivity will be higher and the particle sizes will be greater than if combustion had been completed.

2. The lower flame temperature (or enthalpy) will tend to reduce the radiation and convection heat transfer to the motor contour materials. From the point of view of the materials, this is a beneficial effect.

3. The higher exhaust corrosivity will tend to increase the corrosive attack rates of the exposed contour materials. The oxygen reactions, which do not significantly depend on wall temperature, will dominate. Corrosion rates could conceivably be increased by more than an order of magnitude for either beryllium or aluminum propellants.

4. Any increase in metal, oxide or metal/oxide particle sizes will increase the particle impingement rates along the flow turning sections of the motor contour. Higher impingement rates could cause higher local mechanical erosion. However, a protective deposit may also form, shielding the materials downstream from the corrosive gases. Deposits will also have the beneficial effect of insulating the contour materials, reducing the heat transfer even further. If the deposits contain significant amounts of unburned metal, they are likely to melt and flow faster than the pure oxide. The unburned metal can potentially react with tungsten, to form low melting alloys, but will not significantly harm carbonaceous or graphite materials.

5. Flame temperature and formulation parameters are not sufficient bases for comparison of beryllium and aluminum propellants. Degree of metal combustion and condensed phase deposition characteristics are also required. Direct comparison of the two types of propellants in otherwise identical motors will usually (but not always) show the aluminum propellant to be the less severe. However, beryllium propellants have the greater potential through deposition protection with respect to achieving high motor materials performance. This may require some sacrifice of the theoretical performance advantage of the beryllium system.

6. Materials performance can be better in a low efficiency beryllium propellant exhaust than in a high efficiency aluminum system. It is only required that the poor combustion of beryllium lead to greater deposition protection and lower heat transfer than in the aluminum system.

7. When equivalent degrees of combustion are achieved with an aluminum and beryllium propellant, the higher melting points of the metal and the oxide should lead to higher materials performance in the beryllium system, provided only that deposition protection actually occurs.

8. Without any deposition protection, aluminum propellants should produce the same heat transfer and slightly less corrosion (complete combustion) relative to the beryllium propellants. When no protective deposits form, an incompletely burned beryllium exhaust will always be more corrosive than the aluminum exhaust.

9. In some cases, deposition protection effects may be greater in the aluminum system with the result that comparable beryllium exhausts will appear to be more severe.

10. Incomplete combustion of metal additives necessarily leads to significant theoretical C^* and I_{sp} efficiency losses. The magnitude of the losses is proportional to the metal loading. For the propellants studied in this program, the maximum losses ranged from 20 to 25 percent for 10 to 14 percent beryllium loadings. The two phase drag losses will also be increased when large unburned particles are present or extensive condensed phase flow stratification occurs.

11. High C^* efficiencies are not a positive indication that the motor insulation and nozzle inlet materials have not been exposed to incompletely burned exhaust phases. The metal combustion efficiency should continuously increase with streamline flow distance from the grain surface. The metal combustion efficiency will also vary considerably over a given test period. Short chamber residence times at the beginning of the test and low chamber velocities at the end of the test will tend to promote poor combustion. By averaging the ballistic performance over the entire test, clear indications of poor combustion may be lost.

12. If poor combustion causes significant materials damage early in the test, early failure may occur. More commonly, it will only appear that high average erosion and heat transfer were experienced. This is particularly true for aft closure insulation and nose cap or nozzle inlet sections.

V. NOZZLE HEAT TRANSFER

1. Nozzle convective heat transfer should be treated as a boundary layer phenomenon. Surface temperature, surface chemical reactions, surface roughness, foreign gas injection, exhaust phase segregation, exhaust gas recombination reactions and exhaust gas property effects should all be considered in the convection model.

2. Experimental measurements of convective heat transfer will underestimate the true convective coefficient when oxide deposition, poor metal combustion, nozzle corrosion, and pyrolysis gas injection are important and are not accounted for. Short boundary layer development length, surface roughness, low gas Prandtl number, free stream turbulence and gas specie recombination effects will increase true convective coefficients above predictions which do not involve these factors.

3. Simplified, closed form convection analyses may either overestimate or underestimate convection, depending on the users ability to interpret the actual physical situation. An improved closed form convection equation and method of analysis have been developed in this program. Excellent agreement has been obtained with the motor test results.

4. The convective heat transfer is strongly dependent on the propellant system, grain design, motor/nozzle contour, nozzle materials and nozzle contour roughness. Changes in the exhaust flow field, degree of combustion, deposition and contour characteristics with time will be reflected by the convection.

5. The convective heat transfer associated with beryllium exhausts should ideally be essentially the same as for comparable aluminum exhaust. However, the oxide deposition insulation effect is likely to be significantly different.

6. Radiation heat transfer will be influenced by oxide deposition and poor metal combustion. Apparently, beryllia particle sizes in the combustion chamber will not be similar to alumina particle sizes when the specific combustion mechanisms and rates are different. There may be little tendency for beryllia particles to grow significantly in the rocket exhaust. No unusual beryllia radiation effects have been encountered in this program. It is doubtful that small scale nozzles are exposed to significant radiation. It is speculated that radiation is less important in the beryllium system than for aluminum.

VI. NOZZLE CORROSION

1. Graphite nozzle components and insulation chars will be corroded when they are exposed directly to reactive exhaust species. Carbon is consumed primarily via reactions with the gaseous exhaust species which available oxygen and hydrogen. H_2O, CO_2 and H_2 are the primary attacking species in metalized exhausts. In true double base systems, some nitrogen attack of carbon will occur. Graphite attack by O_2, O, H, OH, $Be(OH)$, $Be(OH)_2$, HCl, etc. are strictly secondary because the contour is never exposed to significant concentrations of these species.

2. Neither the metal or metal oxide species pose a real threat to graphite materials, primarily because the theoretically indicated reactions cannot proceed to equilibrium at significant rates. This is due to the formation of carbide diffusion barriers. The thermal stability of the carbide layer is pressure dependent. Significant beryllia attack of graphite will occur above $2500°K$ at low pressures.

3. The greatest potential difference between the two metal systems stems from the differences in metal combustion and oxide deposition protection. Incomplete combustion of the metal is accompanied by proportional increases in the amounts of H_2O and CO_2 available to react with graphite contour materials. Incomplete combustion, greater condensed phase stratification and less oxide deposition in the beryllium system are the sources of higher observed corrosion of graphite nozzles by beryllium exhausts.

4. Chemical attack of tungsten by carbon is a primary cause of insert failures. The source of the carbon is believed to be graphite-hydrogen corrosion products and insulation pyrolysis products (hydrocarbons) generated upstream of the insert. The formation of low melting tungsten carbides causes surface regression which accelerates plastic deformation, buckling and insert obtrusion. The exposure of tungsten to aluminum or beryllium metal may lead to (not demonstrated as yet) formation of very low melting alloys and a similar failure mode. The source of the metal may be either unburned particles or decomposing metal carbides (formed on graphite surfaces upstream) which flow over the tungsten.

5. The attack of tungsten by gaseous exhaust species is regarded as secondary. H_2O, CO_2, minor oxygen bearing species and the chlorine species will attack tungsten to form gaseous oxides and chlorides. The effect of the gaseous reactions would be most significant when poor metal combustion occurs, provided that the insert surface is not protected by deposits and temperatures are approaching or above $3000°K$. Selective grain boundary attack of tungsten is not well understood but probably involves impurities and carbide formation. The metal oxides will not appreciably attack tungsten at rocket pressures.

6. Above $800-1200°K$, the attack of graphite by oxygen species (H_2O and CO_2) is relatively independent of surface temperature. Essentially all of these species which diffuse to the surface will react. Kinetic reaction rate limitations undoubtedly occur, however, the effect cannot be great and equilibrium can be assumed at the reaction surface for most practical purposes. A check of this assumption can be made by comparing the calculated equilibrium concentrations of H_2O and CO_2 at the reaction surface with the free stream values. Normally the reaction site concentrations will be very close to zero and negligible even if increased by kinetics. The oxygen specie reactions are slightly endothermic.

7. The hydrogen-graphite reaction (to form acetylene) is thermodynamically limited and does not become prominent until surface temperatures exceed about $2400°K$. Ideal reactivity is strongly dependent on temperature thereafter. It is believed that the character of this particular reaction has been misinterpreted in the past. The major issue has been whether or not this reaction is kinetically limited and, if so, to what degree. The questions of whether physical erosion of graphite occurs and to what degree are also involved. Neglect of pyrolysis gas injection, imprecision of the heat transfer analysis, similar imprecision in the boundary layer diffusion mass transfer, neglect of deposition effects and boundary layer reactions between acetylene and H_2O/CO_2 will all tend to promote excessive corrosion rate predictions. This excess is not obviously due primarily to kinetic restriction of the hydrogen-carbon reaction. Pyrolytic graphite, owing to its high degree of orientation and high density, is most likely to exhibit hydrogen

reaction kinetics effects. The result would merely be a ... of the high hydrogen attack rates to somewhat higher surface temperatures (possibly 3000°K). The relatively low degree of orientation and high specific surface area of the polycrystalline graphites favor higher reaction rates. As a first approximation, the hydrogen reaction kinetics are believed to be relatively insignificant for these materials. This applies as well to plastic insulation material chars. The hydrogen-graphite reaction is highly endothermic which imposes severe limitations on the nozzle surface temperature rise. It is actually doubtful that graphite temperatures can rise above about 3300°K in high energy solid propellant exhausts.

8. At surface temperatures above about 3000°K in double base exhausts, nitrogen attack of graphite will produce CN and HCN. These reactions are also thermochemically limited. Becaused of the complexity of the reactions, it is probable that kinetic limitations will exist. Again, the degree of restriction is questionable.

VII. NOZZLE MECHANICAL EROSION

1. Nozzle contour surface material may be removed as a direct result of mechanical actions of the exhaust or spalled off to relieve thermal stress at or near the surface. In many cases, mechanical erosion may be mistakenly interpreted as corrosion. This is most likely to occur when the scale of the erosion process is molecular or granular as compared to bulk material erosion. The surface roughness developed is proportional to the scale of the erosion process. The local increase in heat transfer and corrosion are proportional to the surface roughness. The bulk erosion mechanism of stress relief is probably non-recurring. Grain erosion should exhibit thresholds and will recur until the causal factors disappear.

2. The thermal shock problem is relatively well recognized but somewhat less well understood. Tensile cracks may propagate to the contour in either tungsten or the polycrystalline graphites. Unless entire segments of the nozzle section are lost, the cracks pose little threat. Because the surface crack is a weakness, some preferential grain erosion or corrosion may occur.

3. In conjunction with or in lieu of tensile cracking, it is also possible that compressive or shear failure of the bulk material at the surface may occur. This is most likely to occur with the polycrystalline graphites in the nozzle throat or inlet section before plastic deformation relief occurs (about 2800°K). It is also most likely to occur with high flame temperature propellants. Chamber pressure rise transients, poor metal combustion and oxide deposition may combine to prevent such failures. Increasing the thermal expansion allowance may also relieve the surface compression.

-144-

4. At high surface temperatures, compression induced grain expulsion may occur. This relief mechanism is an alternate to plastic deformation and component buckling. Since tungsten becomes very plastic and the polycrystalline graphites are porous, this erosion mechanism may be limited to pyrolytic graphite. Thus, the spallation of surface nodules is frequently observed with edge oriented washers. This is evidently followed by significant deformation of the washer edges. Crystal reorientation and nodule boundary stress concentrations may be important. As demonstrated in this program, nodule spallation may occur locally as well as over the entire circumference. High heating rates, high flame temperatures and axial restraint against thermal expansion will all affect the surface stress. Since the nodules are so large, this kind of spallation produces extreme roughness and extensive surface regression. When such spallation is averaged over the firing period, the erosion of the pyrolytic graphite may compare with or exceed that of the polycrystalline graphites. Pyrolytic graphite shells are expected to delaminate, buckle or peel rather than eject nodules to relieve stresses.

5. The porous polycrystalline graphite and powder metallurgy tungsten materials may loose surface grains as a combined result of the action of the exhaust and thermally induced surface stresses. These grains are not completely surrounded by or bonded to other grains. Preferential chemical attack at grain boundaries may further weaken the structure. The combination of surface compressive stress and gas shear loads may be relieved by removal of some of the surface grains. The removal of one grain weakens the support of the adjacent grains so there will be a tendency to propagate initial surface defects (upstream). The surface roughness developed will be characteristic of the grain (or pore) size and may augment the convective heat transfer and corrosive attack. The loss of graphite grains without chemical reaction heat absorption is not advantageous. However, the grains which experience the greatest gas shear force, must also be subject to considerably higher chemical attack rates since they project into the boundary layer. It is possible that in some (if not most) cases, the graphite grains are actually corroded away before they can be mechanically removed. This would probably not happen if transpiration or ablation gas injection was occurring.

6. The impaction of condensed phases along the motor contour may locally stress the material beyond its capacity. Impaction will predominantly occur in the aft closure and nozzle inlet regions. It should be noted, however, that the areas which are subjected to particle impingement are also subject to extreme heat transfer, corrosive attack and surface shear. Excessive local erosion is undoubtedly a result of all of these actions, not just impingement.

7. It is presumed that the gas shear action along a carbon or graphite contour may also remove material on the molecular scale at sufficiently high temperatures. This would tend to saturate the boundary layer with carbon and reduce corrosion downstream. However, it is doubtful that molecular erosion actually occurs since the available molecules will be the most likely to react chemically before being sheared away.

8. The most dramatic forms of mechanical erosion should be eliminated, through appropriate motor design and materials selection, rather than analyzed. The overall complexity of the stress and heat transfer problem suggests that there will be no substitute for experimental verification of the effectiveness of design changes to eliminate stress induced erosion.

VIII. OXIDE DEPOSITION

1. When impingement of condensed phases occurs at particular areas along the motor/nozzle contour, a deposit will form unless all particles are rejected during the collision. Thresholds for such rejection, if they exist, have not been found.

2. Oxide and metal/oxide deposits will melt and flow downstream over surfaces where impingement does not occur. The net result if beneficial to the nozzle materials, since the contour is shielded against both corrosion and heat transfer.

3. Eventually, most or all of the nozzle deposits will be expelled from the motor. Both deposit retention and expulsion will contribute to the motor performance losses. Nominal motor performance deviations will occur due to variation in the nozzle throat area caused by deposition and erosion.

4. The specifics of the deposit flow process depend on the properties of the deposit, the amount of the deposit, the exhaust gas shear and the heat sink capacity of the contour forming materials. Deposits may be continuous or discontinuous. Liquid deposits may shield the contour after the partially solid deposits have melted. The high melting point advantage of beryllia (2800°K) is partially offset by the lower thermal conductivity of alumina. Thus, in short tests there may be little difference in the thermal insulation effect afforded by the two oxides.

5. The primary source of deposits is particle impingement. Such impingement is determined by the propellant combustion process, grain design and motor contour. These parameters can conceivably be varied to control the amount of impingement and the times when it occurs. By forcing the exhaust to flow around a submerged nozzle, the nose cap and convergent portion of the nozzle may be entirely shielded from both stagnation flow and impingement/deposition effects. Apparently, submergence to approximately 15 percent will promote effective nose cap shielding.

6. The variation in oxide deposition, with different propellants in identical motors or with the same propellant in different motors, is a major cause of apparent materials performance variations.

7. The thermal insulation and corrosion protection effects do not outlast the deposits. Shortly after the deposits are removed, the nozzle temperatures will closely approach the levels they would have reached without deposits. There will be less total corrosion and possibly no thermal shock or mechanical spallation as a result of deposit protection. Consequently, short time firing data cannot reasonably be extrapolated without considering deposition effects. Scale motor test results should also be treated with great care.

IX. GRAIN DESIGN

1. It has been shown that the solid propellant grain design can have a strong influence on nozzle materials performance. Ideally, the grain should produce a uniform exhaust flow, devoid of free shear and recirculation induced stagnation or turbulence. This is not always possible. In particular, some slotted and star grains produce highly nonuniform flow. The usual result is that the aft closure and nozzle materials are locally subjected to above average flow stagnation and turbulence. The local corrosion, heat transfer and impingement will be increased in these areas. The result will be excessive material degradation and, often, motor failure. In extreme cases, there is little or no hope of developing superior materials or resorting to cooling. Then, the problem must be eliminated through design changes involving the grain and/or the motor contour.

2. The grain and motor aft closure configuration should be arranged to maximize the opportunity for the metal additives to burn completely. The streamline distances, to critical insulation and nozzle surfaces, and the gas velocities should be established to either complete metal combustion or to ensure that protective deposits will form. Otherwise, the materials will exhibit higher surface regression rates than are necessary. To achieve high motor ballistic performance, the metal particles should burn completely before reaching the nozzle throat. In establishing grain designs, the surface agglomeration of metal particles should be considered.

3. Efficient combustion of some beryllium propellants in end burning propellants may not be possible. This is the result of the inherently low chamber velocities associated with end burners. At burn out, internal burning grains also produce low exhaust velocities and combustion efficiency may decay in spite of the increasing streamline path lengths. The flow will be nonuniform across an internal burning grain port, in terms of combustion, due to the great variation in the streamline flow path lengths.

-147-

4. High mass fraction, internal burning grains will produce very high initial exhaust flow velocities and short particle residence times. Poor metal combustion is likely to result for low flame temperature propellants, especially if surface agglomeration occurs. The combination of high flame temperatures (without metal combustion) and potentially high drag heating may compensate for the short stay times.

5. If is not clear whether erosive burning will increase or decrease metal particle agglomeration. Local erosive burning may be induced in a slotted grain. This is due to the effect of the axial slot jets which radially stagnate along the grain surface (opposite a single slot and between multiple slots).

X. NOZZLE DESIGN

1. Any insulation or nozzle material studied in this program can be employed as well in either beryllium or aluminum propellant systems. The specific performance of the materials will be directly determined by (a) propellant combustion efficiency, (b) adequacy of the component thermostructural design, (c) grain-motor-nozzle configuration and (d) oxide deposition characteristics. The ballistic performance of the motor will also depend on these major parameters. In evaluating ballistic performance, nozzle throat area variations caused by deposition, plastic deformation and erosion must be properly accounted for.

2. In the absence of thermal shock fragmentation, tungsten inserts will ultimately fail structurally as a result of excessive plastic deformation. Deformation, buckling and obtrusion can be accelerated by the formation of low melting carbides or metal alloys. Uncooled tungsten inserts should give the best performance in low flame temperature exhausts which achieve either high degree of combustion or extensive oxide deposition protection. In high flame temperature propellants, firing times should be appropriately shortened. Minimizing the corrosion of upstream graphite materials by hydrogen and/or hydrocarbon pyrolysis gas injection will reduce or eliminate tungsten carbide formation at the flame side surface.

3. Pyrolytic graphite can be used with any of the metalized solid propellants. The primary failure mode is high temperature surface spallation of nodules or laminates. Such failures are caused by the development of excessive surface compressive stress which cannot be entirely relieved via plastic deformation. The stresses are primarily induced by differential thermal expansion and, possibly, secondarily by crystal lattice reorientation. Nodule boundary corrosion may be a contributing cause of failure. Apparently, such surface spallation failures occur at surface temperatures above 3000°K when local heating rates are extreme. When surface spallation is controlled, relatively uniform corrosion will be the primary cause of surface regression. The most reactive exhaust species

will be H_2O, CO_2, H_2 and, to a lesser degree N_2. Poor propellant com-bustion accelerates only the H_2O and CO_2 reactions which are not strongly dependent on surface temperature. Sacrificial corrosion of graphite nozzle inlet materials and insulation pyrolysis gas injection will usually (not always) reduce corrosion rates at the nozzle throat.

4. The primary mechanical failure modes for polycrystalline graphite are low temperature surface spallation and grain erosion. Spallation is a thermal stress induced phenomenon somewhat similar to thermal shock. Surface grain erosion may be caused by particle impaction and gas shear loading. It may be accelerated by preferential corrosion of partially graphitized material which supports the graphite grains. Whether grain erosion actually occurs or not probably depends on whether the surface is hydraulically rough or not.

5. Corrosion reactions are the same for all graphites. However, it is argued that the hydrogen reactions will proceed at higher rates with polycrystalline graphites (at the same surface temperature) relative to pyrolytic graphite. The highly endothermic hydrogen reaction will limit the surface temperature rise in proportion to the actual rates of reac-tion. The acetylene reaction product can react with H_2O and CO_2 in the boundary layer or supress the hydrogen reaction rate downstream.

6. The specific performance of ablative insulation materials depends primarily on the local heating rate, corrosion rate, gas shear and particle impingement. Abnormally high exhaust interactions with the insulator surface occur in flow stagnation regions along the aft closure. All four of the above effects peak at about the same place. It is speculated that high corrosion, particularly as a result of incomplete metal combustion, coupled with high gas surface shear is the primary cause of excessive insulation char regression. Higher heating rates are partially compensated for by blowing. Particle impingement may also be a secondary effect with thin chars and when sticking occurs.

XI. MOTOR TESTING

1. Information return from development motor tests has generally been unnecessarily limited. It has been demonstrated in this program that nozzle throat deposition, nozzle thermal response and metal combustion efficiency can be obtained without compromising other test objectives. Motion pictures of firings, post test physical examination of hardware and exhaust plume sampling provide pertinent additional information.

2. The beryllium exhaust erosion corrosion problem is not unique. Similar problems are likely to arise in connection with the development of advanced propellant and motor systems. Early detection and avoidance of these problems would be facilitated by expanding the objectives of future scale and development motor tests.

3. In general, it should be assumed that motor materials performance will depend on motor scale, motor configuration, grain design, propellant formulation, motor pressure level and test duration. Correlation of test results will be difficult or impossible with the limited availability of specific test data. Extrapolation of motor test results should be undertaken with great caution.

XII. ANALYTICAL DEVELOPMENTS

1. Significant progress has been made in the analytical characterization of nozzle heat transfer, corrosion and oxide deposition processes. The dependence of these processes on the major motor design parameters has been demonstrated through post test analysis of nozzle performance. A generalized method for nozzle design and performance analysis has been formulated. The method involves both qualitative and quantitative treatments of the elements of the nozzle performance problem. The method provides a basis for selecting experiments and scale tests to constructively supplement the quantitative analyses.

2. Based on the post-test analysis results in this program, measured nozzle throat heat transfer is potentially a more effective indicator of poor metal combustion than is ballistic performance efficiency. Nozzle throat deposition histories must be obtained from the ballistic performance data to accurately determine the heat transfer, corrosion rate and ballistic performance efficiency.

3. An effective means of analytically predicting nozzle contour deposition histories has not been developed. Qualitative and analytical models have been formulated for future consideration.

4. An improved technique has been developed for estimating nozzle convective heat transfer in high energy solid propellant exhausts. A revised form of the closed form Bartz equation and supplementary thermochemical calculations are employed. Recombination, corrosion, low Prandtl number, recovery and blowing effects have been included. Surface roughness and pyrolysis gas film injection effects can also be covered.

5. An advanced analytical technique for predicting graphite nozzle corrosion by gaseous exhaust species has been partially developed. The improvements in the convective heat transfer analysis are incorporated. The analysis requires the use of unequal specie mass transfer coefficients. Simplified corrosion rate prediction equations can be derived from the more general theory but the essential assumptions are usually physically unrealistic. Major questions have been raised concerning the use of available chemical reaction rate kinetics data.

6. Nozzle heat transfer studies indicate that nozzle failures in the past may often have been the direct result of underestimation of the heat transfer. Similarly, unusually good nozzle performance can be attributed to combinations of poor metal combustion and extensive deposit protection.

SECTION VI (C)

RECOMMENDATIONS

The major recommendations for future work are listed below. These are
based on the program results and their projection to situations not spe-
cifically covered in the present program. The recommendations are not
restricted to beryllium solid propellants or motors except as specifically
stated. More detailed recommendations have previously been presented at the
end of Sections II through V in References 1 through 4.

I. PROPELLANT SELECTION

1. With the objective of minimizing future motor materials and ballistic
   performance problems, it is recommended that the metal combustion
   characteristics be established for candidate propellants. This should
   be done before or in conjunction with early propellant development
   tests. Both analytical and laboratory experimental techniques are
   currently available or can be developed for this purpose. Poor combus-
   tion characteristics should serve as adequate grounds for rejection or
   further development of a propellant, regardless of its ideal performance
   potential.

2. In the earliest possible stages of a rocket motor development, it is
   recommended that tests be conducted to establish the compatibility of
   selected propellants with the actual grain design and motor contour.
   Throat deposition/erosion histories, nozzle thermal response, hardware
   post test analysis and ballistic performance analyses should be conducted
   to clarify the metal combustion efficiency and materials/design per-
   formance. The causes of poor to marginal delivered performance should
   be clearly identified before major motor redesign or rejection are
   undertaken.

3. Double base, composite and CMDB propellants containing beryllium metal
    can be considered for future applications. The majority of these will
    exhibit poor metal combustion in some or all motor applications. With
    proper design, the effects of poor combustion can be minimized. Con-
    figuration, volumn and ballistic performance penalties are likely to
    result. It is recommended that first choice be given to those propellants
    which do not exhibit extensive grain surface agglomeration of beryllium.
    At the same time, the flame temperature without any metal combustion
    should not be below about 2000°K. Ideally, this temperature should be
    close to or above the melting point of the condensed reaction products.
    In cases which are marginal, tailoring should involve metal particle
    size, metal loading, oxidizer particle size and burn rate changes to
    improve combustion. Increasing the propellant oxidation ratio is not
    desirable from a nozzle corrosion point of view. Low chamber pressures
    are not desirable, particularly with composites.

II.   ADVANCED NOZZLE DESIGN

1. Once nozzle deposits are removed, the performance of nozzle materials
    will be essentially the same in completely combusted aluminum and
    beryllium exhausts. Cooled nozzles should be equally effective in
    either system if advantage is not taken of the high melting point of
    beryllia deposits. Before considering the use of cooled nozzles with
    beryllium propellants, it is recommended that the performance limits of
    uncooled designs be established with and without the exploitation of
    oxide deposition protection.

2. In selecting a nozzle design or concept, it is recommended that a
    definite decision be made as to whether oxide deposition is to be
    encouraged or discouraged. Internal gas or liquid metal cooling con-
    cepts will be most successful in extending the oxide deposit protection
    effects. Transpiration and film cooling should be most effective with
    deeply submerged designs which discourage deposit formation. Film
    protection and sacrificial ablation may be effective after deposits are
    removed from the main throat insert and may otherwise delay deposit
    removal. The stability of new material candidates with beryllia should
    be established prior to their use.

3. It is recommended that motor insulation materials be selected with due
    consideration given to (a) their resistance to incompletely burned
    exhaust, (b) their ability to capture condensed phases, (c) the influence
    of pyrolysis gas products on the performance of materials downstream,
    and (d) the consequences of ejecting insulation decomposition products
    into the exhaust plume.

III. MOTOR TESTING

1. It is recommended that future research and development motor testing be related as closely as possible to specific propellants and motor configurations which are candidates for actual systems application. Accurate thrust and pressure data should be obtained in all tests and used to determine nozzle deposition and ballistic performance.

2. Additional motor testing should be conducted to establish or further clarify the dependence of corrosion, heat transfer and deposition on the following:

    (a) Aft closure insulation materials,

    (b) Grain design,

    (c) Nozzle submergence,

    (d) Surface roughness,

    (e) Metal combustion efficiency.

3. It is recommended that the return of heat transfer, corrosion, tungsten carburization, and deposition data be maximized in future motor tests. Correlation of this data should be possible when complete combustion of the metal additives has been achieved in all cases. Such data is also useful in determining when complete combustion is achieved.

4. Geometric scaling is not recommended with beryllium propellants. Scale motor designs should be developed with due consideration to the effects on combustion, deposition, heat transfer and corrosion, relative to the full scale motor.

IV. ANALYSES DEVELOPMENT

1. It is recommended that analytical or semiempirical techniques be developed to predict ignition delays and combustion times for metal particles in the rocket chamber. Fuels such as Al, Be, B, C, BeH_2 and AlH_3, with real size distributions, should be considered. Velocity slip heating, surface reactions, fusion, vaporization, diffusion and radiation should be covered. Parallel laboratory studies should be conducted to improve the characterization of surface agglomeration, particle ignition temperatures and particle ejection mechanics.

2. Analytical or cold flow modeling techniques should be developed or improved for the purpose of determining the detailed exhaust flow inter-actions with the motor/nozzle contour. Emphasis should be placed on locating surface areas which are subject to recirculation, stagnation,

free shear and highly turbulent flow. Such surfaces will be simultaneously subject to significant particle impingement, high corrosion, high heat transfer and extreme gas shear loading.

3. It is recommended that a boundary layer computer program be developed to incorporate the improvements in the characterization of the convective heat transfer and corrosive species diffusion developed in this program.

4. It is recommended that the objectives of future development motor testing be expanded to include the production of basic heat transfer, corrosion, deposition and combustion efficiency data. Individual contractors can use this data directly in the motor/nozzle design process. The Air Force should take the responsibility of promoting the parallel development or improvement of analytical techniques for predicting and correlating the heat transfer, corrosion and deposition. Independent predictions of nozzle and insulation materials performance should be compared with actual results to check the validity and accuracy of the analytical methods.

5. In support of studies dealing with the oxide deposition phenomenon, it is recommended that further work be devoted to determining the important properties of alumina and beryllia. Thermal conductivity, specific heat, density and bulk emissivity data are required for the solid and liquid phases to approximately $5200°F$. The viscosity and surface tension of the liquids should also be measured. The influence of impurities (metal, carbon, silica, silicates, etc.) disolved gases and porosity on the basic properties should be determined.

V. PROGRAM RESULTS

1. It is recommended that the results and conclusions of this program not be regarded as exclusively applicable to beryllium propellants. For the most part, they apply equally as well to fuel rich, hybrid, slurry, gel and liquid propellant systems. Combustion, fluid flow mechanics, heat transfer, corrosion and structural mechanics are common elements to all of these systems.

2. It is recommended that the results of this program and related future work be considered in future systems planning, feasibility and development studies. Alternately, variations of the program technical approach should be effective in developing an understanding of the nature of motor/nozzle materials problems which may arise during advanced systems development.

REFERENCES (U)

1. Smallwood, W. L.,* et al., <u>Beryllium Erosion Corrosion Investigation for Solid Rocket Nozzles (U)</u>, First Quarterly Progress Report, Confidential, Contract AF 04(611)-10753, AFRPL-TR-65-205, November 1965 (AD 367 241).

2. Smallwood, W. L.,* et al., <u>Beryllium Erosion Corrosion Investigation for Solid Rocket Nozzles (U)</u>, Second Technical Progress Report, Confidential, Contract AF 04(611)-1075J, AFRPL-TR-66-71, May 1966 (AD 372 384).

3. Smallwood, W. L.,* et al., <u>Beryllium Erosion Corrosion Investigation for Solid Rocket Nozzles (U)</u>, Third Technical Progress Report, Confidential, Contract AF 04(611)-10753, AFRPL-TR-66-205, November 1966 (AD 377 315).

4. Smallwood, W. L.,* et al., <u>Beryllium Erosion Corrosion Investigation for Solid Rocket Nozzles (U)</u>, Fourth Technical Progress Report, Confidential, Contract AF 04(611)-10753, AFRPL-TR-67-16, February 1967 (AD 379 420).

5. Kuehl, D. K., "Ignition and Combustion of Aluminum and Beryllium," <u>AIAA Journal 3</u>, December 1965, pp 2239-2247.

6. Bartz, D. R., "A Simple Equation for Rapid Estimation of Rocket Nozzle Convective Heat Transfer Coefficients," <u>Jet Propulsion</u>, Vol. 27(1), pp 49-51, January, 1957.

7. Price, F. C., et al, <u>Internal Environment of Solid Rocket Motors</u>, Final Technical Report, Contract AF 04(611)-9072, AFRPL-TDR-64-140, 30 July 1964.

8. McCuen, P. A., et al., <u>A Study of Solid-Propellant Rocket Motor Exposed Materials Behavior</u>, Vidya Report No. 149, Vidya Div. of Itek Corp, February 1965.

REFERENCES (Continued)

9. Lowrie, R., et al., <u>Research on Physical and Chemical Principles Affecting High-Temperature Materials for Rocket Nozzles</u>, Contract No. DA-30-069-ORD-2787, Union Carbide Research Institute, Semi-annual Progress Reports, 30 June and 31 December 1961.

10. <u>Composite Beryllium Propellant Motors For Project Adobe (U)</u>, Final Report, Confidential, Contract AF 04(694)-640, BSD-TR-66-359, Thiokol Chemical Corp., Wasatch Division.

11. Elliott, D. G., Bartz, D. R., and Silver, S., <u>Calculation of Turbulent Boundary Layer Growth and Heat Transfer in Axi-symmetric Nozzles</u>, JPL Tech Report 32-387, February 1963.

12. Svehla, R. A., "Estimated Viscosities and Thermal Conductivities of Gases at High Temperatures," NASA Tech Report R-132, 1962.

13. Brokaw, R. S., "Approximate Formulas for Viscosity and Thermal Conductivity of Gas Mixtures," NASA Tech Note D-2502, November 1964.

14. Hirschfelder, J. O.. Curtiss, C. F., and Bird, R. B., <u>Molecular Theory of Gases and Liquids</u>, Wiley and Sons, 1954.

15. Armour, W. H., et al., <u>An Investigation and Feasibility Demonstration of Nozzles for Restartable Solid Rocket Motors, Final</u> Technical Report, AFRPL-TR-66-53, Aeronutronic Division of Philco-Ford Corp., Newport Beach, California, March 1966.

16. Carlson, D. J., <u>Alumina Absorption and Emittance</u>, Final Technical Report, ARPA Contract Onr 3606(00), Aeronutronic Div of Philco-Ford Corp., Publication N J-2627, 31 May 1964.

17. Bartlett, E. P., "A Systematic Method for Determination of Ablation Rates in a Corrosive Environment," <u>6th Symposium On Ballistic Missile and Aerospace Technology</u>, Vol. III, Academic Press, 1961, pp 103-119.

18. Brinsmade, A. F., and Desmon, L. G., <u>Hypothesis for Correlating Rocket Nozzle Throat Convective Heat Transfer</u>, Allegany Ballistics Laboratory (HPC), Report No. Z-76, November 1964.

19. Armour, W. H., et al., <u>Documentation of Computor Program for Calculation of Rocket Nozzle Convective Heat Transfer</u>, Supplemental Report, Contract AF 04(611)-9904, AFRPL, October 1966.

20. Eckert, E. R. G., and Drake, R. M., Jr., <u>Heat and Mass Transfer</u>, McGraw-Hill, 1959, pp 222-225.

REFERENCES (Continued)

21. Lees, L., "Convective Heat Transfer With Mass Addition and Chemical Reactions," _Third Combustion and Propulsion Colloquium_, AGARD, NATO, March 1958.

22. Rindal, R. A., Flood, D. T., and Kendall, R. M., _Analytical and Experimental Study of Ablation Material for Rocket Engine Application_, NASA CR-54757, May 1966.

23. Schaefer, J. W., and Dahm, T. J., _Studies of Nozzle Ablative Material Performance for Large Solid Boosters_, NASA CR-72080, December 1966.

24. Chapman, D. R., _A Theoretical Analysis of Heat Transfer in Regions of Separated Flow_, NACA TN 3792, October 1956.

25. Fox, J., "Heat Transfer and Air Flow in a Transverse Rectangular Notch," _International Journal of Heat and Mass Transfer_, Vol 8, pp 269-279.

26. Mickley, H. S., and Davis, P. S., _Momentum Transfer for Flow Over a Flat Plate With Blowing_, NACA TN 4017, November 1957.

27. Mastroly, F. R., _Solution of General Heat Transfer Problems Using the IBM 7090 Thermal Analyzer Program_, Lockheed Aircraft Corporation, Report LR 16110, 1963.

28. Mitchell, R. L., et al., _An Investigation and Development of Film Protected-Convectively Cooled Nozzles (U)_, Final Technical Report, Confidential, Contract AF 04(611)-9705, Air Force Rocket Propulsion Laboratory, Philco-Ford Technical Report No. C-3660, 30 Sept 1966.

APPENDIX I (C)

ROCKET MOTOR DESIGN DATA

Propellant, grain, motor and nozzle design data for the motors tested in
this program are presented in this appendix. The data are summarized in
graphical and tabular form. Table III summarizes and compares the major
design features of the motors tested (see also Section 3.3).

1.1 (U) PROGRAM PROPELLANTS

The criteria used in selecting the seven propellants and their ideal per-
formance are discussed in Section 3.1. The propellant formulas are given
in Tables IV, V, and VI. The XSO parameter (excess oxygen) is similar to
the oxidation ratio. Thus, XSO equals the formula gram atoms of oxygen,
less the sum of the formula gram atoms of carbon and metal. The propellants
were tailored to provide equal burn rates at the nominal motor design
pressure of 800 psia. The tests in which each propellant was used are
listed with the formula.

1.2 (U) GRAIN DESIGNS

Cross-sectional views and dimensional data for the five grain designs
employed in this program are shown in Figures 2 through 6. The design
criteria are briefly discussed in Section 3.3. The tests in which each
design was used are indicated on the figures. Note that the end burning
grains were used in two motor configurations. In the remote position, the
initial burning surface was 12 inches farther forward than in the close
position. In the close end burner configuration, the grain was as close
to the nozzle (throat) as the aft closure insulator would allow.

-159-

1.3 (U) MOTOR CONFIGURATIONS

The Aerojet ADOBE (600 pound) hardware was used in all tests. Cross-
sectional schematics of the motor assemblies are shown in Figures 7 through
12. The appropriate tests are indicated on these figures. The motor
assembly procedures are described in detail in Sections 5.2 and 5.3 of
References 2, 3, and 4. Note that minor modifications were made to the
ADOBE barrels after they were damaged on Tests T-1 and T-2. The modifica-
tions allowed for improved sealing between the forward (wood filled) and
aft sections of the motors. The damaged barrel sections were used on Tests
T-3 through T-25. New barrel sections were fabricated by the Air Force
for use in the development Tests, T-51 through T-54.

1.4 (U) NOZZLE DESIGNS

Cross-sectional schematics of the nozzle designs tested in this program
are shown in Figures 13 through 26. The initial nozzle throat diameters
and the nozzle materials are indicated on each figure. Figures 27 through
34 define the critical dimensions and angles for all of the nozzle designs.
Numerical data, corresponding to the letter symbols, are given in Table VII.
Note that otherwise identical nozzles had slightly different throat
diameters when the propellant was changed.

TABLE III. MOTOR DESIGN SUMMARY

Test Number	Propellant	Grain Design	Nozzle Contour	Insulator	Flame Side Materials		Type of Test
					Entrance Cone	Throat	
T-1	Arcocel 191F	Remote End Burner	Conventional, 25° Inlet	Asbestos Phenolic	ATJ Graphite	Pyrolytic Graphite Washers	
T-2	Arcane 24F	Remote End Burner	Conventional, 25° Inlet	Asbestos Phenolic	ATJ Graphite	Pyrolytic Graphite Washers	Beryllium Propellant Formulation Tests
T-3	Arcocel 319BRF	Remote End Burner	Conventional, 25° Inlet	Asbestos Phenolic	ATJ Graphite	Pyrolytic Graphite Washers	
T-4	Arcane 54F	Remote End Burner	Conventional, 25° Inlet	Asbestos Phenolic	ATJ Graphite	Pyrolytic Graphite Washers	
T-5	Arcane 60	Remote End Burner	Conventional, 25° Inlet	Asbestos Phenolic	ATJ Graphite	Pyrolytic Graphite Washers	
T-6	Arcocel 390	Remote End Burner	Conventional, 25° Inlet	Asbestos Phenolic	ATJ Graphite	Pyrolytic Graphite Washers	
T-7	Arcocel 389	Remote End Burner	Conventional, 25° Inlet	Asbestos Phenolic	ATJ Graphite	Pyrolytic Graphite Washers	Aluminum Analog Propellant Tests
T-8	Arcocel 389	Internal Burner Type II	Conventional, 18° Inlet	Asbestos Phenolic	ATJ Graphite	Pyrolytic Graphite Washers	
T-9	Arcocel 191F	Type I	Conventional, 18° Inlet	Asbestos Phenolic	ATJ Graphite	Pyrolytic Graphite Washers	
T-10	Arcocel 191F	Type II	Conventional, 18° Inlet	Asbestos Phenolic	ATJ Graphite	Pyrolytic Graphite Washers	Grain Design Tests
T-11	Arcane 54F	Type I	Conventional, 18° Inlet	Asbestos Phenolic	ATJ Graphite	Pyrolytic Graphite Washers	

TABLE III. MOTOR DESIGN SUMMARY (Continued)

Test Number	Propellant	Grain Design	Nozzle Contour	Flame Side Materials Insulator	Entrance Cone	Throat	Type of Test
T-12	Arcocel 191F	Type II	Submerged	Carbon Cloth	ATJ Graphite	Pyrolytic Graphite Washers	Nozzle Contour Tests
T-13	Arcocel 191F	Type II	Steep Inlet	Asbestos Phenolic	ATJ Graphite	Pyrolytic Graphite Washers	
T-14	Arcocel 319BRF	Type I	Conventional, 18° Inlet	Asbestos Phenolic	ATJ Graphite	Pyrolytic Graphite Washers	Grain Design Tests
T-15	Arcocel 319BRF	Type III	Conventional, 18° Inlet	Asbestos Phenolic	ATJ Graphite	Pyrolytic Graphite Washers	
T-16	Arcocel 191F	Type I	Conventional, 18° Inlet	Asbestos Phenolic	ATJ Graphite	Tungsten	Insulation and Throat Materials Tests
T-17	Arcocel 191F	Type I	Conventional, 18° Inlet	Asbestos Phenolic	Carbon Cloth	Tungsten	
T-18	Arcocel 191F	Type I	Submerged	Carbon Cloth	ATJ Graphite	Tungsten	
T-19	Arcocel 319BRF	Type I	Submerged	Carbon Cloth	ATJ Graphite	Tungsten	
T-20	Arcocel 191F	Type I	Conventional, 18° Inlet	Asbestos Phenolic	Carbon Cloth	Pyrolytic Graphite	
T-21	Arcocel 191F	Close End Burner	Steep Inlet	Asbestos Phenolic	ATJ Graphite	Pyrolytic Graphite	Non-equilibrium Combustion Effects
T-22	Arcane 54F	Close End Burner	Steep Inlet	Asbestos Phenolic	ATJ Graphite	Pyrolytic Graphite	

TABLE III. MOTOR DESIGN SUMMARY (Continued)

Test Number	Propellant	Grain Design	Nozzle Contour	Flame Side Materials			Type of Test
				Insulator	Entrance Cone	Throat	
T-23	Arcocel 191F	Close End Burner (100#)	Submerged	Carbon Cloth	ATJ Graphite	Pyrolytic Graphite Washers	Non-Equilibrium Combustion Effects
T-24	Arcocel 319BRF	Close End Burner (100#)	Steep Inlet	Asbestos Phenolic	ATJ Graphite	Pyrolytic Graphite Washers	
T-25	Arcocel 191F	Type I (100#)	Conventional 18° Inlet	Asbestos Phenolic	ATJ Graphite	Pyrolytic Graphite Washers (Thick)	Heat Sink Size Effect
T-51	Arcocel 191F	Single Slot (500#)	Submerged	Asbestos Phenolic	ATJ Graphite	Pyrolytic Graphite Washers	
T-52	Arcocel 319BRF	Single Slot (500#)	Submerged	Asbestos Phenolic	ATJ Graphite	Pyrolytic Graphite Washers	Scale Effects
T-53	Arcocel 191F	Single Slot (500#)	Deep Submerged	Asbestos Phenolic	ATJ Graphite	Pyrolytic Graphite Washers	
T-54	Arcocel 191F	Single Slot (500#)	Submerged	Asbestos Phenolic	ATJ Graphite	Tungsten	

TABLE IV. BERYLLIUM CMDB PROPELLANT FORMULATION

Test		Arcocel 191F	
T-1	Ingredient		Weight (%)
T-9	Binder:		55.000
T-10			
T-12	Nitrocellulose	18.288	
T-13	TMETN	30.009	
T-16	Nitroglycerin	1.064	
T-17			
T-18	Triacetin	3.574	
T-20	Resorcinol	1.100	
T-21	2-NDPA	0.352	
T-23			
T-25	Ethyl Centralite	0.612	
T-51	Ammonium Perchlorate		31.204
T-53	Beryllium		13.796
T-54			100.000

XSO = 0.150

Test		Arcocel 319BRF	
T-3	Ingredient		Weight (%)
T-14	Binder:		55.000
T-15	Same as Arcocel 191F		
T-19	RDX		26.200
T-24	Ammonium Perchlorate		8.026
T-52	Beryllium		10.774
			100.000

XSO = 0.050

TABLE V. BERYLLIUM COMPOSITE PROPELLANT FORMULATION

Test		Arcane 24F	
		Ingredient	Weight (%)
T-2			
	Binder:		20.000
	Polypropylene Glycol	16.953	
	Trimethyl Propane	0.108	
	Neozone D	0.199	
	Alrosperse 11P	0.530	
	Toluene Disocyanate	2.168	
	Ferric Acetylacetonate	0.042	
	Ammonium Perchlorate		68.053
	Beryllium		11.947
			100.000

XSO = 0.300

Test		Arcane 54F	
		Ingredient	Weight (%)
T-4			
T-11	Binder:		20.000
T-22	Same as Arcane 24F		
	Ammonium Perchlorate		67.019
	Beryllium		12.981
			100.000

XSO = 0.150

-165-

TABLE VI. ALUMINUM ANALOG PROPELLANT FORMULATION

Test	Arcocel 389 (Arcocel 191F Analog)	
	Ingredient	Weight (%)
T-7	Binder:	52.000
T-8	Same as Arcocel 191F	
	Ammonium Perchlorate	24.930
	Aluminum	23.070
		100.000

XSO = 0.150

Test	Arcocel 390 (Arcocel 319BRF Analog)	
T-6	Ingredient	Weight (%)
	Binder:	51.000
	Same as Arcocel 191F	
	Ammonium Perchlorate	4.359
	RDX	26.200
	Aluminum	18.411
		100.000

XSO = 0.050

Test	Arcane 60 (Arcane 54F Analog)	
T-5	Ingredient	Weight (%)
	Binder:	20.000
	Same as Arcane 24F	
	Ammonium Perchlorate	59.360
	Aluminum	22.140
	XSO = 0.150	100.000
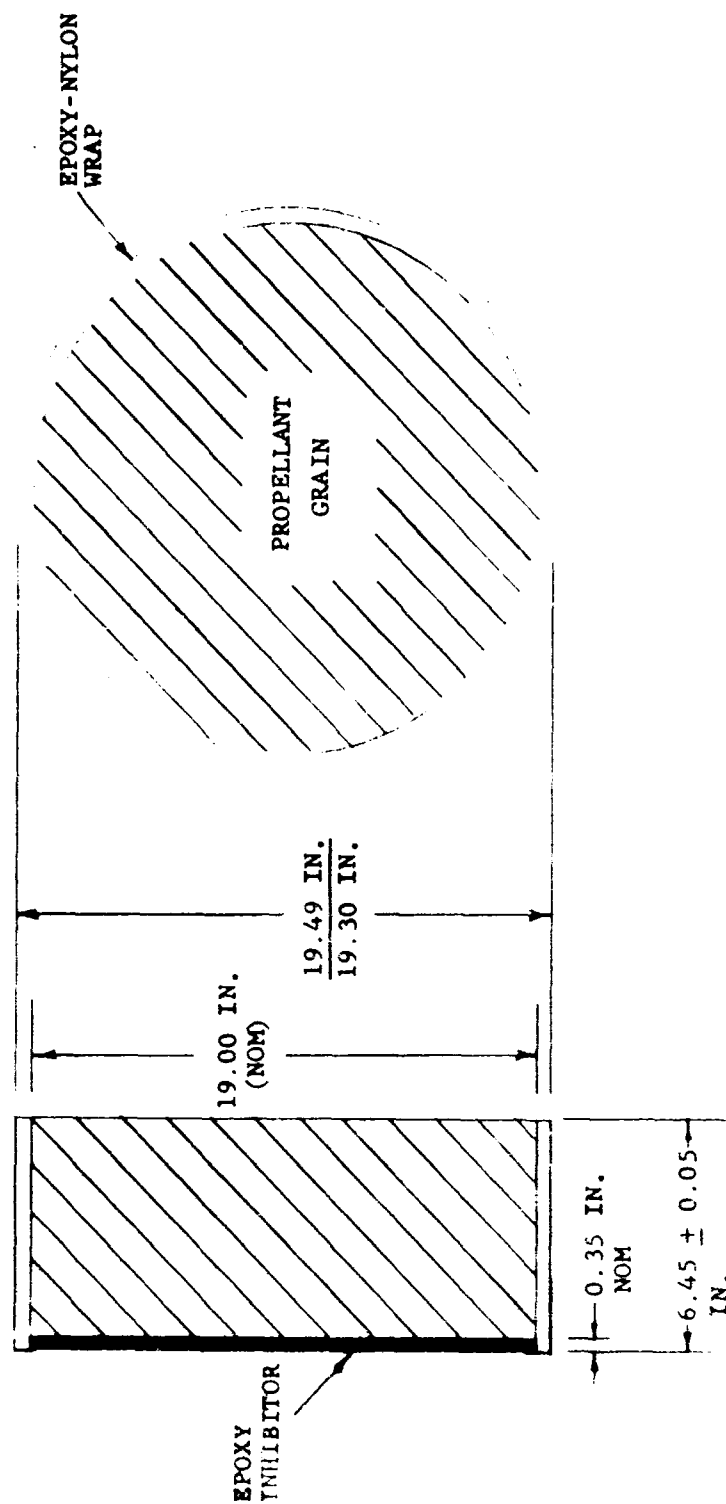
FIGURE 2. END BURNING GRAIN CONFIGURATION
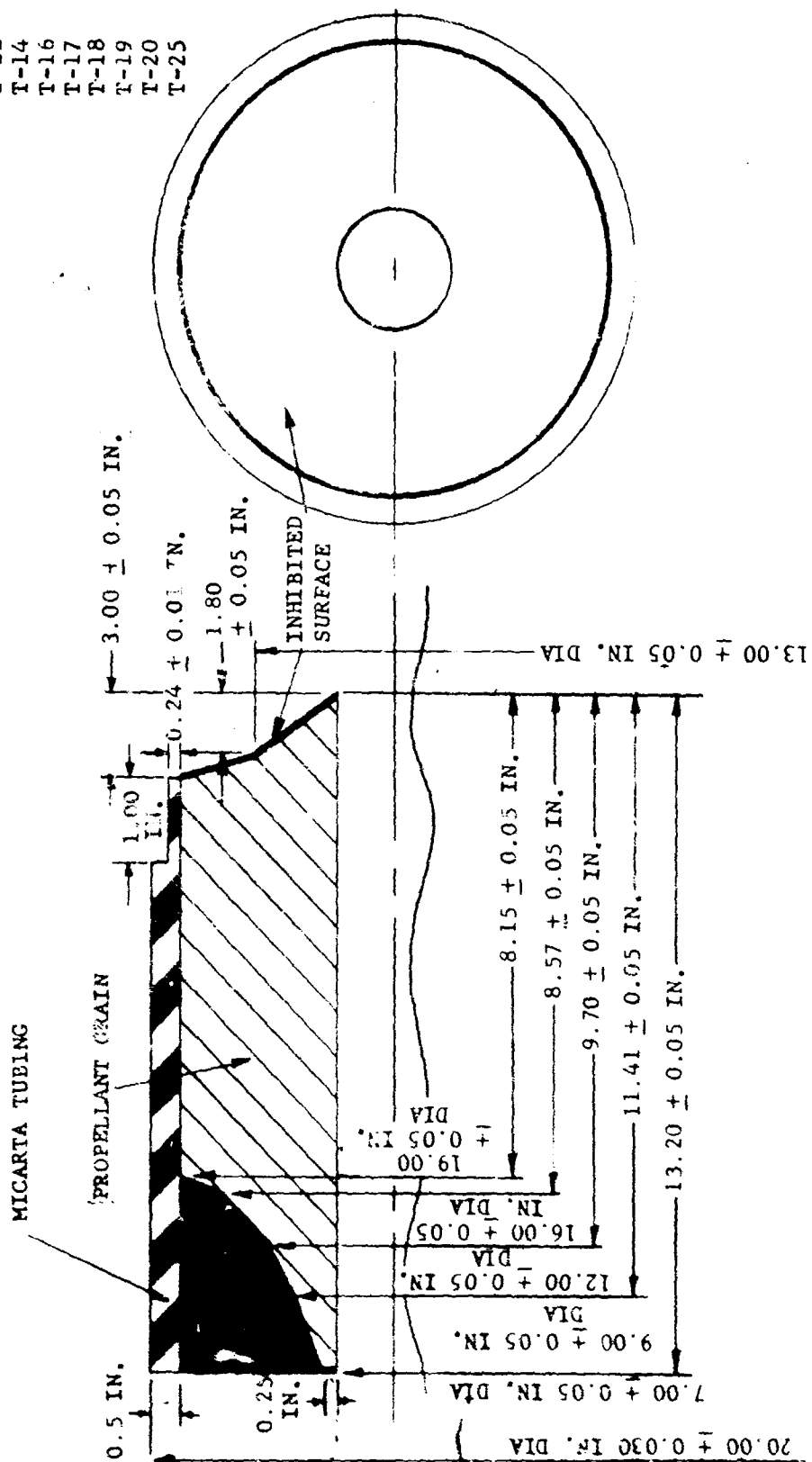
F00808 U

FIGURE 3. INTERNAL BURNING GRAIN I (7 IN. CP)

F00809 U

-168-

TEST

T-8
T-10
T-12
T-13

3.00 ± 0.05 IN.

0.24 ± 0.01 IN.

1.80 ± 0.05 IN.

INHIBITED SURFACE

1.00 IN.

13.00 ± 0.05 IN. DIA

MICARTA TUBING

PROPELLANT GRAIN

10.00 ± 0.05 IN.

0.5 IN.

7.00 ± 0.05 IN. DIA

19.00 ± 0.05 IN. DIA

20.00 ± 0.03 IN. DIA

INHIBITED

1.00 ± 0.10 IN.

SLOT

0.5 IN.
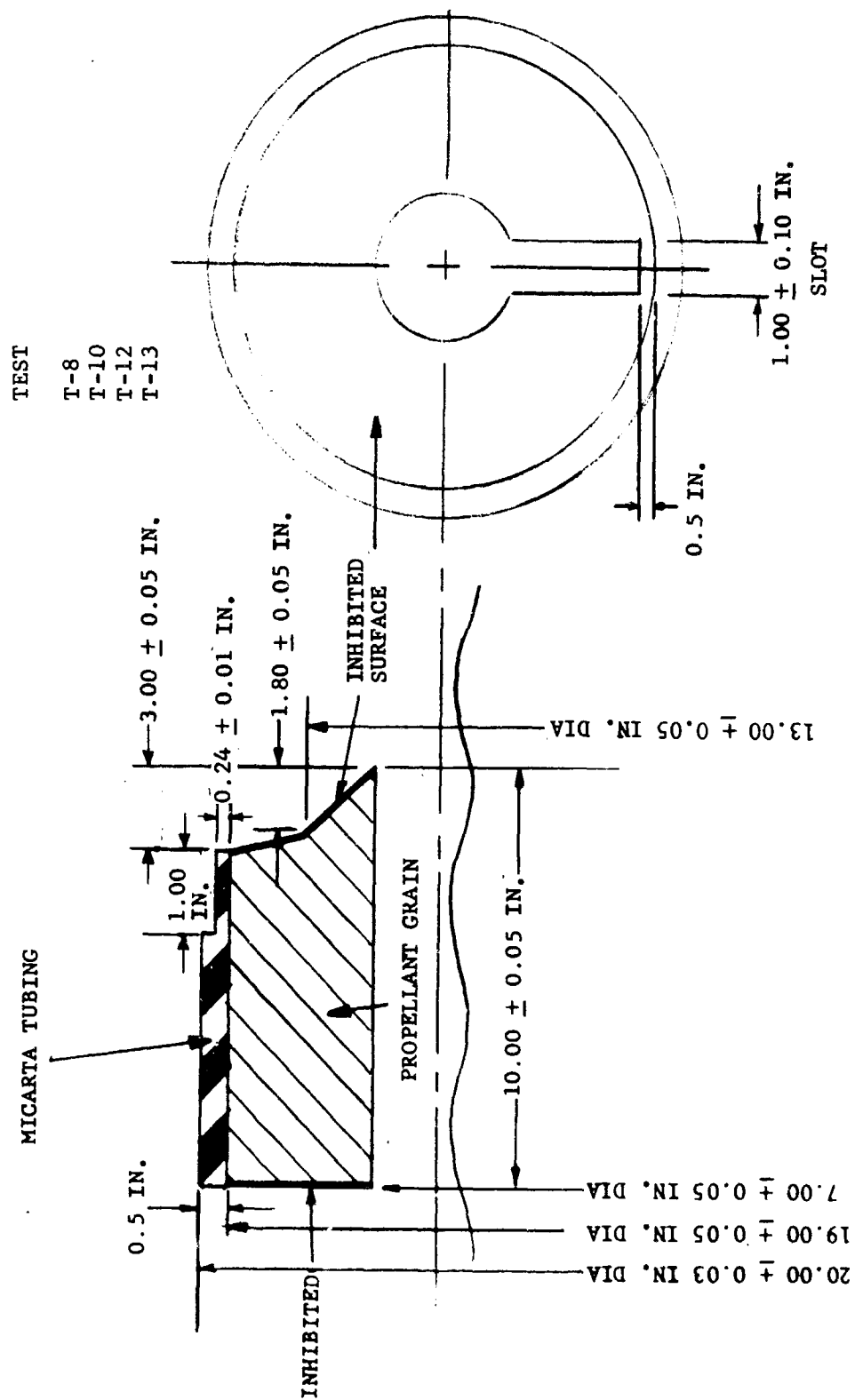
F00810 U

FIGURE 4. INTERNAL BURNING GRAIN II (7 IN. KEY)

-169-
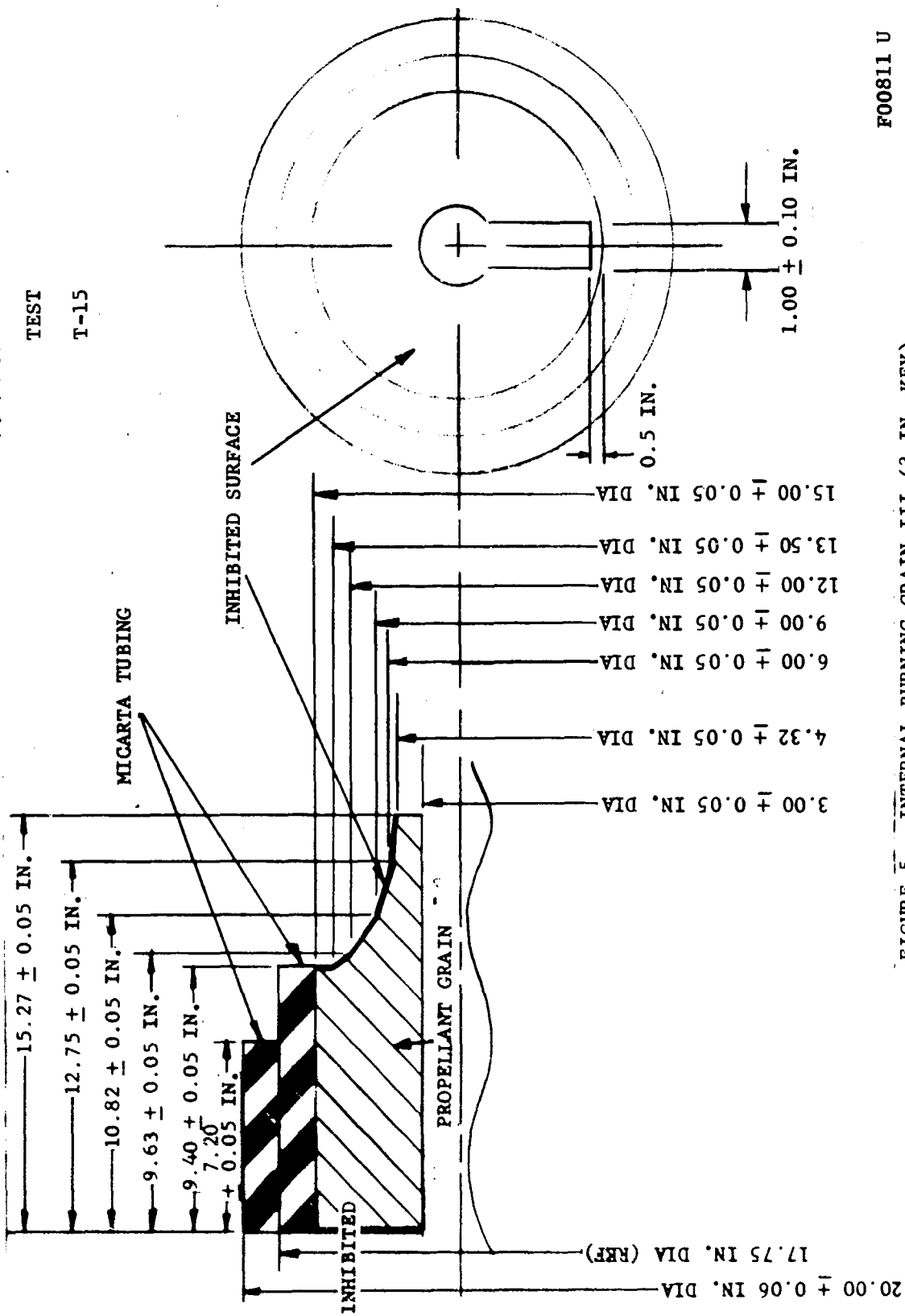
FIGURE 5. INTERNAL BURNING GRAIN III (3 IN. KEY)

TEST
T-15

INHIBITED SURFACE

MICARTA TUBING

PROPELLANT GRAIN

INHIBITED

F00811 U

15.00 ± 0.05 IN. DIA
13.50 ± 0.05 IN. DIA
12.00 ± 0.05 IN. DIA
9.00 ± 0.05 IN. DIA
6.00 ± 0.05 IN. DIA
4.32 ± 0.05 IN. DIA
3.00 ± 0.05 IN. DIA

1.00 ± 0.10 IN.

0.5 IN.

15.27 ± 0.05 IN.
12.75 ± 0.05 IN.
10.82 ± 0.05 IN.
9.63 ± 0.05 IN.
9.40 + 0.05 IN.
7.20 + 0.05 IN.

17.75 IN. DIA (REF)
20.00 ± 0.06 IN. DIA

-170-
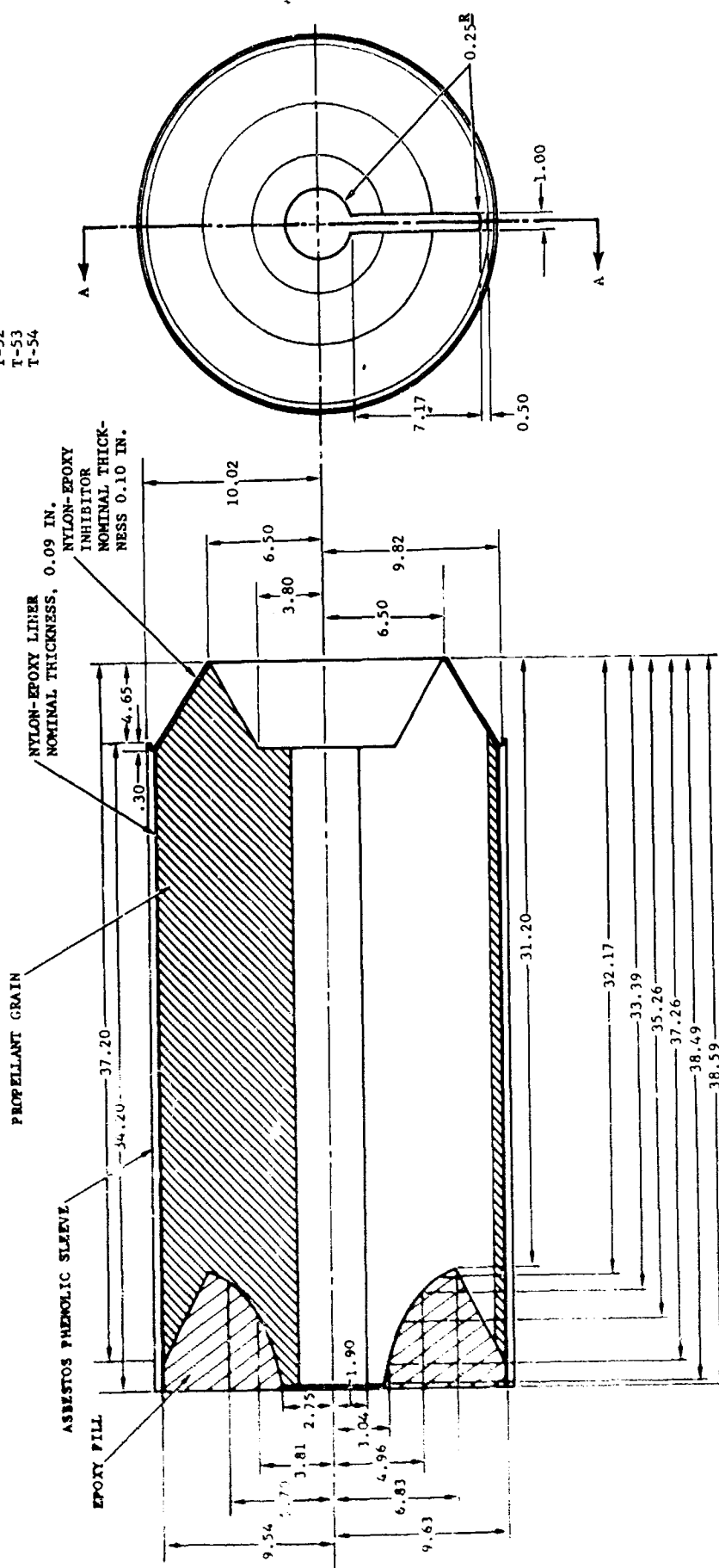
FIGURE 6. 500 POUND INTERNAL BURNING GRAIN

TEST
T-51
T-52
T-53
T-54

NYLON-EPOXY LINER
NOMINAL THICKNESS, 0.09 IN.

NYLON-EPOXY
INHIBITOR
NOMINAL THICK-
NESS 0.10 IN.

PROPELLANT GRAIN

ASBESTOS PHENOLIC SLEEVE

EPOXY FILL

0.25R
1.00
7.17
0.50
10.02
6.50
3.80
9.82
6.50
4.65
.30

37.20
34.20
31.20
32.17
33.39
35.26
37.26
38.49
38.59

1.90
2.75
3.81
1.04
4.96
4.83
6.63
9.54
9.63

-171-

NOZZLE
(T-23)

ASBESTOS
PHENOLIC
AFT CLOSURE
INSULATION

ASBESTOS
PHENOLIC
LINER

INHIBITOR

SEALED
ASBESTOS
PHENOLIC
INSULATION
DISK

SEALED
ALUMINUM
BEARING PLATE

WOOD FILLER
BLOCKS

PROPELLANT
GRAIN

TEST

T-21
T-22
T-23
T-24

F08060 U

FIGURE 7. MOTOR CASE DESIGN - CLOSE END BURNING GRAINS
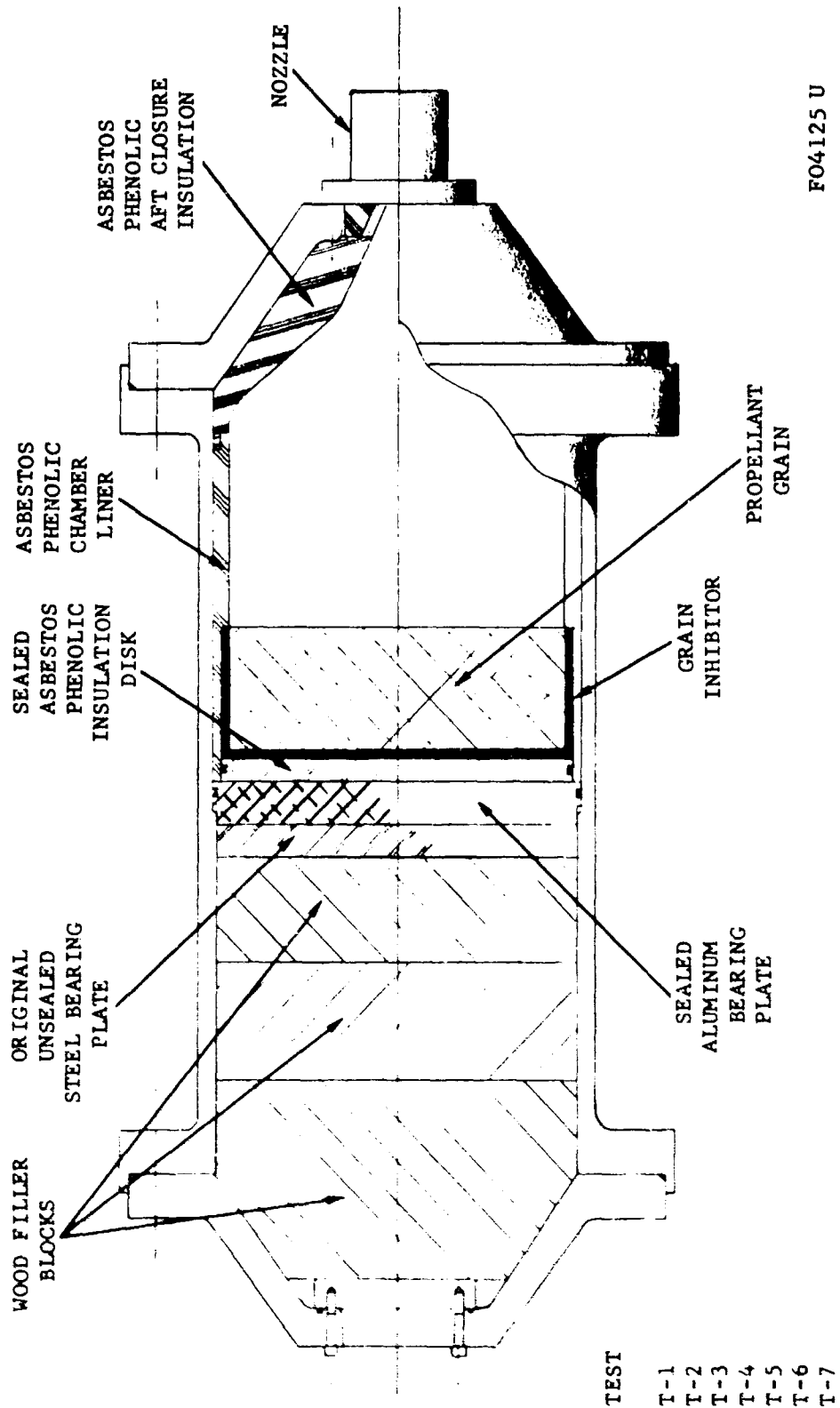
FIGURE 8. MODIFIED MOTOR CASE DESIGN - REMOTE END BURNING GRAINS

NOZZLE

ASBESTOS PHENOLIC AFT CLOSURE INSULATION

ASBESTOS PHENOLIC CHAMBER LINER

SEALED ASBESTOS PHENOLIC INSULATION DISK

PROPELLANT GRAIN

GRAIN INHIBITOR

WOOD FILLER BLOCKS

ORIGINAL UNSEALED STEEL BEARING PLATE

SEALED ALUMINUM BEARING PLATE

FO4125 U

TEST

T-1
T-2
T-3
T-4
T-5
T-6
T-7

-173-

ASBESTOS
PHENOLIC
AFT CLOSURE
INSULATION

NOZZLE

MICARTA
TUBING

GRAIN INHIBITOR

SEALED
ASBESTOS
PHENOLIC
INSULATION
DISK

7 INCH C.P.
PROPELLANT
GRAIN

SEALED
ALUMINUM
BEARING PLATE

WOOD FILLER
BLOCKS

ORIGINAL
UNSEALED
STEEL
BEARING
PLATE

F04126 U

TEST

T-9
T-11
T-14
T-16
T-17
T-18
T-19
T-20
T-25

FIGURE 9. MOTOR CASE DESIGN - INTERNAL BURNING GRAINS TYPE I

-174-

GRAIN INHIBITOR

ASBESTOS PHENOLIC AFT CLOSURE INSULATION

NOZZLE T-10

SEALED PHENOLIC ASBESTOS INSULATION DISK

MICARTA TUBING

SEALED ALUMINUM BEARING PLATE

WOOD FILLER BLOCKS

7 INCH KEY PROPELLANT GRAIN

F04127 U

TEST

T-8
T-10
T-12
T-13
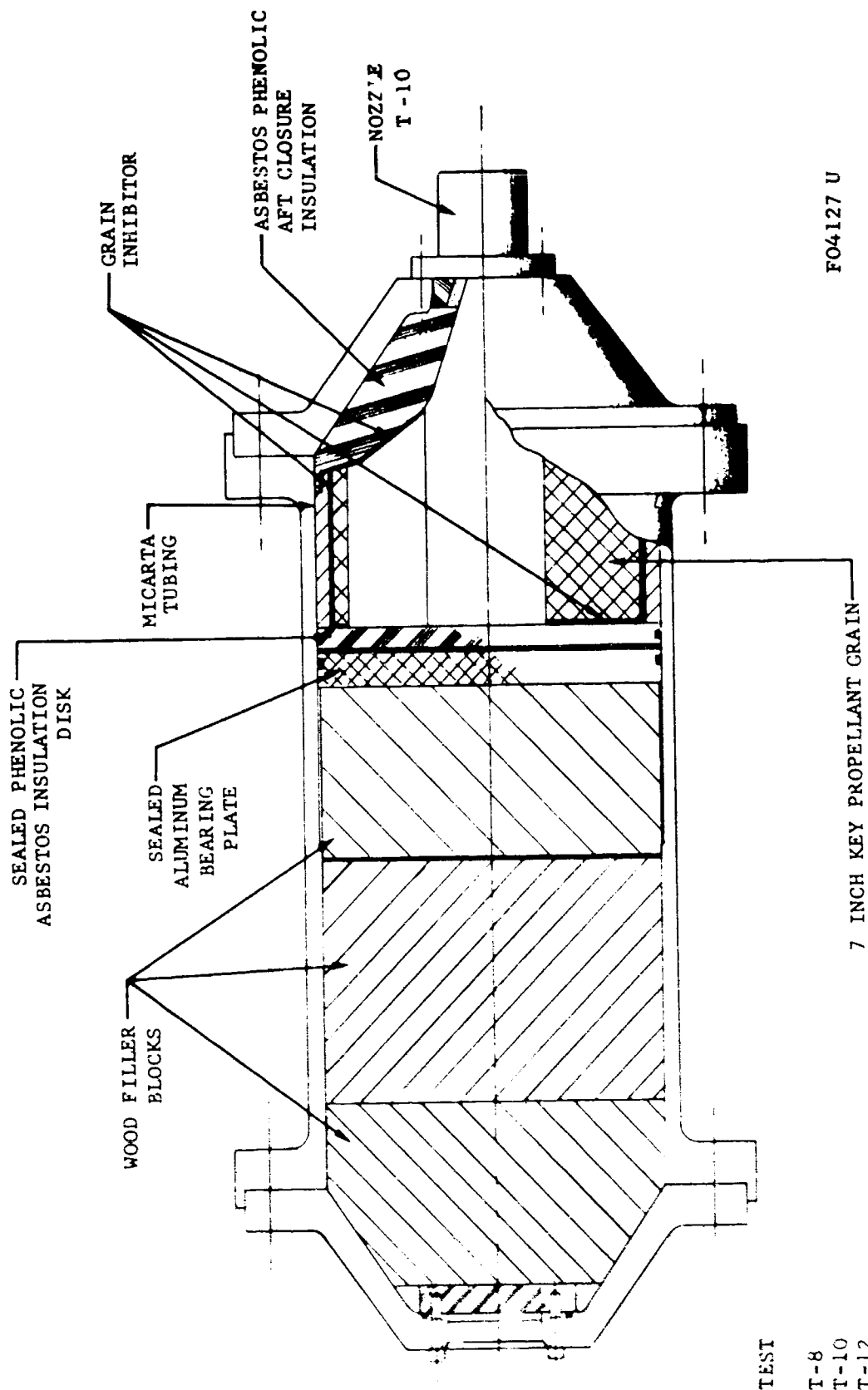
FIGURE 10   MOTOR CASE DESIGN - INTERNAL BURNING GRAINS TYPE II

-175-

GRAIN INHIBITOR

ASBESTOS PHENOLIC AFT CLOSURE INSULATION

NOZZLE

SEALED ASBESTOS PHENOLIC INSULATION DISK

MICARTA TUBING

SEALED ALUMINUM BEARING PLATE

WOOD FILLER BLOCKS

3 INCH KEY PROPELLANT GRAIN

TEST T-15

f04128
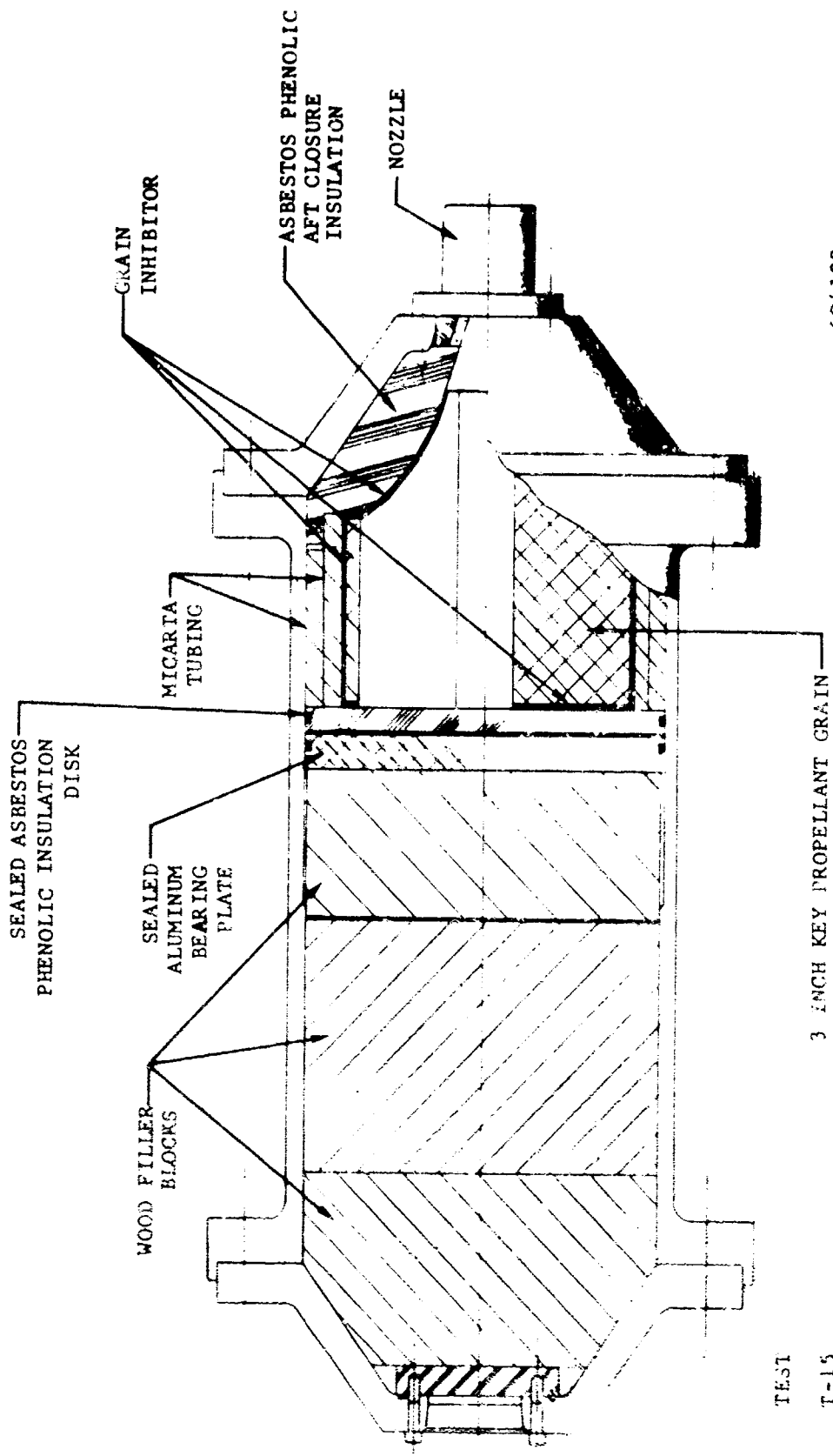
FIGURE 11. MOTOR CASE DESIGN - INTERNAL BURNING GRAIN TYPE III

ASBESTOS PHENOLIC AFT CLOSURE INSULATION

NOZZLE (T-51)

ASBESTOS PHENOLIC LINER (2 SECTIONS)

GRAIN INHIBITOR

PROPELLANT GRAIN

SEALED ASBESTOS PHENOLIC INSULATION DISK

ALUMINUM SPACER DISKS

WOOD FILLER BLOCK
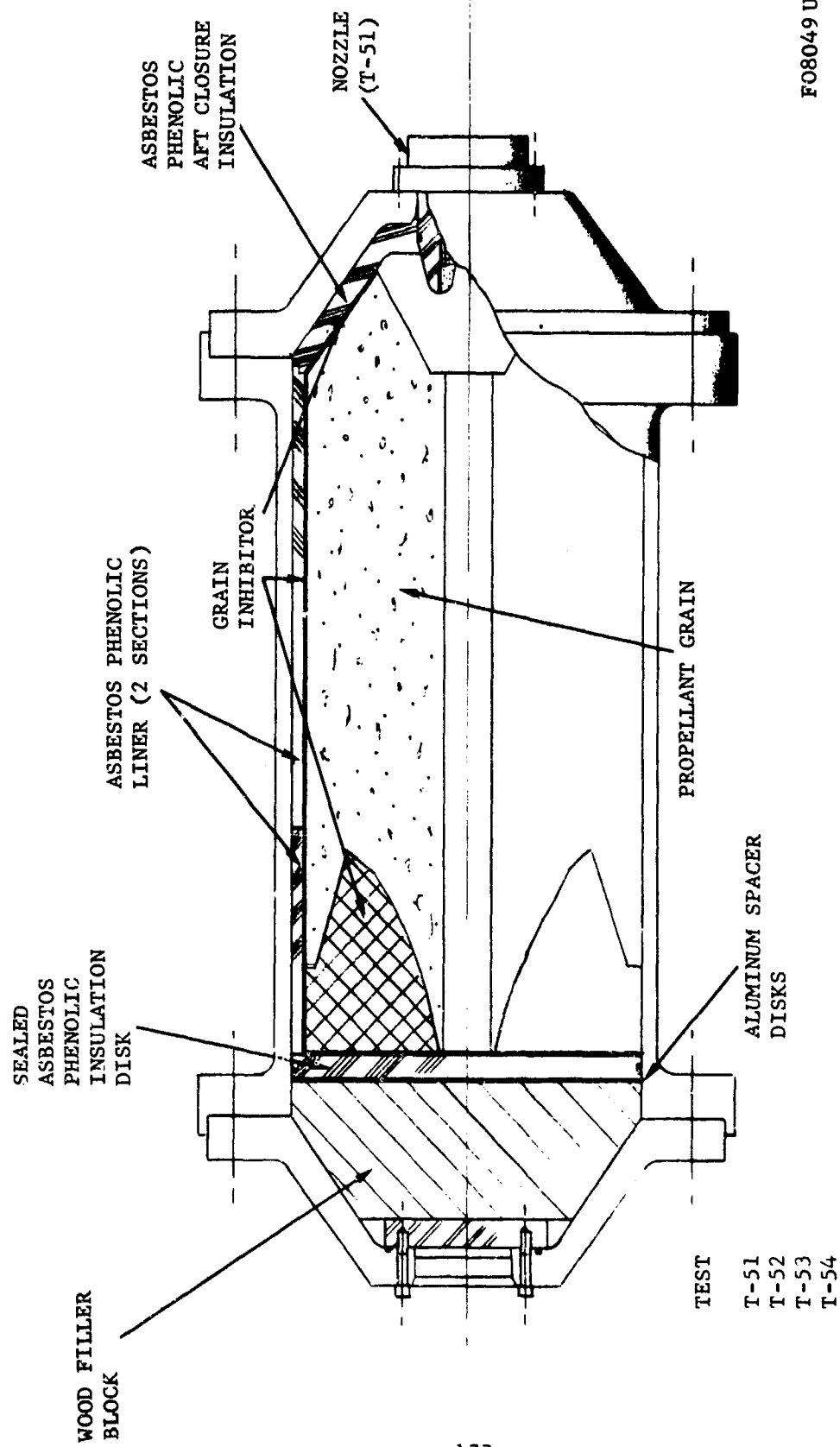
TEST
T-51
T-52
T-53
T-54

F08049 U

FIGURE 12. MOTOR CASE DESIGN - DEVELOPMENT TESTS

-177-
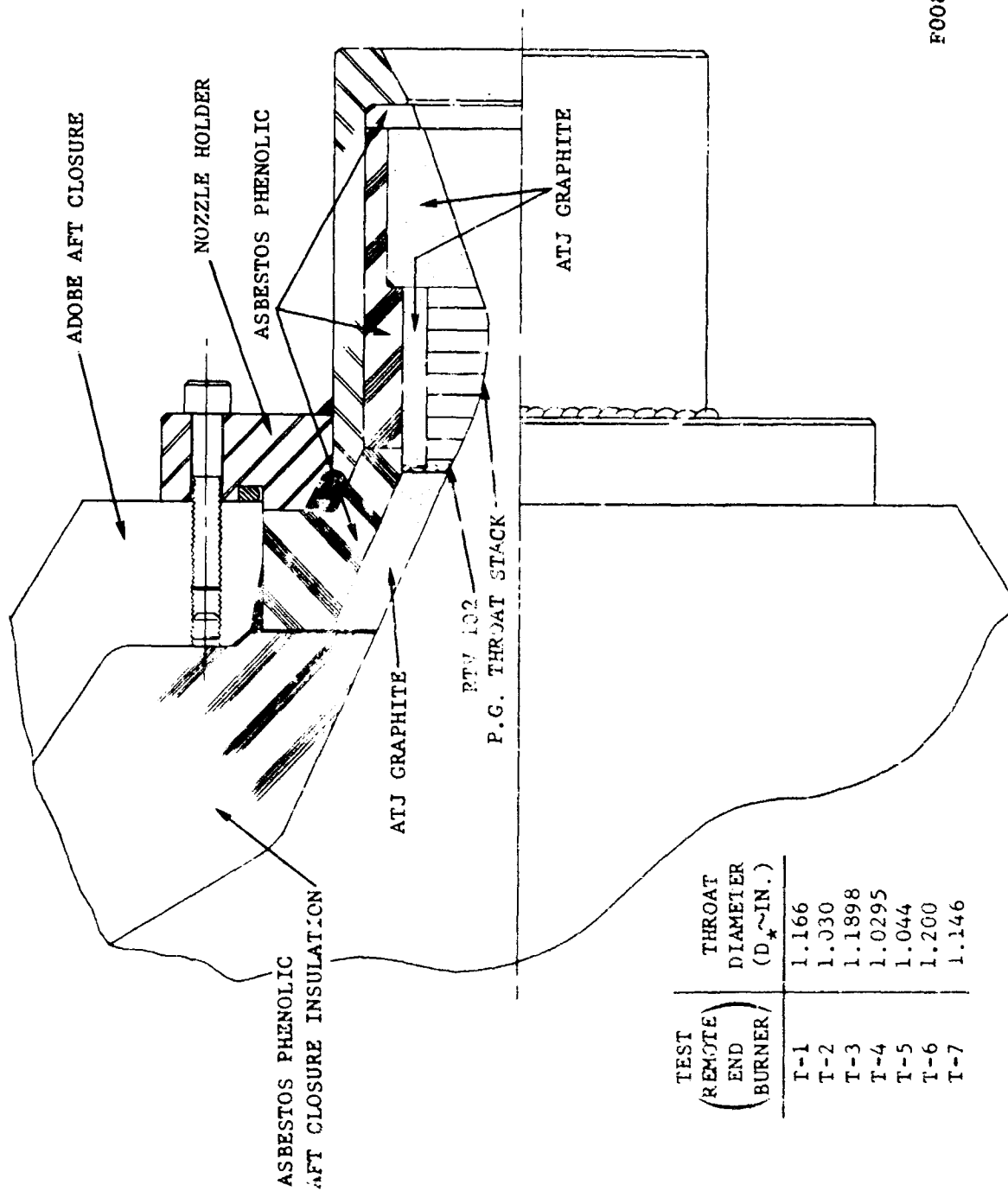
FIGURE 13. NOZZLE DESIGN FOR END BURNING GRAINS

ADOBE AFT CLOSURE

NOZZLE HOLDER

ASBESTOS PHENOLIC

ATJ GRAPHITE

ATJ GRAPHITE

P.G. THROAT STACK

PTV 102

ASBESTOS PHENOLIC
AFT CLOSURE INSULATION

TEST (REMOTE) END BURNER	THROAT DIAMETER $(D_* \sim IN.)$
T-1	1.166
T-2	1.030
T-3	1.1898
T-4	1.0295
T-5	1.044
T-6	1.200
T-7	1.146

F00813 ½

-178-

FIGURE 14. NOZZLE DESIGN (CONVENTIONAL) FOR INTERNAL BURNING GRAINS

ADOBE AFT CLOSURE

NOZZLE HOLDER

ASBESTOS PHENOLIC

ATJ GRAPHITE

ATJ GRAPHITE

PROPELLANT GRAIN

ASBESTOS PHENOLIC
AFT CLOSURE INSULATION

ATJ GRAPHITE

P.G. THROAT STACK

RTV 102

F00814 U

TEST	THROAT DIAMETER D_t ~IN.
T-8	1.213
T-9	1.211
T-10	1.233
T-11	1.080
T-14	1.218
T-15	1.180

-179-

FIGURE 15. NOZZLE DESIGN (SUBMERGED) FOR INTERNAL BURNING GRAINS

F00816 U

TEST	THROAT DIAMETER $D_\star \sim$ IN.
T-12	1.233

ADOBE AFT CLOSURE

SUBMERGED
NOZZLE HOLDER

ASBESTOS PHENOLIC

ATJ GRAPHITE

ASBESTOS PHENOLIC
AFT-CLOSURE INSULATION

PROPELLANT GRAIN

ATJ GRAPHITE

P.G.
THROAT STACK

RTV 102

F00815 U

TEST	THROAT DIAMETER $D_*\sim$IN.
T-13	1.238
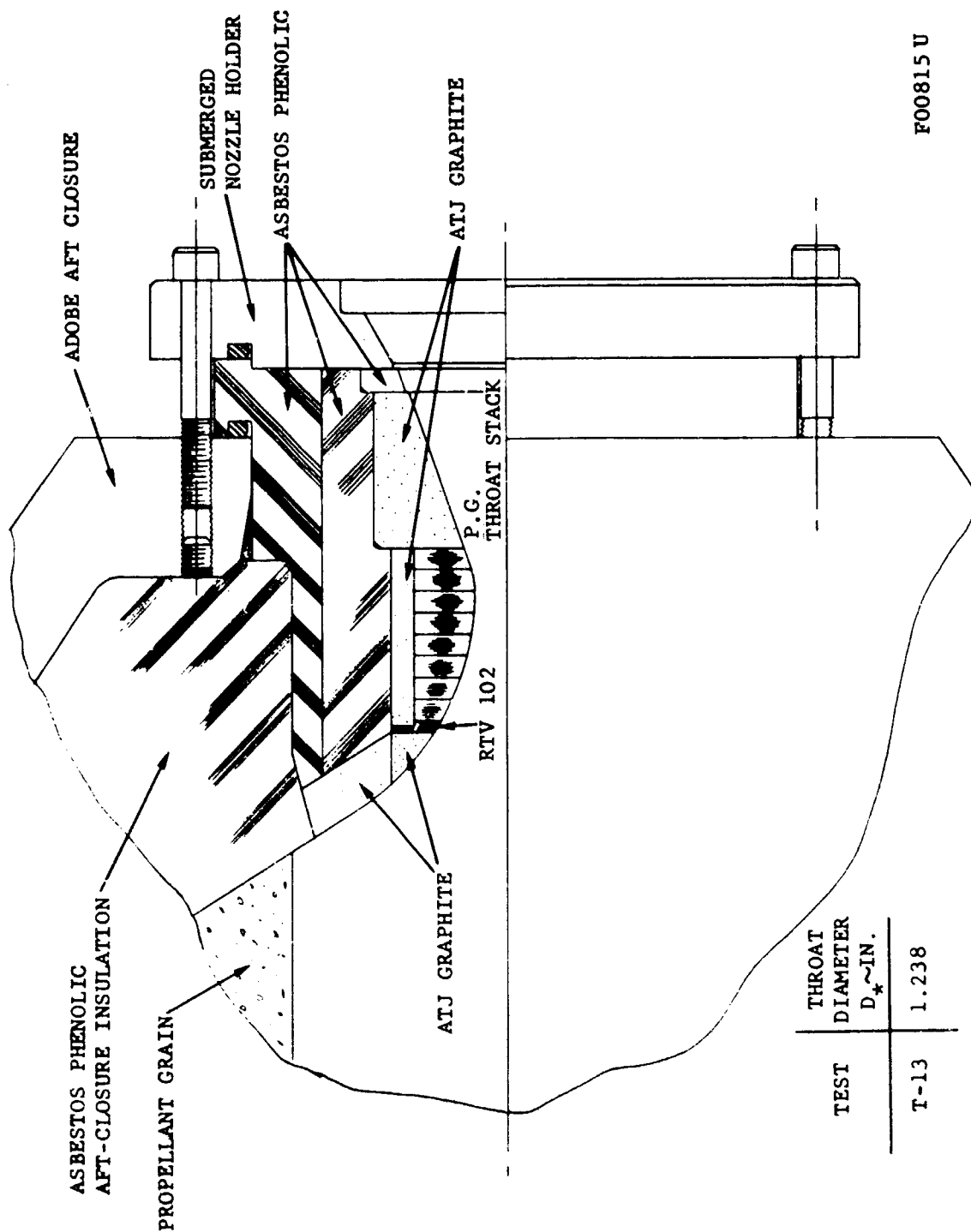
FIGURE 16. NOZZLE DESIGN (STEEP INLET) FOR INTERNAL BURNING GRAINS

-181-

TEST	THROAT DIAMETER $(D_* \sim IN.)$
T-16	1.214

ASBESTOS PHENOLIC

POLYCRYSTALLINE GRAPHITE

DUAL ASBESTOS PHENOLIC AFT CLOSURE INSULATION

ARC-CAST, ROLLED AND EXTRUDED TUNGSTEN THROAT INSERT

RTV102

PYROLYTIC GRAPHITE WASHER

POLYCRYSTALLINE GRAPHITE

TYPE I GRAIN

F04129 U
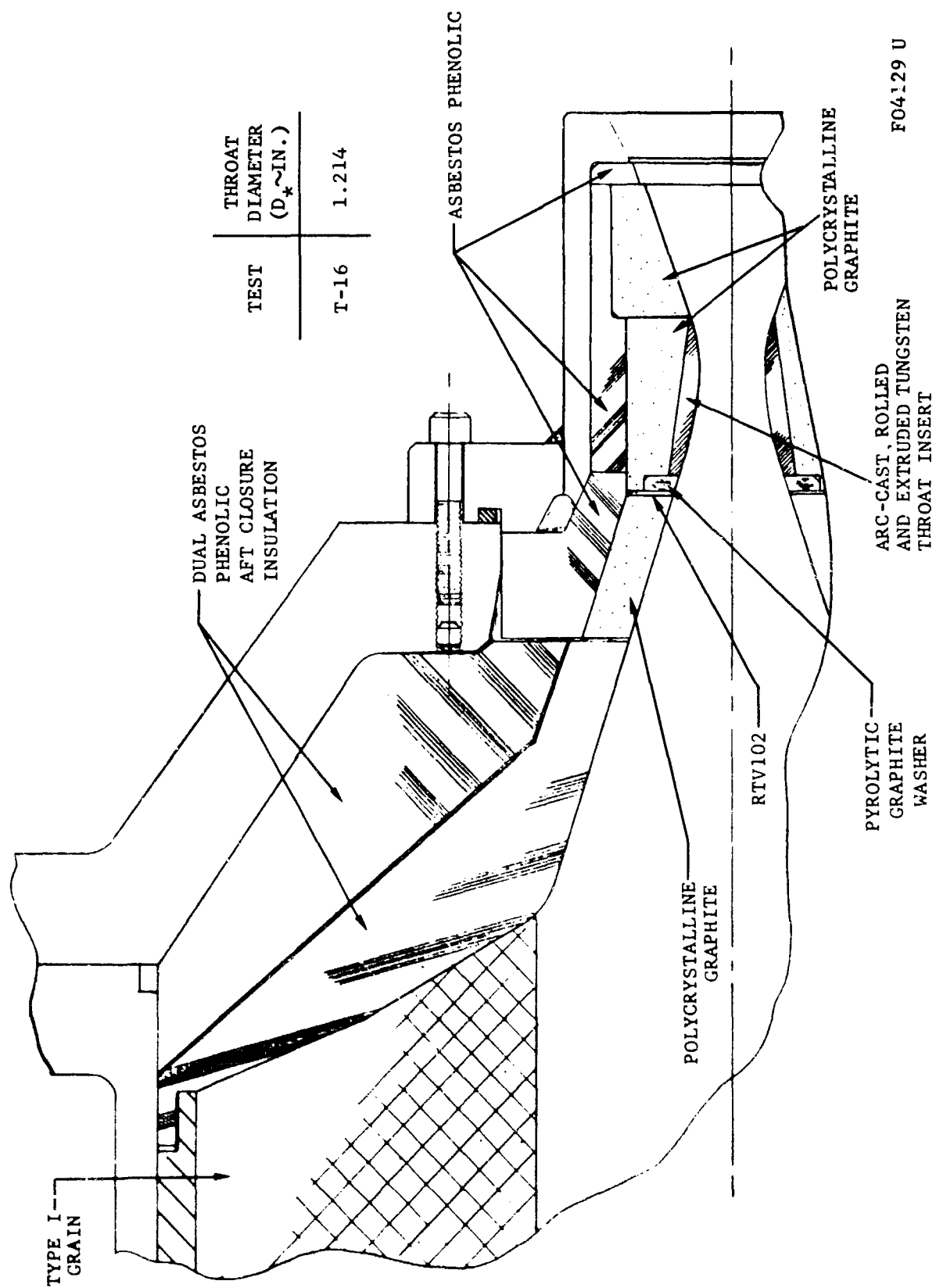
FIGURE 17. NOZZLE DESIGN FOR TEST T-16

DUAL ASBESTOS PHENOLIC AFT CLOSURE INSULATION

TYPE I GRAIN

CARBON CLOTH PHENOLIC

ASBESTOS PHENOLIC

POLYCRYSTALLINE GRAPHITE

PYROLYTIC GRAPHITE WASHER

ARC-CAST, ROLLED AND EXTRUDED TUNGSTEN THROAT INSERT

TEST	THROAT DIAMETER $(D_* \sim IN.)$
T-17	1.214
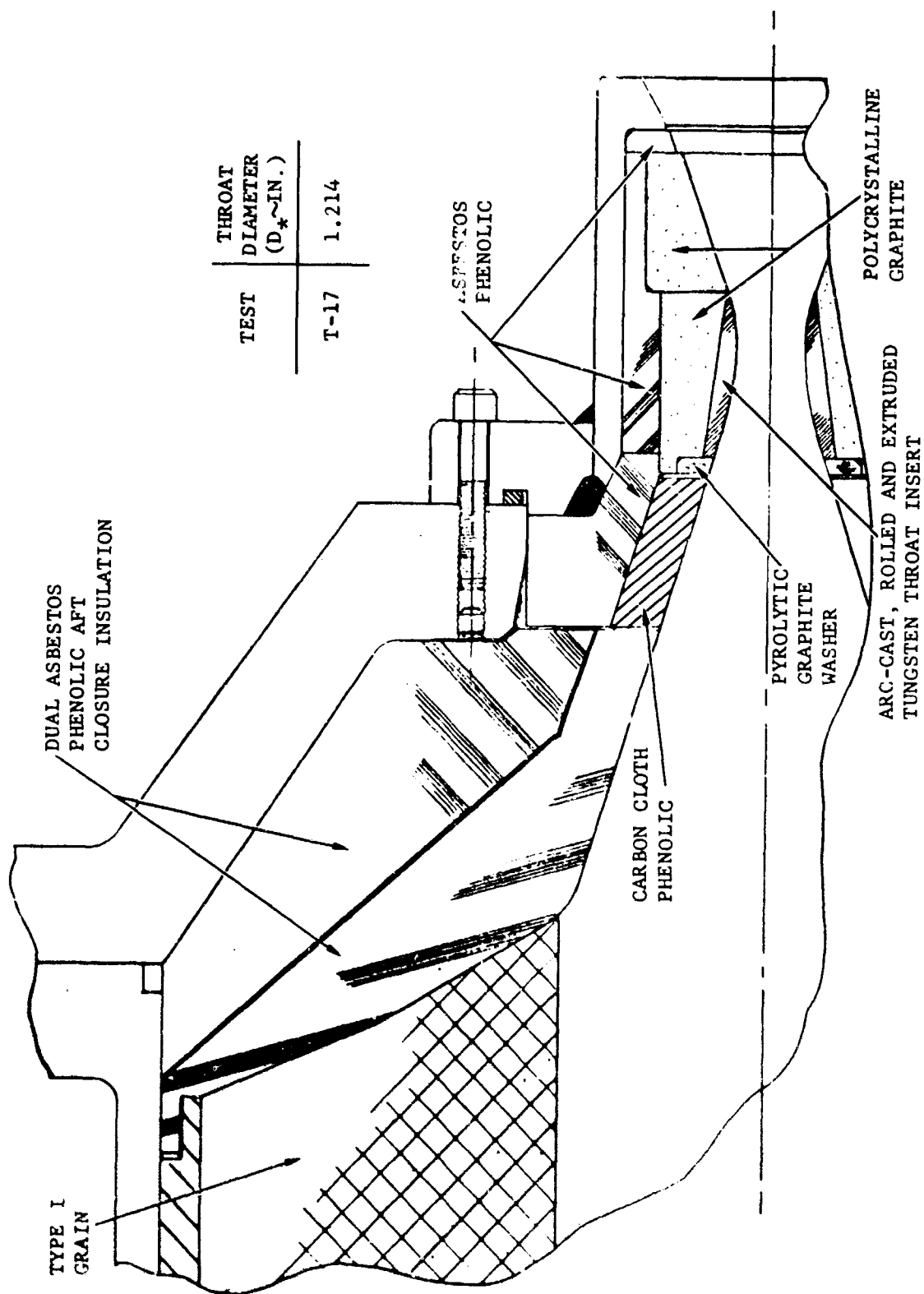
FO4130 U

FIGURE 18.   NOZZLE DESIGN FOR TEST T-17

-183-

DUAL ASBESTOS PHENOLIC AFT CLOSURE INSULATION

ASBESTOS PHENOLIC

POLYCRYSTALLINE GRAPHITE

ARC-CAST, ROLLED AND EXTRUDED TUNGSTEN THROAT INSERT

F04131U

TYPE I GRAIN

CARBON CLOTH PHENOLIC

POLYCRYSTALLINE GRAPHITE

PYROLYTIC GRAPHITE WASHER

RTV-102
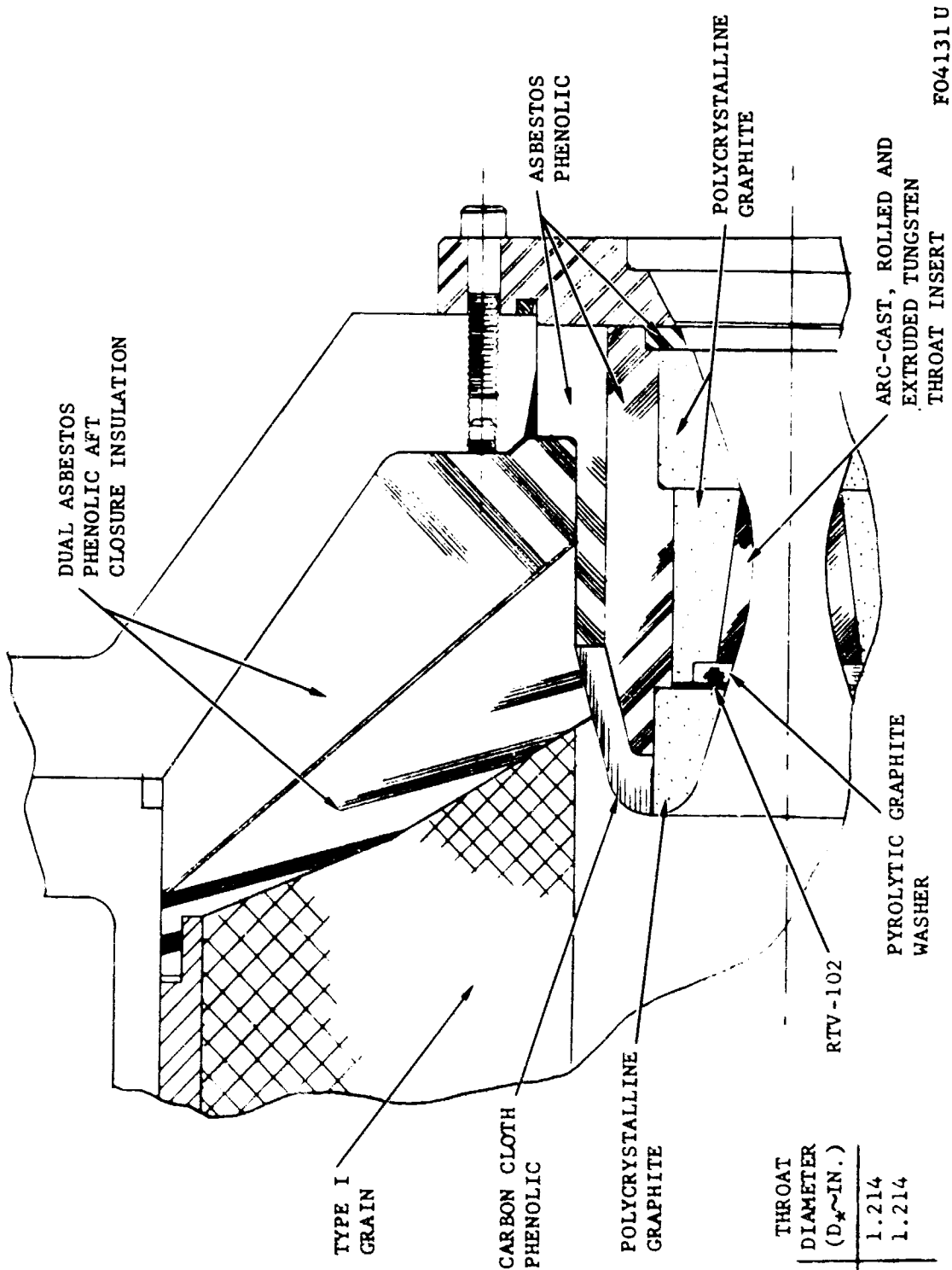
FIGURE 19. NOZZLE DESIGN FOR TESTS T-18 AND T-19

TEST	THROAT DIAMETER ($D_*\sim$IN.)
T-18	1.214
T-19	1.214

TEST	THROAT DIAMETER $(D_* \sim IN.)$
T-20	1.214

DUAL ASBESTOS PHENOLIC AFT CLOSURE INSULATION

ASBESTOS PHENOLIC

POLYCRYSTALLINE GRAPHITE

CARBON CLOTH PHENOLIC

RTV-102

EDGE-GRAIN PYROLYTIC GRAPHITE THROAT STACK

TYPE I GRAIN
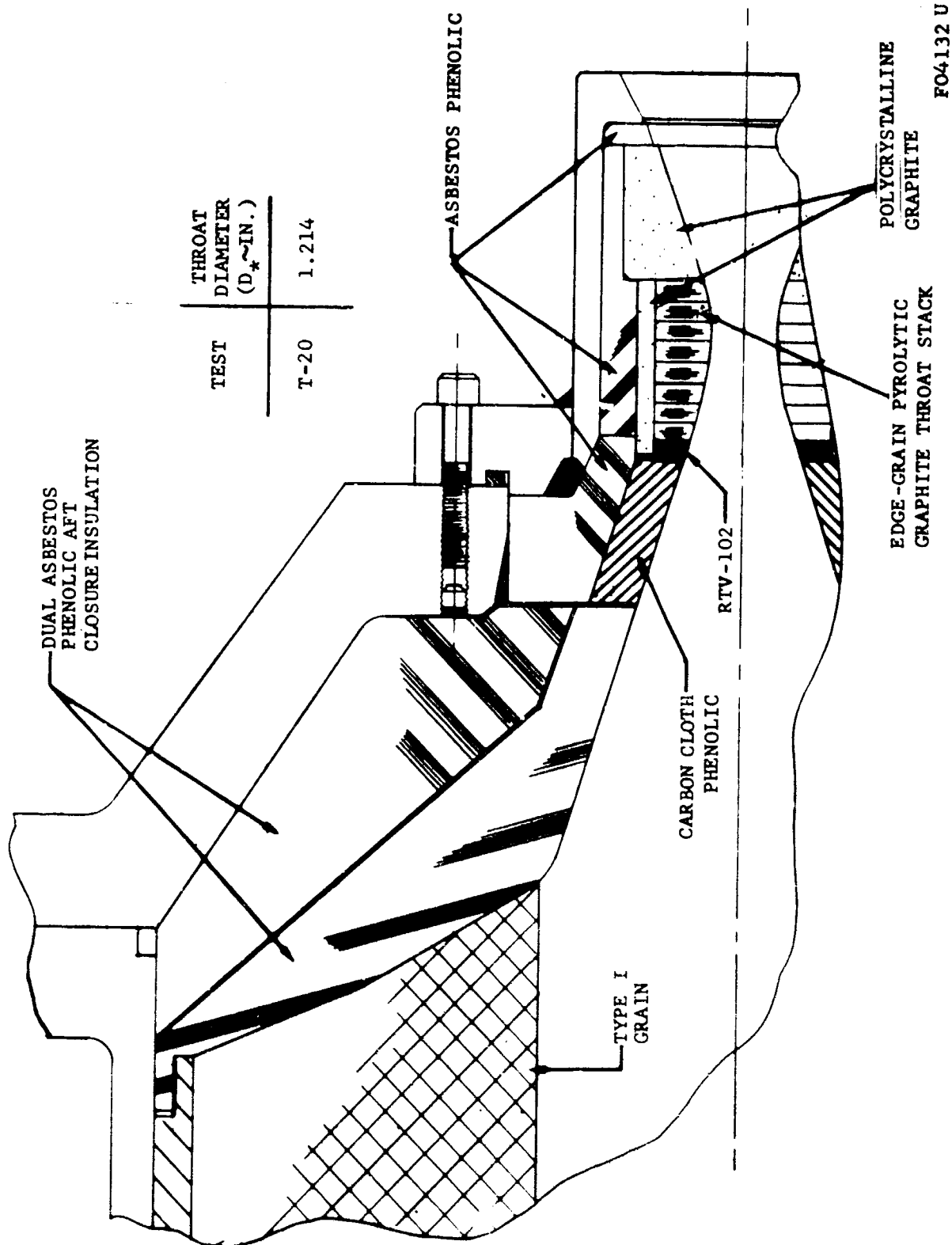
FO4132 U

FIGURE 20. NOZZLE DESIGN FOR TEST T-20

-185-
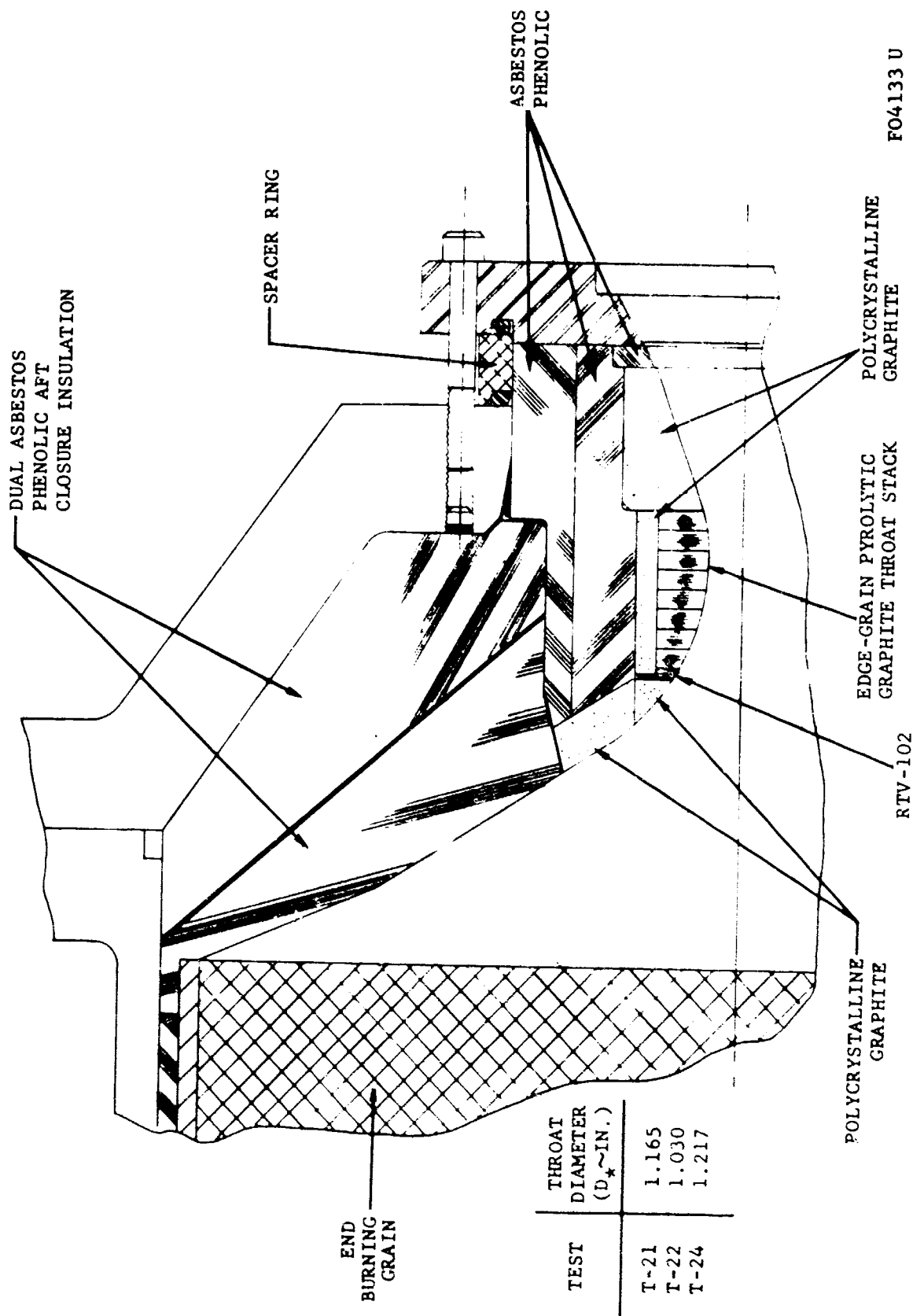
FIGURE 21. NOZZLE DESIGN FOR TESTS T-21, T-22 AND T-24

F04133 U

TEST	THROAT DIAMETER ($D_\star \sim$ IN.)
T-21	1.165
T-22	1.030
T-24	1.217

ASBESTOS PHENOLIC

ASBESTOS PHENOLIC

ATJ GRAPHITE

PYROLYTIC GRAPHITE

CARBON CLOTH PHENOLIC

ATJ GRAPHITE

PROPELLANT GRAIN

F08061U

TEST	THROAT DIAMETER $(D_\star \sim IN.)$
T-23	1.179
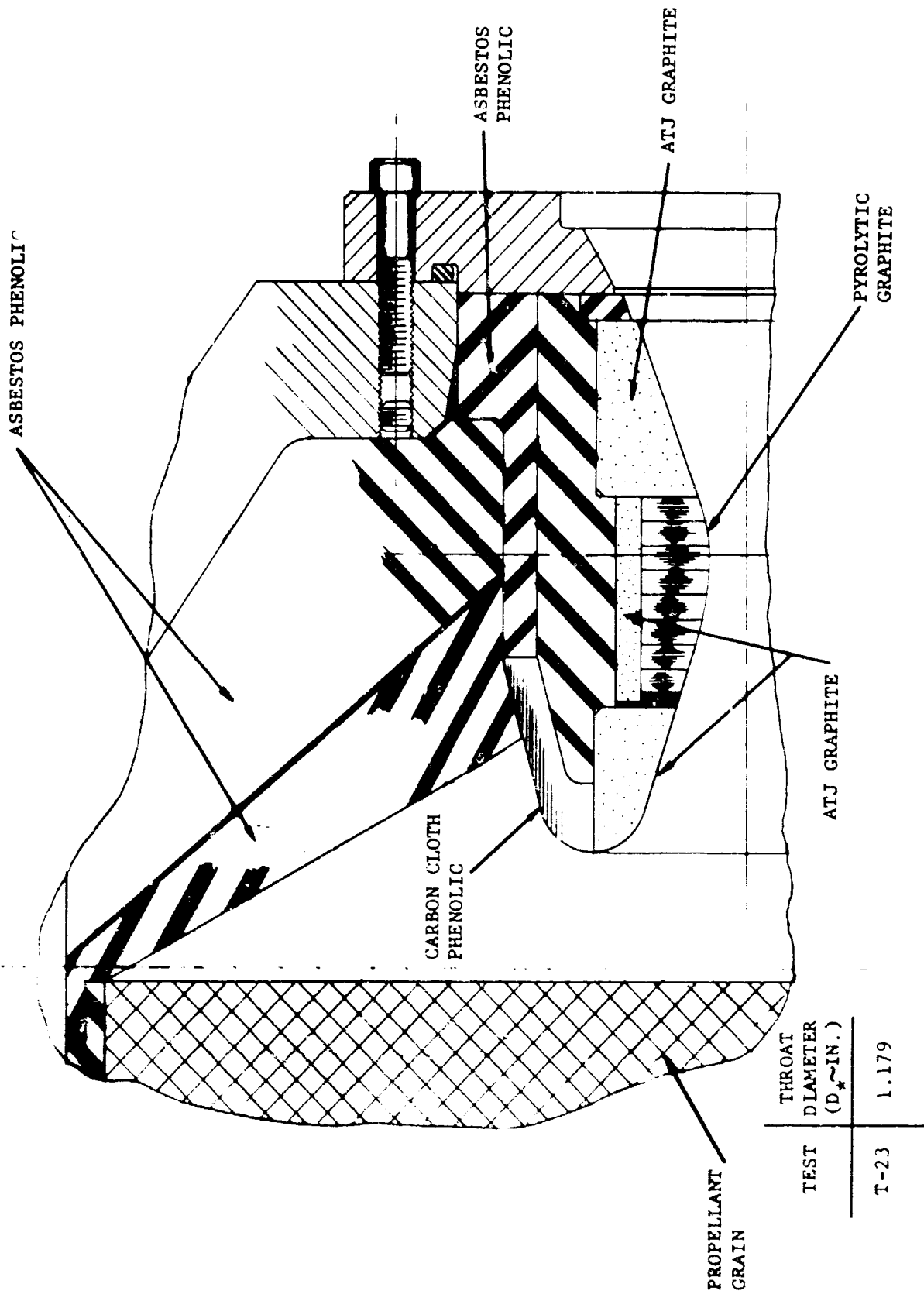
FIGURE 22. NOZZLE DESIGN FOR TEST T-23

STEEL

ATJ GRAPHITE

ASBESTOS PHENOLIC

ASBESTOS PHENOLIC

PYROLYTIC GRAPHITE

RTV SILICONE

ATJ GRAPHITE

PROPELLANT GRAIN
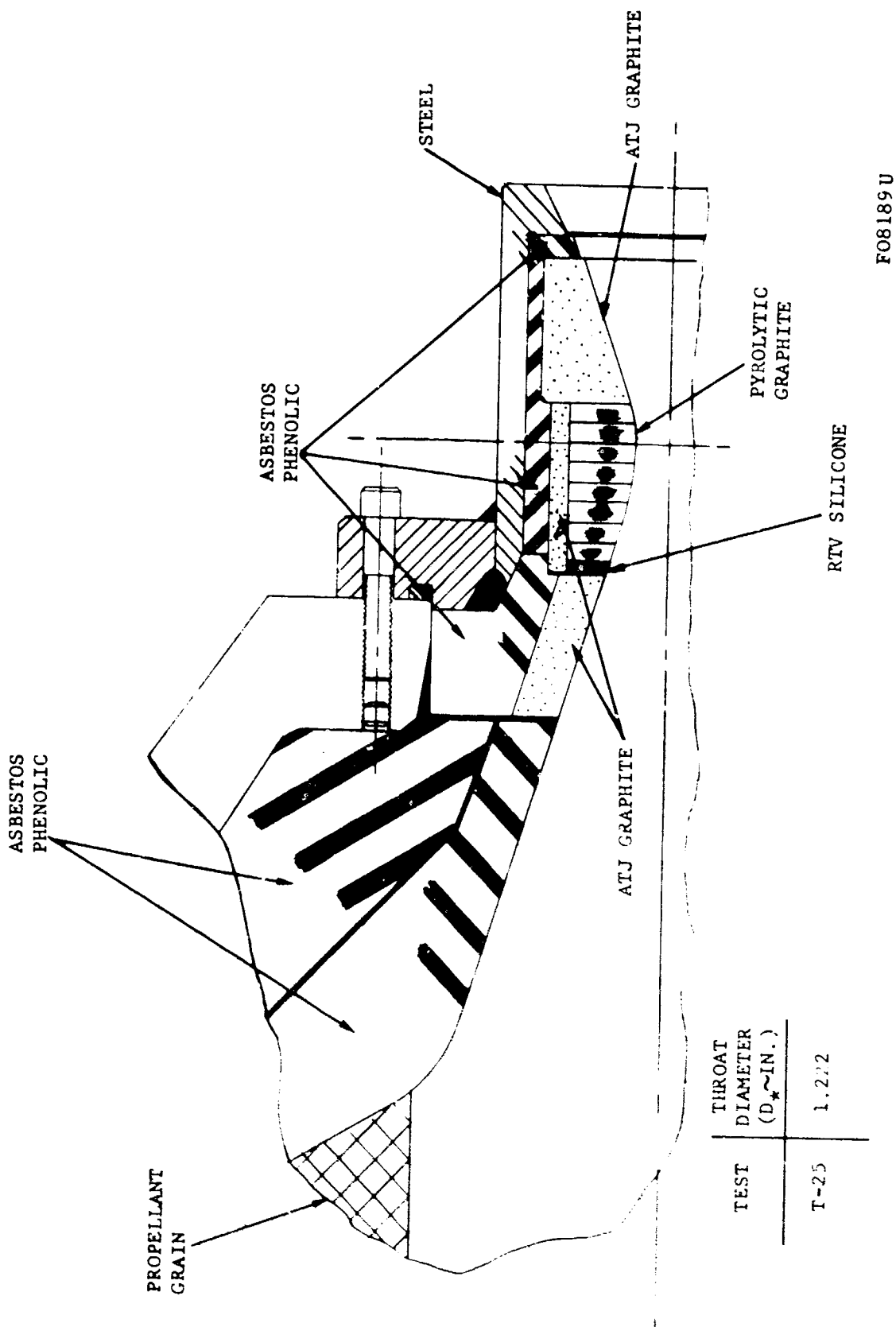
F08189 U

FIGURE 23. NOZZLE DESIGN FOR TEST T-25

TEST	THROAT DIAMETER $(D_\star \sim IN.)$
T-25	1.2'2

-188-
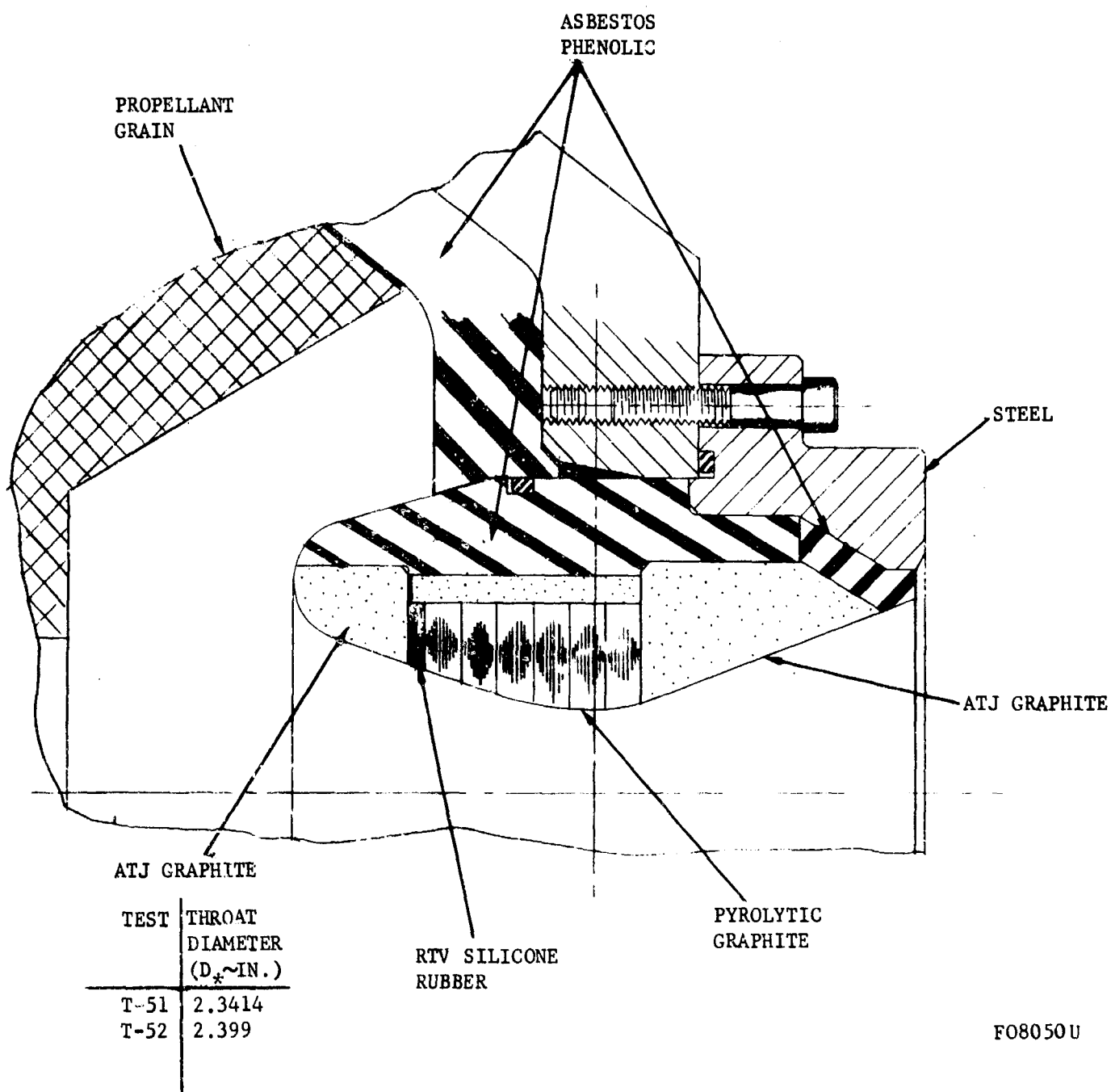
FIGURE 24. NOZZLE DESIGN FOR TESTS T-51 AND T-52

TEST	THROAT DIAMETER $(D_*\sim\text{IN.})$
T-51	2.3414
T-52	2.399

FO8050U
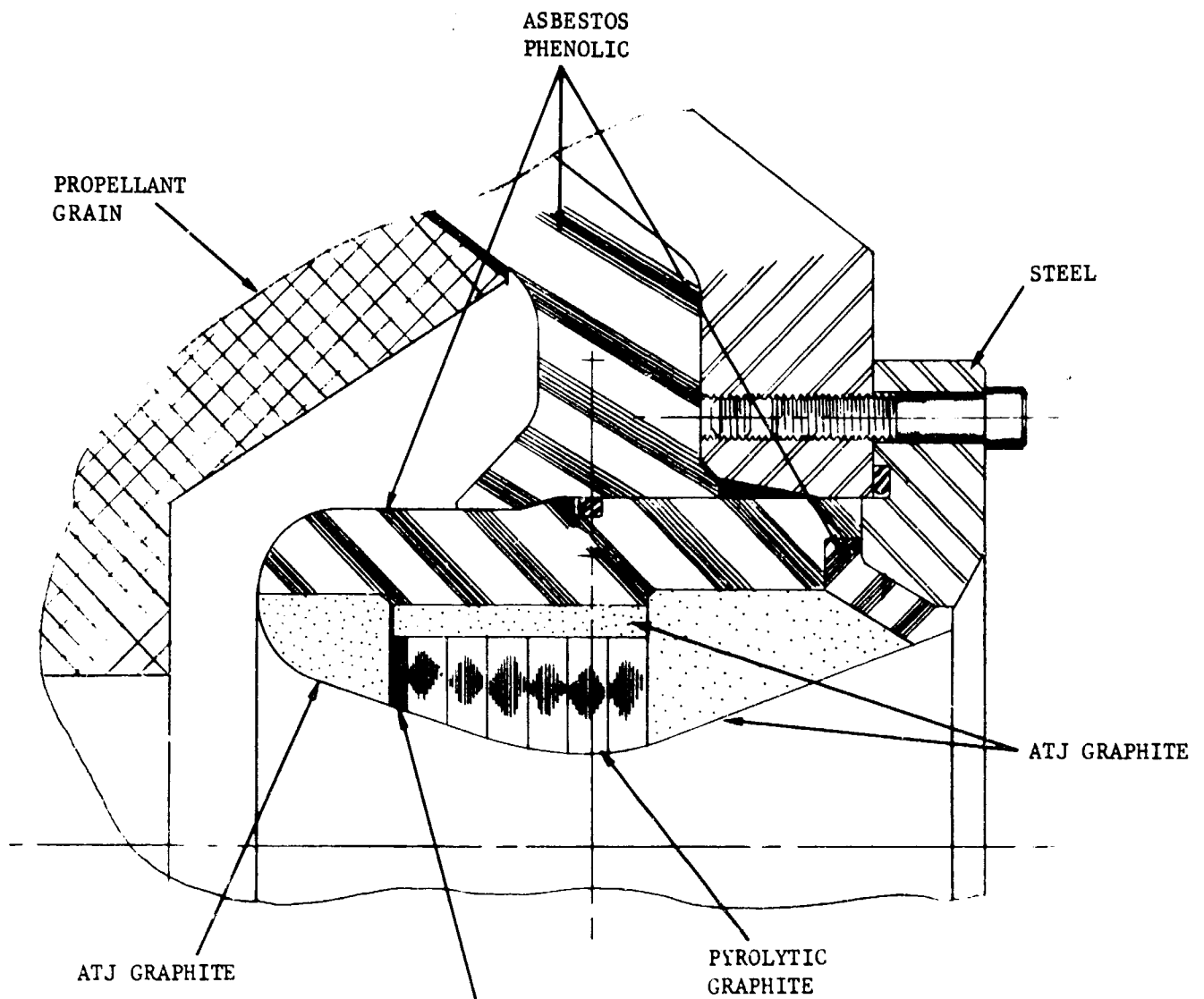
TEST	THROAT DIAMETER (D*- IN.)
T-53	2.340

F08200U

FIGURE 25.   NOZZLE DESIGN FOR TEST T-53
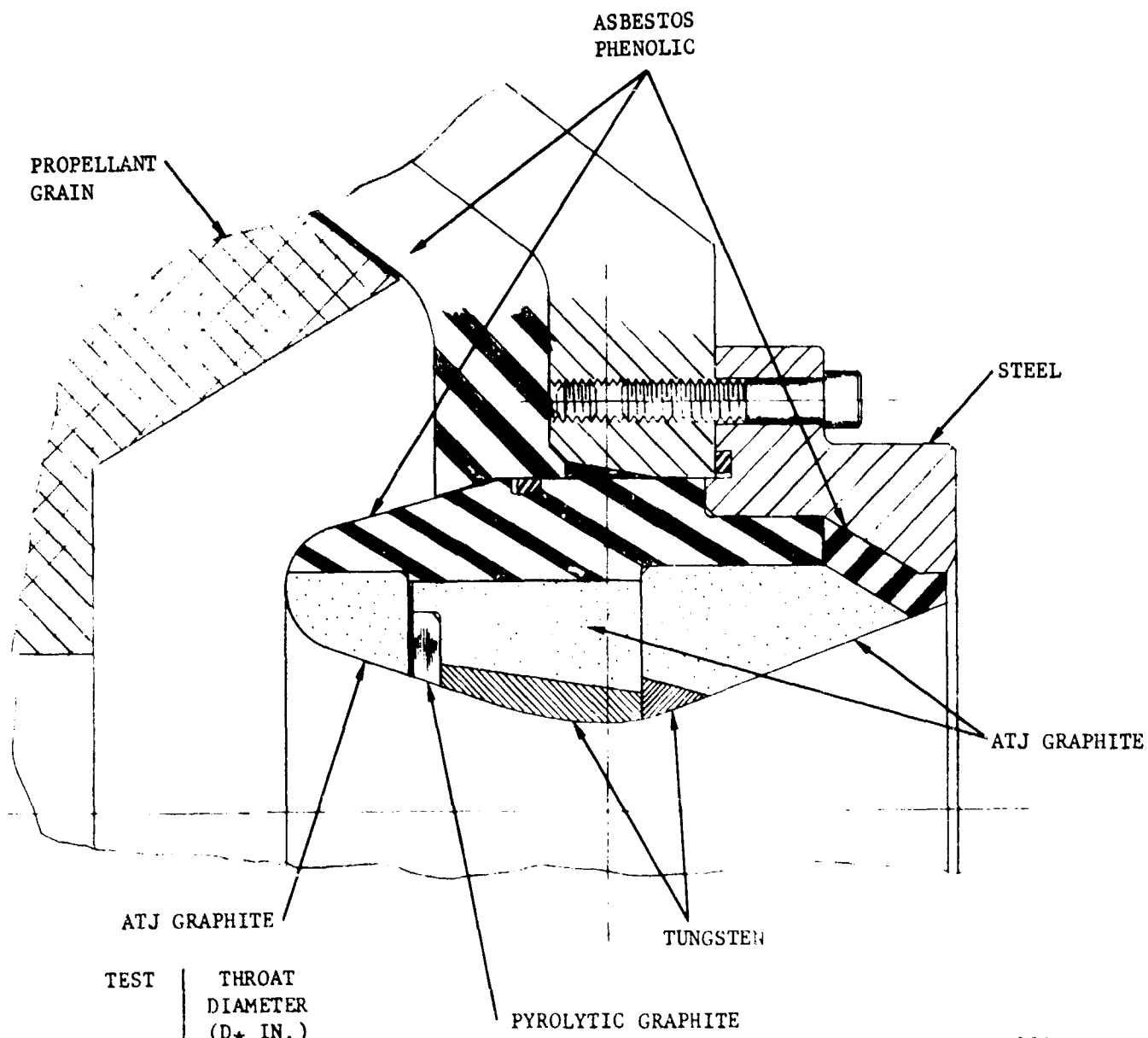
FIGURE 26. NOZZLE DESIGN FOR TEST T-54

TEST	THROAT DIAMETER (D_* IN.)
T-54	2.340

F08201U

-191-
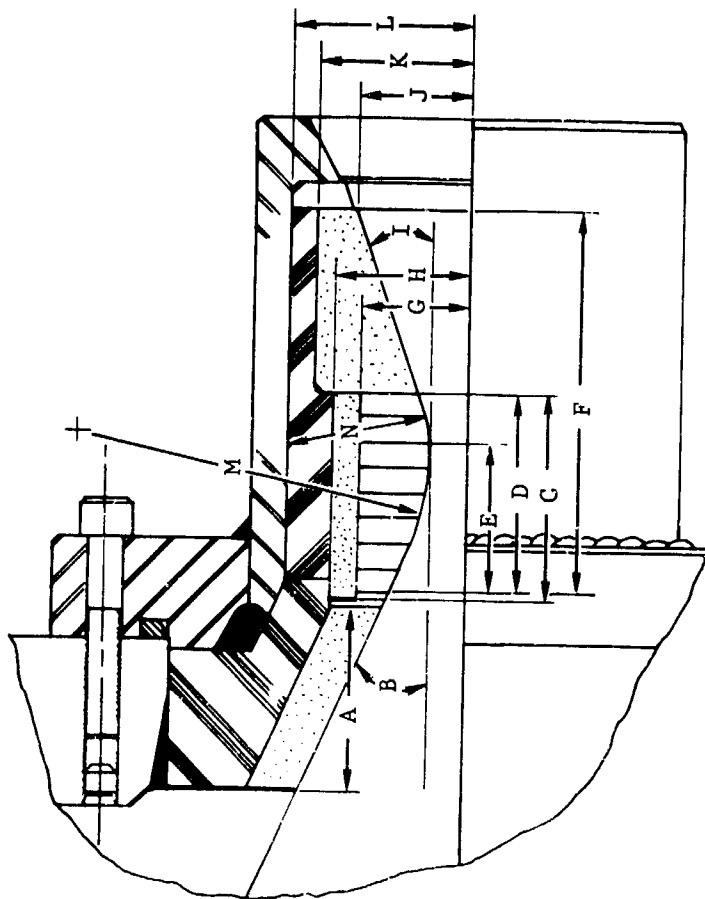
FIGURE 27. DIMENSION CODE FOR T-1 THROUGH T-11,
T-14, T-15, T-20 AND T-25 NOZZLES
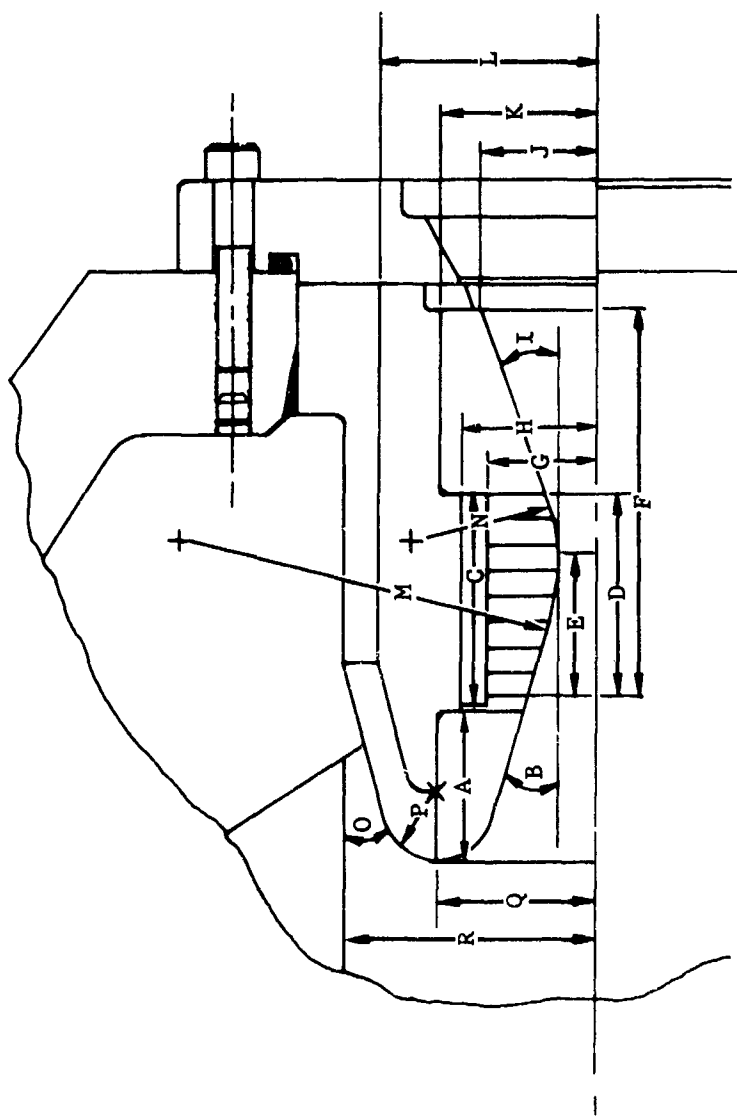
F11024 U

FIGURE 28. DIMENSION CODE FOR T-12 AND T-23 NOZZLES

F11025 U
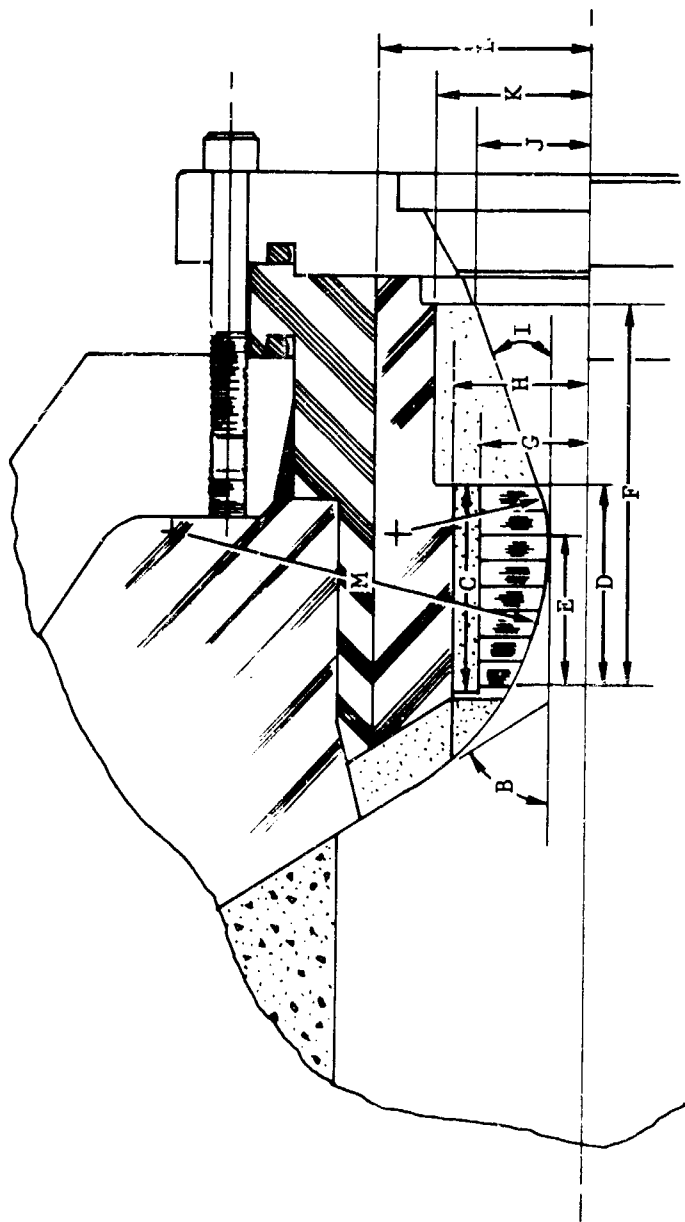
F11026 U

FIGURE 29. DIMENSION CODE FOR T-13, T-21, T-22 AND T-24 NOZZLES
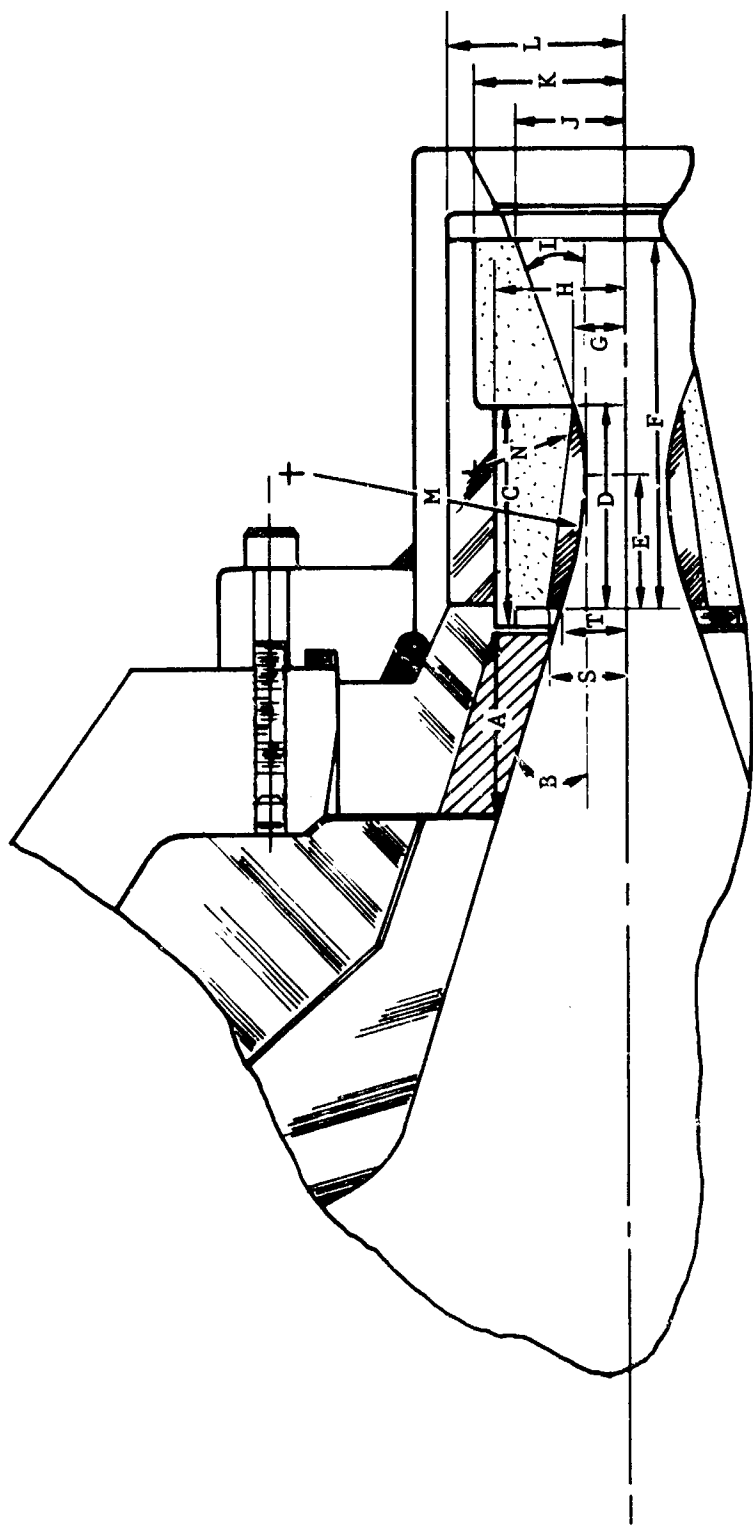
FIGURE 30. DIMENSION CODE FOR T-16 AND T-17 NOZZLES

F11027 U
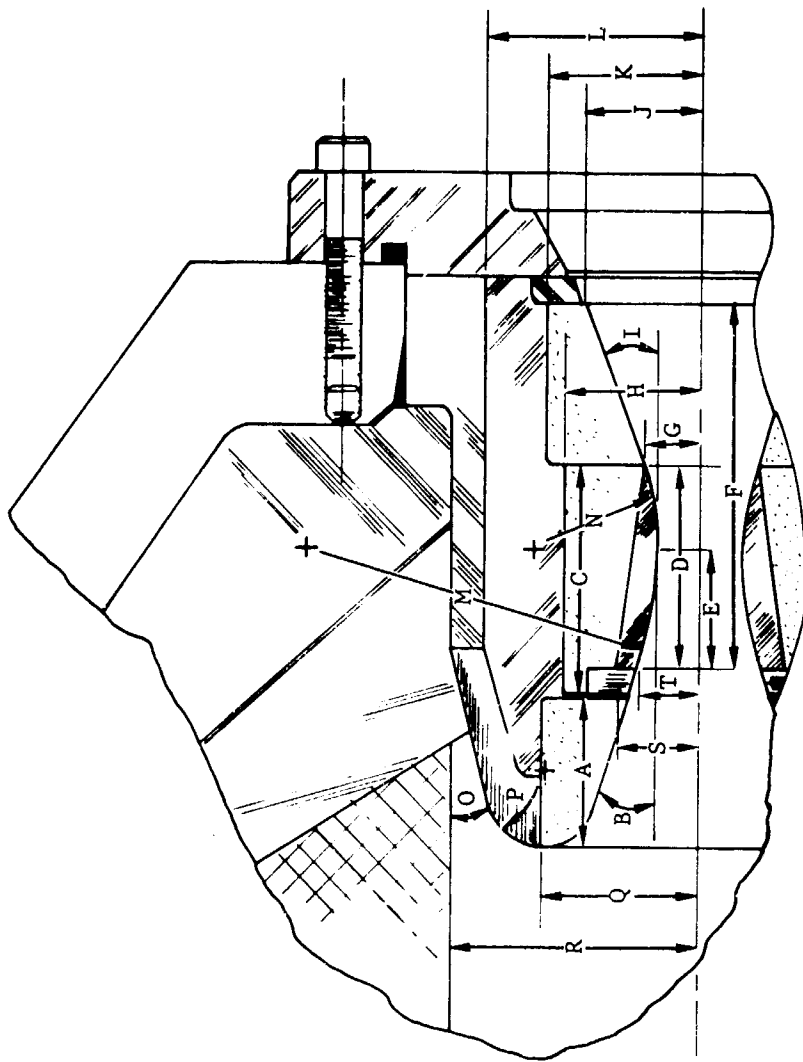
F11028 U

FIGURE 31.   DIMENSION CODE FOR T-18 AND T-19 NOZZLES
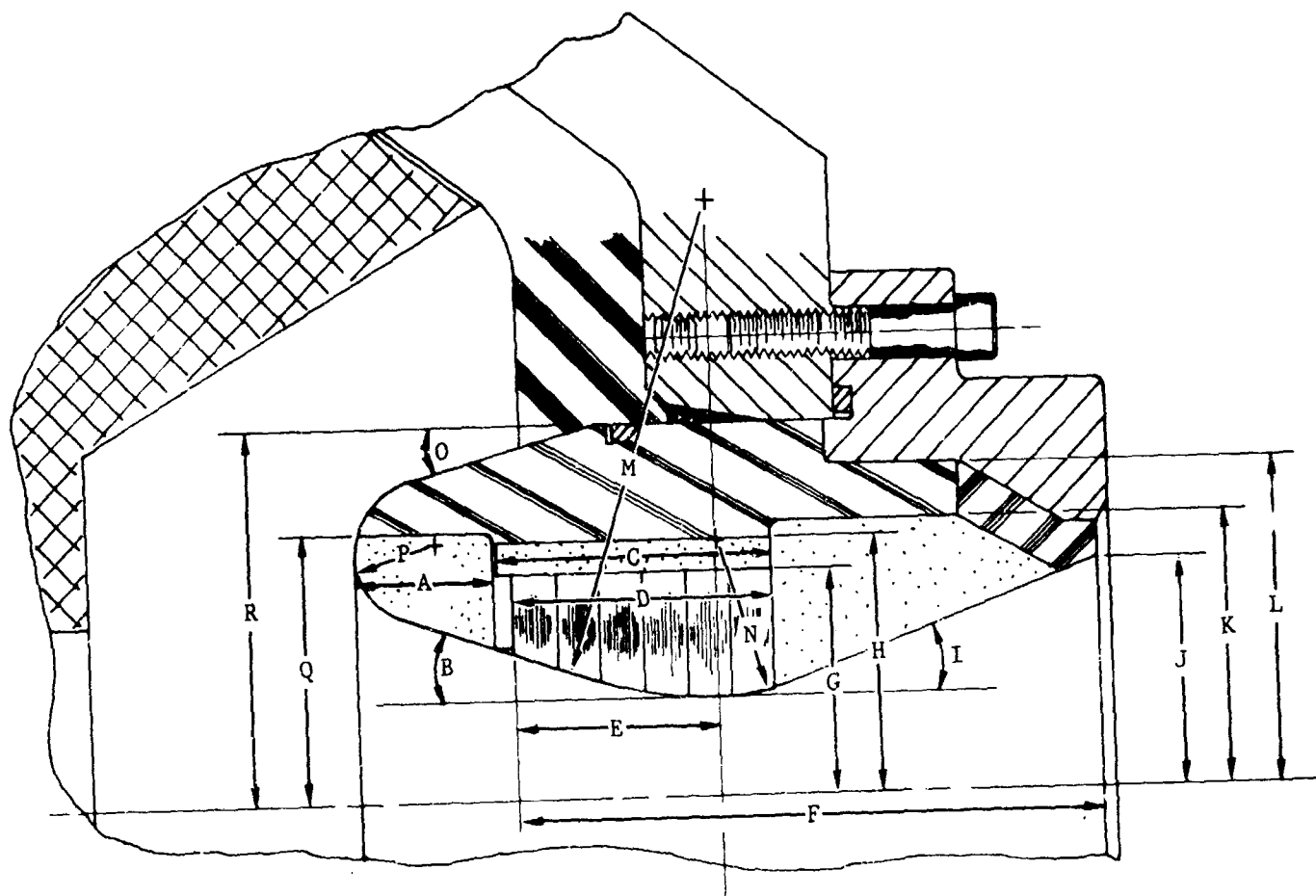
FIGURE 32. DIMENSION CODE FOR T-51 AND T-52 NOZZLES

F11029 U
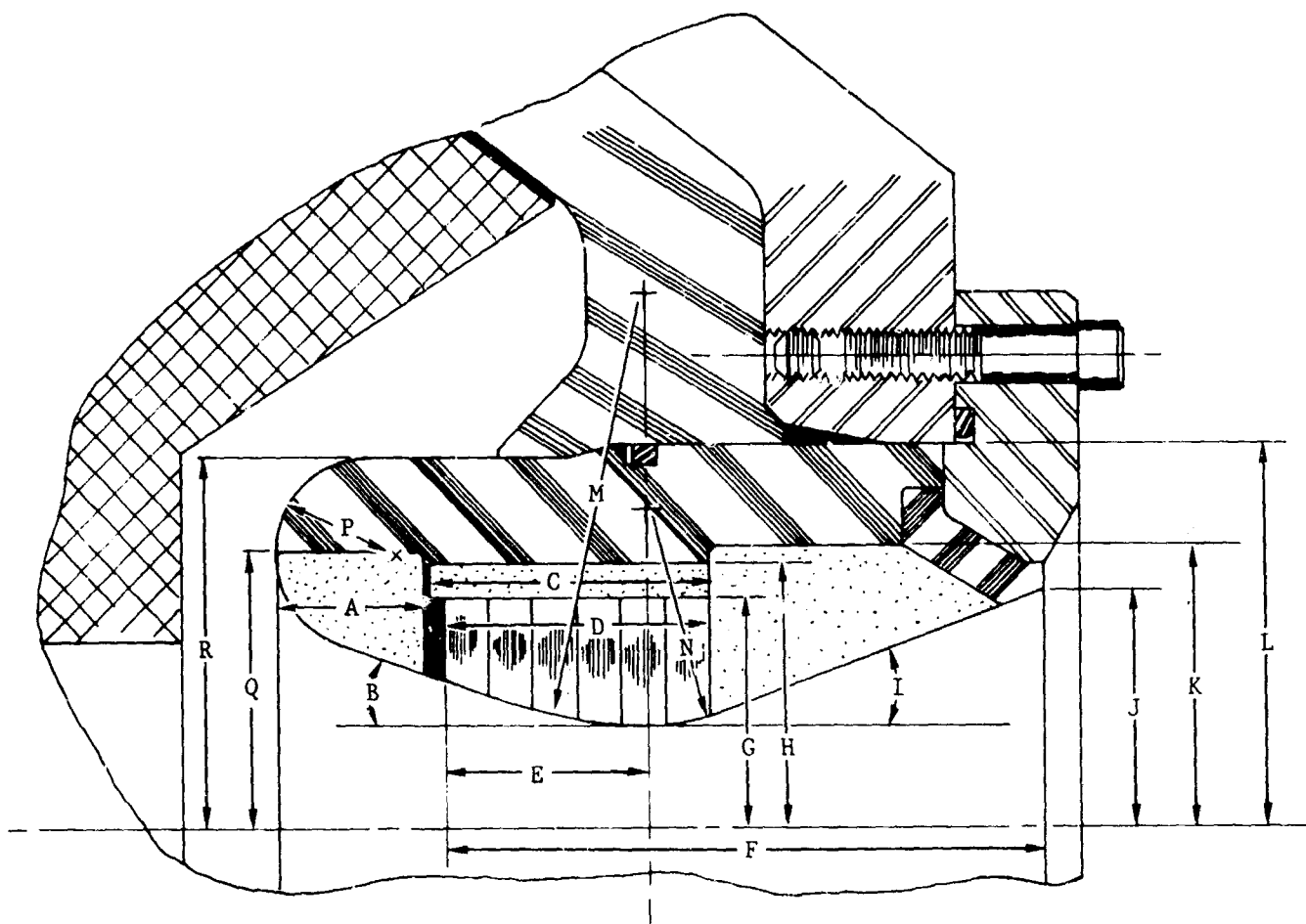
F11030 U

FIGURE 33.   DIMENSION CODE FOR T-53 NOZZLE
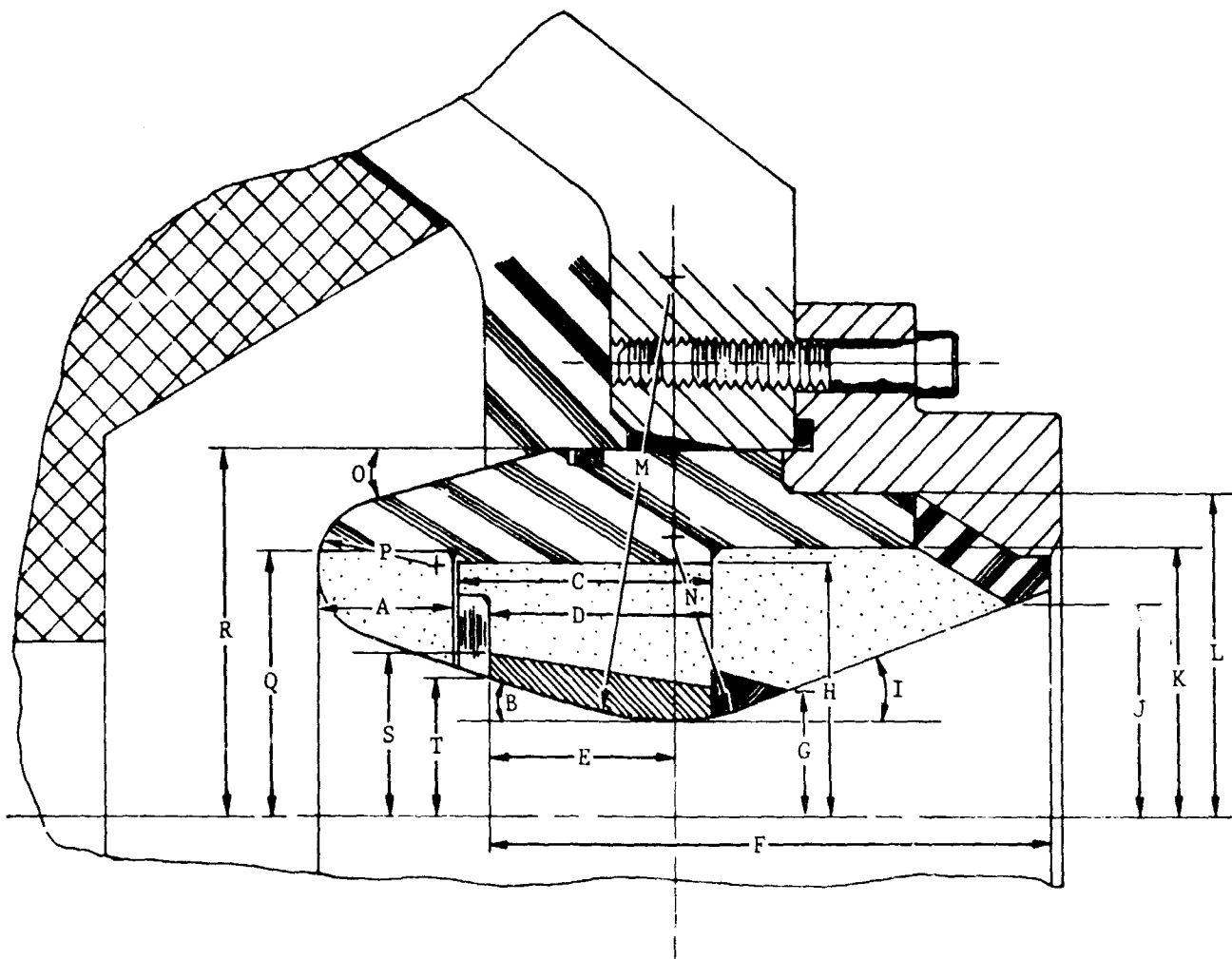
F11031U

FIGURE 34. DIMENSION CODE FOR T-54 NOZZLE

TABLE VII. SUMMARY OF ESSENTIAL NOZZLE DESIGN DIMENSIONS

DIMENSIONS (KEYED TO ALPHABETIC SYMBOLS OF FIGURES 27 THROUGH 34) NOTE FIGURE CALLOUT IN TABLE

Test	Figure	D*	A	B	C	D	E	F	G	H	I	J	K	L	M	N	O	P	Q	R	S	T
T-1	27	1.1660	2.340 →	25°	2.80 →	2.70 →	2.00 →	5.10 →	1.50 →	1.875 →	20° →	1.564 →	2.155 →	2.50 →	4.00 →	1.00 →						
T-2		1.0300																				
T-3		1.1898																				
T-4		1.0295																				
T-5		1.0440																				
T-6		1.2000																				
T-7		1.1460																				
T-8		1.2150		18°																		
T-9		1.2120																				
T-10		1.2330																				
T-11		1.0800																				
T-12	28	1.2330	2.027	60°										3.00	5.25	2.00	15°	0.75	2.2185	3.4975		
T-13	29	1.2380	-											3.00	4.00	1.00						
T-14	27	1.2180	2.340	18°										2.50	4.00	1.00						
T-15	27	1.1800	2.340	→											4.00	1.00						
T-16	30	1.2140	2.340			2.636	1.690		0.79			1.5735		3.00 →	6.00	2.50					1.147 →	0.85 →
T-17	30	1.2140	2.340			→	2.00		→					→	→	2.45						
T-18	31	1.2140	2.027									1.564		3.00	4.00	2.00	15°	0.75	2.2185	3.4975		
T-19	31	1.2140	2.027									1.5815		3.00	3.87	1.50	15°	0.75	2.2185	3.4975		
T-20	27	1.2140	2.340			2.70			1.50			1.55		2.50	5.25	2.00						
T-21	29	1.1650	-	60°																		
T-22	29	1.0300	-	60°																		
T-23	28	1.1790	2.027	18°					1.75			1.5825		3.00	3.93	2.00	15°	0.75	2.2185	3.4975		
T-24	29	1.2170	-	60°								1.594				2.00						
T-25	27	1.2220	2.340	18°	1.595	3.00				2.125		1.564	2.250	2.50	6.00	2.45						
T-51	32	2.3410	1.670 →	18°		3.00			2.44	2.8125 →	20° →	2.56 →	3.0625 →	3.6175 →	4.58 →	2.34 →	15°	0.72	3.00 →	4.120 →	1.8125	1.596
T-52	32	2.3990															15°	0.72				
T-53	33	2.3400			1.5825	2.670			1.50								-	1.170				
T-54	34	2.3400	→	→													15°	0.72				

APPENDIX II (U)

MOTOR TEST INSTRUMENTATION

2.1 PRESSURE AND THRUST

The following ballistic data were taken during each motor test: (1) axial
thrust, (2) chamber pressure, and (3) ambient pressure. It was anticipated
that the motors used in the small scale tests would normally produce about
1000 to 1500 pounds thrust at chamber pressures between 600 and 1000 psi.
Two strain gage, dual bridge axial thrust mounts (0-1000 and 0-2000 psig)
were used. The data were recorded on a digital system at 17 to 18 milli-
second intervals. For redundancy, an oscillograph was also used to record
chamber pressure and thrust. In the development motor tests, two dual
bridge strain gage axial thrust mounts (0-10,000 pound range) were used.
Two pressure transducers (0-1000 and 0-2000 psig) were used. The data were
recorded on the digital recording system at about 3.5 millisecond intervals.
For redundancy, an oscillograph was used to record the thrust and chamber
pressure.

Pressure transducers on the development test motors were somewhat undepend-
able. The No. 2 transducer was inoperative on Tests T-51 and T-53 and it
was plugged during Test T-54. The No. 1 transducer performed adequately
on all tests except T-54 where it apparently plugged for a few seconds in
the middle of the run. The cause of the failures of the No. 2 transducer
is not clear. It is believed that the pressure port was plugged by: (1)
the cab-o-sil used to bond the aft closure insulator to the propellant grain,
(2) debris from the ignitor, and/or (3) metal oxide deposits from the aft
closure.

2.2 THERMOCOUPLE DESIGNS

The thermal instrumentation plan and thermocouple performance are discussed
at length in Sections 4.3 of References 1 through 4. The majority of the
thermocouples used were of the standard, spring loaded, bayonette type.
Both the type K, chromel-alumel, and type S, platinum/platinum-rhodium,
thermocouples were used. A special, submerged thermocouple design (Figure 35)
was used in nozzles T-12 and T-13. The relatively poor performance of this
thermocouple prompted the development of the improved model shown in
Figure 36. This design was used on Tests T-18, T-19, T-21 through T-24,
and T-51 through T-54. These and the majority of the bayonette type thermo-
couples gave excellent data. The thermocouple performance for all tests is
summarized in Table VIII.

A special radiometer (Figure 37) was fabricated and used on Test T-3. The
radiometer performance is shown in Figure 38. These results are discussed
in Section 2.5.b and 4.3.a of Reference 2.

2.3 PLUME PARTICLE SAMPLERS

Exhaust plume particle samples were collected during each of the program
motor tests. Two, simple, grab samplers were installed approximately
50 feet from the nozzle along the motor axis. The design shown in Figure 39
was used in Tests T-1 through T-7. It featured a wide variety of sample
collectors. Based on these early results, the sampler shown in Figure 40
was designed and used on the remaining tests. The second sampler uses small
glass bottles, open at one end, to collect the sample. The analyses of the
samples are discussed in Sections 3.4 of References 2, 3, and 4. The per-
formance and installation of the samplers are discussed in Sections 4.3 of
References 2, 3, and 4.

2.4 NOZZLE THERMOCOUPLE LOCATIONS

The locations of the thermocouples in each type of nozzle tested are shown
in Figures 41 through 51. The actual temperature data is given in Section 2.5
(Tests T-1 through T-7) of Reference 2, Appendix A (T-8 through T-23 and
T-25) of Reference 3, and Appendix A (T-24 and T-51 through T-54) of
Reference 4. It should be noted that much of the temperature data was
not actually used in this program. The temperature data are also available
in digital form.

END VIEW

EPOXY PLUG

THERMOCOUPLE
LEAD WIRE

SIDE VIEW

STAINLESS STEEL

COMPRESSION SPRING

CERAMIC TUBE

THERMOCOUPLE
JUNCTION
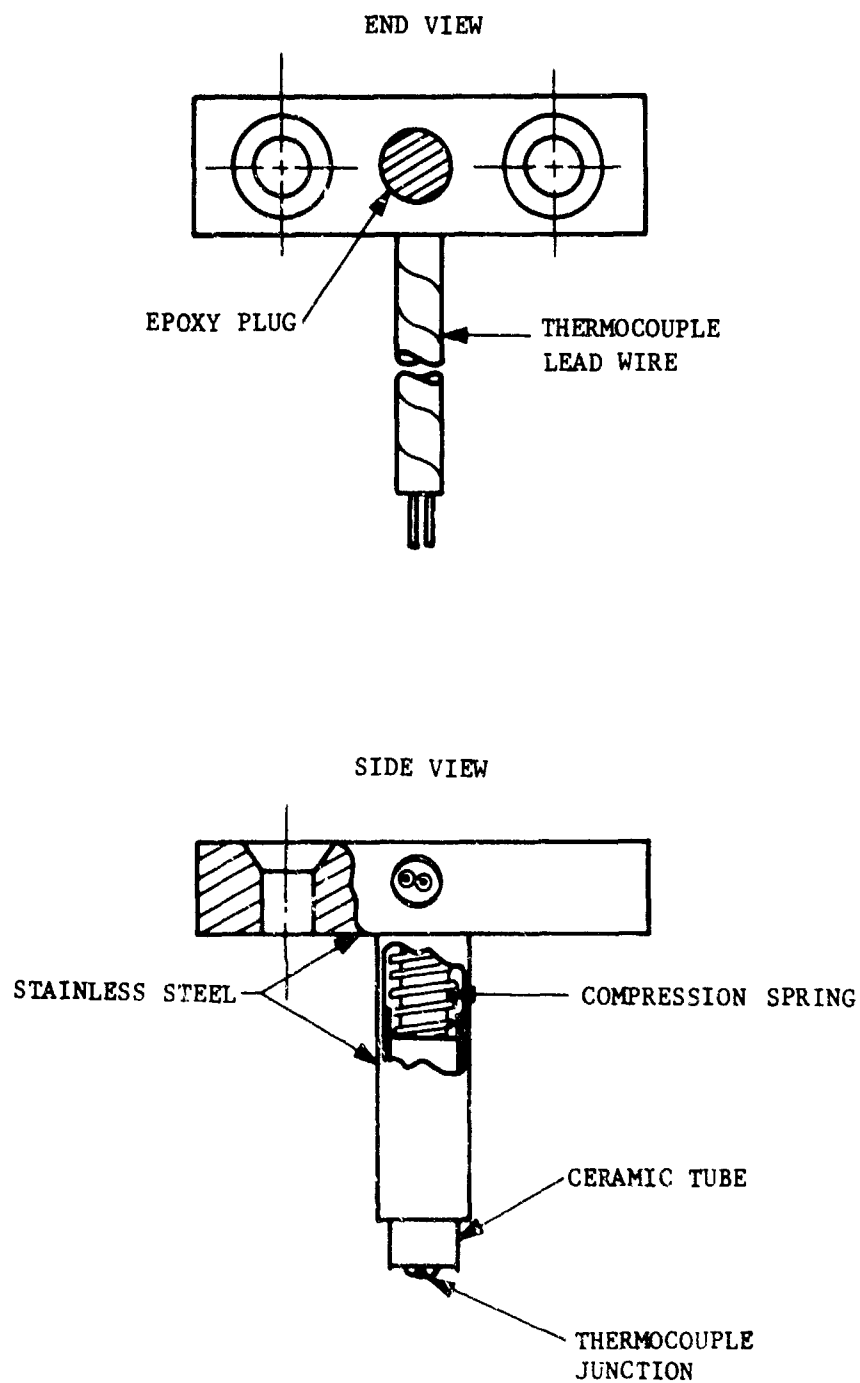
FO4121 U

FIGURE 35. HY-CAL ENGINEERING SPECIAL SUBMERGED THERMOCOUPLE

-203-

SLOT FILLED WITH EPOXY AFTER
THERMOCOUPLE INSTALLATION

THERMOCOUPLE LEAD WIRE
WITH FIBERGLASS INSULATION

METAL RETAINER

COMPRESSION
SPRING

CERAMIC
CEMENT

WASHER

CERAMIC
TUBE

ASBESTOS
PHENOLIC

ATJ GRAPHITE

THERMOCOUPLE
SENSOR TIP

PYROLYTIC
GRAPHITE

F04122 U
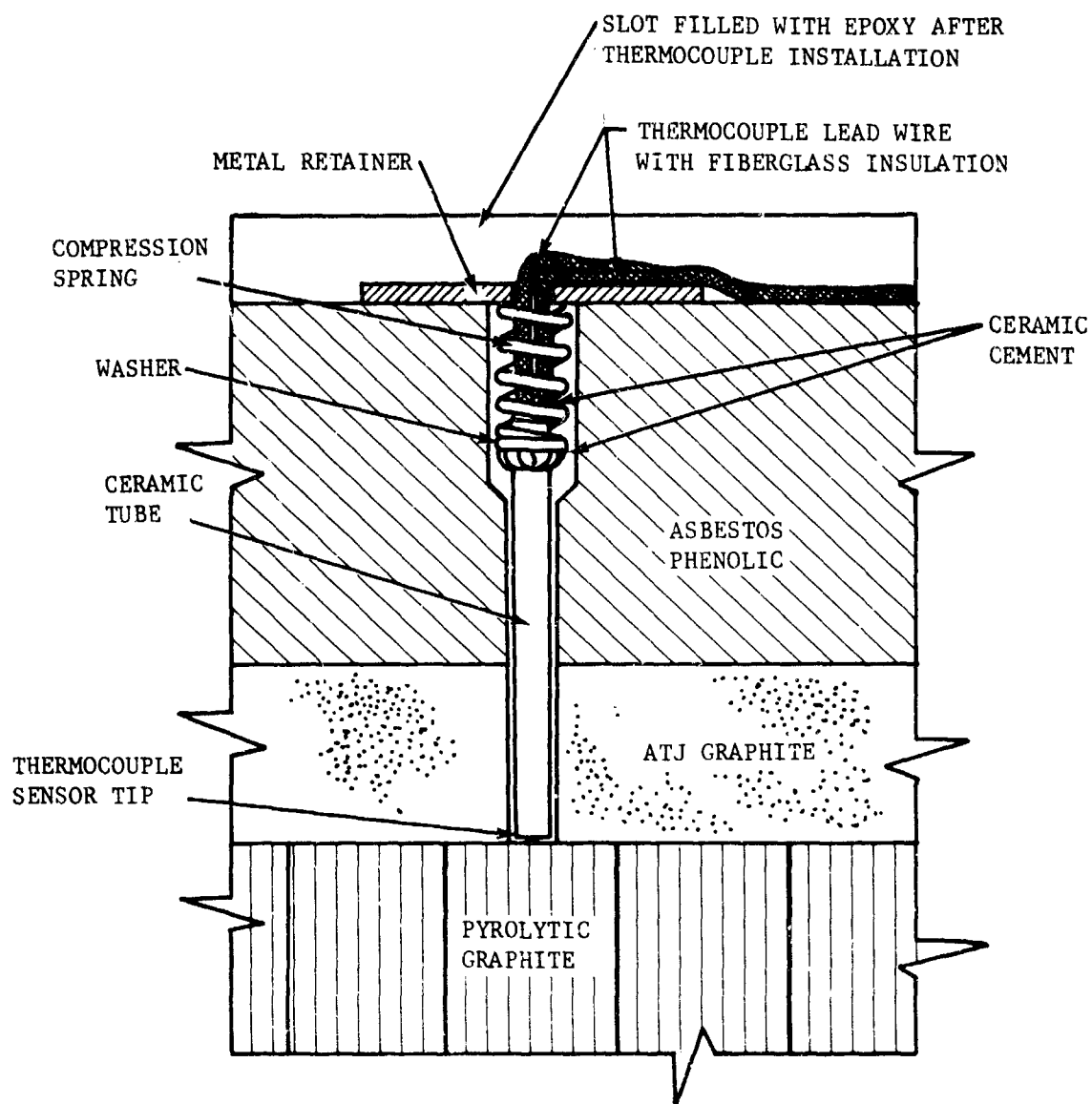
FIGURE 36.   AERONUTRONIC SPECIAL SUBMERGED THERMOCOUPLE DESIGN
             (TYPICAL INSTALLATION)

TABLE VIII. QUALITY OF THERMOCOUPLE DATA

Thermocouple Port Number

Test Number	1	2	3	4	5	6	7	8	9	10	11	12	13	14	15	16	17	18	19	20	21	23	24	25	121	101	122	102	123	103	2	7
T-1		KG	SG	KF	SG	KG	KG	SF	SG	SG	SG	SG	KU	KU	KU																	
T-2	SP		SP		SP			SG	SG	SG	KP	SF	KG	KG	KG																	
T-3	SP		SG	KG	SG		KF	SG	SG	SG	KG	SG			RG																	
T-4	SG		SG	KU	SF		KU	SU			KG	SG																				
T-5	SG		KG	KG	KG		KG		SG	SG	KG	SG	RU																			
T-6	SG		KF	KF	KF		KG		SG	SG	KF	SG																				
T-7	SG		KG		KG		KG		SG	SG		SG																				
T-8	SU		KG				KG		KU	KU	KG	KP				KG	KP	KG														
T-9			KF				KF		SG	SG	KG	SG				SG	KU															
T-10	SG		KP				KG		SU	SP	KF	SG				SU	KG	KF														
T-11			KG						SG	SG	KG	SP				SU	KG															
T-12							SU		SG	SU		SG									SG											
T-13							SU		SP	SP		SU							SU	SP	SP											
T-14			KU				KP		SP	SP	KP	SP				SP	KP															
T-15	SP		KG				KF		SG	SG	KG	SF				SG	KG	KG														
T-16		KG	KG				KG	SG	SG	SP		SG				SG	KG															
T-17		KG					KG	SP	SG			SF																				
T-18							KG	SG				SG							SG		SG											
T-19							KU	SG	SG			SG							SG		SG											
T-20							KG		SG	SP	KF	SG																				
T-21							KG			SU		SG							SG			KG										
T-22							KG		SG	SG		SG							SP	SP		KG	SG	SG								
T-23							KG		SG	SP		SG								SF		KG	SG	SP								
T-24							KG		SG	SG		SG										KG	SG	SG								
T-25			KU				KP	SU	KP	SP	KP	SG				SP	KF															
T-51																									SG	SG	SG	SG	SG	SG	KG	KG
T-52																									SG	SG	SG	SG	U	SG	KG	KG
T-53																									U	U	SG	SG	SG	SG	KG	KF
T-54																									SG*	SG*	SG*	SG*	SG*	SG*	KG*	KG

Thermocouples exposed from back side early in run.
Insert ejected exposing thermocouples, data good until that time.

Symbol

R   Radiometer
S   Platinum/platinum 10% rhodium thermocouple
K   Chromel/alumel thermocouple

G   Good - 1, 2, 3, 4
F   Fair - 1, 2, 3
P   Poor - 1 or 2 or 3
U   Unusable - none
*   Good until insert ejected

Where

1   Equilibration temperature
2   Startup transient
3   Cooldown transient
4   Smooth curves
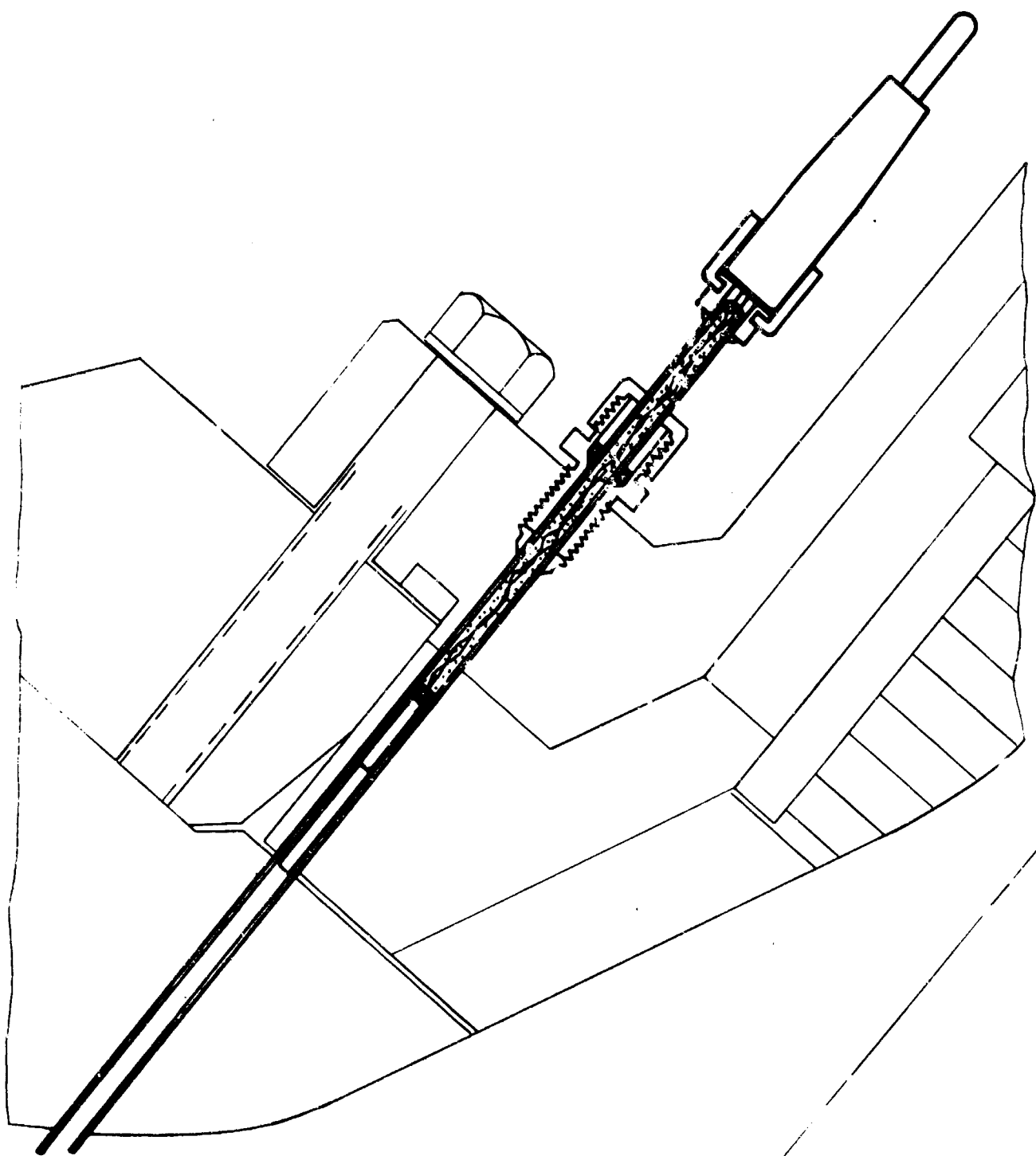
F00806 U

FIGURE 37. RADIOMETER
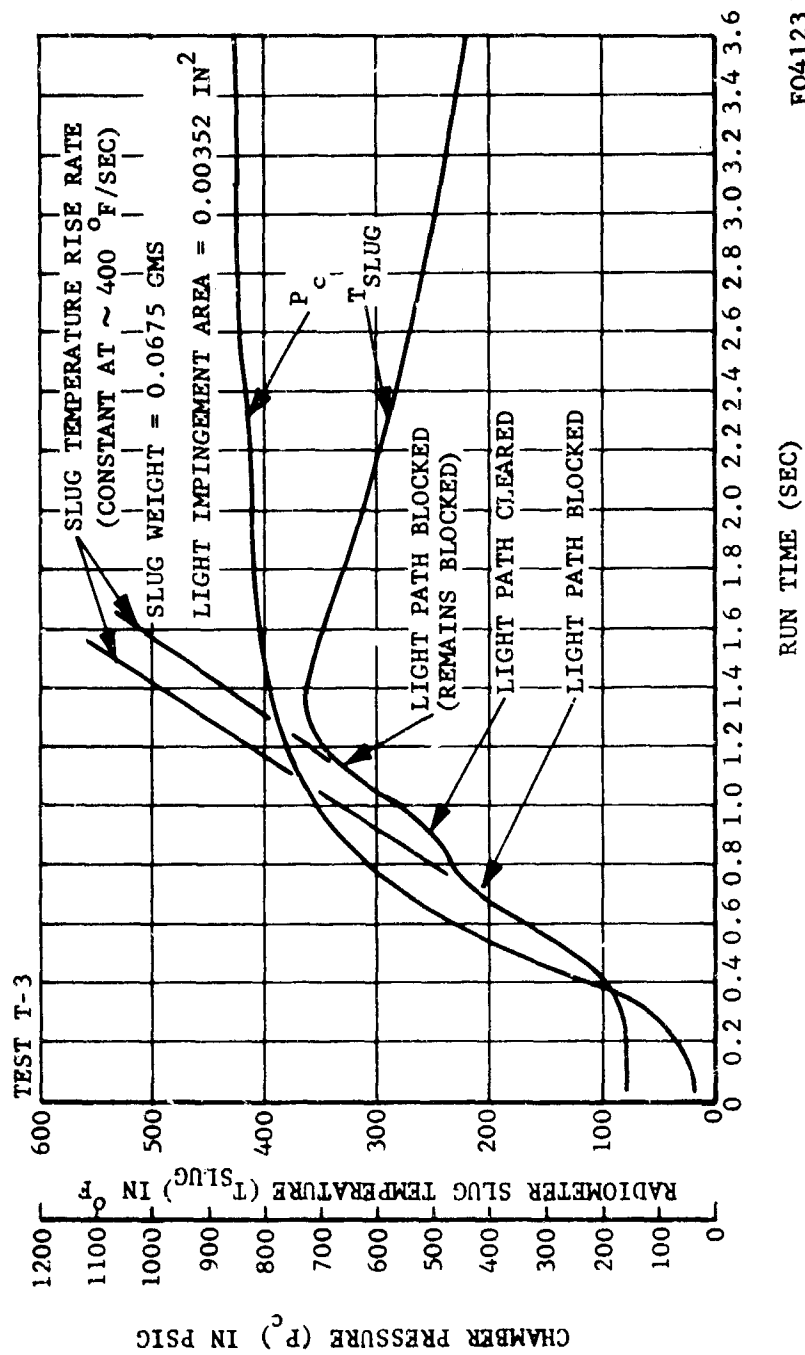
FIGURE 38. RADIOMETER PERFORMANCE

F04123 U

FLOW →

TOP VIEW

EXHAUST PLUME
CENTER LINE

FLOW
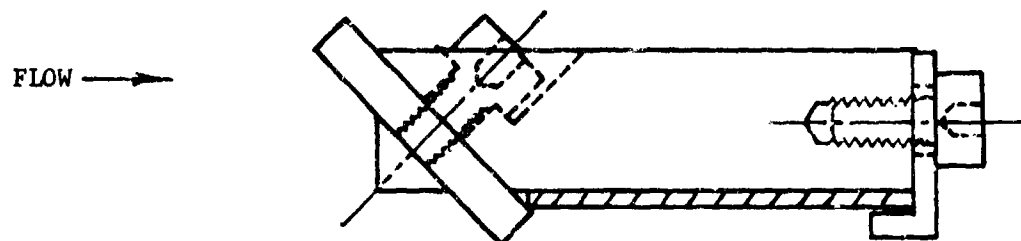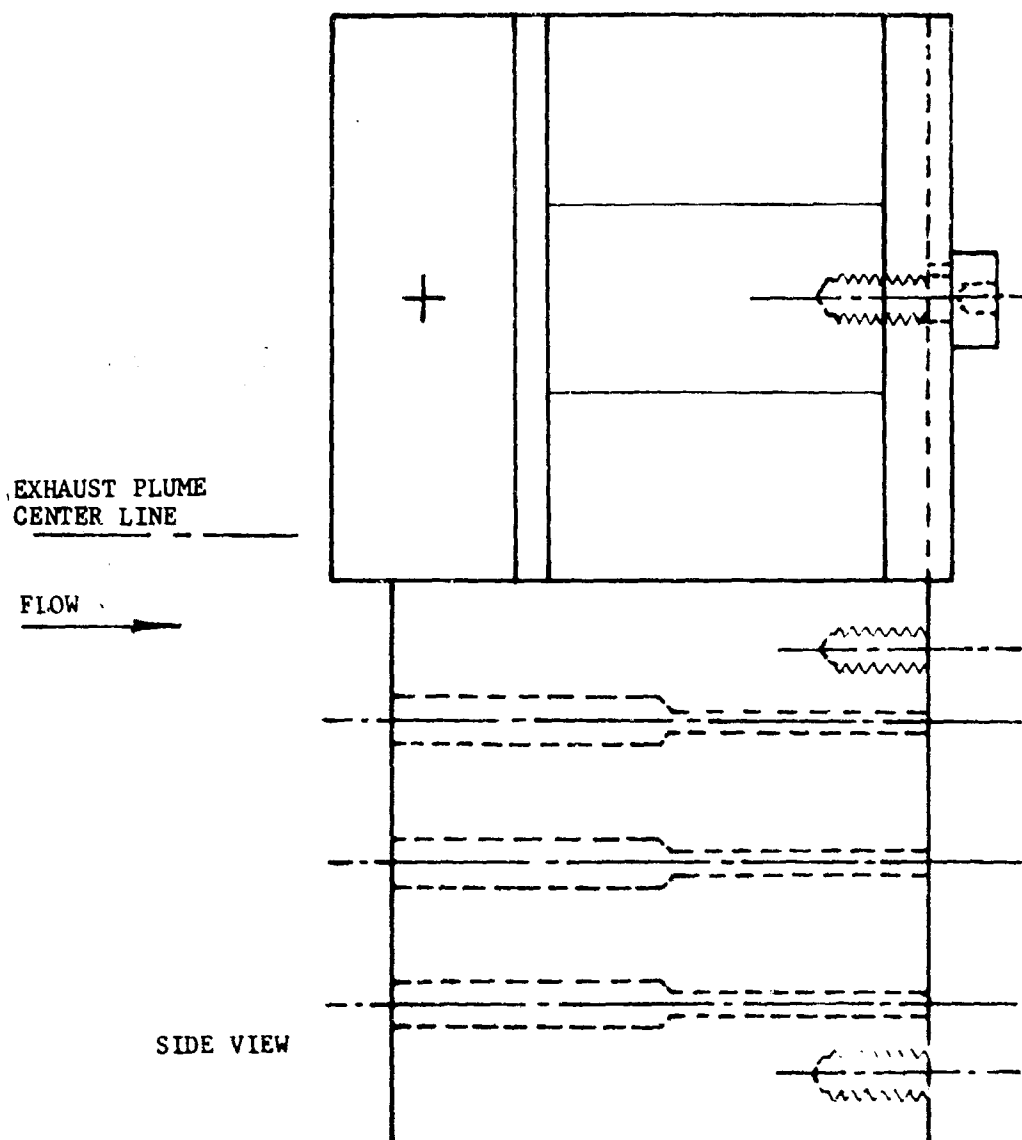
SIDE VIEW

F00807 U

FIGURE 39.   EXHAUST PLUME PARTICLE SAMPLER

-208-

RUBBER WASHER

BOTTLE

36 IN.

NOZZLE ℄

TO NOZZLE ← 22 FT →
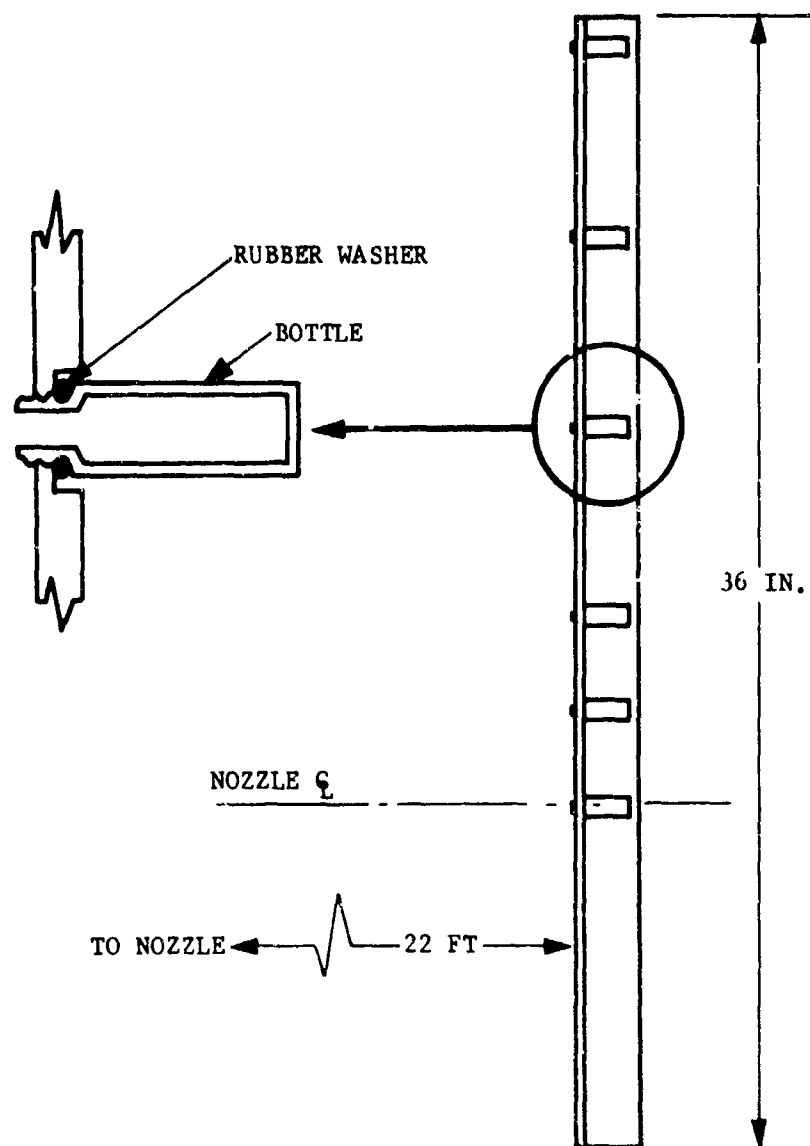
FO4124 U

FIGURE 40. EXHAUST PLUME PARTICLE SAMPLER NO. 2
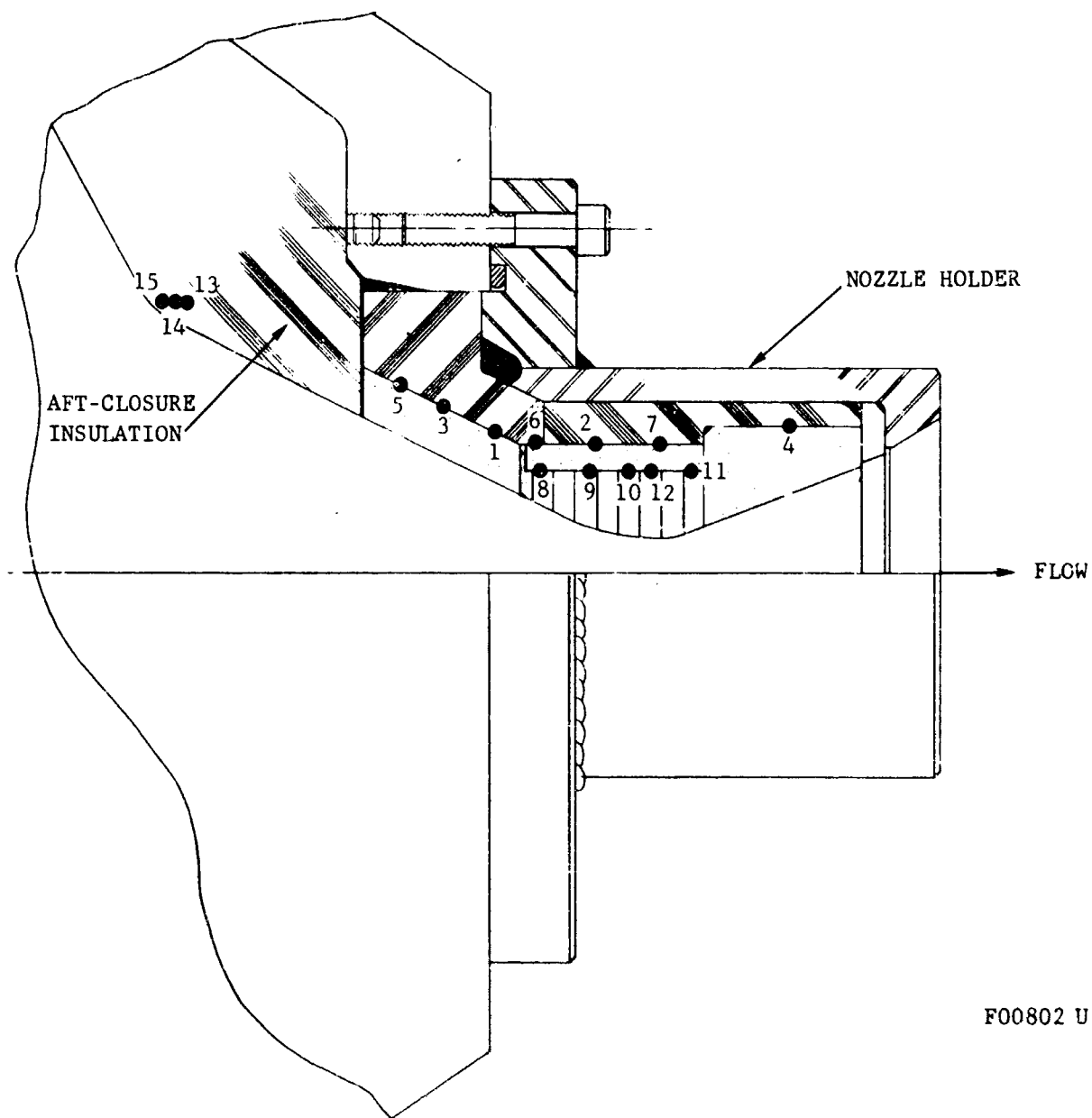
FIGURE 41. THERMOCOUPLE LOCATIONS ON NOZZLES T-1 THROUGH T-7

F00802 U
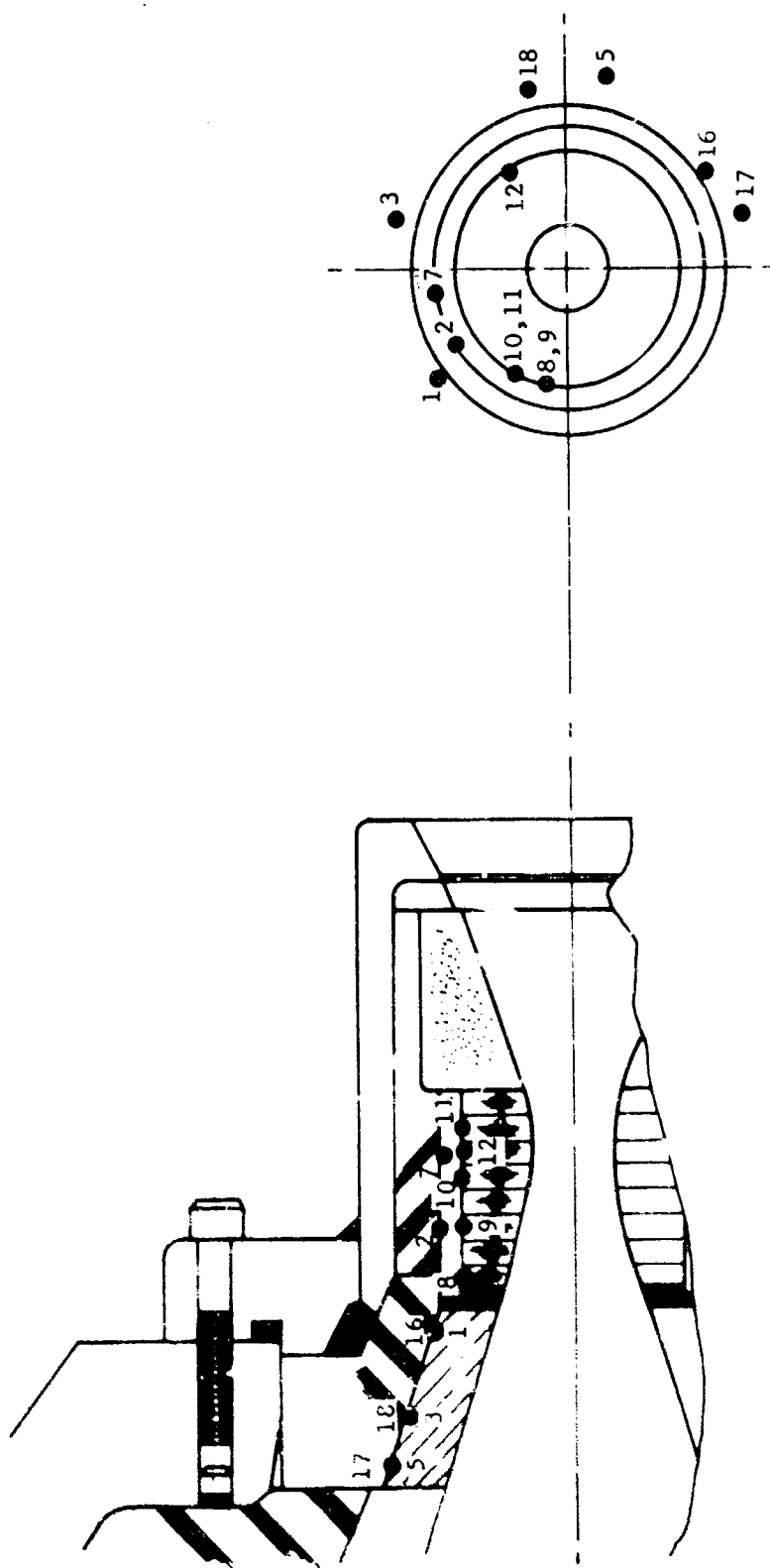
CIRCUMFERENTIAL LOCATIONS
(END VIEW)

F11032 U

LOCATIONS ILLUSTRATED IN ONE PLANE
(SIDE VIEW)

FIGURE 42. THERMOCOUPLE LOCATIONS FOR NOZZLE T-8 THROUGH T-11, T-14, T-15, AND T-20

-211-

CIRCUMFERENTIAL LOCATIONS
(END VIEW)

LOCATIONS ILLUSTRATED IN ONE PLANE
(SIDE VIEW)
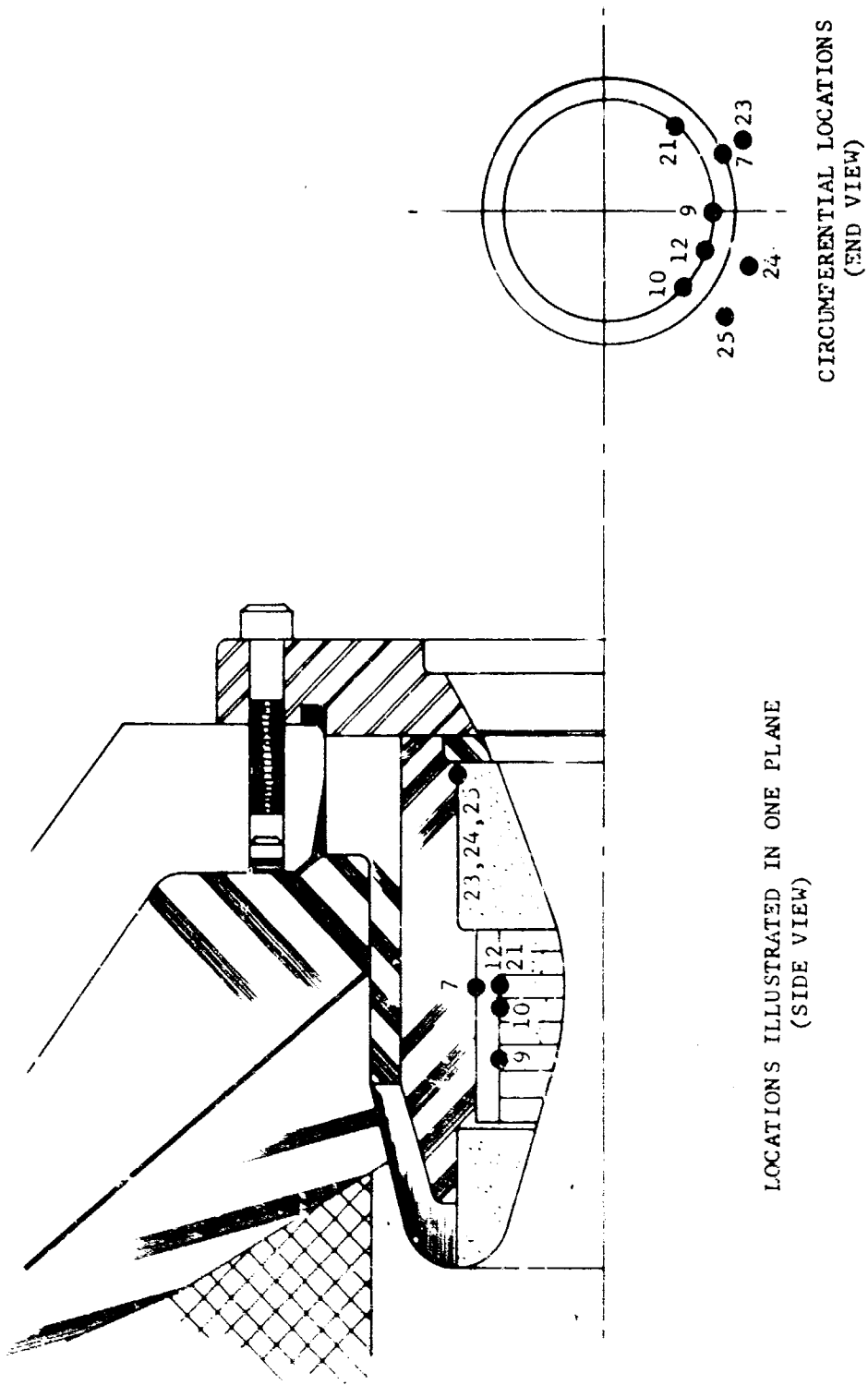
FIGURE 43. THERMOCOUPLE LOCATIONS FOR NOZZLE T-12 AND T-23

F11033 U

-212-

CIRCUMFERENTIAL LOCATIONS
SIDE VIEW

F04119 U

LOCATIONS ILLUSTRATED IN ONE PLANE
SIDE VIEW
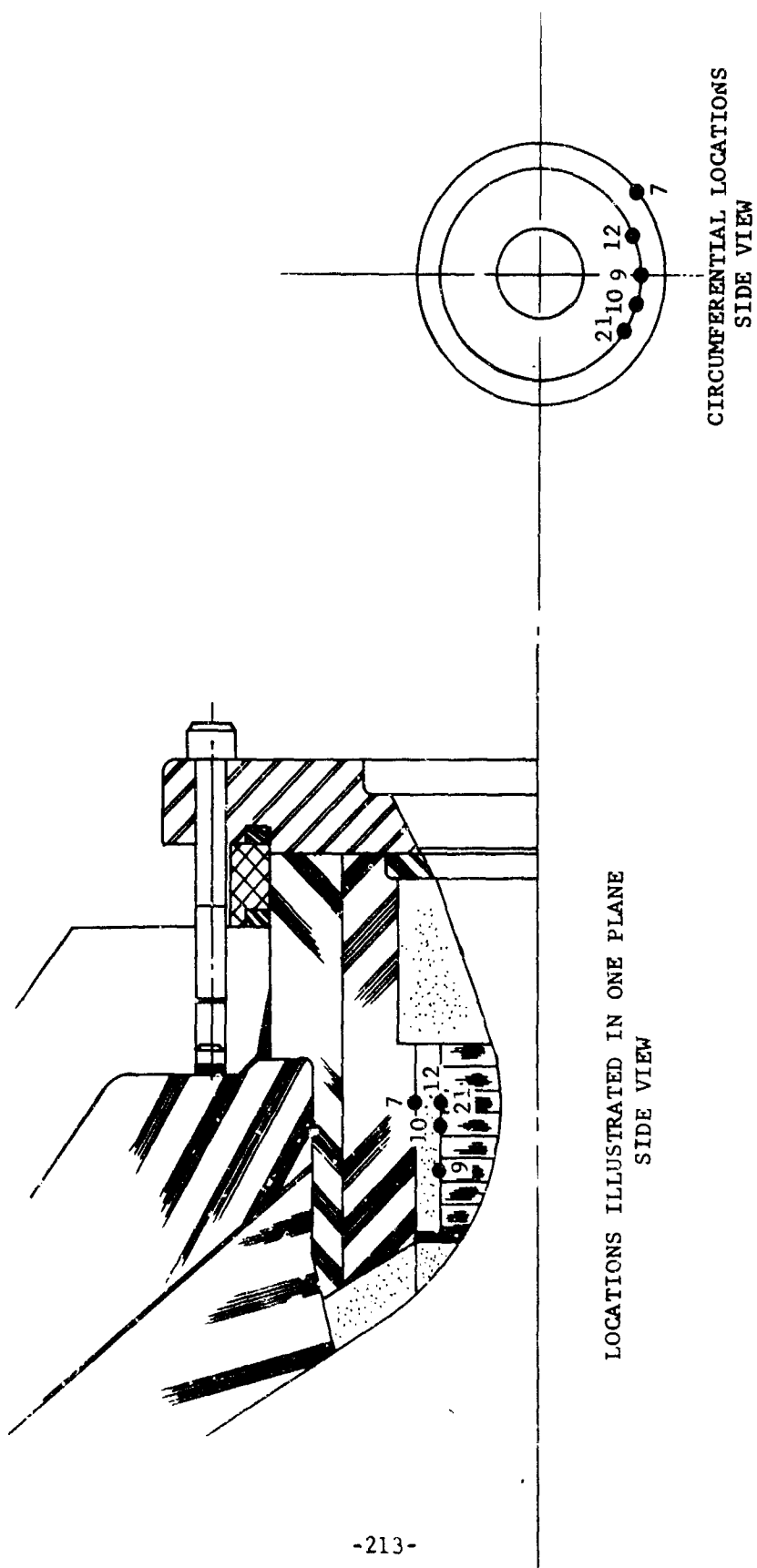
FIGURE 44. THERMOCOUPLE LOCATIONS FOR NOZZLE T-13

-213-
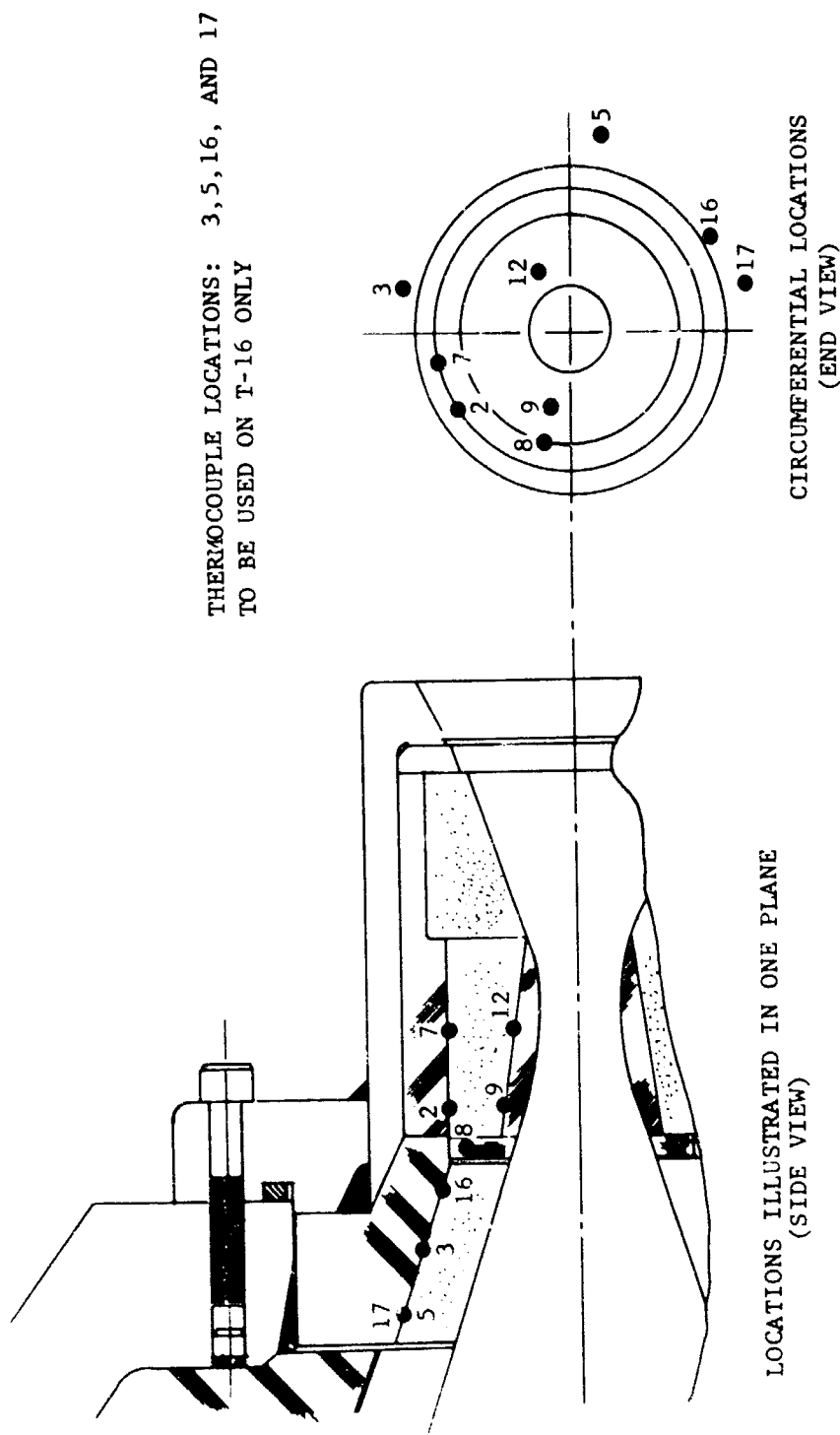
THERMOCOUPLE LOCATIONS: 3, 5, 16, AND 17
TO BE USED ON T-16 ONLY

CIRCUMFERENTIAL LOCATIONS
(END VIEW)

LOCATIONS ILLUSTRATED IN ONE PLANE
(SIDE VIEW)

FIGURE 45. THERMOCOUPLE LOCATIONS FOR NOZZLE T-16, AND T-17

10896U

-244-

CIRCUMFERENTIAL LOCATIONS
(END VIEW)

LOCATION ILLUSTRATED IN ONE PLANE
(SIDE VIEW)
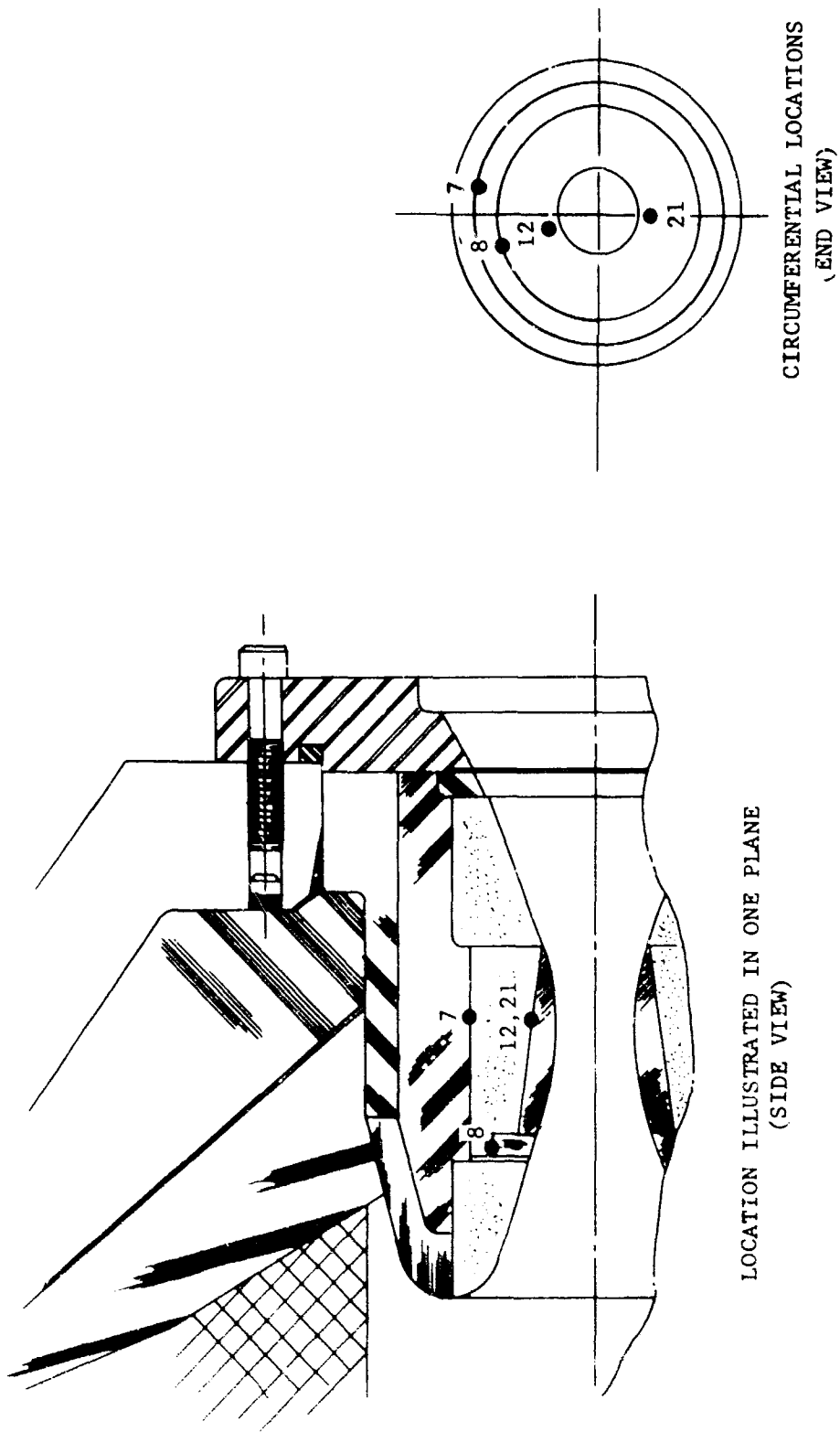
FIGURE 46. THERMOCOUPLE LOCATIONS FOR NOZZLES T-18 AND T-19

10897U
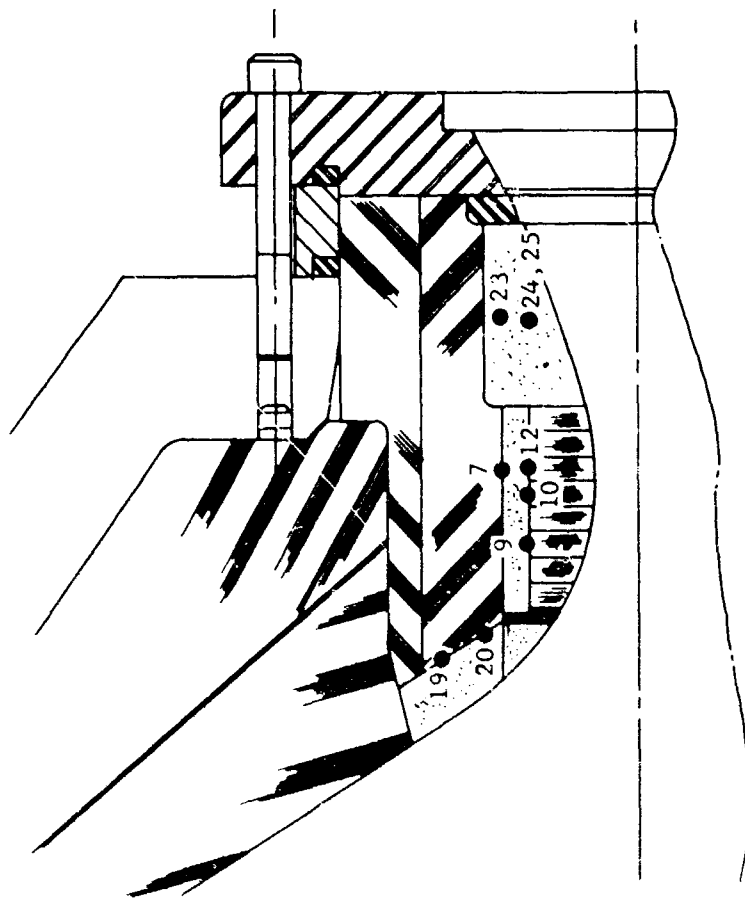
LOCATIONS ILLUSTRATED IN ONE PLANE
(SIDE VIEW)
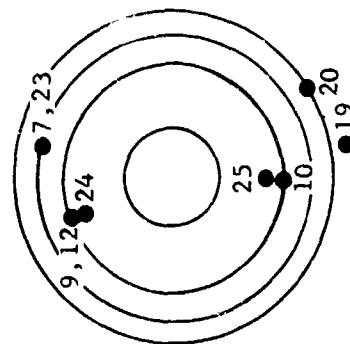
CIRCUMFERENTIAL LOCATIONS
(END VIEW)

F04120 U

FIGURE 47. THERMOCOUPLE LOCATIONS FOR NOZZLES T-21 T-22, AND T-24

CIRCUMFERENTIAL LOCATIONS
(END VIEW)

F08184 U

LOCATIONS ILLUSTRATED IN ONE PLANE
(SIDE VIEW)
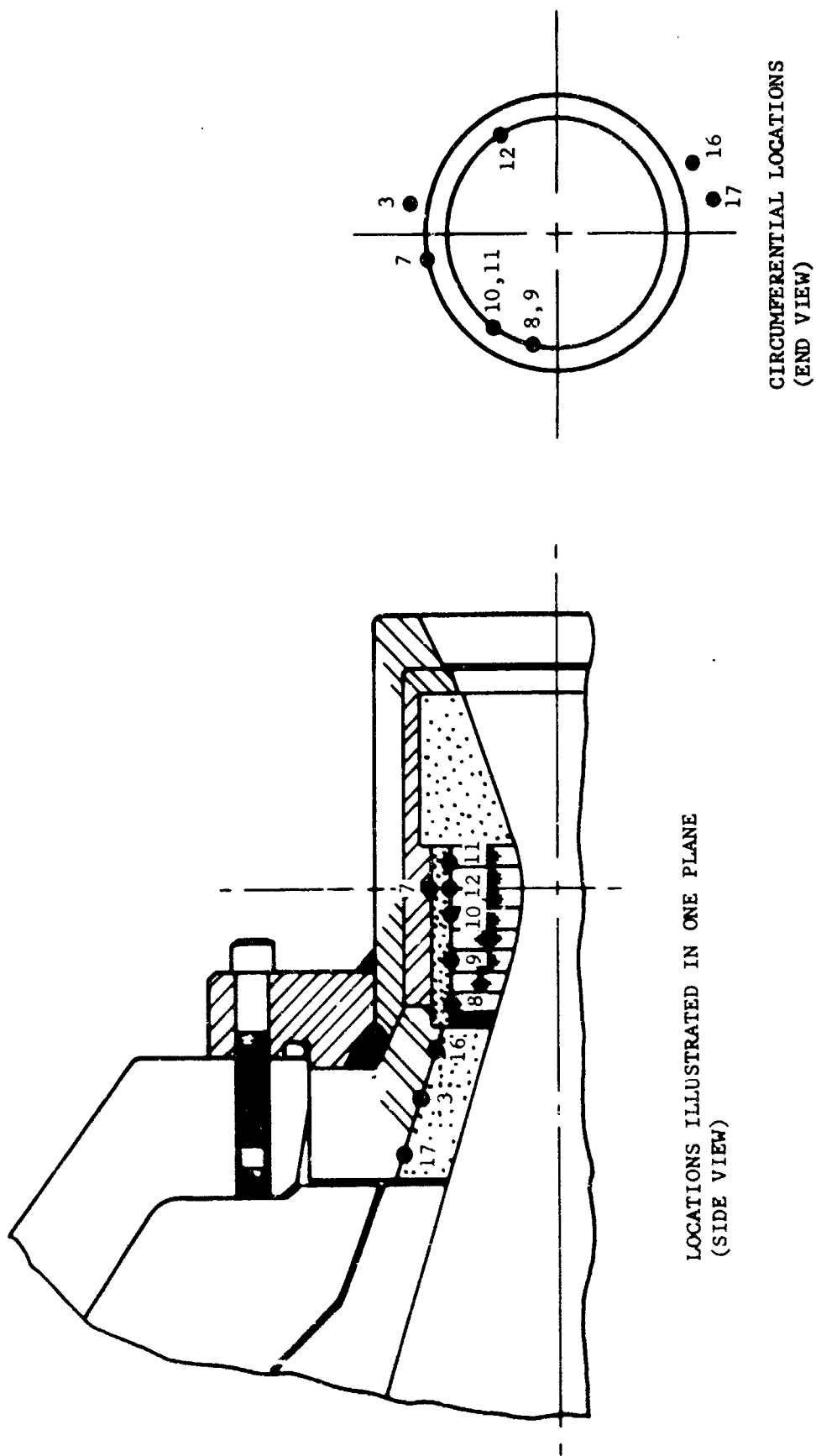
FIGURE 48. THERMOCOUPLE LOCATIONS FOR NOZZLE T-25

LOCATIONS ILLUSTRATED IN ONE PLANE
(SIDE VIEW)

CIRCUMFERENTIAL LOCATIONS
(END VIEW)
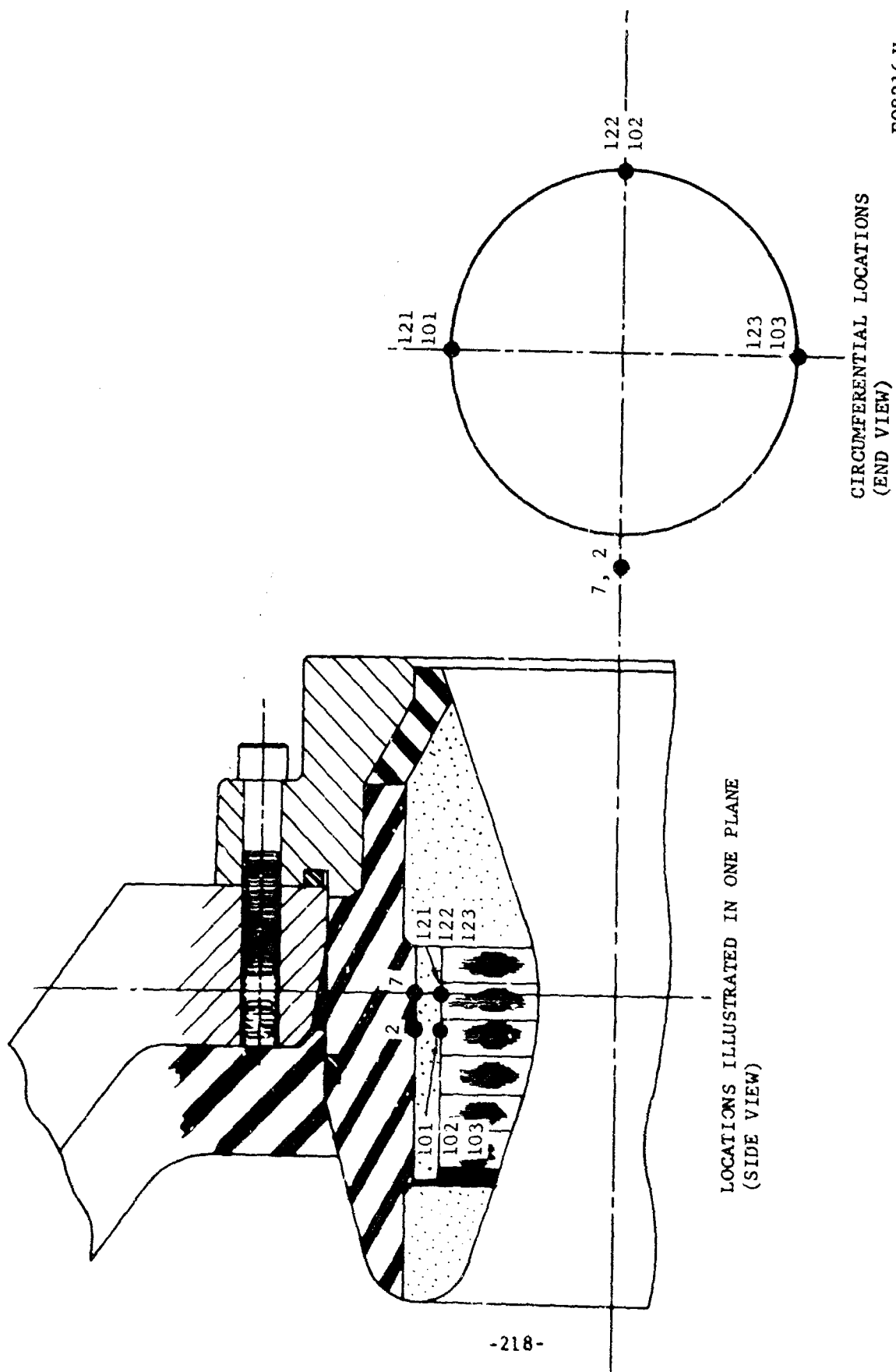
FIGURE 49. THERMOCOUPLE LOCATIONS FOR NOZZLES T-51 AND T-52

F08216 U

CIRCUMFERENTIAL LOCATIONS
(END VIEW)

F08074 U

LOCATIONS ILLUSTRATED IN ONE PLANE
(SIDE VIEW)
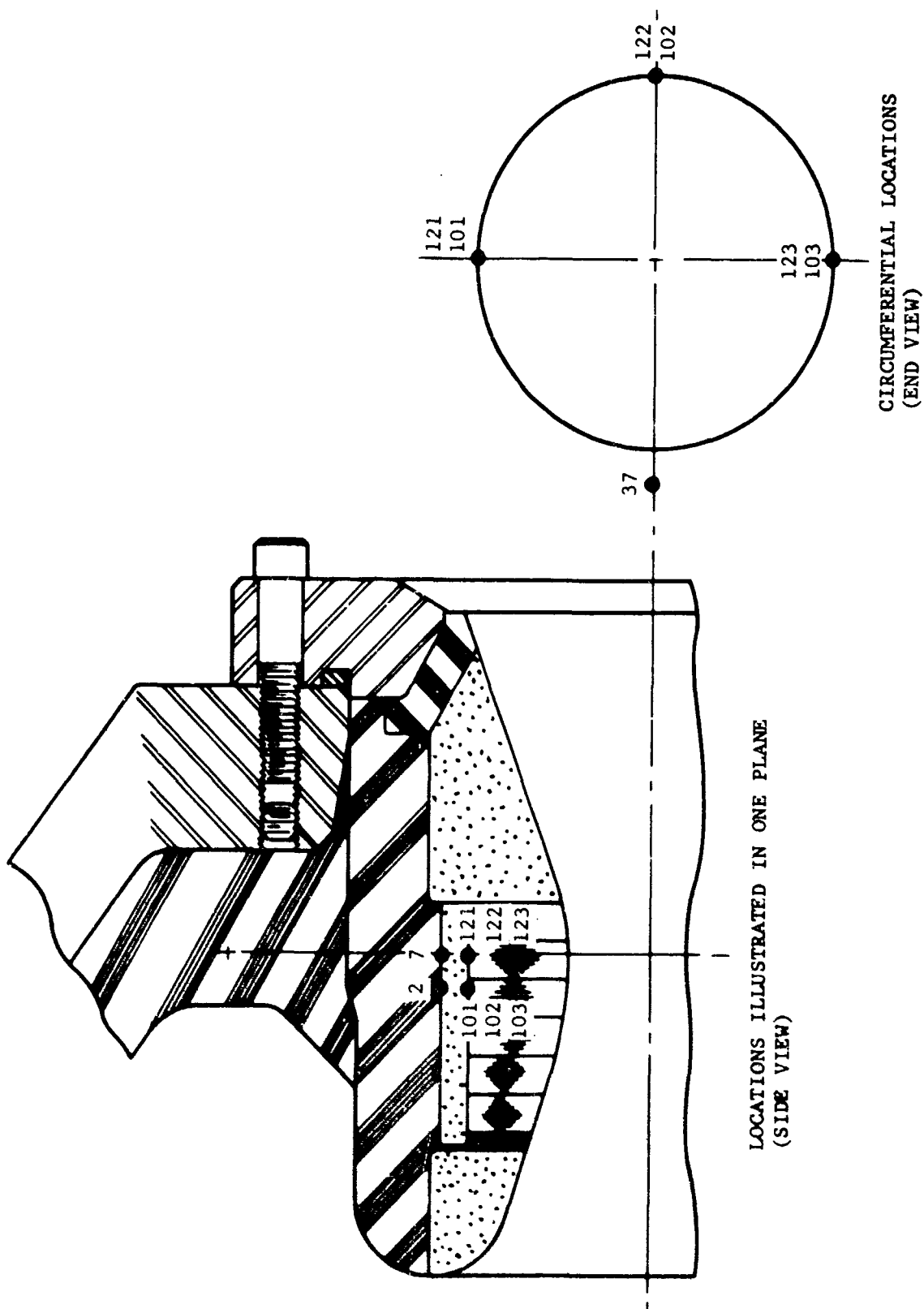
FIGURE 50. THERMOCOUPLE LOCATIONS FOR NOZZLE T-53
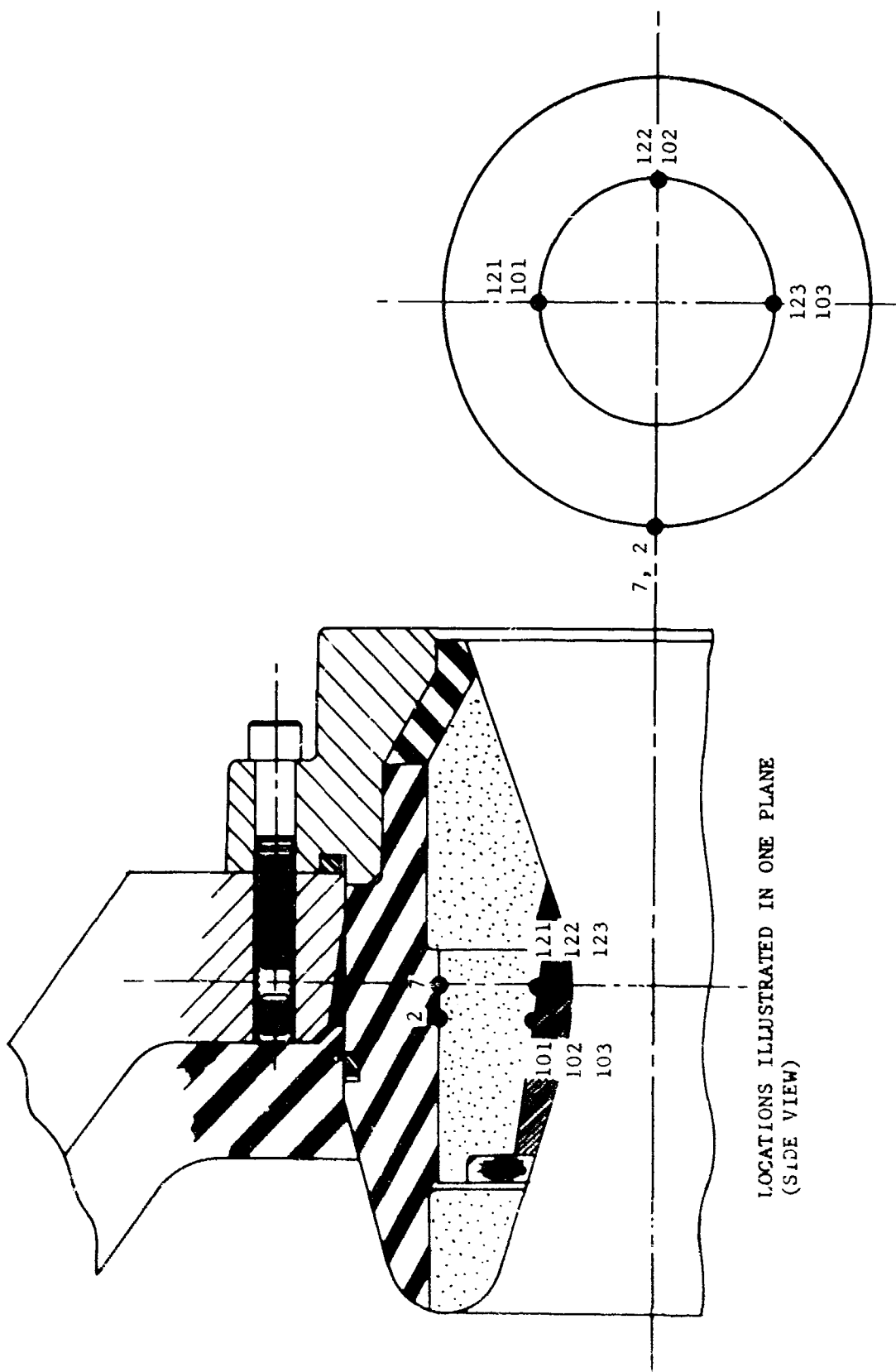
-219-

CIRCUMFERENTIAL LOCATIONS
(END VIEW)

F08073 U

LOCATIONS ILLUSTRATED IN ONE PLANE
(SIDE VIEW)

FIGURE 51.   THERMOCOUPLE LOCATIONS FOR NOZZLE T-54

APPENDIX III (C)

PRESSURE AND THRUST DATA

Measured motor pressure and thrust data for each of the program motor tests are presented in Figures 52 through 80. These data may also be found and are discussed in Sections 5.2 and 5.3 of References 2, 3 and 4. The instrumentation used to obtain the data are discussed briefly in Appendix II of this report and in Section 4.3 of References 1 through 4. Two sets of measurements were obtained on each firing. In many cases, only one pressure history was actually obtained due to oxide plugging of one aft closure pressure port. In general, the most reasonable curves are presented when both sets of pressure and thrust data were recorded.

It should be noted that each grain was designed to provide a nominally neutral pressure at 800 psia. This condition was not usually achieved due to: (1) minor variations in burning rates, (2) deposition/erosion induced throat area variations, and (3) erosive burning (slotted grains). Tests T-6, T-24 and T-52 were hangfires. Apparently, ignition was marginal on Tests T-1, T-2, T-4, T-5, T-15, T-51 and, possibly, T-23. On T-54, the tungsten throat insert was ejected at 20 seconds. Partial plugging of the pressure port apparently occurred at 5 seconds on T-54. The estimated pressure is shown as a dashed line (until the port cleared) in Figure 80. The minor fluctuations in the pressure and thrust curves are believed to be real. Such fluctuations appeared to correspond to the expulsion of slag deposits as observed in the motion pictures of the firings.

-221-
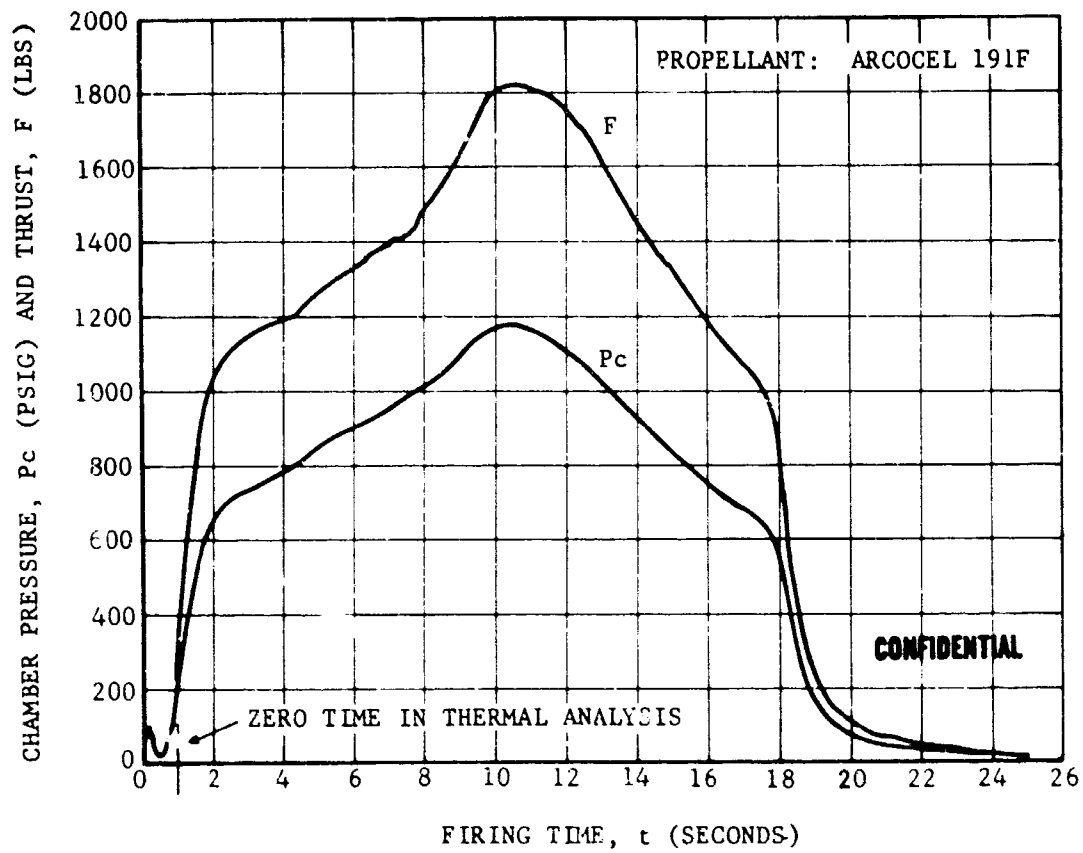
FIGURE 52.   CHAMBER PRESSURE AND THRUST VERSUS FIRING TIME TEST T-1
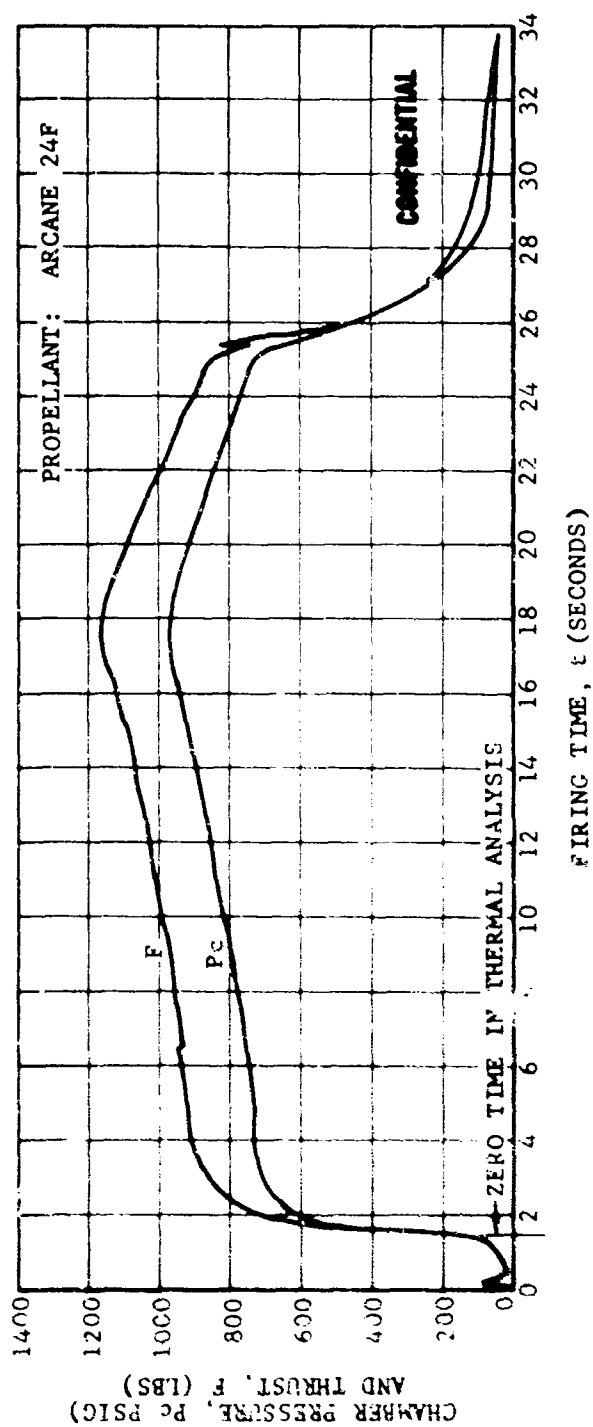
FIGURE 53. CHAMBER PRESSURE AND THRUST VERSUS FIRING TIME TEST T-2
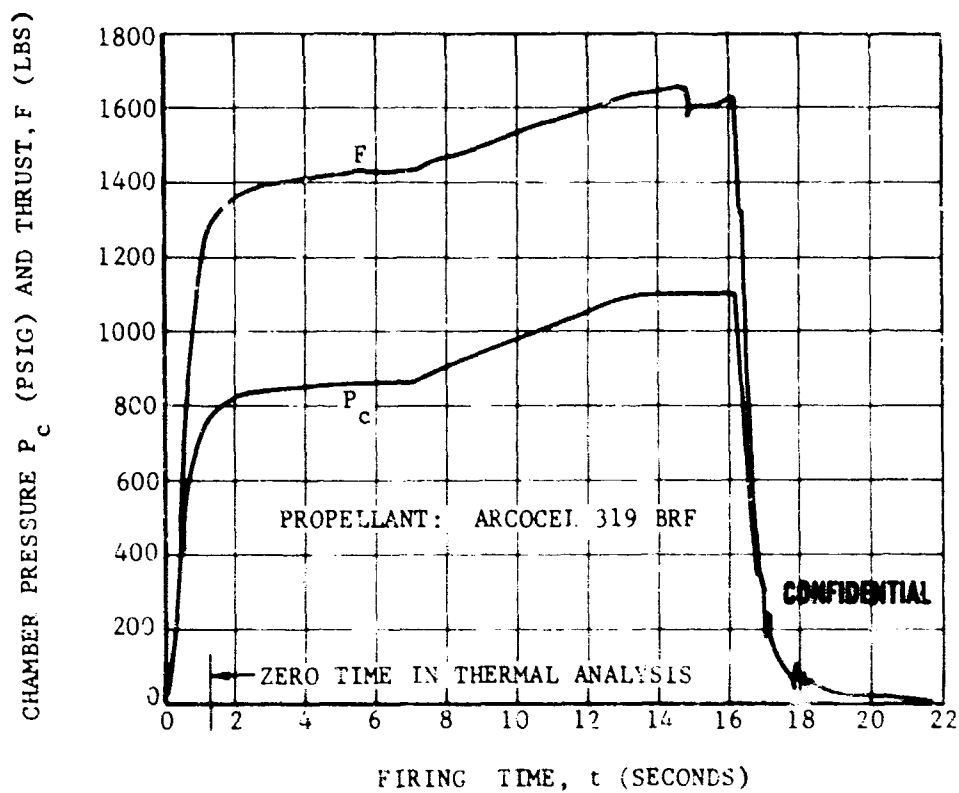
F04136 C

FIGURE 54.   CHAMBER PRESSURE AND THRUST VERSUS FIRING
TIME TEST T-3
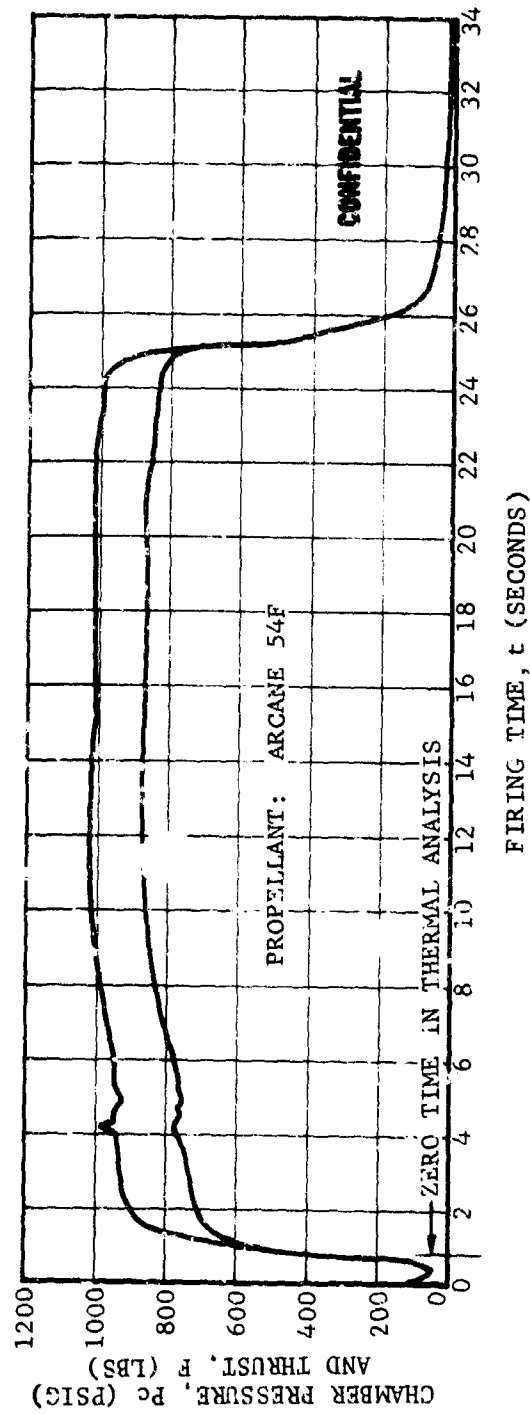
FO4137 C

FIGURE 55. CHAMBER PRESSURE AND THRUST VERSUS FIRING TIME TEST T-4
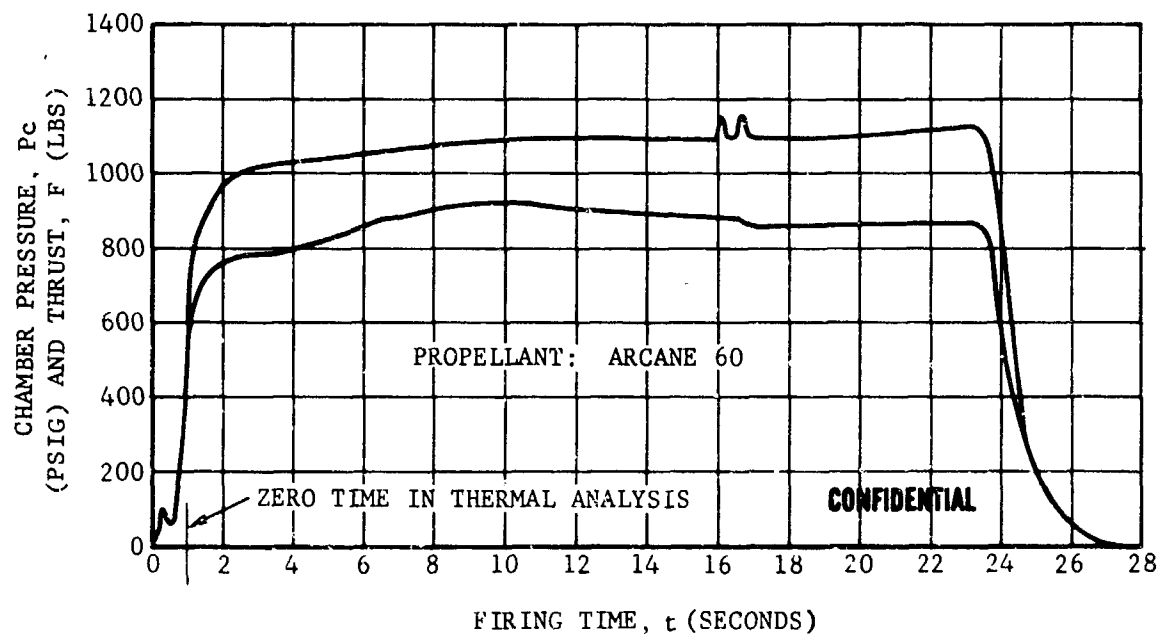
F04138 C

FIGURE 56. CHAMBER PRESSURE AND THRUST VERSUS FIRING TIME TEST T-5
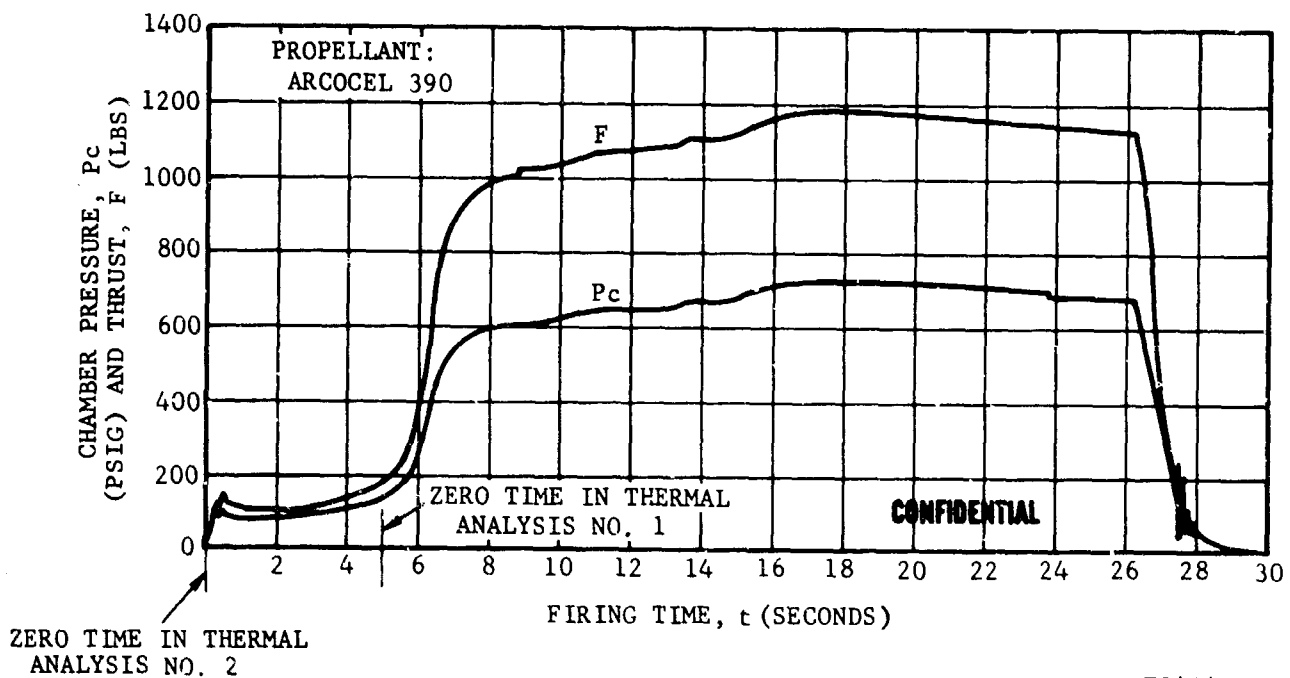
FIGURE 57. CHAMBER PRESSURE AND THRUST VERSUS FIRING TIME TEST T-6
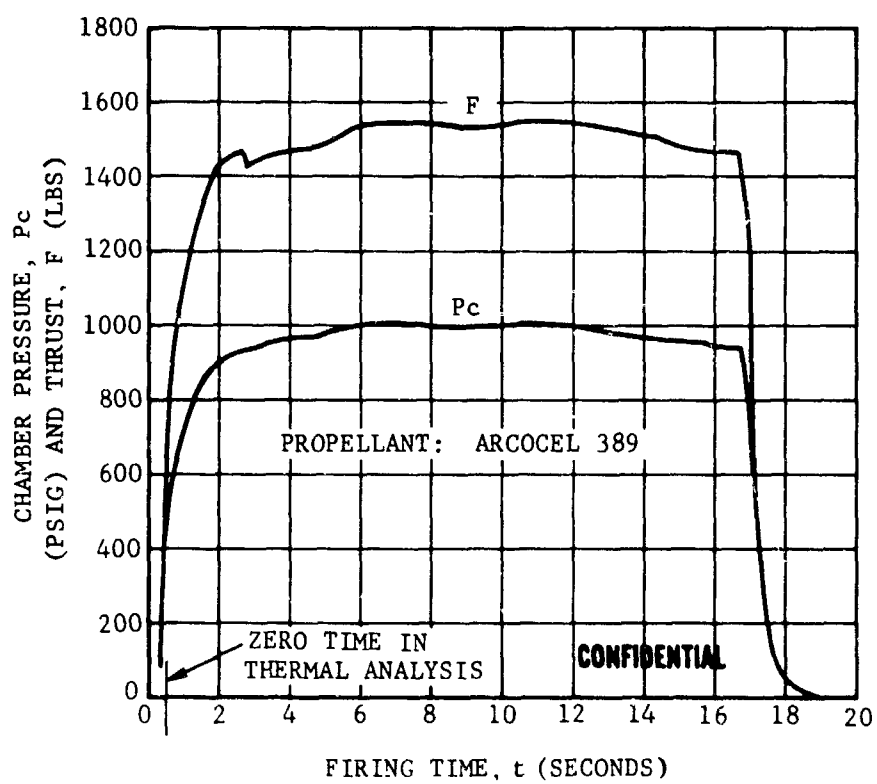
F04140 C

FIGURE 58. CHAMBER PRESSURE AND THRUST VERSUS FIRING TIME   TEST T-7

F04141 C
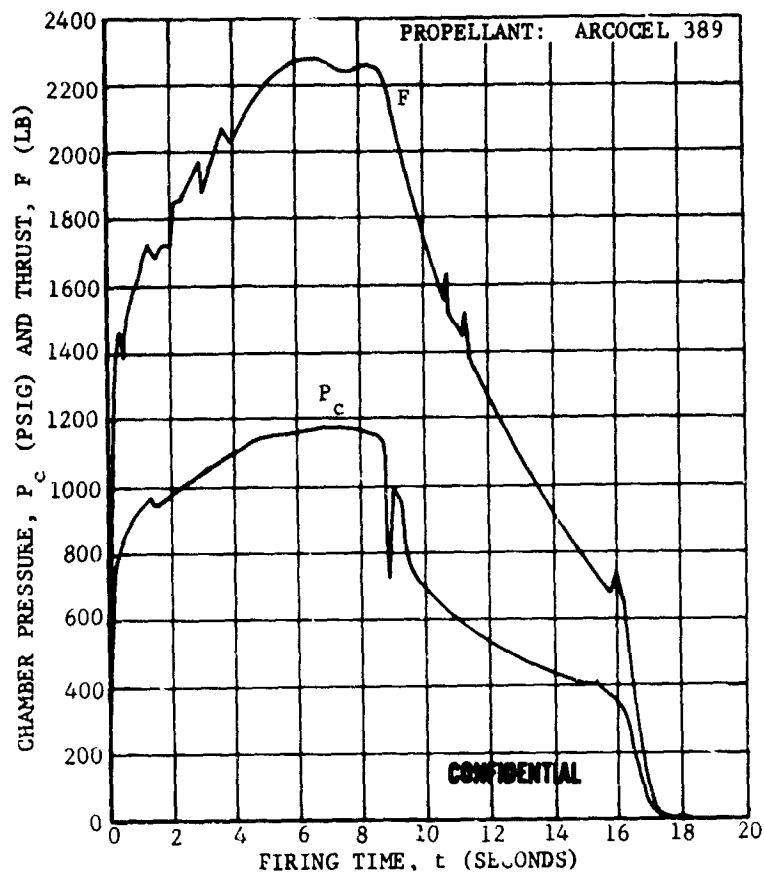
FIGURE 59. CHAMBER PRESSURE AND THRUST VERSUS FIRING TIME TEST T-8
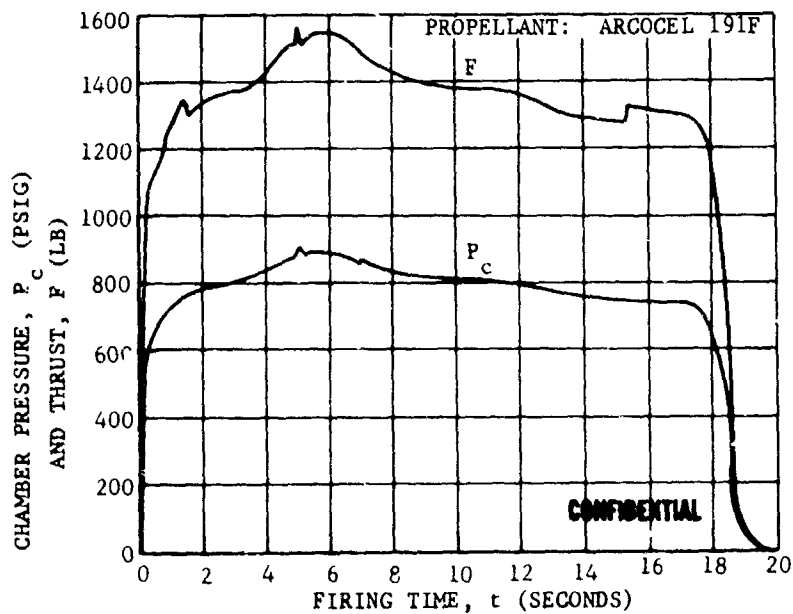
FIGURE 60. CHAMBER PRESSURE AND THRUST VERSUS FIRING TIME TEST T-9

FIGURE 61. CHAMBER PRESSURE AND THRUST VERSUS FIRING TIME TEST T-10

F08069C
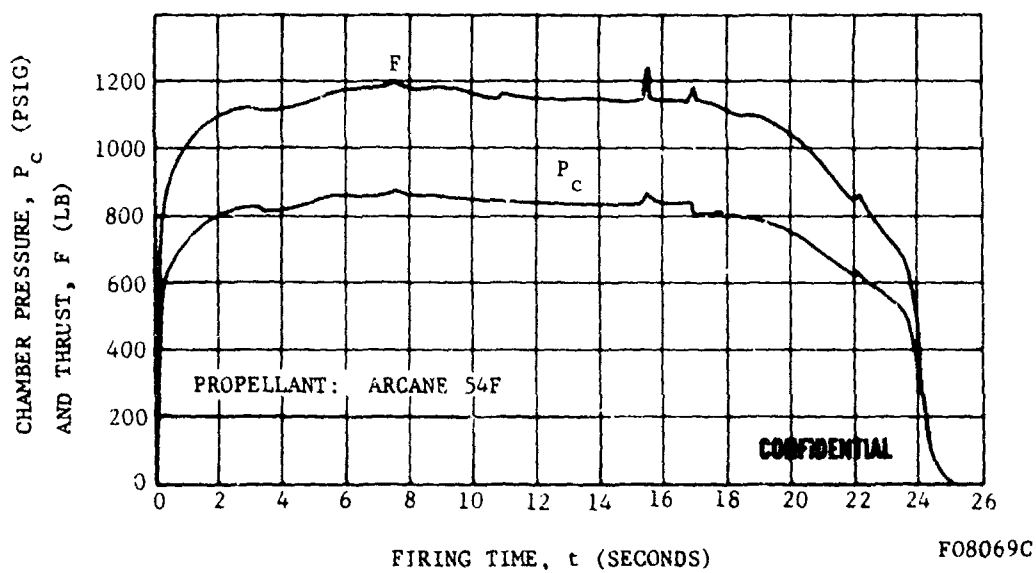
FIGURE 62. CHAMBER PRESSURE AND THRUST VERSUS FIRING TIME TEST T-11

FIGURE 61.   CHAMBER PRESSURE AND THRUST VERSUS FIRING TIME TEST T-10

FIGURE 62.   CHAMBER PRESSURE AND THRUST VERSUS FIRING TIME TEST T-11
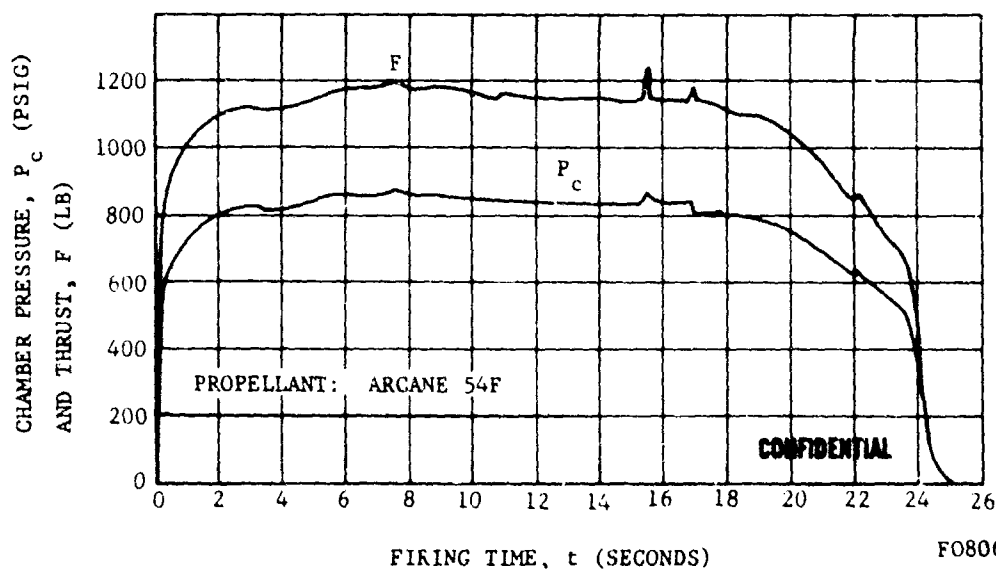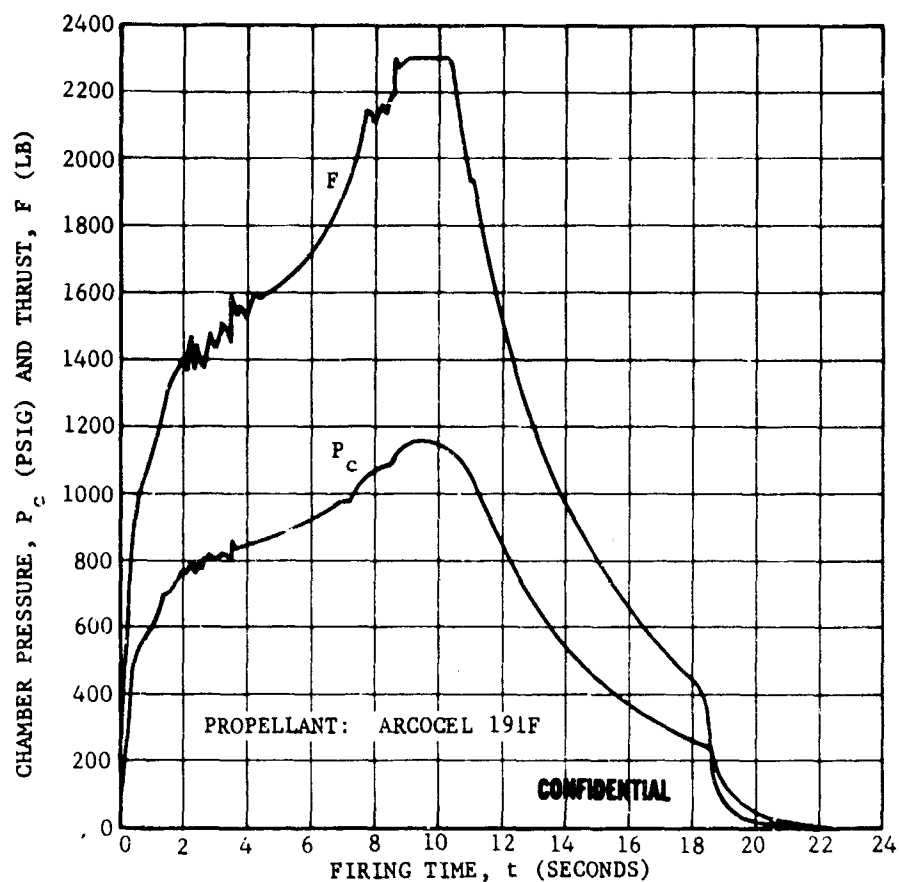
FIGURE 63.   CHAMBER PRESSURE AND THRUST VERSUS FIRING TIME TEST T-12
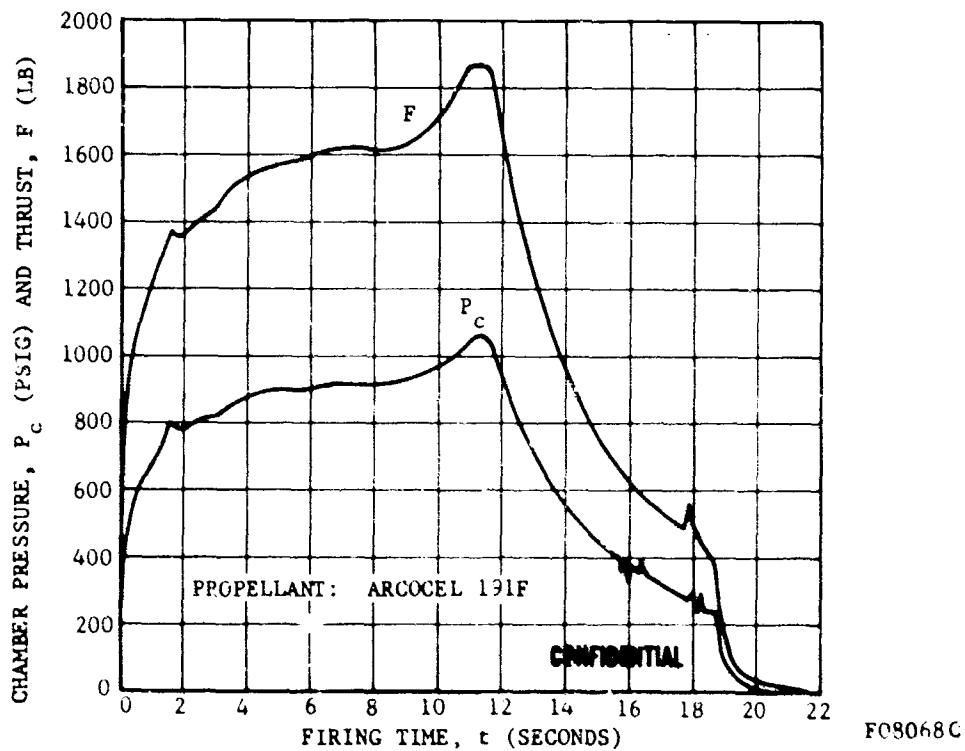
FIGURE 64.   CHAMBER PRESSURE AND THRUST VERSUS FIRING TIME TEST T-13

-231-
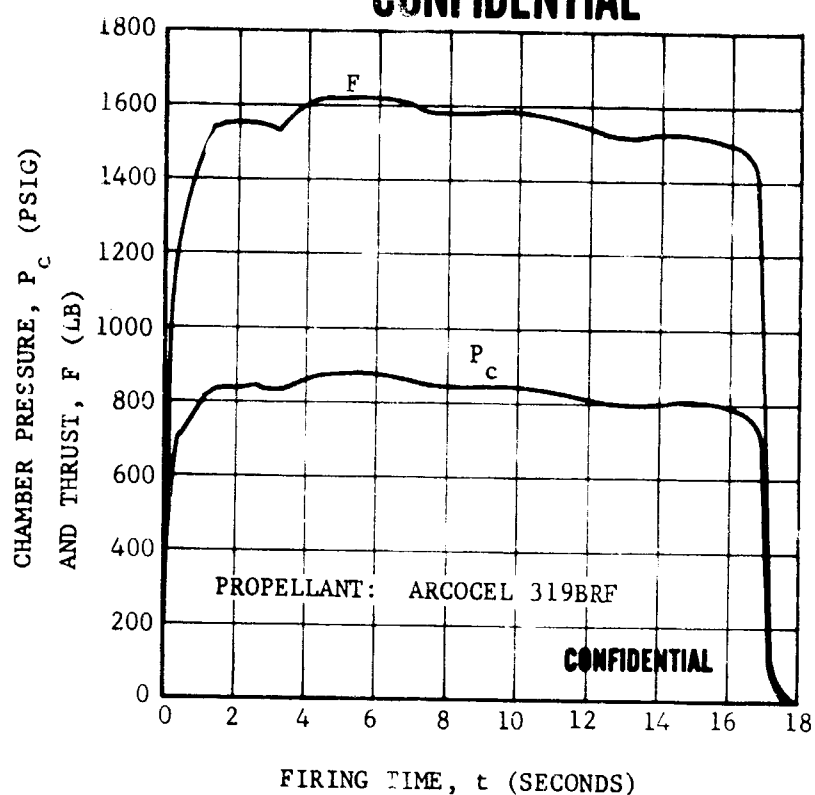
FIGURE 65. CHAMBER PRESSURE AND THRUST VERSUS FIRING TIME TEST T-14
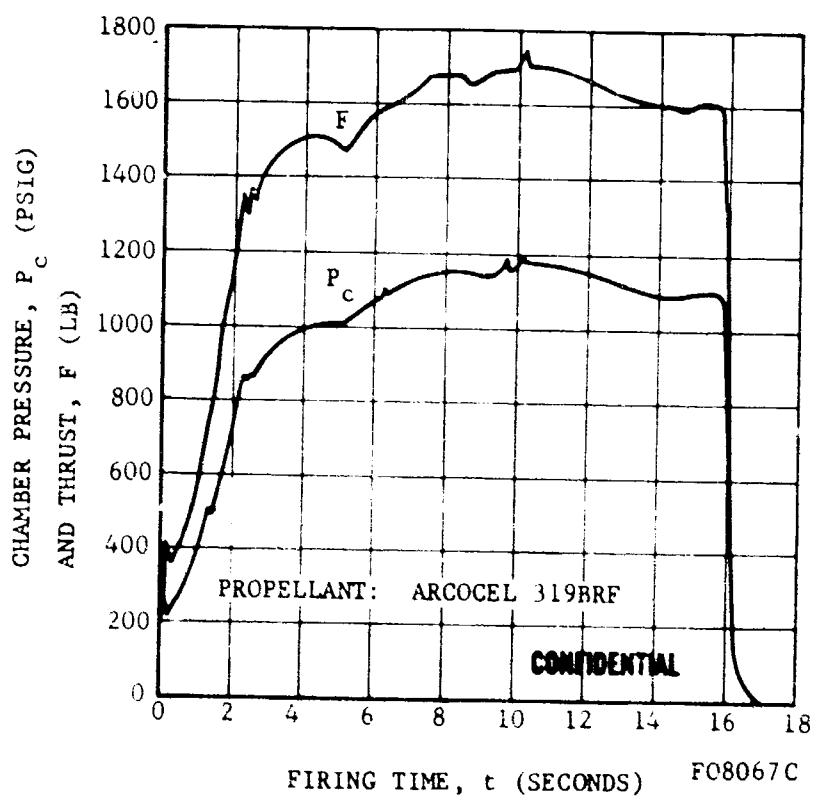
FIGURE 66. CHAMBER PRESSURE AND THRUST VERSUS FIRING TIME TEST T-15
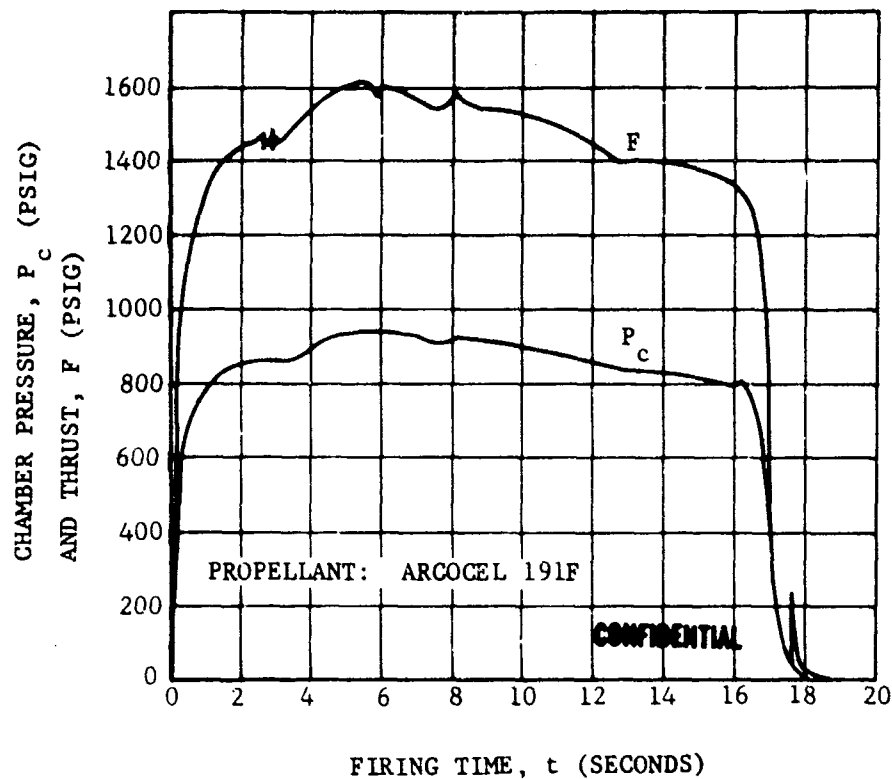
FIGURE 67. CHAMBER PRESSURE AND THRUST VERSUS FIRING TIME TEST T-16
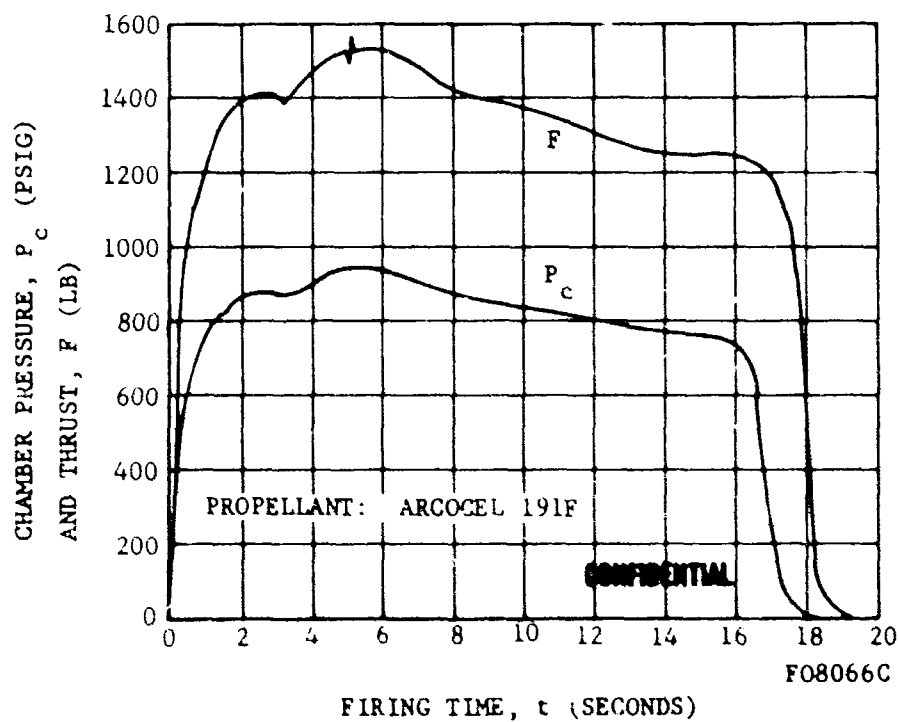
FIGURE 68. CHAMBER PRESSURE AND THRUST VERSUS FIRING TIME TEST T-17

-233-
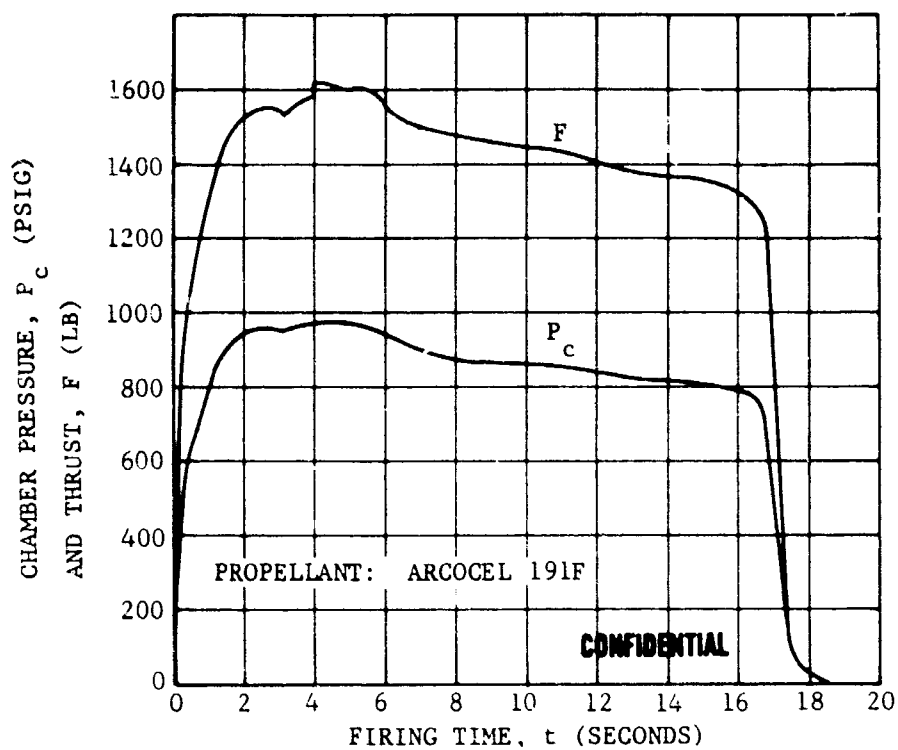
FIGURE 69. CHAMBER PRESSURE AND THRUST VERSUS FIRING TIME TEST T-18
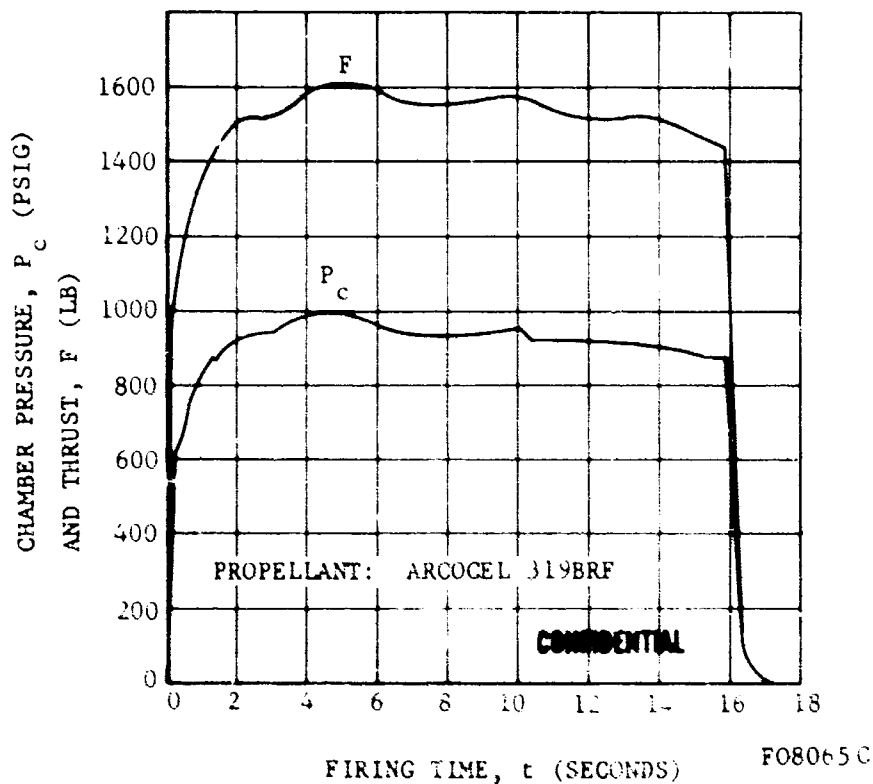
FIGURE 70. CHAMBER PRESSURE AND THRUST VERSUS FIRING TIME TEST T-19
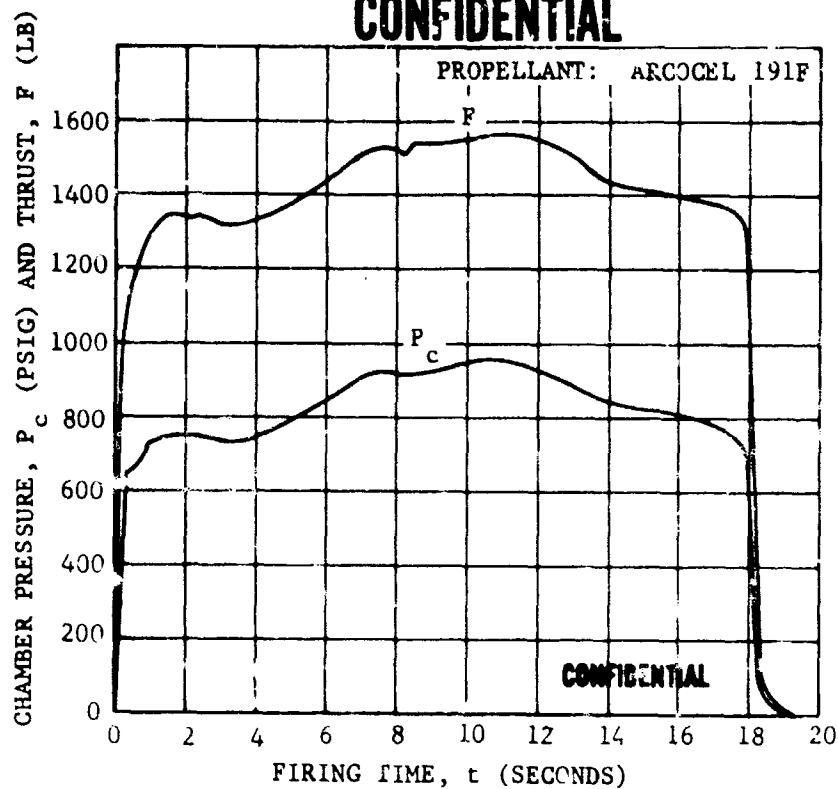
-234-

FIGURE 71. CHAMBER PRESSURE AND THRUST VERSUS FIRING TIME TEST T-20

F08064C

FIGURE 72. CHAMBER PRESSURE AND THRUST VERSUS FIRING TIME TEST T-21

FIGURE 71.   CHAMBER PRESSURE AND THRUST VERSUS FIRING TIME TEST T-20

F08064C
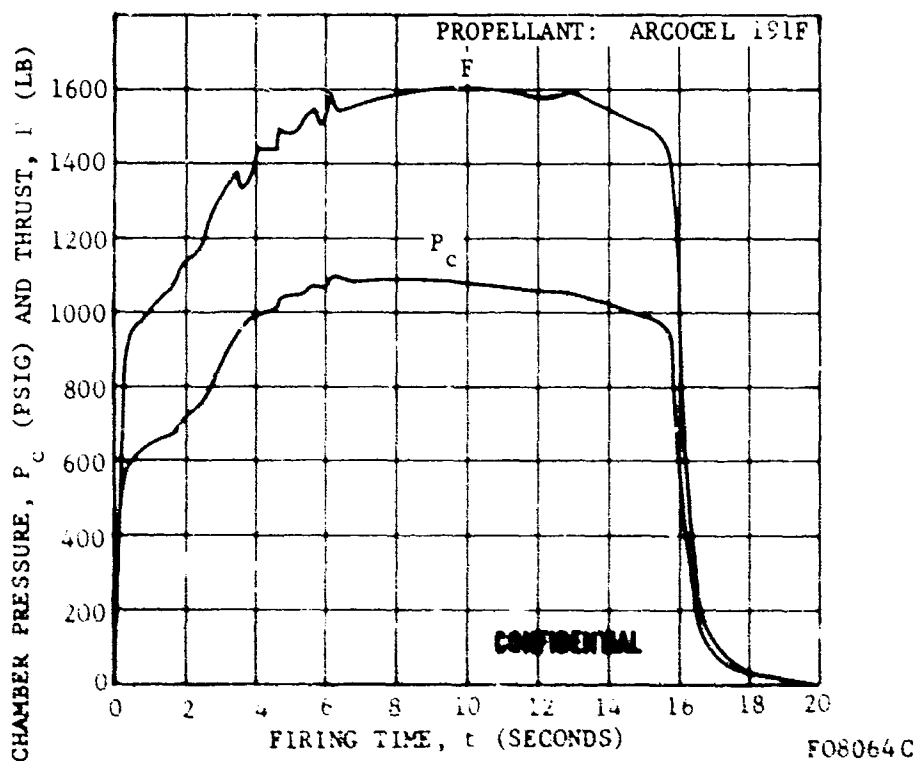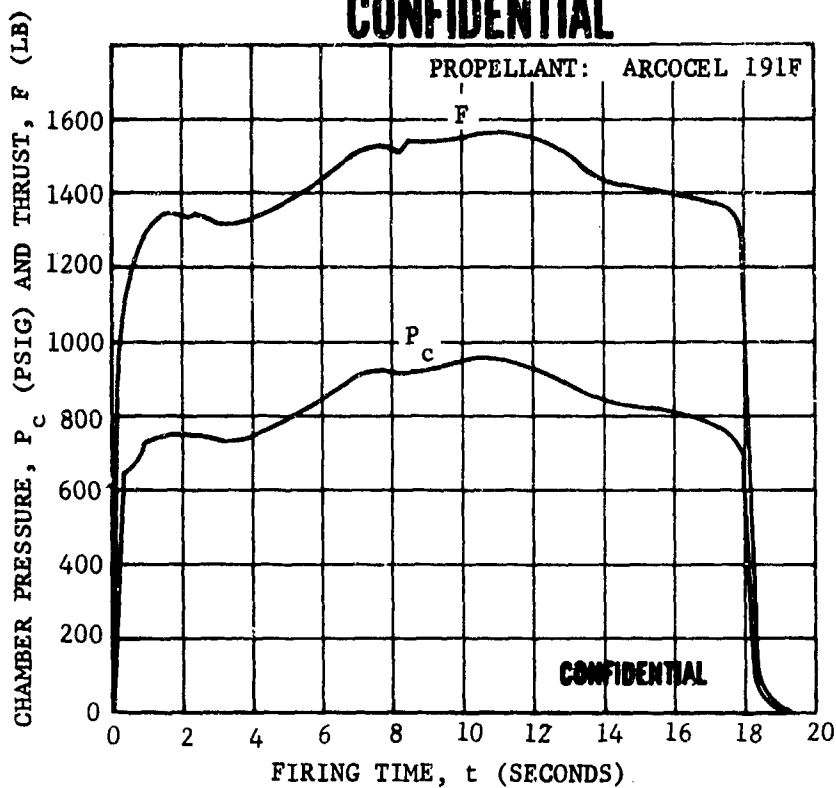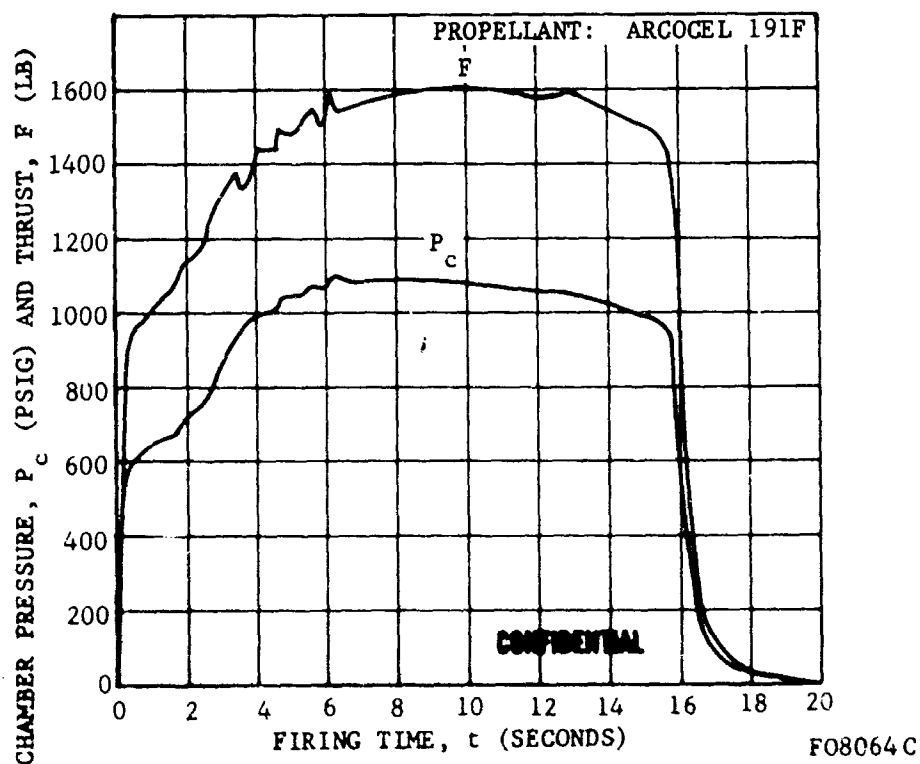
FIGURE 72.   CHAMBER PRESSURE AND THRUST VERSUS FIRING TIME TEST T-21
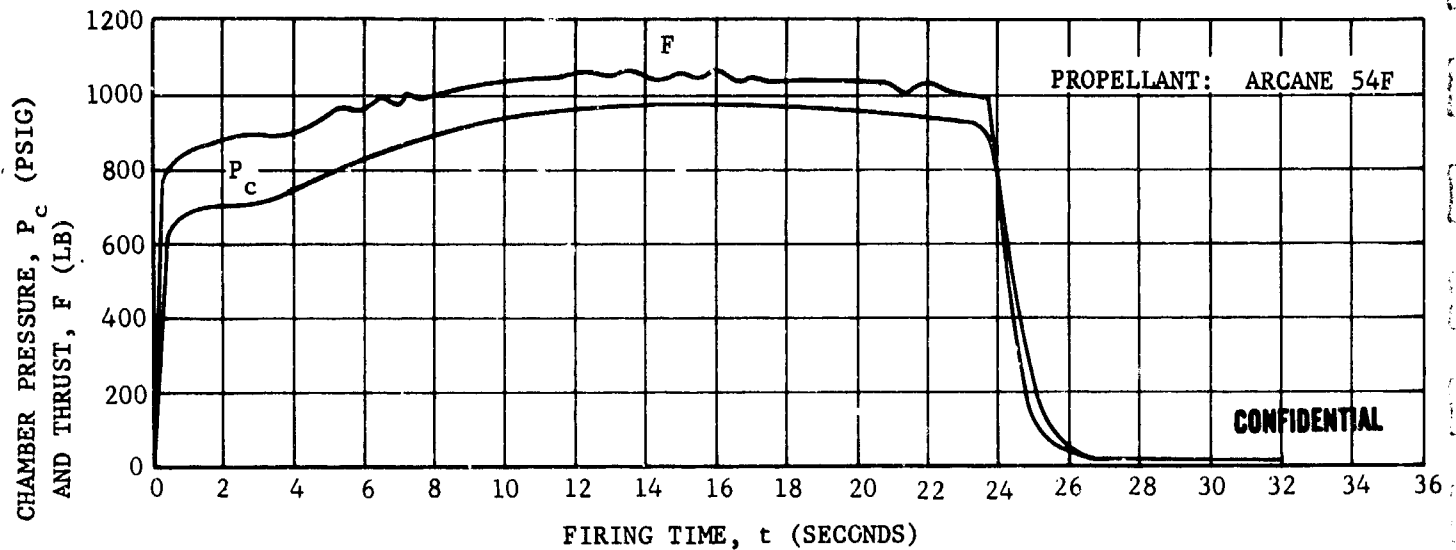
FIGURE 73. CHAMBER PRESSURE AND THRUST VERSUS FIRING TIME TEST T-22

F08063C
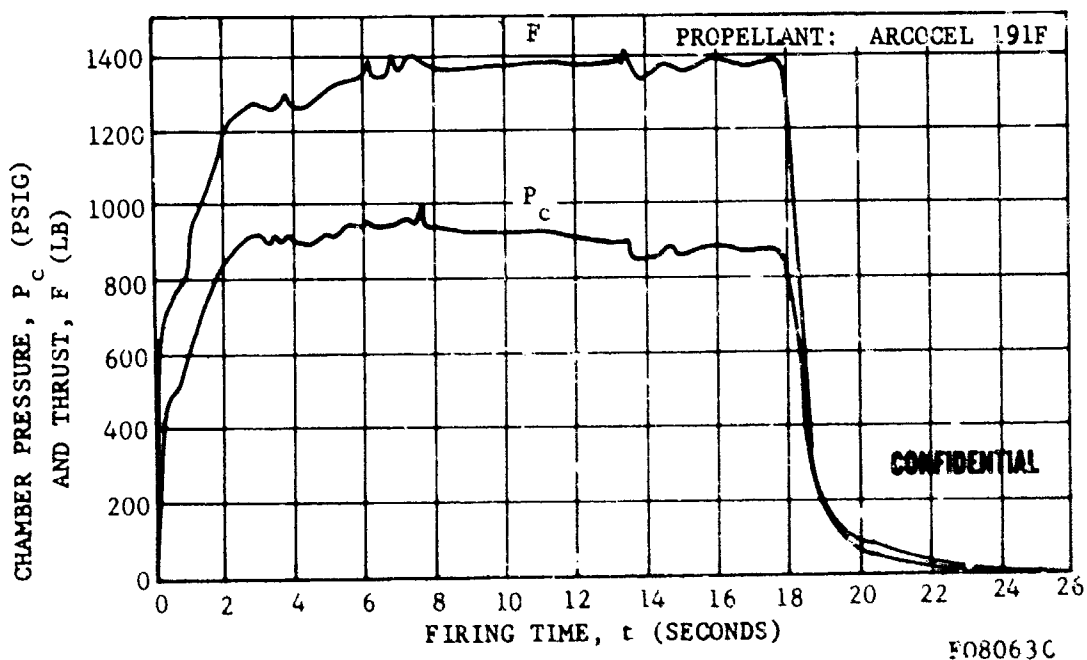
FIGURE 74. CHAMBER PRESSURE AND THRUST VERSUS FIRING TIME TEST T-23
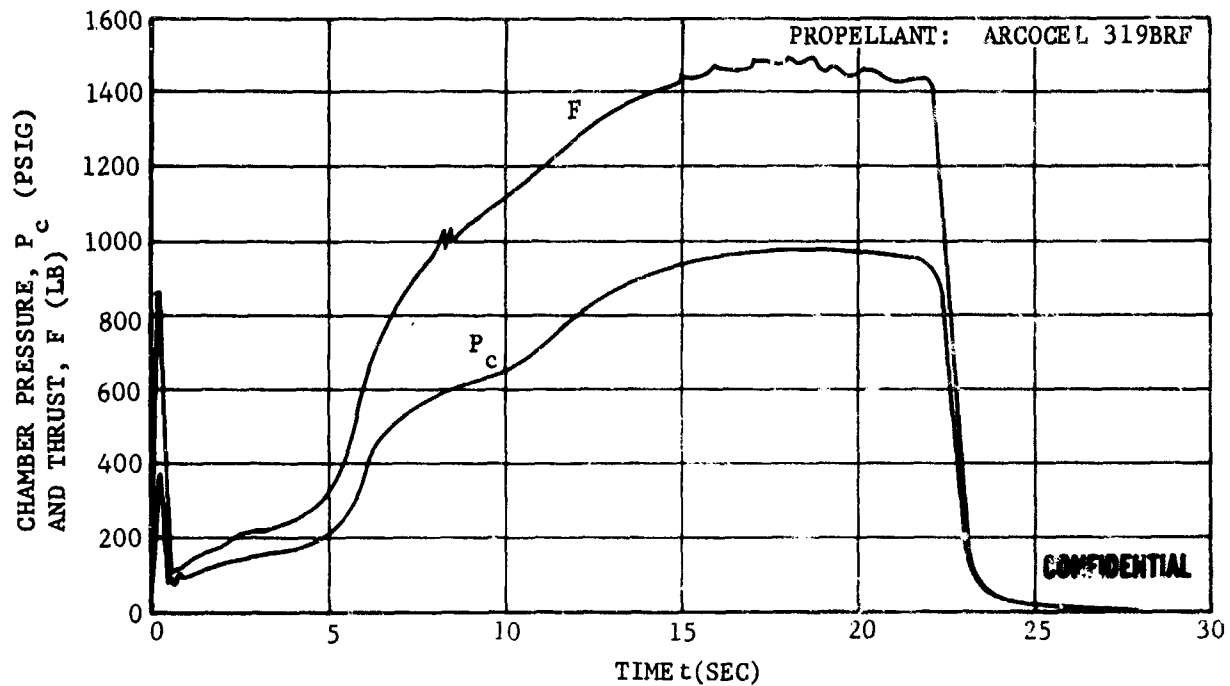
FIGURE 75. CHAMBER PRESSURE AND THRUST VERSUS FIRING TIME TEST T-24
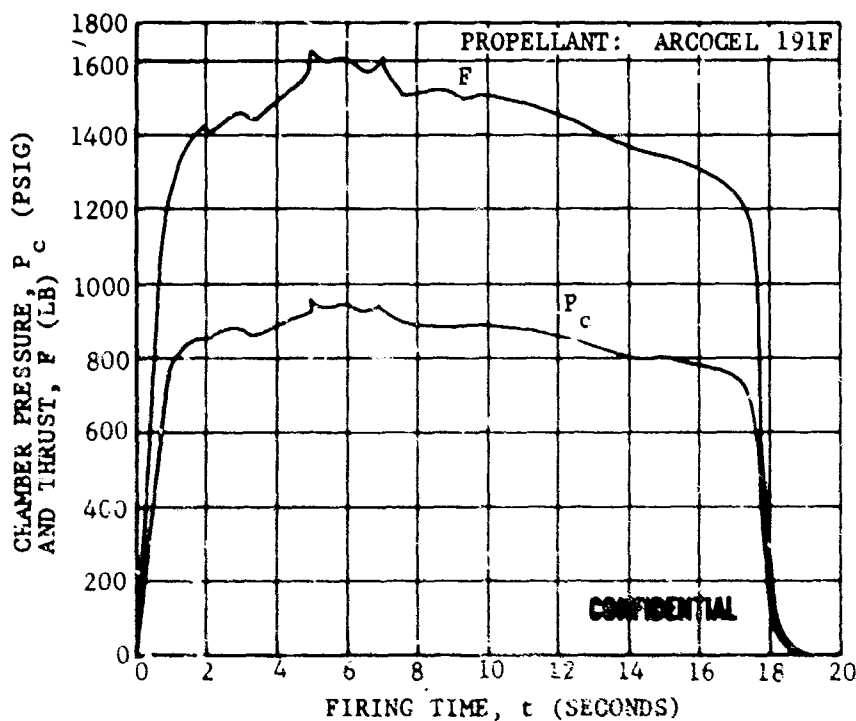
FIGURE 76. CHAMBER PRESSURE AND THRUST VERSUS FIRING TIME TEST T-25
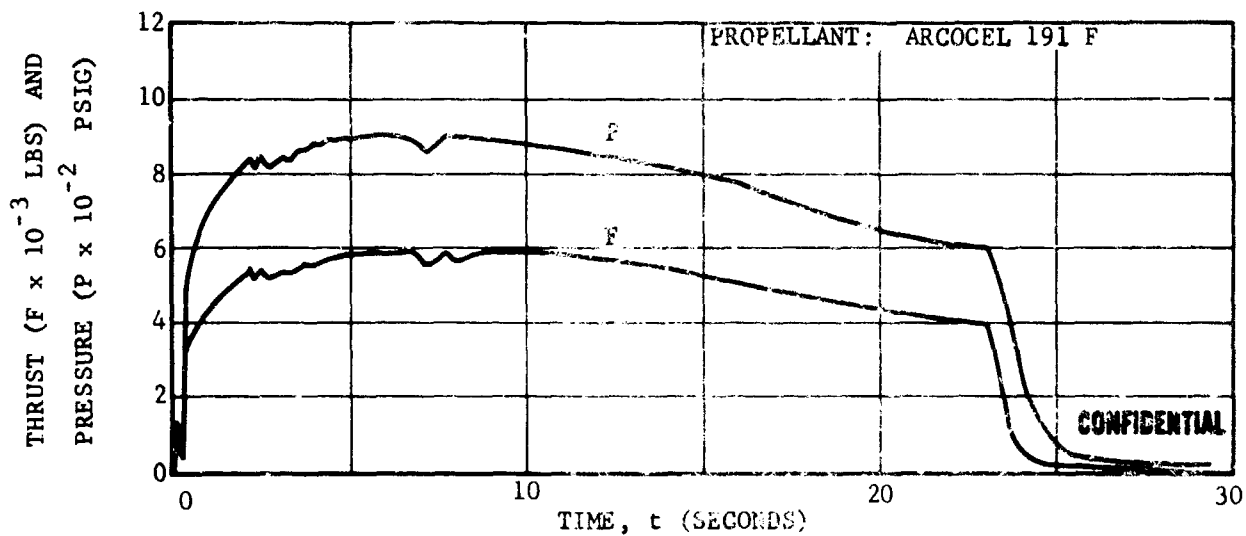
FIGURE 77. CHAMBER PRESSURE AND THRUST VERSUS FIRING TIME TEST T-51
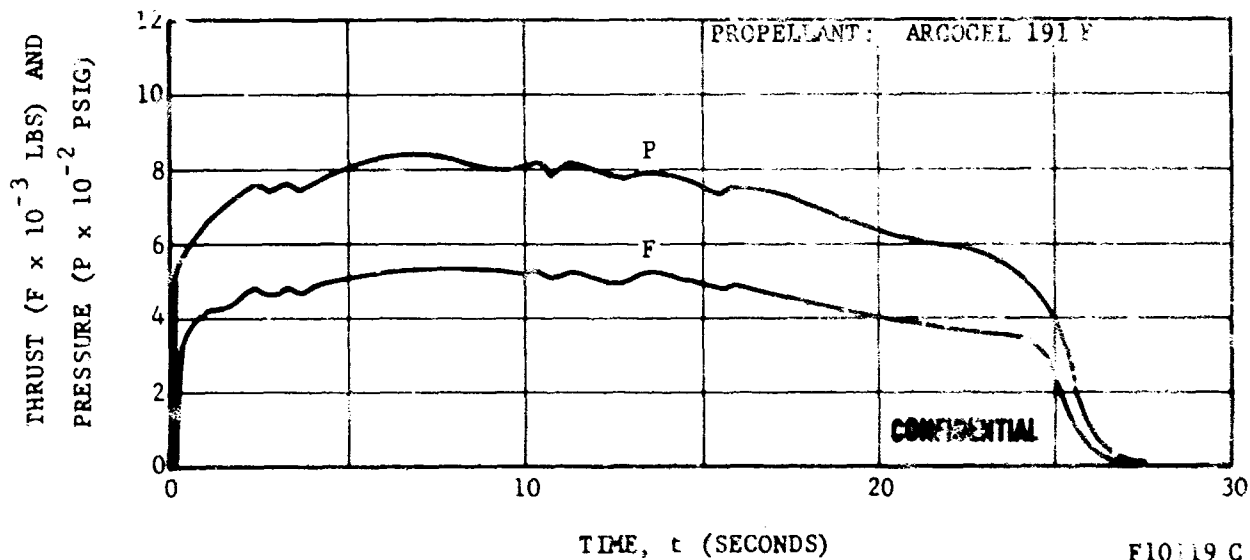
FIGURE 78. CHAMBER PRESSURE AND THRUST VERSUS FIRING TIME TEST T-53
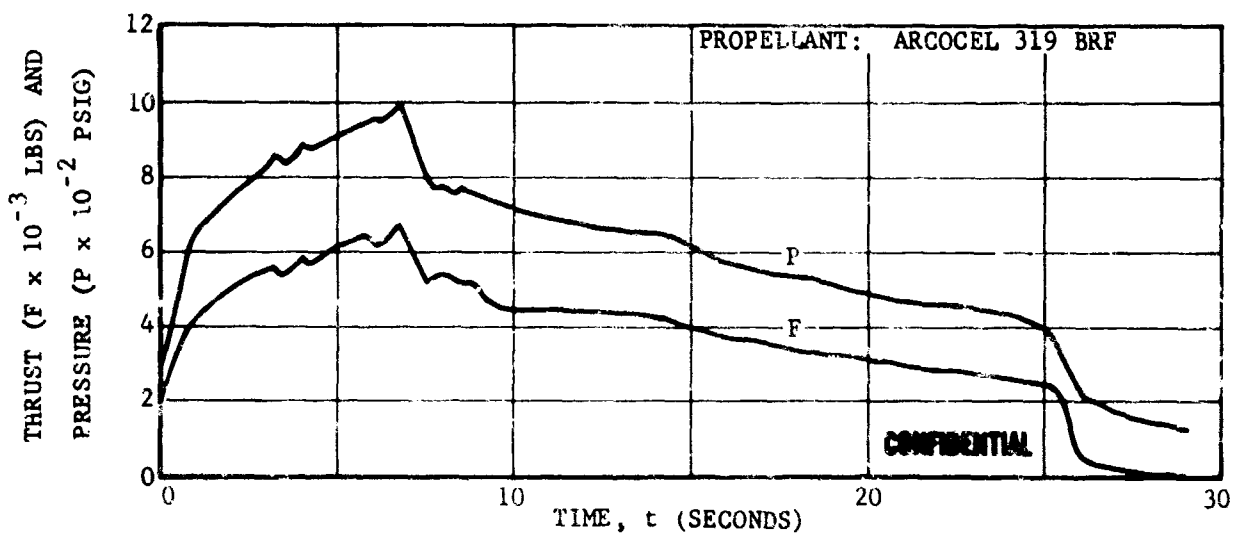
FIGURE 79. CHAMBER PRESSURE AND THRUST VERSUS FIRING TIME TEST T-52

F10120 C
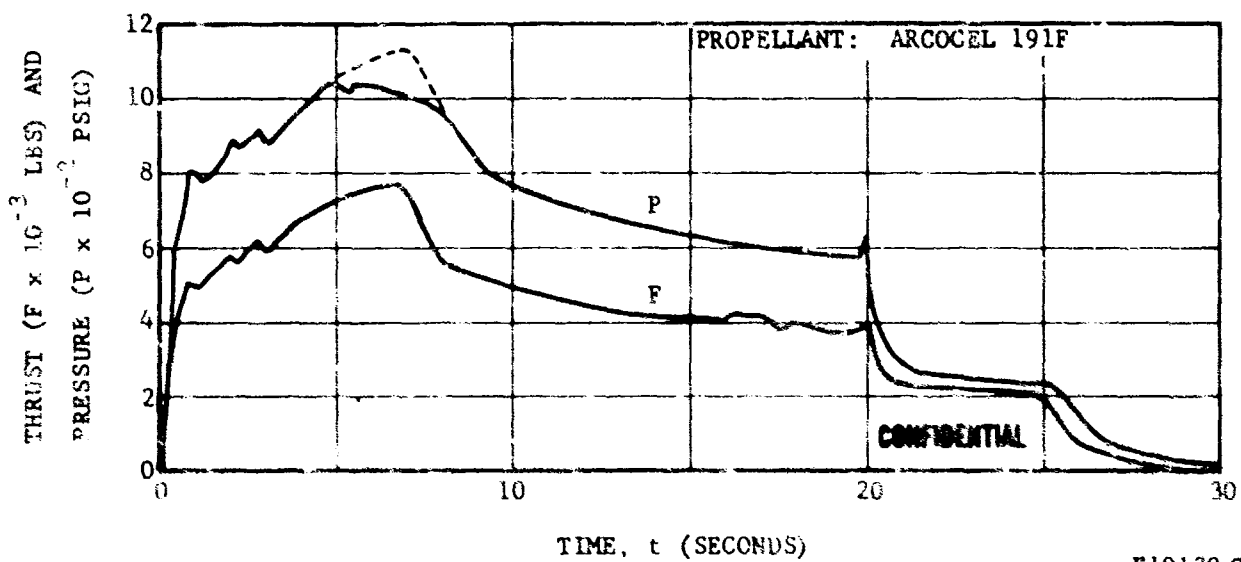
FIGURE 80. CHAMBER PRESSURE AND THRUST VERSUS FIRING TIME TEST T-54

APPENDIX IV (C)

NOZZLE CROSS SECTIONS

This appendix contains selected photographs of the tested nozzles and aft closure insulators. Over 100 additional photographs of the hardware, in the as received condition and with loose deposits removed, may be found in Sections 3.4 of References 2, 3 and 4. Section 3.4 of Reference 4 also shows cross sections of 5 Aerojet ADOBE nozzles.

Figures 81 through 88 show hardware from Tests T-1 through T-7. Each of the seven program propellants was used in these otherwise identical tests. The nearly perfect nozzle condition and most of the residual oxide deposits can be seen. Figure 82 shows an aft closure insulation cross section. It was typical of this series of tests that no char erosion could be measured. This was apparently the result of oxide deposition protection which also reduced the extent of charing. Note the radial-axial crack in the upstream washer in Figure 88. Also note the char profile in the nozzle throat insulation sections. There are no significant differences in the appearance of the nozzles tested with beryllium or aluminum propellants.

Figures 89 through 96, 102, 103 and 104 show hardware from the grain design test series (T-8 through T-11, T-14 and T-15). The Type I grain (circular port) was used with the two CMBD and Arcane 54F composite formulations on Tests T-9, T-11 and T-14. The nozzles are shown in Figures 92, 96 and 102 were in essentially the same condition as those from the end burning grain series (T-1 through T-7). The aft closure cross section in Figure 91 shows typical erosion of the asbestos phenolic with the Type I grains. Figures 89 and 93 show the aft closure insulators from Tests T-8 and T-10. These are typical of the Type II, slotted grain tests. Note that grooving opposite the grain slot was less pronounced on T-8 which used the aluminum analog of the Arcocel 191F tested in T-10. As shown in Figure 90, there

-240-

was no observable grooving of the T-8 nozzle. Figures 94 and 95 show the top and bottom halves of the T-10 nozzle. While two grooves could be seen in the ATJ entrance section, only the bottom groove extended into the throat section of the T-10 nozzle. Figures 103 and 104 show the grooving incurred on Test T-15, the only test in which the Type III slotted grain design was used.

Figures 97 through 101 show the nozzles from Tests T-12 and T-13, the nozzle contour subseries. The condition of the carbon cloth/ATJ nose cap, Figure 97, was typical of the shallow submerged design used in the small motor tests. Two distinct grooves were formed in the ATJ entrance section, Figure 98, but only the bottom groove was pronounced in the throat section of the T-12 nozzle, Figure 99. The effect of the gas leak on the T-13 aft closure and nozzle can be seen in Figures 100 and 101. The bottom groove, opposite the grain slot, can also be seen in Figure 101.

The nozzles from the materials evaluation subseries, T-16 through T-20, are shown in Figures 105 through 111. The Type I grain design was used on all of these tests. The Arcocel 191F propellant was used on all but T-19 (Arcocel 319BRF) and conventional nozzle contours were used on all but T-18 (submerged). No cracks were found in the T-16 tungsten insert; the others were cracked axially during machining. The T-17 insert, Figures 106 and 107, developed an axial surface groove which was associated with the original axial crack. It also developed a circumferential crack at the throat during or after the test. This insert was preceded by a carbon cloth inlet section. The T-18 nozzle, Figures 108 and 109, was in excellent condition as was the T-19 nozzle, Figure 110. Figure 111 shows the typical condition of the carbon cloth entrance section used on T-17 and T-20.

The close end burner series, Tests T-21 through T-24, were designed to adversely effect the metal combustion efficiency of the beryllium propellants. The nozzles are shown in Figures 112 through 115. These nozzles were in excellent condition. The T-25 nozzle was designed with a thicker throat heat sink and was tested with a Type I grain. The nozzle was in excellent condition as shown in Figure 116.

The larger development nozzles are shown in greater detail in Figures 117 through 134. The aft closure insulator from Test T-51 is shown in Figures 117 and 118. The condition of this insulator is also typical of those from Tests T-53 and T-54. Note that the insulator was nearly burned through at the top in line with the grain slot. Considerably less erosion occurred on Test T-52 (Arcocel 319BRF, hangfire) as shown in Figure 123. The extensive erosion of the asbestos phenolic nose cap insulation and the ATJ nose cap slots can be seen in Figures 119, 124, 126, 131, and 132 (all four tests). The grooves in the nozzle throat sections of the T-51 and T-53 nozzles are shown in Figures 120, 122, 127 and 129. The groove extension into the exit cone of the T-53 nozzle is shown in Figure 130. The unaffected sections of the T-51, T-52 and T-53 nozzles are shown in Figures 121, 125 and 128 for

comparison. The condition of the T-54 nozzle, Figures 132 and 133 was essentially the same as the others, except for the missing tungsten inserts. The extent of insert deformation and surface carbide formation can be seen in Figure 134. Note that the tungsten insert was expelled from the motor 20 seconds after ignition.

FIGURE 81. NOZZLE FROM TEST T-1 - CROSS SECTION

FIGURE 82. SECTION OF ASBESTOS-PHENOLIC AFT CLOSURE FROM TEST T-1
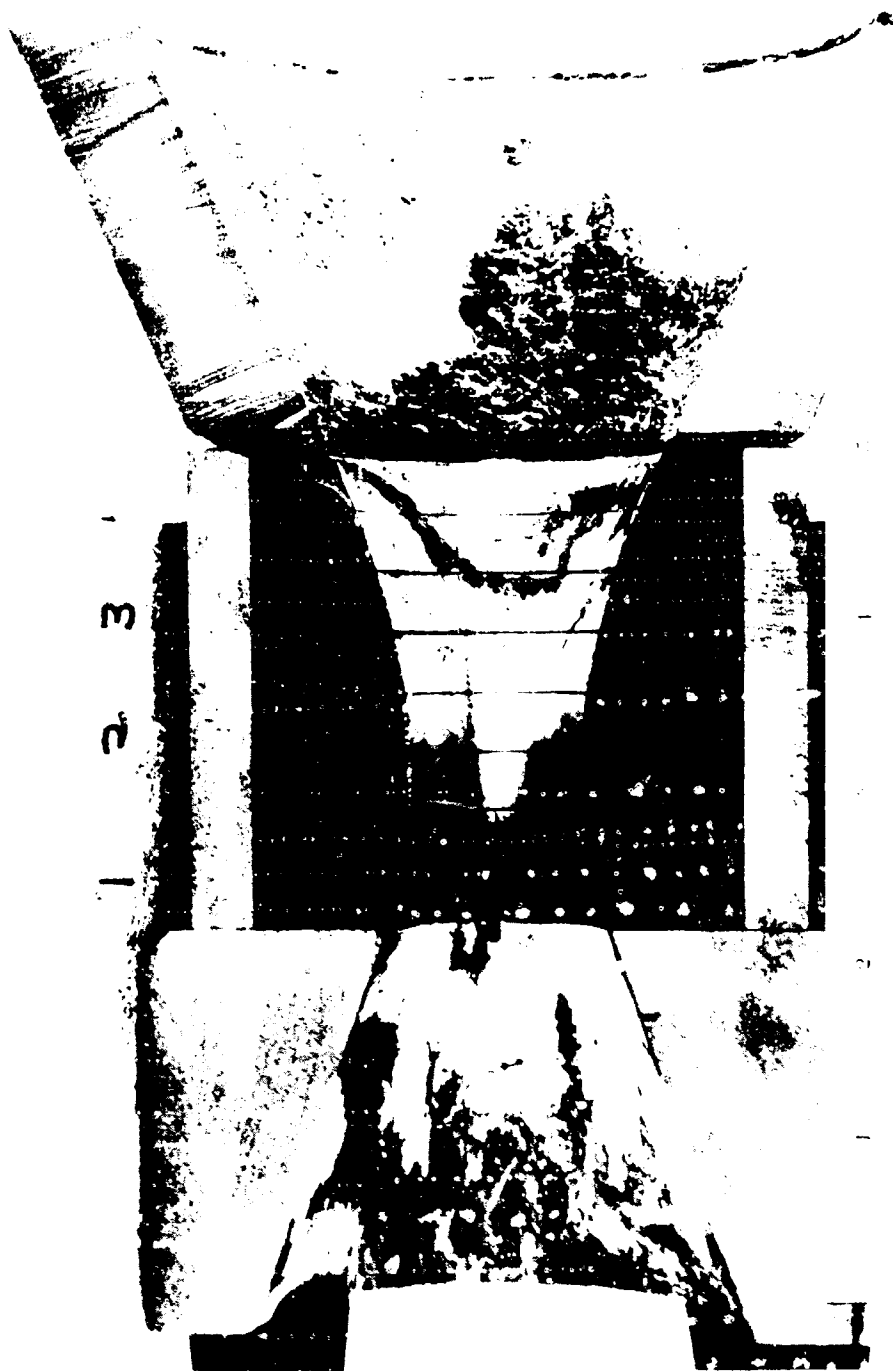
FIGURE 83. NOZZLE FROM TEST T-2 - CROSS SECTION

FIGURE 84. NOZZLE FROM TEST T-3 - CROSS SECTION

FIGURE 85. NOZZLE FROM TEST T-4 - CROSS SECTION

FIGURE 86. NOZZLE FROM TEST T-5 - CROSS SECTION

CONFIDENTIAL
FO4080

-248-

FIGURE 87. NOZZLE FROM TEST T-6 - CROSS SECTION

CONFIDENTIAL

FO4085 C

FIGURE 88. NOZZLE FROM TEST T-7 - CROSS SECTION

FIGURE . AFT CLOSURE INSULATOR - TEST 1

FIGURE 90. NOZZLE FROM TEST T-8 - CROSS SECTION

ORIGINAL
CONTOUR
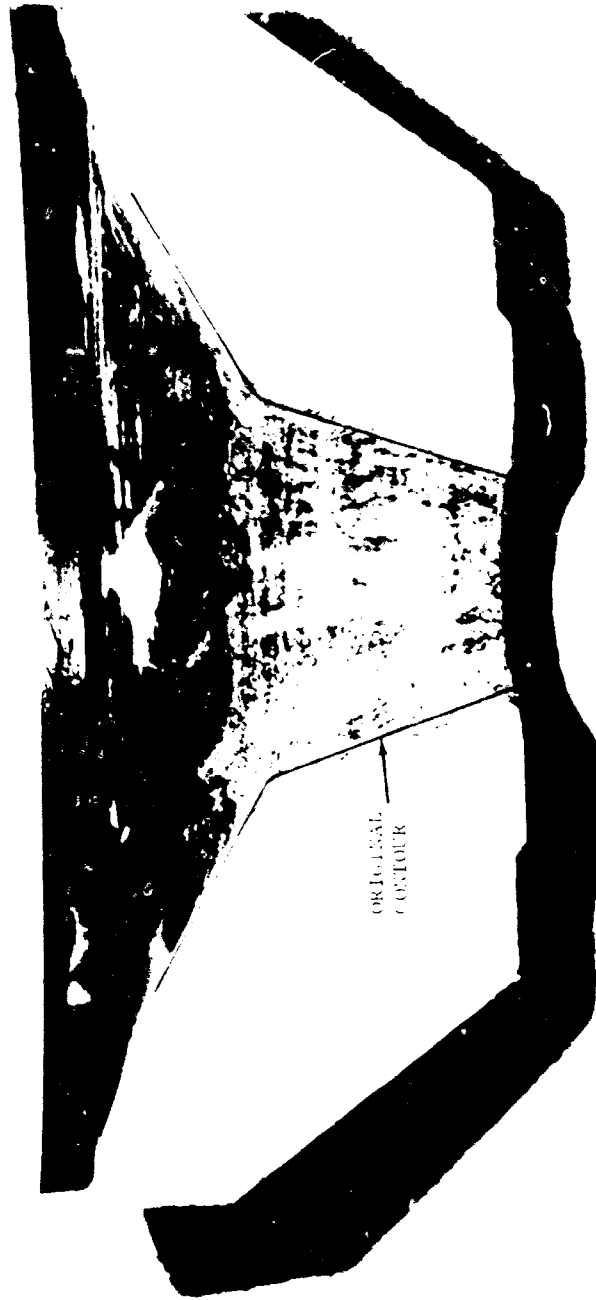
FIGURE 91. AFT CLOSURE INSULATOR CROSS SECTION - TEST T-9
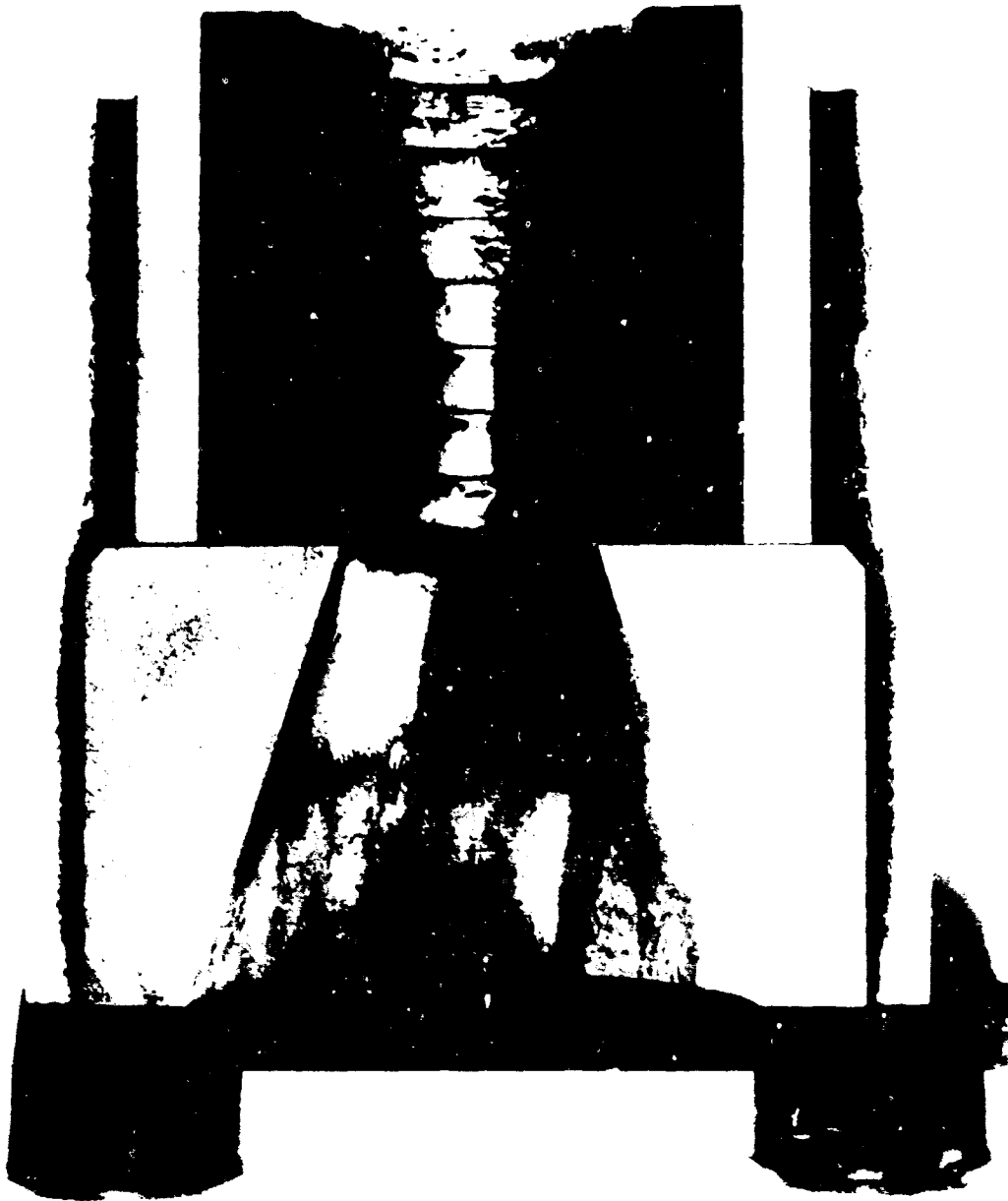
FIGURE 93. AFT CLOSURE INSULATOR - TEST T-19

FIGURE 94. NOZZLE FROM TEST T-10 - CROSS SECTION (TOP HALF)

GROOVE AREA →

FLOW →

FIGURE 95. NOZZLE FROM TEST T-10 - CROSS SECTION (BOTTOM HALF)

FIGURE 96. NOZZLE FROM TEST T-11 - CROSS SECTION
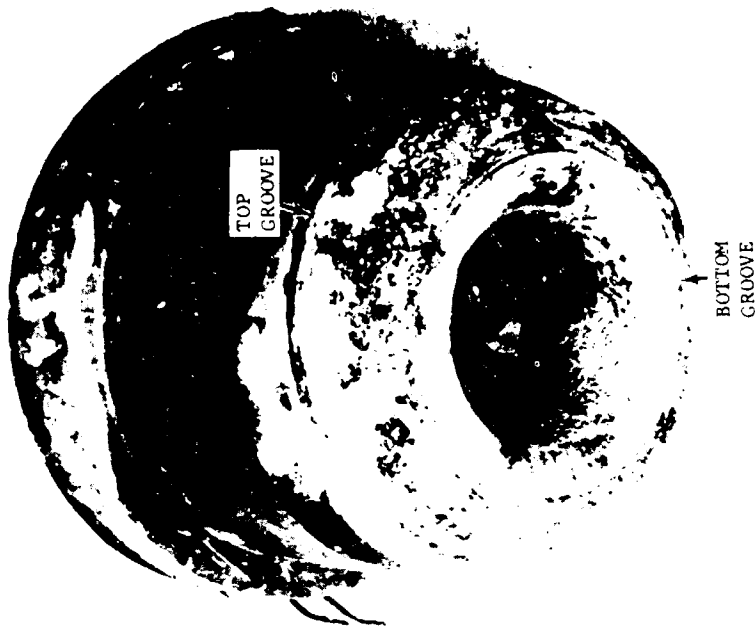
FIGURE 97. SUBMERGED NOZZLE FROM TEST T-12 (SOOT REMOVED)

F07085 C

FIGURE 98. ATJ GRAPHITE ENTRANCE CONE - TEST T-12

BOTTOM
GROOVE

FIGURE 99. NOZZLE THROAT SECTION - TEST T-12 (THROAT APPROACH VIEW)

- 293 -

FIGURE 100. AFT CLOSURE INSULATOR DAMAGE - TEST T-13

CONFIDENTIAL

F07091 C

-262-

TOP

BURN
THROUGH
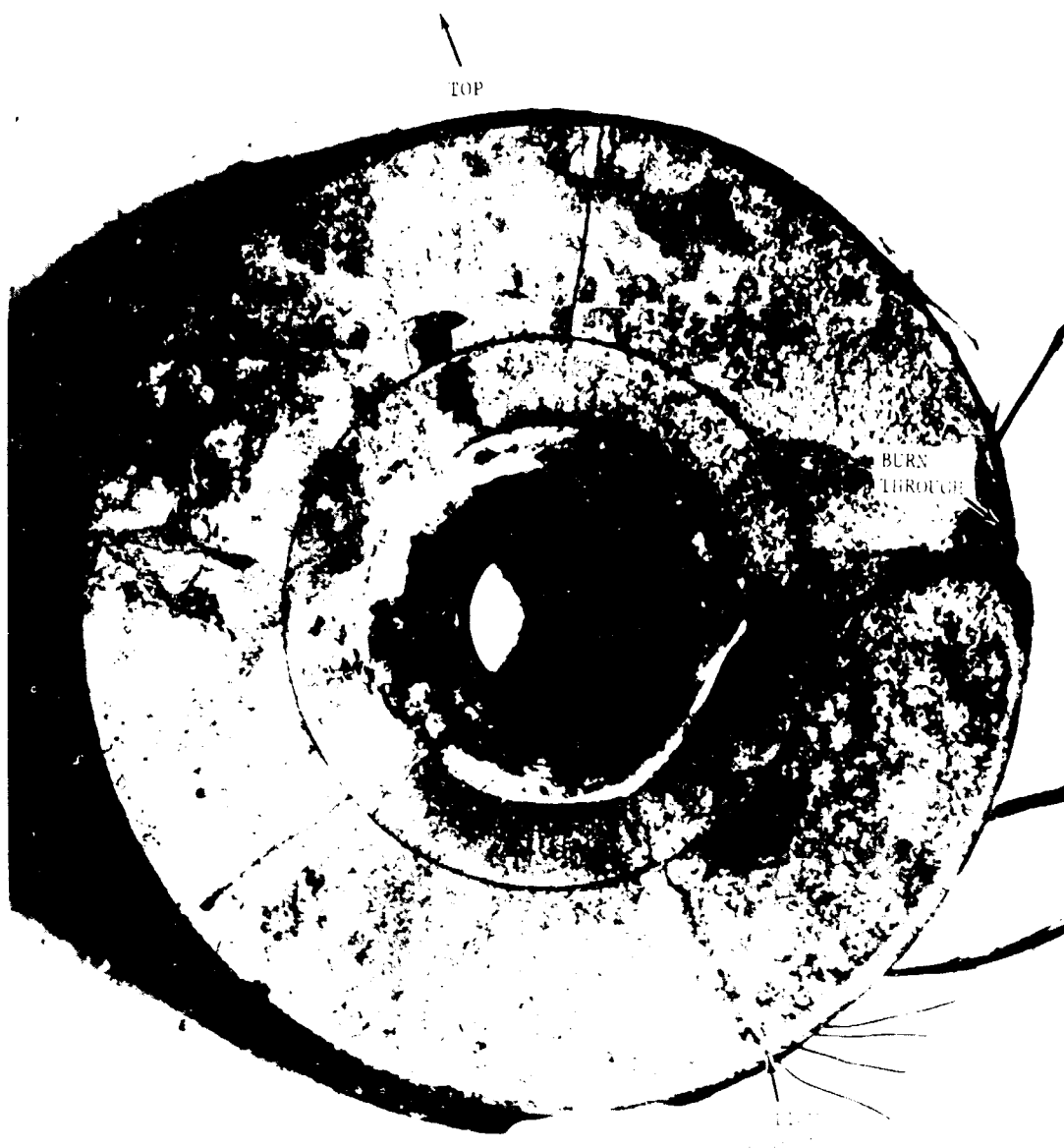
FIGURE 1-1. NOZZLE FROM TEST T-15 - ENTRANCE CONE VIEW (LOOSE DEPOSITS REMOVED)

FIGURE 102. NOZZLE FROM TEST T-1. - CROSS SECTION

FIGURE 141. DOUBLE DRUM TEST T-1 - FWD AT AFTER-40° VIEW

FIGURE 104. NOZZLE FROM TEST T-1) - CROSS SECTION
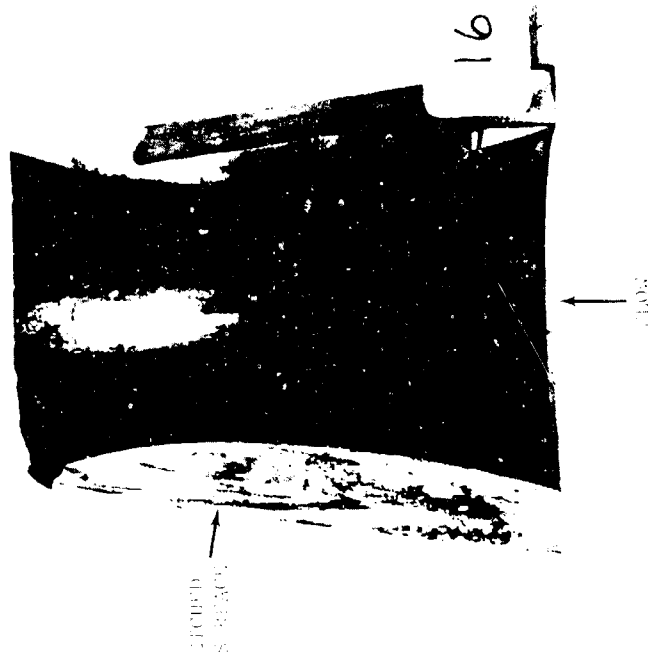
FIGURE 105. TUNGSTEN INSERT - TEST T-16
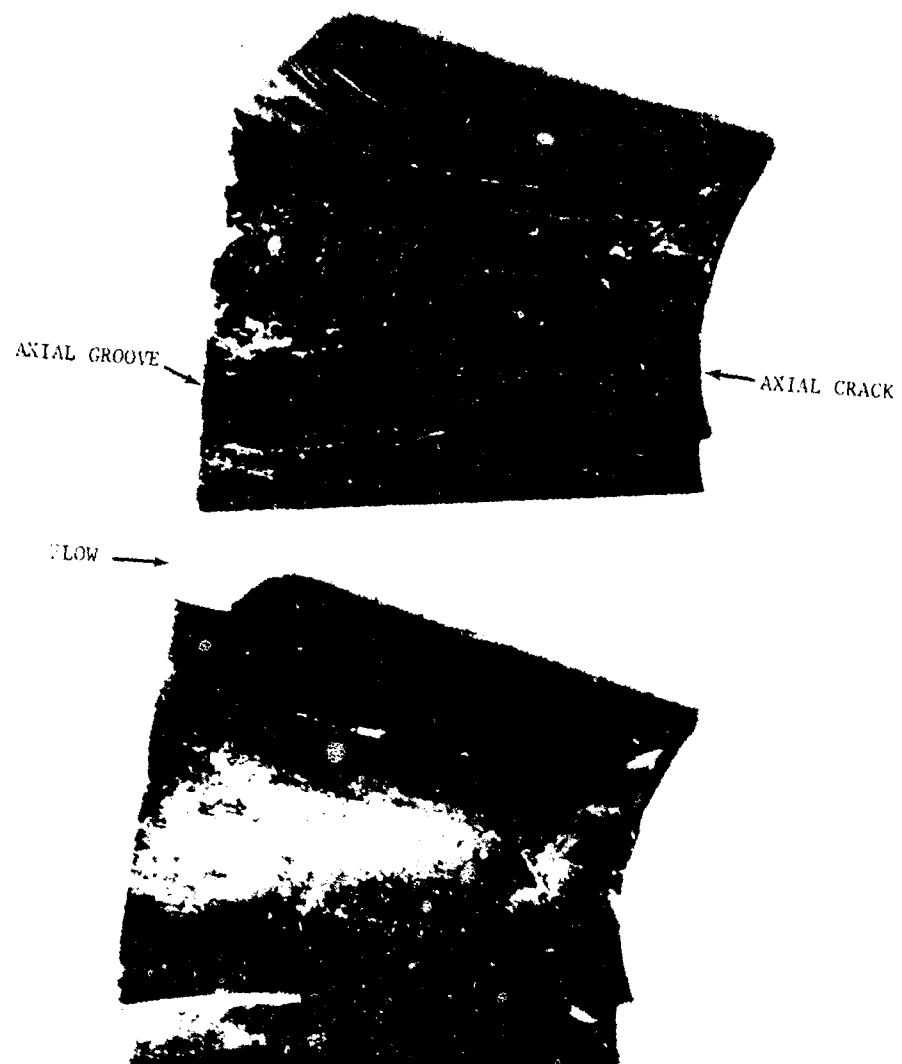
FIGURE 106. TUNGSTEN INSERT FROM TEST T-4 (BEFORE DEPOSIT REMOVAL)
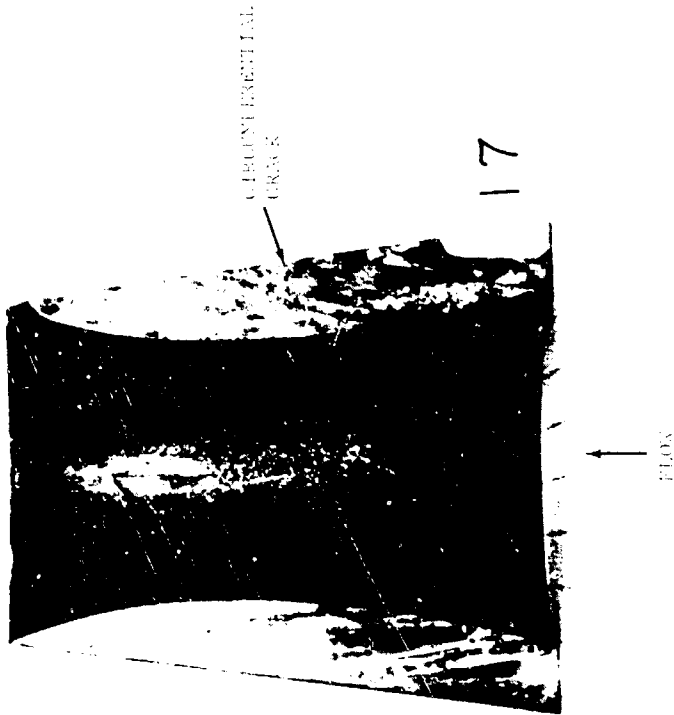
CONFIDENTIAL
F07115C

FIGURE 167. TUNGSTEN INSERT FROM TEST T-17 (DEPOSITS REMOVED, ETCHED)

FIGURE 108. NOZZLE FROM TEST T-18 - NOSE CAP VIEW (LOOSE DEPOSITS REMOVED)

CONFIDENTIAL

AXIAL
CRACK

18
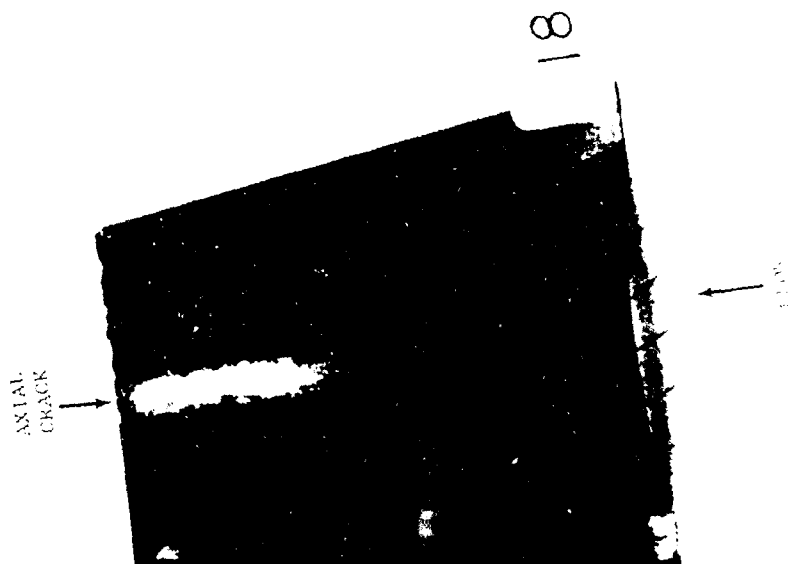
FIGURE 109. TUNGSTEN INSERT FROM TEST T-18 (LOOSE DEPOSITS REMOVED)

FIGURE 110.   NOZZLE FROM TEST T-19 - CROSS SECTION
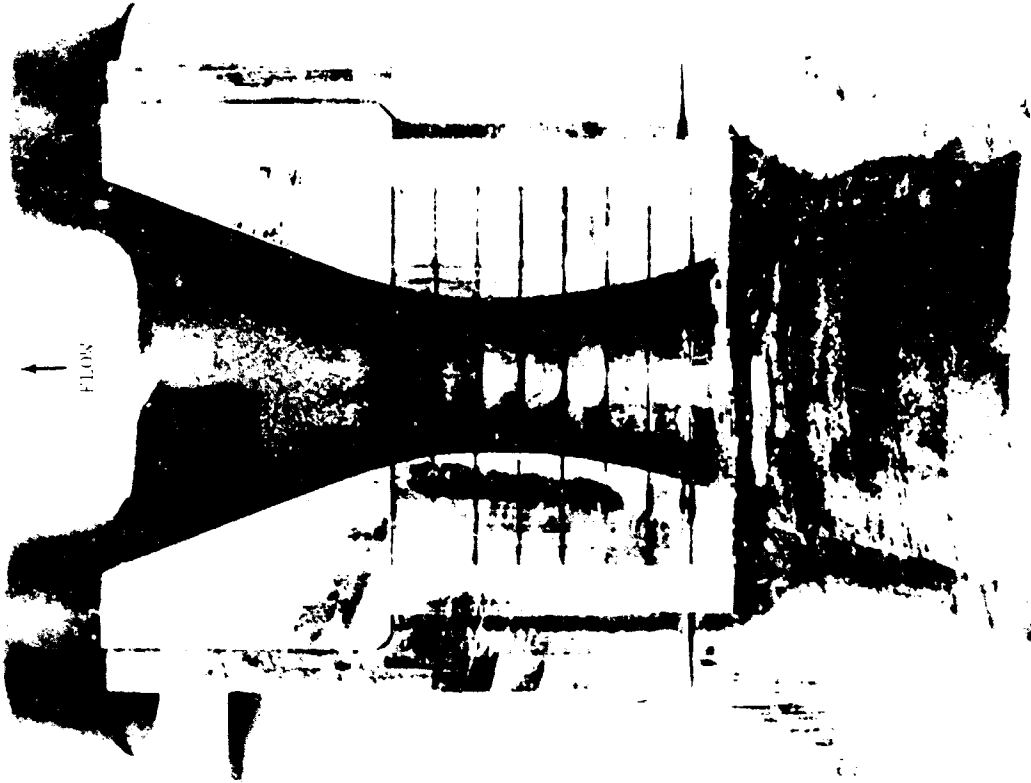
FIGURE 111. NOZZLE FROM TEST T-20 - CROSS SECTION

CONFIDENTIAL
FU7i29 C

FLOW
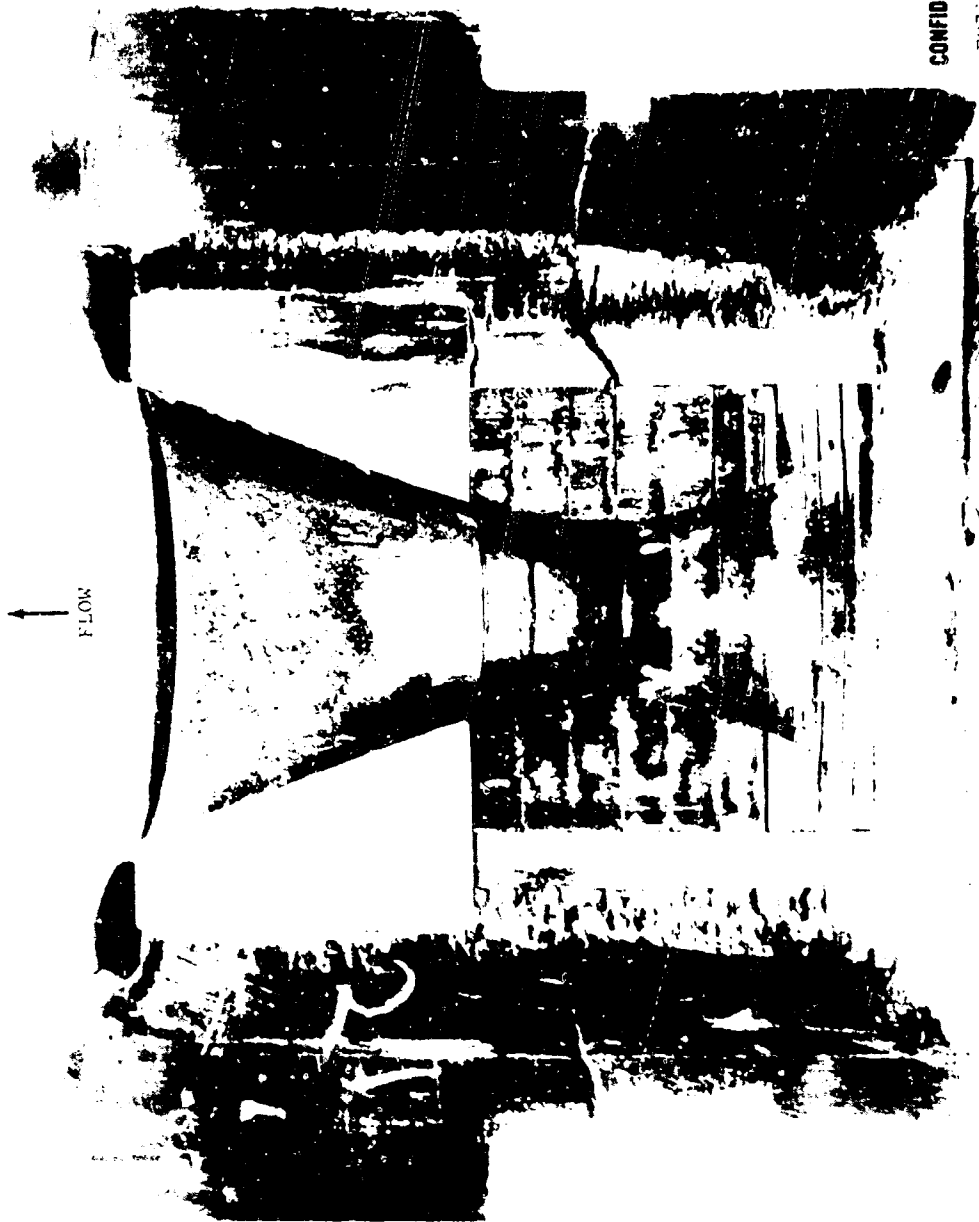
FIGURE 112. NOZZLE FROM TEST T-21 - CROSS SECTION
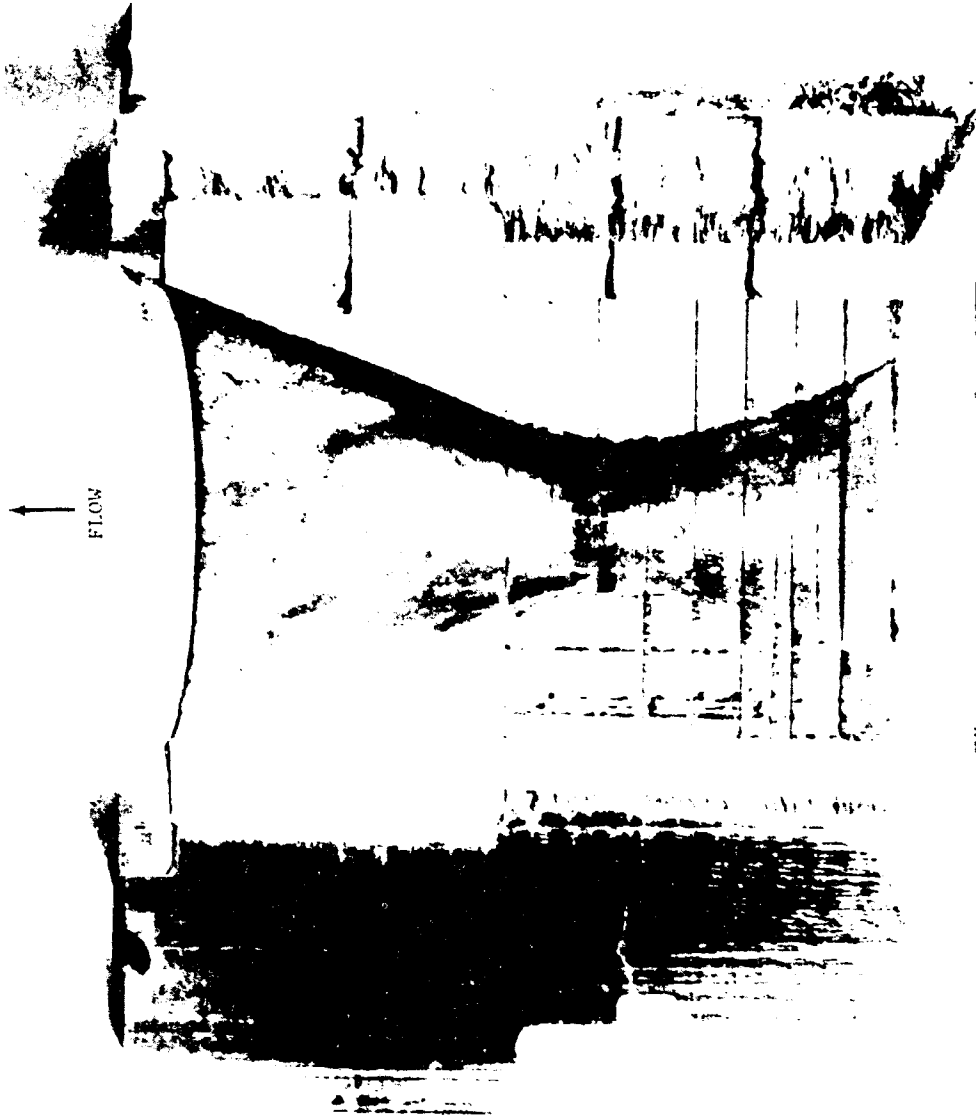
FIGURE 113. NOZZLE FROM TEST T-22 - CROSS SECTION

FLOW

FLOW →
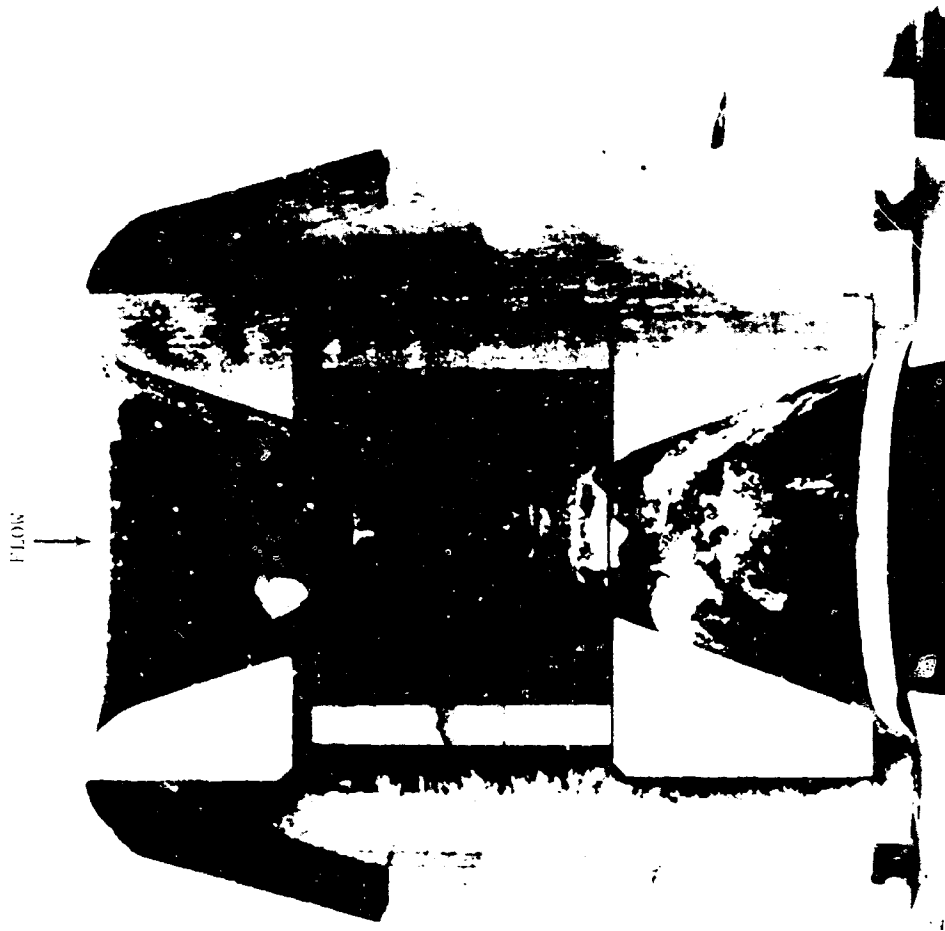
FIGURE 114. SUBMERGED NOZZLE FROM TEST T-23 - CROSS SECTION

FIGURE 115. NOZZLE FROM TEST T-24 - CROSS SECTION

FIGURE 116. NOZZLE FROM TEST T-25 — CROSS SECTION
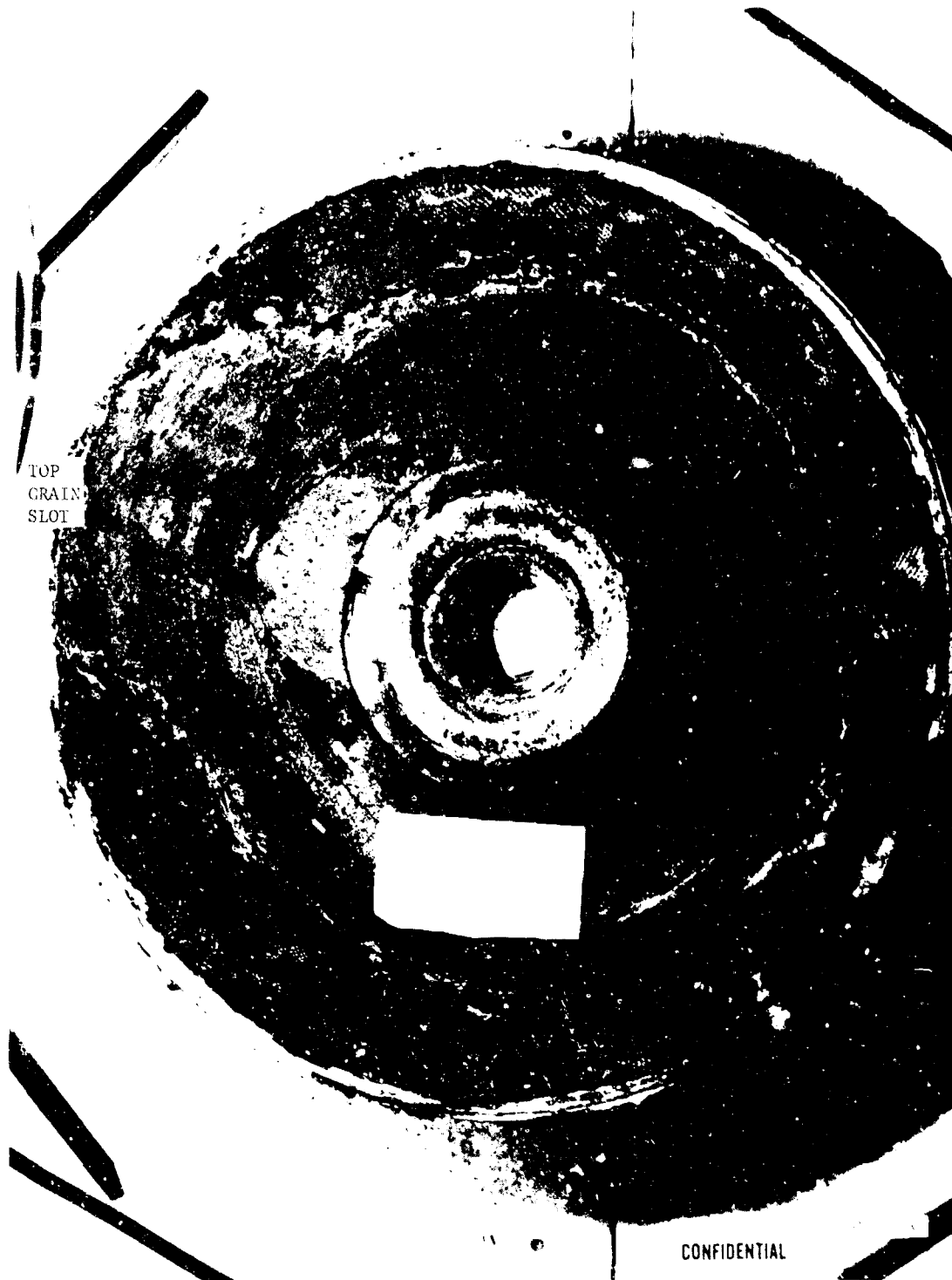
FIGURE 117. AFT CLOSURE INSULATOR - TEST T-51
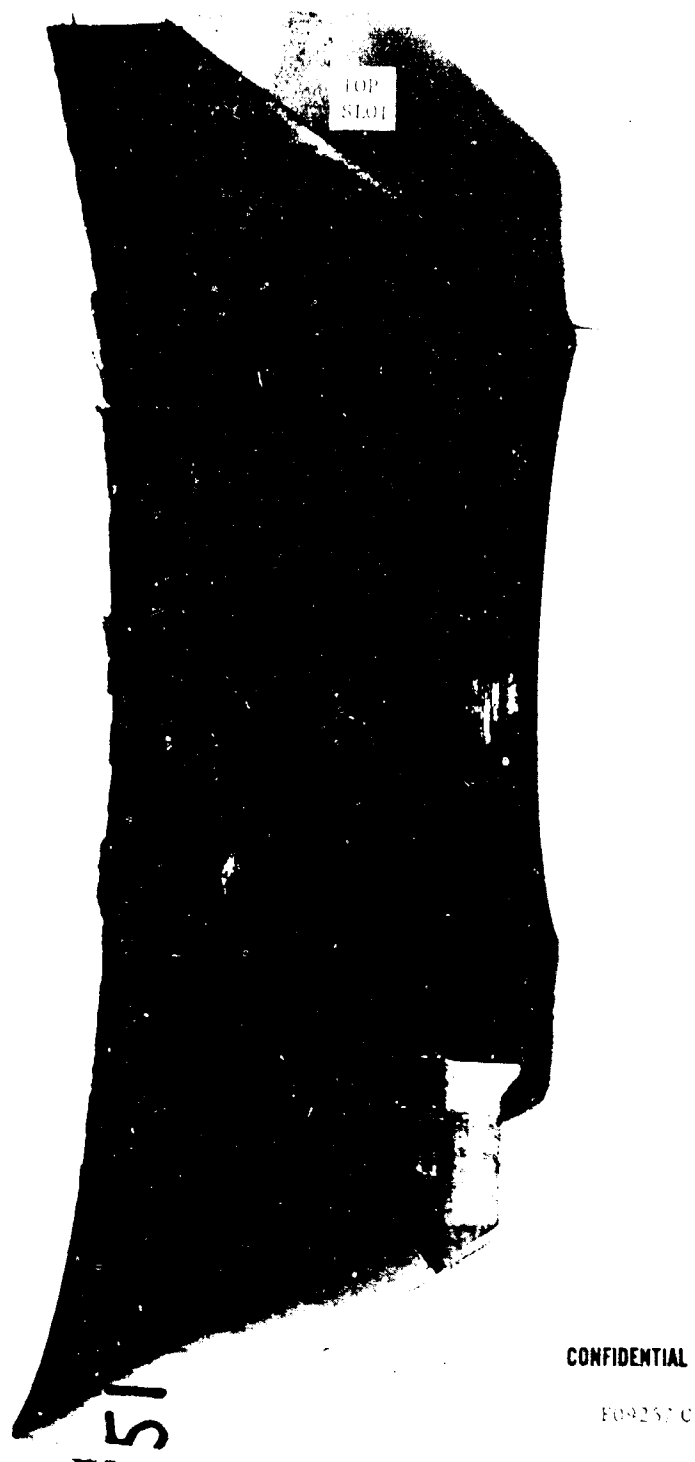
CONFIDENTIAL

FIGURE 118. AFT CLOSURE INSULATOR SECTIONED IN LINE WITH GRAIN
SLOT - TEST T-51
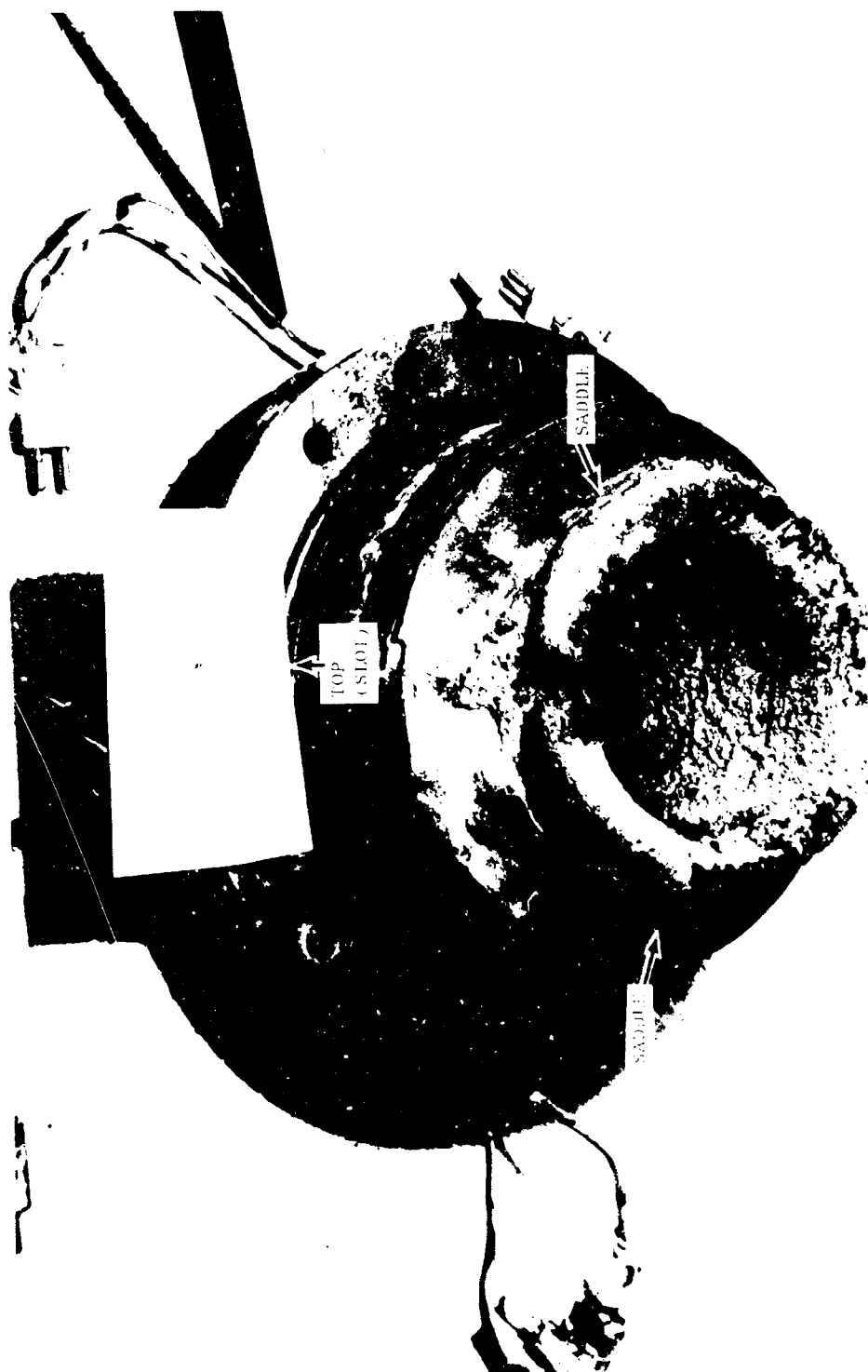
FIGURE 119. NOZZLE FROM TEST T-51 - AS RECEIVED

← FLOW
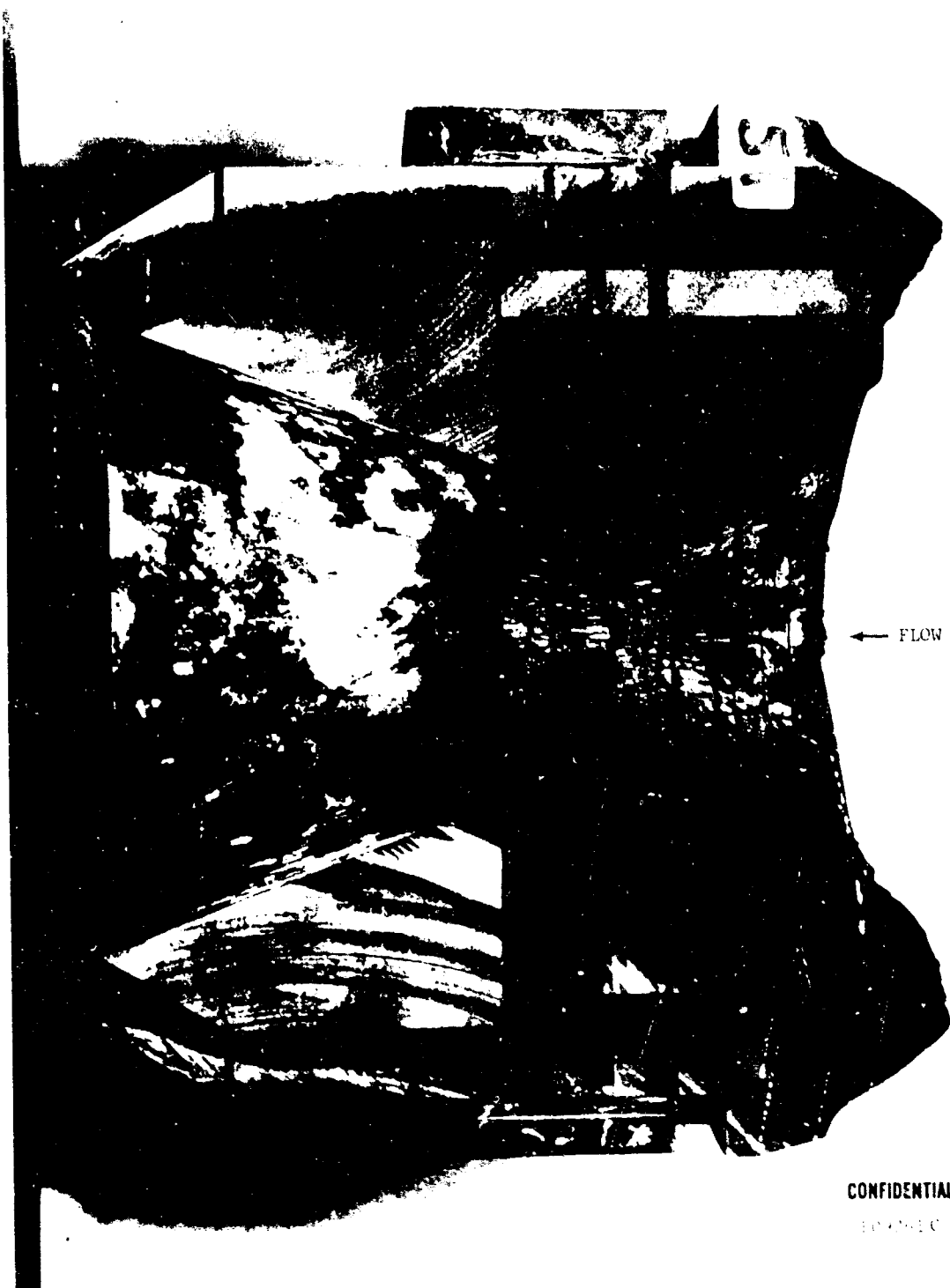
FIGURE 120. NOZZLE CROSS SECTION - TOP HALF - TEST T-51

FIGURE 141. NOZZLE CROSS SECTION - BOTTOM HALF - TEST T-51

← FLOW
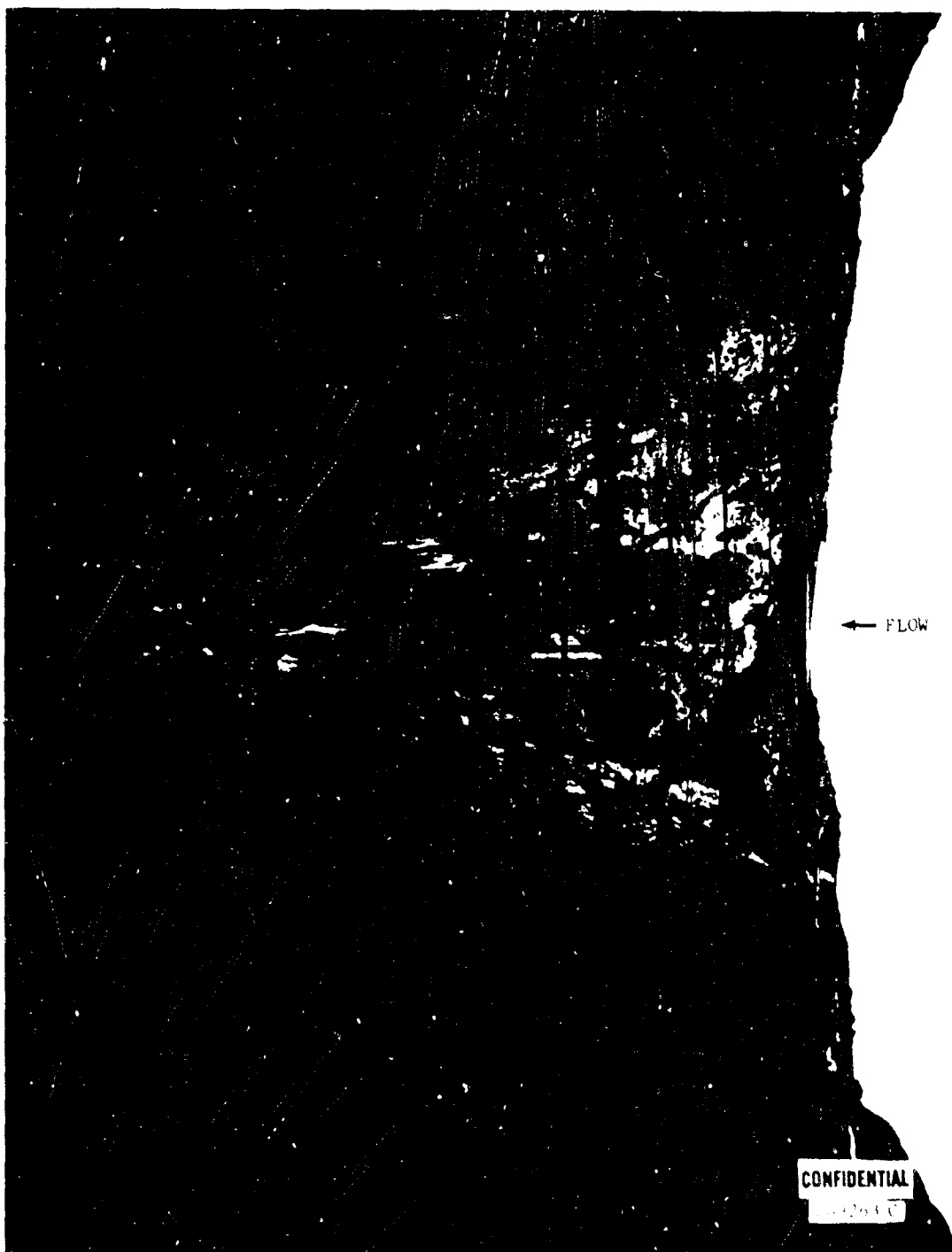
CONFIDENTIAL

FIGURE 122. TYPICAL PANEL FLOW - TOP HALF - TEST T-51

TOP
(SLOT)

FIGURE 123. AFT CLOSURE INSULATOR SECTIONED IN LINE WITH GRAIN
SLOT - TEST C-32

TOP
(SLOT)

FLOW

FIGURE 124. NOZZLE CROSS SECTION - TOP HALF - TEST F-52

FIGURE 125. NACELLE CROSS SECTION - BOTTOM HALF - TEST T-32

FIGURE 121. SADDLE TEST P-52 - AS RECEIVED

TOP
SLOT

FIGURE 127. NOZZLE CROSS SECTION - TOP HALF - TEST F-2

FLOW →

FIGURE 1-?, NOZZLE CROSS SECTION - BOTTOM HALF - TEST T-5A

FIGURE 129. NOZZLE THROAT SECTION - TOP HALF - TEST T-53

- 291 -

FIGURE 130. NOZZLE EXIT CONE - TOP HALF - TEST T-53
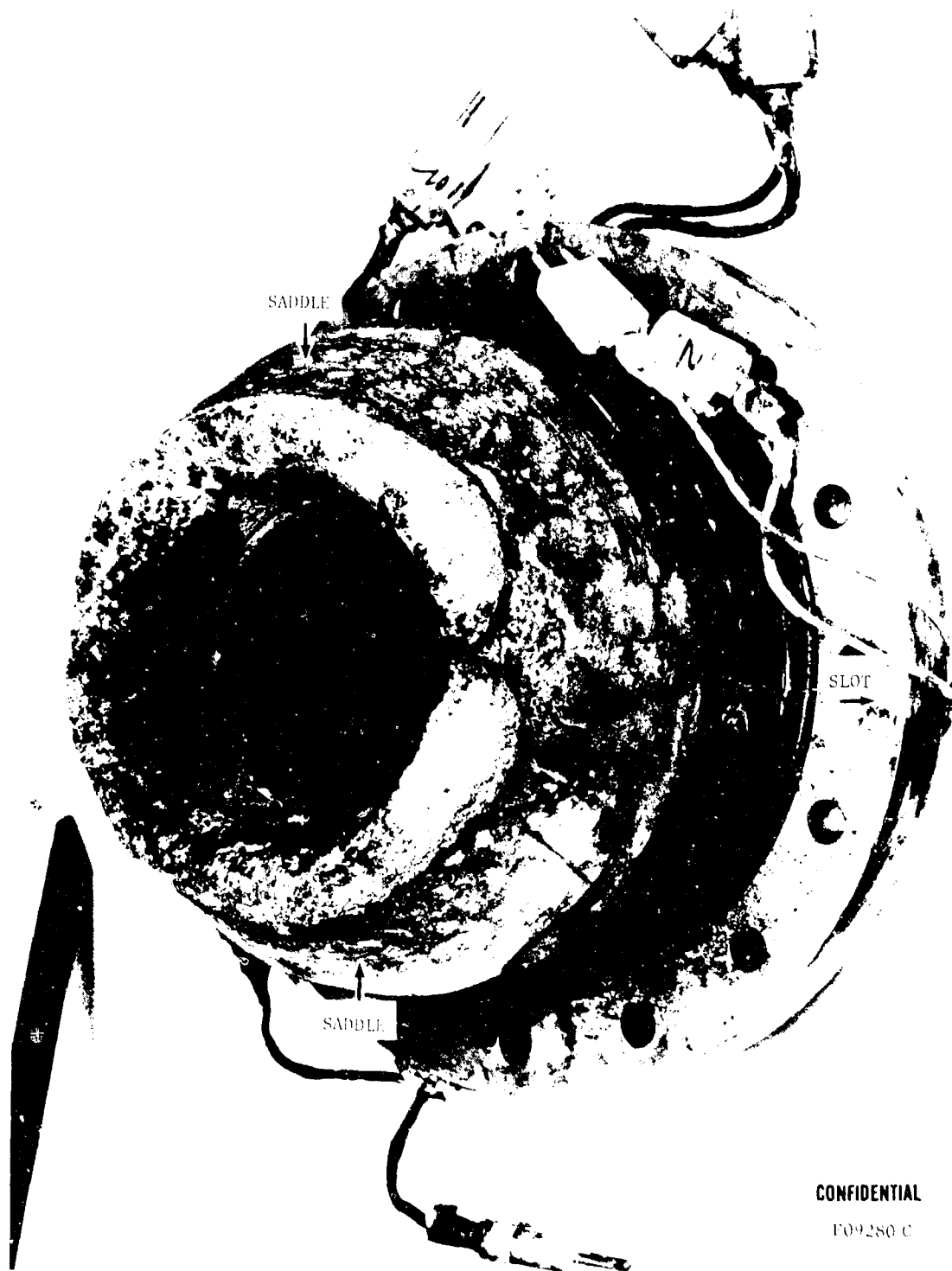
FIGURE 131. NOZZLE FROM TEST T-54 - AS RECEIVED
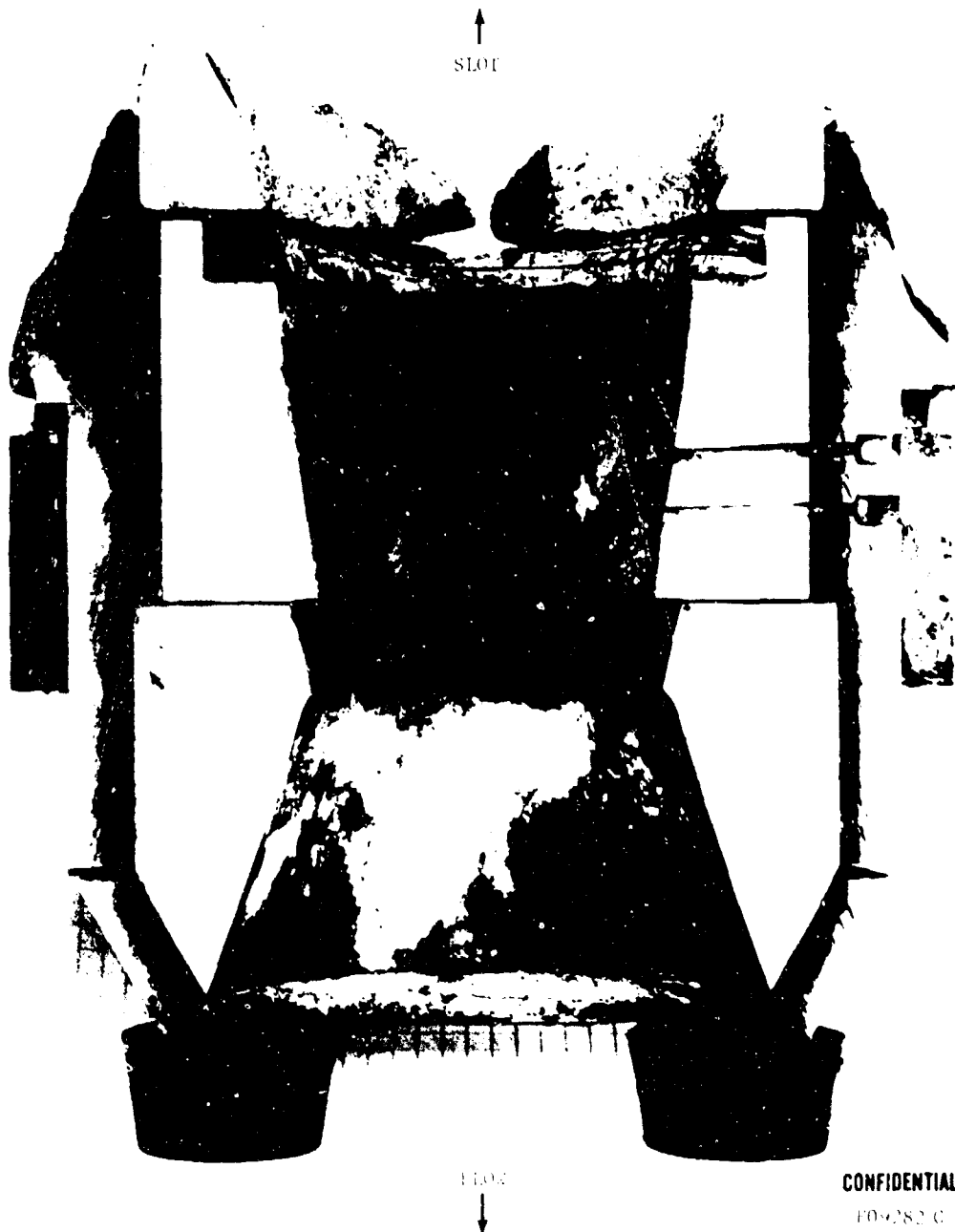
FIGURE 132. NOZZLE CROSS SECTION - TOP HALF - TEST T-54
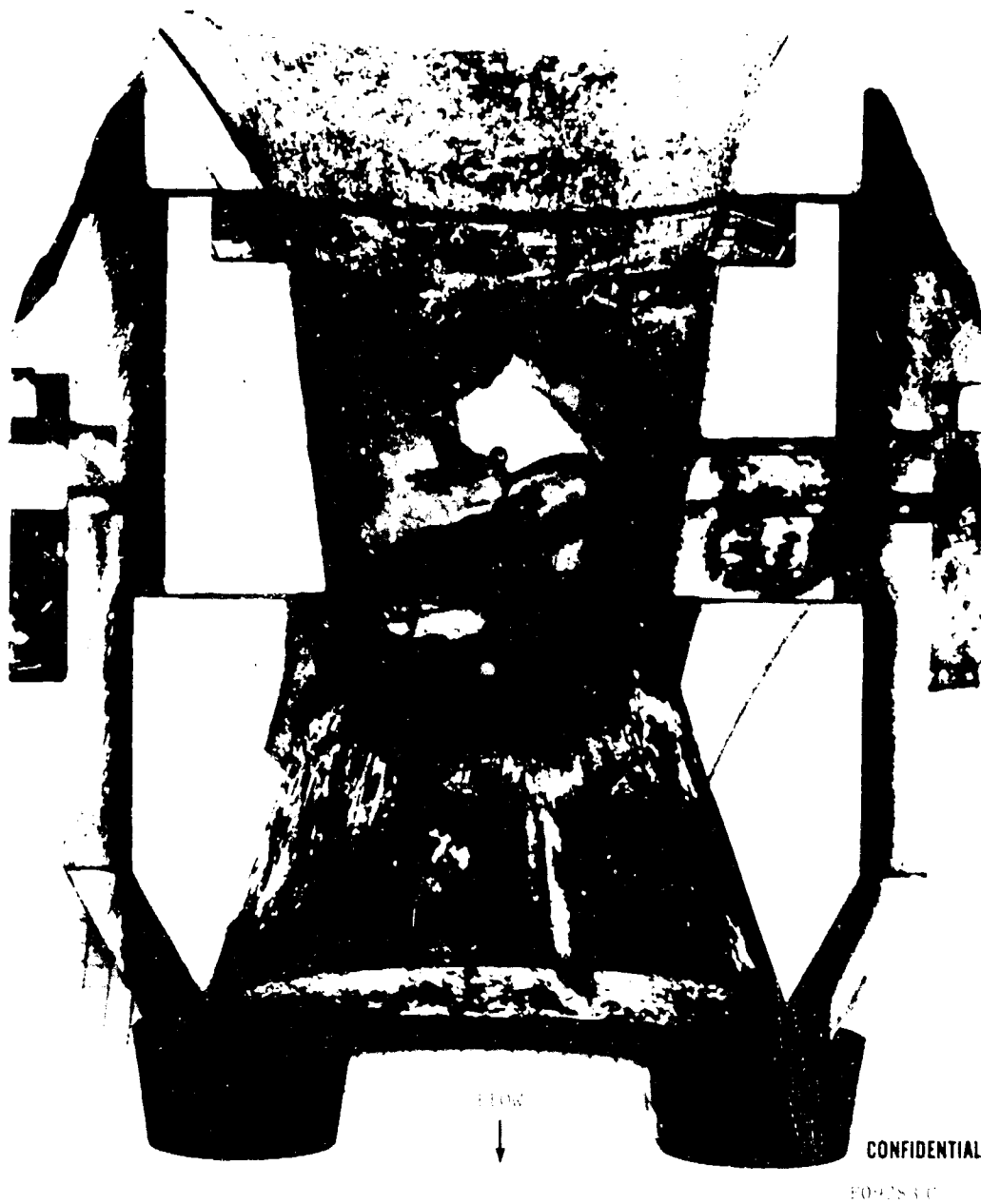
FIGURE 133. NOZZLE CROSS SECTION - BOTTOM HALF - TEST T-54

FIGURE 134. TUNGSTEN INSERT - CLEANED INSIDE SURFACE - TEST T-54

APPENDIX V (C)

THROAT DEPOSITION/EROSION HISTORIES

5.1 (U) PROGRAM TEST DATA

Several methods were developed to permit the calculation of throat area
variations through the motor firing period. The first techniques devel-
oped are described in Section 5.2 of Reference 2. Basically, the Kn
method uses the measured pressure history and adjusted grain burning rate
data. The F/P method uses measured pressure and thrust data. An improved
version of the F/P method is described in Section 5.2 of Reference 4. The
Kn method used in this program is most effective when approximately neutral
burning is achieved. Significant deviations from neutral burning were
experienced on the majority of the program tests. The Kn method is believed
to have given results which are inferior to the F/P results. However, the
frequent occurrence of thrust stand resonance made it necessary to use the
Kn method on some tests.

Figures 135 through 163 present the deposition/erosion curves used in the
nozzle thermal and ballistic performance analyses. The original F/P (or
C_f) technique was used for Tests T-1 through T-7. Thereafter, the improved
F/P technique (Reference 4) was used. Both Kn and F/P results are shown in
Figures 135 through 141 and 160. When only one curve is shown, the method
used is indicated on the figure. Minor changes in the deposit histories
for Tests T-1 through T-7 were made by combining the results of the Kn and
original F/P method results. These data may be found in Figures 139 through
145 in Reference 2. The grain burning rate data used in the Kn analysis
may be found in Section 5.2 of Reference 2 and Appendix B of Reference 4.

The improved F/P technique was subsequently used to reevaluate the deposition data on Tests T-1, T-2, T-3, T-7, and T-21 through T-24. These results are compared with the Kn results in Figures 164 through 167. The improved F/P method results would lead to improvements in the thermal analysis results as discussed in Section 5.2 of Reference 4.

5.2 (U) COMPARISON OF DEPOSIT HISTORIES

Composite plots of the nozzle throat deposit histories were presented in Section 4.2 of References 3 and 4. These are repeated in this appendix as Figures 168 through 181. These comparisons were made to determine the influence of the major design parameters on the deposition phenomenon and, consequently, on nozzle heat transfer, corrosion and motor ballistic performance. There are apparently strong effects on grain design, propellant formulation, nozzle submergence and stay time. The characteristics and magnitude of the deposit curves for each grain design appear to be reproducible. It should be noted that the deposit histories calculated by the improved F/P method shown in Figures 164 through 167 have not been used in Figures 168 through 181. If this were done, it is not expected that significant revision of the discussion of the deposit history comparisons would be required. Such discussions may be found in Sections 4.2 of References 3 and 4.

5.3 (U) THIOKOL ADOBE NOZZLES

Ballistic performance data from the Thiokol ADOBE motor test program (Reference 10) were used to find throat deposition/erosion histories for selected nozzles by the improved F/P method. The results are shown in Figures 182 through 186. The nozzles and motors were identical in these tests except for the indicated variation of the throat heat sink or heat barrier design. Approximately 3600 pounds of Thiokol TPH-1092 were used in each TU-152 motor. A nearly neutral, cup type grain design was used in these tests. Note that the throat radius histories reflect the throat heat sink capacity effect and that erosion rates may be measured directly from the curves.

*USED IN THERMAL ANALYSIS
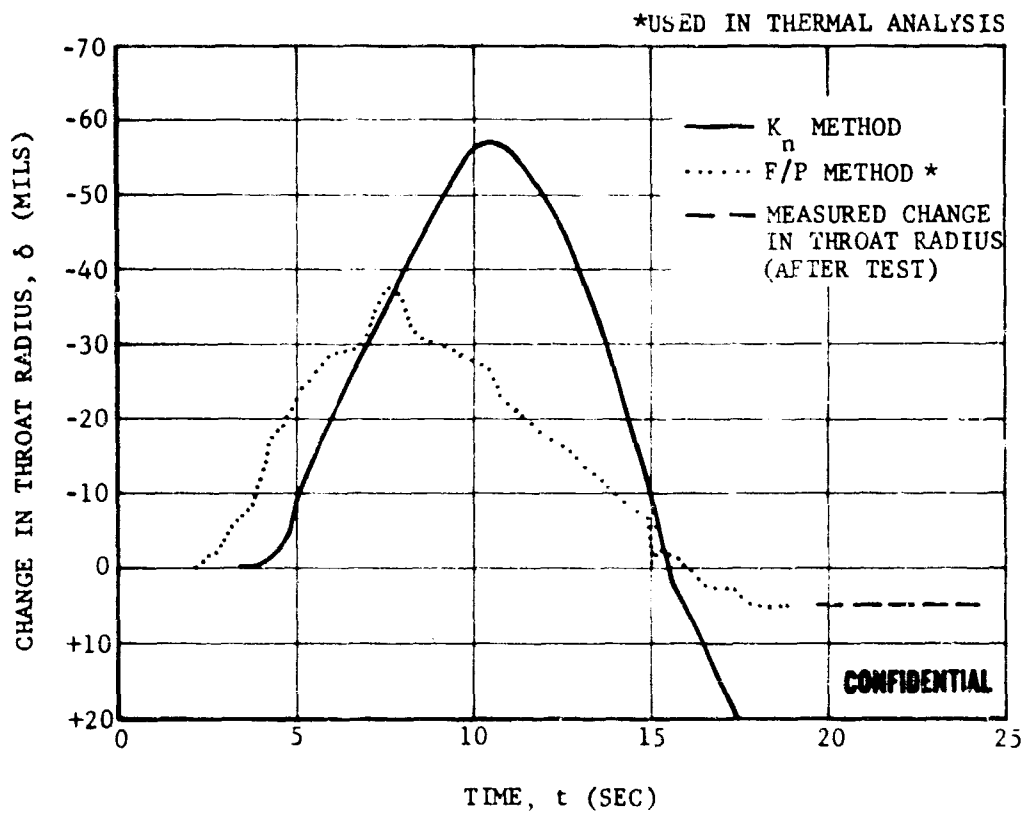
FIGURE 135. CHANGE IN NOZZLE THROAT RADIUS VERSUS FIRING TIME TEST T-1

F04149 C

*USED IN THERMAL ANALYSIS
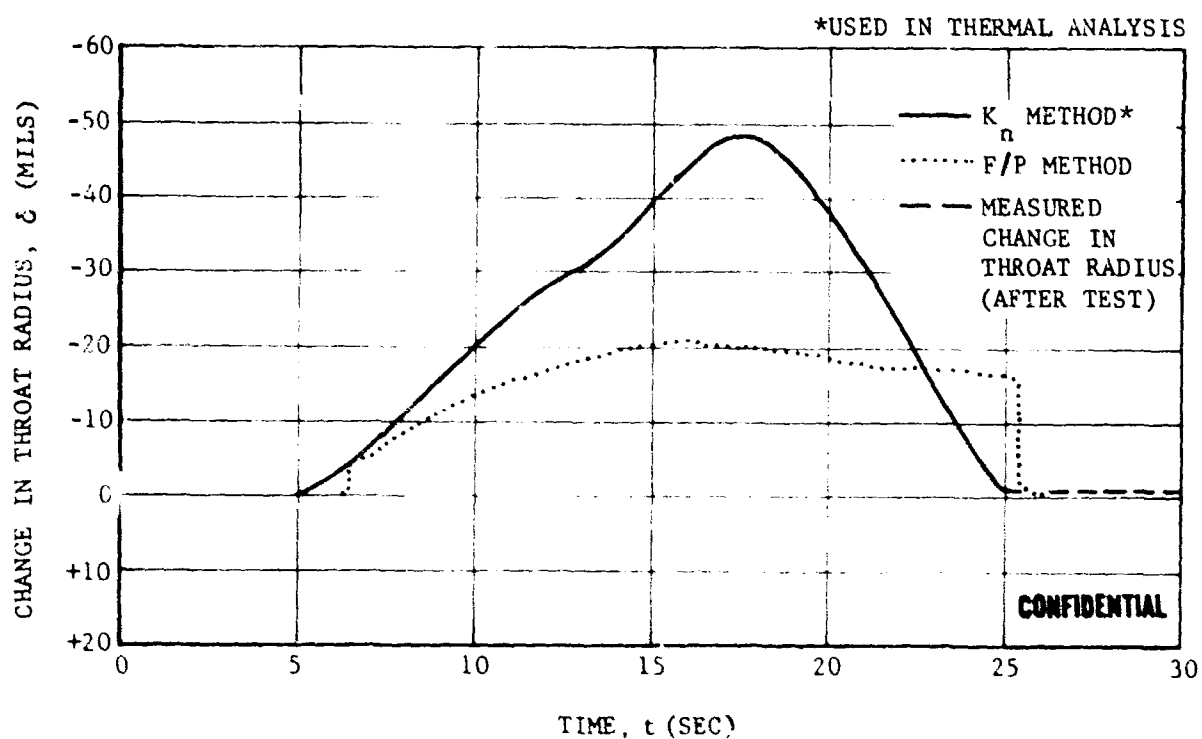
FIGURE 136. CHANGE IN NOZZLE THROAT RADIUS VERSUS FIRING TIME   TEST T-2
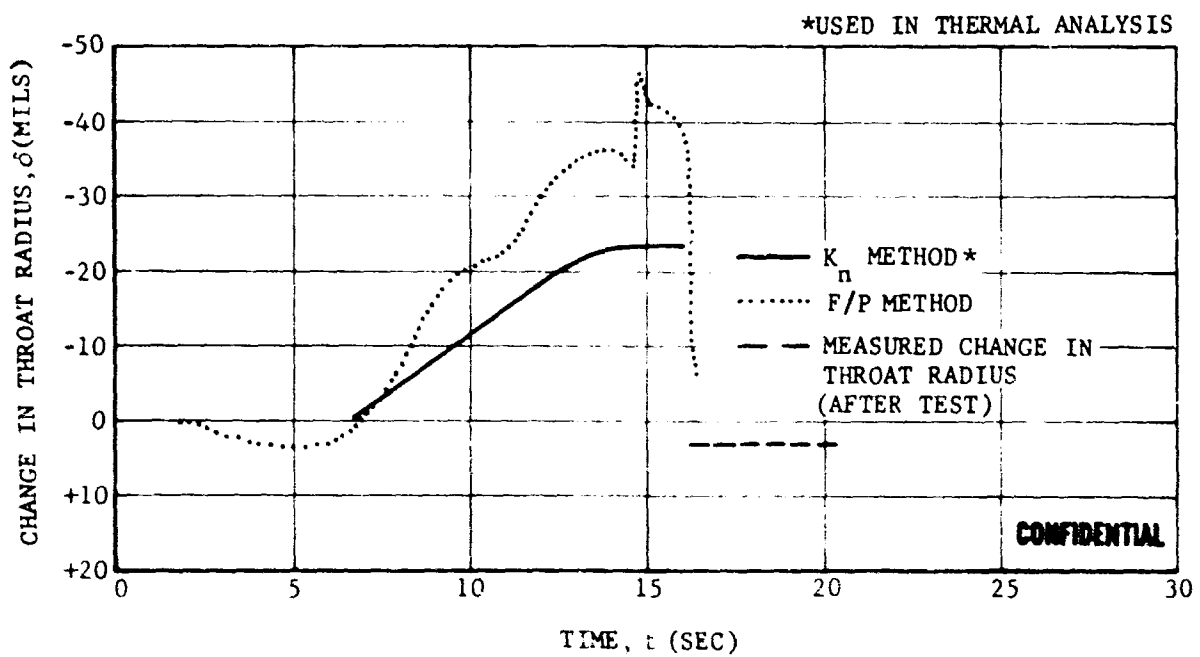
F04150 C

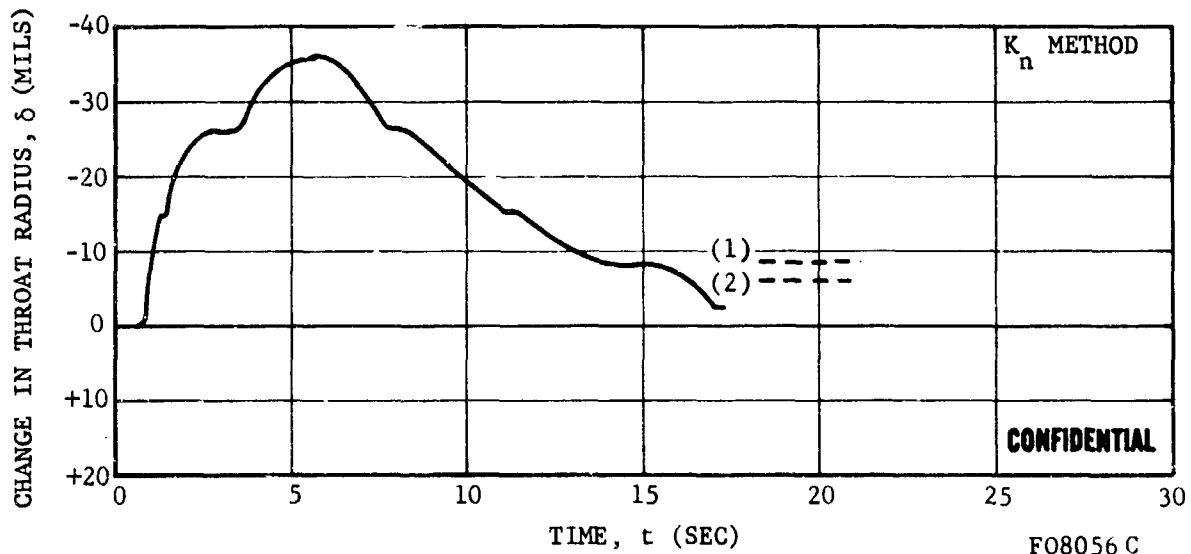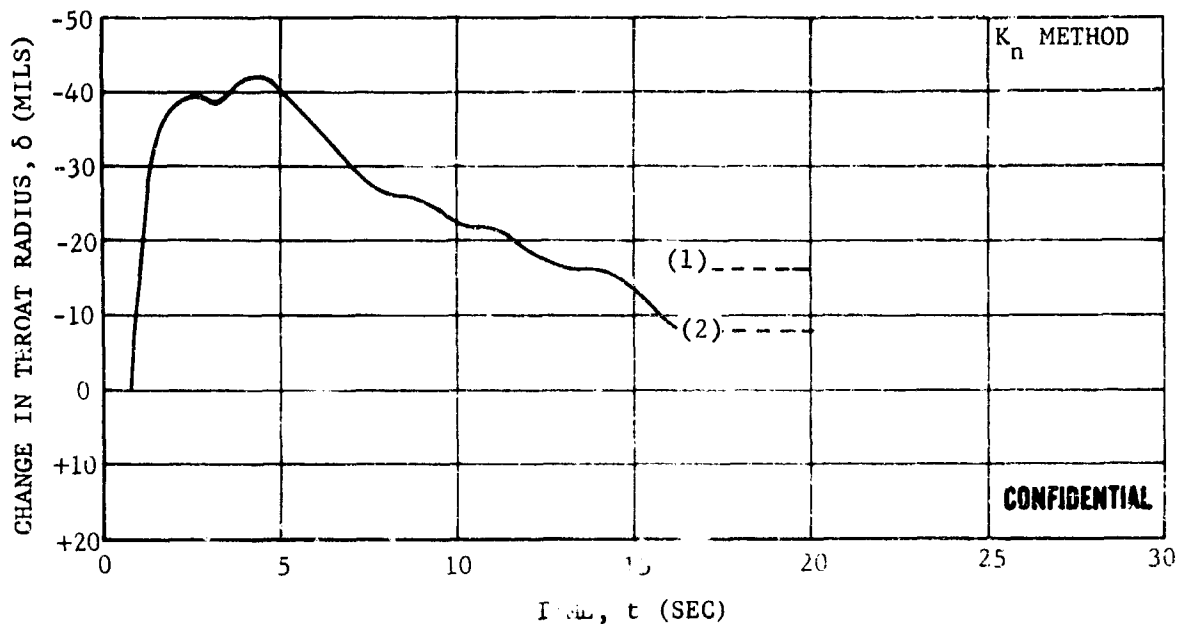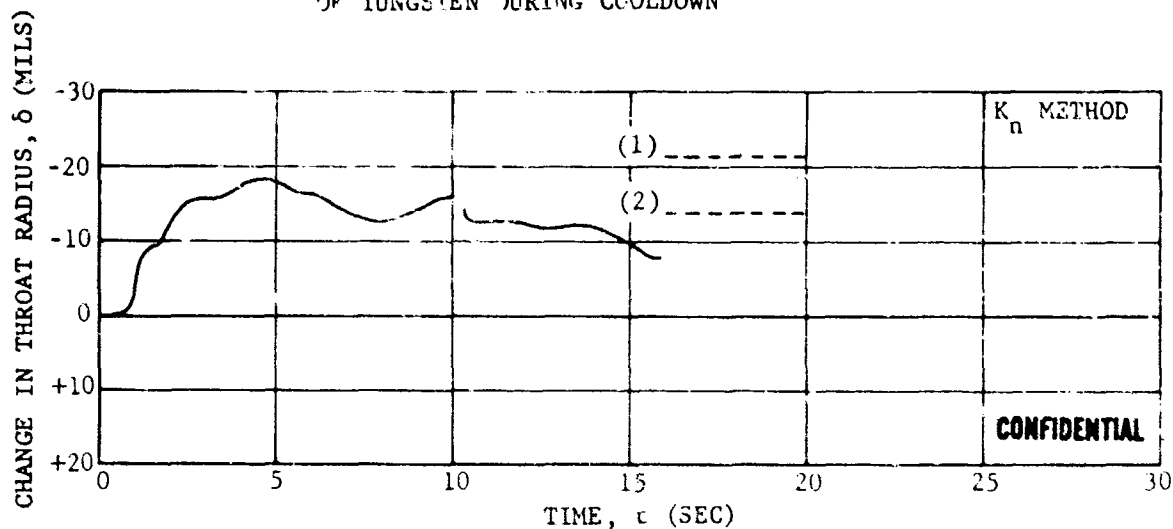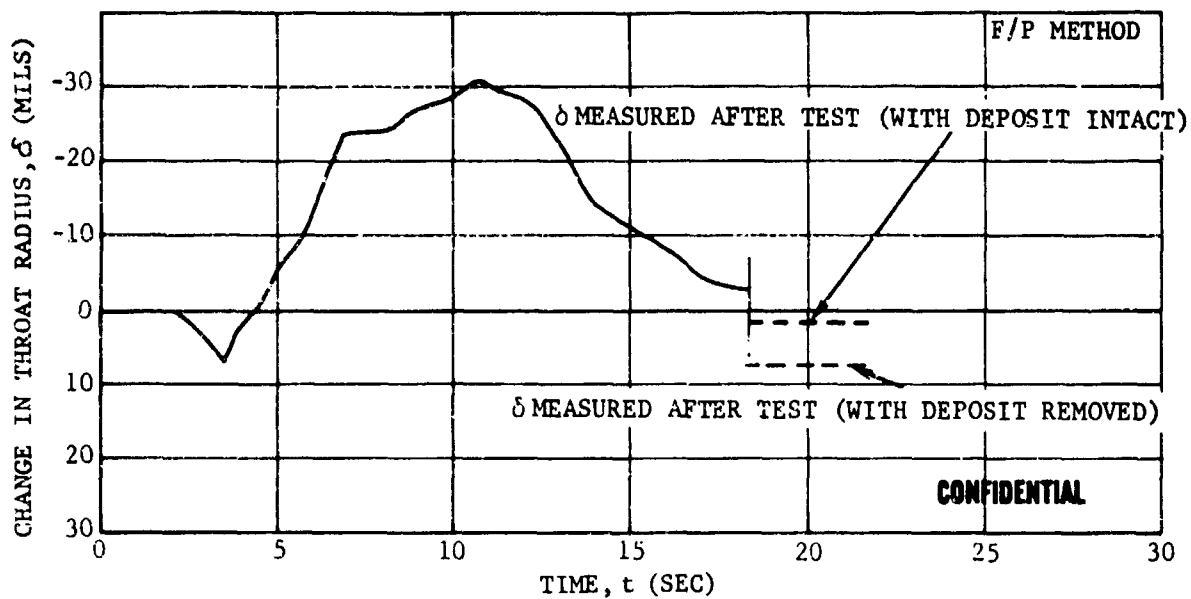FIGURE 137. CHANGE IN NOZZLE THROAT RADIUS VERSUS FIRING TIME TEST T-3
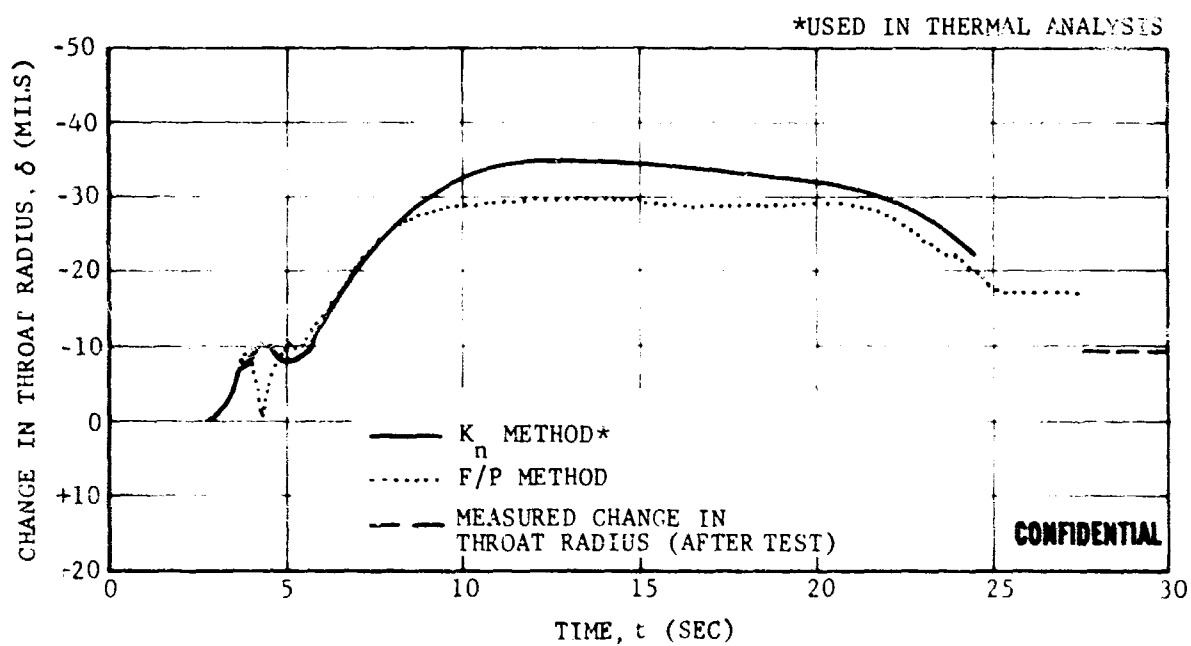
F04151 C

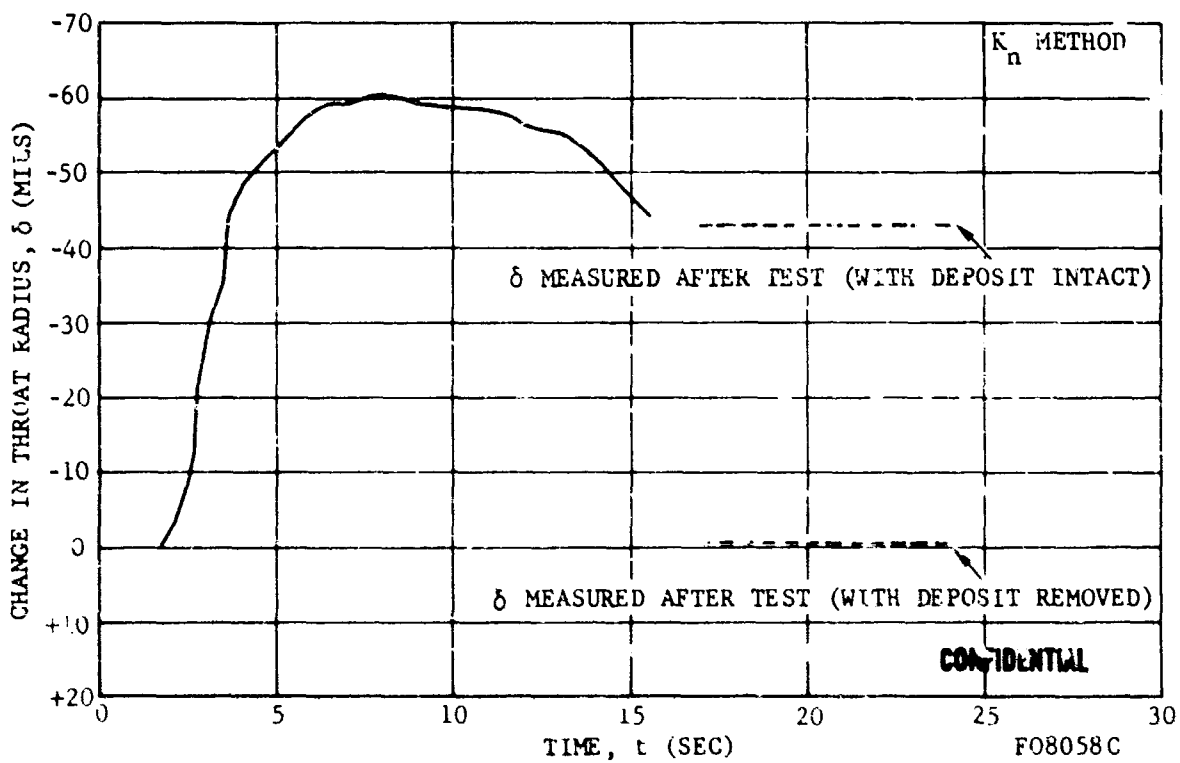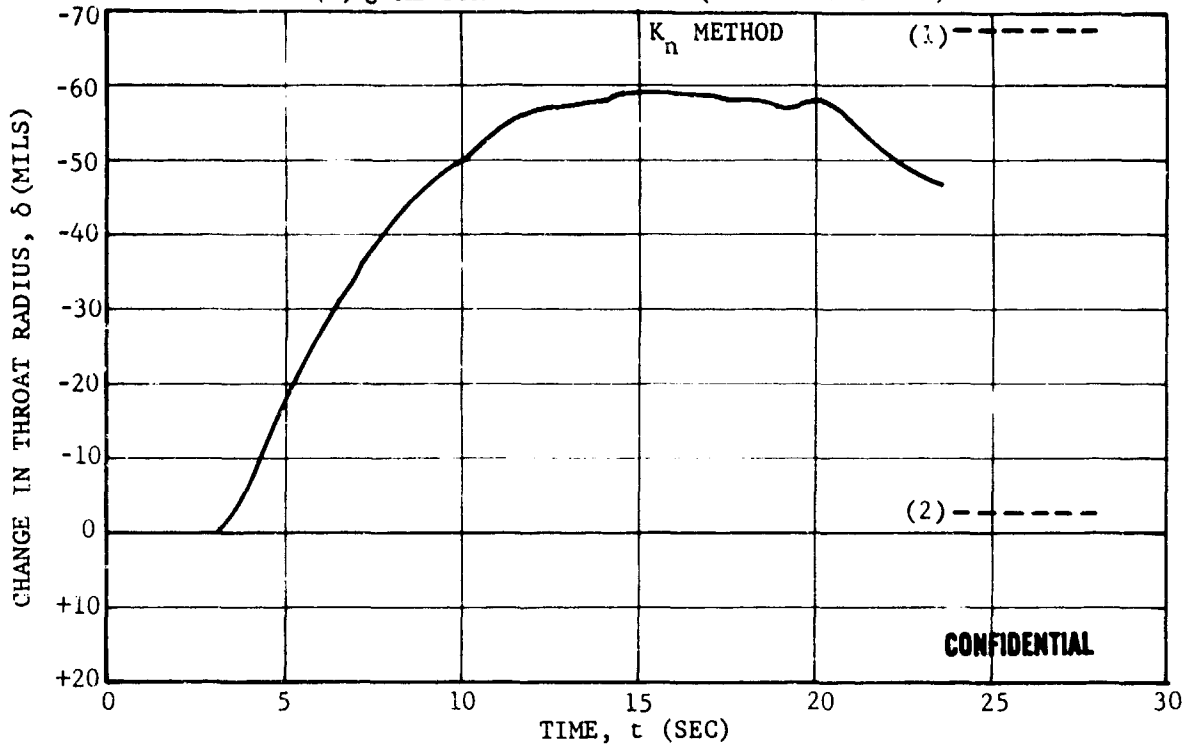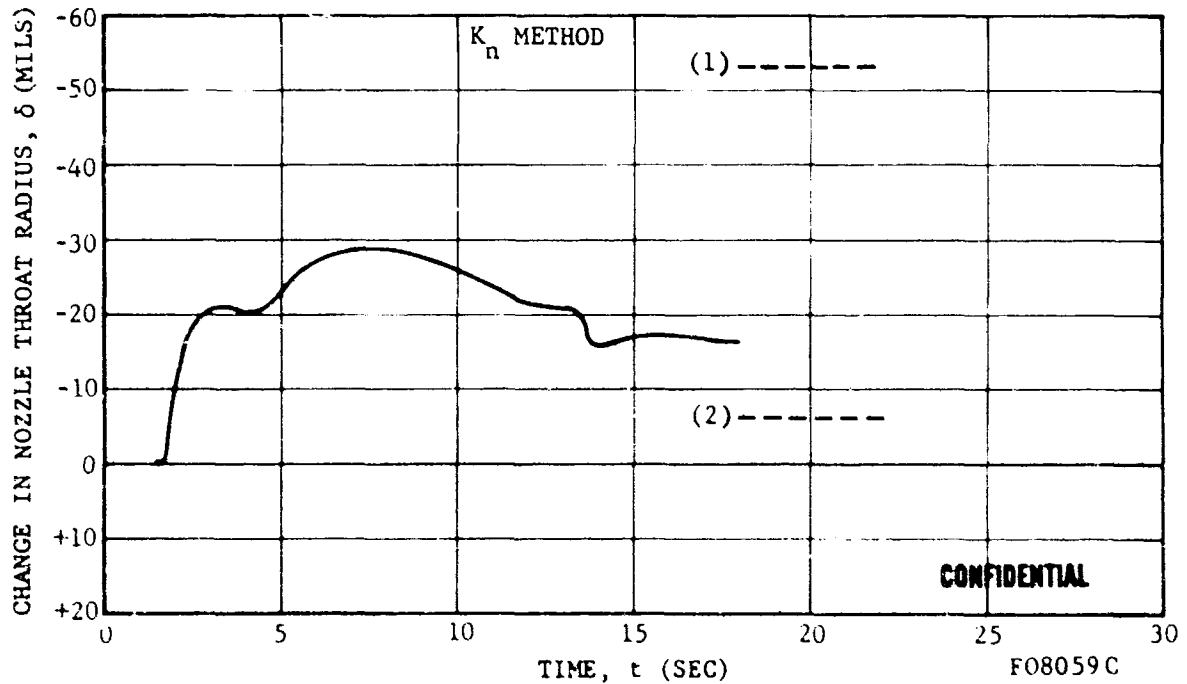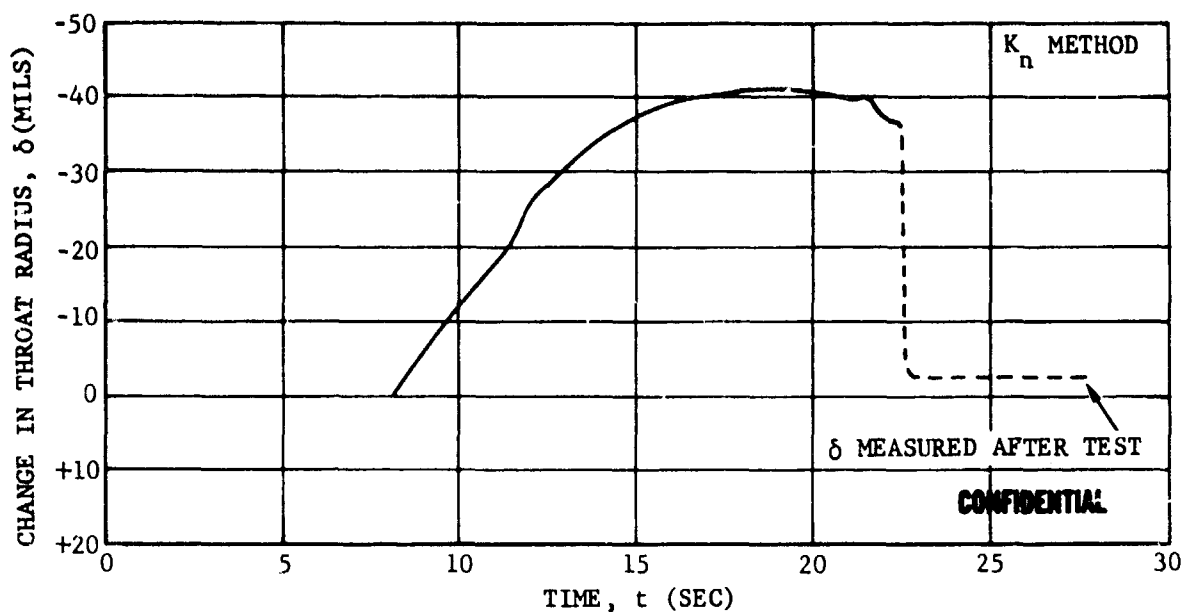FIGURE 138. CHANGE IN NOZZLE THROAT RADIUS VERSUS FIRING TIME   TEST T-4

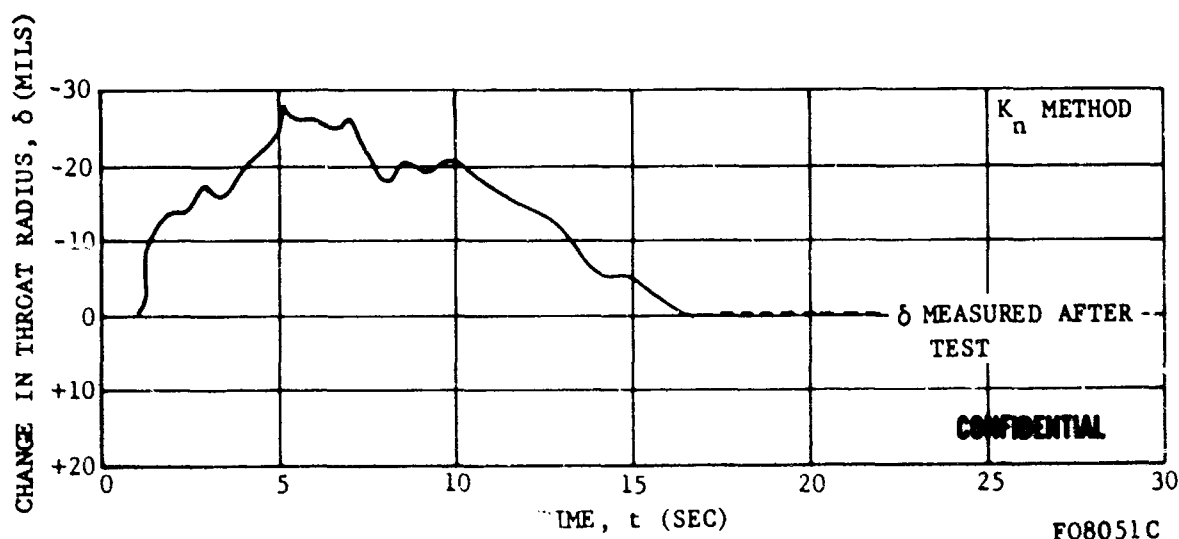FO4152 C

*USED IN THERMAL ANALYSIS
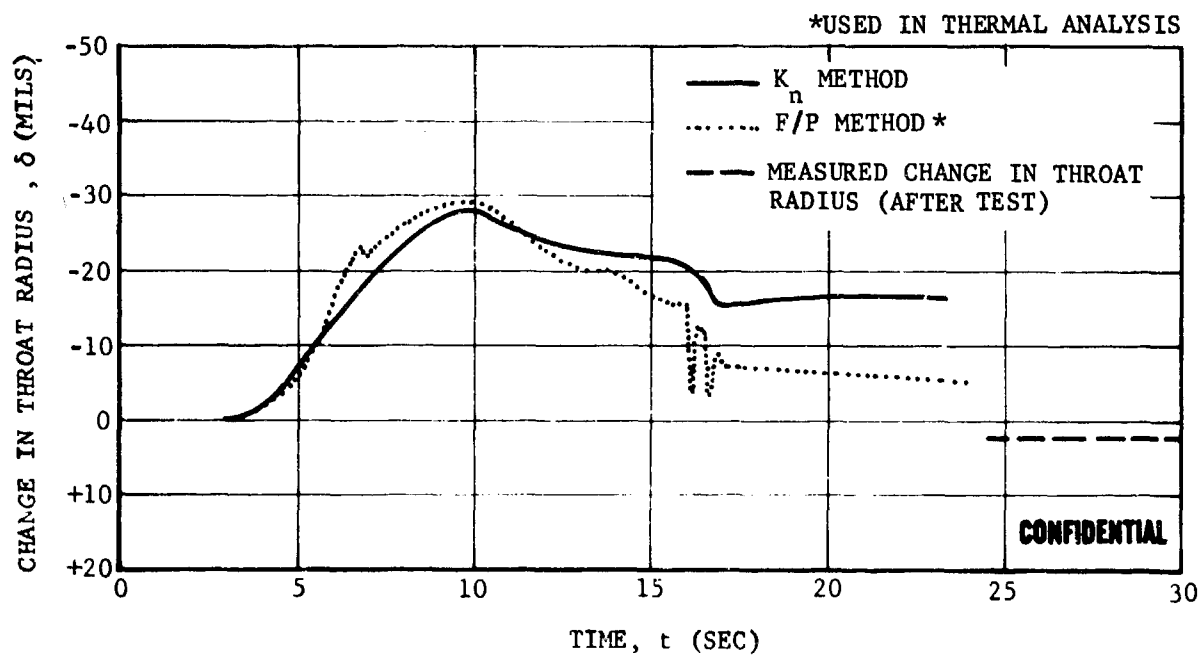
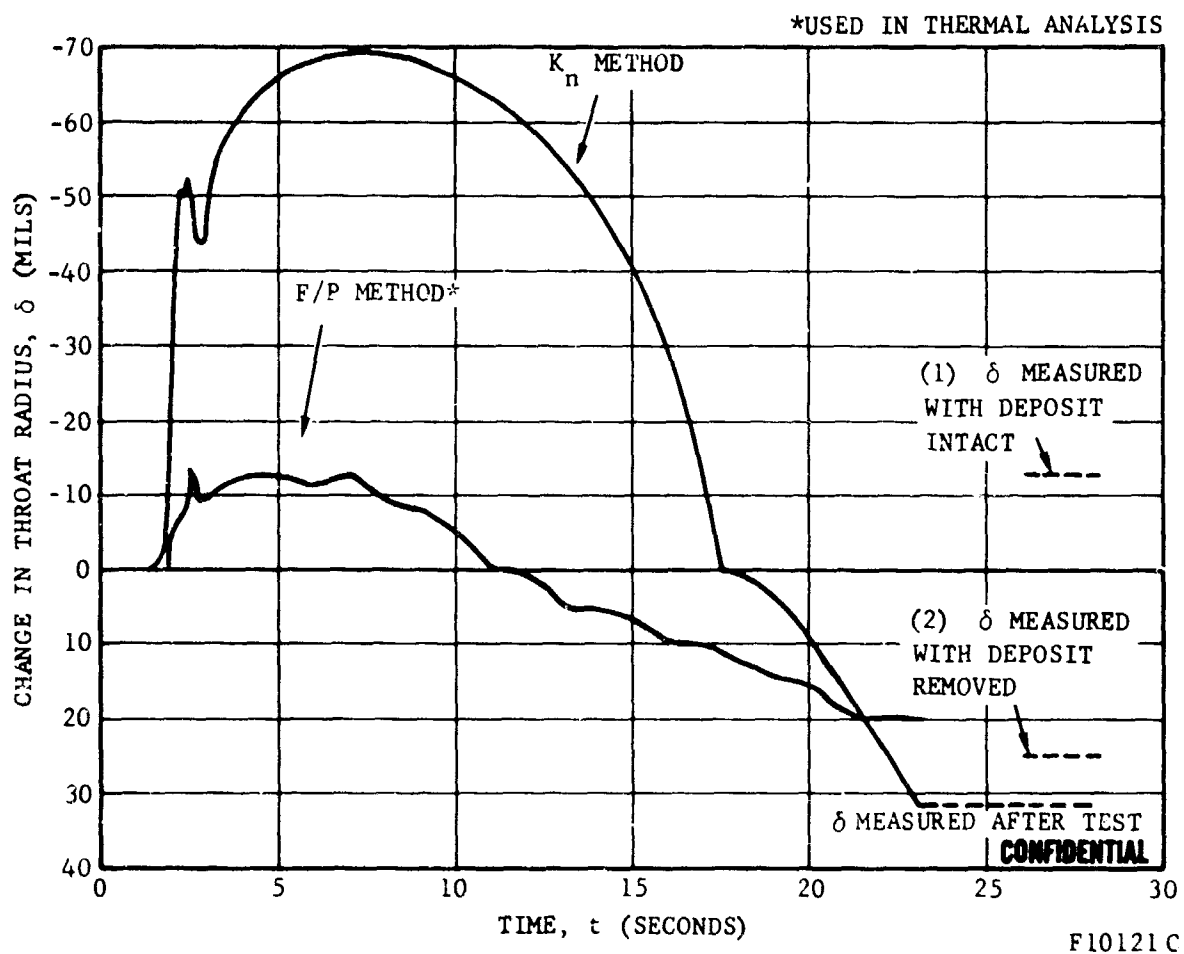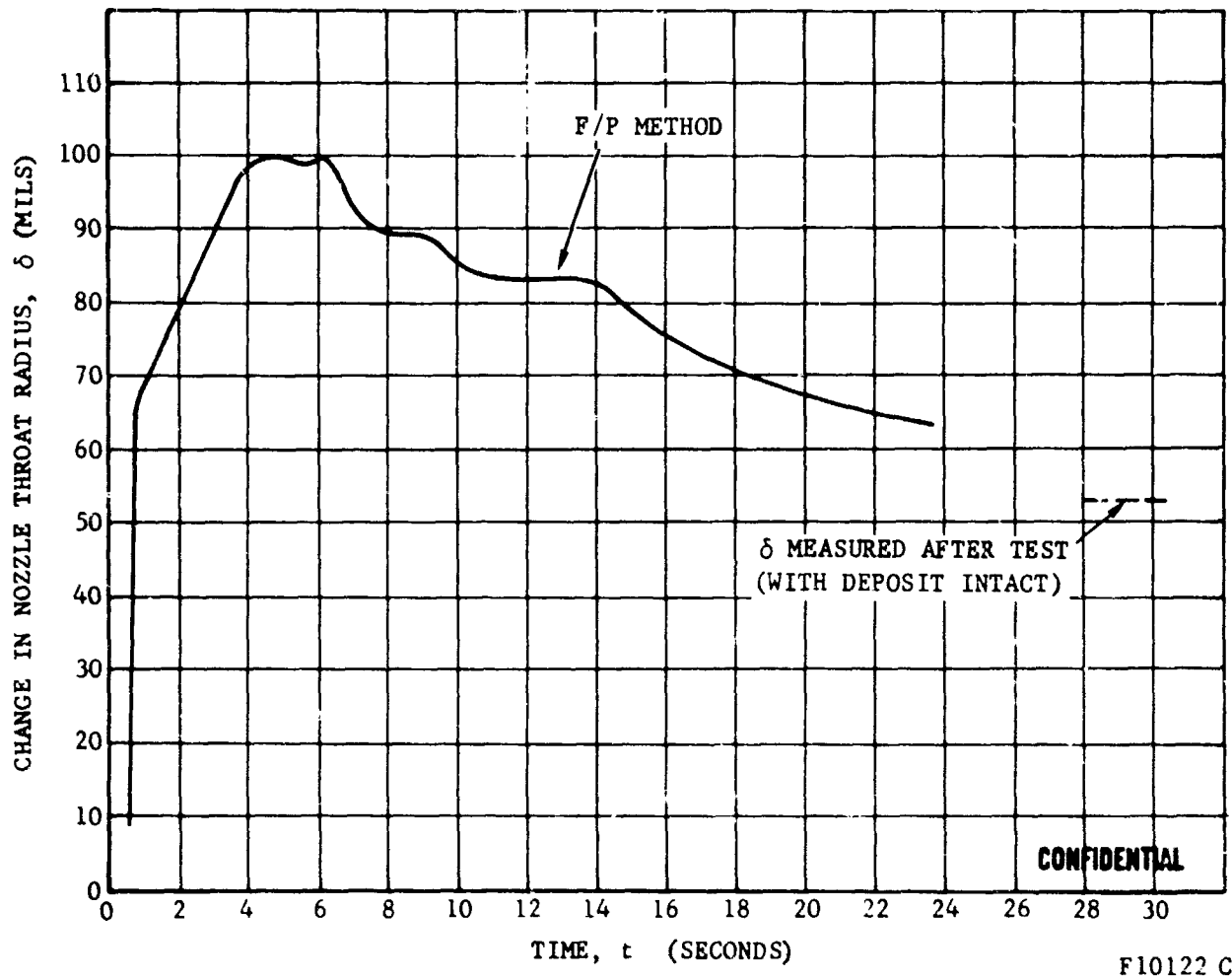FIGURE 139. CHANGE IN NOZZLE THROAT RADIUS VERSUS FIRING TIME TEST T-5
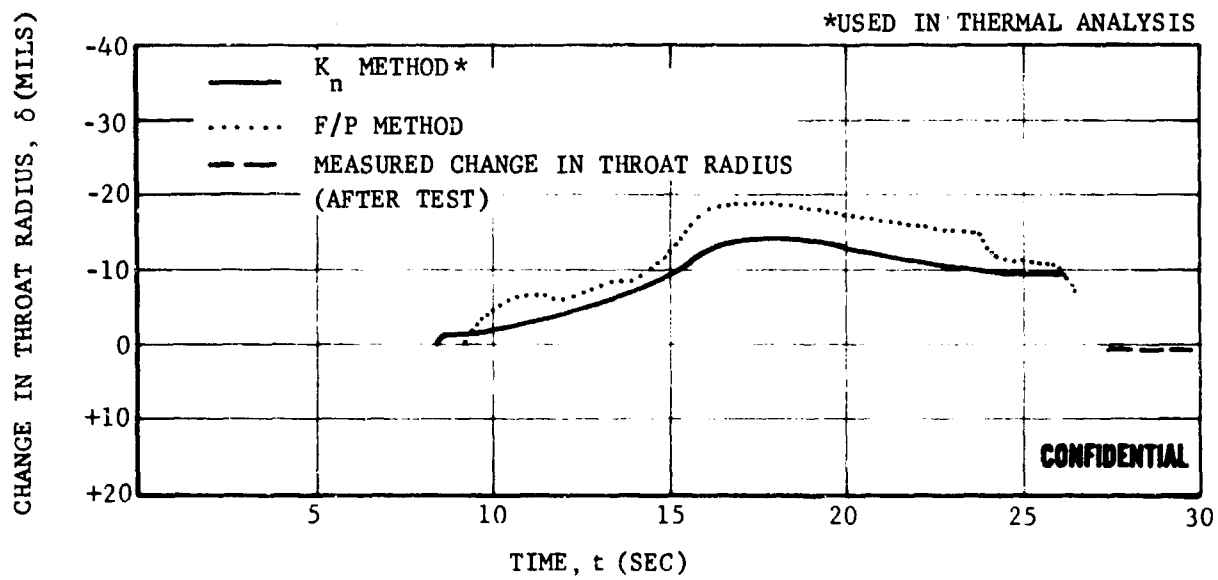
FO4153 C

FIGURE 140. CHANGE IN NOZZLE THROAT RADIUS VERSUS FIRING TIME TEST T-6

F04154 C
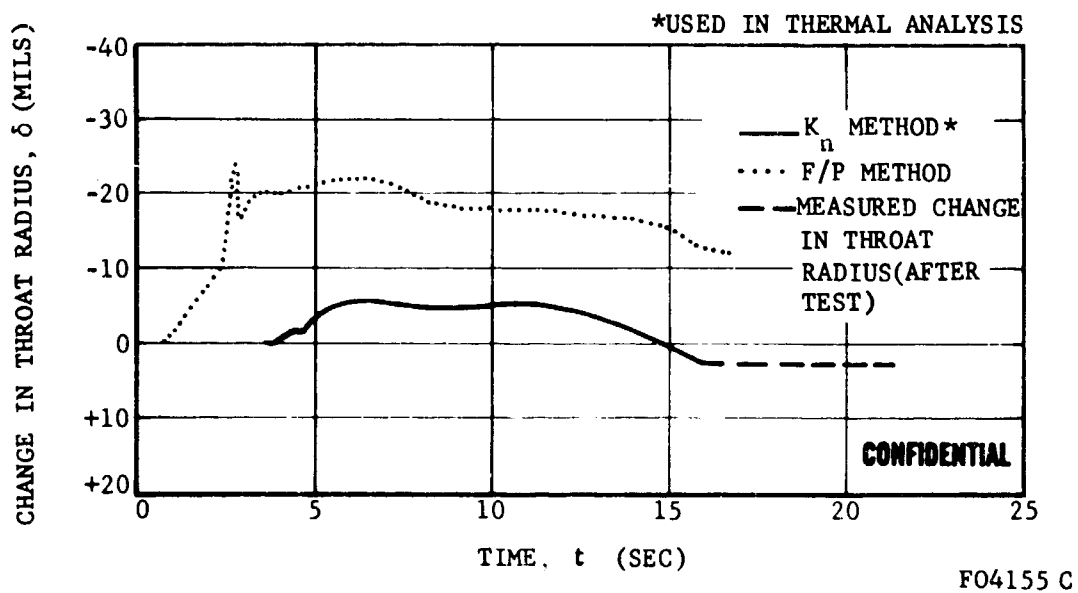
FIGURE 141. CHANGE IN NOZZLE THROAT RADIUS VERSUS FIRING TIME   TEST T-7
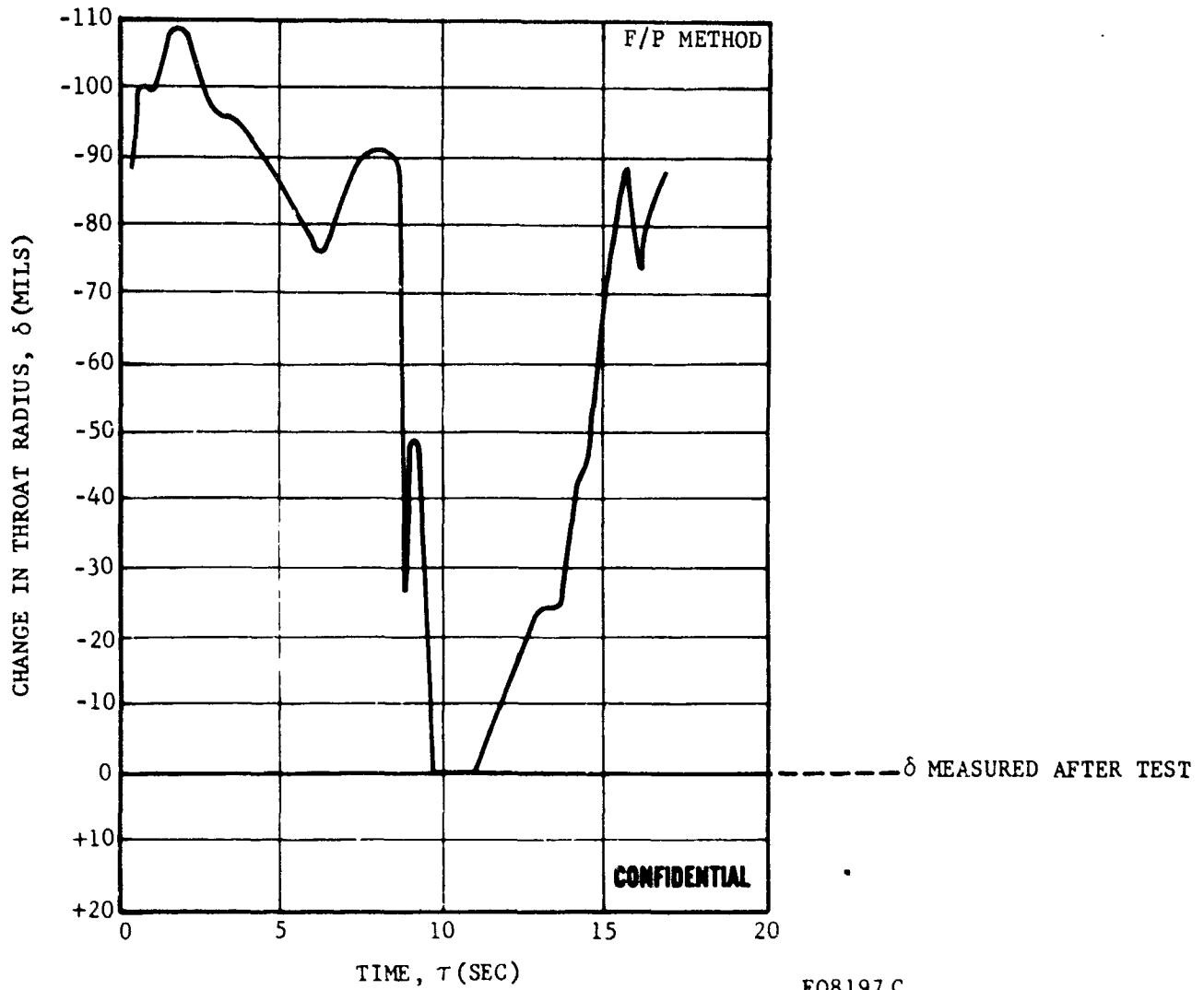
FIGURE 142. CHANGE IN NOZZLE THROAT RADIUS VS FIRING TIME TEST T-8
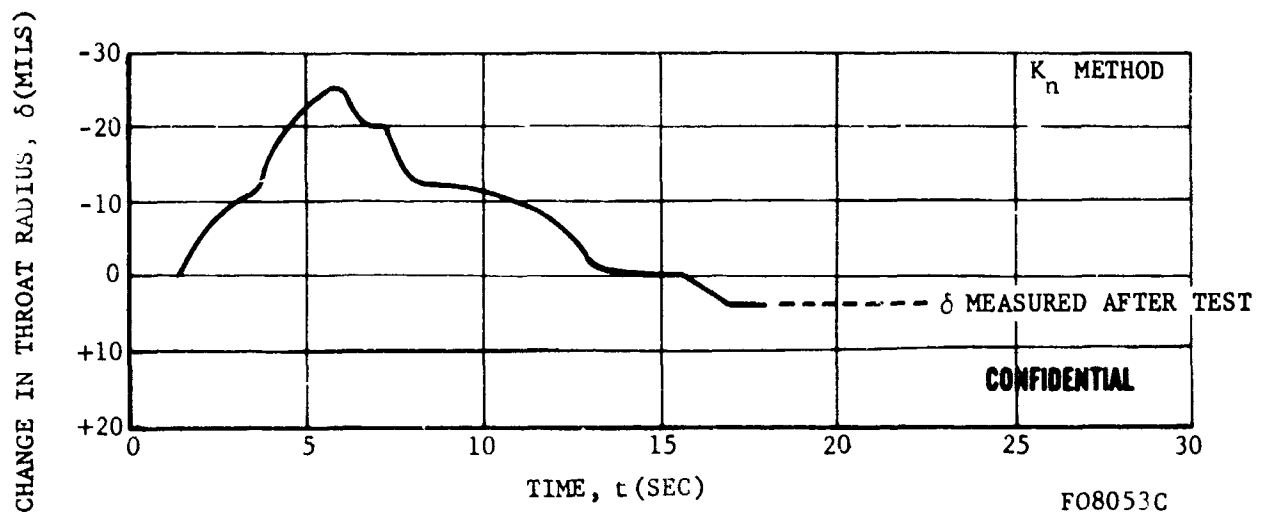
FIGURE 143. CHANGE IN NOZZLE THROAT RADIUS VS FIRING TIME TEST T-9
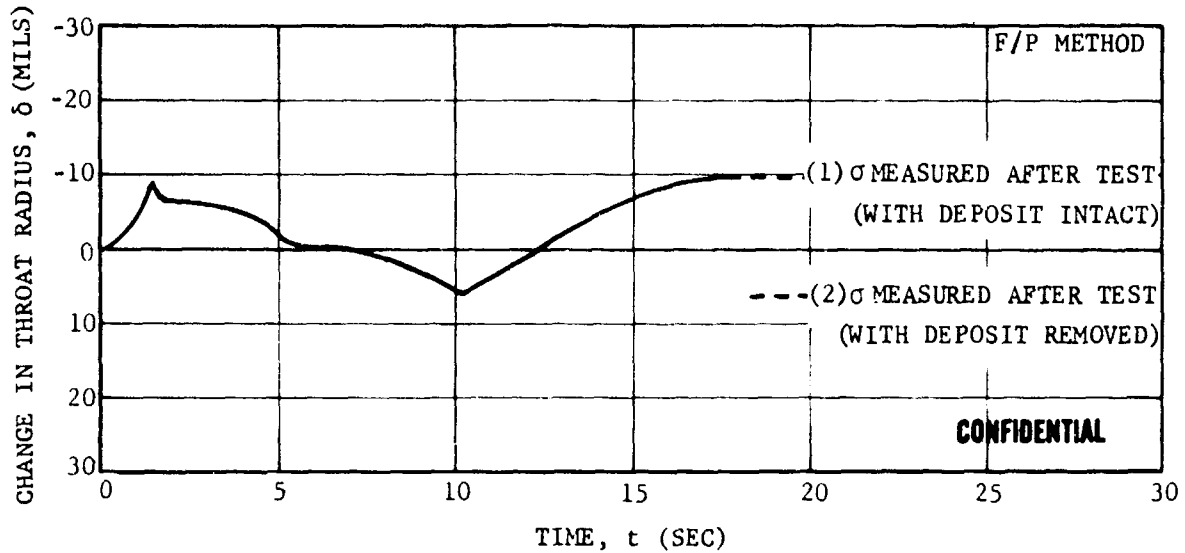
FIGURE 144. CHANGE IN NOZZLE THROAT RADIUS VERSUS FIRING TIME TEST T-10

F08052 C
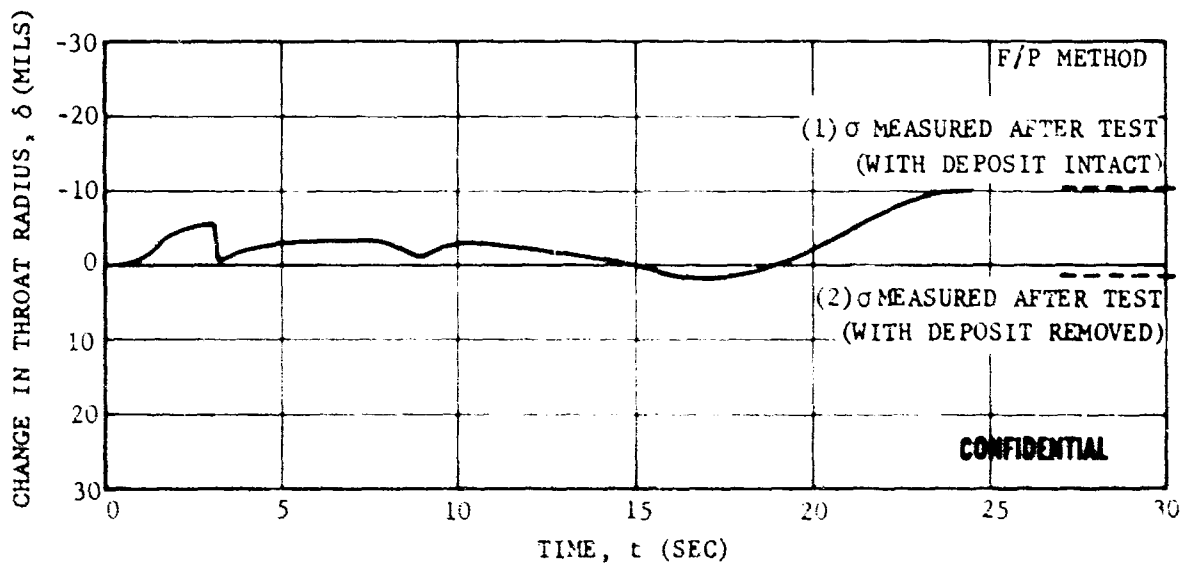
FIGURE 145. CHANGE IN NOZZLE THROAT RADIUS VERSUS FIRING TIME TEST T-11
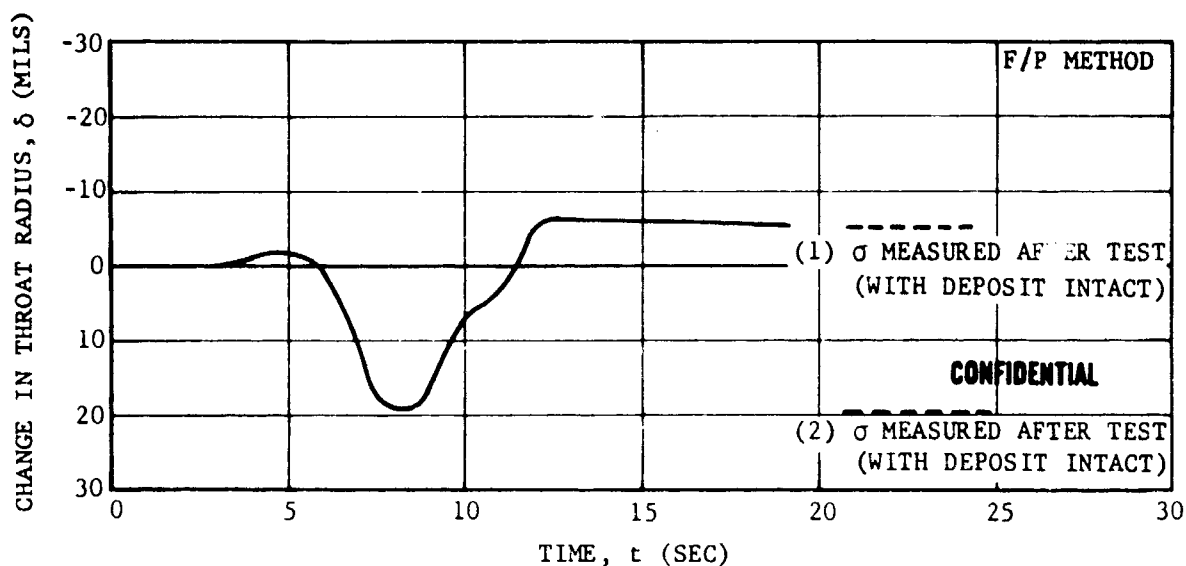
FIGURE 146. CHANGE IN NOZZLE THROAT RADIUS VERSUS FIRING TIME TEST T-12
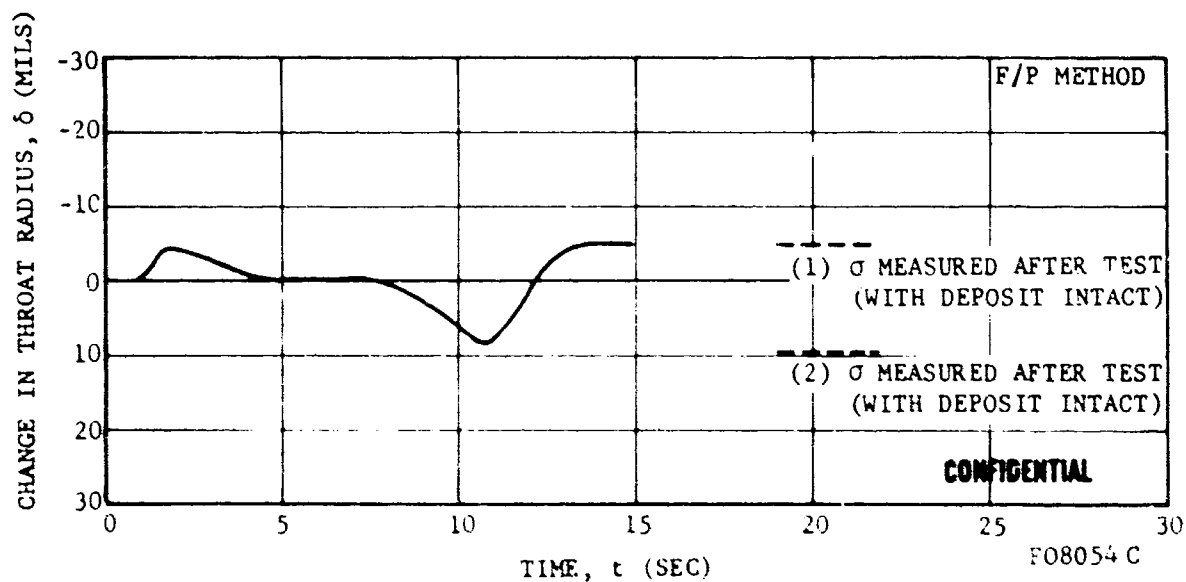
FIGURE 147. CHANGE IN NOZZLE THROAT RADIUS VERSUS FIRING TIME TEST T-13
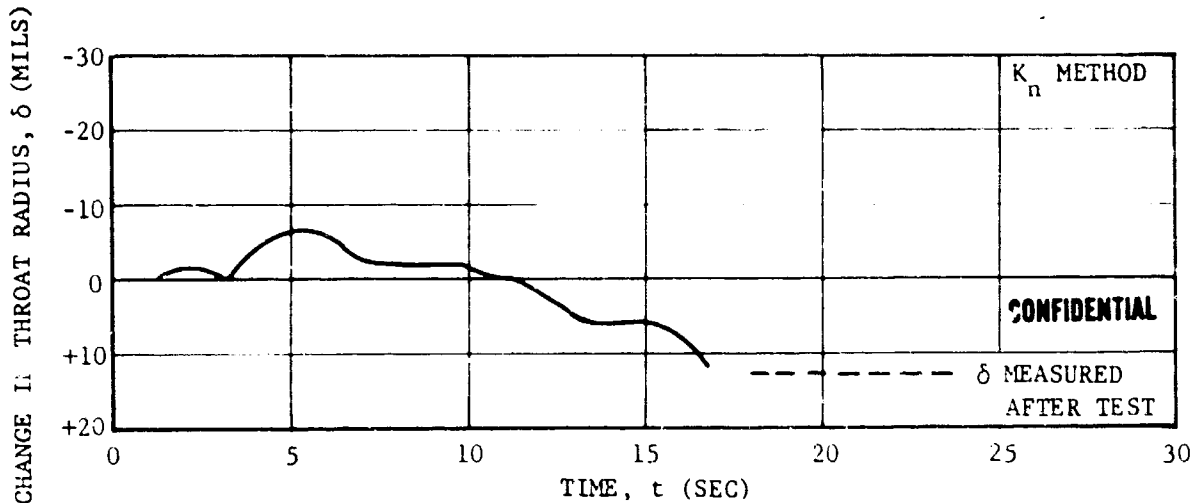
FIGURE 148.   CHANGE IN NOZZLE THROAT RADIUS VERSUS FIRING TIME TEST T-14
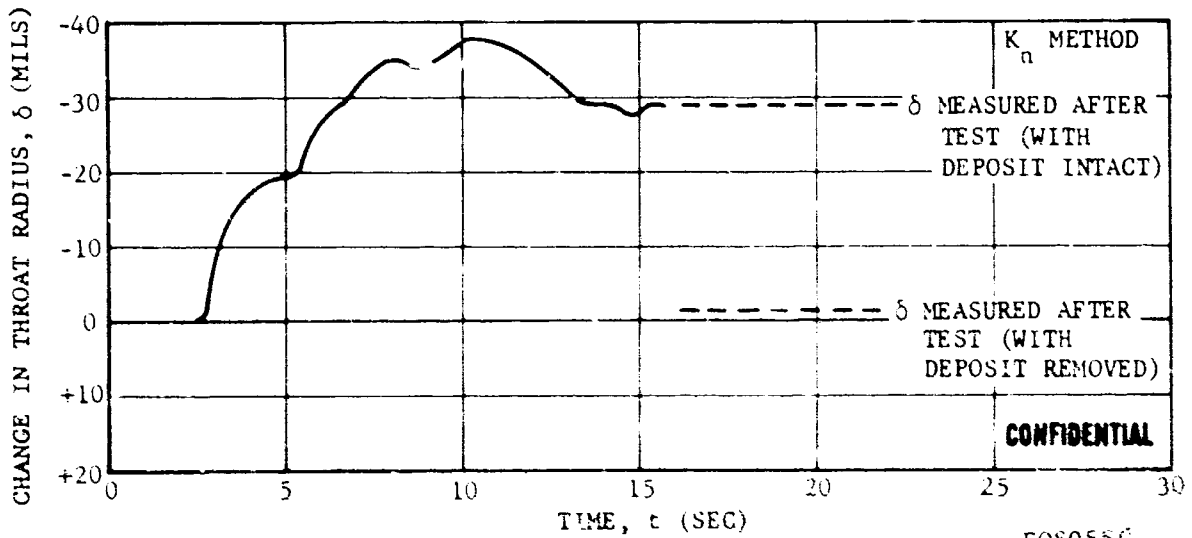
FIGURE 149.   CHANGE IN NOZZLE THROAT RADIUS VERSUS FIRING TIME TEST T-15

(1) δ MEASURED AFTER TEST (WITH DEPOSIT INTACT)

(2) δ MEASURED AFTER TEST (WITH DEPOSIT REMOVED)
THROAT SHRINKAGE DUE TO PLASTIC DEFORMATION
OF TUNGSTEN DURING COOLDOWN
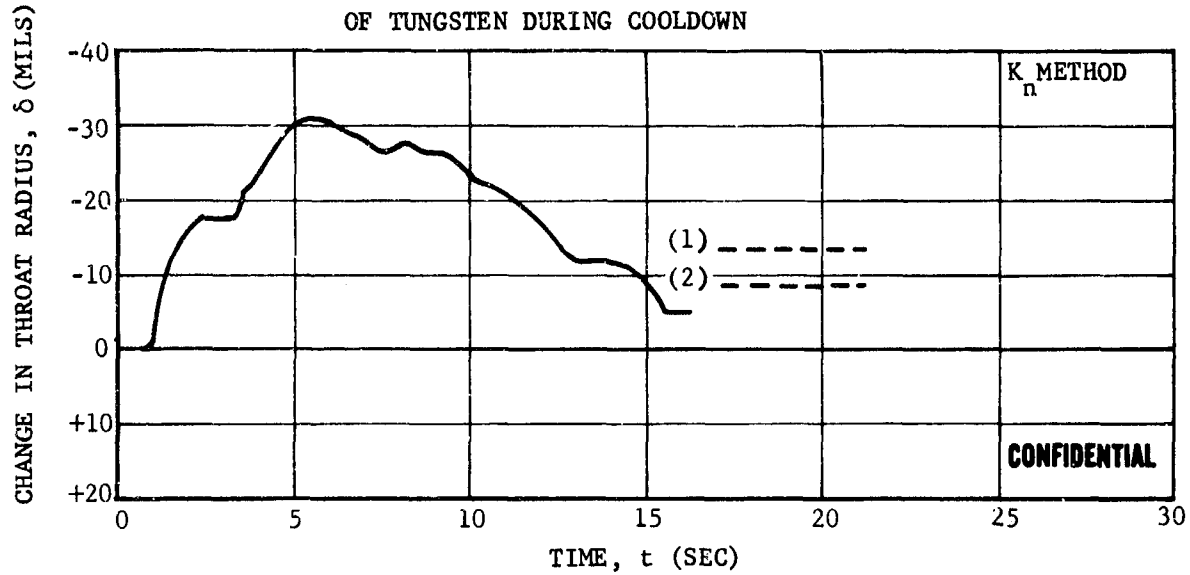
FIGURE 150. CHANGE IN NOZZLE THROAT RADIUS VERSUS FIRING TIME TEST T-16

FIGURE 151. CHANGE IN NOZZLE THROAT RADIUS VERSUS FIRING TIME TEST T-17

-311-

FIGURE 152. CHANGE IN NOZZLE THROAT RADIUS VERSUS FIRING TIME TEST T-18

    (1) δ MEASURED AFTER TEST (WITH DEPOSIT INTACT)

    (2) δ MEASURED AFTER TEST (WITH DEPOSIT REMOVED)
        THROAT SHRINKAGE DUE TO PLASTIC DEFORMATION
        OF TUNGSTEN DURING COOLDOWN

F08057 C

FIGURE 153. CHANGE IN NOZZLE THROAT RADIUS VERSUS FIRING TIME TEST T-19

FIGURE 154. CHANGE IN NOZZLE THROAT RADIUS VERSUS FIRING TIME TEST T-20

FIGURE 155. CHANGE IN NOZZLE THROAT RADIUS VERSUS FIRING TIME TEST T-2.

(1) δ MEASURED AFTER TEST (DEPOSIT INTACT)
(2) δ MEASURED AFTER TEST (DEPOSIT REMOVED)

FIGURE 156.   CHANGE IN NOZZLE THROAT RADIUS VERSUS FIRING TIME TEST T-22

FIGURE 157.   CHANGE IN NOZZLE THROAT RADIUS VERSUS FIRING TIME TEST T-23

FIGURE 158. CHANGE IN NOZZLE THROAT RADIUS VERSUS FIRING TIME TEST T-24

FIGURE 159. CHANGE IN NOZZLE THROAT RADIUS VERSUS FIRING TIME TEST T-25

FIGURE 160. CHANGE IN NOZZLE THROAT RADIUS VERSUS FIRING TIME, TEST T-51

FIGURE 161. CHANGE IN NOZZLE THROAT RADIUS VERSUS FIRING TIME, TEST T-52
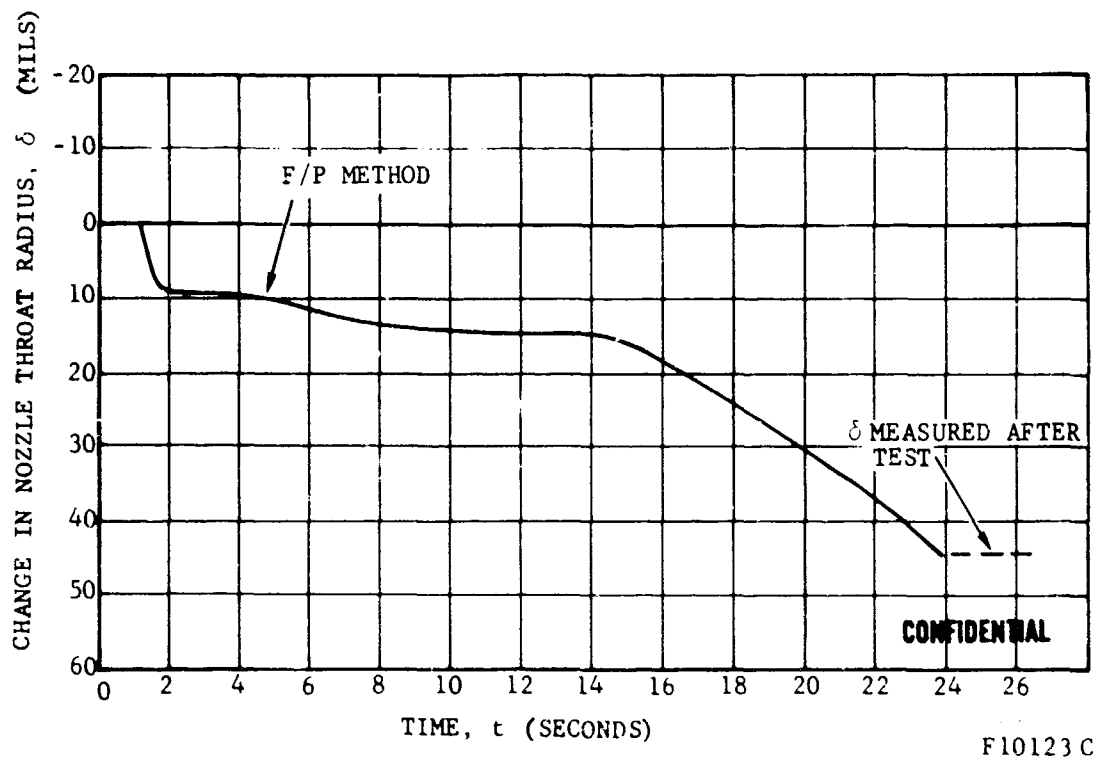
FIGURE 162. CHANGE IN NOZZLE THROAT RADIUS VERSUS FIRING TIME, TEST T-53
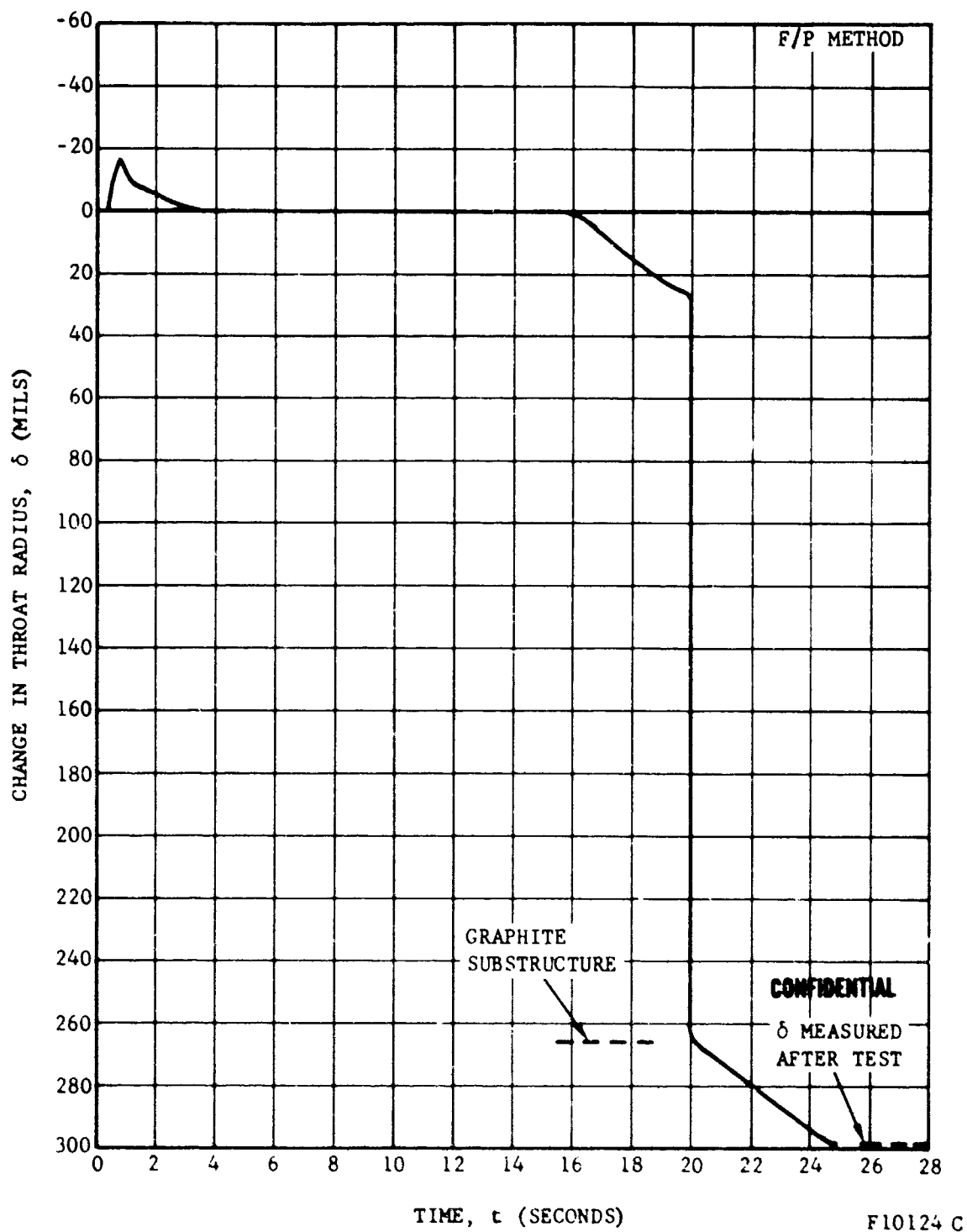
FIGURE 163. CHANGE IN NOZZLE THROAT RADIUS VERSUS FIRING TIME, TEST T-54
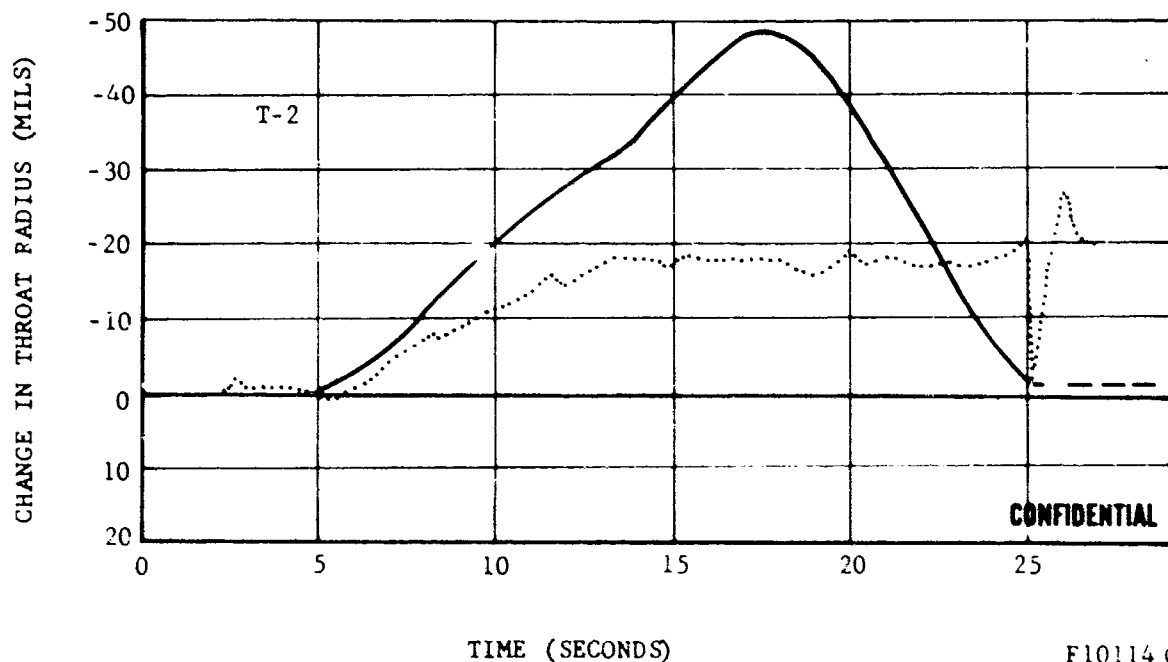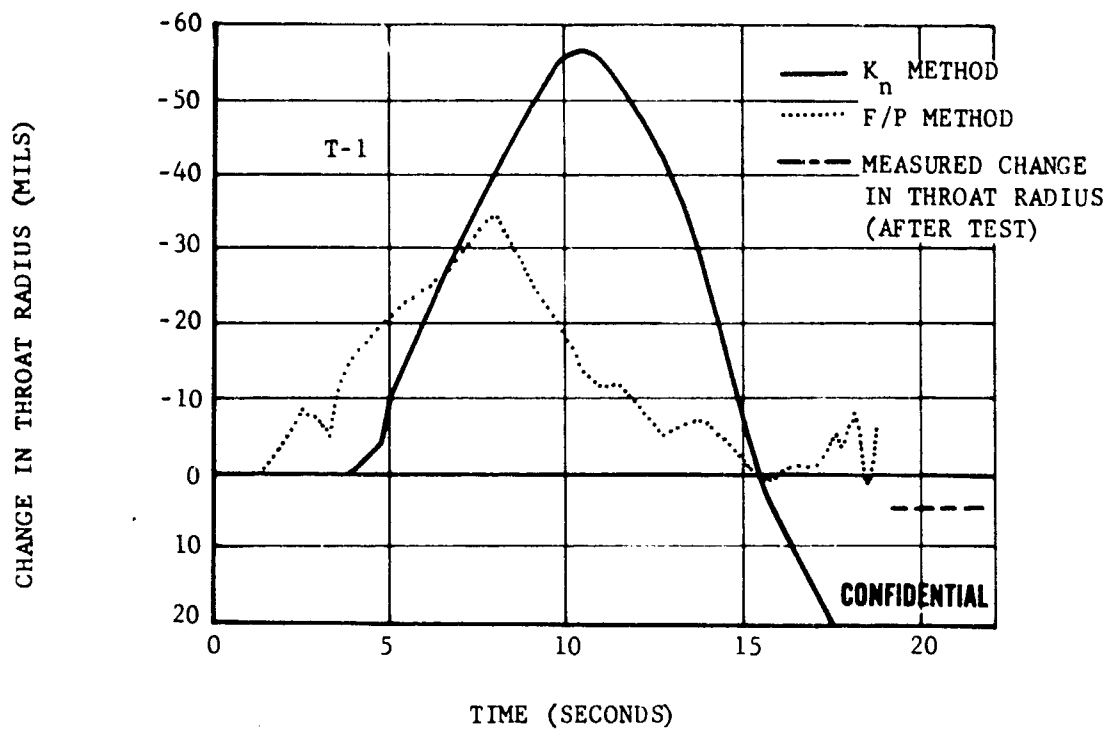
FIGURE 164. NOZZLE THROAT RADIUS VERSUS FIRING TIME FOR
TESTS T-1 AND T-2
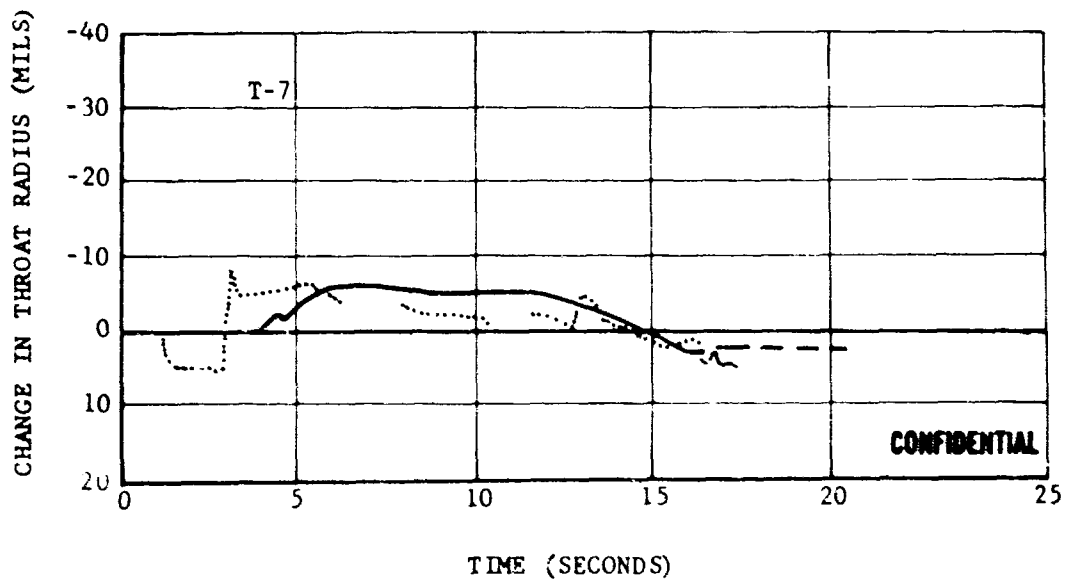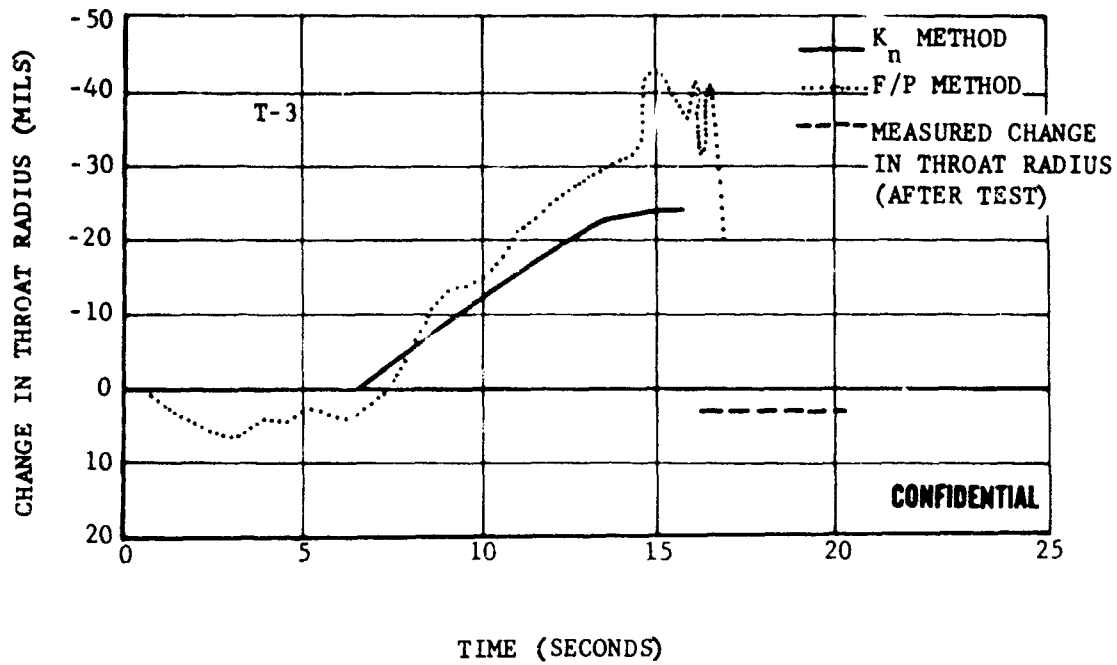
FIGURE 165. CHANGE IN NOZZLE THROAT RADIUS VERSUS TIME FOR
TESTS T-3 AND T-7

F10115C

-321-
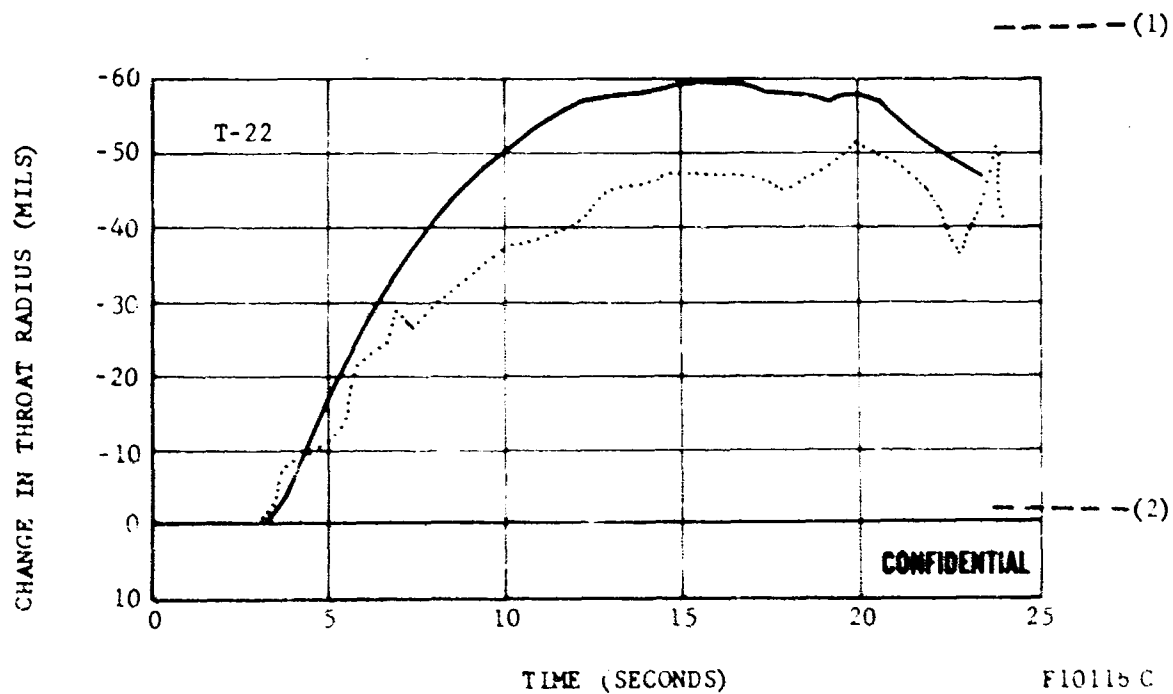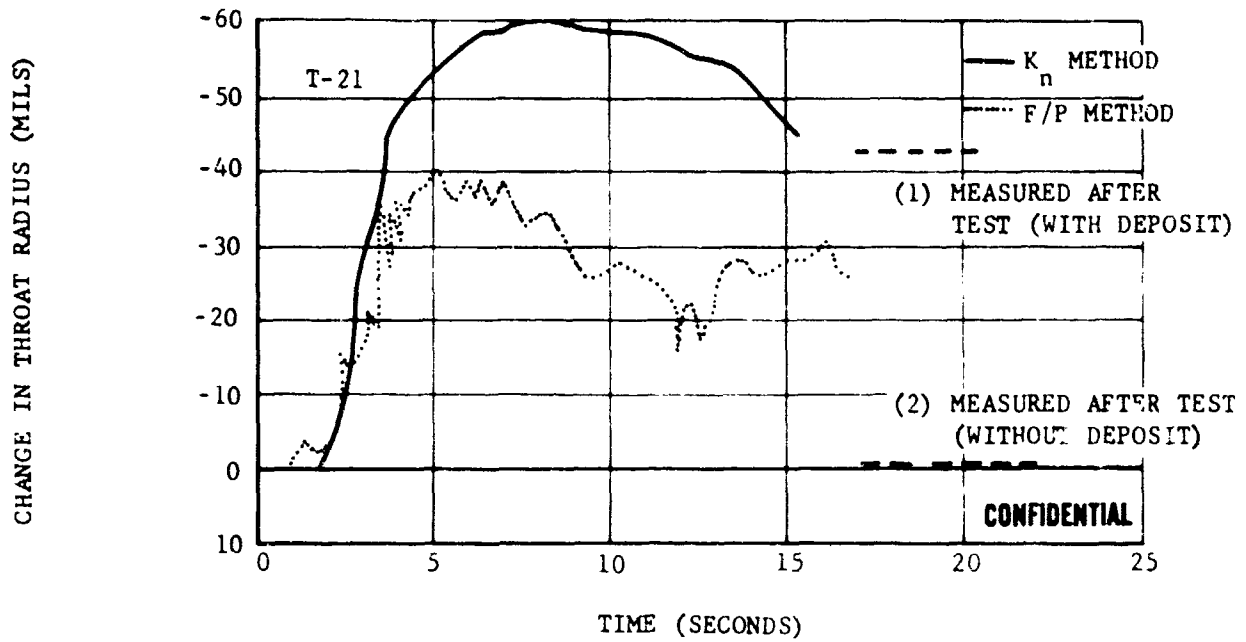
FIGURE 166. CHANGE IN THROAT RADIUS VERSUS FIRING TIME FOR
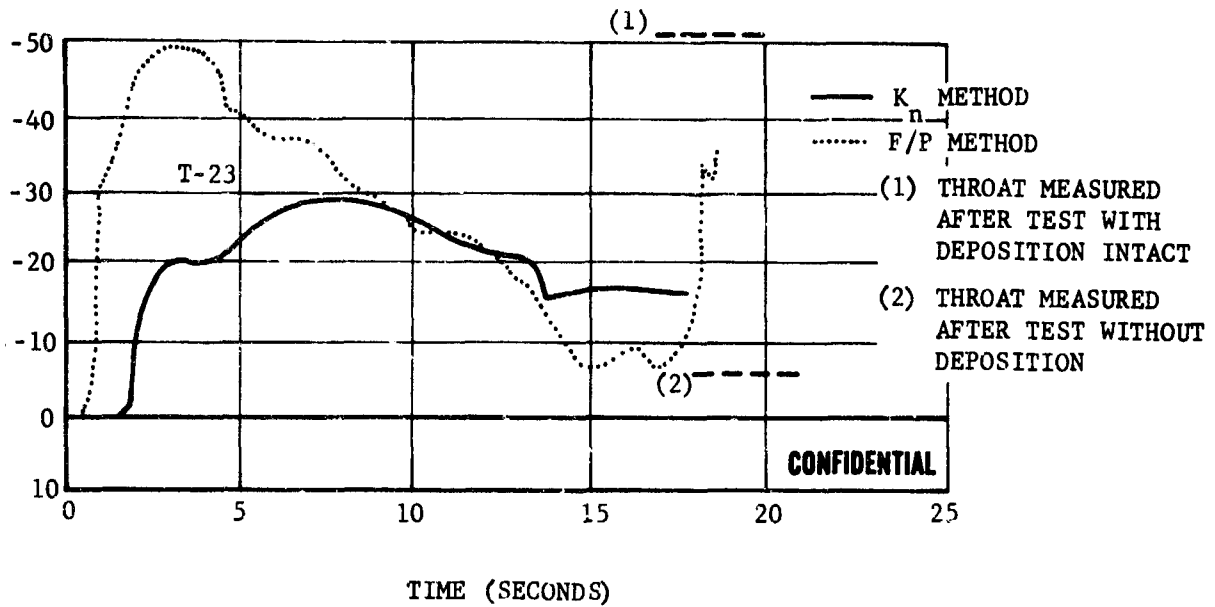TESTS T-21 AND T-22
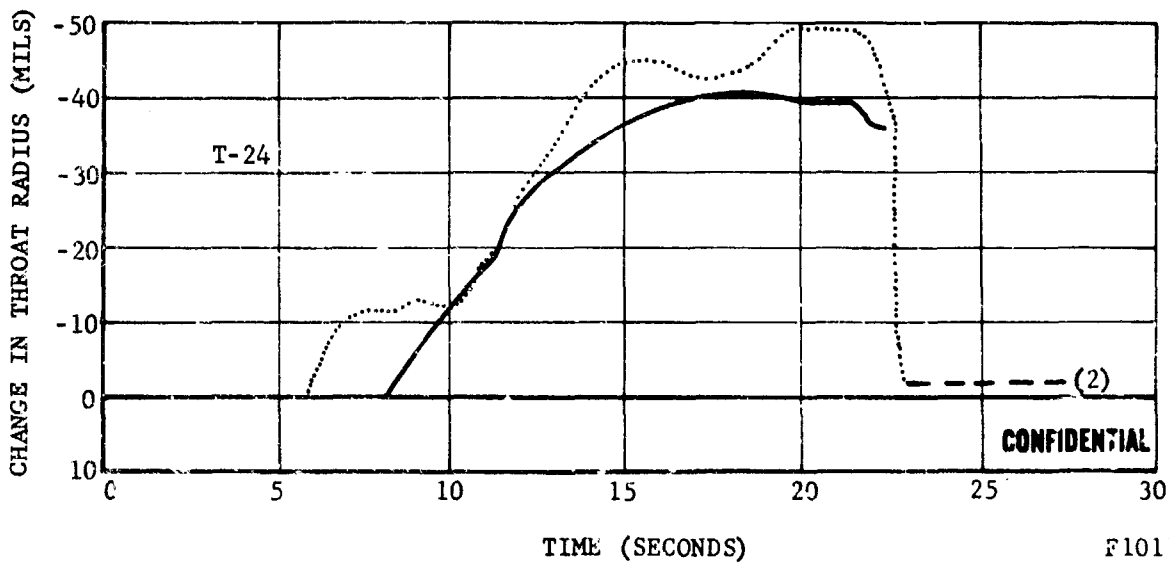
FIGURE 167.   CHANGE IN NOZZLE THROAT RADIUS VERSUS FIRING TIME
FOR TESTS T-23 AND T-24
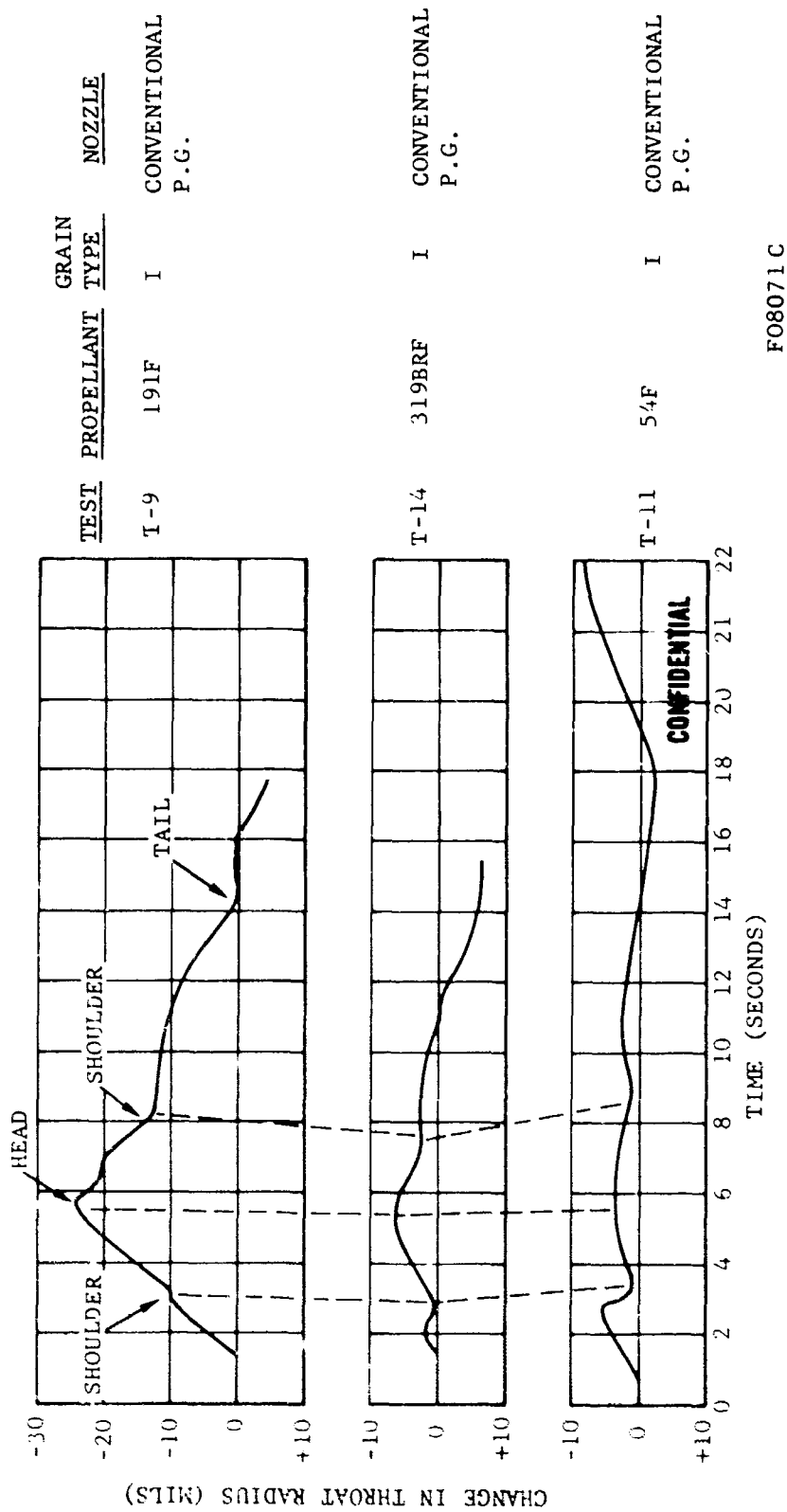
FIGURE 163. PROPELLANT EFFECTS ON THROAT DEPOSIT HISTORY (I)

F08071C

TEST	PROPELLANT	GRAIN TYPE	NOZZLE
T-9	191F	I	CONVENTIONAL P.G.
T-14	319BRF	I	CONVENTIONAL P.G.
T-11	54F	I	CONVENTIONAL P.G.

NOTE: ALL TESTS HAVE SHOWN ARE CLOSE END-BURNING GRAIN
AND STEEP INLET PYROLYTIC GRAPHITE NOZZLES
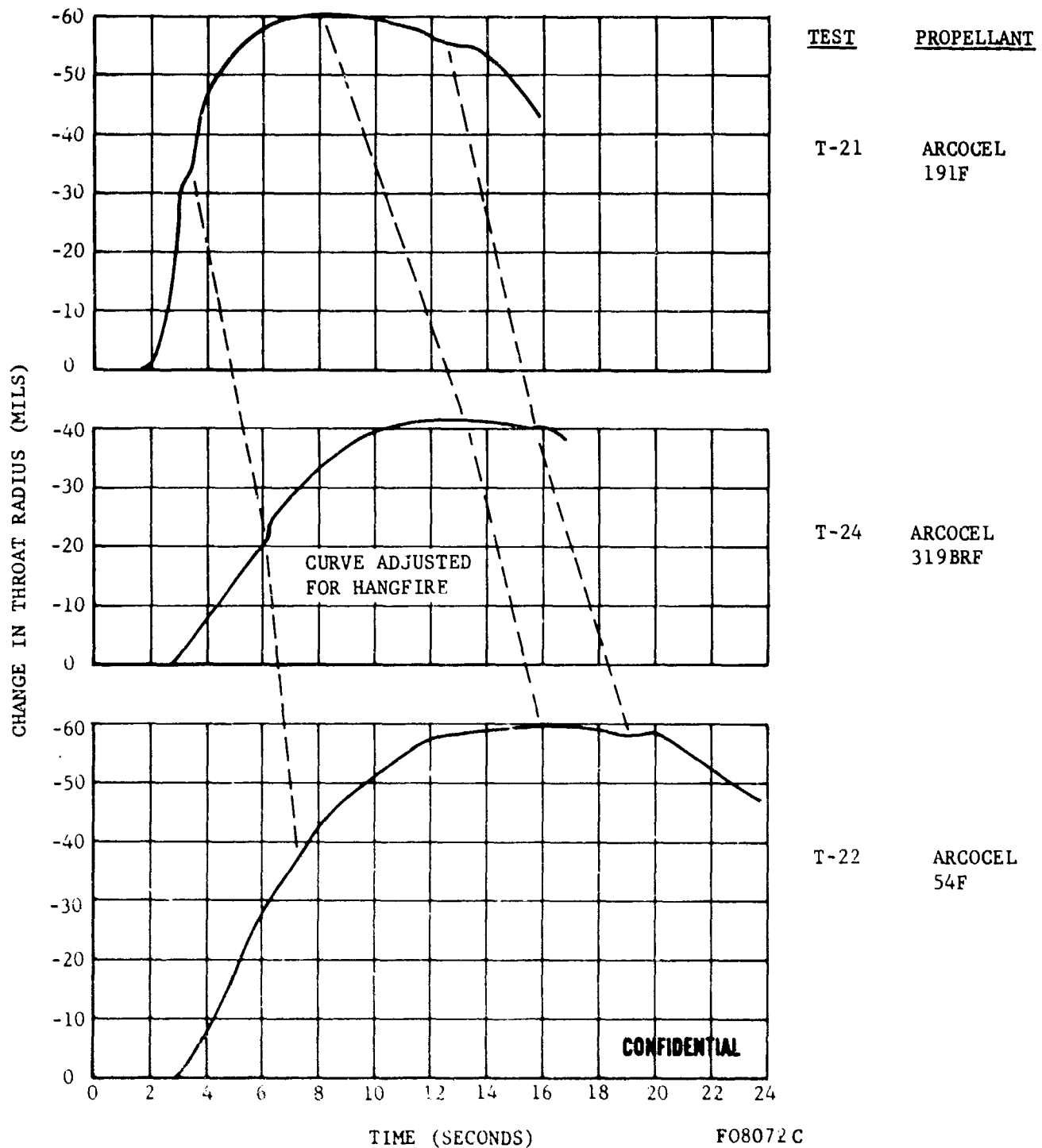

FIGURE 169. PROPELLANT EFFECTS ON THROAT DEPOSIT HISTORY (II)

F08072C

NOTES:

ALL NOZZLES ARE CONVENTIONAL PYROLYTIC GRAPHITE
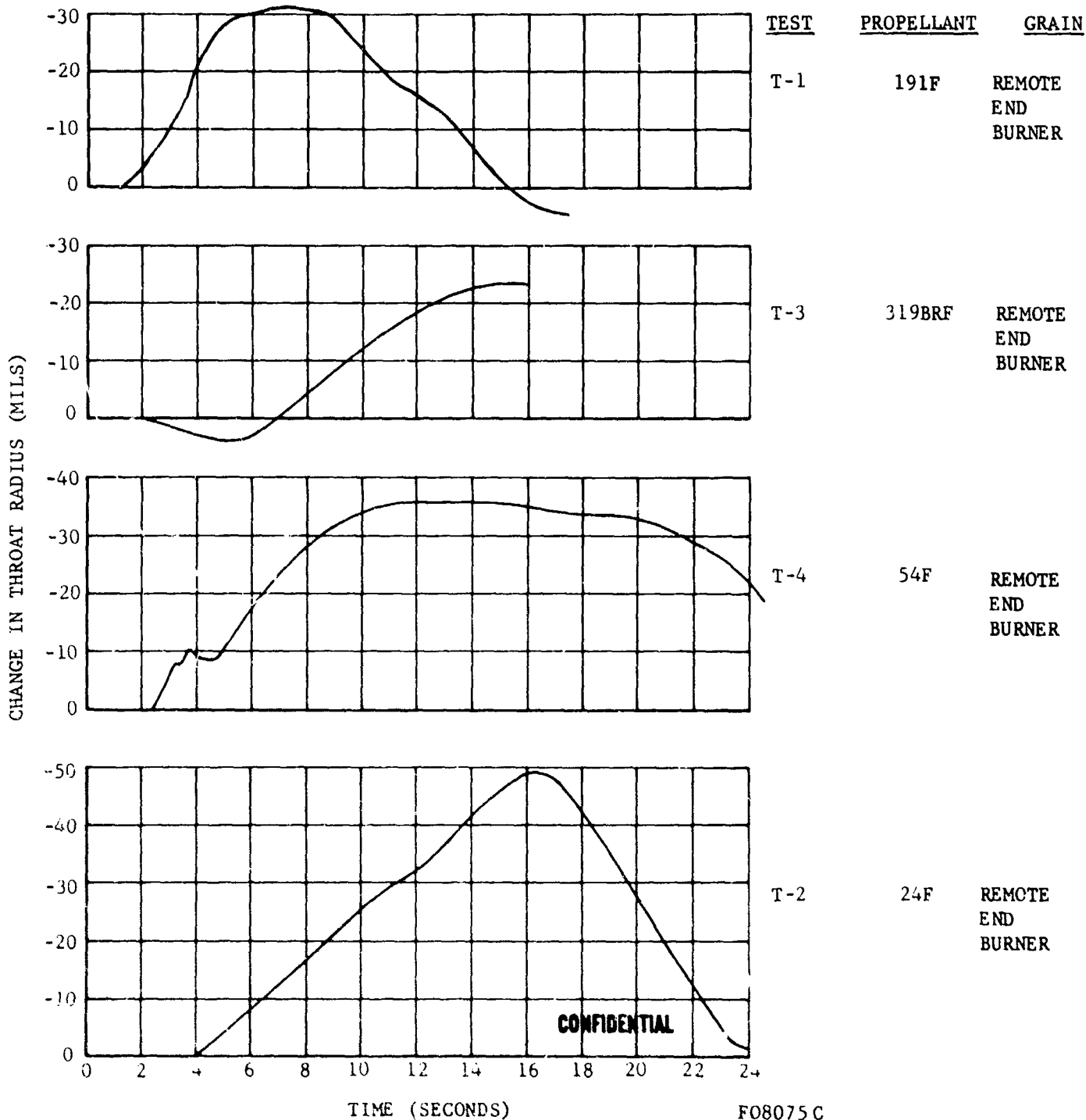
TIME SCALE ADJUSTED TO ELIMINATE IGNITER SPIKES

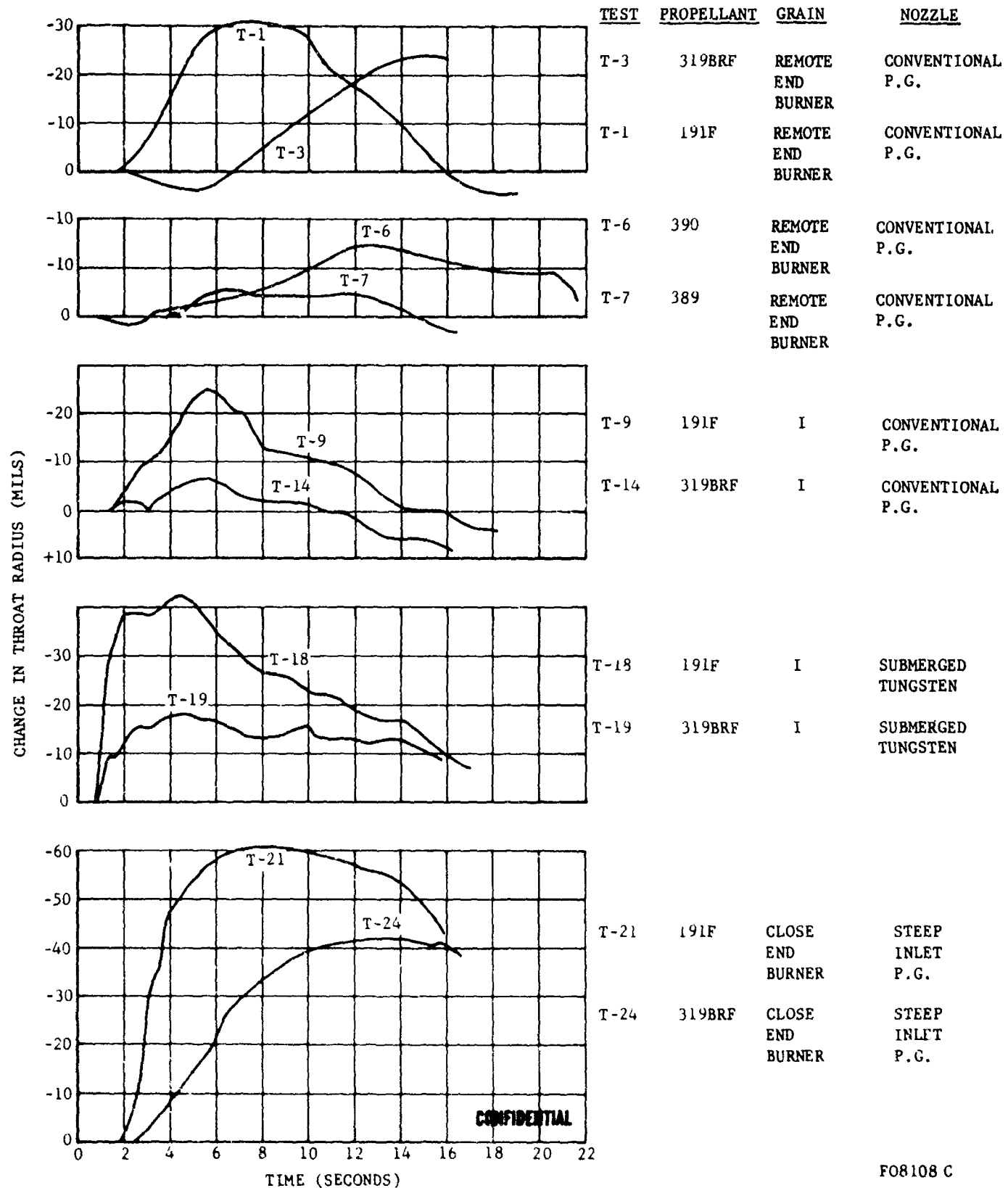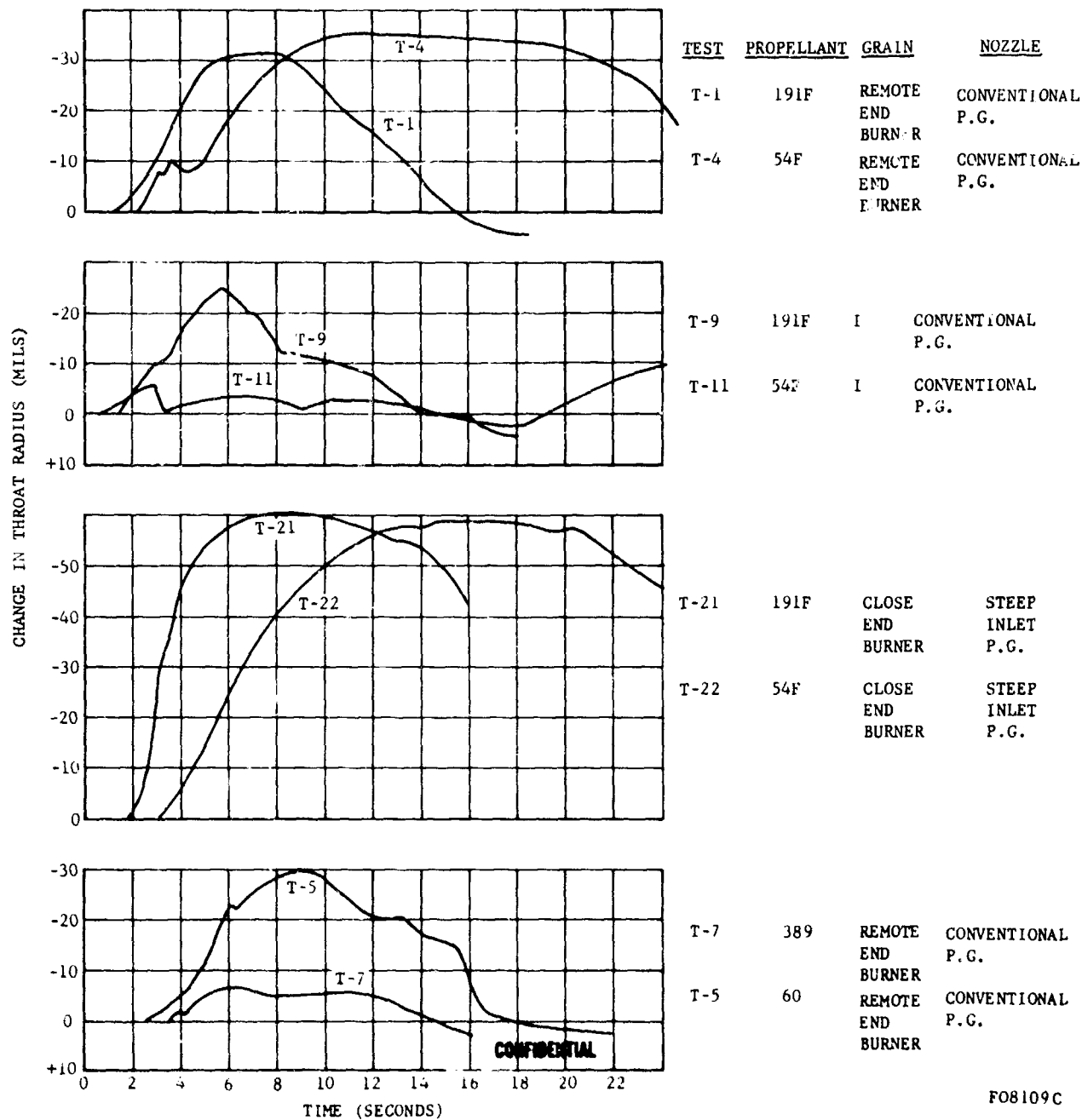| TEST	PROPELLANT	GRAIN
T-1	191F	REMOTE END BURNER
T-3	319BRF	REMOTE END BURNER
T-4	54F	REMOTE END BURNER
T-2	24F	REMOTE END BURNER

CHANGE IN THROAT RADIUS (MILS)

TIME (SECONDS)

F08075C

FIGURE 170. PROPELLANT EFFECTS ON THROAT DEPOSIT HISTORY (III)

FIGURE 171. PROPELLANT EFFECTS ON THROAT DEPOSIT HISTORY (IV)

F08108 C

-327-

FIGURE 172. PROPELLANT EFFECTS ON THROAT DEPOSIT HISTORY (V)

TEST	PROPELLANT	GRAIN	NOZZLE
T-3	319BRF	REMOTE END BURNER	CONVENTIONAL P.G.
T-4	54F	REMOTE END BURNER	CONVENTIONAL P.G.
T-14	319BRF	I	CONVENTIONAL P.G.
T-11	54F	I	CONVENTIONAL P.G.
T-24	319BRF	CLOSE END BURNER	STEEP INLET P.G.
T-22	54F	CLOSE END BURNER	STEEP INLET P.G.
T-6	390	REMOTE END BURNER	CONVENTIONAL P.G.
T-5	60	REMOTE END BURNER	CONVENTIONAL P.G.

F08110 C
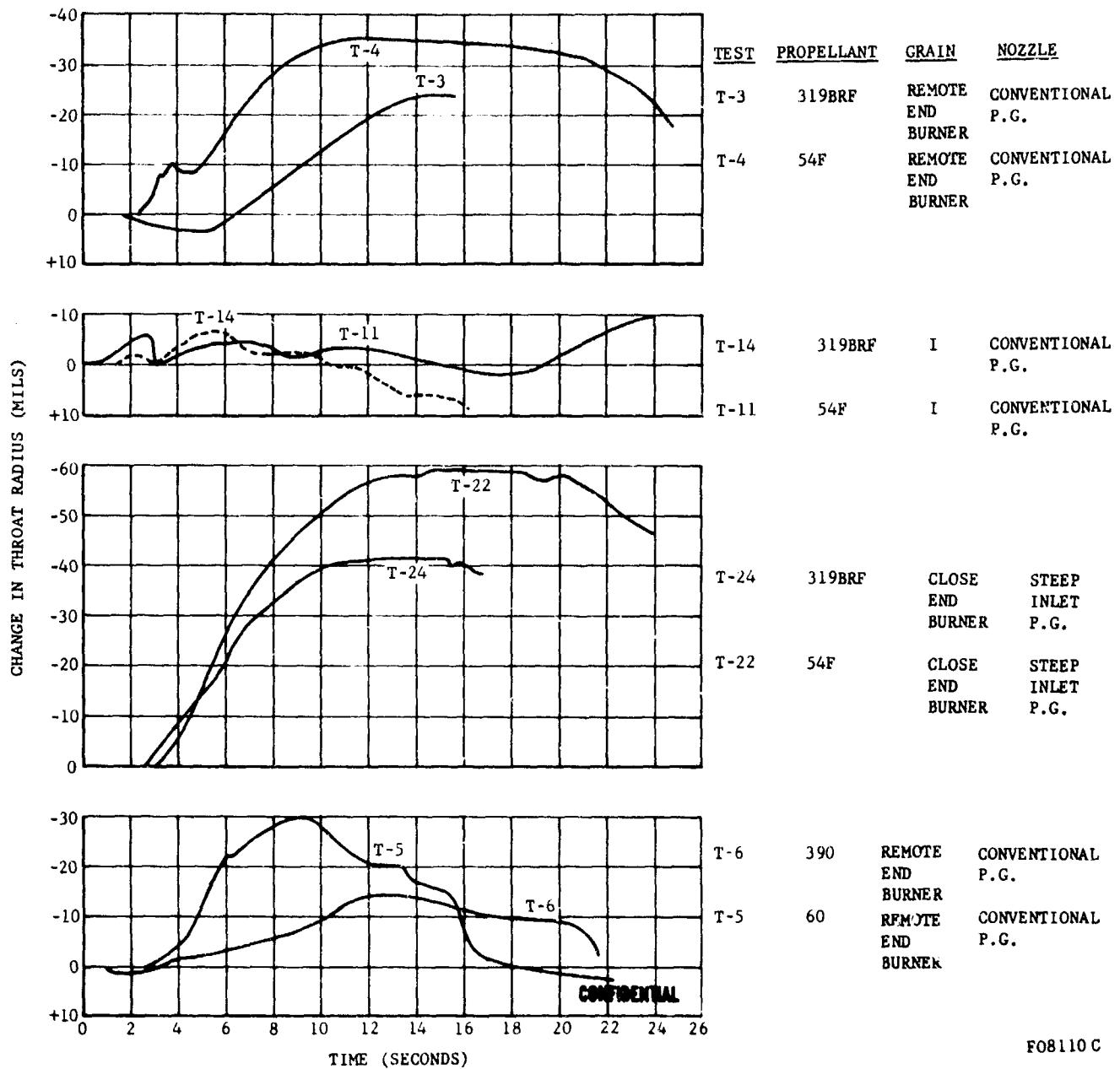
FIGURE 173.   PROPELLANT EFFECTS ON THROAT DEPOSIT HISTORY (VI)

-329-

TEST	PROPELLANT	NOZZLE CONTOUR
T-9	191F	CONVENTIONAL
T-11	54F	CONVENTIONAL
T-16	191F	CONVENTIONAL
T-17	191F	CONVENTIONAL
T-25	191F	CONVENTIONAL

T-14	319BRF	CONVENTIONAL
T-18	191F	SUBMERGED
T-19	319BRF	SUBMERGED

NOTE: S = SHOULDER
       H = HEAD
       T = TAIL

FO8113C
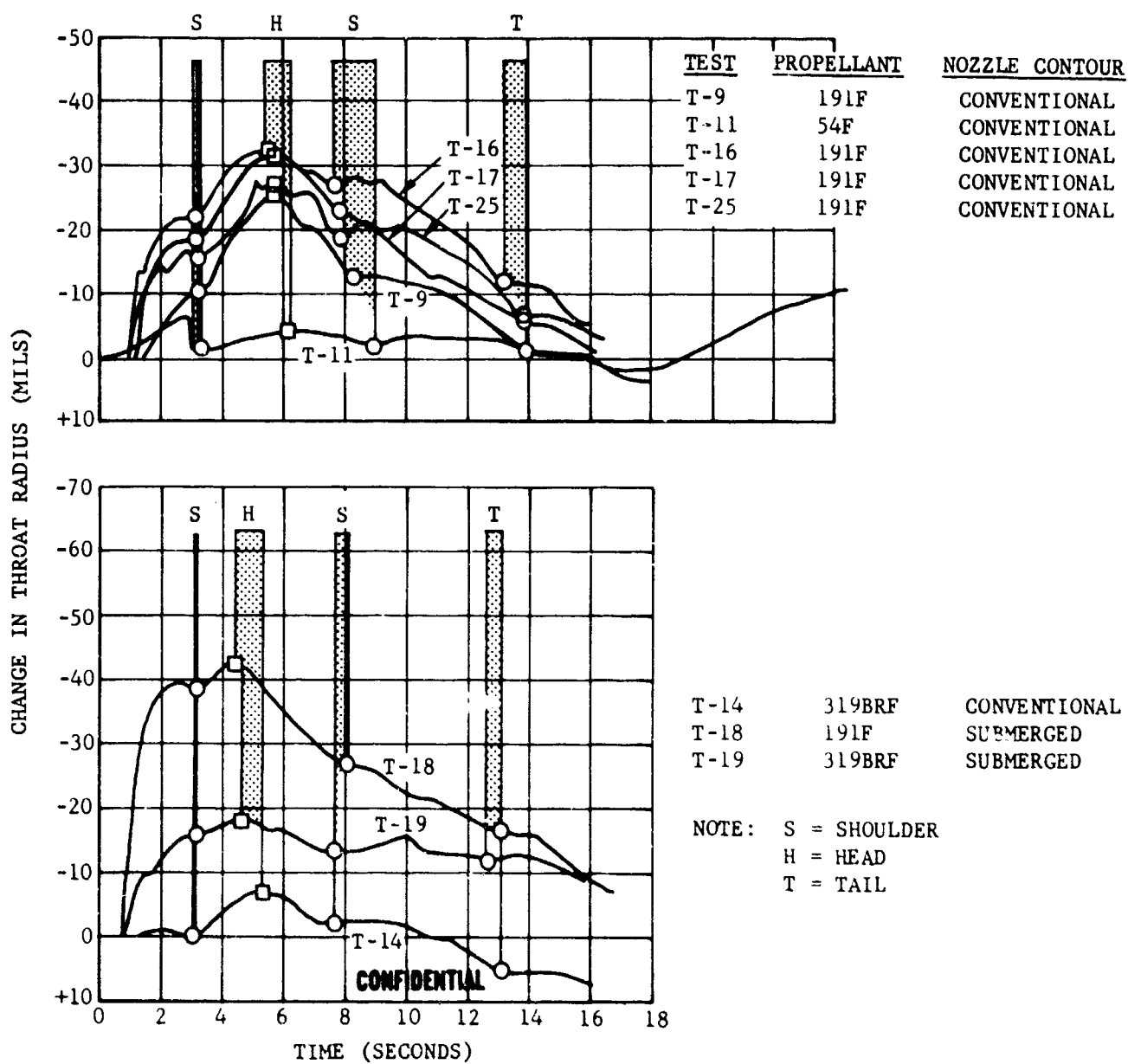
FIGURE ... EFFECT OF GRAIN TYPE ON THROAT DEPOSIT HISTORY (I)
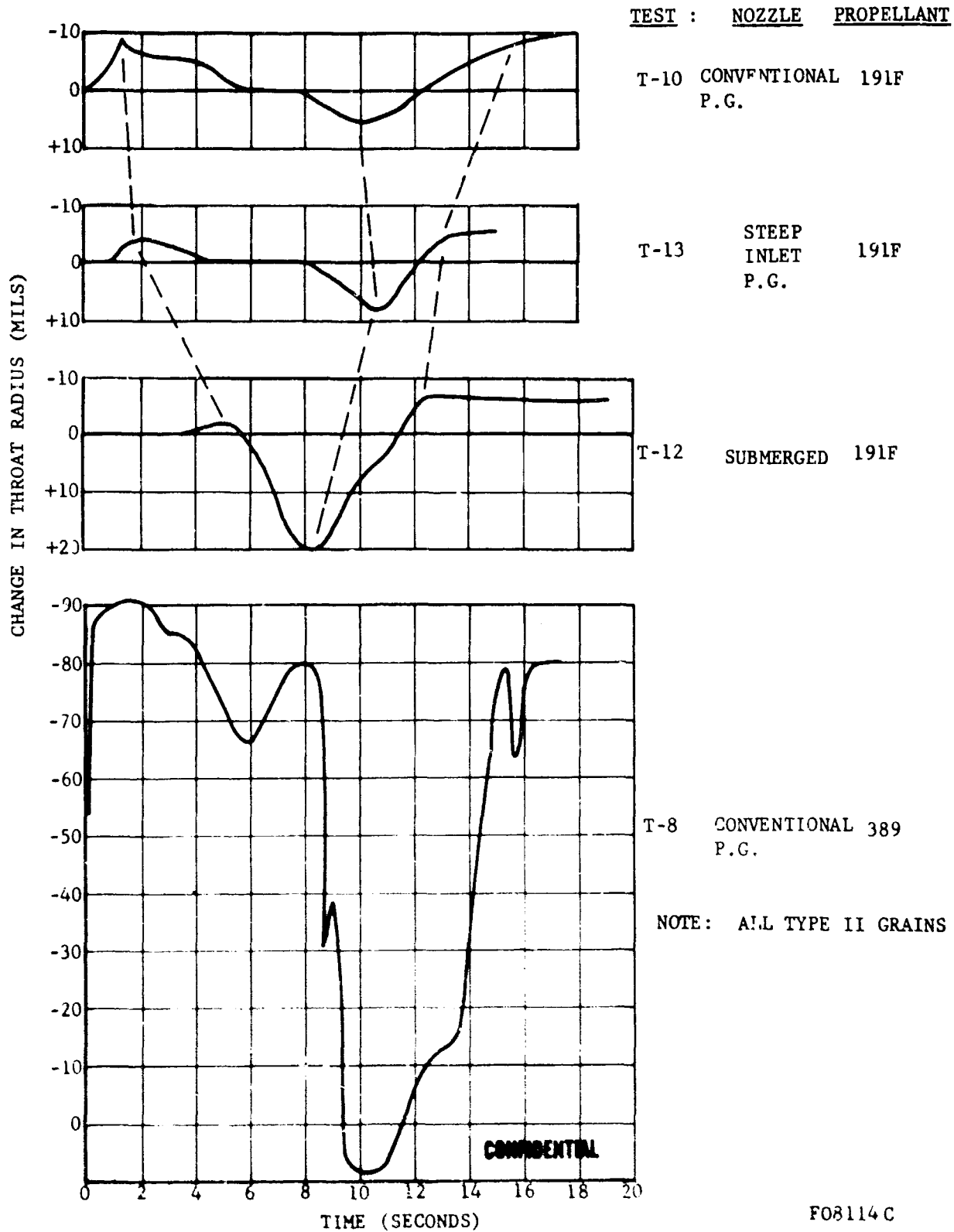
FIGURE 175. EFFECT OF NOZZLE AND GRAIN TYPE ON THROAT DEPOSIT HISTORY

-331-

FIGURE 176. EFFECT OF GRAIN TYPE ON THROAT DEPOSIT HISTORY (II)
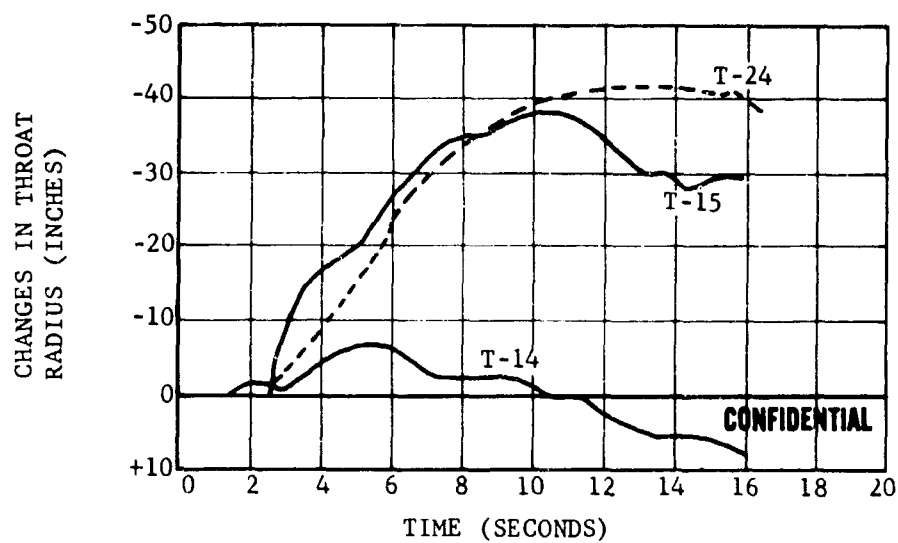
TEST	PROPELLANT ,	GRAIN	NOZZLE
T-14	319BRF	I	CONVENTIONAL P.G.
T-15	319BRF	III	CONVENTIONAL P.G.
T-24	319BRF	CLOSE END BURNER	STEEP INLET P.G.

F08115 C
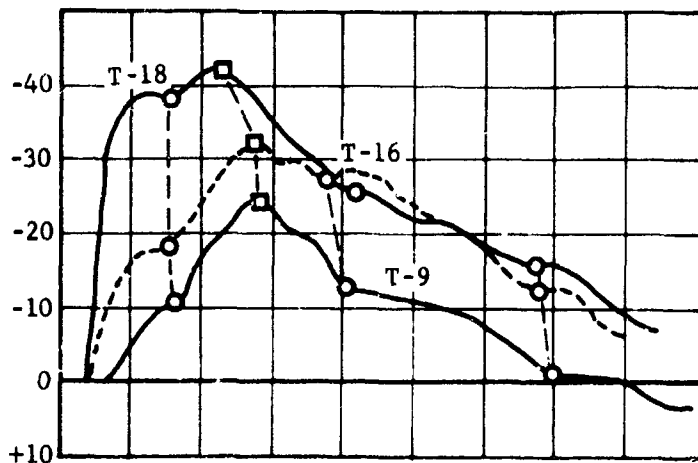
TEST	PROPELLANT	GRAIN	NOZZLE
T-9	191F	I	CONVENTIONAL P.G.
T-16	191F	I	SUBMERGED TUNGSTEN
T-18	191F	I	SUBMERGED TUNGSTEN
T-19	319BRF	I	SUBMERGED TUNGSTEN
T-14	319BRF	I	CONVENTIONAL P.G.
T-21	191F	CLOSE END BURNER	STEEP INLET P.G.
T-23	191F	CLOSE END BURNER	SUBMERGED P.G.
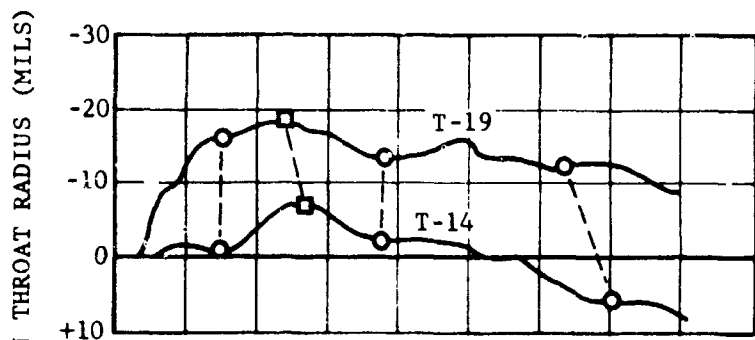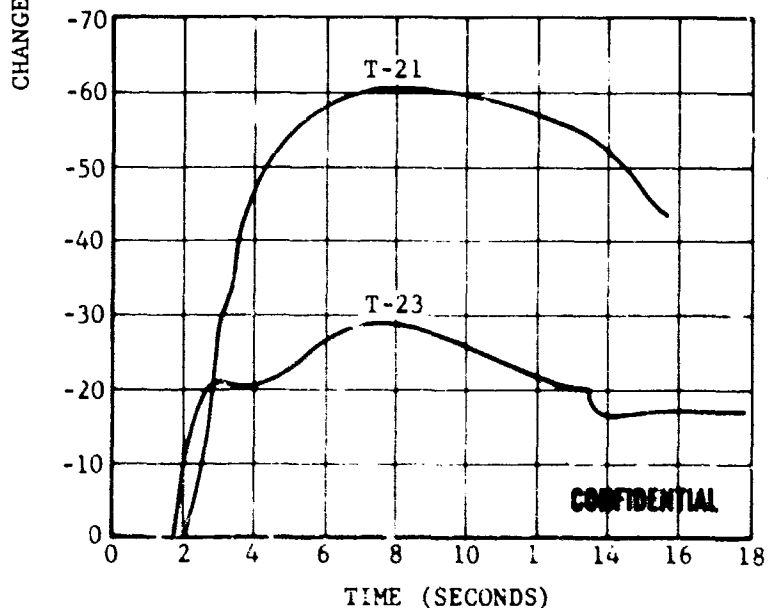
CHANGE IN THROAT RADIUS (MILS)

TIME (SECONDS)

FO8116C

FIGURE 177. NOZZLE EFFECTS ON THROAT DEPOSIT HISTORY

-333-

TEST	PROPELLANT	GRAIN	NOZZLE
T-25	191F	I	CONVENTIONAL P.G. (THICK HEAT SINK)
T-9	191F	I	CONVENTIONAL P.G.

TEST	PROPELLANT	GRAIN	NOZZLE
T-16	191F	I	CONVENTIONAL TUNGSTEN
T-25	191F	I	CONVENTIONAL P.G. (THICK HEAT SINK)
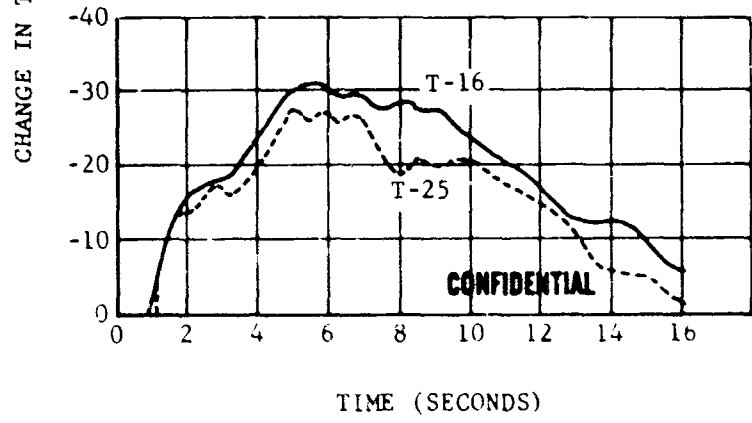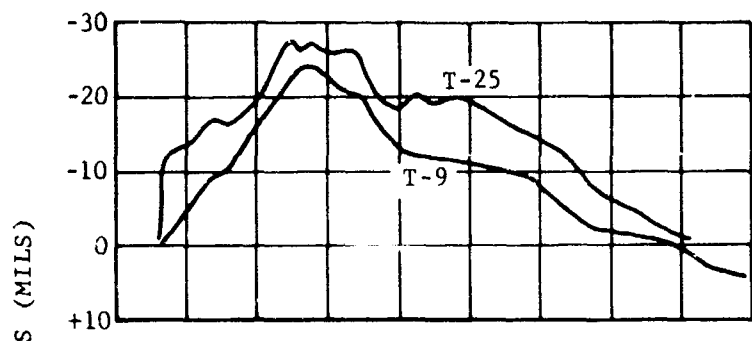
F08117C

FIGURE 178. EFFECTS OF HEAT SINK ON THROAT DEPOSIT HISTORY

NOTE:

191F PROPELLANT
{
T-16
T-17
} GRAIN TYPE I CONVENTIONAL TUNGSTEN NOZZLE

T-9
T-20
} GRAIN TYPE I CONVENTIONAL P.G. THROAT

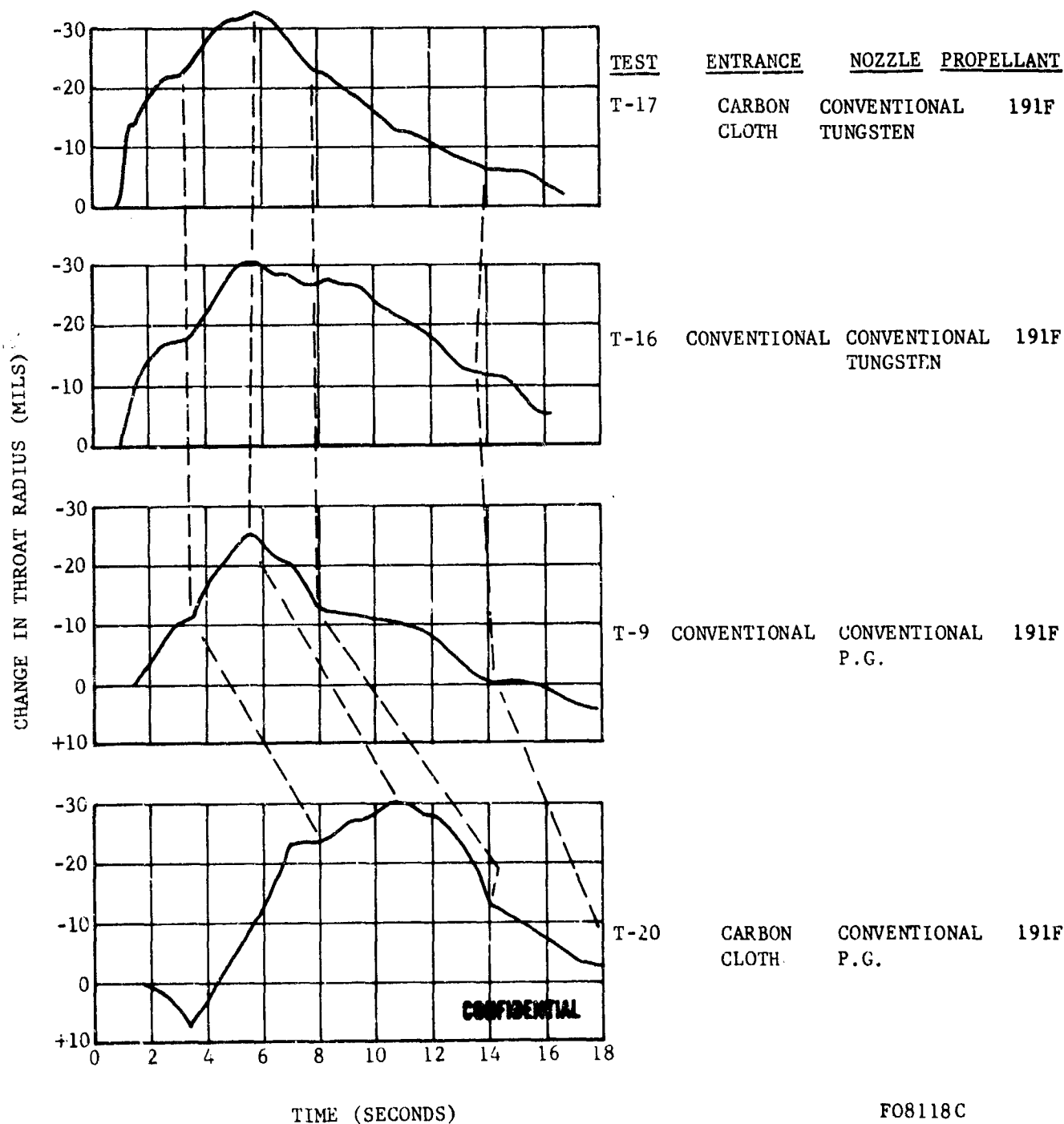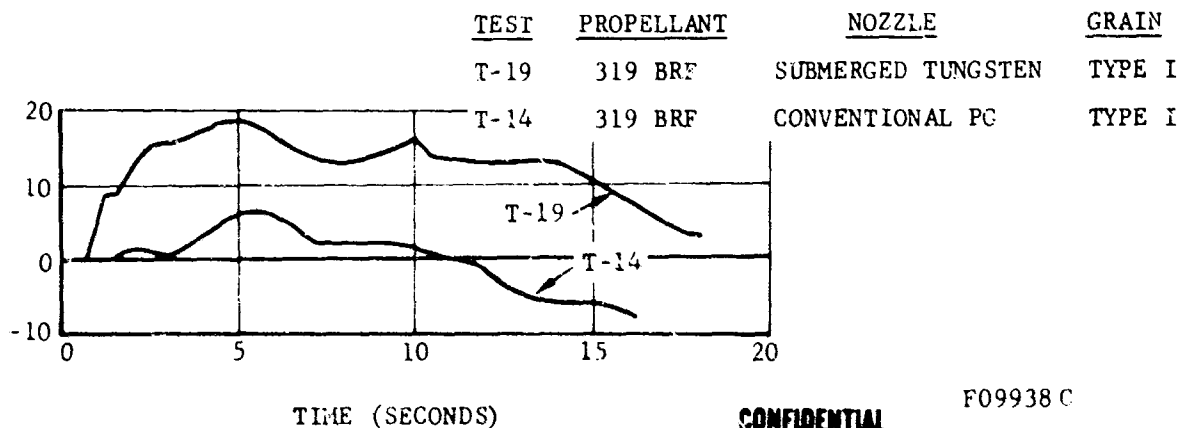| TEST	ENTRANCE	NOZZLE	PROPELLANT
T-17	CARBON CLOTH	CONVENTIONAL TUNGSTEN	191F
T-16	CONVENTIONAL	CONVENTIONAL TUNGSTEN	191F
T-9	CONVENTIONAL	CONVENTIONAL P.G.	191F
T-20	CARBON CLOTH	CONVENTIONAL P.G.	191F

CHANGE IN THROAT RADIUS (MILS)

TIME (SECONDS)

F08118C

FIGURE 179. EFFECT OF CARBON CLOTH ENTRANCE ON THROAT DEPOSIT HISTORY

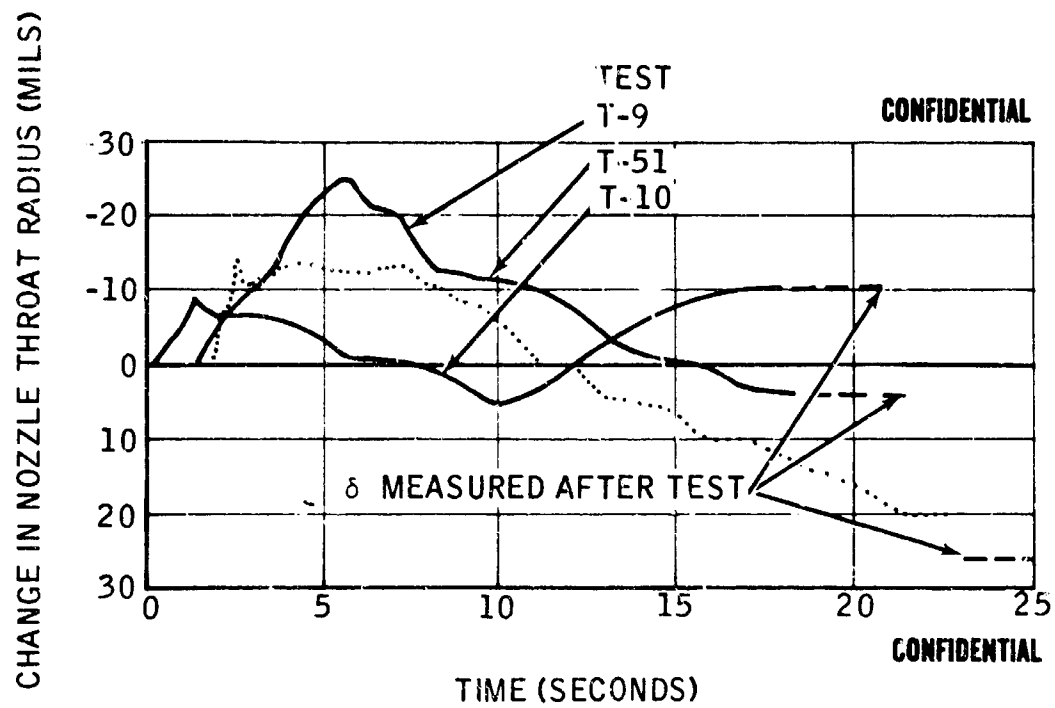| TEST	PROPELLANT	NOZZLE	GRAIN
T-10	191F	CONVENTIONAL PG	TYPE II
T-12	191F	SUBMERGED TUNGSTEN	TYPE II

TEST	PROPELLANT	NOZZLE	GRAIN
T-18	191F	SUBMERGED TUNGSTEN	TYPE I
T-16	191F	CONVENTIONAL TUNGSTEN	TYPE I
T-9	191F	CONVENTIONAL PG	TYPE I

TEST	PROPELLANT	NOZZLE	GRAIN
T-19	319 BRF	SUBMERGED TUNGSTEN	TYPE I
T-14	319 BRF	CONVENTIONAL PG	TYPE I

CHANGE IN NOZZLE THROAT RADIUS (MILS)

TIME (SECONDS)
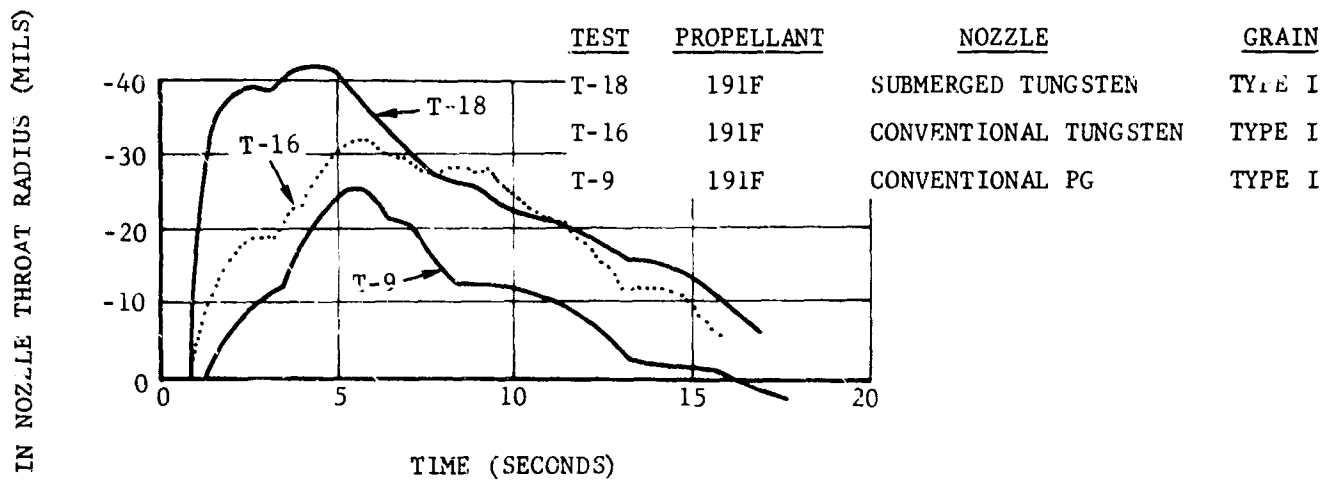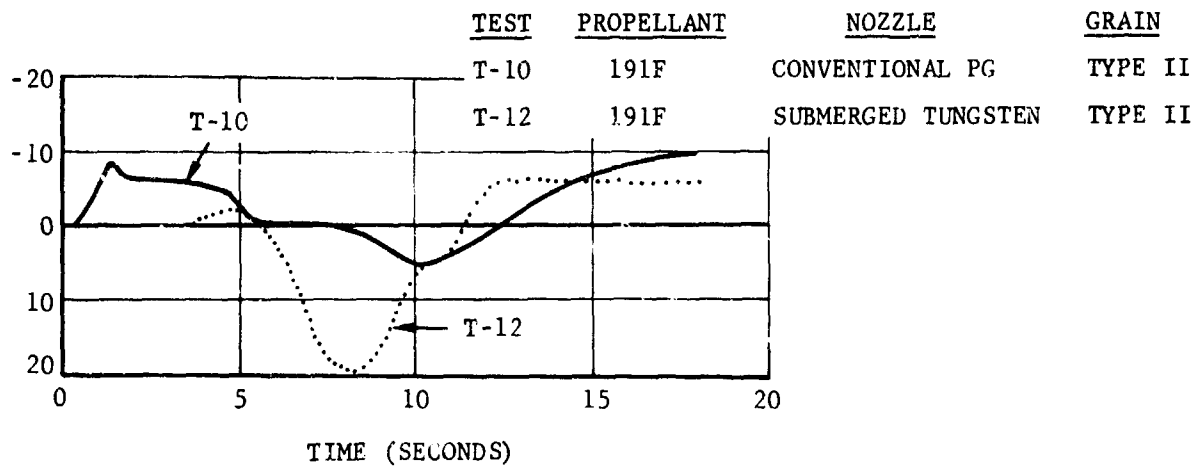
F09938 C

FIGURE 180. EFFECT OF NOZZLE SUBMERGENCE ON THROAT DEPOSITION

-336-

FIGURE 181.   CHANGE IN NOZZLE THROAT RADIUS TEST T-9, T-10, AND T-51

FIGURE 182.   CHANGE IN NOZZLE THROAT RADIUS VERSUS FIRING TIME, THIOKOL TEST TU-380.07

F10154C

FIGURE 183. CHANGE IN NOZZLE THROAT RADIUS VERSUS FIRING TIME, THIOKOL TEST TU-380.04

F10155 C

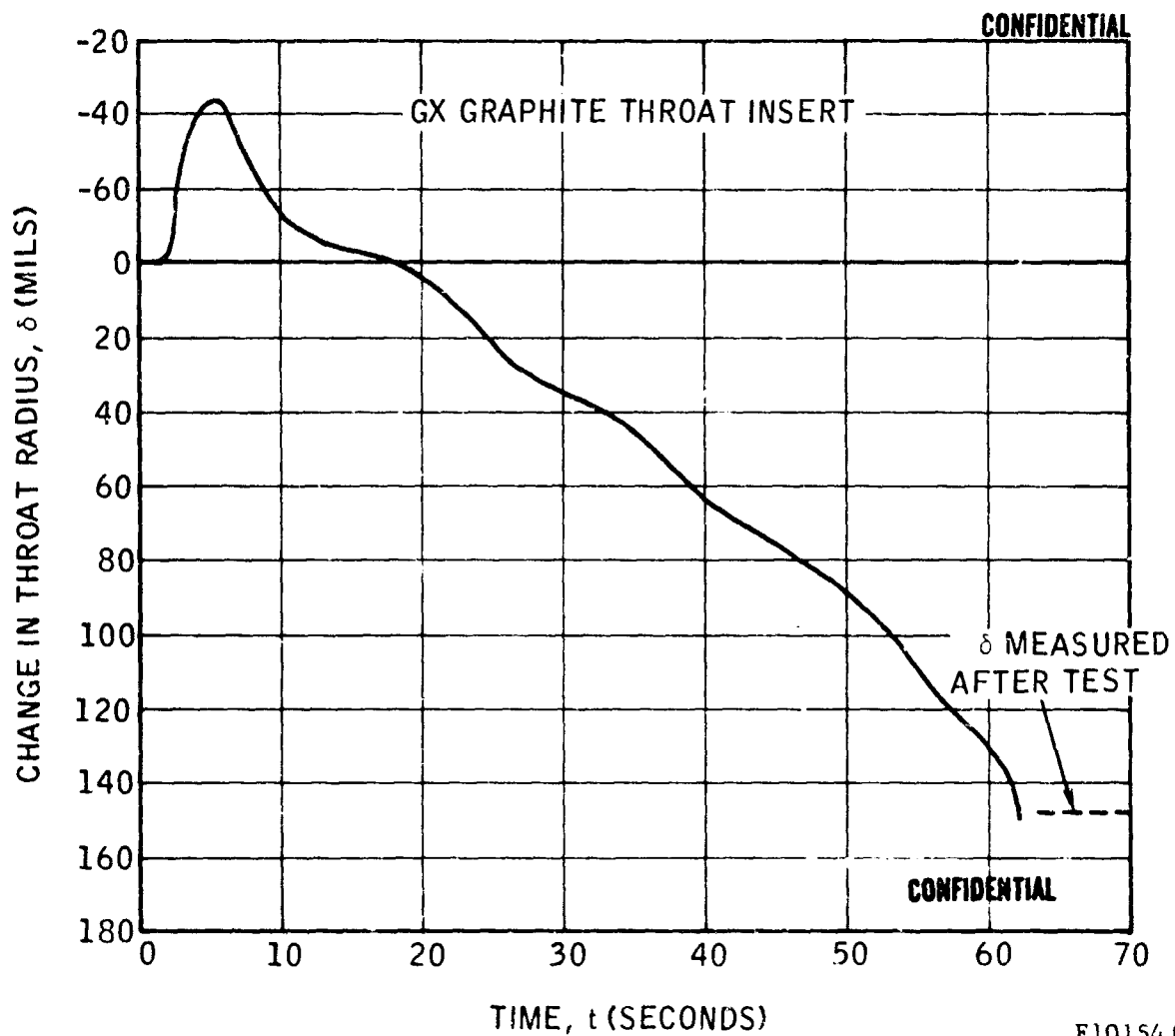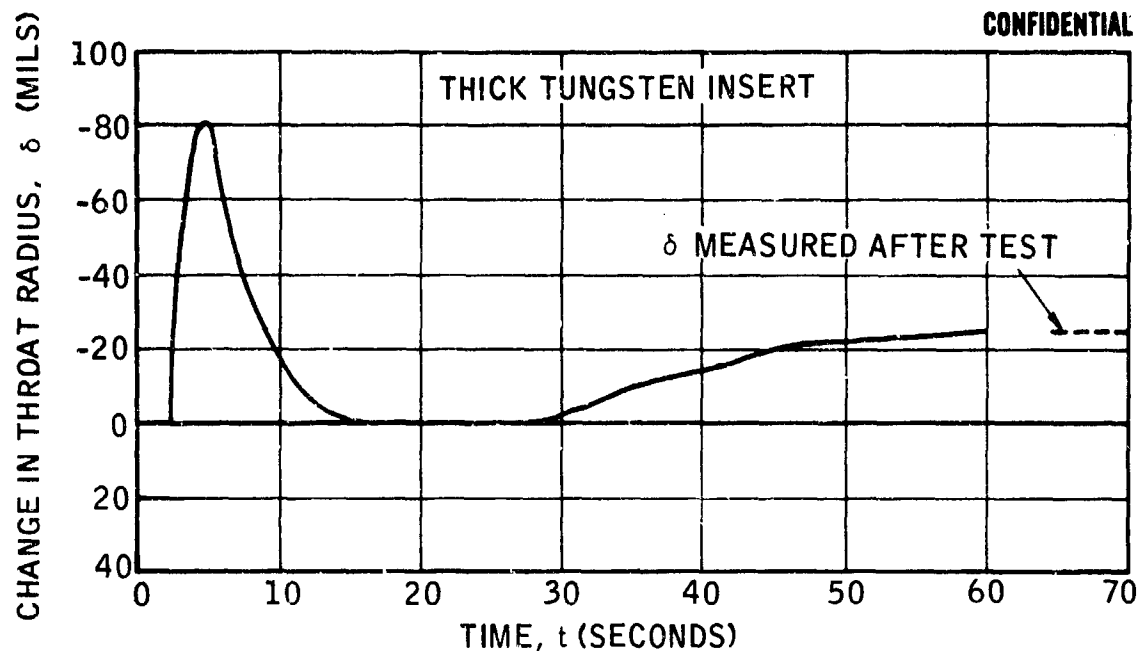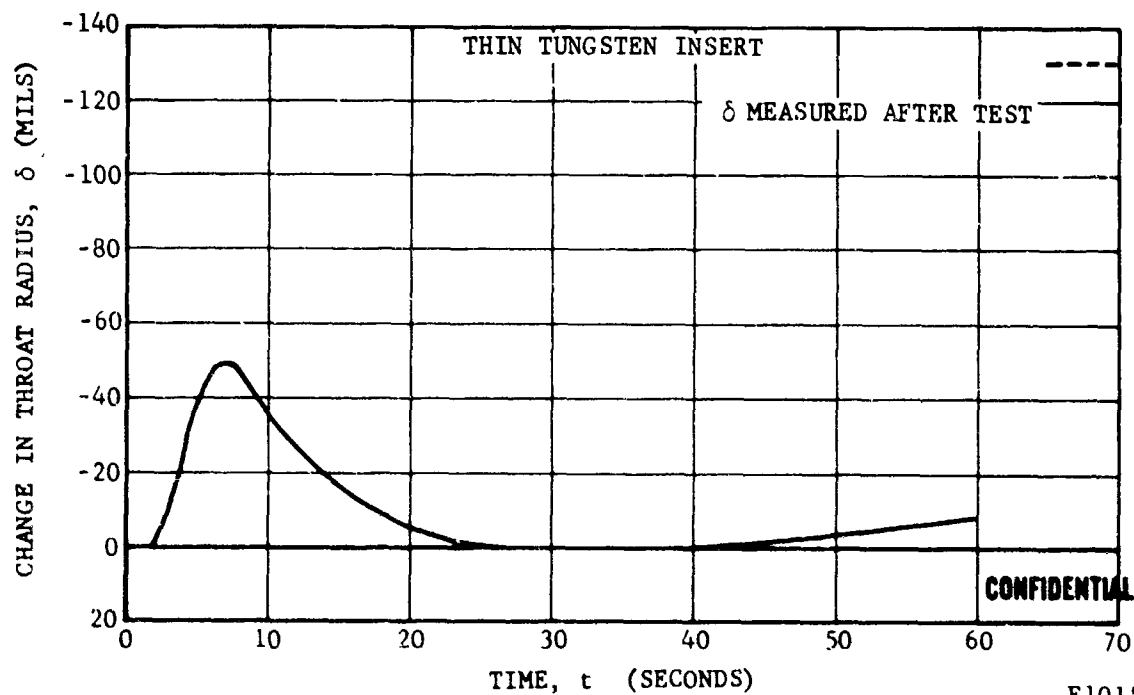FIGURE 184. CHANGE IN NOZZLE THROAT RADIUS VERSUS FIRING TIME, THIOKOL TEST TU-380.12

FIGURE 185.   CHANGE IN NOZZLE THROAT RADIUS VERSUS FIRING TIME, THIOKOL TEST TU-380.10

FIGURE 186. CHANGE IN NOZZLE THROAT RADIUS VERSUS FIRING TIME, THIOKOL TEST TU-380.05

APPENDIX VI (C)

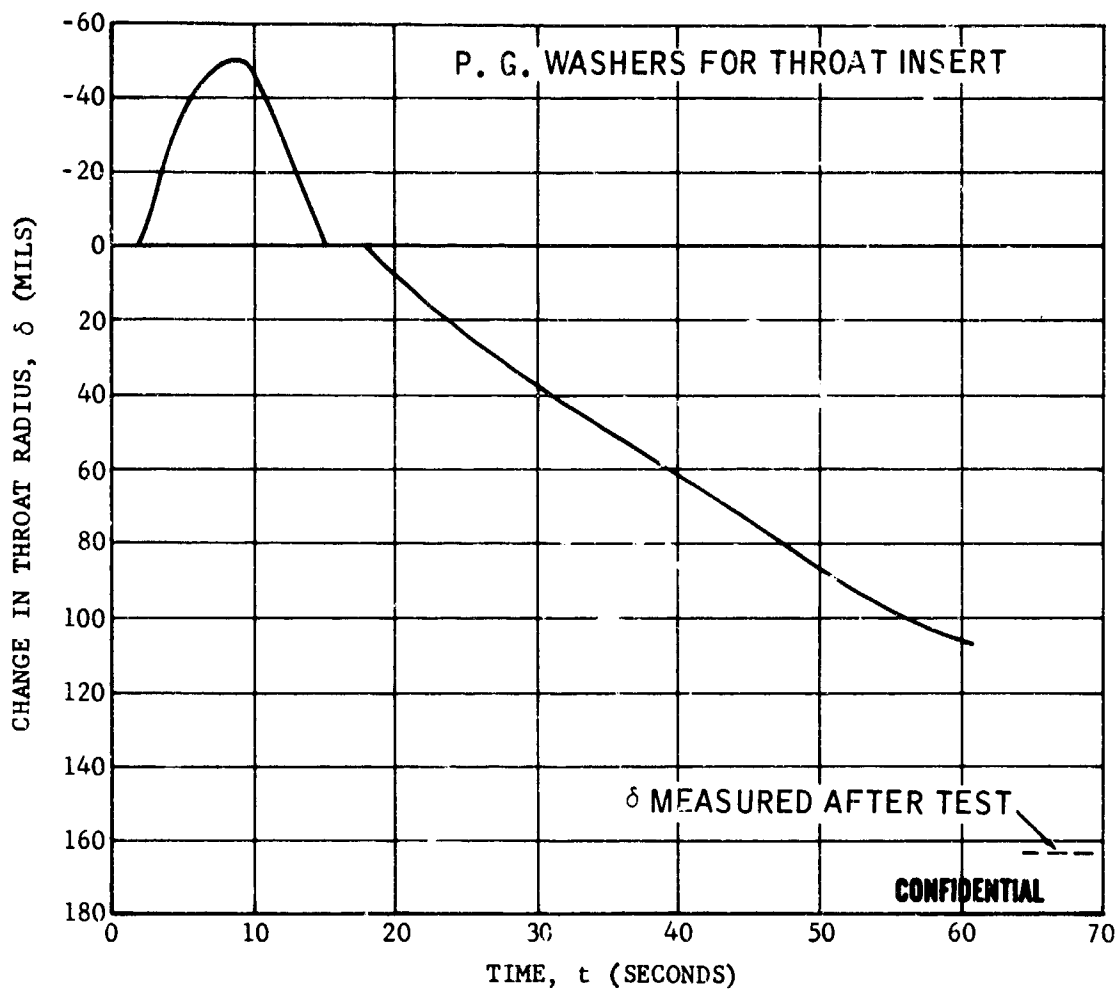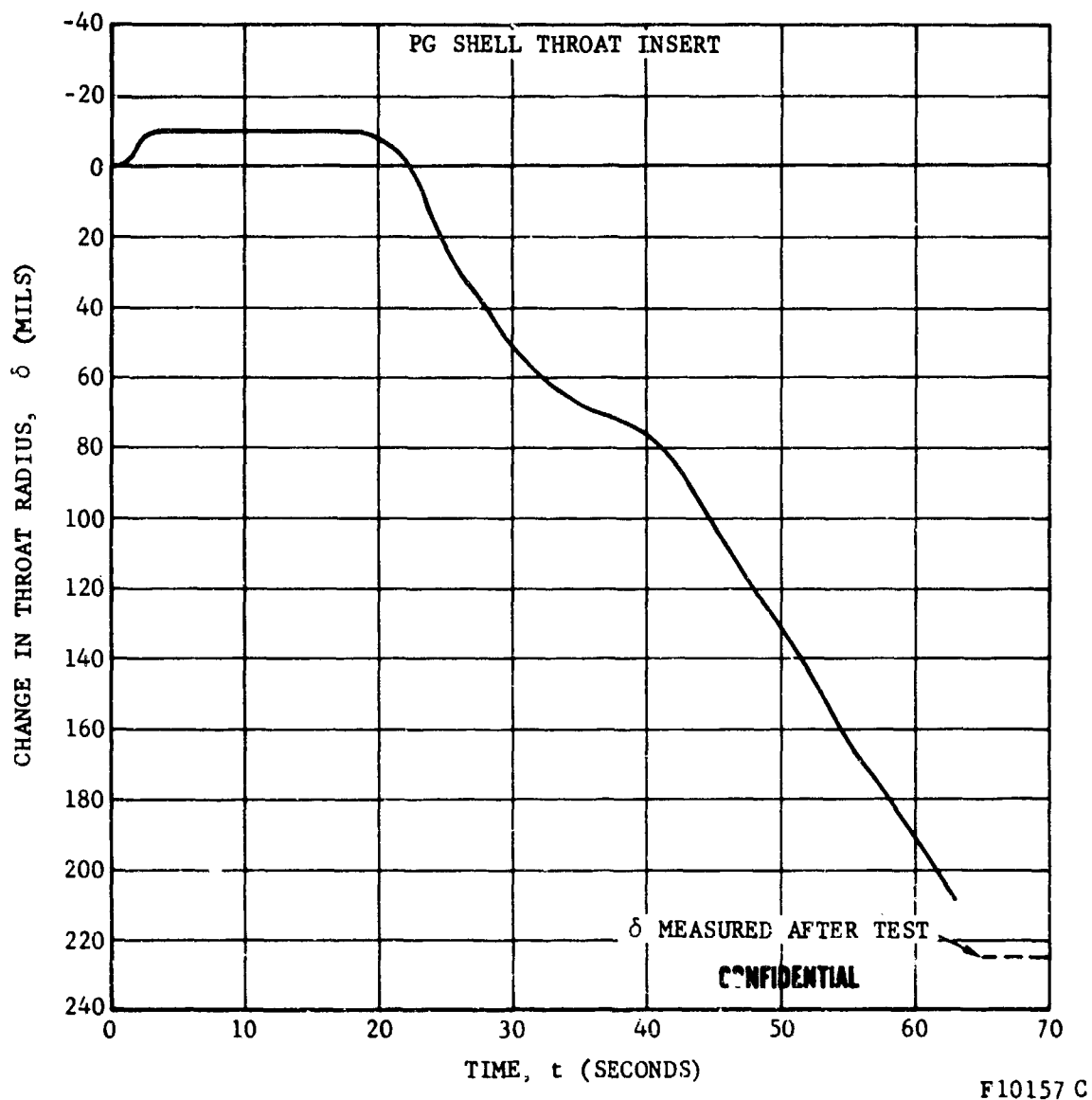BALLISTIC PERFORMANCE DATA

Ballistic performance data were obtained for the majority of the motor
tests conducted. It was expected that performance efficiency data would
reflect the average degree of metal combustion for comparison purposes.
This goal was only partially realized in that the results are not entirely
consistent with other evidence obtained from the nozzle post test analyses.
Basically, the combination of errors in the uniaxial thrust measurement
and the calculated deposit histories are believed to be serious. More
refined estimates of combustion efficiency would probably require measure-
ment of motor weight changes and side thrust measurements. Improvements
in the pressure measurements would also be desirable.

Action time, propellant weight, pressure, thrust, C* and impulse data are
given in Tables IX and X for the small motor tests and in Table XI for the
development motor tests. Two methods were used to compute the C* and
impulse. The TSI method assumed a linear change in throat area between
the initial and final measured values. The ADP method used on integral
average throat area to account for the throat deposition calculated for
each nozzle. Both methods use integrally averaged pressure and thrust
data while assuming that the entire propellant mass is expelled over the
action time. There are slight differences in the definition of action
time in the two methods. The TSI results were computer calculated while
the ADP results were hand calculated. The ADP results are regarded as the
more reasonable.

The raw performance data was converted to efficiencies which are shown in
Table XII. These data were then adjusted to approximately account for the
slag, heat transfer and divergence losses. Such losses were estimated
from visual examination of the tested hardware, the motion pictures of the

tests and the results of the thermal analyses. The results are shown in Table XIII. A number of errors were found in similar data presented in References 3 and 4. These have been corrected and Table XIII supercedes the earlier presentations. The ideal ballistic performance, for each of the program propellants, is presented as a function of pressure in Figure 187. These data were used to determine the ideal performance corresponding to the integral average chamber pressure for each test.

More extensive discussion of the ballistic performance data and analyses may be found in Sections 2.3 of References 2, 3 and 4. Section 3.5 of this report should also be consulted.

TABLE IX.   BALLISTIC DATA, TESTS T-1 THROUGH T-7

Test Number	Propellant	Action Time, t_a (seconds)	Propellant Weight (lb)	Chamber Pressure (psig)		Thrust (lb)		C^* (fps)			I_{SP} (seconds)	
				P_c max	P_c	F max	$\bar{F}$	C^*_{EO} (800 psia)	C^*_{TSI}	C^*_{ADP}	I_{SP} TSI	I_{SP} ADP
T-1	Arocel 191F	19.4	101.28	1180	818	1820	1230	5448	5386 to 5401	5170	232 to 236	235
T-2	Arcane 24F	28.8	105.734	965	723	11	367	5420	5453 to 5535	5055	229 to 236	235
T-3	Arocel 319BRF	17.5	98.11	1105	737	1655	1372	5510	5704 to 5755	5525	246	245
T-4	Arcane 54F	26.2	105.562	880	799	1020	929	5297	5338 to 5414	4890	233	231
T-5	Arcane 60	24.96	112.40	925	830	1120	1019	5123	5062 to 5108	4910	225 to 226	226
T-6	Arocel 390	27.54	107.55	720	536	1180	868	5279	5023 to 5041	4910	220	222
T-7	Arocel 389	17.24	110.59	1010	935	1550	1430	5197	4893 to 4904	4800	226	223

TABLE X. BALLISTIC DATA, TESTS T-8 THROUGH T-25

Test Number	Propellant	Action time (seconds)	Propellant Weight (lb)	Chamber Pressure psig		Thrust (lb)		C* eq (800 psia)	C* fps		ISP (seconds)	
				Pc max	Pc	F max	F		C* TSI	C* ADP	ISP TSI	ISP ADP
T-8	Arcocel 165	16.95	114.31	1170	759.17	2300	1603	5197	5182	5168		238
T-9	Arcocel 191F	18.74	106.01	895	774.60	1550	1332	5448	5182	5168		235
T-10	Arcocel 191F	18.00	107.93	1390	822.56	2670	1513	5448	5402	5317		252
T-11	Arcon 567	24.40	107.53	675	775.16	1190	1120	5420	5259	5233	236 o 241	254
T-12	Arcocel 1191F	19.2	108.95	1170	729.90	2200	1346	5448	5270	5065	238	237
T-13	Arcocel 1191F	19	107.80	106.0	726.84	1890	1272	5448		5026		224
T-14	Arcocel 3191RF	17.2	102.70	880	812.67	1620	1590	5510	5259	5204	249 to 252	254
T-15	Arcocel 3191RF	16.4	95.55	1180	986.22	1740	1453	5510	6038	5583	241 to 248	249
T-16	Arcocel 1191F	17.4	104.47	935	835.98	1600	1412	5448	5170 to 5215	5083	236	235
T-17	Arcocel 1191F	18.3	104.45	935	798.36	1540	1295	5448	5199 to 5244	5040	226	227
T-18	Arcocel 1191F	17.5	104.44	970	841.03	1620	1390	5448	5180 to 5235	4920	232	233
T-19	Arcocel 319RRF	16.40	102.18	985	895.03	1620	1483	5510	5250 to 5309	5222	237	238
T-20	Arcocel 1191F	18.15	105.22	935	826.78	1750	1413	5448		5163		244
T-21	Arcocel 1191F	16.90	99.73	1090	933.37	1610	1386	5448	5527 to 5539	4669	236 to 237	236
T-22	Arcene 567	25.40	103.42	980	857.13	1060		5420	5741 to 5758	.017	235	234
T-23	Arcocel 1191F	20.10	103.92	1000	811.19	1420	1197	5448		4784		232
T-24	Arcocel 3191RF	23.20	100.99	975	636.12	1490	994	5510		5267		229
T-25	Arcocel 1191F	17.80	104.81	950	828.20	1630	1397	5448		5167		237

TABLE XI. BALLISTIC DATA, TESTS T-51 THROUGH T-54

Test No.	Propellant	Action Time, ta(sec)	Propellant Weight (lb)	Chamber Pressure (psia)		Thrust (lb)		C*(fps)			ISP (seconds)
				$P_{c\,max}$	P_c	F_{max}	F	$C^{*}eq$	C^{*} TSI	C^{*} ADP	ISP ADP
T-51	Arcocel 191F	25.0	496.71	910	710	5950	4760	5448	5343	5070	239.5
T-52	Arcocel 319BKP	29.1	483.92	1000	610	6720	3855	5510	---	5290	231.5
T-53	Arcocel 191F	26.2	493.75	830	685	5350	4430	5448	5351	5280	235.0
T-54*	Arcocel 191F	30.5	497.08	1180	---	7700	---	5448	---	---	---

*Nozzle throat insert ejected. Ballistic performance was not computed.

TABLE XII. CORRECTED BALLISTIC PERFORMANCE EFFICIENCY DATA

Propellant	Grain Type	Nozzle Type	Test Number	Chamber Pressure Average (psig)	C* Measured Average (ft/sec)	C* Efficiency (percent)	ISP Measured (sec)	ISP Efficiency (percent)
191F	I	Conv PG	9	774.6	5010	91.5	235	84.8
191F	I	Conv PG	20	826.8	5163	95.0	244	87.5
191F	I	Conv PG	25	828.2	5190	95.0	237	85.2
191F	I	Conv W	16	835.9	5083	93.3	235	84.2
191F	I	Conv W	17	798.4	5040	92.-	227	81.8
191F	I	Sub W	18	841.0	4810	88.1	233	83.4
191F	EB (remote)	Conv PG	1	804.2	5164	95.0	235	84.4
191F	EB (close)	STP PG	21	933.3	4669	84.9	236	83.5
191F	EB (close)	Sub PG	23	811.2	4784	87.9	232	83.3
191F	II	Conv PG	10	822.6	5317	97.7	252	90.4
191F	II	Sub PG	12	729.9	5065	93.1	237	86.8
191F	II	STP PG	13	726.8	5026	92.3	224	81.5
319BRF	I	Conv PG	14	812.7	5204	94.5	254	89.9
319BRF	1	Sub W	19	895.8	5222	95.0	238	83.5
319BRF	EB (remote)	Conv PG	3	894.9	5494	99.6	245	86.0
319BRF	EB (close)	STP PG	24	636.1	5267	95.6	228	82.8
319BRF	III	Conv PG	15	986.2	5500	99.5	249	86.8
54F	I	Conv PG	11	775.2	5233	96.5	254	91.2
54F	EB (remote)	Conv PG	4	788.8	4898	90.3	231	82.8
54F	EB (close)	STP PG	22	857.1	4790	88.2	234	83.3
247	EB (remote)	Conv PG	2	706.3	5041	93.5	236	86.0
389	EB (remote)	Conv PG	7	962.8	4840	93.4	223	84.1
389	II	Conv PC	8	799.2	-	-	238	91.3
390	EB (remote)	Conv PC	6	525.3	4918	3.2	222	88.0
60	EB (remote)	Conv PC	5	814.6	4882	95.2	226	87.3
191F	500 lb	Sub PG	51	710.0	5370	98.8	239.5	95.8
319BRF	500 lb	Sub PG	52	610.0	5290	96.2	231.5	91.2
191F	500 lb	Sub PG	53	685.0	5310	97.8	235.0	93.8
191F	500 lb	Sub W	54	-	-	-	-	-

TABLE XIII. ADJUSTED BALLISTIC PERFORMANCE EFFICIENCIES

| | Estimated Losses Due to: | | | | | | Adjusted Efficiency | |
| | Slag Effect | | Heat Transfer | | Divergence | | | |
Test	C* (percent)	ISP (percent)	C* (percent)	ISP (percent)	20° Angle (percent)	Side Thrust (percent)	C* (percent)	ISP (percent)
T-1	3	3	2	2-1/2	3	1	100.0	93.9
T-2	3	3	2	2-1/2	3	1	98.5	95.5
T-3	2	2	2	2-1/2	3	1/2	103.6	94.0
T-4	3	3	2	2-1/2	3	1/2	95.3	91.8
T-5	3	3	1-1/2	2	3	1	99.7	96.3
T-6	2	2	1-1/2	2	3	1/2	96.7	95.5
T-7	2	2	2	2-1/2	3	0	97.4	91.6
T-8	2-1/2	2-1/2	1-1/2	2	3	1	-	99.8
T-9	2	2	1-1/2	2	3	1	95.0	92.8
T-10	2-1/2	2-1/2	1-1/2	2	3	1/2	101.7	98.4
T-11	1	1	1-1/2	2	3	0	99.0	97.1
T-12	2-1/2	2-1/2	1	1-1/2	3	1	96.6	94.8
T-13	2-1/2	4-1/2	1-1/2	2	3	1	96.3	92.0
T-14	1-1/2	1-1/2	1-1/2	2	3	0	97.5	96.4
T-15	1	1	1	1-1/2	3	0	101.5	92.3
T-16	2	2	1-1/2	2	3	1	96.8	92.2
T-17	2	2	1-1/2	2	3	1	96.0	89.8
T-18	1	1	1	1-1/2	3	1	90.1	89.9
T-19	1	1	1-1/2	2	3	0	97.5	89.5
T-20	2	2	2	2-1/2	3	1/2	99.0	95.5
T-21	3	3	2	2-1/2	3	0	89.9	92.0
T-22	3	3	2	2-1/2	3	0	93.2	91.6
T-23	1	1	1	1-1/2	3	1/2	89.9	89.3
T-24	3	3	2	2-1/2	3	0	100.6	91.3
T-25	1-1/2	1-1/2	1-1/2	2	3	1	98.0	92.7
T-51	1	1	1	1-1/2	3	1/2	100.8	101.8
T-52	1	1	1	1-1/2	3	1/2	98.2	97.2
T-53	1/2	1/2	1	1-1/2	3	1/2	99.3	99.3
T-54	1	1	1	1-1/2	3	1/2	-	-
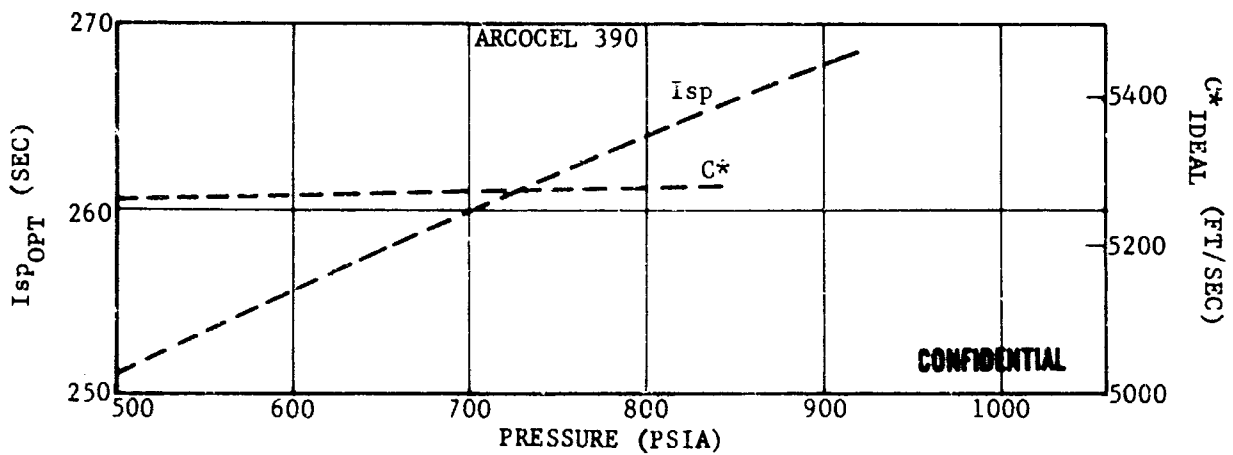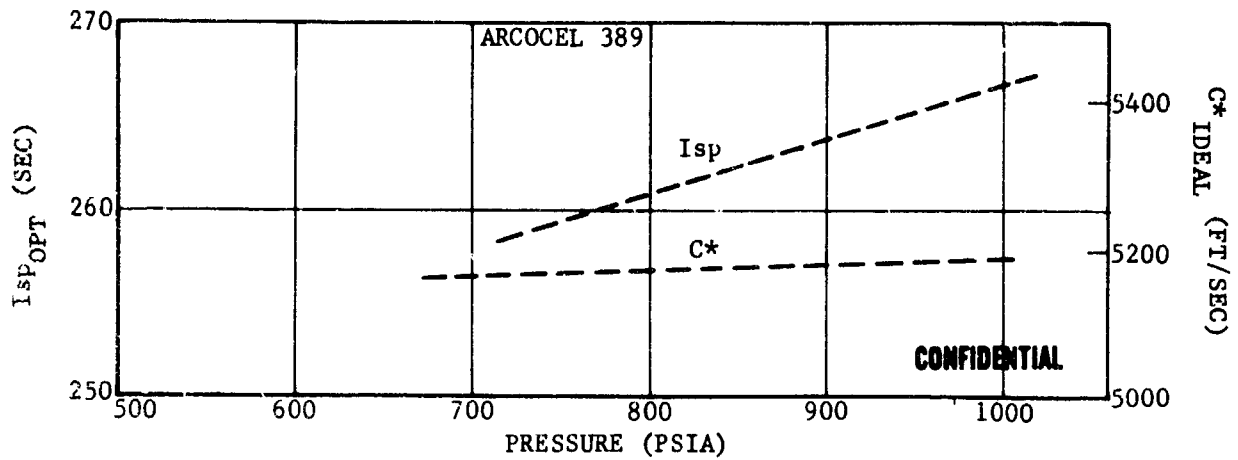
FIGURE 187. IDEAL BALLISTIC PERFORMANCE

F11034 C

-349-
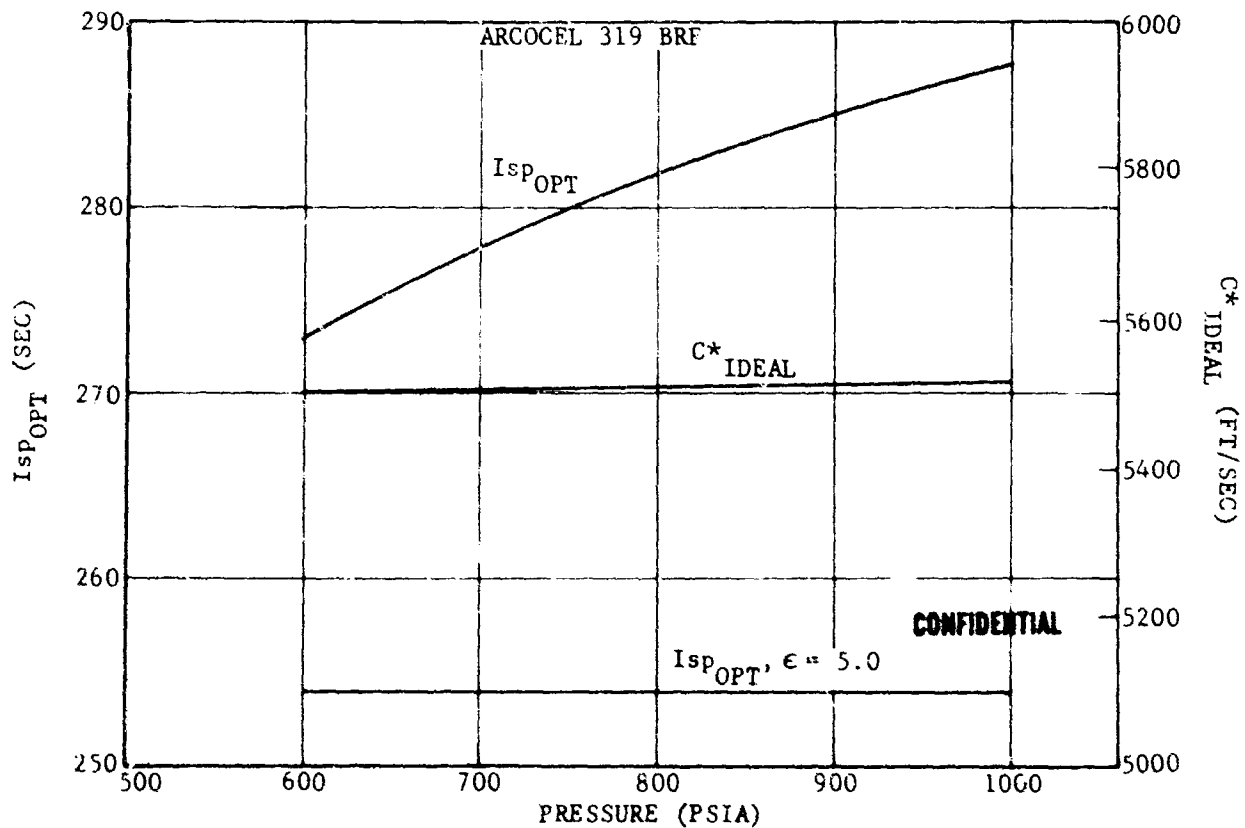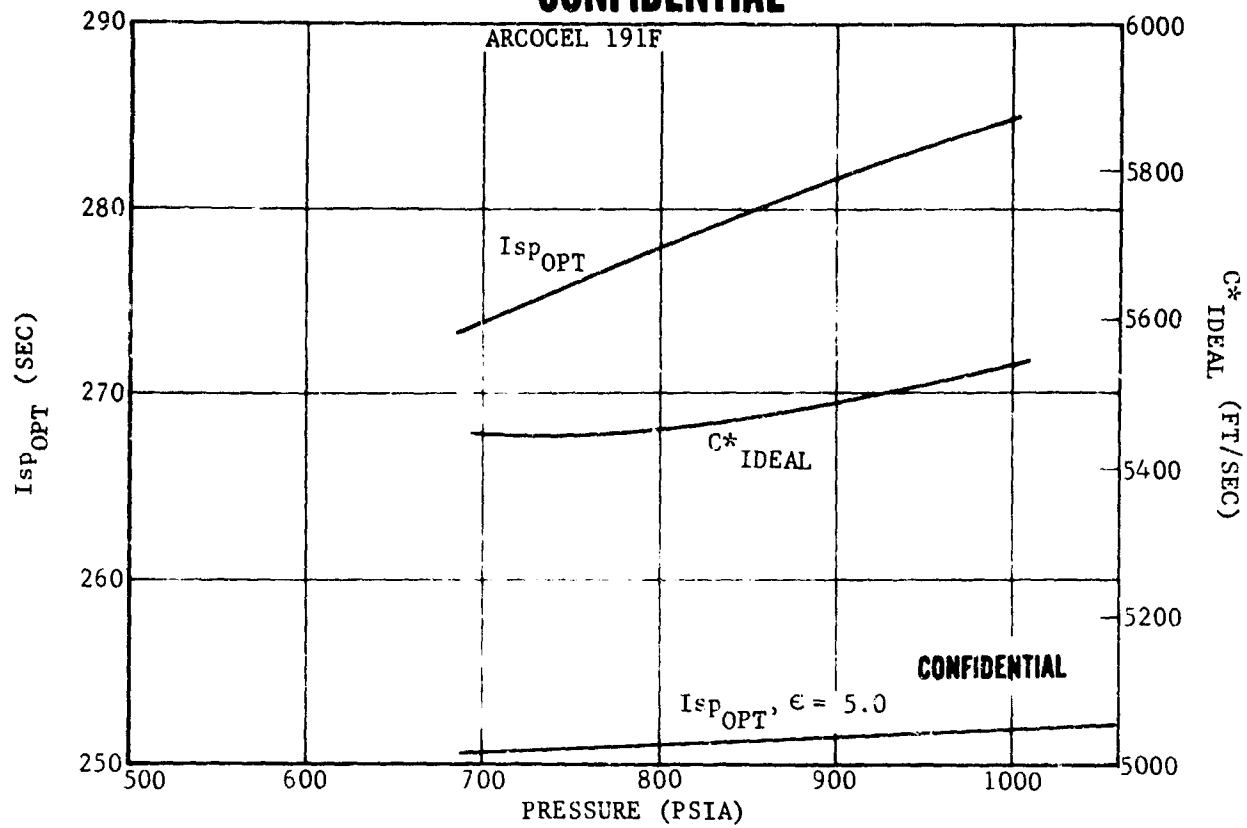
FIGURE 187. IDEAL BALLISTIC PERFORMANCE (Continued)

F11035C
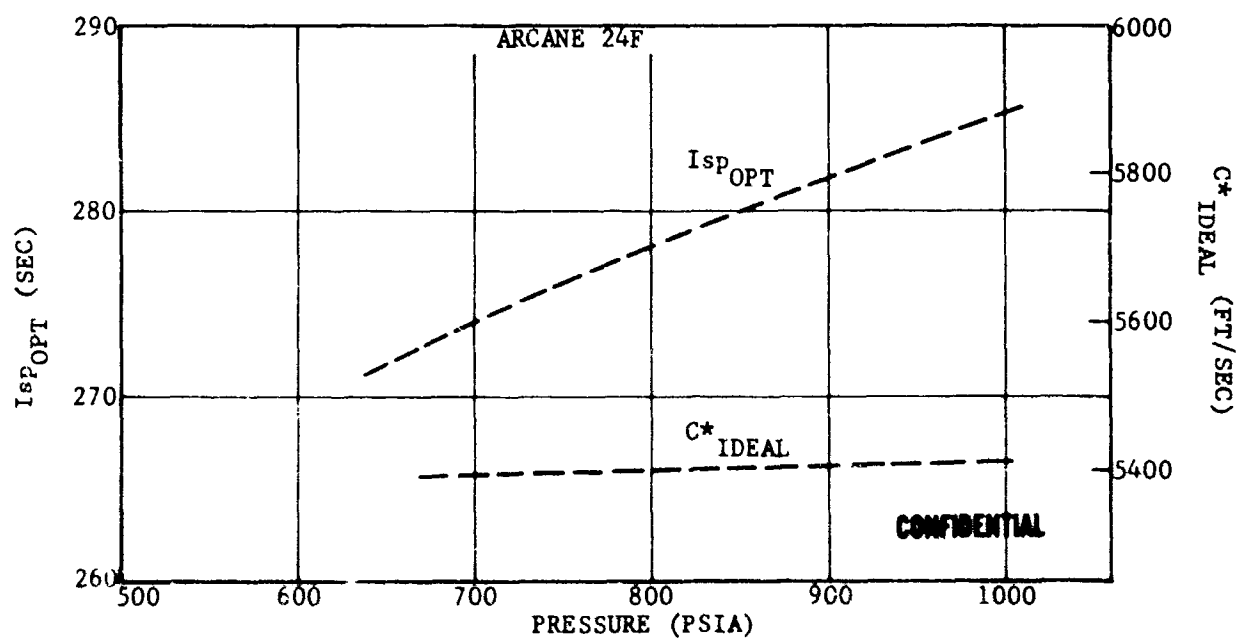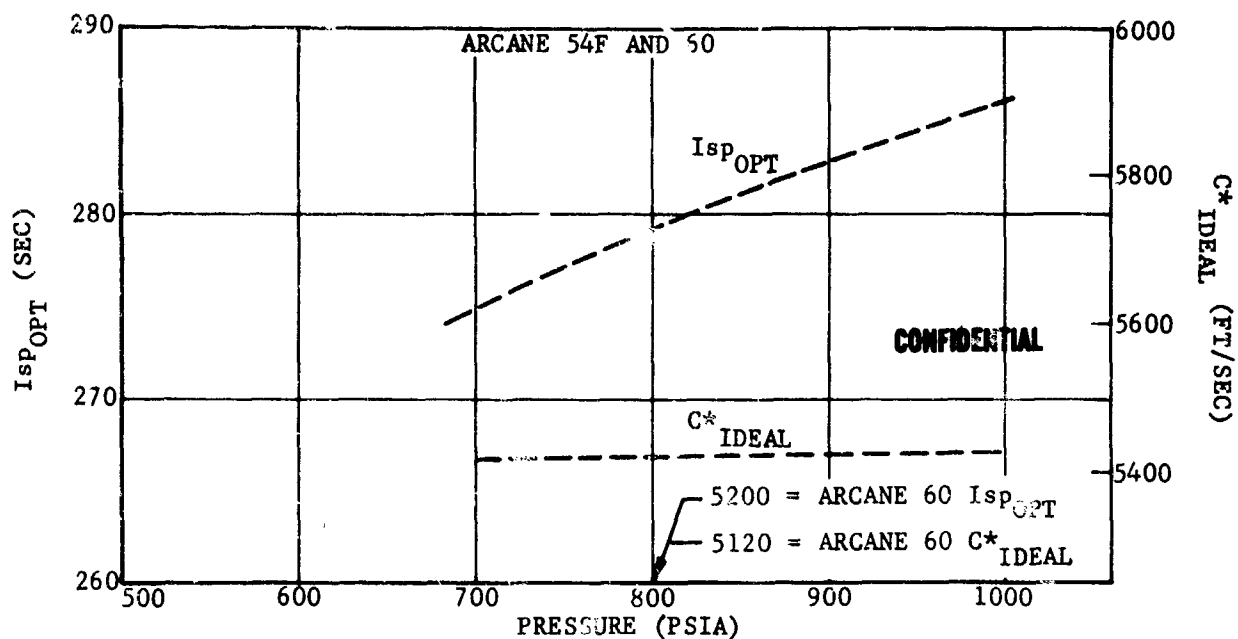
FIGURE 18?.   IDEAL BALLISTIC PERFORMANCE (Concluded)

F 11036 C

APPENDIX VII (U)

EXHAUST FLOW FIELDS

A primary objective of the motor test program was to clarify the depend-
ence of nozzle performance on grain and nozzle contour design. The test
results emphatically illustrate the importance of nonuniform exhaust flow.
Basically, the nozzle deposition, heat transfer and corrosion/erosion
reflect the character of the gaseous and condensed exhaust flow fields.
Consequently, the flow fields associated with the several grain design/nozzle
contour combinations were estimated. No attempt was made to develop ana-
lytical techniques capable of handling the two phase flow with combustion
transients and flow nonuniformities. Instead, the gas streamlines and
relative particle impingement were estimated from experience gained in the
cold flow modeling studies (Section 3.2), two phase flow theory and poten-
tial flow theory.

Figure 188 illustrates the flow field and impingement for the simplest
case, the remotely located end burning grain and a conventional nozzle
contour (Tests T-1 through T-7). Except for metal combustion transients,
little or no dependence on time would be expected with this design.
Figure 189 shows the flow field for the end burning grain combined with
the steep inlet nozzle contour (Tests T-21, T-22 and T-24). Note that
the grain is in the extreme aft position. With this design, impingement
rates are expected to increase slightly with time. Figure 190 shows the
expected results for Test T-23 in which a submerged nozzle was used with
the end burner in the aft position. The flow fields and relative impinge-
ment are shown in Figures 191 and 192 for the Type I grain design (7 inch
circular port) with the conventional and submerged nozzles. Figure 191
applies to Tests T-9, T-11, T-14, T-16, T-17, T-20 and T-25. Figure 192
applies to Tests T-18 and T-19. Note that major variations in the
impingement with time are expected. The end burning and Type I grains

-352-

produce uniform exhaust flow fields with each of the nozzle contours. Some recirculation flow is indicated behind the submerged nozzles for which boundary layer development lengths will be relatively short. Significant condensed phase flow stratification would be expected with the submerged and steep inlet designs.

The slotted grains were selected for test in order to introduce a relatively simple deviation from the uniform exhaust flow field. The Type II and III grains are compared in Figure 193. The gas flow field for the Type II grain is shown in Figure 194. Note that the radial slot velocity will be much greater for the Type II relative to the Type III design. The shear layers and mixing regions will be proportionately more extensive for the Type II grain. Note that the radial stagnation, 180 degrees from the grain slot, apparently developed a second slot which resulted in the progressive/regressive grain burning. The increased turbulence associated with the radial stagnation was responsible for the formation of the nozzle grooves 180 degrees from the grain slot. The nozzle grooves formed in line with the grain slot may have resulted from the free shear layer turbulence or centrifuging of burning metal particles away from the wall. The anticipated effects of introducing additional grain slots are shown in Figure 195. Basically, two nozzle grooves could be formed for each grain slot. In some cases the grooves in line with the grain slots should essentially disappear. Evidently, erosive burning will occur with most slotted grain designs.

The initial flow fields and relative impingement rates for the development nozzles are illustrated in Figures 196 and 197. The strength of the radial slot flow for the 500-pound grain design is between that of the Type II and the Type III design. The initial port to throat area ratio was approximately 4.3 for the 500-pound grain compared to 37 and 11.5 for the Type II and III designs. Evidently, the radial jet stagnation flow caused slotting of the nose cap and erosive grain burning. The nozzles were submerged enough to prevent nozzle grooving 180 degrees from the grain slot. The radially oriented free shear layers probably were the cause of the "saddles" formed in the nose caps.

The estimated grain/nozzle flow field effects are discussed in greater detail in Sections 2.4 of References 3 and 4. Nozzle grooving is discussed in Section III of this report.
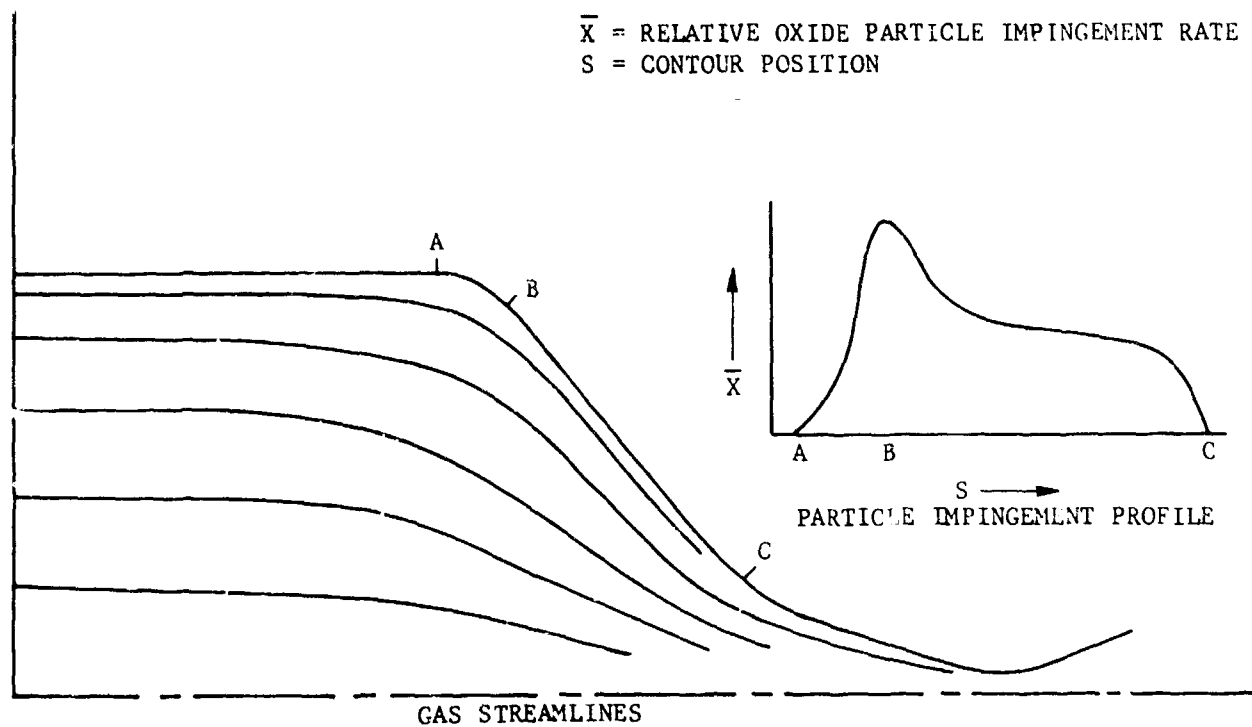
FIGURE 188. STREAMLINES AND IMPINGEMENT PROFILE - REMOTE ENDBURNER WITH CONVENTIONAL NOZZLE

FO8186 U

$\overline{X}$ = RELATIVE OXIDE PARTICLE IMPINGEMENT RATE
S = CONTOUR POSITION
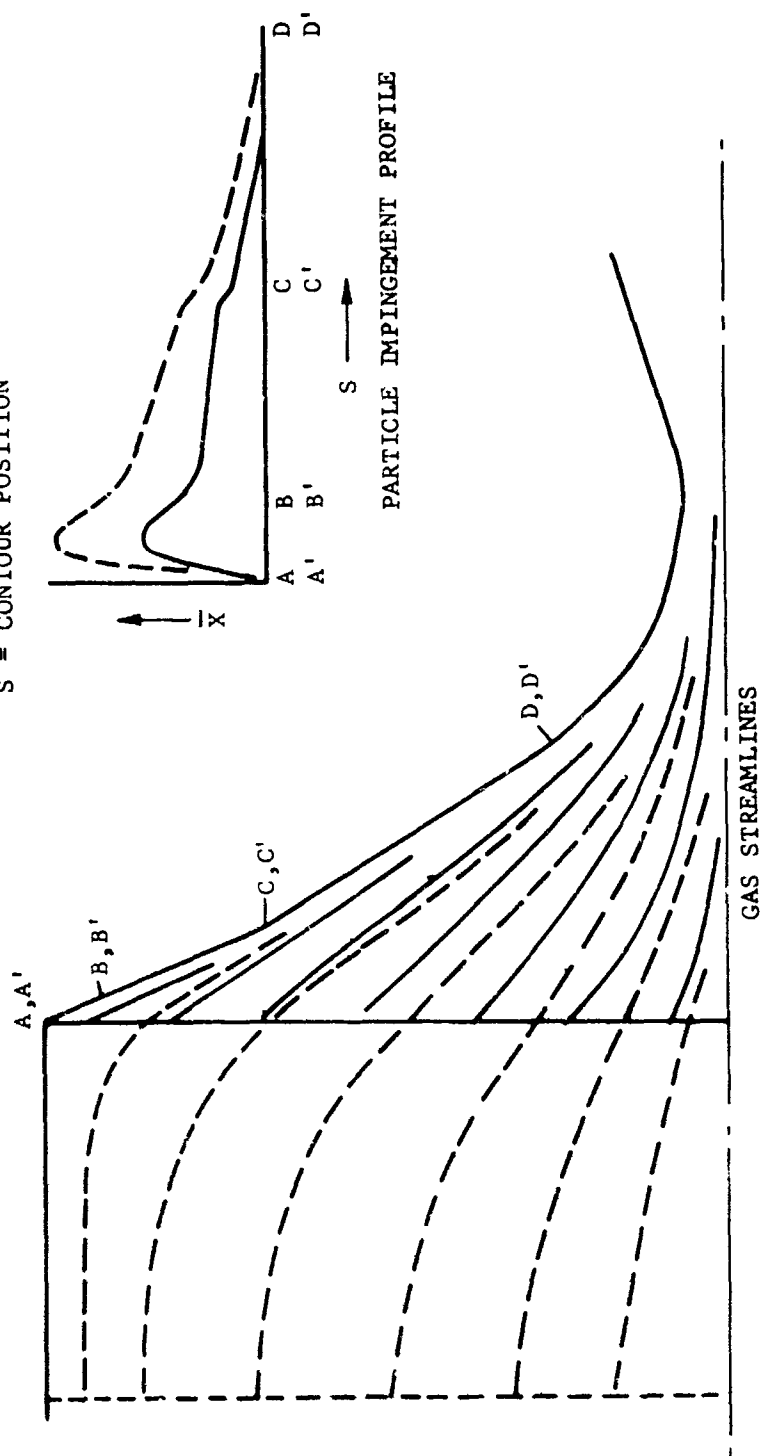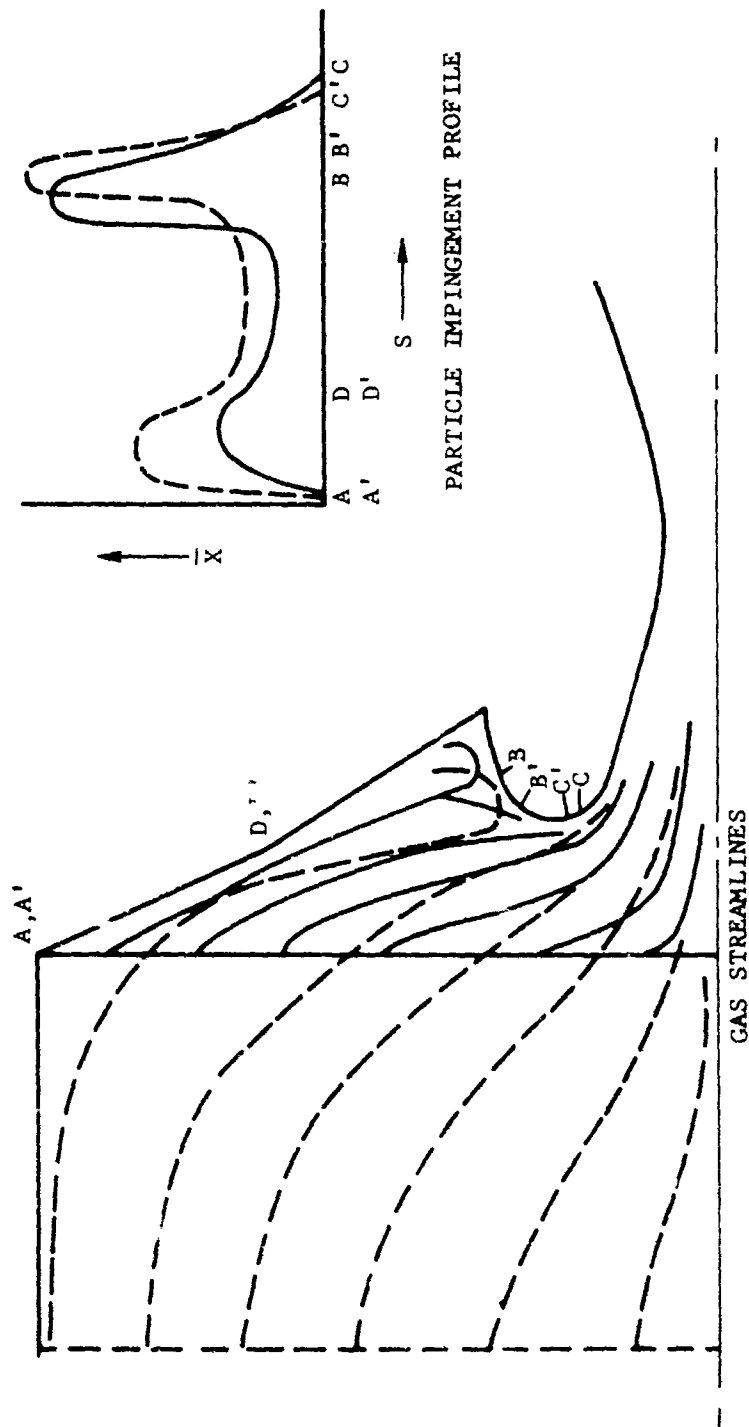
PARTICLE IMPINGEMENT PROFILE

GAS STREAMLINES

F08188 U

FIGURE 189. STREAMLINES AND IMPINGEMENT PROFILES - CLOSE
END BURNING GRAIN WITH STEEP INLET NOZZLE

$\overline{X}$ = RELATIVE OXIDE PARTICLE IMPINGEMENT RATE

S = CONTOUR POSITION

PARTICLE IMPINGEMENT PROFILE

GAS STREAMLINES

FIGURE 190. STREAMLINES AND IMPINGEMENT PROFILE - CLOSE
END BURNING GRAIN WITH A SUBMERGED NOZZLE

F08187 U

-356-

$\overline{X}$ = RELATIVE OXIDE PARTICLE IMPINGEMENT RATE
S = CONTOUR POSITION

PARTICLE IMPINGEMENT PROFILE
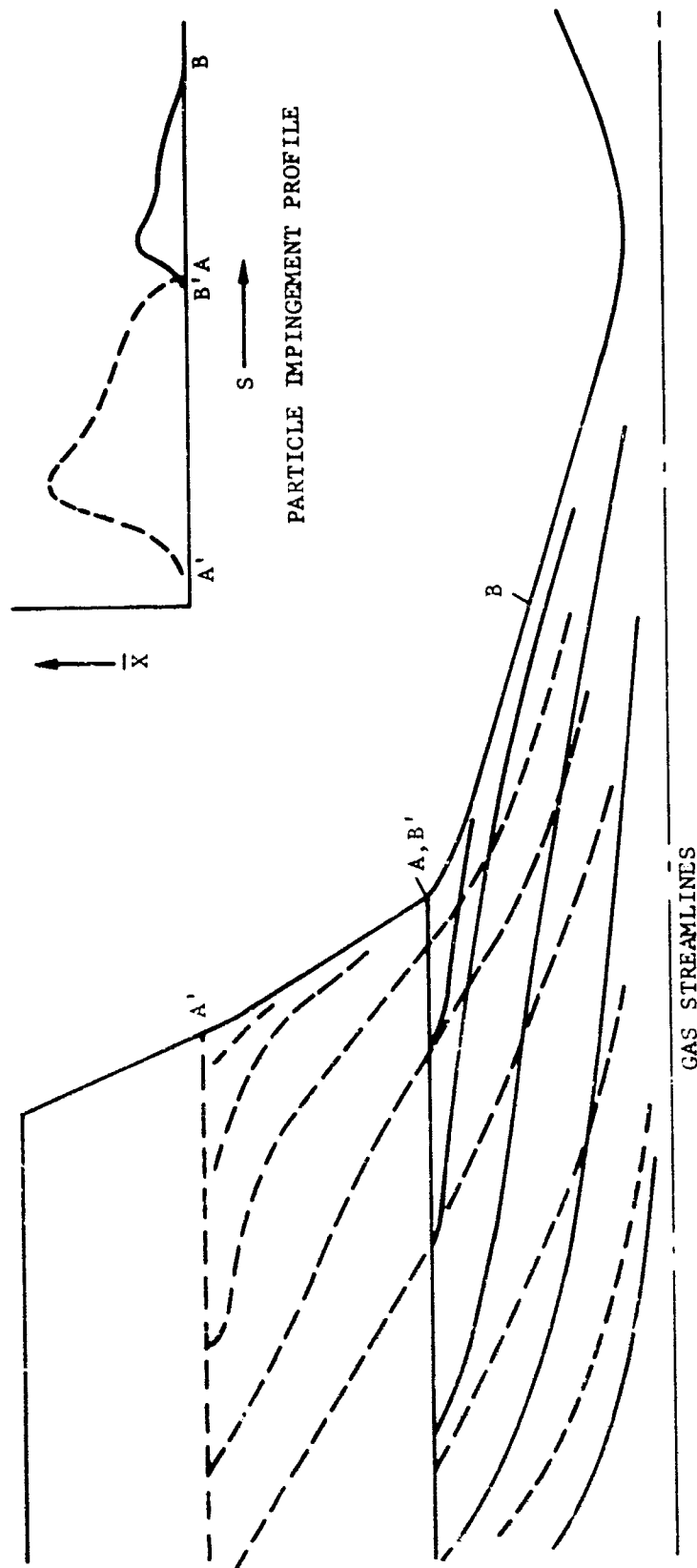
GAS STREAMLINES

F08190 U

FIGURE 191. STREAMLINES AND IMPINGEMENT PROFILES -
TYPE I GRAIN WITH CONVENTIONAL NOZZLE

-357-

$\bar{X}$ = RELATIVE OXIDE PARTICLE IMPINGEMENT RATE
S = CONTOUR POSITION

PARTICLE IMPINGEMENT PROFILE

GAS STREAMLINES

F08191U

FIGURE 192. STREAMLINES AND IMPINGEMENT PROFILES -
TYPE 1 GRAIN WITH SUBMERGED NOZZLE

-358-

NOZZLE CONTOUR OF T-15

NOZZLE CONTOUR OF T-8
AND T-10 (T-12 AND T-13
NOT SHOWN)

FLOW →

FLCW →

5-1/2"

3" DIA

5-1/2"

7" DIA

1"

1"

TYPE III DESIGN

TYPE II DESIGN
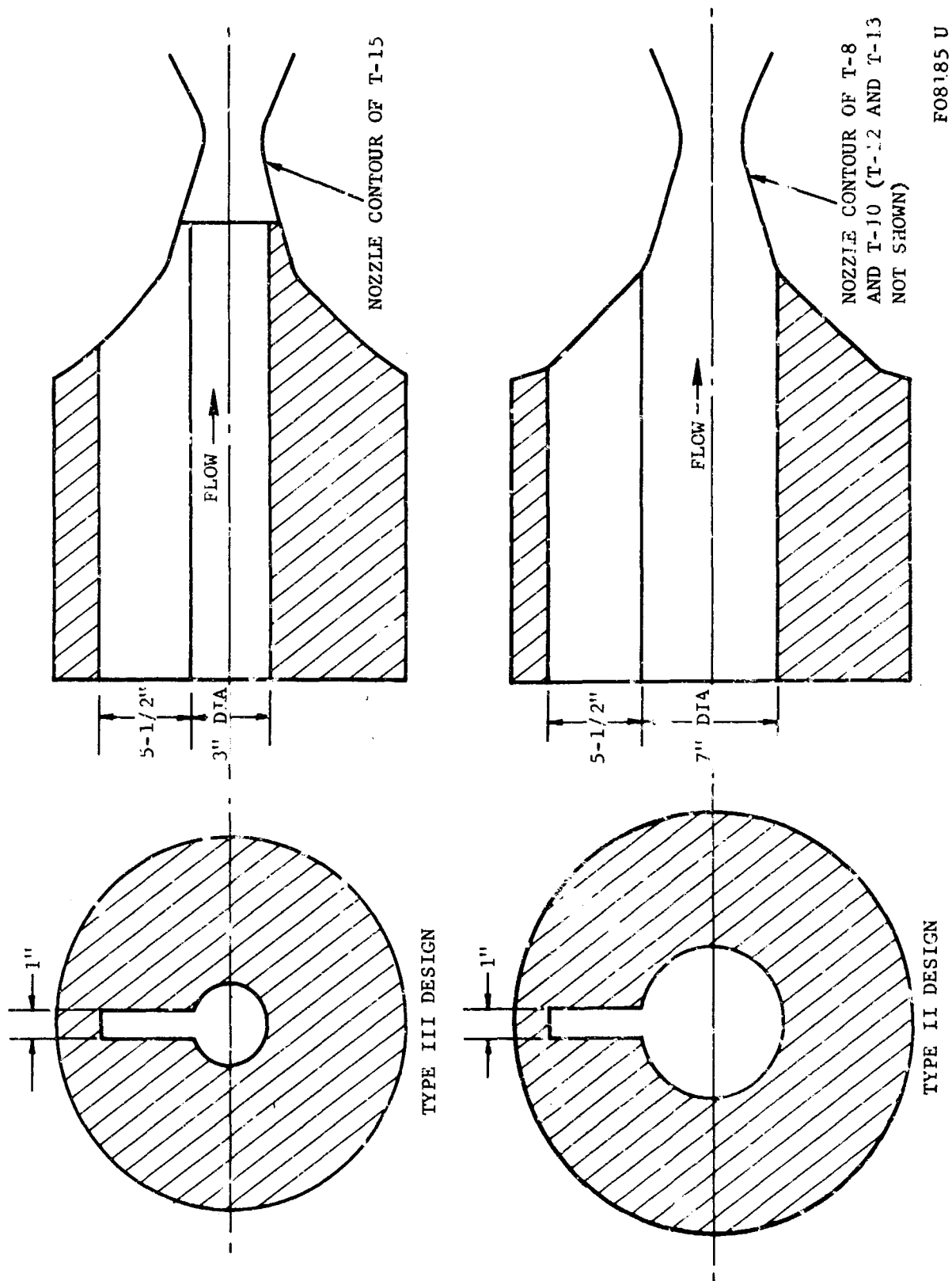
F08185 U

FIGURE 193. SLOTTED GRAIN DESIGNS FOR SMALL MOTOR TESTS

FREE SHEAR LAYERS

MIXING REGION

θ

0°

180°
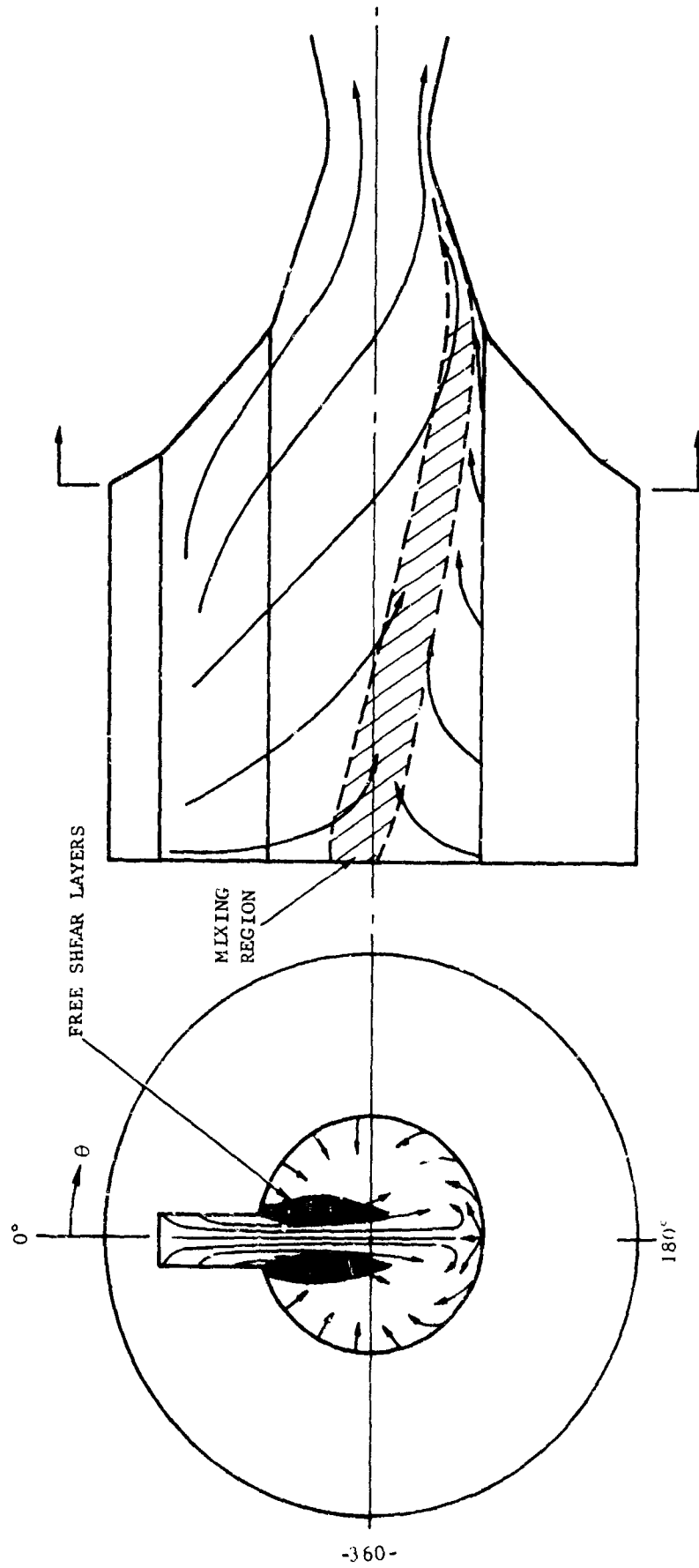
FIGURE 194. ESTIMATED FLOW FIELD - TYPE II SLOTTED GRAIN

F08179 U

-360-
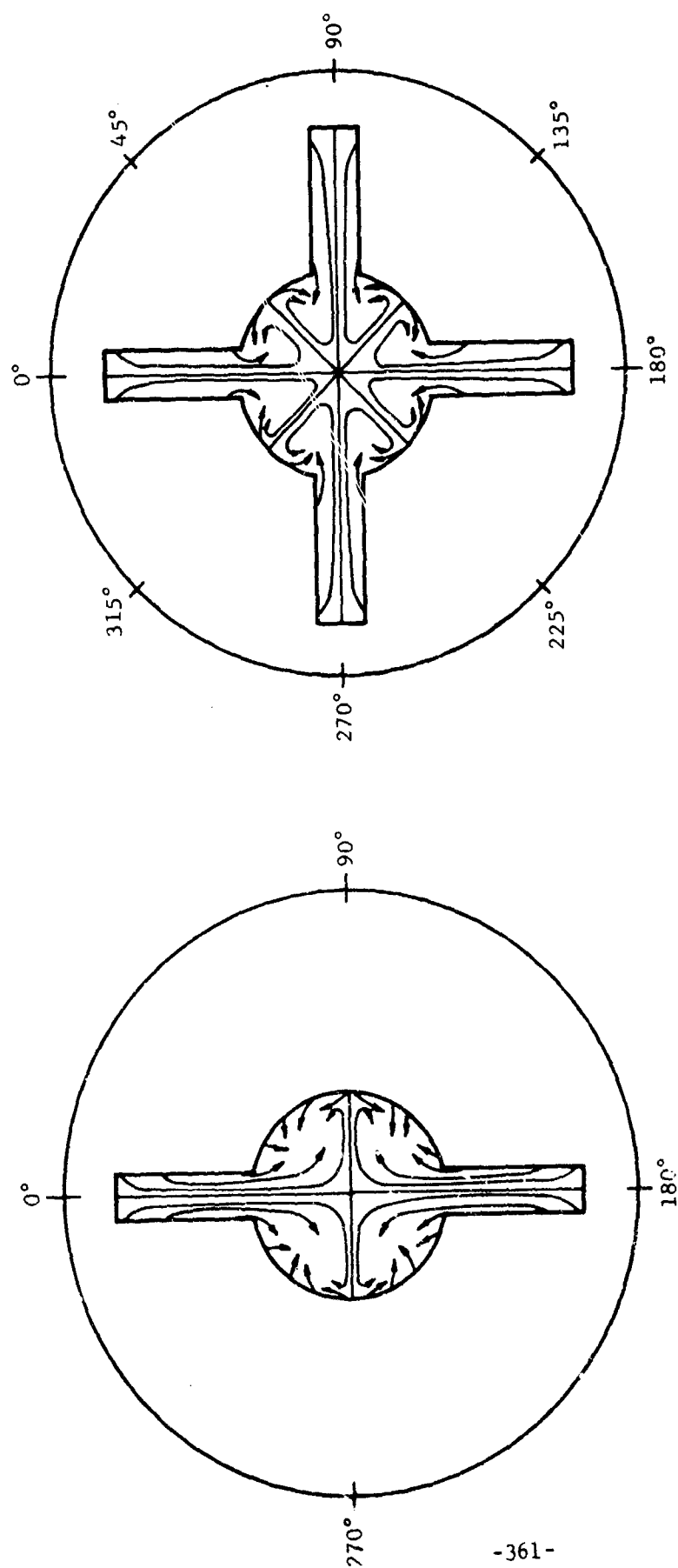
SIGNIFICANT AFT CLOSURE INSULATION AND NOZZLE GROOVES
WILL FORM AT EACH ANGULAR POSITION INDICATED

F08178 U

FIGURE 195.   ESTIMATED EFFECTS OF MULTIPLE GRAIN SLOTS ON FLOW FIELD

-361-
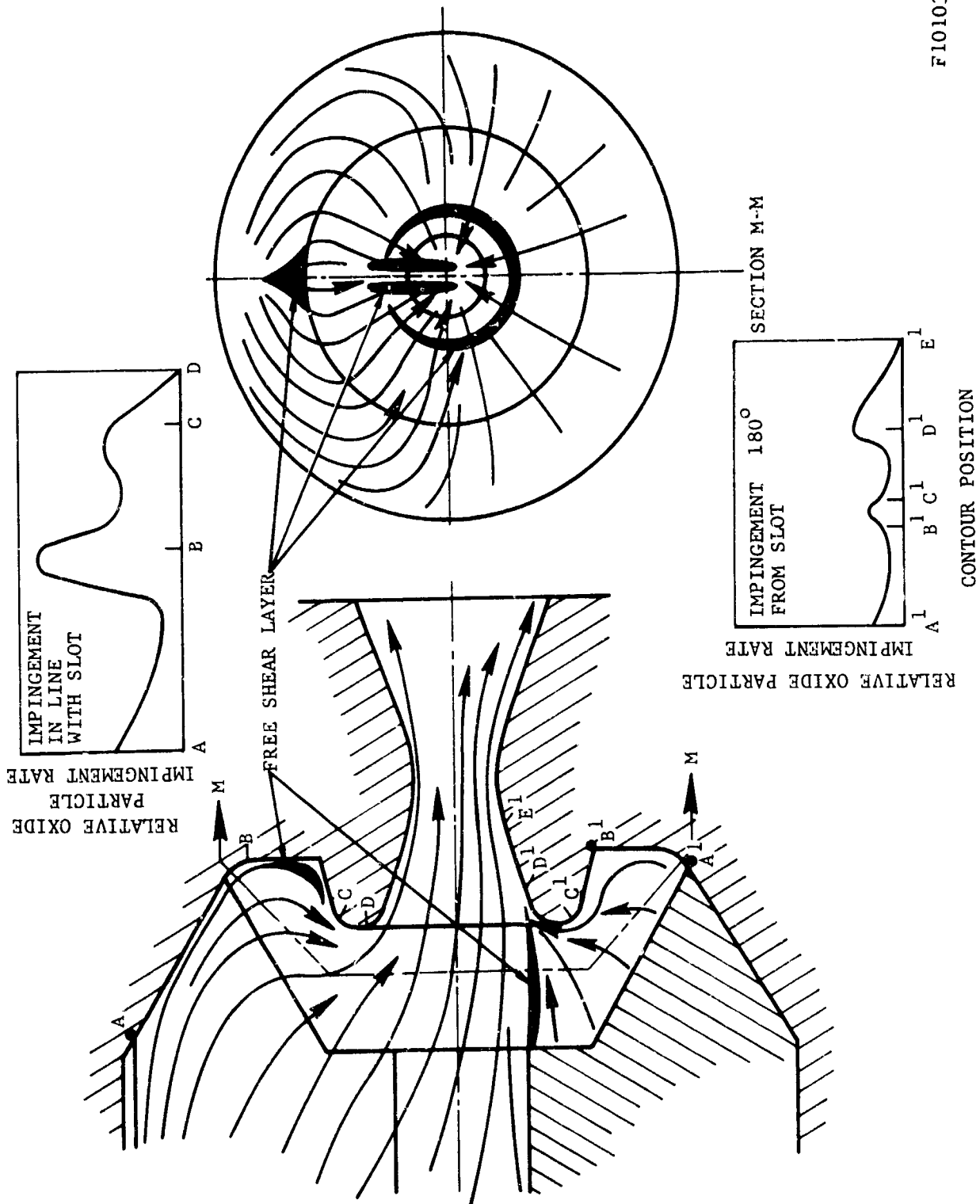
FIGURE 196. STREAMLINES AND IMPINGEMENT PROFILES AT ZERO BURN TIME - TESTS T-51, T-52, AND T-54

F10103 U

-362-

IMPINGEMENT
IN LINE
WITH SLOT

RELATIVE OXIDE PARTICLE
IMPINGEMENT RATE

CONTOUR POSITION

IMPINGEMENT 180°
FROM SLOT

RELATIVE OXIDE PARTICLE
IMPINGEMENT RATE

CONTOUR POSITION

FREE SHEAR LAYER
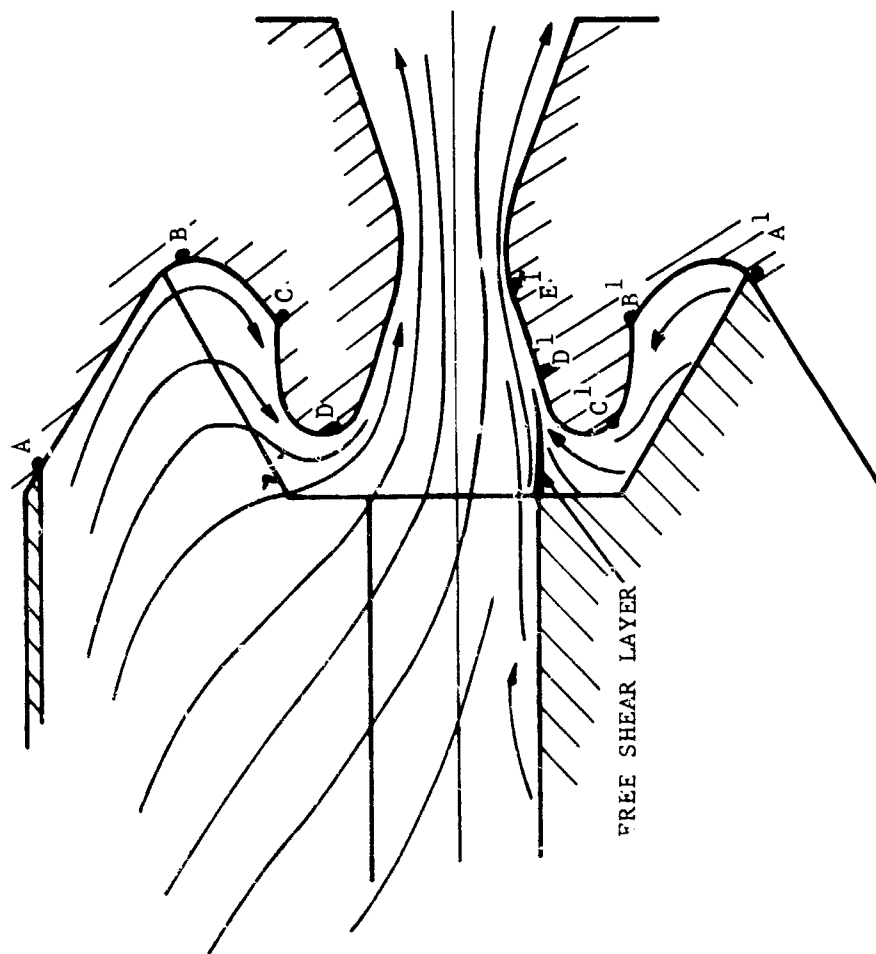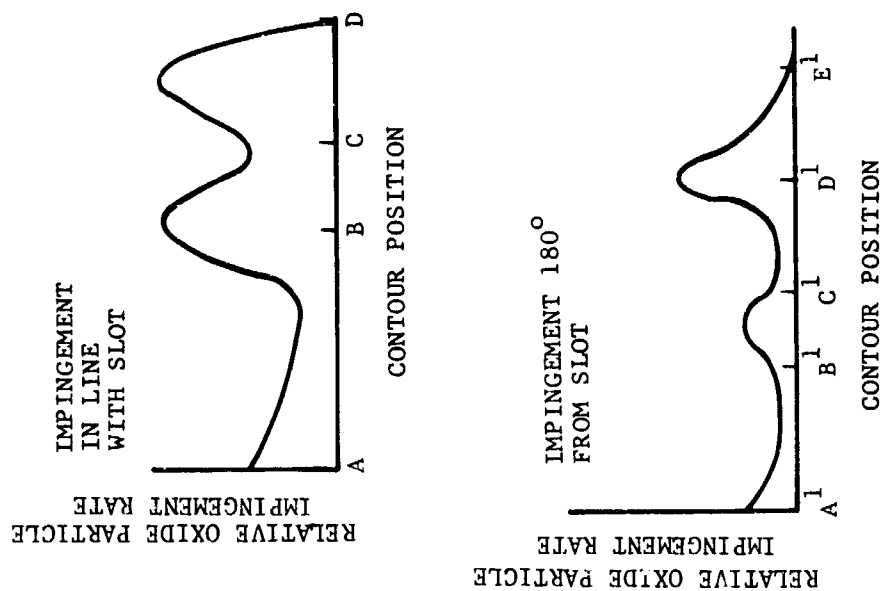
F10104 U

FIGURE 197. STREAMLINES AND IMPINGEMENT PROFILES AT ZERO BURN TIME - TEST T-53

APPENDIX VIII (C)

NOZZLE THROAT HEAT TRANSFER DATA

8.1 (U) THROAT TEMPERATURE HISTORIES

The primary objectives of the nozzle thermal analyses were to (1) establish the nozzle surface temperature history with deposit effects included and (2) estimate the boundary layer convective heat transfer coefficients for each test. These objectives were achieved only at the nozzle throat station where the deposit thickness history was reasonably well known. The calculation procedures outlined in Sections 2.5.c of References 1 through 4 were highly successful when applied to the pyrolytic graphite heat sink nozzles. At the throat station, radiation, deposit flow energy transport and deposit heat of fusion effects were judged to be negligible. Heat absorbed in chemical corrosion reactions was also neglected. This latter assumption is quite reasonable for the majority of the tests since little corrosion occurred. Axial conduction effects (pyrolytic graphite) were excluded and it was assumed that the graphite components were perfectly insulated at the outer radius.

The transient conduction analysis was constrained by the total heat absorption which was determined from the local equilibration temperature measurement along with the known specific heat and mass of the throat washer. The thermal equilibration of the throat washer occurred about 60 seconds after burnout. Thus, the throat washer served as a calorimeter. The measured chamber pressure history was input to permit the use of a pressure dependent (0.8 power) heat transfer coefficient. The calculated throat deposit histories (Appendix V) were input to the analysis. Successive estimates of the heat transfer coefficient ultimately satisfied the total heat absorption constraint. The calculated and measured back wall temperatures were then compared. Good agreement

was normally obtained. In a few cases, disagreement was resolved by recalculating the throat deposit histories, using an alternate method or improving the arithmetic. It should be noted that the agreement in the calculated and measured throat back wall temperatures is far from perfect. This is undoubtedly the consequence of (1) temperature measurement errors, (2) deposit history errors, (3) averaging effects, (4) procedural errors, and (5) inadequate thermal property data. The thermal property data employed in this program are given in Table XIV. The analysis of the tungsten insert thermal response was more difficult and the results were less satisfactory. The procedures employed in handling the axial conduction effects are described in Section 2.5 of Reference 3.

TABLE XIV. MATERIAL THERMAL PROPERTIES EMPLOYED
IN THROAT CONDUCTION-DEPOSIT ANALYSIS

Material	Temperature (°F)	Density (lb/in^3)	Local Specific Heat (Btu/lb °F)	Thermal Conductivity (Btu/in.sec °F) x 10^4
BeO	-	0.080	0.60	1.85
Al$_2$O$_3$	-	0.133	0.35	0.60
Pyrolytic	250	0.0792	-	54.0
Graphite	350		0.274	-
(a-b Direction)	500		0.30	-
	750		0.34	-
	1000		0.38	-
	1500		0.44	-
	1750		-	26.4
	2000		0.48	-
	2500		-	16.2
	3000		0.52	13.0
	4000		0.541	11.4
	5000	0.0792	0.552	11.3
ATJ Graphite	350	0.0625	same	13.2
(average of	1000		as	9.3
with and	2000		P.G.	5.9
against grain)	3000			4.6
	4000			3.8
	5000			3.2
Tungsten	500	0.675	0.0335	17.0
	5500	0.675	0.0460	11.0

The results are shown in Figures 198 through 227. Each figure shows the throat deposit history the calculated back wall temperature the measured back wall temperature, the throat surface temperature, the assumed exhaust recovery temperature and the calculated pressure dependent heat transfer coefficient. The majority of the figures also indicate the calculated

-365-

deposit surface temperature history. Assuming that the deposit thickness, composition and thermal properties have been reasonably well characterized, the quality of the results can be judged in several ways. First, compare the calculated and measured back wall temperatures. In many cases there appear to be systematic variations. Next, examine the surface temperature when the oxide deposit disappears. It should be, and usually is, close to the oxide melting point. Finally, examine the oxide surface temperature when the thickness is at or near its peak value. Again, this should be at or slightly above the oxide melting point to provide for liquid oxide flow.

It should be noted that no data are presented for Tests T-8, T-13 and T-54. These are absent for lack of thermal data due to instrumentation problems or nozzle failures. Attempts to resolve the poor agreement of measured and calculated temperatures on Test T-25 were unsuccessful. The results for Test T-53 are not satisfactory since no deposits were included in the analysis. The slotted grain tests show considerable circumferential variation in measured back wall temperature. This is associated with nonuniform flow field and deposition effects. It should also be noted that the use of an ideal recovery temperature in the analyses necessarily leads to reduced heat transfer coefficients when poor metal combustion occurs. The corrosion heat absorption was apparently significant enough on Tests T-51 and T-53 to influence the results.

## 8.2 (U) HEAT TRANSFER COEFFICIENT COMPARISON

The calculated heat transfer coefficients were adjusted to the nominal motor pressure of 800 psia for comparison. The results are given in Tables XV through XVIII. Predicted heat transfer coefficients for the program propellants are given in Table XIX. The analysis used to predict the convective coefficients is described in Section 2.5.a of Reference 4. The heat transfer coefficient data are discussed in Section 3.5 of this report. The (equilibrium) average boundary layer specific heat data are given in Figures 228 through 230 for the program propellants. Note that the heat of fusion effect was ignored in forming the $\bar{h}/\bar{C}p$ parameter.

CONDITIONS

$T_{r_*} = 6150°F$

$h_{g.s.} = 0.0075 \left(\frac{P}{870}\right)^{0.8}$
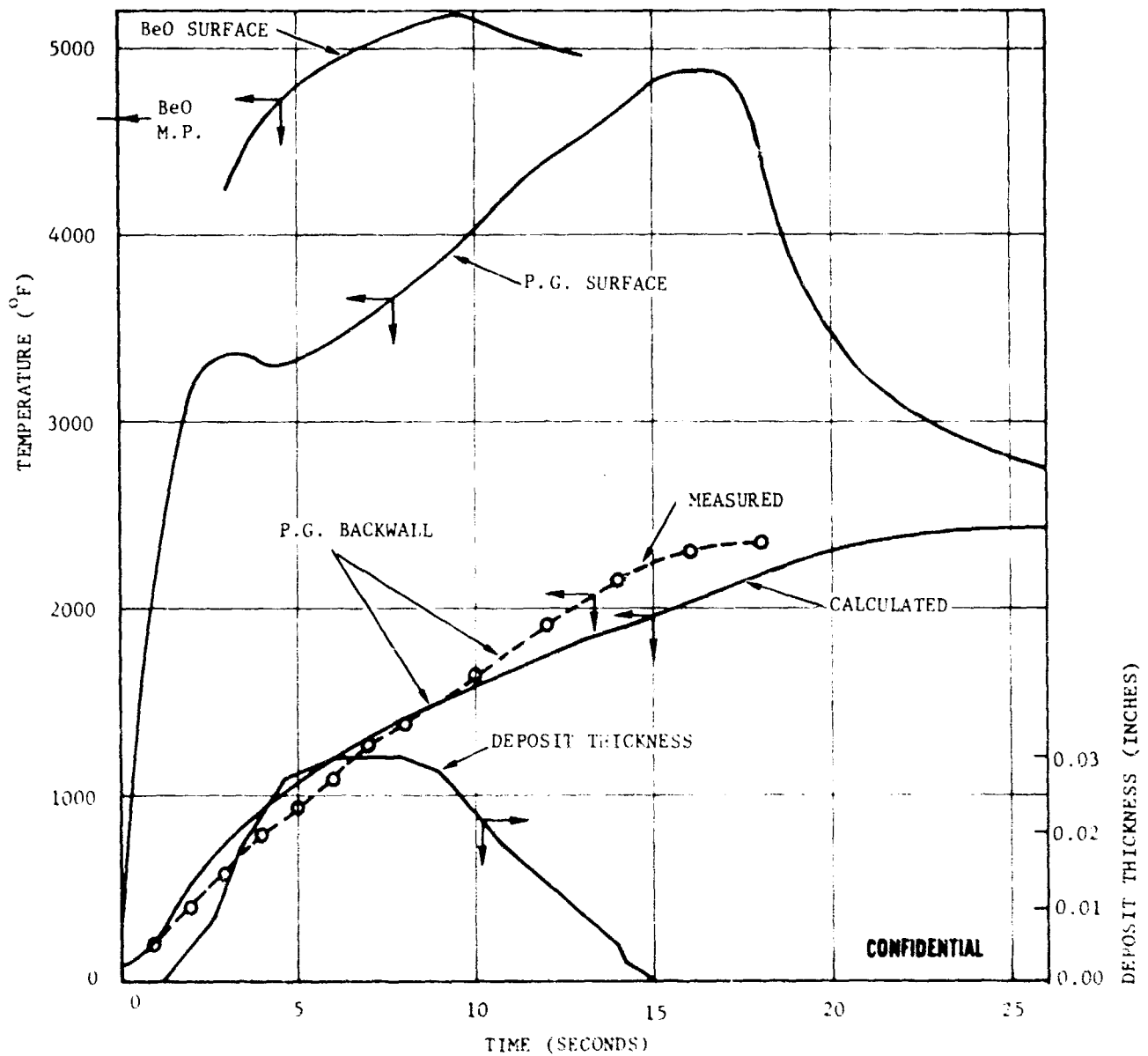
FIGURE 198.   THROAT TEMPERATURE RESPONSE WITH DEPOSITION - TEST T-1

F08192 C

-367-

CONDITIONS

$T_{r_*} = 5560°F$

$h_{g.s.} = 0.0056 \left(\dfrac{P}{840}\right)^{0.8}$
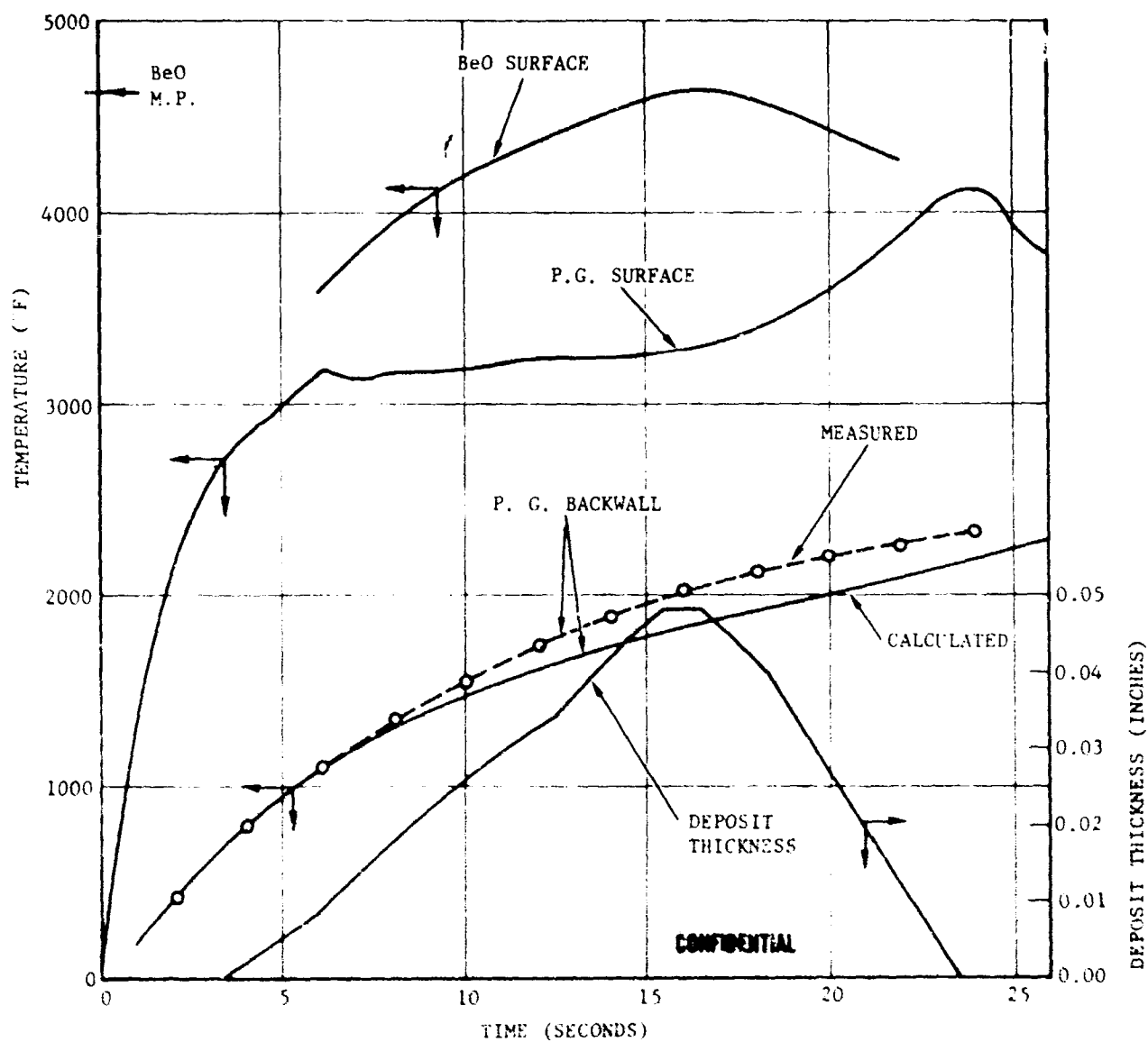
FIGURE 199. THROAT TEMPERATURE RESPONSE WITH DEPOSITION - TEST T-2

F08193 C

-368-

CONDITIONS

$$T_{r_\star} = 5790°F$$

$$h_{g.s.} = 0.0073 \left(\frac{P}{902}\right)^{0.8}$$
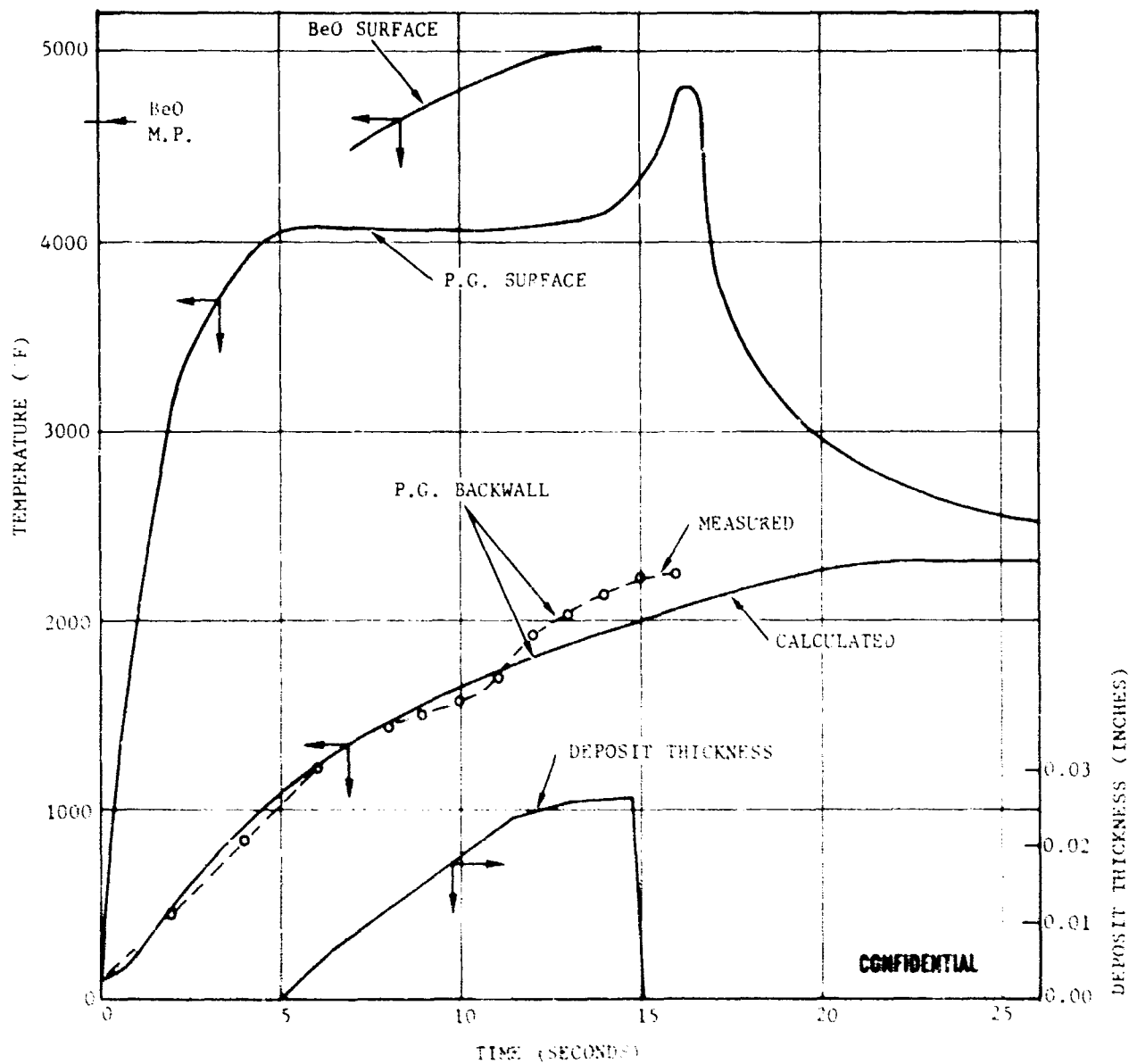
FIGURE 200.   THROAT TEMPERATURE RESPONSE WITH DEPOSITION - TEST T-3

F08194 C

-369-

CONDITIONS

$$T_{r_*} = 5590°F$$

$$h_{g.s.} = 0.0067 \left(\frac{P}{834}\right)^{0.8}$$
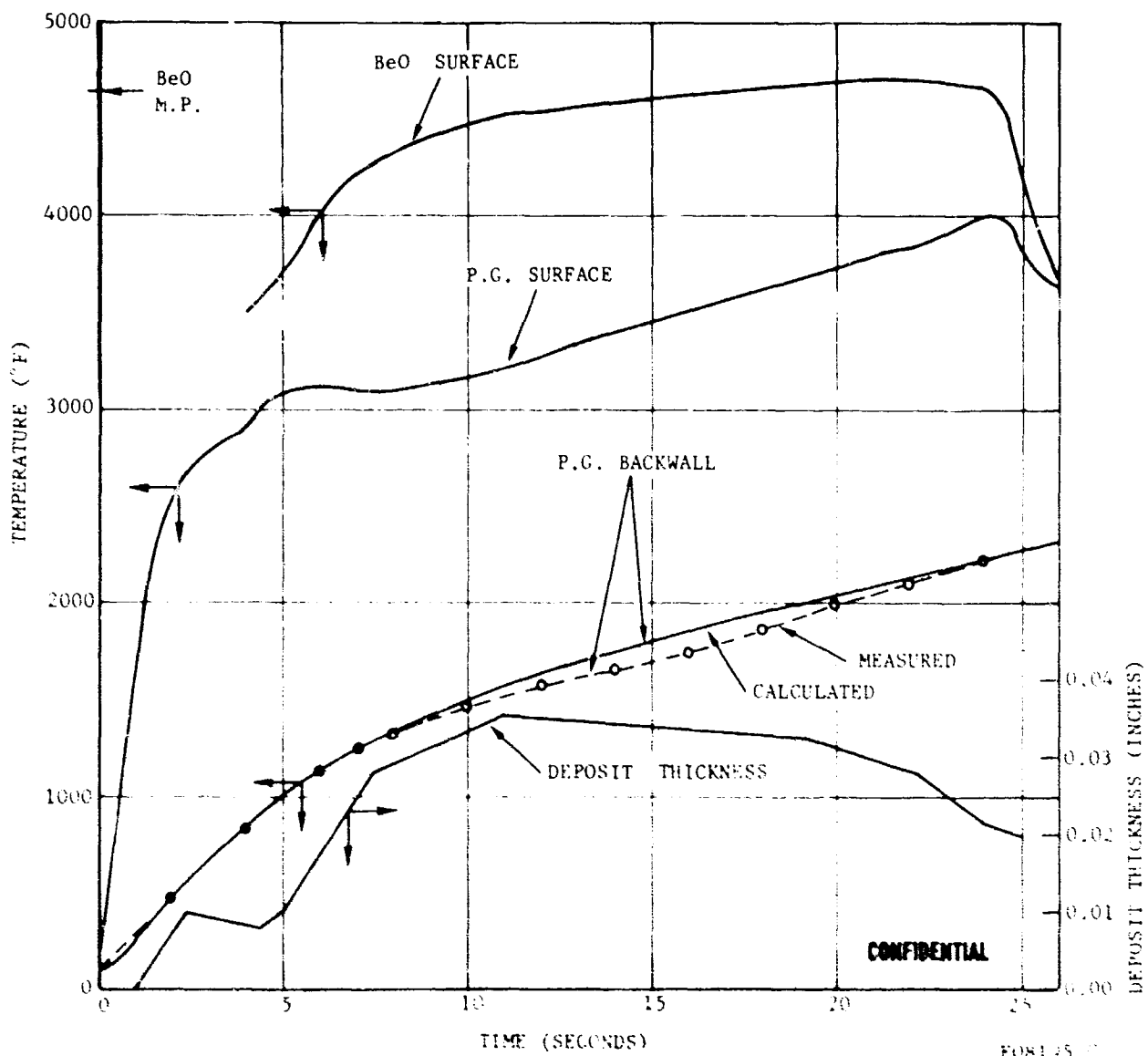
FIGURE 201. THROAT TEMPERATURE RESPONSE WITH DEPOSITION - TEST T-4

CONDITIONS

$$T_{r_*} = 5630°F$$
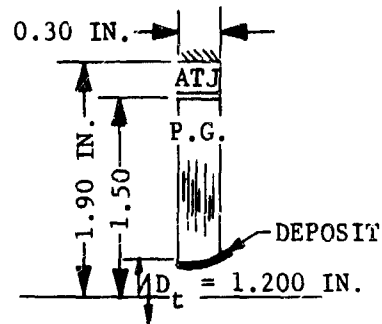
$$h_{g.s.} = 0.0040 \left(\frac{P}{853}\right)^{0.8}$$
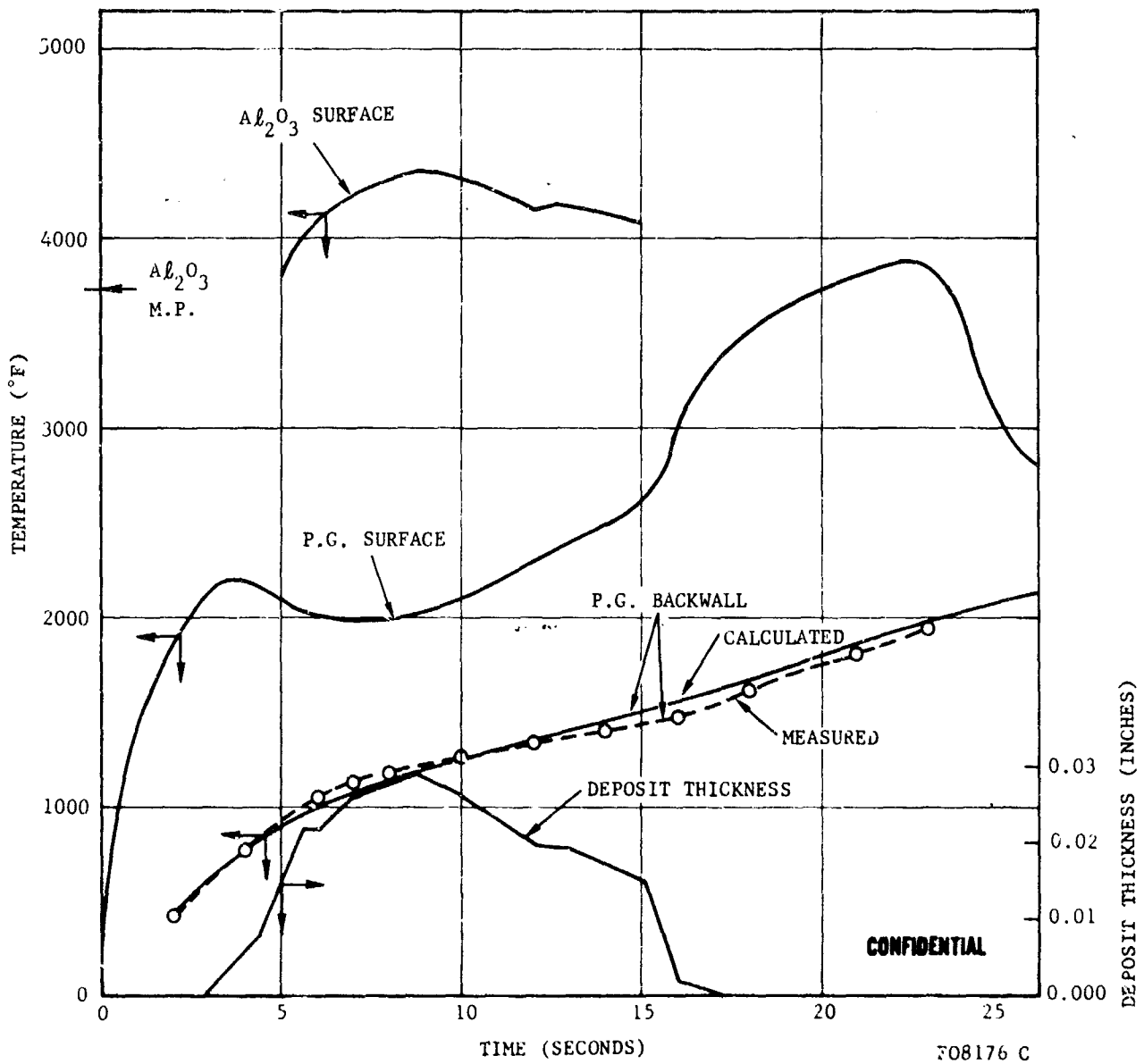
FIGURE 202. THROAT TEMPERATURE RESPONSE WITH DEPOSITION - TEST T-5

-371-

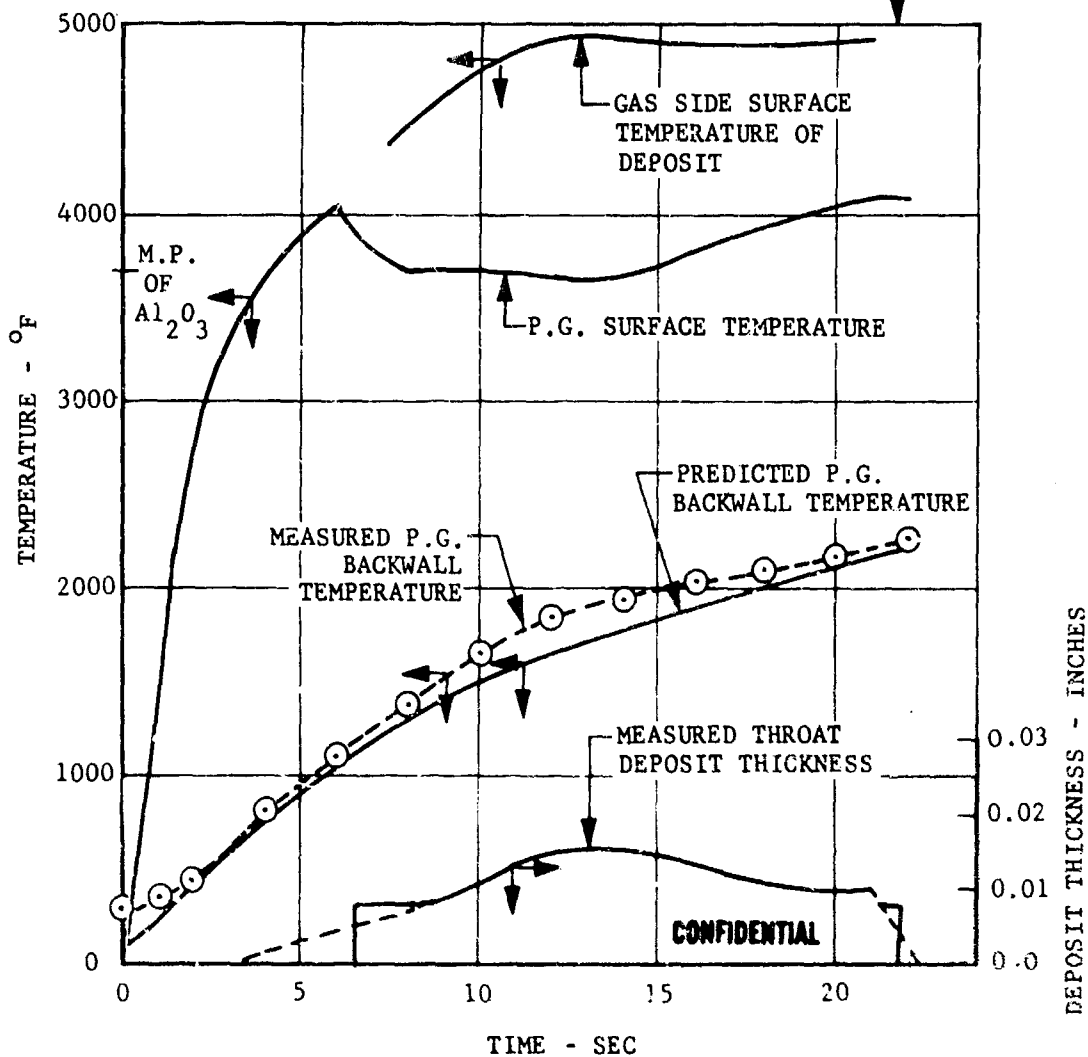PARAMETERS USED IN ANALYSIS

THROAT RECOVERY
    TEMPERATURE : 6260 $^{\circ}$R

$h = 0.00138 \ (P/100)^{0.8}$ BTU/IN^{2}SEC$^{\circ}$F

P.G.-ATJ CONTACT   0.013
CONDUCTANCE   BTU/IN^2 SEC $^{\circ}$F

0.30 IN.

ATJ

P.G.

1.90 IN.

1.50

DEPOSIT

D_t = 1.200 IN.

END OF FIRING

FINAL MEASURED THROAT DIAMETER = 1.202 IN.

GAS SIDE SURFACE
TEMPERATURE OF
DEPOSIT

M.P. OF Al$_2$O$_3$

P.G. SURFACE TEMPERATURE

PREDICTED P.G.
BACKWALL TEMPERATURE

MEASURED P.G.
BACKWALL
TEMPERATURE

MEASURED THROAT
DEPOSIT THICKNESS

CONFIDENTIAL

TEMPERATURE - $^{\circ}$F

DEPOSIT THICKNESS - INCHES

TIME - SEC

F04045 C

FIGURE 203.   THROAT TEMPERATURE RESPONSE WITH DEPOSITION FOR FIRING T-6 (#1)
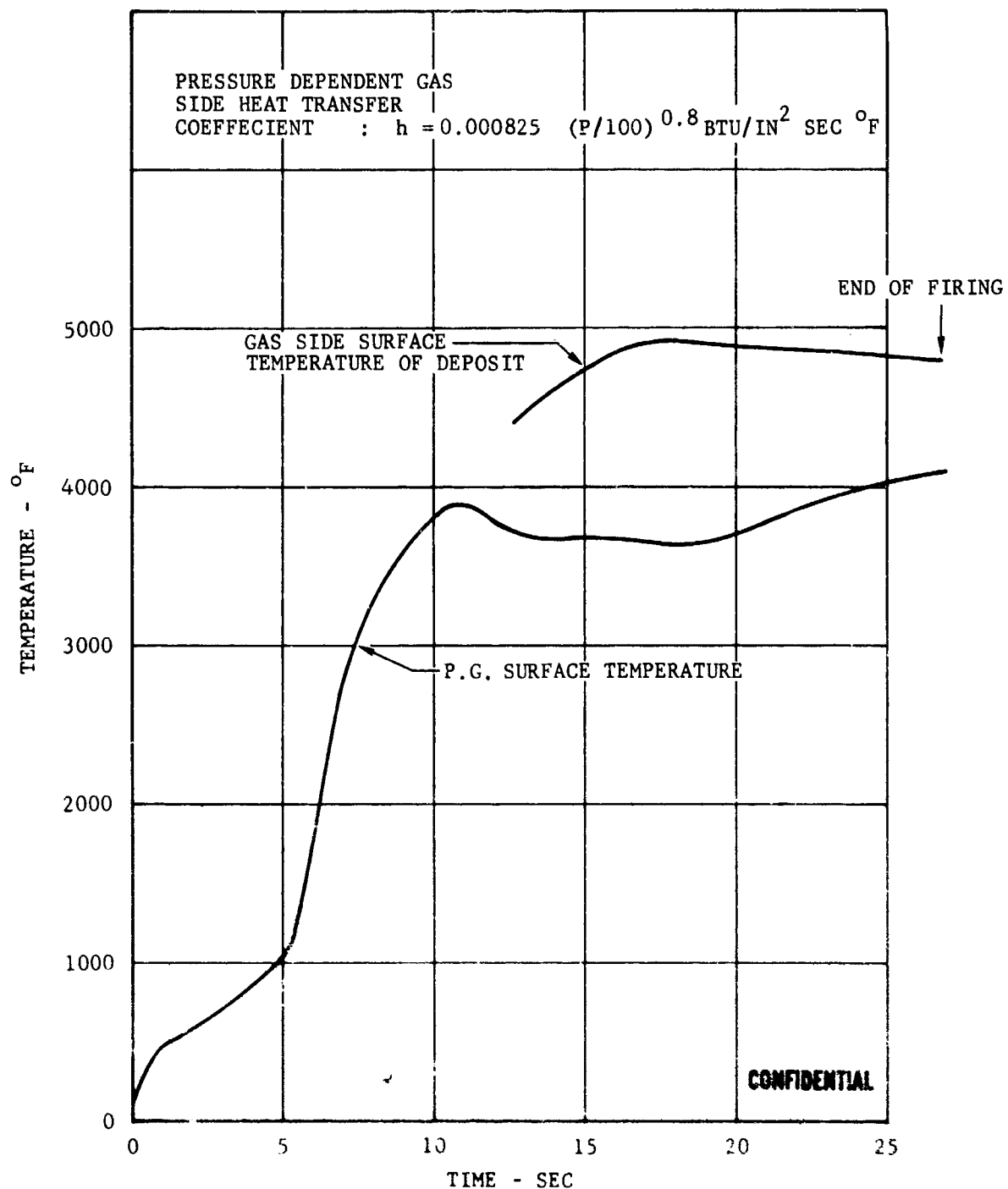
PRESSURE DEPENDENT GAS
SIDE HEAT TRANSFER
COEFFECIENT : $h = 0.000825 \; (P/100)^{0.8} BTU/IN^2 SEC \, ^\circ F$

END OF FIRING

GAS SIDE SURFACE
TEMPERATURE OF DEPOSIT

P.G. SURFACE TEMPERATURE

TEMPERATURE - $^\circ F$

TIME - SEC

CONFIDENTIAL

F04046 C

FIGURE 2)4. THROAT TEMPERATURE RESPONSE WITH DEPOSITION FOR FIRING
T-6 (#2)

-373-

CONDITIONS

$T_{r_*} = 6200°F$

$h_{g.s.} = 0.0080 \left(\dfrac{P}{952} \right)^{0.8}$
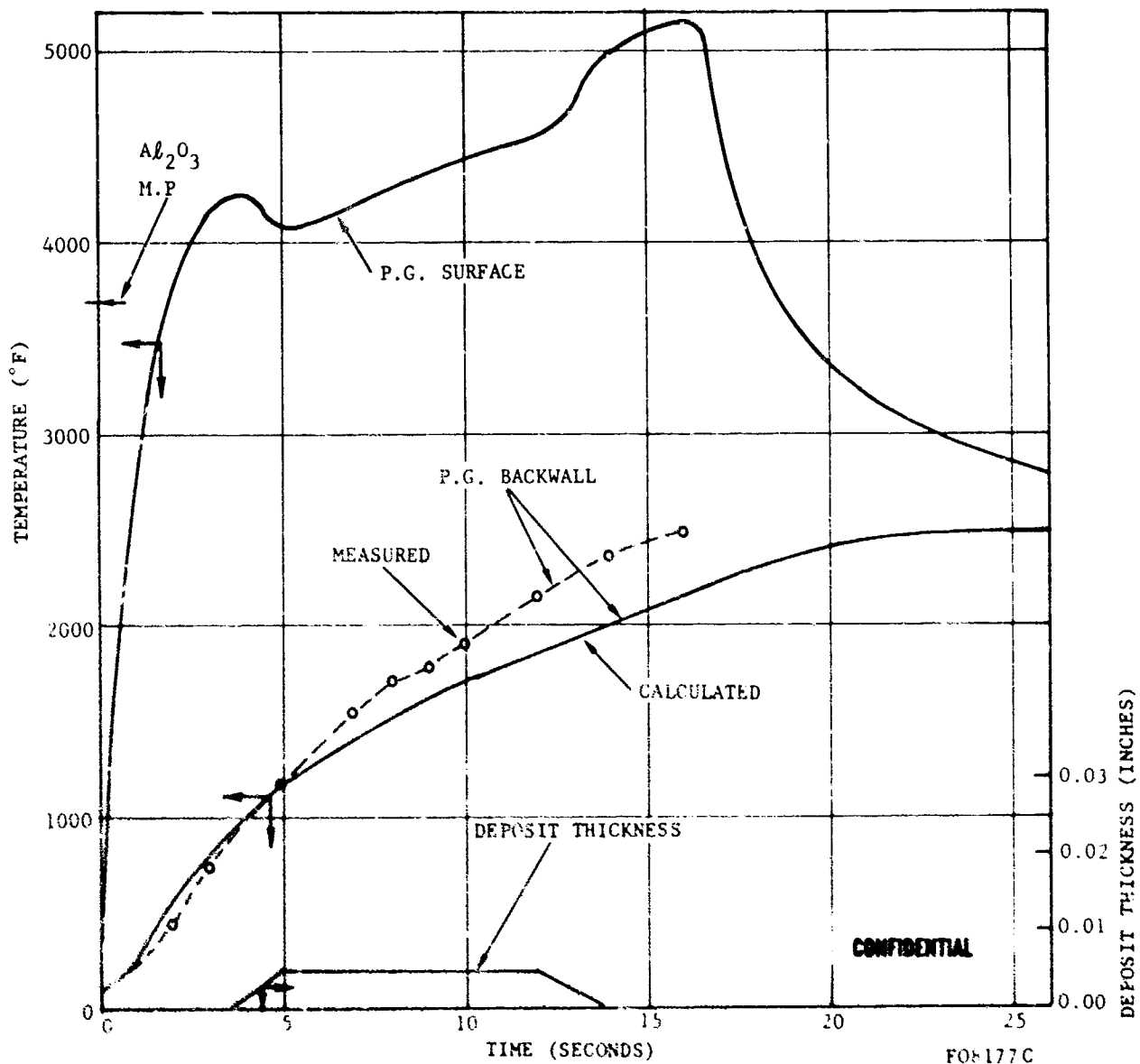
FIGURE 205. THROAT TEMPERATURE RESPONSE WITH DEPOSITION - TEST T-7
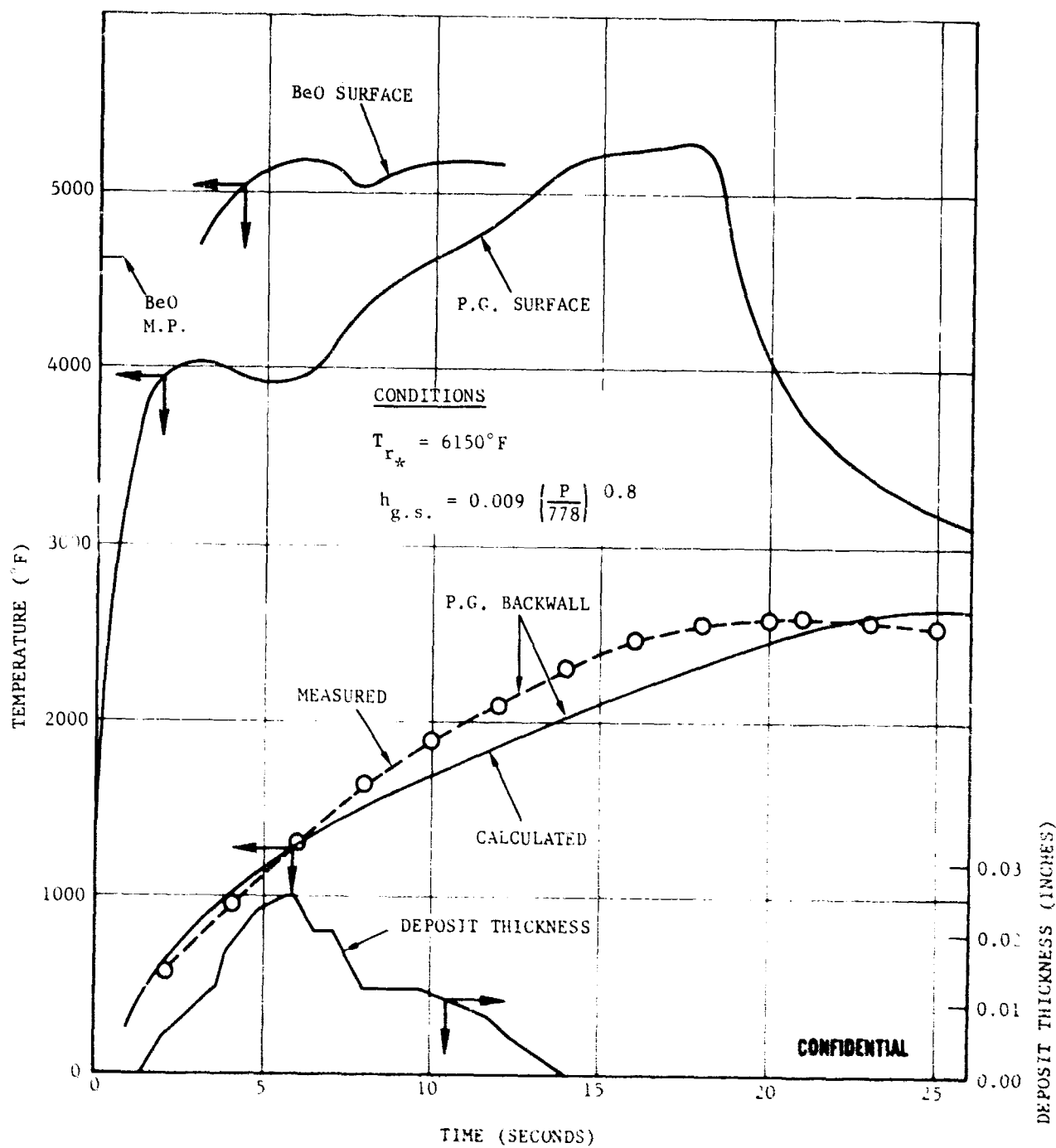
FIGURE 206. THROAT TEMPERATURE RESPONSE WITH DEPOSITION - TEST T-9

F08196 C
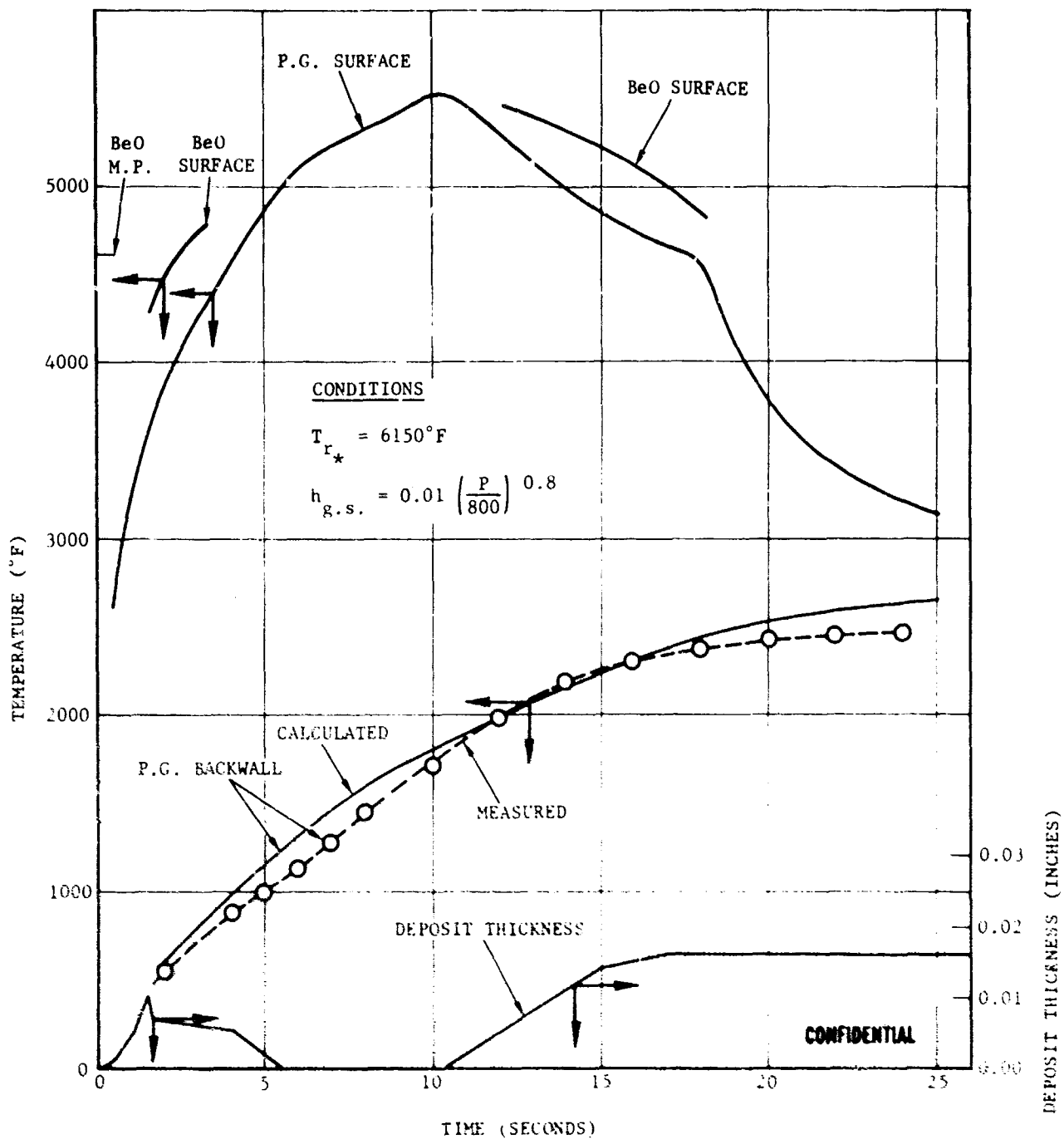
FIGURE 207. THROAT TEMPERATURE RESPONSE WITH DEPOSITION - TEST T-10
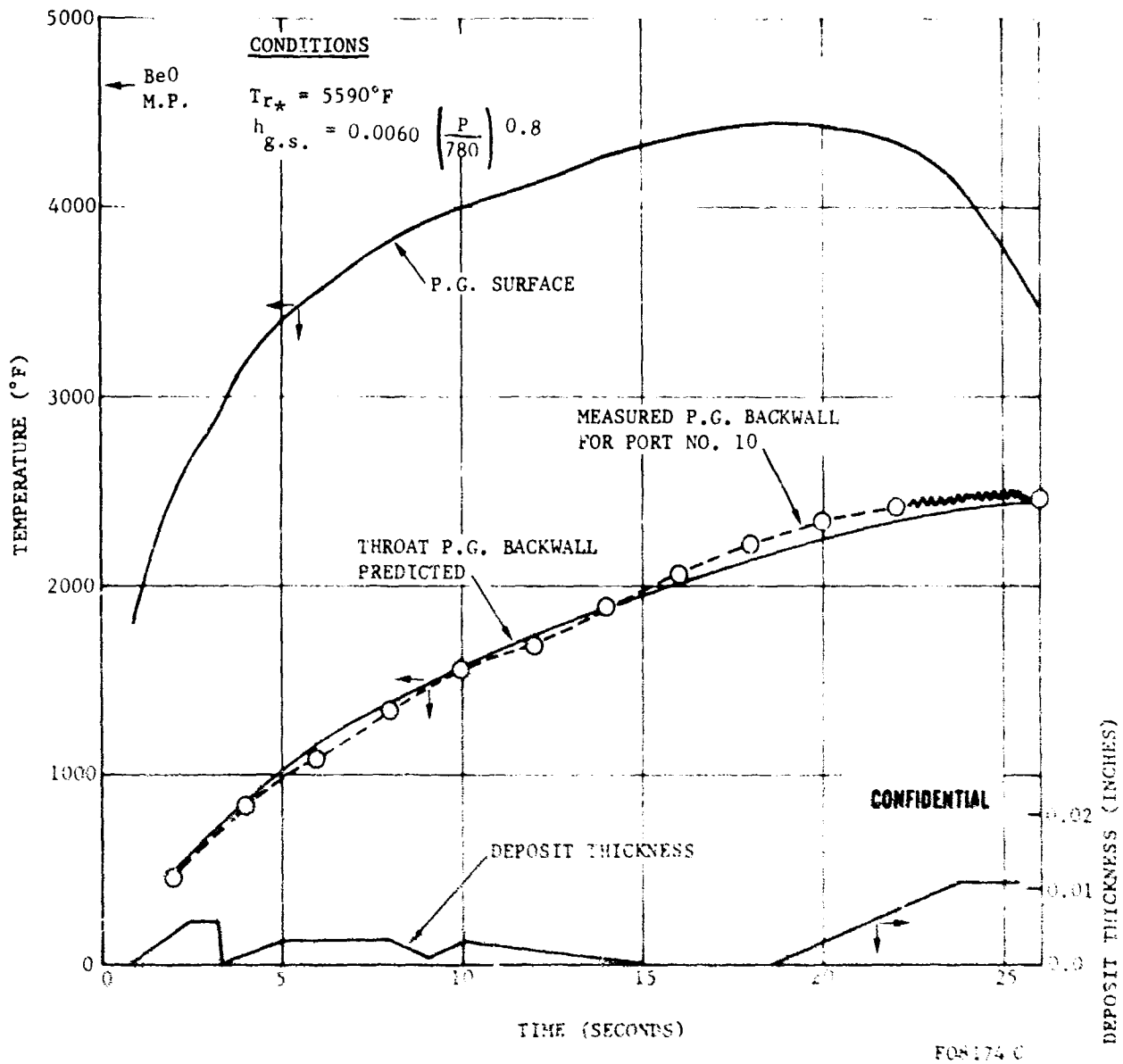
FIGURE 208.   THROAT TEMPERATURE RESPONSE
WITH DEPOSITION - TEST T-11
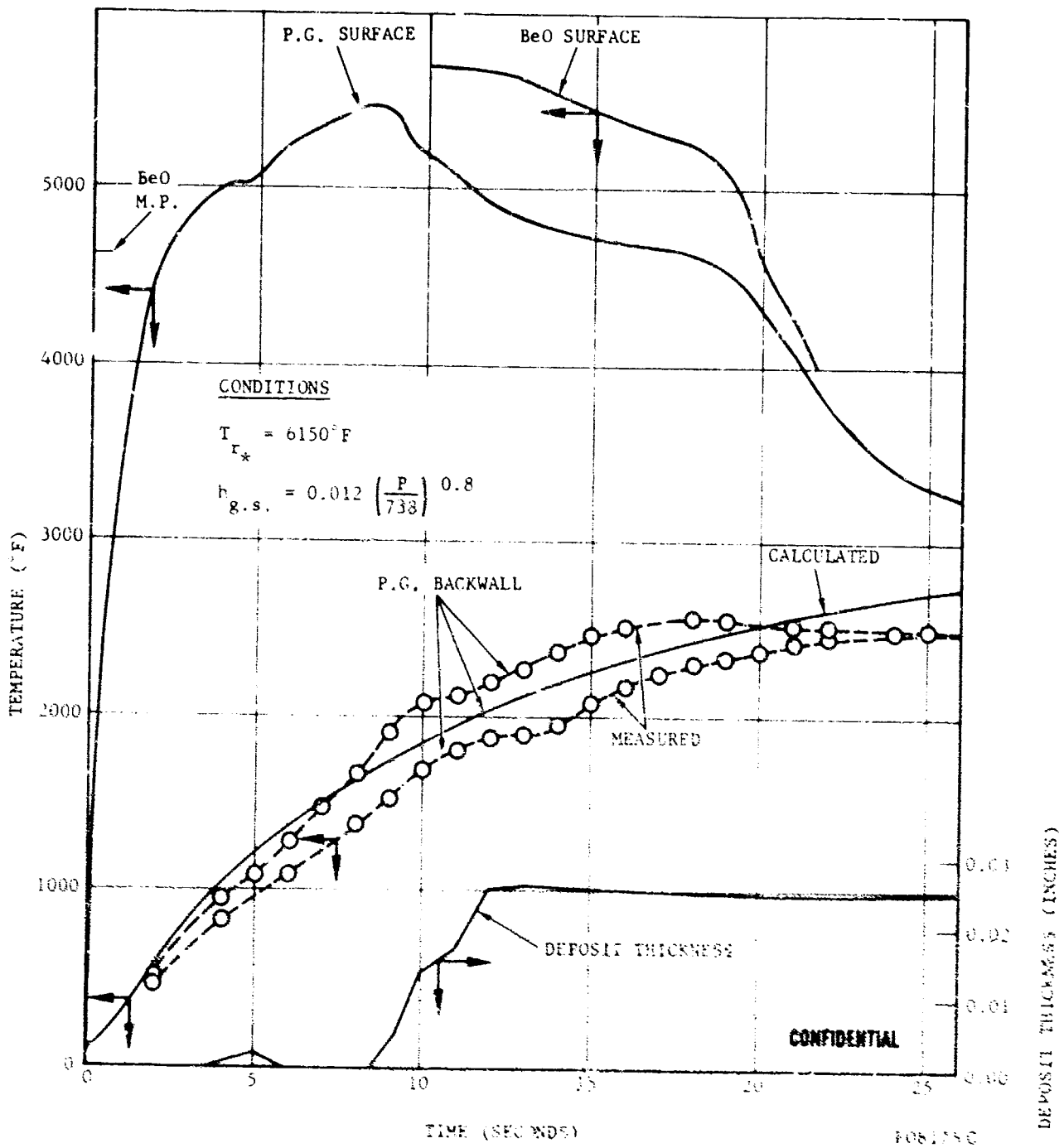
FIGURE 209. THROAT TEMPERATURE RESPONSE WITH DEPOSITION - TEST T-12

-378-

CONDITIONS

$$T_{r_*} = 5790°F$$

$$h_{g.s.} = 0.0074 \left(\frac{P}{814}\right)^{0.8}$$

FIGURE 210.   THROAT TEMPERATURE RESPONSE WITH DEPOSITION - TEST T-14

F08202 C

CONDITIONS

$T_{r_*} = 5790°F$

$h_{g.s.} = 0.0053 \left(\frac{P}{995}\right)^{0.8}$

FIGURE 211. THROAT TEMPERATURE RESPONSE WITH DEPOSITION - TEST T-15

F08203 C

FIGURE 212. THROAT TEMPERATURE RESPONSE WITH DEPOSITION, TEST 1-16

F08204 C

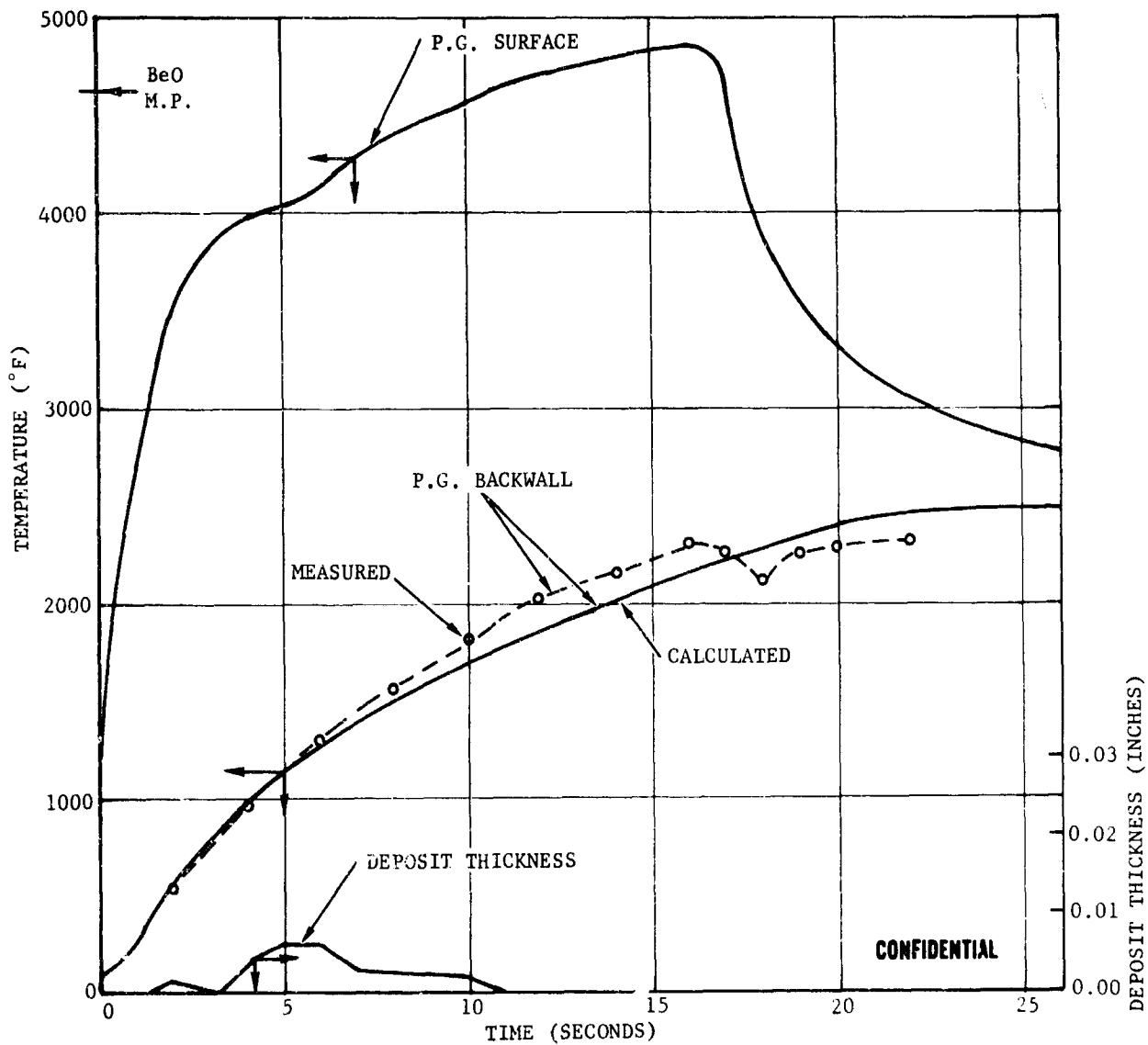FIGURE 213. TEMPERATURE RESPONSE WITH DEPOSITION AT UPSTREAM AREA
RATIO OF 1.03, TEST T-16

F08205 C
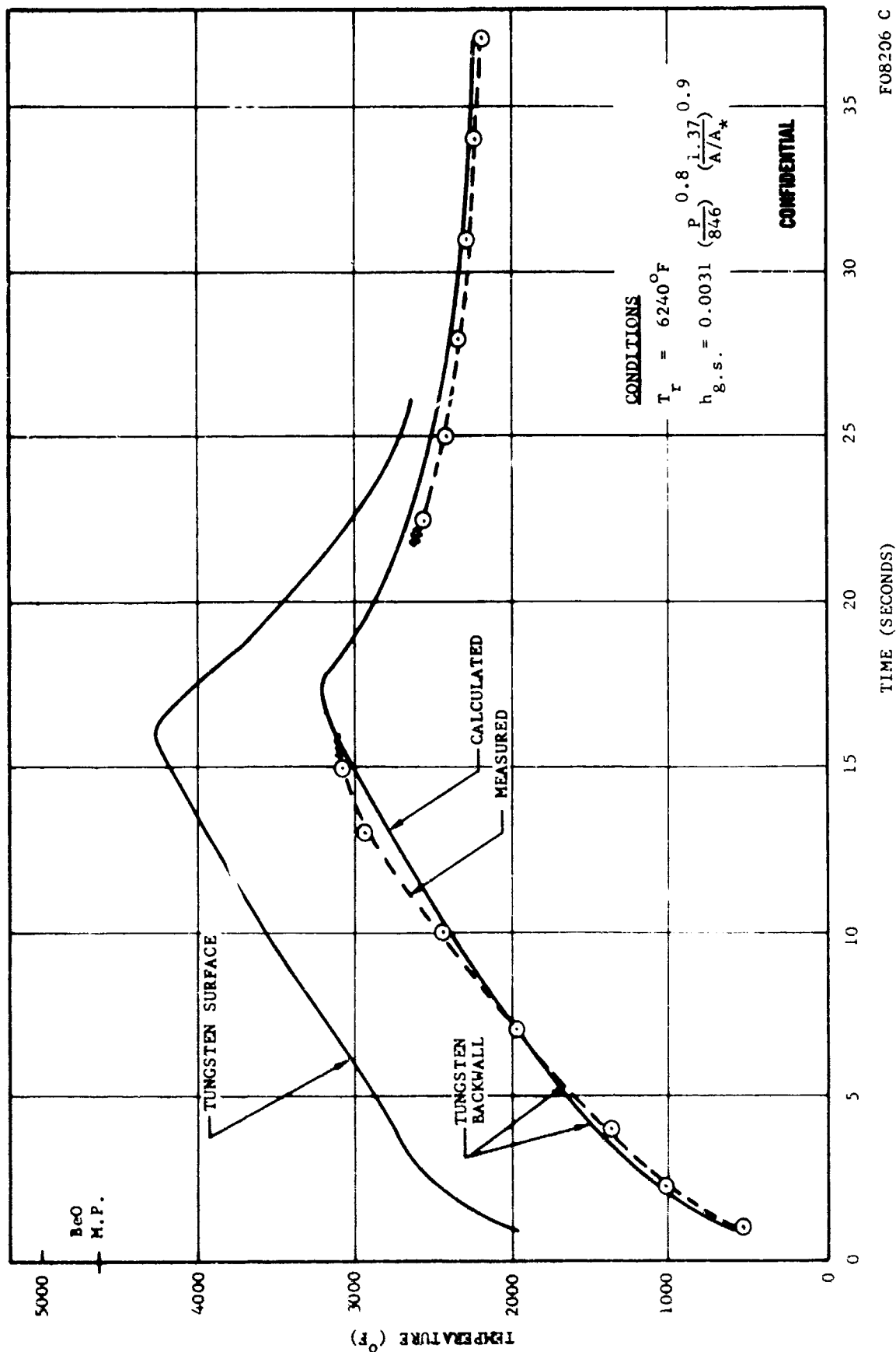
FIGURE 214. TEMPERATURE RESPONSE WITH DEPOSITION AT UPSTREAM AREA RATIO OF 1.37, TEST T-16

CONDITIONS

$T_r = 6240°F$

$h_{g.s.} = 0.0031 \left(\frac{P}{846}\right)^{0.8} \left(\frac{1.37}{A/A_*}\right)^{0.9}$

F08206 C
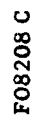
FIGURE 215. THROAT TEMPERATURE RESPONSE WITH DEPOSITION, TEST T-17

CONDITIONS

$T_r = 6240°F$

$h_{g.s.} = 0.0028 \left(\frac{P}{800}\right)^{.8} \left(\frac{1.37}{A}\right)^{.9}{}_{*}$

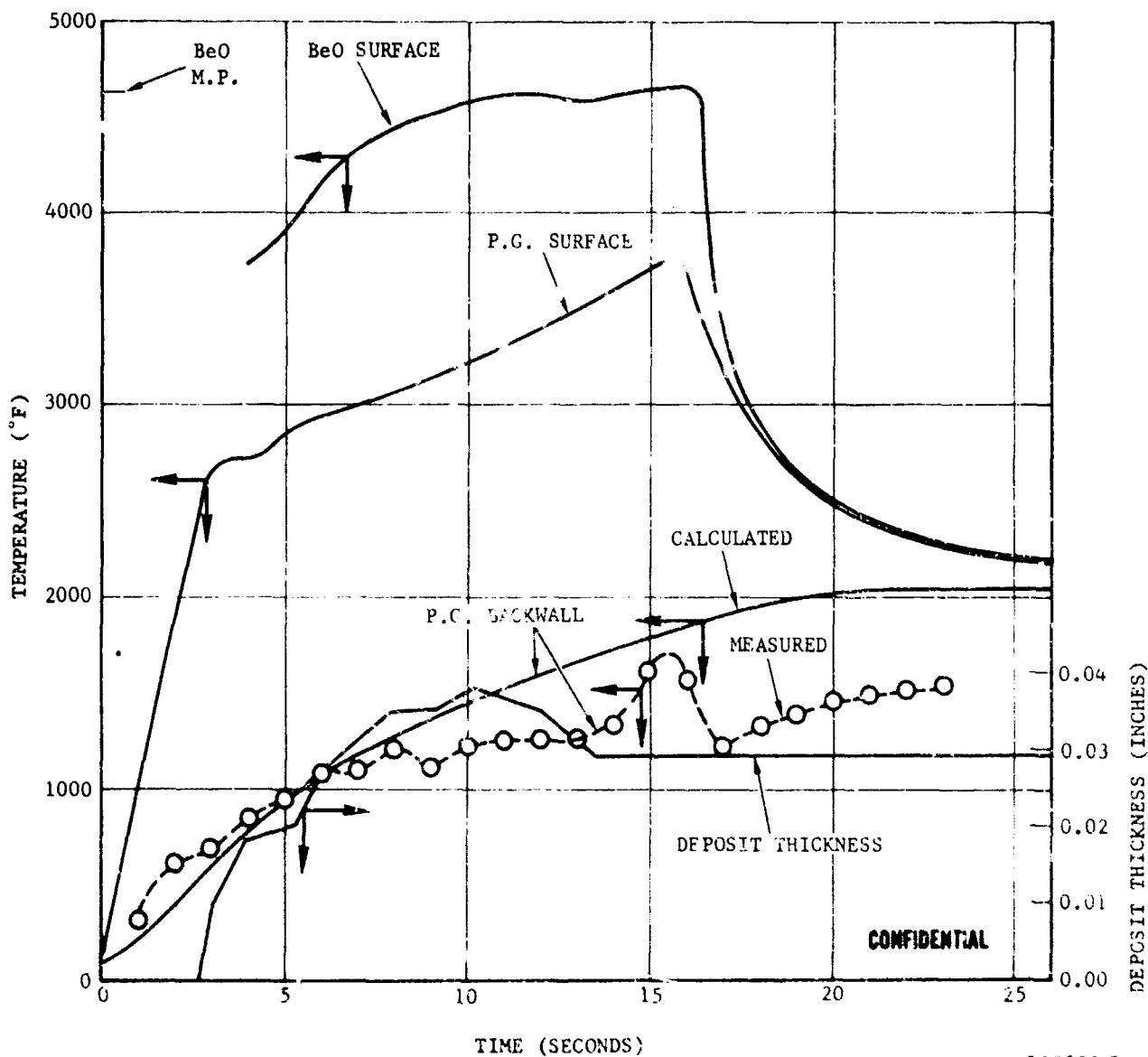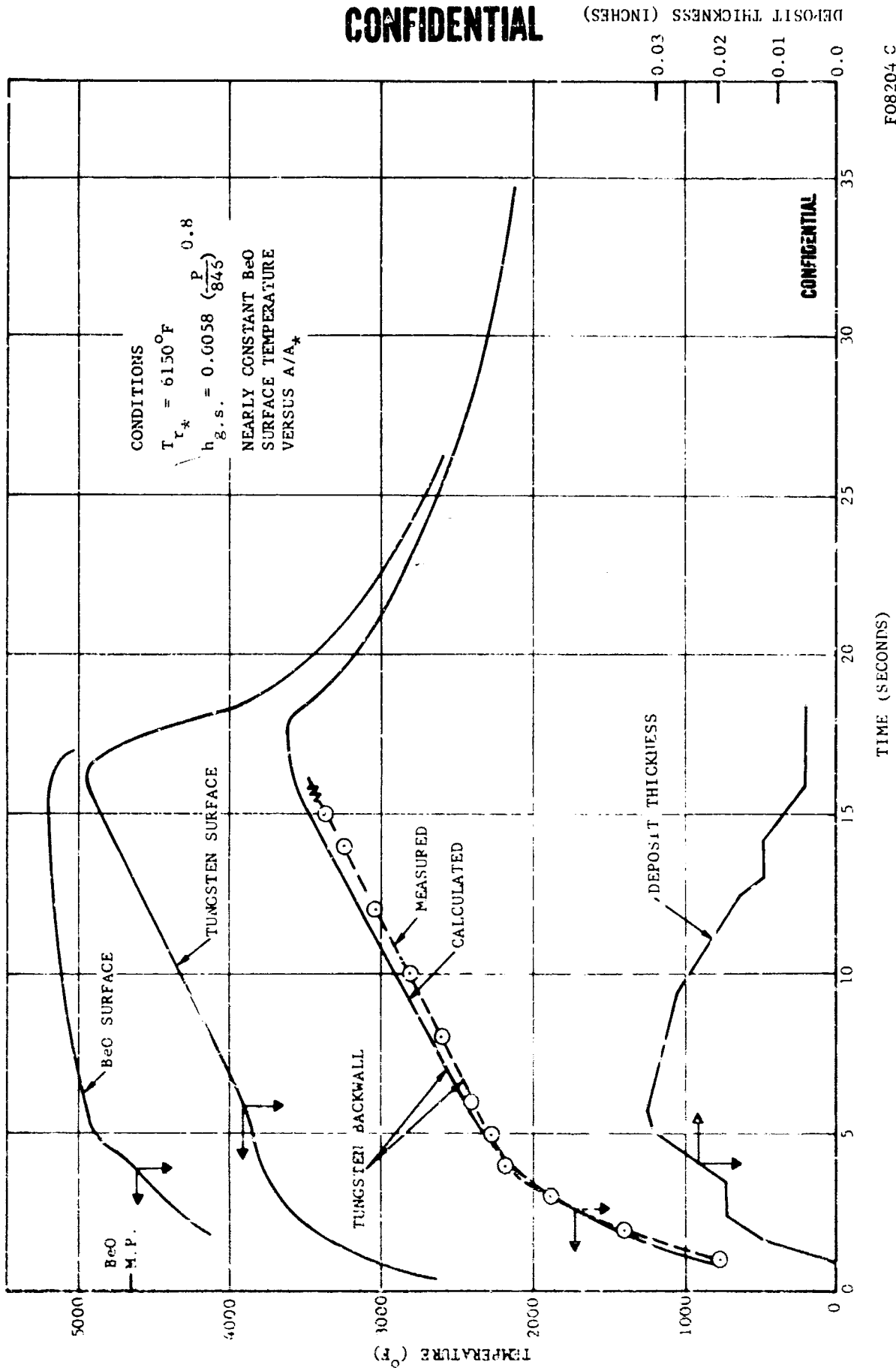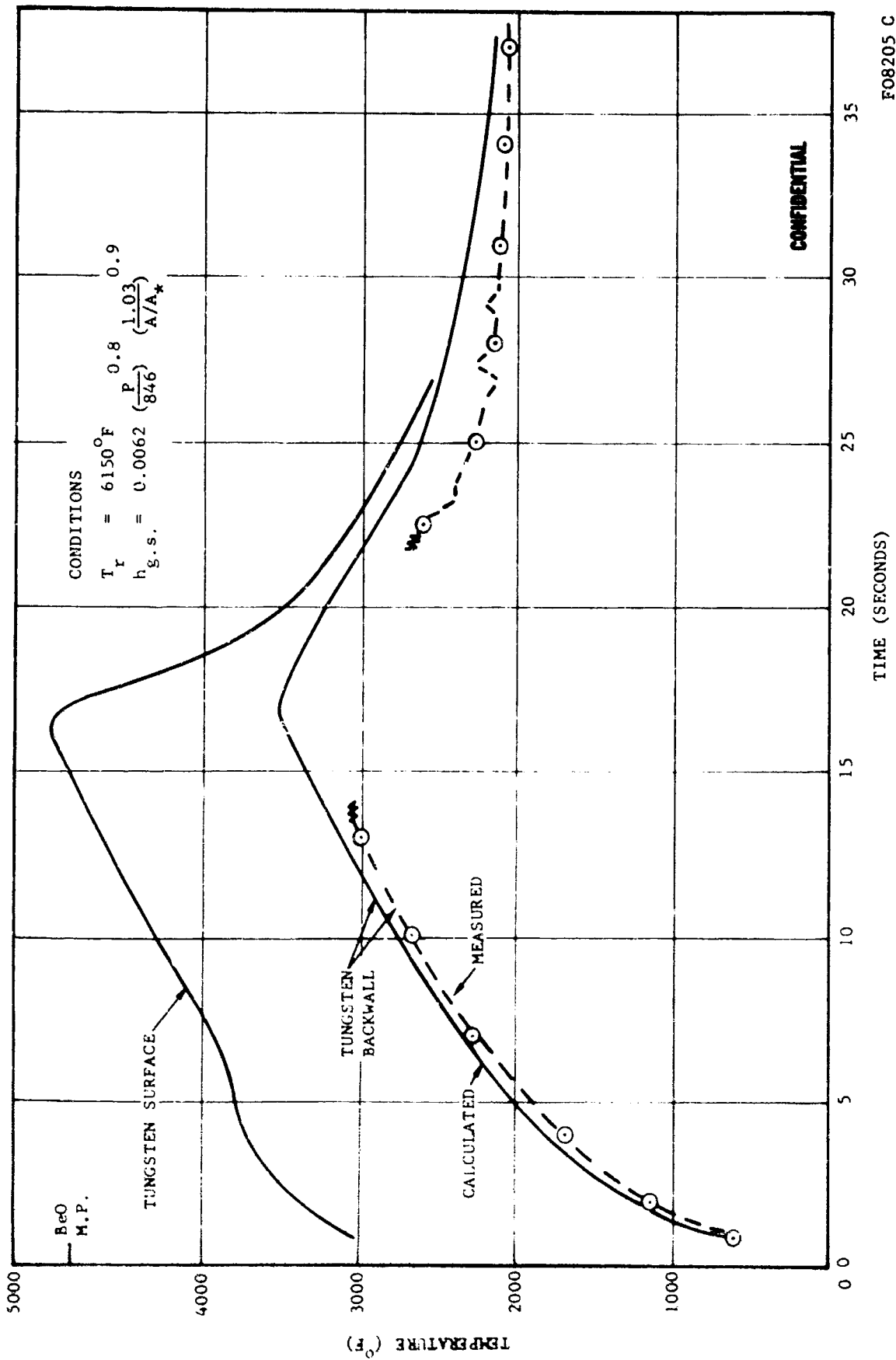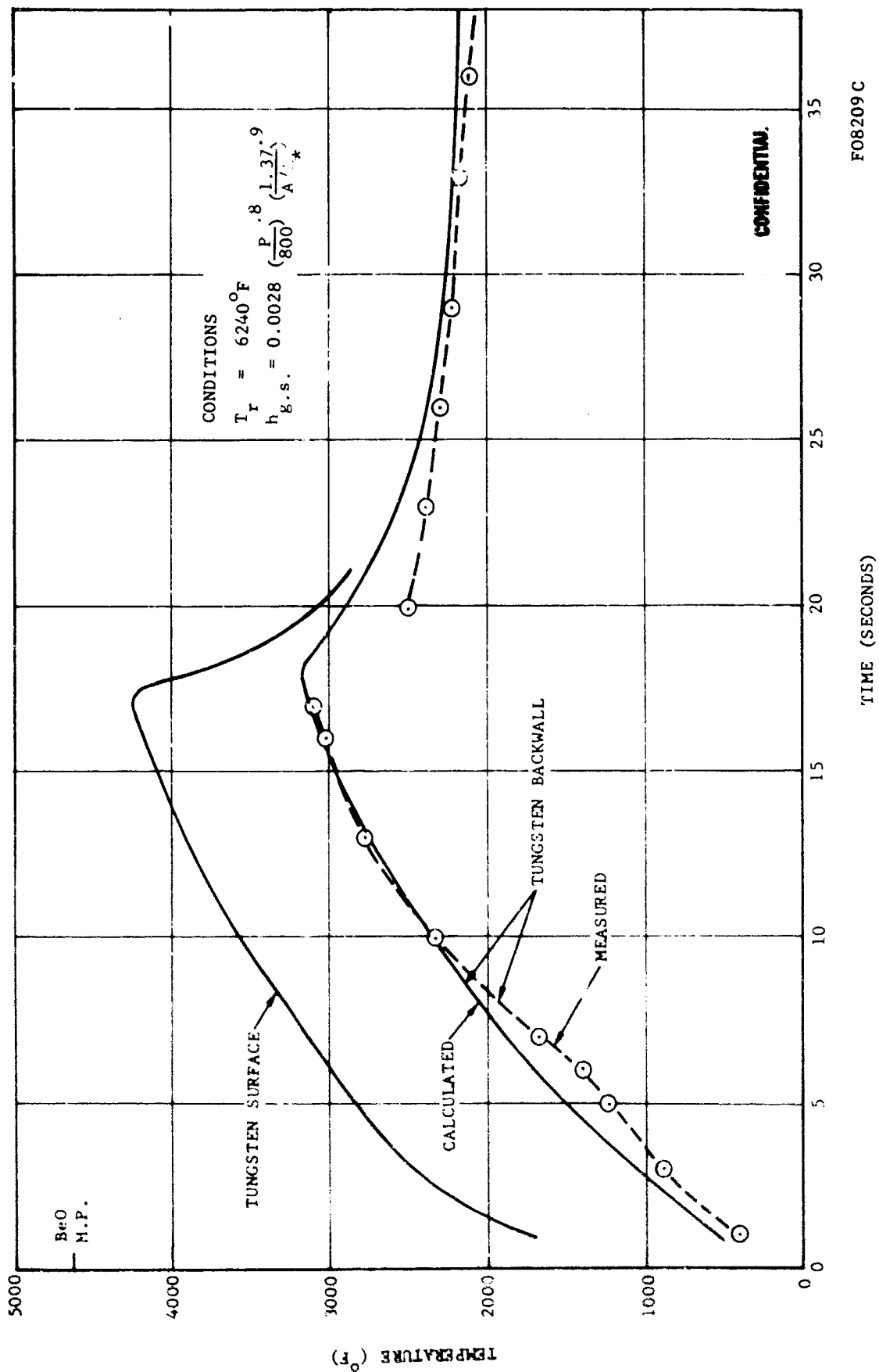FIGURE 216. TEMPERATURE RESPONSE WITH DEPOSITION AT UPSTREAM AREA
RATIO OF 1.37, TEST T-17

F08209 C
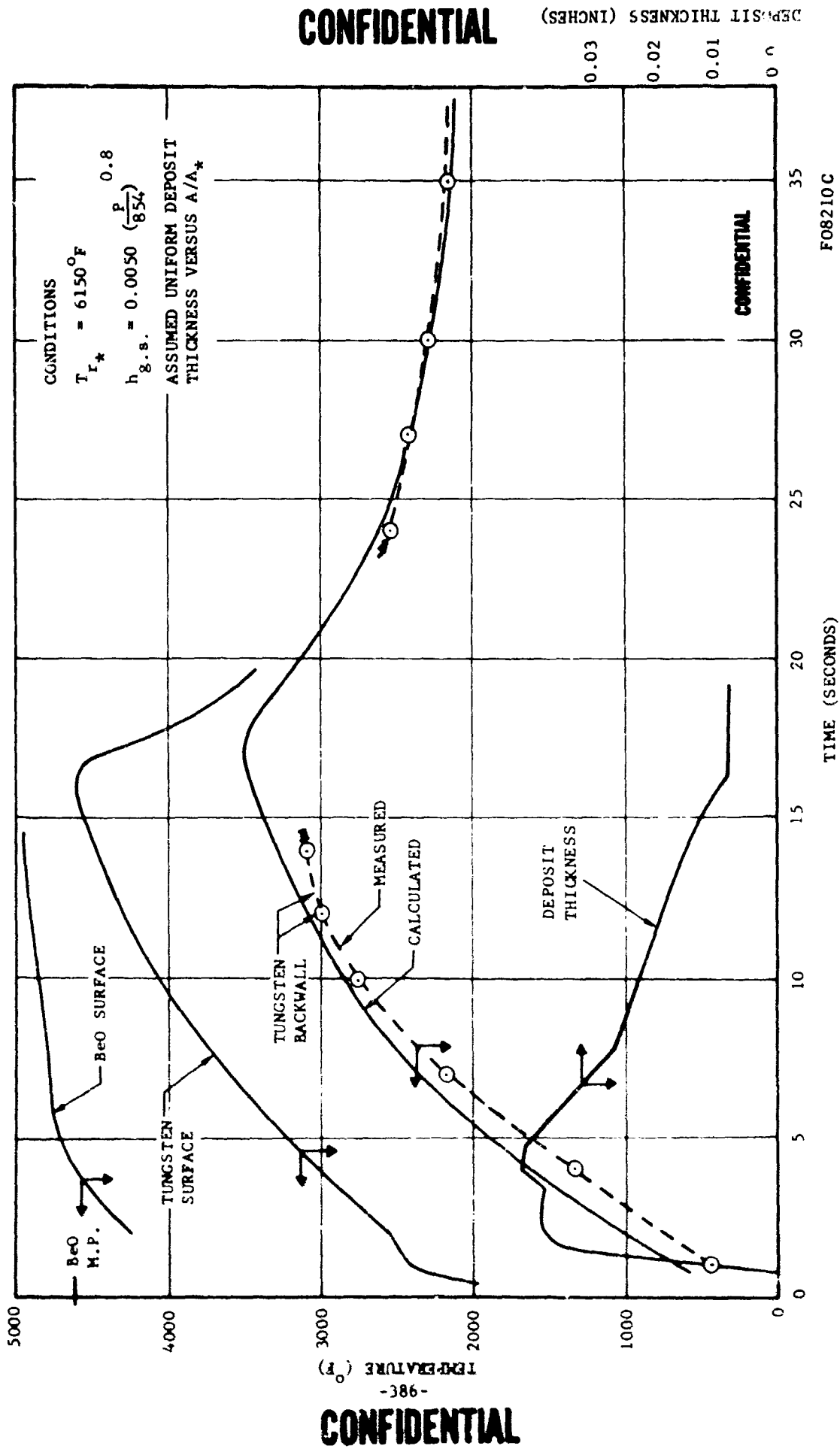
FIGURE 217. THROAT TEMPERATURE RESPONSE WITH DEPOSITION, TEST T-18

CONFIDENTIAL

FIGURE 218. THROAT TEMPERATURE RESPONSE WITH DEPOSITION, TEST T-19

F08211 C

-387-
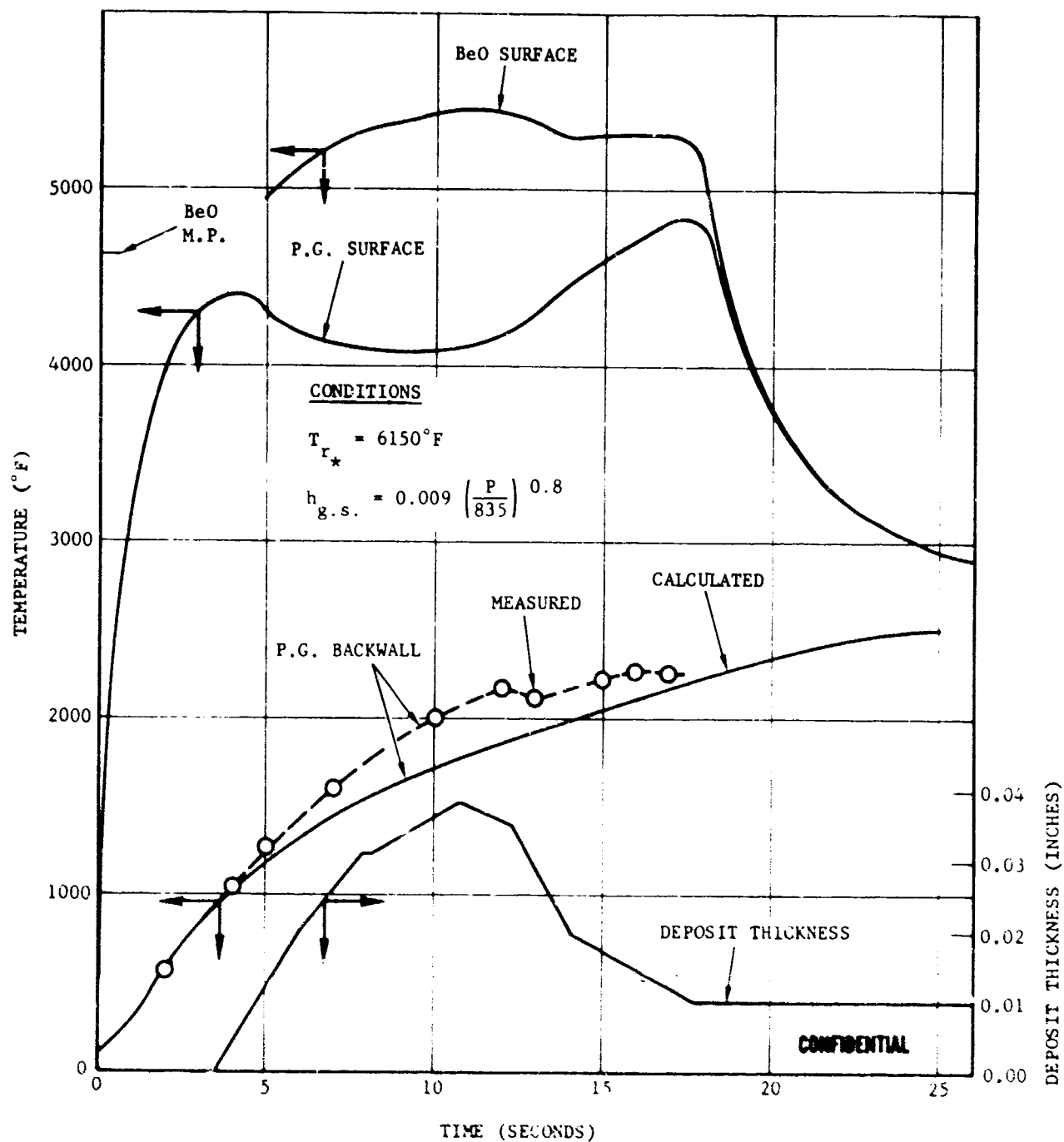
CONFIDENTIAL

FIGURE 219. THROAT TEMPERATURE RESPONSE WITH DEPOSITION - TEST T-20

F08212 C

CONDITIONS

$T_{r_*} = 6150°F$

$h_{g.s.} = 0.004 \left(\dfrac{P}{946} \right)^{0.8}$
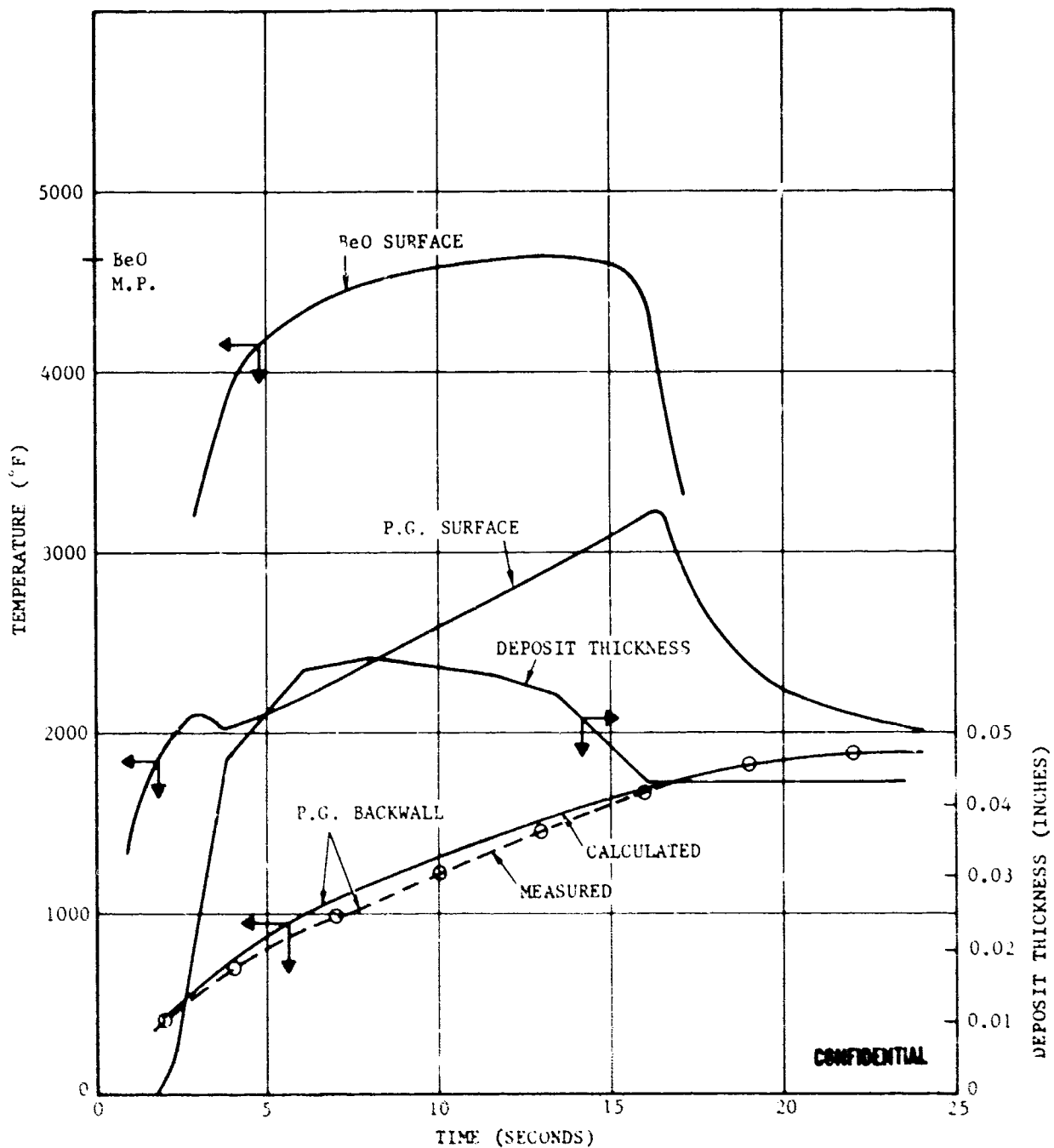
FIGURE 220. THROAT TEMPERATURE RESPONSE WITH DEPOSITION - TEST T-21

708213 C

CONDITIONS

$T_{r_\star} = 6150°F$

$n_{g.s.} = 0.004 \left(\frac{P}{946} \right)^{0.8}$
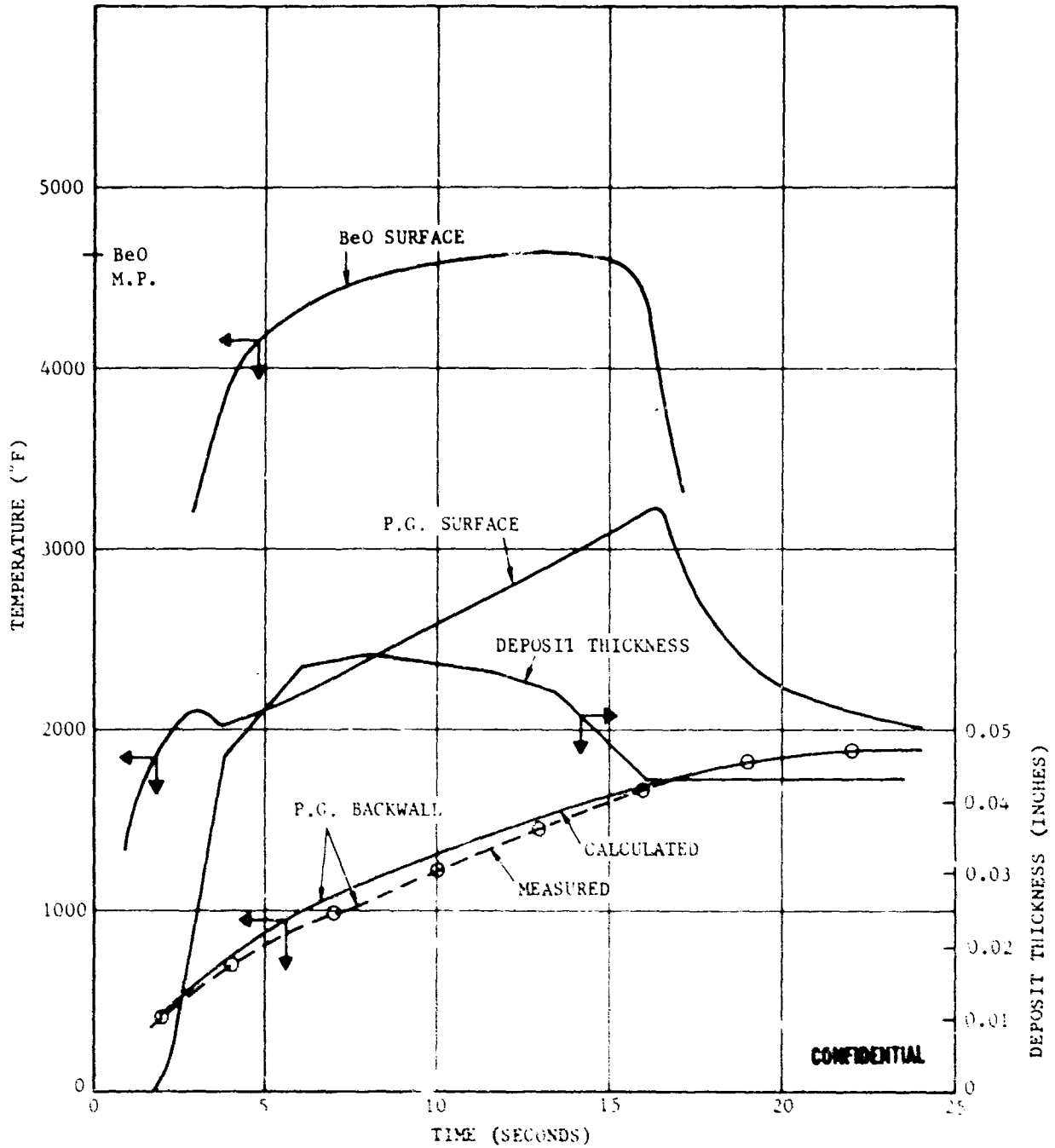
FIGURE 220. THROAT TEMPERATURE RESPONSE WITH DEPOSITION - TEST T-21

F08213 C

CONDITIONS

$T_{r_*} = 5590°F$

$h_{g.s.} = 0.0062 \left(\dfrac{P}{865}\right)^{0.8}$
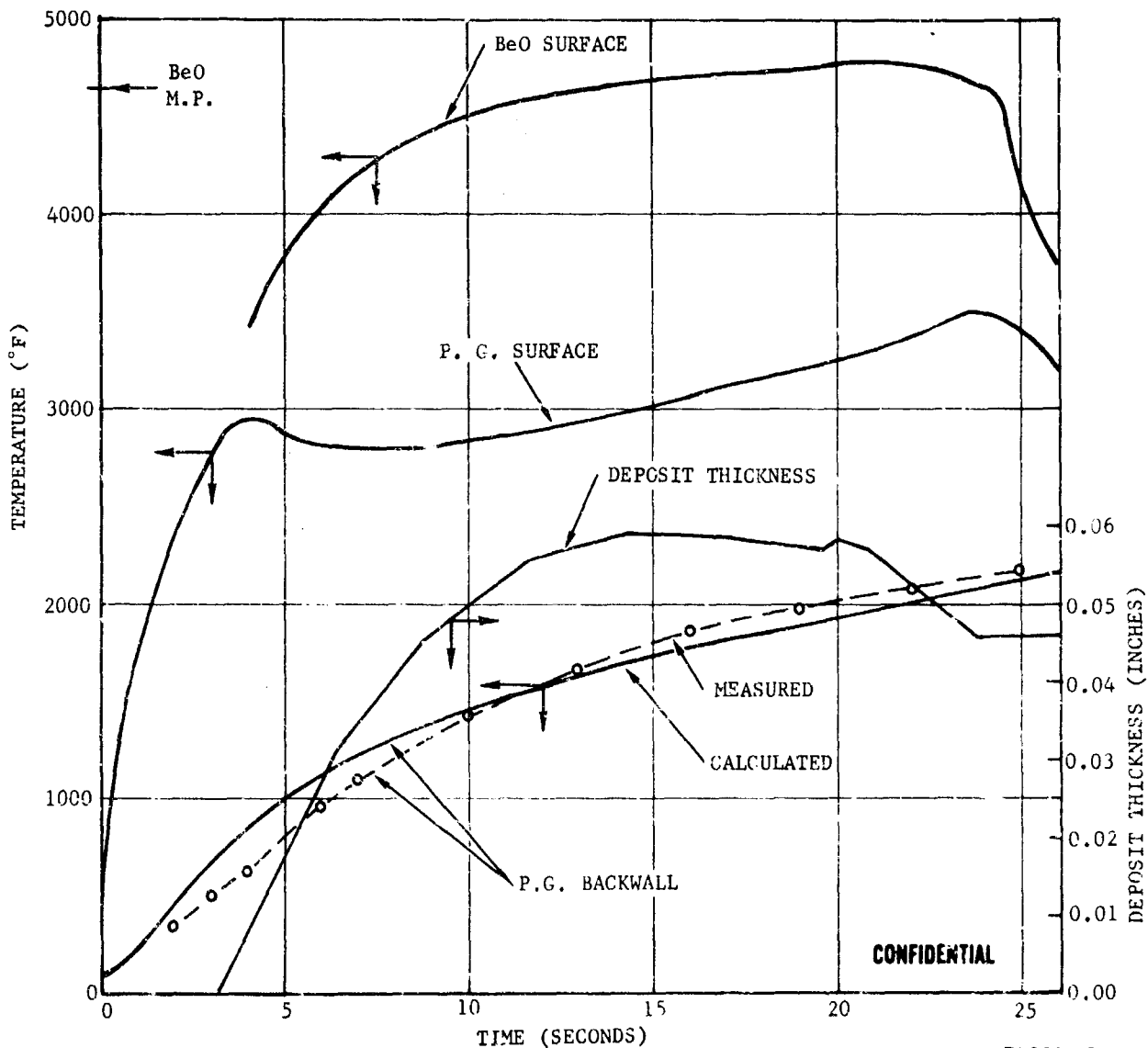
FIGURE 221. THROAT TEMPERATURE RESPONSE WITH DEPOSITION - TEST T-22

F08214 C

CONDITIONS

$T_{r_*} = 6150°F$

$h_{g.s.} = 0.0060 \left(\dfrac{P}{850}\right)^{0.8}$
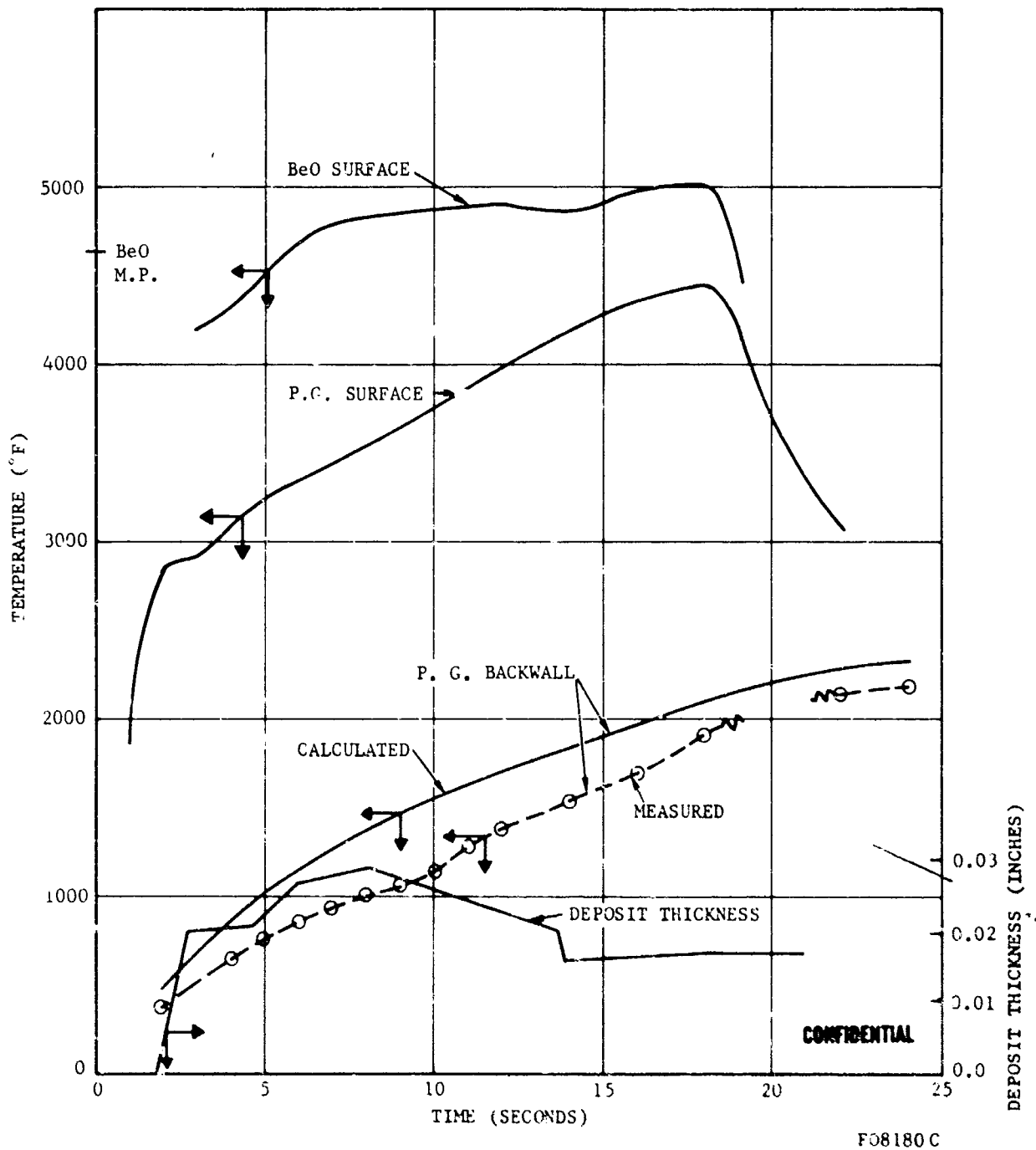
FIGURE 222.   THROAT TEMPERATURE RESPONSE WITH DEPOSITION - TEST T-23

-391-
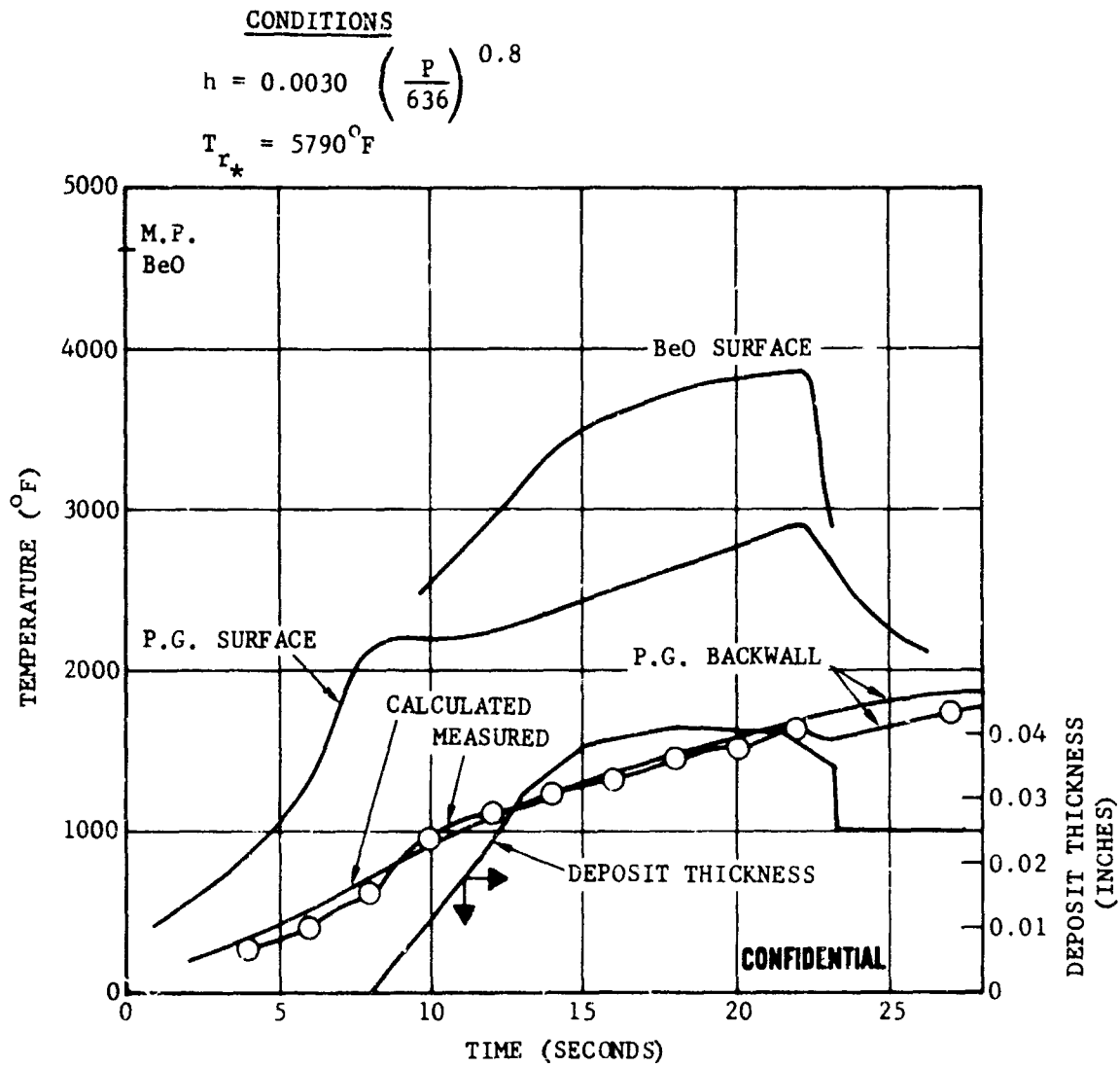
FIGURE 223. THROAT TEMPERATURE RESPONSE WITH DEPOSITION, TEST T-24

CONDITIONS

$T_{r_*} = 6150°F$

$h_{g.s.} = 0.0072 \left(\frac{P}{830}\right)^{0.8}$
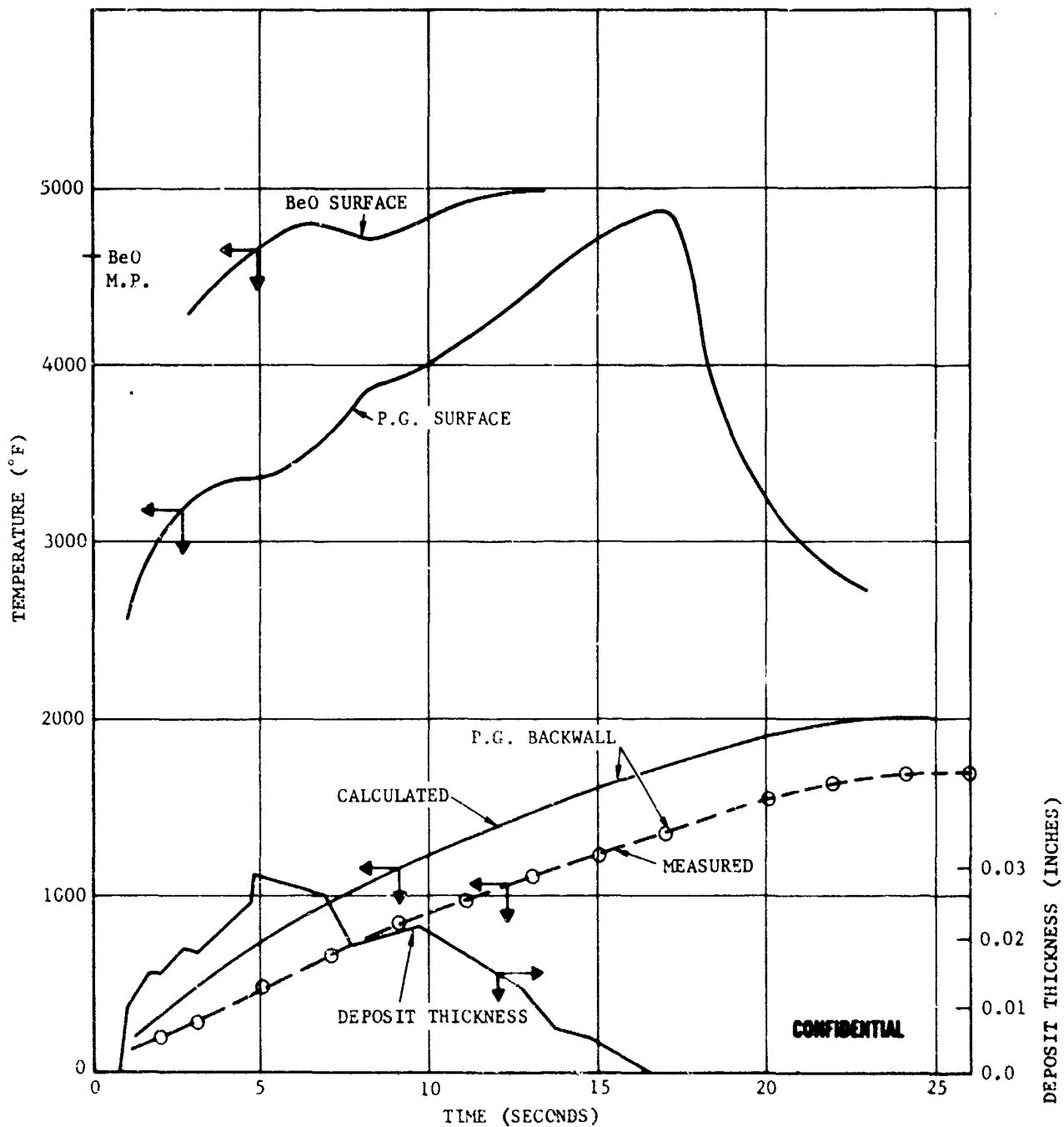
FIGURE 224. THROAT TEMPERATURE RESPONSE WITH DEPOSITION - TEST T-25

CONDITIONS

$$h = 0.010 \left(\frac{P}{773} \right)^{0.8}$$

$$T_{r_*} = 6150°F$$
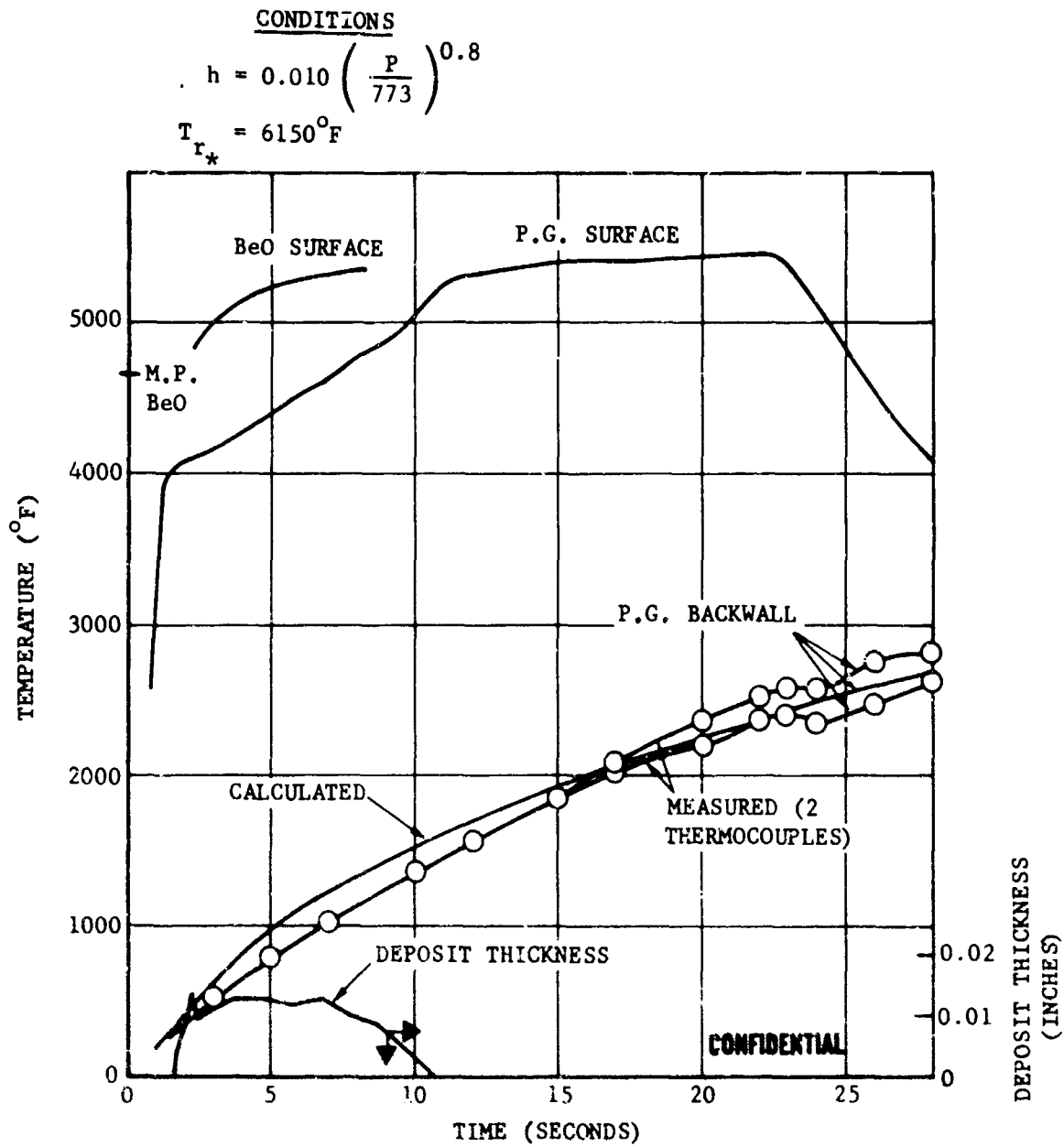
FIGURE 225. THROAT TEMPERATURE RESPONSE WITH DEPOSITION, TEST T-51

F10109 C

CONDITIONS

$$h = 0.0067 \left(\frac{P}{625} \right)^{0.8}$$

$$T_{r_*} = 5790\,^{\circ}F$$
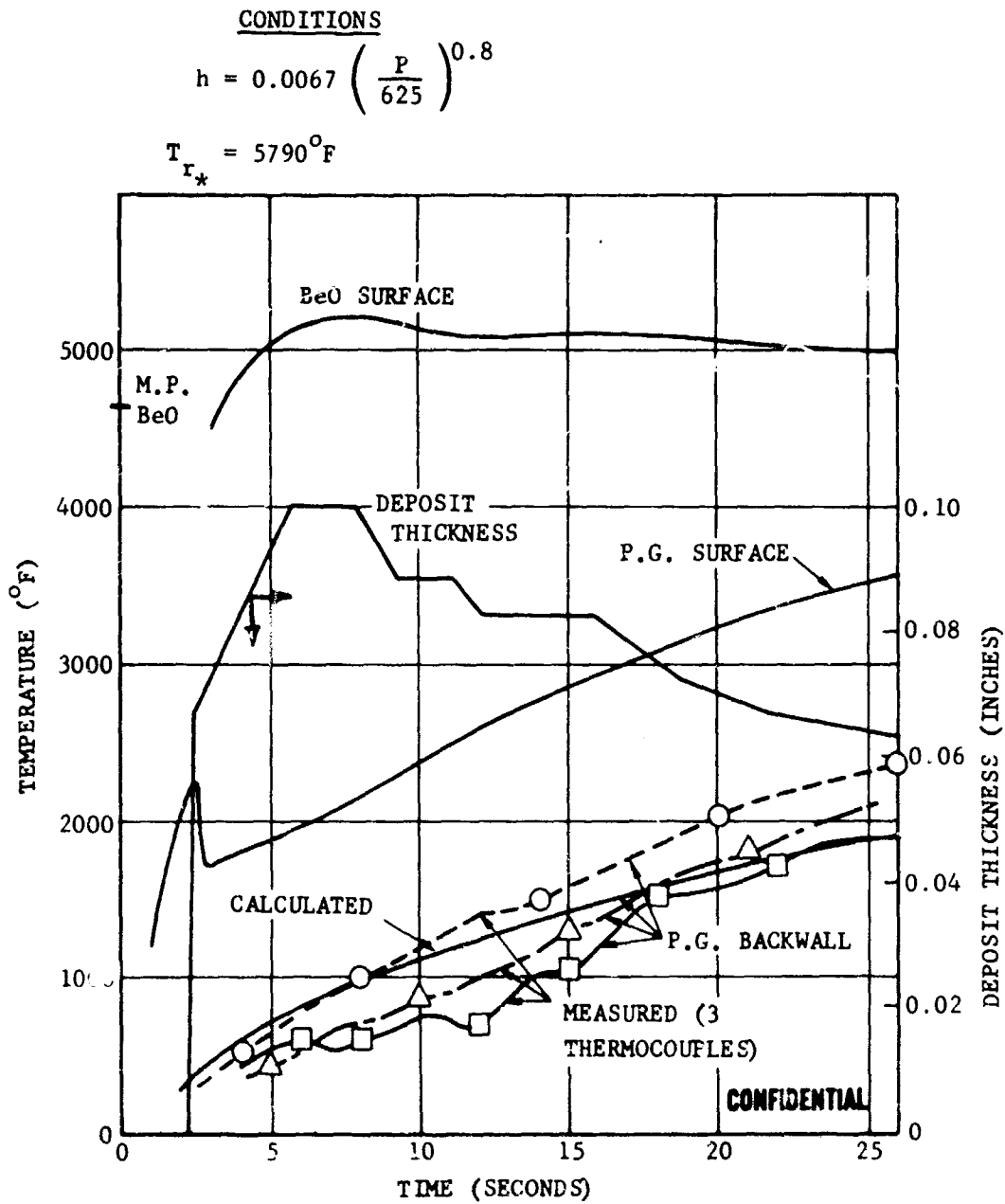
FIGURE 226. THROAT TEMPERATURE RESPONSE WITH DEPOSITION, TEST T-52
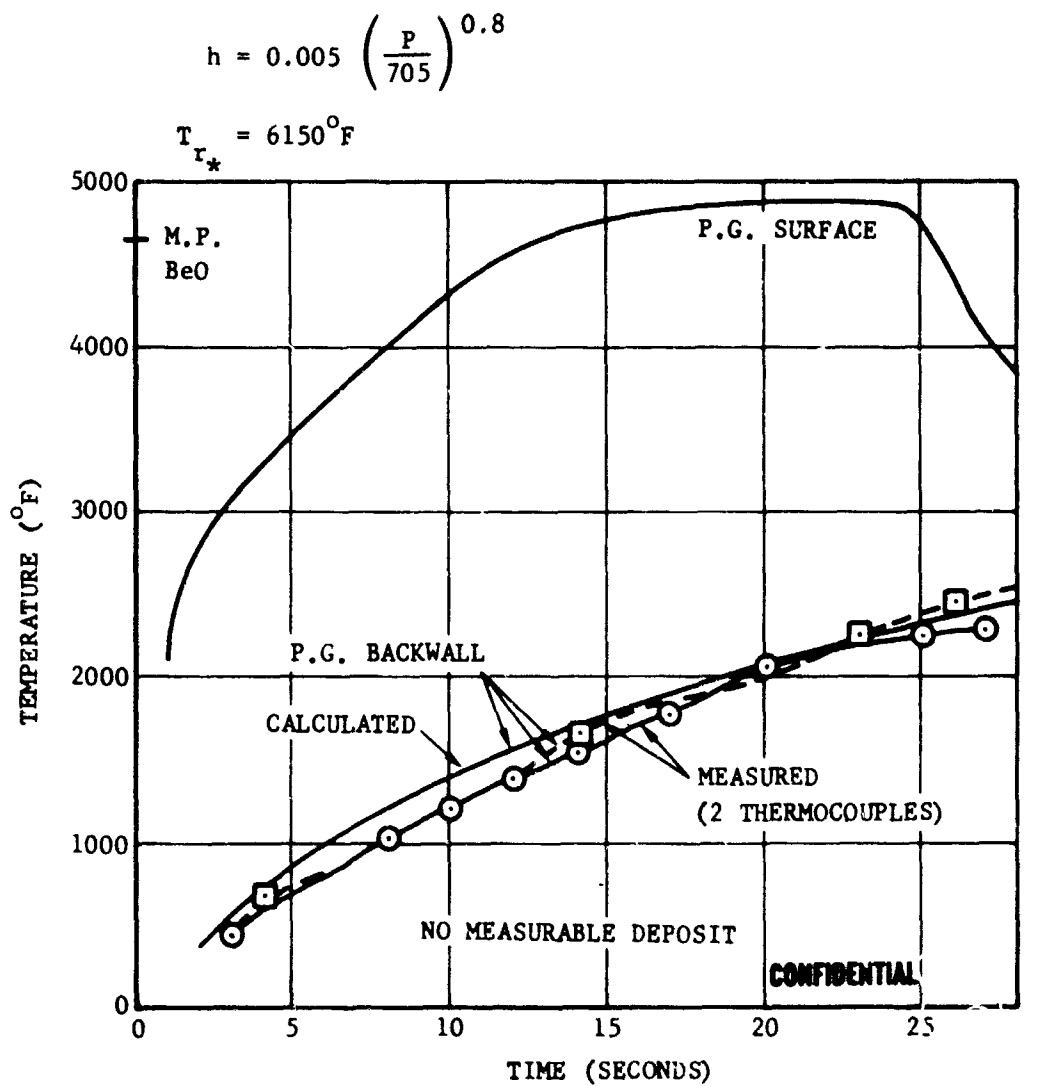
F10110 C

$$h = 0.005 \left(\frac{P}{705}\right)^{0.8}$$

$$T_{r_*} = 6150^{\circ}F$$

FIGURE 227. THROAT TEMPERATURE RESPONSE WITH DEPOSITION, TEST T-53

F10111 C

$$h = 0.005 \left(\frac{P}{705}\right)^{0.8}$$

$$T_{r_*} = 6150^{\circ}F$$
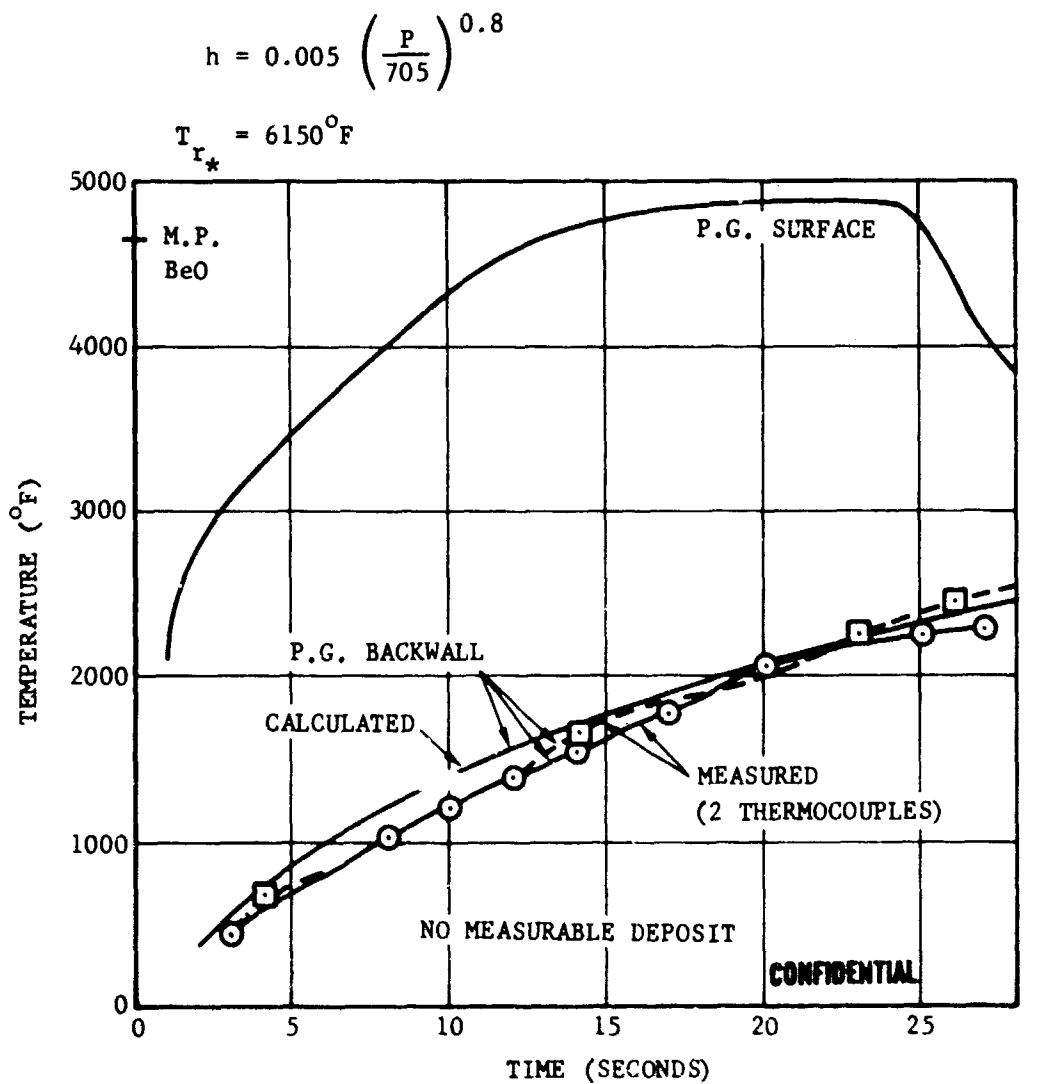
FIGURE 227. THROAT TEMPERATURE RESPONSE WITH DEPOSITION, TEST T-53

TABLE XV. INFLUENCE OF GRAIN GEOMETRY ON THROAT HEAT TRANSFER

Test	Propellant	Grain-Nozzle Geometry	$\bar{h}_{800}$ (Btu/in.^{2}sec$°$F)	$\bar{h}_{800}/\bar{C}_p$ (lb/in.^{2}sec)
T-1	191F	Remote end burner 25° conventional nozzle	0.0070	0.0070
T-9	191F	7" port - Type I 18° conventional nozzle	0.0092	0.0092
T-10	191F	7" port - Type II (slotted) 18° conventional nozzle	0.010	0.010
T-21	191F	Close end burer 55° steep inlet nozzle	0.0035	0.0039
T-3	319BRF	Remote end burner 25° conventional nozzle	0.0066	0.0083
T-14	319BRF	7" port - Type I 18° conventional nozzle	0.0073	0.0092
T-15	319BRF	3" port - Type III (slotted) 18° conventional nozzle	0.0045	0.0059
T-24	319BRF	Close end burner 55° steep inlet nozzle	0.0036	0.0051
T-4	54F	Remote end burner 25° conventional nozzle	0.0065	0.0069
T-11	54F	7" port - Type I 18° conventional nozzle	0.0061	0.0070
T-22	54F	Close end burner 55° steep inlet nozzle	0.0059	0.0064
T-7	389	Remote end burner 25° conventional nozzle	0.0070	0.0090
T-8	389	7" port - Type II (slotted) 18° conventional nozzle	No data	-

TABLE XVI.   INFLUENCE OF NOZZLE GEOMETRY ON THROAT HEAT TRANSFER

Test	Propellant	Grain-Nozzle Geometry	$\bar{h}_{800}$ (Btu/in.^{2}sec°F)	$\bar{h}_{800}/\bar{C}_p$ (lb/in.^{2}sec)
T-10	191F	7" port - Type II (slotted) 18° conventional nozzle	0.010	0.010
T-12	191F	7" port - Type II (slotted) submerged nozzle	0.013	0.0118
T-13	191F	7" port - Type II (slotted) 55° steep inlet nozzle	No data	-
T-21	191F	Close end burner 55° steep inlet nozzle	0.0035	0.0039
T-23	191F	Close end burner submerged nozzle	0.0057	0.0060
T-16	191F	7" port - Type I 18° conventional nozzle, W throat	0.0059	0.0059
T-18	191F	7" port - Type I submerged nozzle, W throat	0.0048	0.0051
T-51	191F	3.8" port - Type II (slotted) "Shallow" submerged nozzle	0.010	0.0092
T-53	191F	3.8" port - Type II (slotted) "Deep" submerged nozzle	0.0055	0.0058

TABLE XVII. INFLUENCE OF PROPELLANT FORMULATION ON THROAT HEAT TRANSFER

Test	Propellant	Grain-Nozzle Geometry	$\bar{h}_{800}$ (Btu/in.^{2}sec$^\circ$F)	$\bar{h}_{800}/\bar{C}_p$ (lb/in.^{2}sec)
T-1	191F	Remote end burner 25° conventional nozzle	0.0070	0.0070
T-2	24F	Remote end burner 25° conventional nozzle	0.0054	0.0072
T-3	319BRF	Remote end burner 25° conventional nozzle	0.0066	0.0086
T-4	54F	Remote end burner 25° conventional nozzle	0.0065	0.0072
T-5	60 (Al)	Remote end burner 25° conventional nozzle	0.0038	0.0061
T-6	390 (Al)	Remote end burner 25° conventional nozzle	0.0072	0.0116
T-7	389 (Al)	Remote end burner 25° conventional nozzle	0.0070	0.0090
T-9	191F	7" port - Type I 18° conventional nozzle	0.0092	0.0092
T-11	54F	7" port - Type I 18° conventional nozzle	0.0061	0.0070
T-14	319BRF	7" port - Type I 18° conventional nozzle	0.0073	0.0092
T-21	191F	Close end burner 55° steep inlet nozzle	0.0035	0.0039
T-22	54F	Close end burner 55° steep inlet nozzle	0.0059	0.0064
T-24	319BRF	Close end burner 55° steep inlet nozzle	0.0036	0.0051

TABLE XVII (Continued)

Test	Propellant	Grain-Nozzle Geometry	$\bar{h}_{800}$ (Btu/in.^{2}sec°F)	$\bar{h}_{800}/\bar{C}_p$ (lb/in.^{2}sec)
T-8	389 (A1)	7" port - Type II (slotted) 18° conventional nozzle	No data	-
T-10	191F	7" port - Type II (slotted) 18° conventional nozzle	0.010	0.010
T-18	191F	7" port - Type I Submerged Nozzle: W-ATJ Throat	0.0048	0.0051
T-19	319BRF	7" port - Type I Submerged Nozzle: W-ATJ Throat	0.0042	0.0056
T-51	191F	3.8" port - Type II (slotted) "Shallow" Submerged Nozzle	0.010	0.0092
T-52	319BRF	3.8" port - Type II (slotted) "Shallow" Submerged Nozzle	0.0082	0.0097

TABLE XVIII. INFLUENCE OF NOZZLE MATERIAL ON THROAT HEAT TRANSFER

Test	Propellant	Grain-Nozzle Geometry	Material	$\bar{h}_{800}$ (Btu/in.^{2}sec$^\circ$F)	$\bar{h}_{800}/\bar{c}_p$ (lb/in.^{2}sec)
T-9	191F	7" port - Type I 18° conventional nozzle	Throat: P.G. Entrance: ATJ	0.0092	0.0092
T-16	191F	7" port - Type I 18° conventional nozzle	Throat: W-ATJ Entrance: ATJ	0.0059	0.0059
T-17	191F	7" port - Type I 18° conventional nozzle	Throat: W-ATJ Entrance: Carbon Phenolic	0.0052	0.005
T-20	191F	7" port - Type I 18° conventional nozzle	Throat: P.G. Entrance: Carbon Phenolic	0.0087	0.0087
T-14	319BRF	7" port - Type I 18° conventional nozzle	Throat: P.G. Entrance: ATJ	0.0073	0.0092
T-19	319BRF	7" port - Type I 18° conventional	Throat: W-ATJ Entrance: ATJ	0.0042	0.0056
T-51	191F	3.8" port - Type II (slotted) "Shallow" submerged nozzle	Throat: P.G. Entrance: ATJ	0.010	0.0092
T-54	191F	3.8" port - Type II (slotted) "Shallow" submerged nozzle	Throat: W-ATJ Entrance: ATJ	No data	-

TABLE XIX. THEORETICAL CONVECTIVE COEFFICIENTS FOR PROGRAM PROPELLANTS

Propellant	$\dfrac{P_c\,g}{C^*}$	$\left(\dfrac{\mu_c C^*}{D_t P_c g}\right)^{0.2}$	$C_f/2$	$F(P_r)$	C_h	$\left(\dfrac{h}{c_p}\right)_{800}$
Arcocel 191F	4.724	0.0641	0.00151	1.193	0.00197	0.00931
Arcocel 319BRF	4.672	0.0636	0.00148	1.179	0.00191	0.00892
Arcane 54F	4.749	0.0634	0.00144	1.238	0.00188	0.00883
Arcane 24F	4.769	0.0633	0.00143	1.205	0.00185	0.00882
Arcocel 389	4.970	0.0635	0.00148	1.165	0.00191	0.00949
Arcocel 390	4.876	0.0630	0.00144	1.166	0.00185	0.00902
Arcane 60	5.024	0.0626	0.00142	1.224	0.00185	0.00529

$$\frac{P_c\,g}{C^*} \sim \frac{lbm}{in^2-sec}$$

$$\frac{h}{c_p} \sim \frac{lbm}{in^2-sec}$$

$$F(P_r) = \left[1 - P_r + \ln\left(\frac{6}{5P_r+1}\right)\right]$$
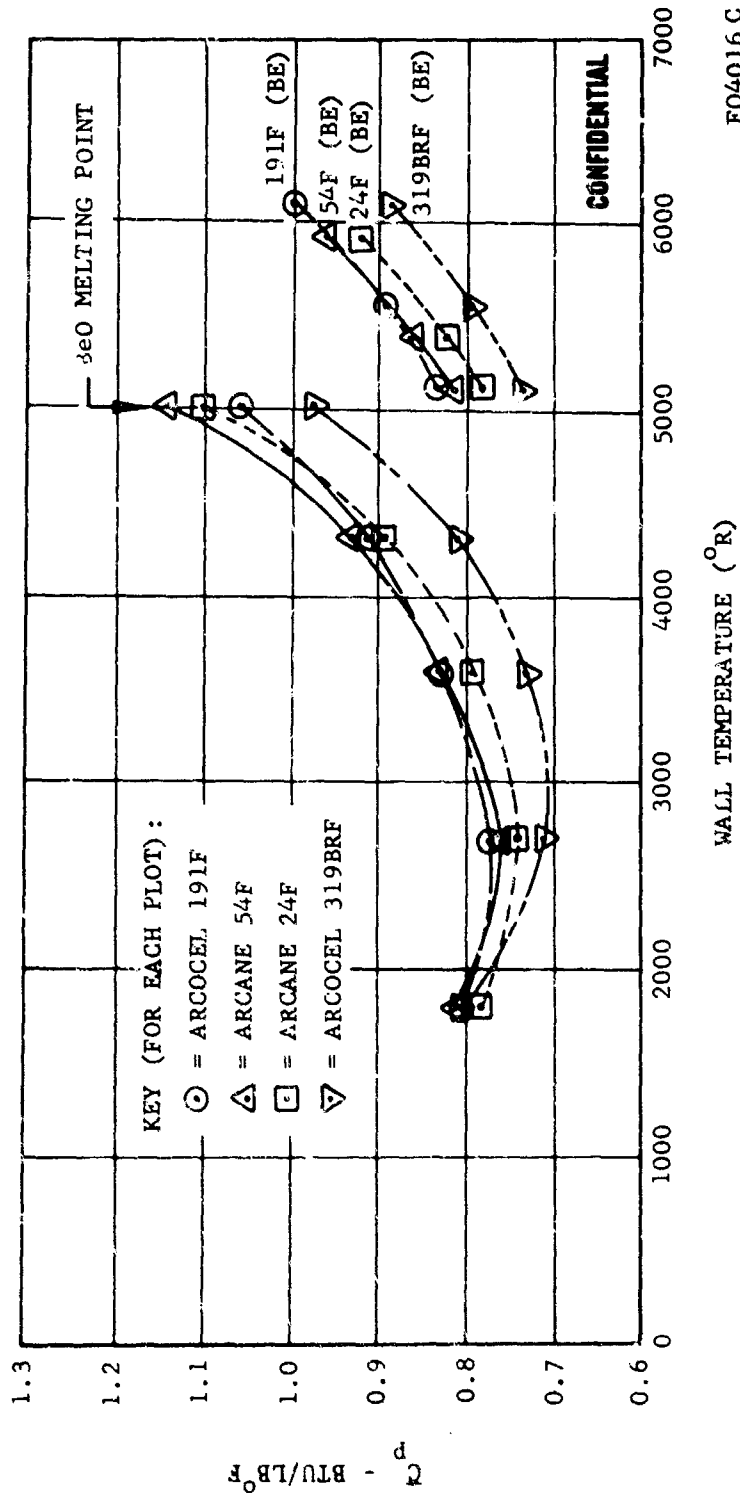
FIGURE 228. AVERAGE BOUNDARY LAYER SPECIFIC HEAT FOR BERYLLIUM
PROPELLANTS - 800 PSIA

F04016 C
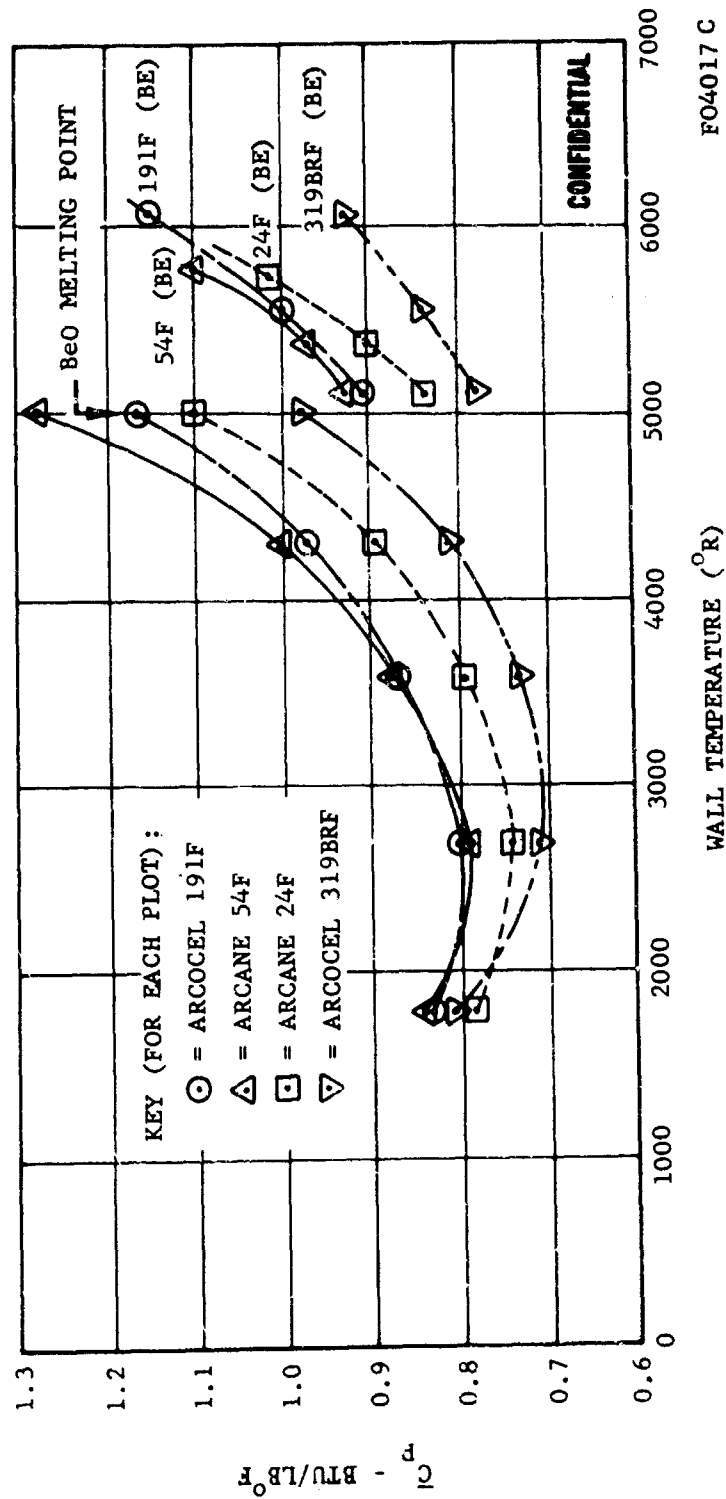
FIGURE 229. AVERAGE BOUNDARY LAYER SPECIFIC HEAT FOR BERYLLIUM
PROPELLANTS - 400 PSIA

F04017 C
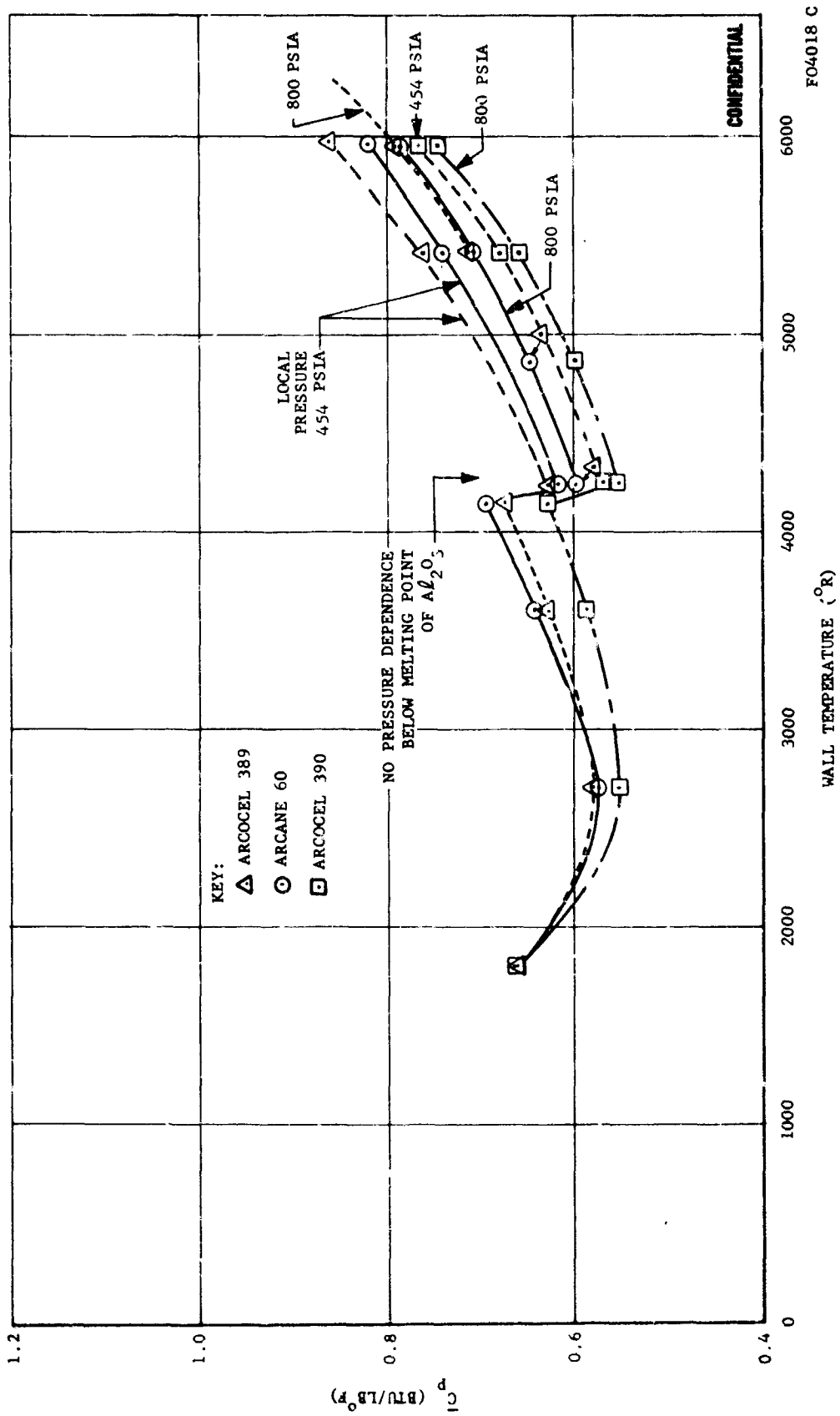
FIGURE 230. AVERAGE BOUNDARY LAYER SPECIFIC HEAT FOR ALUMINUM PROPELLANTS

-405-

APPENDIX IX (C)

NOZZLE THROAT CORROSION DATA

This appendix presents a tabulated summary of the nozzle throat corrosion data obtained in this program. These results were originally presented and discussed in Sections 2.2 of References 2, 3 and 4. Table XX shows the results of the effort to establish the threshold surface temperatures for corrosion of pyrolytic graphite by the program propellant exhausts. Table XXI presents the measured radial regression and other pertinent data for the tests in which corrosion occurred. The symbols used in Table XXI are defined in Table XXII. Table XXIII compares several corrosion rate predictions with the adjusted rates for the tests in which corrosion occurred. The prediction methods are described on Pages 15-18 of Reference 3. Note that the $\overset{\circ}{R}$ prediction column indicates extreme corrosion rates at temperatures above 5000°F. This prediction method assumes total similarity between heat and mass transfer. Comparison of the predicted and measured values would suggest that this assumption is not reasonable. The similarity assumption has also been attacked on theoretical grounds in this program. The data presented in this appendix also serve to illustrate the extreme complexity of obtaining good corrosion data. Improved definitions of the heat transfer and deposition processes are evidently required before the corrosion rates can be correctly interpreted.

TABLE XX. COMPARISON OF CORROSION THRESHOLD WITH TEST RESULTS

		Surface Temperature of Graphite Throat at:		
Test	Propellant	Deposit Arrival (°F)	Start of Corrosion (°F)	Theoretical Corrosion Threshold (°F)
T-1	191F	2500	-	1000-1900
T-2	24F	1700	-	600-1700
T-3	319BRF	-	2500	1400-2300
T-4	54F	2600	-	900-1900
T-5	60	2150	-	800-1900
T-6	390	-	2000	1500-2300
T-7	389	4200	-	1000-1800
T-8	389	-	-	-
T-9	191F	3400	-	1000-1900
T-10	191F	2000	-	1000-1900
T-11	54F	1800	-	900-1900
T-12	191F	5000	-	1000-1900
T-13	191F	-	-	-
T-14	319BRF	2900	-	1400-2300
T-15	319BRF	-	2200	1400-2300
T-20	191F	-	4000	1000-1900
T-21	191F	1900	-	1000-1900
T-22	54F	2800	-	900-1900
T-23	191F	2800	-	1000-1900
T-24	319BRF	-	-	-
T-25	191F	2300	-	1000-1900
T-51	191F	4100	-	1000-1900
T-52	319BRF	2200	-	1400-2300
T-53	191F	-	2500	1000-1900

TABLE XXI. EXPERIMENTAL CORROSION PARAMETER DATA

Propellant	Test	P	$\bar{h}_c$	C_p	R	ΔT	ΔT̄	Δr_max	Δr_min	Corrected ΔR	$\dot{R}$	Grain Type, Nozzle Contour
	-	psig	Btu/in²sec°F	Btu/lb°F	-	°F	Mils	Mils	Mils	Mils	Mils/sec	-
Arcane 247	T-2	740	0.0056	0.80	0.08	3800-3900	-1	-	-	1	1*	REB-Conv
Arcane 547	T-11	830	0.0060	0.90	0.09	4320-4400	2	2.5	-1.5	4	2	CP-Conv
Arcane 60	T-5	860	0.0043	0.60	0.07	3480-3880	3	5	1	6	1.3	REB-Conv
Arcocel 191F	T-1	700	0.0075	0.95	0.13	4840-4880	5	6	4	7	4	REB-Conv
Arcocel 191F	T-9	740	0.0090	1.03	0.26	5240-5280	4	4	3.5	6	4.3	CP-Conv
Arcocel 191F	T-10	1300	0.0106	1.10	0.32	5240-5500	6	10	1.5	7	2.3	Key II-Conv
Arcocel 191F	T-12	1000	0.0120	1.10	0.32	5260-5480	19	22.5	16	21	9.5	Key II-Subm
Arcocel 191F	T-13	960	-	-	-	-	8	35	2	5	1.7	Key II-Steep
Arcocel 191F	T-20	740	0.0090	0.85	0.06	4040-4400	7	-	-	9	6	CP-Conv
Arcocel 191F	T-25	760	0.0072	0.93	0.10	4700-4800	-0.3	-	-	1	1*	CP-Conv
Arcocel 191F	T-51	710	0.10	1.09	0.32	5200-5450	20	-	-	22	2	500#-Subm.
Arcocel 191F	T-53	685	0.055	0.95	0.10	2500-4900	44	-	-	46	2-3	500#-Subm.
Arcocel 389	T-7	950	0.0080	0.80	0.22	5040-5150	3	3	2	5	3	REB-Conv
Arcocel 319RF	T-3	1060	0.0073	0.75	0.01	2500-4000	3	5	1	6	2	REB-Conv
Arcocel 319RF	T-14	800	0.0074	0.80	0.12	4680-4840	12	-	-	14	2.5	CP-Couv
Arcocel 319RF	T-15	900	0.0053	0.70	0.002	2200-2500	-1.5	22	-9	3	3*	Key III-Conv
Arcocel 390	T-6	500	0.0060	0.53	0.01	2000-3000	1	2	1	3	2	REB-Conv

*Estimated, assuming corrected corrosion occurred over 1 second period

TABLE XXII. DEFINITION OF SYMBOLS USED IN TABLE XXI

$\bar{P}$: Average chamber pressure over the period when throat corrosion actually occurred. The average nozzle throat pressure can be obtained by multiplying $\bar{P}$ by 0.575.

$\bar{h}_c$: Average gas side, throat heat transfer coefficient over the entire firing. The value given is corrected to the average coefficient over the time when corrosion actually occurred by multiplying by the ratio of $\bar{P}$ to the average pressure over the entire firing, raised to the 0.8 power.

$\bar{C}_p$: Average equilibrium boundary layer specific heat, at the wall temperature when corrosion occurred.

$\bar{B}$: Average thermodynamic saturation parameter, at the wall temperature when corrosion occurred, for the particular propellant, taken from Figures 14 and 15, Reference 1, and from similar plots which have not been published. Note that these B values are for the case of inert condensed oxides.

ΔT: Range of throat surface temperature during period when corrosion occurred.

$\overline{\Delta r}$: Average change in throat radius. Average of at least four measurements of the throat diameter after removal of soot and beryllia deposits.

Δr_{max}: One half of the maximum measurement of post-test throat diameter change.

Δr_{min}: One half of the minimum measurement of post-test throat diameter change.

ΔR: One half of the measured throat diameter change which most logically represents the corrosion for each particular nozzle. One or more diameter measurements, excluding those which reflect grooves and/or minimum values, were selected or averaged. Then, the throat regression values were corrected by adding two mils to account for the thermal expansion effect.

$\dot{R}$: Average corrosion rate over the estimated time period when corrosion occurred, based on ΔR.

TABLE XXIII. PREDICTED AND MEASURED CORROSION RATES

Propellant	Test	$\overset{\circ}{R} = \dfrac{h_c\ B}{C_p\ W}$ (mils/sec)	$\overset{\circ}{R}_{H_2O}$ (mils/sec)	$\overset{\circ}{R}_{H_2}$ (mils/sec)	$\overset{\circ}{R}_{Measured}$ (mils/sec)
Arcane 24F	T-2	7	4.6	0.1	1*
Arcane 54F	T-11	7	2.9	0.6	2
Arcane 60	T-5	7	4.6	0.1	1.3-2.6
Arcocel 191F	T-1	13	2.9	1.3	4-8
Arcocel 191F	T-9	28	3.2	2.6	4.3
Arcocel 191F	T-10	37	5.0	4.7	2.3
Arcocel 191F	T-12	44	5.3	5.1	9.5
Arcocel 191F	T-13	-	-	-	1.7
Arcocel 191F	T-20	8	3.7	0.5	6
Arcocel 191F	T-25	10	2.8	1.0	1*-2*
Arcocel 191F	T-51	37	5.0	4.7	2-4
Arcocel 191F	T-53	7	2.8	1.0	2-6
Arcocel 389	T-7	27	6.4	3.2	3-6
Arcocel 319BRF	T-3	1.2	1.3	0	2
Arcocel 319BRF	T-14	14	1.2	1.2	2.5
Arcocel 319BRF	T-15	0	0.9	0	3*
Arcocel 390	T-6	1.4	1.9	0	2

---

*Estimated, assuming corrected corrosion occurred over a one second period.

DOCUMENT CONTROL DATA - R&D

(Security classification of title, body of abstract and indexing annotation must be entered when the overall report is classified)

1. ORIGINATING ACTIVITY (Corporate author)	2a. REPORT SECURITY CLASSIFICATION
Space and Re-entry Systems Division Philco-Ford Corporation Newport Beach, California 92663	Confidential
	2b. GROUP GP-4

3. REPORT TITLE

Beryllium Erosion Corrosion Investigation For Solid Rocket Nozzles (U)

4. DESCRIPTIVE NOTES (Type of report and inclusive dates)

Final Report, 1 June 1965 - 17 March 1967

5. AUTHOR(S) (Last name, first name, initial)

Smallwood, W. L., et. al.

6. REPORT DATE	7a. TOTAL NO. OF PAGES	7b. NO. OF REFS
June 1967	444	28

8a. CONTRACT OR GRANT NO.	9a. ORIGINATOR'S REPORT NUMBER(S)
AF 04 (611) - 10753	CG - 3969
b. PROJECT NO	
c.	9b. OTHER REPORT NO(S) (Any other numbers that may be assigned this report)
d.	AFRPL - TR - 67 - 82

10. AVAILABILITY/LIMITATION NOTICES In addition to security requirements which must be met, this document is subject to special export controls and each transmittal to foreign governments or foreign nationals may be made only with prior approval of AFRPL (RPPR-STINFO), Edwards, California 93523.

11. SUPPLEMENTARY NOTES	12. SPONSORING MILITARY ACTIVITY
Qualified requestors may obtain copies of this report from DDC.	Air Force Rocket Propulsion Laboratory Edwards Air Force Base Edwards, California 93523

13. ABSTRACT

Contract AF04(611)-10753 was conducted over the period June 1965 to March 1967. The program was directed toward understanding erosion corrosion mechanisms of nozzle heat sink and insulation materials in state-of-the-art beryllium solid propellant exhausts. The major task was the design, fabrication and evaluation of the results of the 29 motor tests. Primary design variables included propellant, grain design, motor configuration, nozzle contour, materials and nozzle scale. Four beryllium propellants were tested in 5 designs (100 and 500 pound grains) in 25 tests. Aluminum analogs were used in 4 tests. Submerged, conventional and steep inlet nozzles were designed to exceed 5000°F with pyrolytic graphite, ATJ graphite, dense tungsten, carbon cloth and asbestos phenolic materials. The hardware, wall deposits and exhaust plume particles are described. Measured nozzle temperatures and ballistic performance were used to determine throat temperature, corrosion and oxide deposition histories. Design parameter effects on nozzle and ballistic performance and material failure mechanisms are discussed. Supporting chemical reaction, arc plasma, cold flow modeling, data correlation and analytical studies are described. A generalized model for nozzle design and performance evaluation is presented. The model includes improved heat transfer, corrosion and deposition analyses. Standard materials can be used with either beryllium or aluminum propellants in properly designed motors. Poor nozzle and ballistic performance relates to incomplete metal combustion and inadequate thermostructural design. Oxide deposits are thermally and chemically protective. Most of the conclusions and recommendations pertain also to liquid, hybrid and other solid systems

DD FORM 1473 (1 JAN 64)

14. KEY WORDS	LINK A		LINK B		LINK C	
	ROLE	WT	ROLE	WT	ROLE	WT
Solid Propellants						
Beryllium Propellants						
Rocket Motor Tests						
Nozzle Design						
Corrosion						
Heat Transfer						
Two Phase Flow						
Oxide Deposition						
Graphite						
Tungsten						
Failure Mechanisms						

INSTRUCTIONS

1. ORIGINATING ACTIVITY: Enter the name and address of the contractor, subcontractor, grantee, Department of Defense activity or other organization *(corporate author)* issuing the report.

2a. REPORT SECURITY CLASSIFICATION: Enter the overall security classification of the report. Indicate whether "Restricted Data" is included. Marking is to be in accordance with appropriate security regulations.

2b. GROUP: Automatic downgrading is specified in DoD Directive 5200.10 and Armed Forces Industrial Manual. Enter the group number. Also, when applicable, show that optional markings have been used for Group 3 and Group 4 as authorized.

3. REPORT TITLE: Enter the complete report title in all capital letters. Titles in all cases should be unclassified. If a meaningful title cannot be selected without classification, show title classification in all capitals in parenthesis immediately following the title.

4. DESCRIPTIVE NOTES: If appropriate, enter the type of report, e.g., interim, progress, summary, annual, or final. Give the inclusive dates when a specific reporting period is covered.

5. AUTHOR(S): Enter the name(s) of author(s) as shown on or in the report. Enter last name, first name, middle initial. If military, show rank and branch of service. The name of the principal author is an absolute minimum requirement.

6. REPORT DATE: Enter the date of the report as day, month, year; or month, year. If more than one date appears on the report, use date of publication.

7a. TOTAL NUMBER OF PAGES: The total page count should follow normal pagination procedures, i.e., enter the number of pages containing information.

7b. NUMBER OF REFERENCES: Enter the total number of references cited in the report.

8a. CONTRACT OR GRANT NUMBER: If appropriate, enter the applicable number of the contract or grant under which the report was written.

8b, 8c, & 8d. PROJECT NUMBER: Enter the appropriate military department identification, such as project number, subproject number, system numbers, task number, etc.

9a. ORIGINATOR'S REPORT NUMBER(S): Enter the official report number by which the document will be identified and controlled by the originating activity. This number must be unique to this report.

9b. OTHER REPORT NUMBER(S): If the report has been assigned any other report numbers *(either by the originator or by the sponsor)*, also enter this number(s).

10. AVAILABILITY/LIMITATION NOTICES: Enter any limitations on further dissemination of the report, other than those

imposed by security classification, using standard statements such as:

(1) "Qualified requesters may obtain copies of this report from DDC."

(2) "Foreign announcement and dissemination of this report by DDC is not authorized."

(3) "U. S. Government agencies may obtain copies of this report directly from DDC. Other qualified DDC users shall request through

_____."

(4) "U. S. military agencies may obtain copies of this report directly from DDC. Other qualified users shall request through

_____."

(5) "All distribution of this report is controlled. Qualified DDC users shall request through

_____."

If the report has been furnished to the Office of Technical Services, Department of Commerce, for sale to the public, indicate this fact and enter the price, if known.

11. SUPPLEMENTARY NOTES: Use for additional explanatory notes.

12. SPONSORING MILITARY ACTIVITY: Enter the name of the departmental project office or laboratory sponsoring *(paying for)* the research and development. Include address.

13. ABSTRACT: Enter an abstract giving a brief and factual summary of the document indicative of the report even though it may also appear elsewhere in the body of the technical report. If additional space is required, a continuation sheet shall be attached.

It is highly desirable that the abstract of classified reports be unclassified. Each paragraph of the abstract shall end with an indication of the military security classification of the information in the paragraph, represented as (TS), (S), (C), or (U).

There is no limitation on the length of the abstract. However, the suggested length is from 150 to 225 words.

14. KEY WORDS: Key words are technically meaningful terms or short phrases that characterize a report and may be used as index entries for cataloging the report. Key words must be selected so that no security classification is required. Identifiers, such as equipment model designation, trade name, military project code name, geographic location, may be used as key words but will be followed by an indication of technical context. The assignment of links, rules, and weights is optional

GPO 890-551

-422-